Transactions of the ASME®

Journal of Applied Mechanics

Published Quarterly by The American Society of Mechanical Engineers

VOLUME 65 • NUMBER 3 • SEPTEMBER 1998

Transactions of the ASME, Journal of Applied Mechanics (ISSN 0021-8936) is published quarterly (Mar., June, Sept., Dec.) for $240.00 per year by The American Society of Mechanical Engineers, Three Park Avenue, New York, NY 10016. Periodicals postage paid at New York, NY and additional mailing office. POSTMASTER: Send address changes to Transactions of the ASME, Journal of Applied Mechanics, c/o THE AMERICAN SOCIETY OF MECHANICAL ENGINEERS, 22 Law Drive, Box 2300, Fairfield, NJ 07007-2300. **CHANGES OF ADDRESS** must be received at Society headquarters seven weeks before they are to be effective. Please send old label and new address. **PRICES:** To members, $40.00; to nonmembers, $240.00; single issue, $96.00. Add $40.00 (airmail $60.00) for postage to countries outside the United States and Canada.

TECHNICAL PAPERS

(Contents continued on outside back cover)

This journal is printed on acid-free paper, which exceeds the ANSI Z39.48-1992 specification for permanence of paper and library materials.♾ ™

♻ 85% recycled content, including 10% post-consumer fibers.

CONTENTS (CONTINUED)

BRIEF NOTES

DISCUSSIONS

ERRATUM

ANNOUNCEMENTS AND SPECIAL NOTICES

Self-Similar Crack Expansion Method for Three-Dimensional Cracks Under Mixed-Mode Loading Conditions

Yonglin Xu
Research Assistant Professor of Civil Engineering.

B. Moran
Associate Professor of Civil Engineering, Mem. ASME.

T. Belytschko
Walter P. Murphy Professor of Computational Mechanics, Fellow ASME.

Department of Civil Engineering, Northwestern University, Evanston, IL 60208

Three-dimensional planar cracks under mixed-mode loading conditions are investigated by using the self-similar crack expansion method with the boundary integral equation technique. For a planar crack under general loading (tensile and shear) conditions, the normal displacement and tangential displacements on the crack surface exhibit uncoupled characteristics. However, the tangential displacements in the two directions are generally coupled. In this paper, two coupled boundary integral equations for a crack subject to shear loading are solved using the analytically numerical method, where the integrals on elements are estimated by using the explicit expression of the close form of the integrals. Combination of the self-similar crack expansion method and the analytically numerical method results in good accuracy, with errors in stress intensity factors of penny-shaped cracks and elliptical cracks less than one percent. This numerical analysis is applicable to the analysis of cracks with arbitrary geometry.

1 Introduction

Stress intensity factor analysis for three-dimensional cracks under mixed-mode loading conditions has received great attention in the past three decades due to its importance in fatigue life prediction of materials and design criterion of structures. With the advent of computer technology, the numerical analysis in fracture is rapidly growing in the application of engineering.

Boundary integral equations for three-dimensional cracks under mixed-mode loading conditions have been well established in the literature (Cruse, 1988; Murakami and Nemat-Nasser, 1982; Weaver, 1977). It is apparent that for a planar crack, the displacements induced by tensile loading and by shear loading are uncoupled. Thus, a three-dimensional planar crack under mixed-mode loading conditions can be independently dealt with as a planar crack under tensile loading and under shear loading. However, for a crack under shear loading, the displacements in the two tangential directions of the crack surface are generally coupled. Thus, double displacement unknowns on the crack surface are required for the solution of the two coupled boundary integral equations. Only for some special cases, these two tangential displacements can be solved separately. For example, the material Poisson's ratio approaches zero, which has been discussed by Xu et al. (1998a). In this paper, the more complicated problems—cracks under shear loading with coupled boundary integral equations—are mainly discussed by using the self-similar expansion method associated with analytically numerical method.

For more efficiently evaluating the stress intensity factors of three-dimensional cracks, Xu et al. (1997) proposed the self-similar crack expansion method based on the previous energy consideration (Cruse and Besunner, 1975; Cruse and Meyers, 1977). In the self-similar crack expansion method, the stress intensity factors are estimated as the crack propagates in the self-similar manner. Based on the line integral technique by Guo et al. (1995) for the regular integrals, Xu et al. (1997) extended this technique to estimate both singular and regular integrals on the elements of cracks, and obtained the closed form of the integrals. The use of the present self-similar crack expansion method is limited to cracks in an infinite body and semi-infinite body under uniform loading. However, these limitations can be circumvented by using the weight function method (Rice, 1972) and the improved self-similar crack expansion method (Xu, 1998b). The objective of the paper is to extend the self-similar crack expansion method to three-dimensional planar cracks under mixed-mode loading conditions. Fortunately, all the integrals for the crack under shear loading can be estimated analytically. The calculations show good accuracy of stress intensity factors, with errors less than one percent for penny-shaped cracks and elliptical cracks as compared to analytical solutions.

2 Basic Formulation for Crack Under Mixed-Mode Loading Conditions

The boundary integral equations for a three-dimensional planar crack (Fig. 1) can be written as

$$\sigma_{ij}(\mathbf{x}) = \int_{\Omega} S_{ijk}(\mathbf{x}, \boldsymbol{\xi}) \quad \Delta u_k(\boldsymbol{\xi}) d\Omega(\mathbf{x}, \boldsymbol{\xi}) \tag{2.1}$$

where $\Delta u_k(\boldsymbol{\xi})$ represents the displacement jump across the crack surface, and the functions S_{ijk} for isotropic materials are

$$\begin{aligned} S_{ijk} = \frac{\mu}{4\pi(1-\nu)r^3} \{ & 3[(1-2\nu)\delta_{ij}r_{,k} + \nu(\delta_{ik}r_{,j} + \delta_{jk}r_{,i}) \\ & - 5r_{,i}r_{,j}r_{,k}]r_{,l}n_l + n_i[(1-2\nu)\delta_{jk} + 3\nu r_{,k}r_{,j}] \\ & + n_j[(1-2\nu)\delta_{ik} + 3\nu r_{,k}r_{,i}] \\ & + n_k[3(1-2\nu)r_{,i}r_{,j} - (1-4\nu)\delta_{ij}]\}. \end{aligned} \tag{2.2}$$

Contributed by the Applied Mechanics Division of THE AMERICAN SOCIETY OF MECHANICAL ENGINEERS for publication in the ASME JOURNAL OF APPLIED MECHANICS.

Discussion on the paper should be addressed to the Technical Editor, Professor Lewis T. Wheeler, Department of Mechanical Engineering, University of Houston, Houston, TX 77204-4792, and will be accepted until four months after final publication of the paper itself in the ASME JOURNAL OF APPLIED MECHANICS.

Manuscript received by the ASME Applied Mechanics Division, Dec. 17, 1996; final revision, July 25, 1997. Associate Technical Editor: J. W. Ju.

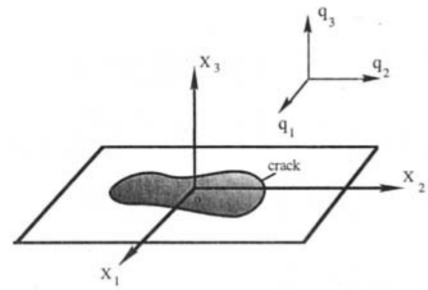

Fig. 1 A planar crack in the x_1–x_2 plane under mixed-mode loading conditions

For the typical case of a three-dimensional planar crack located in the x_1–x_2 plane (Fig. 1), Eq. (2.1) can be written as

$$\sigma_{3j}(\mathbf{x}) = \int_{\Omega} S_{3jk}(\mathbf{x}, \boldsymbol{\xi})\Delta u_k(\mathbf{x}, \boldsymbol{\xi}) d\Omega(\boldsymbol{\xi}) \quad (j = 1, 2, 3) \tag{2.3}$$

where

$$S_{333} = \frac{\mu}{4\pi(1-\nu)r^3}$$

$$S_{3jk} = \frac{\mu}{4\pi(1-\nu)r^3}[(1-2\nu)\delta_{jk} + 3\nu r_{,j} r_{,k}], \quad (j, k = 1, 2) \tag{2.4}$$

or the functions S_{3jk} can be written as

$$\begin{pmatrix} S_{311} & S_{312} & S_{313} \\ S_{321} & S_{322} & S_{323} \\ S_{331} & S_{332} & S_{333} \end{pmatrix} = \frac{\mu}{4\pi(1-\nu)r^3}$$

$$\times \begin{pmatrix} (1-2\nu) + 3\nu\dfrac{(\xi-x)^2}{r^2} & 3\nu\dfrac{(\xi-x)(\eta-y)}{r^2} & 0 \\ 3\nu\dfrac{(\xi-x)(\eta-y)}{r^2} & (1-2\nu) + 3\nu\dfrac{(\eta-y)^2}{r^2} & 0 \\ 0 & 0 & 1 \end{pmatrix}. \tag{2.5}$$

It is obvious from Eq. (2.5) that the normal displacement and tangential displacement of a three-dimensional planar crack are uncoupled; i.e., the normal displacement on the crack surface induces the normal stress in the crack plane, and the tangential displacements produce the shear stresses in the crack plane. On the other hand, the tangential displacements in the two directions (x and y-directions) are generally coupled. In a special case, the crack displacements may be uncoupled as the Poisson's ratio of the material approaches zero and the right side of (2.5) becomes a unit matrix. Therefore, the displacements in the three directions can be dealt with separately. This case of a crack with uncoupled tangential displacements has been discussed in detail by Xu et al. (1998a).

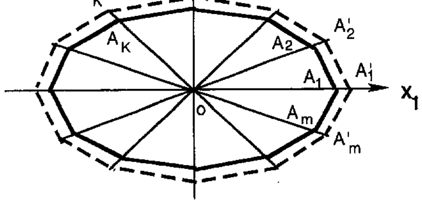

Fig. 2 Crack expansion similarly

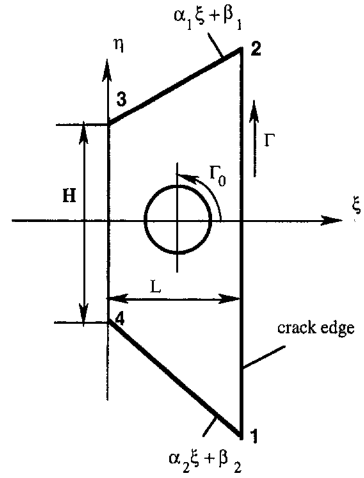

Fig. 3 An element near the crack edge

Following the method by Xu et al. (1997b), we may find a function ϕ_{3jk} satisfied $\nabla^2\phi_{3jk} = -S_{3jk}$ and thus, the integral Eq. (2.3) can be written as an equation with lower singularity as

$$\sigma_{3j}(\mathbf{x}) = \int_{\Omega} F_{3jkt}(\mathbf{x}, \boldsymbol{\xi})\Delta u_{k,t}(\boldsymbol{\xi}) d\Omega(\boldsymbol{\xi}) \tag{2.6}$$

where function $F_{3jkt} = \phi_{3jk,t}$ is a differentiation of function ϕ_{3jk} with respect to x_t. These functions F_{3jkt} have been given by Xu et al. (1998a). In the special case ($\nu = 0$), the integral equations of a planar crack under shear loading can be written as

$$\sigma_{3j}(x, y) = \frac{E}{8\pi(1-\nu^2)}\int_{\Omega}\left\{\frac{(\xi-x)}{r^3}\Delta u_{j,\xi} + \frac{(\eta-y)}{r^3}\Delta u_{j,\eta}\right\} d\Omega(\xi, \eta). \tag{2.7}$$

These two equations can be solved separately and the form of the equations are similar to that of a crack under tensile loading. In this paper, the more complicated case, a crack with coupled tangential displacements, is mainly discussed.

3 Self-Similar Crack Expansion Method for Cracks Under Shear Loading

At a crack tip, the stress intensity factors (K_{II} and K_{III}) can be determined by the asymptotic field of the crack-tip displacement as

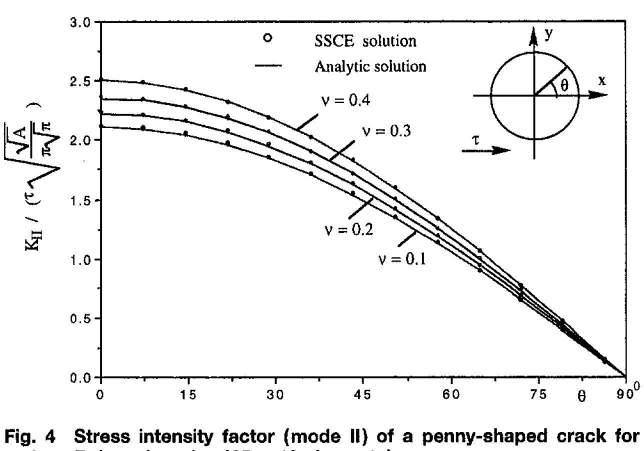

Fig. 4 Stress intensity factor (mode II) of a penny-shaped crack for various Poisson's ratios (25 × 13 elements)

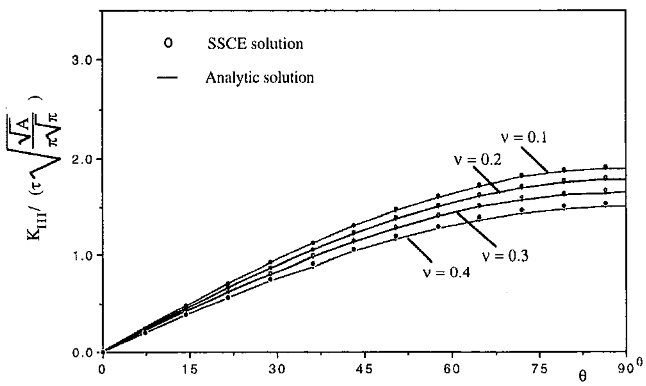

Fig. 5 Stress intensity factors (mode III) of a penny-shaped crack for various Poisson's ratios (25 × 13 elements)

$$u_n = \frac{1-\nu}{\mu}\sqrt{\frac{2r}{\pi}}K_{\mathrm{II}}, \quad u_t = \frac{1}{\mu}\sqrt{\frac{2r}{\pi}}K_{\mathrm{III}} \tag{3.1}$$

where u_n is the crack-tip displacement in the crack edge normal direction and u_t in the crack edge tangential direction. The self-similar crack expansion method simplifies the calculation of stress intensity factors, and stress intensity factors can be calculated more accurately than if they were determined solely by the traditional method of examining the local displacement around the crack tip. Thus, the relationship between the energy release rate and the displacements on the crack surface (for mode II and III) may be employed. For a crack in the x_1–x_2 plane under shear tractions q_1 and q_2, this gives

$$\delta\frac{1}{2}\int_\Omega (q_1\Delta u_1 + q_2\Delta u_2)d\Omega = \int_\Gamma \left\{\frac{1-\nu^2}{E}K_{\mathrm{II}}^2 + \frac{1+\nu}{E}K_{\mathrm{III}}^2\right\}\delta a(s)d\Gamma \tag{3.2}$$

where $\delta a(s)$ is the crack advance as a function of a crack-edge contour parameter s, and Γ is the boundary of the crack. For details of the relationship between strain energy and the energy release rate one can refer to Rice (1985). If a crack expands self-similarly (Fig. 2), the change in crack size can be written as

$$\delta a(s) = \alpha a(s) \tag{3.3}$$

where α is a parameter, and $a(s)$ is the distance from the crack edge to the similarity center. The stress intensity factors around the crack edge can be expressed as

$$K_{\mathrm{II}}(s) = f_{\mathrm{II}}(s)K_{\mathrm{II0}} \quad K_{\mathrm{III}}(s) = f_{\mathrm{III}}(s)K_{\mathrm{II0}} \tag{3.4}$$

where $f_{\mathrm{II}}(s)$ and $f_{\mathrm{III}}(s)$ are distribution functions of the stress intensity factors, which can be determined from the displacement at the crack tip, and K_{II0} is a reference stress intensity factor of mode II at the reference point. The distance between the crack edge and the similarity center at the reference point is denoted by a_0.

For a crack under remote shear tractions q_1 and q_2, the left side of (3.2) can be written as $(1/2)(q_1\delta V_1 + q_2\delta V_2)$, where V_1 and V_2 is the so-called crack-opening volume in the x_1-directions and x_2-direction. Here V_1 and V_2 are induced by shear loading, while V_3 is induced by normal loading. The crack-opening volume can be expressed as $V = \beta a_0^3$ as long as the three-dimensional crack expands self-similarly as described by (3.3). Thus, the variation of the crack volume can be written as

$$\delta V = \frac{3V}{a_0}\delta a_0 \quad \text{or} \quad \delta V = 3V\alpha. \tag{3.5}$$

Substituting (3.3) and (3.4) into the right side of (3.2) and using (3.5) on the left side of (3.2) yields

$$\frac{3}{2}(q_1V_1 + q_2V_2) = \frac{1-\nu^2}{E}K_{\mathrm{II0}}^2\int_\Gamma\left\{f_{\mathrm{II}}^2(s) + \frac{1}{(1-\nu)}f_{\mathrm{III}}^2(s)\right\}a(s)d\Gamma. \tag{3.6}$$

Hence, a modified reference stress intensity factor can be written as

$$K_{\mathrm{II0}}^* = \sqrt{\frac{\frac{3}{2}E(q_1V_1 + q_2V_2)}{(1-\nu^2)\int_\Gamma\left\{f_{\mathrm{II}}^2(s) + \frac{1}{(1-\nu)}f_{\mathrm{III}}^2(s)\right\}a(s)d\Gamma}}. \tag{3.7}$$

To obtain $f_{\mathrm{II}}(s)$ and $f_{\mathrm{III}}(s)$, the relative crack-tip displacements Δu_n and Δu_t need to be known. The stress intensity factors can be obtained by using (3.4), where K_{II0} is replaced by K_{II0}^*.

4 Numerical Implementation and Integral Evaluation on Elements

To evaluate the integral Eqs. (2.6), the crack can be discretized as $N = m \times n$ elements, where m is the number of segments in the circumferential direction and n is the number of segments in the radial direction as described in the previous paper (Xu et al., 1997). Except for m triangular elements around the crack center, the other $m \times (n-1)$ elements are trapezoidal elements. Displacements in the elements are approximated by

$$\Delta u_j = \sum_{K=1}^{4} N_K(x, y)\Delta u_{jK}, \tag{4.1}$$

similar to the analysis of a crack under tensile loading by Xu et al. (1997). The discrete form of the integral Eq. (4.1) can be written as

$$\sigma_{3j} = \int_\Omega (F_{3jk\xi}N_{K,\xi} + F_{3jk\eta}N_{K,\eta})\Delta u_{jK}d\Omega \quad (j, k = 1, 2) \tag{4.2}$$

where Δu_{jK} ($j = 1, 2$; $K = 1, 2, 3, 4$) represent the crack-opening displacements in the x_j direction at the element nodes, and the derivatives of the shape functions may be written as

$$N_{K,\xi} = A_K + B_K\eta, \quad N_{K,\eta} = C_K + D_K\xi. \tag{4.3}$$

Table 1 Normalized stress intensity factors of an elliptical crack under shear loading

Element	$K_{\mathrm{II}}/\left(\tau\sqrt{\frac{\sqrt{A}}{\pi\sqrt{\pi}}}\right)$ ($\alpha = 0$)	Error	$K_{\mathrm{III}}/\left(\tau\sqrt{\frac{\sqrt{A}}{\pi\sqrt{\pi}}}\right)$ ($\alpha = 90$)	Error
13 × 7	1.934	3.20 percent	2.106	0.52 percent
25 × 13	1.897	1.23 percent	2.105	0.48 percent
35 × 17	1.905	1.65 percent	2.104	0.43 percent
65 × 23	1.890	0.83 percent	2.102	0.32 percent
Analytic	1.8740		2.0952	

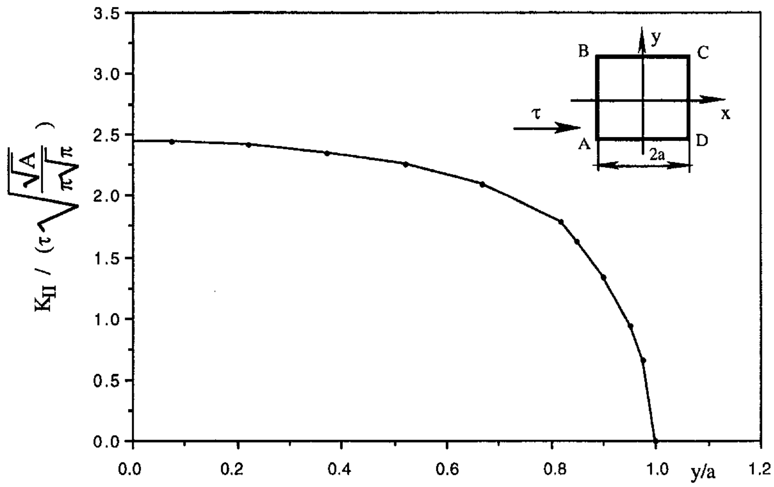

Fig. 6 Stress intensity factors (Mode II) on side CD for a square crack (n = 0.3) under shear loading (45 × 13 elements)

Therefore, Eq. (4.2) becomes

$$\sigma_{3j} = \sum_{n=1}^{N} J_{nj} \tag{4.4a}$$

$$J_{nj} = \int_{\Omega_n} \{F_{3jk\xi}(A_K + B_K y) + F_{3jk\eta}(C_K + D_K x) + F_{3jk\xi}B_K(\eta - y) + F_{3jk\eta}D_K(\xi - x)\}\,\Delta u_{jK} d\Omega. \tag{4.4b}$$

Note that for a three-dimensional crack under tensile loading only three functions need to be evaluated, while for the crack under shear loading 12 integrals need to be evaluated since more complicated functions F_{3jkt} in (2.6). These 12 functions ($I_1 \sim I_{12}$) are as follows:

$$I_1 = \int_{\Omega_\epsilon} \frac{(\xi - x)^3}{r^5} d\Omega, \quad I_2 = \int_{\Omega_\epsilon} \frac{(\xi - x)(\eta - y)^2}{r^5} d\Omega,$$

$$I_3 = \int_{\Omega_\epsilon} \frac{(\xi - x)^2(\eta - y)}{r^5} d\Omega, \quad I_4 = \int_{\Omega_\epsilon} \frac{(\eta - y)^3}{r^5} d\Omega,$$

$$I_5 = \int_{\Omega_\epsilon} \frac{(\xi - x)^3(\eta - y)}{r^5} d\Omega, \quad I_6 = \int_{\Omega_\epsilon} \frac{(\xi - x)^2(\eta - y)^2}{r^5} d\Omega,$$

$$I_7 = \int_{\Omega_\epsilon} \frac{(\xi - x)(\eta - y)^3}{r^5} d\Omega, \quad I_8 = \int_{\Omega_\epsilon} \frac{(\xi - x)}{r^3} d\Omega,$$

$$I_9 = \int_{\Omega_\epsilon} \frac{(\eta - y)}{r^3} d\Omega, \quad I_{10} = \int_{\Omega_\epsilon} \frac{(\xi - x)^2}{r^3} d\Omega,$$

$$I_{11} = \int_{\Omega_\epsilon} \frac{(\xi - x)(\eta - y)}{r^3} d\Omega, \quad I_{12} = \int_{\Omega_\epsilon} \frac{(\eta - y)^2}{r^3} d\Omega, \tag{4.5}$$

where $r = \sqrt{(\xi - x)^2 + (\eta - y)^2}$. The evaluation of these integrals will be discussed for both regular and singular elements.

For integrals in the regular elements, the integrals (4.5) can be evaluated by line integrals as

$$I_k = \int_{\Gamma_\epsilon} (A_{k\xi} n_\xi + A_{k\eta} n_\eta) d\Gamma \quad (k = 1 \sim 12) \tag{4.6}$$

where (n_ξ, n_η) are components of the unit normal to the element boundary, and functions $A_{k\xi}$ and $A_{k\eta}$ are listed in Appendix A. The corresponding integrals for functions $A_{k\xi}$ and $A_{k\eta}$ can be estimated in a similar way to Xu et al. (1997).

For integrals in the singular elements, it is convenient to directly use the line integrals for (4.6). The reason for this is that the singular integral, defined as the Cauchy principal value of the integral, can be expressed as (see Fig. 3)

$$I = \int_{\Gamma} f(\xi, \eta, x, y) ds - \int_{\Gamma_0} f(\xi, \eta, x, y) ds. \tag{4.7}$$

Fortunately, the line integral on Γ_0 is zero as the radius of Γ_0 approaches 0.

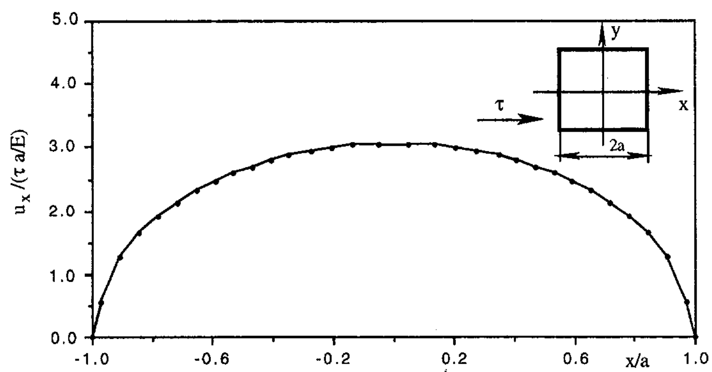

Fig. 7 Displacement in the x-direction for a square crack (33 × 15 elements)

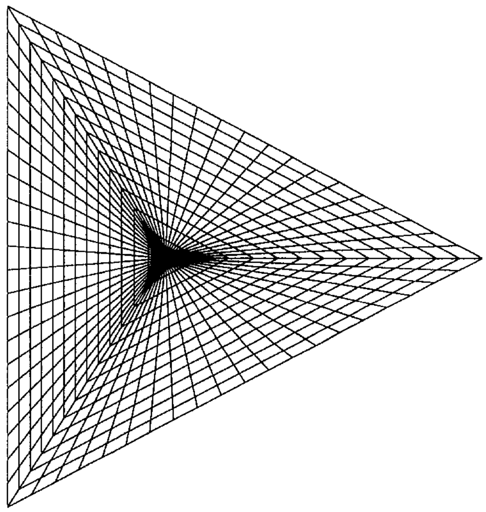

Fig. 8 Triangular crack with 61 × 13 elements

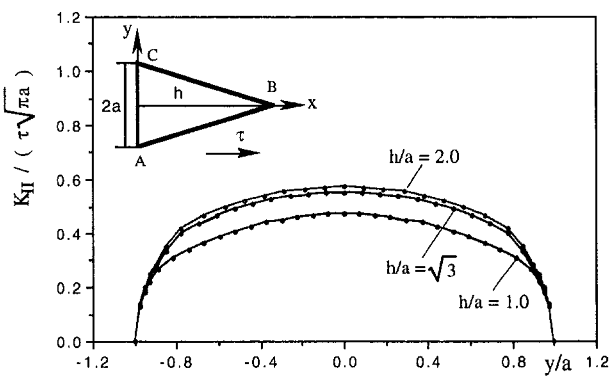

Fig. 9 Stress intensity factors of triangular cracks along AC

The integral for a singular element near the crack edge or crack tip is a special singular integral which contains two singularities. However, it is still possible to transform these two-dimensional singular integrals to one-dimensional regular integrals which are easier to evaluate precisely. The procedure is as follows:

The crack-opening displacement in the local coordinate system (ξ, η) in Fig. 3 may be expressed in the form

$$\Delta u_k = \frac{\sqrt{L-\xi}}{\sqrt{L}}\left[\frac{\eta-\eta_4}{\eta_3-\eta_4}\Delta u_{k3} + \frac{\eta_3-\eta}{\eta_3-\eta_4}\Delta u_{k4}\right] \quad (k = 1, 2) \quad (4.8)$$

where $L = \xi_2 - \xi_3$, the nodal displacements Δu_{k1} and Δu_{k2} vanish because of the zero displacement condition at the crack edge. Equation (4.8) indicates that the displacement has a linear variation in the tangential (η) direction and varies with the square root of the distance from the crack edge in the normal (ξ) direction. The derivatives of the displacement are

$$\Delta u_{k,\xi} = -\frac{1}{2H\sqrt{L(L-\xi)}}[(\eta-\eta_4)\Delta u_{k3} + (\eta_3-\eta)\Delta u_{k4}] \quad (4.9)$$

$$\Delta u_{k,\eta} = \frac{\sqrt{L-\xi}}{H\sqrt{L}}[\Delta u_{k3} - \Delta u_{k4}] \quad (4.10)$$

where $H = \eta_3 - \eta_4$. On the other hand, in the global coordinate system (x_1', x_2', x_3'), the function φ_{i3k} can be written as

$$\varphi_{i3k} = \frac{E}{8\pi(1-\nu^2)}\left\{\frac{\delta_{ik}}{r} - \nu\frac{(\xi_i'-x_i')(\xi_k'-x_k')}{r^3}\right\}. \quad (4.11)$$

Note functions φ_{i3k} satisfy $\nabla^2\phi_{3jk} = -S_{3jk}$ and $\varphi_{i3k,t} = F_{3jkt}$. In the local coordinate system, (4.11) can be written as

$$\varphi_{i3k} = \frac{E}{8\pi(1-\nu^2)}\left\{\frac{\delta_{ik}}{r} - \frac{\nu}{r^3}[\alpha_{ik}(\xi-x)^2 + \beta_{ik}(\xi-x)(\eta-y) + \gamma_{ik}(\eta-y)^2]\right\} \quad (4.12)$$

where

$$\alpha_{ik} = \delta_{1i}\delta_{1k}\cos^2\alpha + \delta_{1i}\delta_{2k}\sin\alpha\cos\alpha + \delta_{2i}\delta_{2k}\sin^2\alpha$$

$$\beta_{ik} = -2\delta_{1i}\delta_{1k}\sin\alpha\cos\alpha + \delta_{1i}\delta_{2k}(\cos^2\alpha - \sin^2\alpha) + 2\delta_{2i}\delta_{2k}\sin\alpha\cos\alpha$$

$$\gamma_{ik} = \delta_{1i}\delta_{1k}\sin^2\alpha - \delta_{1i}\delta_{2k}\sin\alpha\cos\alpha + \delta_{2i}\delta_{2k}\cos^2\alpha. \quad (4.13)$$

In Eq. (4.13), α denotes the normal direction of the crack edge of a tip element.

Substitution of (4.8) and (4.12) into Eqs. (4.4) yields

$$J_{n1} = \frac{E}{8\pi(1-\nu^2)}\frac{1}{2H\sqrt{L}}\{(\eta_4u_3 - \eta_3u_4)\sum_{m=1}^{5}a_mI_m + (-u_3+u_4)\sum_{m=6}^{10}a_{m-5}I_m + (u_3-u_4)\sum_{m=11}^{15}a_{m-5}I_m + (\eta_4v_3 - \eta_3v_4)\sum_{m=1}^{5}b_mI_m + (-v_3+v_4)\sum_{m=6}^{10}b_{m-5}I_m + (v_3-v_4)\sum_{m=11}^{15}b_{m-5}I_m\}$$

$$J_{n2} = \frac{E}{8\pi(1-\nu^2)}\frac{1}{2H\sqrt{L}}\{(\eta_4u_3 - \eta_3u_4)\sum_{m=1}^{5}b_mI_m + (-u_3+u_4)\sum_{m=6}^{10}b_{m-5}I_m + (u_3-u_4)\sum_{m=11}^{15}b_{m-5}I_m$$

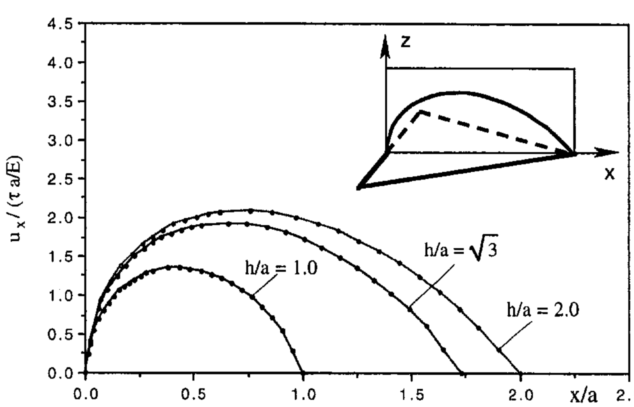

Fig. 10 Crack-opening displacements of triangular cracks under shear loading

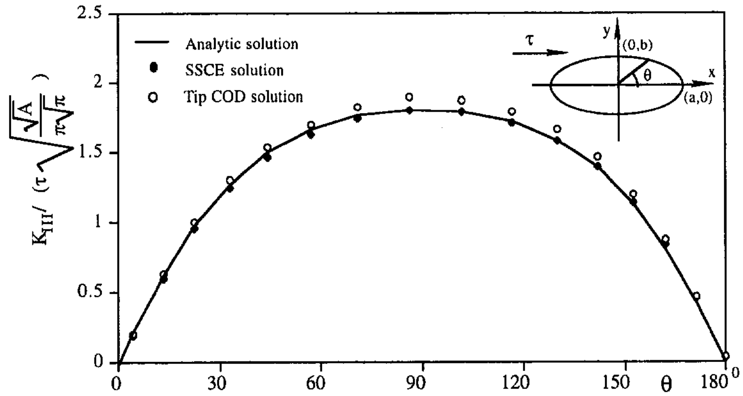

Fig. 11 Stress intensity factors of an elliptic crack ($b/a = 0.75$) under shear loading

$$+ (\eta_4 v_3 - \eta_3 v_4) \sum_{m=1}^{5} c_m I_m + (-v_3 + v_4) \sum_{m=6}^{10} c_{m-5} I_m + (v_3 - v_4) \sum_{m=11}^{15} c_{m-5} I_m \} \quad (4.14)$$

where the coefficients a_k, b_k, c_k for $k \le 7$ are

$$a_1 = -(1 + \nu 2 \cos^2 \alpha) \quad b_1 = -\nu 2 \sin \alpha \cos \alpha$$
$$c_1 = -(1 + \nu 2 \sin^2 \alpha)$$
$$a_2 = \nu 2 \sin \alpha \cos \alpha \quad b_2 = -\nu(\cos^2 \alpha - \sin^2 \alpha)$$
$$c_2 = -\nu 2 \sin \alpha \cos \alpha$$
$$a_3 = \nu 3 \cos^2 \alpha \quad b_3 = -\nu 3 \sin \alpha \cos \alpha \quad c_3 = \nu 3 \sin^2 \alpha$$
$$a_4 = -3a_2 \ b_4 = -\nu 3(\cos^2 \alpha - \sin^2 \alpha) \ c_4 = \nu 6 \sin \alpha \cos \alpha$$
$$a_5 = \nu 3 \sin^2 \alpha \quad b_5 = -\nu 3 \sin \alpha \cos \alpha \quad c_5 = \nu 3 \cos^2 \alpha$$
$$a_6 = -\nu 2 \sin \alpha \cos \alpha \quad b_6 = -\nu(\cos^2 \alpha - \sin^2 \alpha)$$
$$c_6 = -\nu 2 \sin \alpha \cos \alpha$$
$$a_7 = 1 + \nu 2 \sin^2 \alpha \quad b_7 = \nu 2 \sin \alpha \cos \alpha$$
$$c_7 = -(1 + \nu 2 \cos^2 \alpha) \quad (4.15)$$

and the coefficients for $k = 8 \sim 10$ can be given by using $a_k = a_{k-5}$, $b_k = b_{k-5}$, and $c_k = c_{k-5}$. The functions I_m ($m \le 15$) represent 15 integrals on the crack-tip elements as

$$I_1 = \int_{\Omega_e} \frac{\xi - x}{r^3\sqrt{L - \xi}} d\Omega \quad I_2 = \int_{\Omega_e} \frac{\eta - y}{r^3\sqrt{L - \xi}} d\Omega$$
$$I_3 = \int_{\Omega_e} \frac{(\xi - x)^3}{r^5\sqrt{L - \xi}} d\Omega \quad I_4 = \int_{\Omega_e} \frac{(\xi - x)^2(\eta - y)}{r^5\sqrt{L - \xi}} d\Omega$$
$$I_5 = \int_{\Omega_e} \frac{(\xi - x)(\eta - y)^2}{r^5\sqrt{L - \xi}} d\Omega \quad I_6 = \int_{\Omega_e} \frac{(\xi - x)\eta}{r^3\sqrt{L - \xi}} d\Omega$$
$$I_7 = \int_{\Omega_e} \frac{(\eta - y)\eta}{r^3\sqrt{L - \xi}} d\Omega \quad I_8 = \int_{\Omega_e} \frac{(\xi - x)^3\eta}{r^5\sqrt{L - \xi}} d\Omega$$
$$I_9 = \int_{\Omega_e} \frac{(\xi - x)^2(\eta - y)\eta}{r^5\sqrt{L - \xi}} d\Omega \ I_{10} = \int_{\Omega_e} \frac{(\xi - x)(\eta - y)^2\eta}{r^5\sqrt{L - \xi}} d\Omega$$
$$I_{11} = \int_{\Omega_e} \frac{(\xi - x)\sqrt{L - \xi}}{r^3} d\Omega \quad I_{12} = \int_{\Omega_e} \frac{(\eta - y)\sqrt{L - \xi}}{r^3} d\Omega$$
$$I_{13} = \int_{\Omega_e} \frac{(\xi - x)^2(\eta - y)\sqrt{L - \xi}}{r^3} d\Omega$$
$$I_{14} = \int_{\Omega_e} \frac{(\xi - x)(\eta - y)^2\sqrt{L - \xi}}{r^3} d\Omega$$
$$I_{15} = \int_{\Omega_e} \frac{(\eta - y)^3\sqrt{L - \xi}}{r^3} d\Omega \quad (4.16)$$

where $r = \sqrt{(\xi - L/2)^2 + \eta^2}$. Among these 15 integrals, the first five integrals ($I_1 \sim I_5$) have higher singularity in the integrals, while the other ten integrals ($I_6 \sim I_{15}$) can be transformed to regular integrals through integration by parts. By using the technique by Xu et al. (1997), these 15 two-dimensional integrals can be transformed into one-dimensional regular integrals. Where the source point (x, y) is at the center of the trapezoidal element, i.e., $x = (L/2)$ and $y = 0$. The equations for the two sides between nodes 2–3 and nodes 1–4 (see Fig. 3) are $\eta = \alpha_1\xi + \beta_1$ and $\eta = \alpha_2\xi + \beta_2$, respectively. By taking advantage

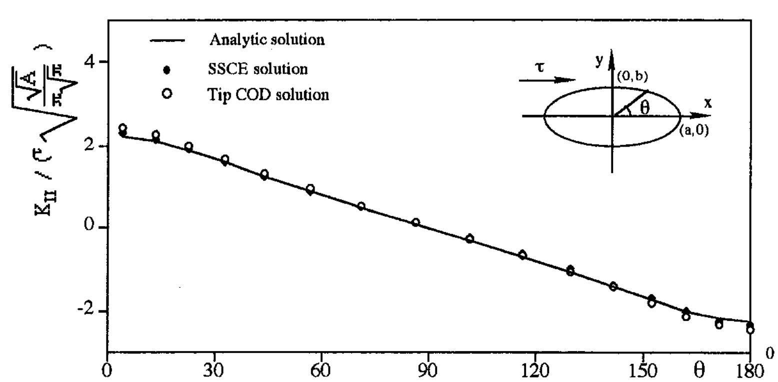

Fig. 12 Stress intensity factors of an elliptic crack under shear loading (31 × 13 elements)

of the trapezoidal geometry and integrating in the η direction, these integrals can be expressed as

$$I_k = F_k(\alpha_1, \beta_1) - F_k(\alpha_2, \beta_2), \quad (k = 1, 2, \ldots 15) \quad (4.17)$$

and the functions $F_k(\alpha, \beta)$ are listed in the Appendix B. In this way, all the integrals are expressed as regular integrals and can be precisely evaluated.

5 Numerical Results for Stress Intensity Factors of Cracks Under Shear Loading

The self-similar crack expansion method, associated with analytically numerical evaluation in the element integrals, shows good accuracy for the analysis of three-dimensional cracks under shear loading. A penny-shaped crack with radius a under shear loading τ in the x-direction is discretized into 25×13 elements. Stress intensity factors for various Poisson's ratios of materials are shown in Figs. 4 and 5. The least-square method might be used for determining displacements of Δu_x and Δu_y for $m(n-1)+1$ nodes in terms of $2m \times n$ equations on the crack surface. The results agree well with the analytical solution by Kassir and Sih (1975) where the analytical solutions for stress intensity factors are

$$K_{\mathrm{II}} = \frac{4}{(2-\nu)\sqrt{\pi}} \tau\sqrt{a} \cos\theta,$$

$$K_{\mathrm{III}} = \frac{4(1-\nu)}{(2-\nu)\sqrt{\pi}} \tau\sqrt{a} \sin\theta. \quad (5.1)$$

Stress intensity factors of the crack ($\nu = 0.3$), K_{II} at points A ($\theta = 0$ deg) and K_{III} at point B ($\theta = 90$ deg) for 65×23 elements are $K_{\mathrm{II}} = 2.3655\tau\sqrt{a/\pi}$ and $K_{\mathrm{III}} = 1.6578\tau\sqrt{a/\pi}$ as compared with the analytical solution $2.35294\tau\sqrt{a/\pi}$ and $1.64706\tau\sqrt{a/\pi}$. The errors are less than one percent.

The stress intensity factors of an elliptical crack at the points A and B with axis ratio $b/a = 0.8$, $\nu = 0$ under shear loading, the calculation shows high accuracy of stress intensity factors, with errors less than one percent as more than 65×23 elements are used. The analytical form for an elliptical crack with axis length a and b ($a > b$) under uniform shear loading in the x-direction is

$$K_{\mathrm{II}} = \tau\left(\frac{\pi b^3}{a}\right)^{1/2} \times \frac{k^2 \cos\alpha}{[(k^2-\nu)E(k) + \nu k_1^2 K(k)](b^2\cos^2\alpha + a^2\sin^2\alpha)^{1/4}}$$

$$K_{\mathrm{III}} = \tau(\pi ab)^{1/2} \times \frac{(1-\nu)k^2 \sin\alpha}{[(k^2-\nu)E(k) + \nu k_1^2 K(k)](b^2\cos^2\alpha + a^2\sin^2\alpha)^{1/4}}. \quad (5.2)$$

Functions $K(k)$ and $E(k)$ in (5.2) are the elliptic integrals of the first kind and the second kind, respectively. $k = \sqrt{1-(b/a)^2}$ and $k_1 = b/a$.

For a rectangular crack under shear loading in the direction parallel to the x-axis, stress intensity factors K_{II} on the side CD is shown in Fig. 6. Displacements in the x-direction (along the x-axis) are shown in Fig. 7.

For triangular cracks with various geometry ($h/a = 1, \sqrt{3}$, 2) under shear loading τ in the x-direction, the discretized elements for a triangular crack with $h/a = \sqrt{3}/2$ are plotted in Fig. 8. Normalized stress intensity factors along the crack edge AC are shown in Fig. 9, where AC $= 2a$, and AB $=$ BC $= \sqrt{a^2+h^2}$. Also as plotted in Fig. 10 are the crack-opening displacements along the x-axis for triangular cracks with various ratio of h/a. It is interesting that for the crack with three equivalent sides of length ($h/a = \sqrt{3}/2$), the maximum displacement is at the center of the triangular crack. However, it may not be true for all other kinds of triangular cracks.

6 Conclusion and Discussion

Stress intensity factors for three-dimensional cracks under shear loading can be accurately calculated by using the self-similar crack expansion method, associated with the analytically numerical evaluation of the cracks. In general, the boundary integral equations for cracks under shear loading show coupled characteristics. The unknowns on the crack surface will be doubled as compared to the cracks under tensile loading and thus, a rational treatment of the problems may require more efforts in the numerical analysis.

For the boundary integral equations of three-dimensional cracks under shear loading, the regular and singular integrals on the elements of the crack surface can be evaluated by using the explicit expressions of the closed form. However, more functions need to be estimated as compared with cracks under tensile loading. By using the self-similar crack expansion method, the accuracy of the cracks under shear loading is comparable to that of the cracks under tensile loading, with errors in stress intensity factors around the crack edge less than one percent.

The self-similar crack expansion method generally gives better values of stress intensity factors than the conventional method (tip crack-opening displacement method) where the stress intensity factors of a crack are directly obtained from the crack-opening displacement by using (3.1). Figures 11 and 12 show the stress intensity factors obtained by the tip crack-opening displacement method and the self-similar crack expansion method in comparison with the analytical solution. The self-similar crack expansion method provides more accurate results than the tip crack-opening displacement method for stress intensity factor analysis. The use of the present self-similar crack expansion method is limited to cracks in an infinite (including semi-infinite) body, and is also limited to cracks under uniform loading. The first limitation can be circumvented by using the improved self-similar crack expansion method (Xu, 1998b), and the second limitation can be circumvented by using the combination of the weight function method (Rice, 1972) and the self-similar crack expansion method.

Acknowledgment

The support of the National Institute of Standards and Technology and the Army Office of Research are gratefully acknowledged. The authors are grateful for helpful suggestions and comments by the reviewers.

References

Cruse, T. A., and Besunner, P. M., 1975, "Residual life prediction for surface cracks in complex structural details," *Journal of Aircraft*, Vol. 12, pp. 369–375.

Cruse, T. A., and Meyers, G. J., 1977, "Three-dimensional fracture mechanics analysis," *J. Struct. Divn., ASCE*, Vol. 103, pp. 309–320.

Cruse, T. A, 1988, *Boundary element analysis in computational fracture mechanics*, Kluwer, Dordrecht, The Netherlands.

Guo, Q., Wang, J. J., Clifton, R. J., and Mertaugh, L. J., 1995, "Elastic Analysis of Planar Cracks of Arbitrary Shape," ASME JOURNAL OF APPLIED MECHANICS, Vol. 62, pp. 108–115.

Kassir, M. K., and Sih, G. C., 1975, *Three-Dimensional Crack Problems*, Noordhoff International Publishing Leyden.

Murakami, Y., and Nemat-Nasser, 1982, "Interacting dissimilar semi-elliptical surface flaws under tension and bending," *Engineering Fracture Mechanics*, Vol. 16, No. 3, pp. 373–386.

Rice, J. R., 1972, "Some remarks on elastic crack-tip stress fields," *International Journal of Solids and Structures*, Vol. 8, pp. 751–758.

Rice, J. R. 1985, "First Order Variation in Elastic Fields due to Variation Location of a Planar Crack Front," ASME *Journal of Applied Mechanics*, Vol. 52, pp. 571–579.

Weaver, J., 1977, "Three-dimensional crack analysis," *International Journal of Solids and Structures*, Vol. 13, pp. 321–333.

Xu, Y., Moran B., and Belytschko T., 1997, "Self-Similar Crack Expansion Method for Three-Dimensional Crack Analysis," ASME JOURNAL OF APPLIED MECHANICS, Vol. 64, pp. 729–737.

Xu, Y., Moran B., and Belytschko T., 1998a, "Uncoupled characteristics of three-dimensional planar cracks," *International Journal of Engineering Science*, Vol. 36, No. 4, pp. 33–48.

Xu, Y., 1998b, "Self-Similar Crack Expansion Method for two-dimensional cracks under mixed mode loading conditions," *Engineering Fracture Mechanics*, Vol. 59, No. 2, pp. 165–182.

APPENDIX A

Functions $A_{K\xi}$, $A_{K\eta}$ ($K = 1, 2, 3, \ldots 12$)

$$A_{1\xi} = \frac{1}{3}\left\{\frac{(\xi-x)^2}{r^3} + \frac{(\xi-x)^4}{r^5} - \frac{2}{r}\right\},$$

$$A_{1\eta} = \frac{1}{3}\left\{\frac{(\xi-x)^3(\eta-y)}{r^5} + 2\,\frac{(\xi-x)(\eta-y)}{r^3}\right\}$$

$$A_{2\xi} = -\frac{1}{3}\left\{\frac{(\eta-y)^2}{r^3} - \frac{(\xi-x)^2(\eta-y)^2}{r^5}\right\},$$

$$A_{2\eta} = \frac{1}{3}\,\frac{(\xi-x)(\eta-y)^3}{r^5}$$

$$A_{3\xi} = \frac{1}{3}\,\frac{(\xi-x)^3(\eta-y)}{r^5},$$

$$A_{2\eta} = -\frac{1}{3}\left\{\frac{(\xi-x)^2}{r^3} - \frac{(\xi-x)^2(\eta-y)^2}{r^5}\right\},$$

$$A_{4\xi} = \frac{1}{3}\left\{\frac{(\xi-x)(\eta-y)^3}{r^5} + 2\,\frac{(\xi-x)(\eta-y)}{r^3}\right\},$$

$$A_{4\eta} = \frac{1}{3}\left\{\frac{(\eta-y)^2}{r^3} + \frac{(\eta-y)^4}{r^5} - \frac{2}{r}\right\}$$

$$A_{5\xi} = \frac{-1}{15}\left\{\frac{2(\eta-y)}{r} + \frac{(\xi-x)^2(\eta-y)}{r^3} - \frac{3(\xi-x)^4(\eta-y)}{r^5}\right\}$$

$$A_{5\eta} = \frac{-1}{15}\left\{\frac{3(\xi-x)^5(\eta-y)}{r^5}\right\}$$

$$A_{6\xi} = \frac{1}{15}\left\{\frac{2(\xi-x)^3}{r^3} + \frac{3(\xi-x)^3(\eta-y)^2}{r^5}\right\},$$

$$A_{6\eta} = \frac{1}{15}\left\{\frac{2(\eta-y)^3}{r^3} + \frac{3(\xi-x)^2(\eta-y)^3}{r^5}\right\}$$

$$A_{7\xi} = \frac{-1}{15}\left\{\frac{3(\eta-y)^5}{r^5}\right\}$$

$$A_{7\eta} = \frac{-1}{15}\left\{\frac{2(\xi-x)}{r} + \frac{(\xi-x)(\eta-y)^2}{r^3} - \frac{3(\xi-x)(\eta-y)^4}{r^5}\right\}$$

$$A_{8\xi} = -\frac{1}{r} + \frac{(\xi-x)^2}{r^3} \quad A_{8\eta} = \frac{(\xi-x)(\eta-y)}{r^3}$$

$$A_{9\xi} = \frac{(\xi-x)(\eta-y)}{r^3} \quad A_{9\eta} = -\frac{1}{r} + \frac{(\eta-y)^2}{r^3}$$

$$A_{10\xi} = \frac{1}{3} + \frac{(\xi-x)^3}{r^3}$$

$$A_{10\eta} = \frac{1}{3}\left\{\frac{2(\eta-y)}{r} + \frac{(\xi-x)^2(\eta-y)}{r^3}\right\}$$

$$A_{11\xi} = \frac{1}{3}\left\{-\frac{(\eta-y)}{r} + \frac{(\xi-x)^2(\eta-y)}{r^3}\right\}$$

$$A_{11\eta} = \frac{1}{3}\left\{-\frac{(\xi-x)}{r} + \frac{(\xi-x)(\eta-y)^2}{r^3}\right\}$$

$$A_{12\xi} = \frac{1}{3}\left\{\frac{2(\xi-x)}{r} + \frac{(\xi-x)(\eta-y)^2}{r^3}\right\}$$

$$A_{12\eta} = \frac{1}{3}\left\{\frac{(\eta-y)^3}{r}\right\}$$

APPENDIX B

Functions $F_m(\alpha, \beta)$ ($m = 1, 2, 3 \ldots, 15$)

$$F_1(\alpha,\beta) = \frac{2}{\sqrt{L}}\left\{\frac{\alpha}{\sqrt{\left(\frac{1}{2}\right)^2 + \left(\frac{\beta}{L}\right)^2}} - \alpha\int_0^1 \frac{\sqrt{1-\xi}\left[(1+\alpha^2)\xi + \left(\frac{\alpha\beta}{L} - \frac{1}{2}\right)\right]}{\left[\left(\xi-\frac{1}{2}\right)^2 + \left(\alpha\xi + \frac{\beta}{L}\right)^2\right]^{3/2}}\,d\xi\right\} + \frac{\operatorname{sgn}\left(\frac{\alpha L}{2} + \beta\right)}{\sqrt{L}}\left\{\sqrt{2}\,\lg(3 + 2\sqrt{2})\right.$$

$$\left. + \frac{1 - \alpha^2 - 4\alpha\frac{\beta}{L}}{r_0\left[r_0 + \left|\frac{\beta}{L} + \frac{\alpha}{2}\right|\right]}\right\} + \frac{2\operatorname{sgn}\left(\frac{\alpha L}{2} + \beta\right)}{\sqrt{L}}\left\{\int_0^1 \frac{\sqrt{1-\xi}\left(\frac{\alpha}{2} + \frac{\beta}{L}\right)\left[\alpha(2\xi-1) - (1-\alpha^2)\left(\alpha\xi + \frac{\beta}{L}\right)\right]}{r^3\left[r + \left|\frac{\alpha}{2} + \frac{\beta}{L}\right|\right]}\,d\xi\right.$$

$$\left. - \int_0^1 \frac{\sqrt{1-\xi}\left[(1+\alpha^2)\left(\xi - \frac{1}{2}\right) + \alpha\left(\alpha + \frac{2\beta}{L}\right)\right]\left[\left(\xi-\frac{1}{2}\right) + \alpha\left(a\xi + \frac{\beta}{L}\right)\right]}{r^2\left[r + \left|\frac{\alpha}{2} + \frac{\beta}{L}\right|\right]^2}\,d\xi\right\}$$

$$F_2(\alpha,\beta)=\frac{-2}{\sqrt{L}}\left\{\frac{1}{\sqrt{\left(\frac{1}{2}\right)^2+\left(\frac{\beta}{L}\right)^2}}-\int_0^1\frac{\sqrt{1-\xi}\left[(1+\alpha^2)\xi+\left(\frac{\alpha\beta}{L}-\frac{1}{2}\right)\right]}{\left[\left(\xi-\frac{1}{2}\right)^2+\left(\alpha\xi+\frac{\beta}{L}\right)^2\right]^{3/2}}\,d\xi\right\}$$

$$F_3(\alpha,\beta)=\frac{2}{3}F_1-\frac{2}{3\sqrt{L}}\left\{\frac{\beta/L}{2r_0^3}-\int_0^1\frac{\sqrt{1-\xi}\,[2\alpha\xi-\alpha/2+\beta/L]}{r^3}-\frac{\sqrt{1-\xi}3(\alpha\xi+\beta/L)(\xi-1/2)p}{r^5}\,d\xi\right\}$$

$$F_4(\alpha,\beta)=-\frac{2}{3\sqrt{L}}\left\{\frac{1}{4r_0^3}+\int_0^1\left[\frac{\sqrt{1-\xi}(2\xi-1)}{r^3}-\frac{\sqrt{1-\xi}3(\xi-1/2)^2p}{r^5}\right]d\xi\right\}$$

$$F_5(\alpha,\beta)=F_1(\alpha,\beta)-F_3(\alpha,\beta)$$

$$F_6(\alpha,\beta)=2\sqrt{L}\left\{\frac{1}{2r_0}-\int_0^1\frac{\sqrt{1-\xi}}{r^3}-\frac{\sqrt{1-\xi}(\xi-1/2)p}{r^3}\,d\xi\right\}$$

$$F_7(\alpha,\beta)=\sqrt{L}\left\{\frac{-2\beta/L}{r_0}+\lg\left(\frac{r_0+\beta/L}{r_0-\beta/L}\right)-\int_0^1\sqrt{1-\xi}\left[\frac{2\alpha}{r}-\frac{(\alpha\xi+\beta/L)p}{r^3}-\frac{p+\alpha r}{r(r+\alpha\xi+\beta/L)}-\frac{p-\alpha r}{r(r-\alpha\xi-\beta/L)}\right]d\xi\right.$$

$$F_8(\alpha,\beta)=\frac{2}{3}\sqrt{L}\left\{\frac{1}{8r_0^3}-\int_0^1\sqrt{1-\xi}\left[\frac{3(\xi-1/2)^2}{r^3}-\frac{3(\xi-1/2)p}{r^5}\right]d\xi\right.$$

$$F_9(\alpha,\beta)=\frac{2}{3}\sqrt{L}\left\{\left(\frac{\beta/L}{r_0}\right)^3+\int_0^1\sqrt{1-\xi}\left[\frac{3(\alpha\xi+\beta/L)^2\alpha}{r^3}-\frac{3(\alpha\xi+\beta/L)^3p}{r^5}\right]d\xi\right\}$$

$$F_{10}(\alpha,\beta)=2\sqrt{L}\left\{\left[\frac{1}{2r_0}-\frac{1}{24r_0^3}\right]+\int_0^1\sqrt{1-\xi}\left[\frac{(\xi-1/2)^2}{r^3}-\frac{(\xi-1/2)^3p}{r^5}-\frac{1}{r}+\frac{(\xi-1/2)p}{r^3}\right]d\xi\right.$$

$$F_{11}(\alpha,\beta)=\sqrt{L}\left\{\alpha\int_0^1\frac{\sqrt{1-\xi}}{r}\,d\xi+\operatorname{sgn}\left(\frac{\alpha L}{2}+\beta\right)\int_0^1\frac{-(\alpha/2+\beta/L)^2-1/2(1+\alpha^2)\xi+1/2(\alpha^2-1)+2\alpha\beta/L}{\left[\sqrt{1-\xi}\left|\frac{\alpha}{2}+\frac{\beta}{L}\right|+1/\sqrt{2}r\right]}\,d\xi\right.$$

$$F_{12}(\alpha,\beta)=-\sqrt{L}\left\{\int_0^1\frac{\sqrt{1-\xi}}{r}\,d\xi\right\}\qquad F_{13}(\alpha,\beta)=\frac{-1}{3}\sqrt{L}\int_0^1\frac{(\xi-1/2)^2\sqrt{1-\xi}}{r^{3/2}}\,d\xi$$

$$F_{14}(\alpha,\beta)=\sqrt{L}\,\frac{\operatorname{sgn}\left(\frac{\alpha L}{2}+\beta\right)}{3}$$
$$\times\int_0^1\frac{-\left(\alpha\xi+\frac{\beta}{L}\right)^6-\frac{1}{2}\left(\xi-\frac{1}{2}\right)\left\{\left(\alpha\xi+\frac{\beta}{L}\right)^4+\left[\left(\alpha\xi+\frac{\beta}{L}\right)^2+\left(\xi-\frac{1}{2}\right)^2\right]^2+\left(\alpha\xi+\frac{\beta}{L}\right)^2\left[\left(\alpha\xi+\frac{\beta}{L}\right)^2+\left(\xi-\frac{1}{2}\right)^2\right]\right.}{r^3\left[\operatorname{sgn}\left(\frac{\alpha L}{2}+\beta\right)\sqrt{1-\xi}\,(\alpha\xi+\beta/L)^3-1/\sqrt{2}r^3\right]}\,d\xi$$

$$F_{15}(\alpha,\beta)=\sqrt{L}\int_0^1\sqrt{1-\xi}\left[\frac{(\xi-1/2)^2}{3r^3}-\frac{1}{r}\right]d\xi$$

where

$$r=\sqrt{\left(\xi-\frac{1}{2}\right)^2+\left(\alpha\xi+\frac{\beta}{L}\right)^2},\quad r_0=\frac{1}{2}+\frac{\beta}{L}$$

and sgn (x), the sign function, is defined as 1 when x is positive and -1 when x is negative.

The Elastodynamic Green's Function for a Torsional Ring Source

Yichi Lu
Southwest Research Institute,
P.O. drawer 28510,
San Antonio, TX 78228-0510
Assoc. Mem. ASME

The elastodynamic Green's function for a torsional ring source in a homogeneous, linear elastic medium is derived using the Fourier-Hankel transform. The Green's function is found to possess the same logarithmic singularity as the Legendre function of half-degree of the second kind.

Introduction

Magnetostrictively generated and detected torsional modes have been proposed and tested for ultrasonic pipe inspection (Mohr and Höller, 1976; Kwun and Teller, 1994). Here, magnetostriction refers to the physical phenomenon that when a ferromagnetic or ferrimagnetic material is magnetized, its dimensions change (Cullity, 1972). The lowest torsional mode has a unique property in that it propagates at the shear wave velocity and is nondispersive, while the second lowest torsional mode has the largest displacement near the external and internal surfaces.

When there are only axially symmetric scatterers like welds or circumferential cracks, the incidence of torsional waves results in torsional waves only, even though the mode amplitude may change and new torsional modes may be generated. In this case, numerical calculations can be greatly simplified if an elastodynamic Green's function for a torsional ring source is available and used. The elastostatic Green's functions for ring sources and corresponding integral equations for axially symmetric elastostatic problems appeared in the 1970s (Kermanidis, 1975; Cruse et al., 1977; Mayr et al., 1980; Hartmann, 1989), where the Green's functions were expressed in terms of either half-order Legendre functions or complete elliptic integrals. The elastodynamic Green's functions for ring sources, however, do not exist.

We report here the derivation of the elastodynamic Green's function for a torsional ring source using the Fourier-Hankel transform. The Green's function is found to possess the same order of singularity as the Legendre function of half-order of the second kind.

The Green's Function for a Torsional Ring Source

Consider an axisymmetric torsional ring source in the cylindrical coordinate system (r, θ, z), where the ring source is located at $r = r'$, $z = z'$. Since we study only axisymmetric problems, there is only one nonvanishing displacement, $u_\theta(r, z)$, polarized in the θ direction. The equation of motion for $u_\theta(r, z)$ is

$$\left(\nabla^2 - \frac{1}{r^2} + k_T^2\right) u_\theta(r, z) = 0, \tag{1}$$

where $k_T = \omega / c_T$ is the shear wave number, $c_T = \sqrt{\mu/\rho}$ is the shear wave velocity, μ is the shear modulus, ρ is the density, $\omega = 2\pi f$ is the circular frequency, f is the frequency, and

$$\nabla^2 = \frac{1}{r}\frac{\partial}{\partial r}\left(r \frac{\partial}{\partial r}\right) + \frac{\partial^2}{\partial z^2}. \tag{2}$$

The equation of motion for the Green's function, $G_\theta(r, z; r', z')$, can be written as

$$\left(\nabla^2 - \frac{1}{r^2} + k_T^2\right) G_\theta(r, z; r', z') = -\frac{1}{\mu}\frac{\delta(r' - r)\delta(z' - z)}{r}, \tag{3}$$

where $\delta(r' - r)\delta(z' - z)/r$ represents the torsional ring source.

We use the Fourier transform for the axial coordinate z, and the Hankel transform for the radial coordinate r. The Fourier transform is defined as

$$G_\theta(r, z; r', z') = \frac{1}{2\pi}\int_{-\infty}^{\infty} G_\theta^*(r, \eta; r', z') e^{i\eta z} d\eta, \tag{4a}$$

$$G_\theta^*(r, \eta; r', z') = \int_{-\infty}^{\infty} G_\theta(r, z; r', z') e^{-i\eta z} dz, \tag{4b}$$

while the Hankel transform is defined as

$$G_\theta^*(r, \eta; r', z') = \int_0^\infty \bar{G}_\theta^*(\xi, \eta; r', z') J_1(\xi r)\xi d\xi, \tag{5a}$$

$$\bar{G}_\theta^*(\xi, \eta; r', z') = \int_0^\infty G_\theta^*(r, \eta; r', z') J_1(\xi r) r dr, \tag{5b}$$

where η and ξ are transform parameters. We obtain

$$\bar{G}_\theta^*(\xi, \eta; r', z') = \frac{e^{-i\eta z'} J_1(\xi r')}{\mu[\eta^2 - (k_T^2 - \xi^2)]}. \tag{6}$$

Substituting Eq. (6) into Eq. (5a) and Eq. (5a) into Eq. (4a), and using the residue theorem, we obtain

$$G_\theta(r, z; r', z') = \frac{i}{2\mu}\int_0^\infty \frac{e^{i|z - z'|\sqrt{k_T^2 - \xi^2}}}{\sqrt{k_T^2 - \xi^2}} J_1(\xi r') J_1(\xi r)\xi d\xi, \tag{7}$$

where

$$\operatorname{Im}(\sqrt{k_T^2 - \xi^2}) > 0, \tag{8}$$

in order to satisfy the radiation condition.

Contributed by the Applied Mechanics Division of THE AMERICAN SOCIETY OF MECHANICAL ENGINEERS for publication in the ASME JOURNAL OF APPLIED MECHANICS.

Discussion on the paper should be addressed to the Technical Editor, Professor Lewis T. Wheeler, Department of Mechanical Engineering, University of Houston, Houston, TX 77204-4792, and will be accepted until four months after final publication of the paper itself in the ASME JOURNAL OF APPLIED MECHANICS.

Manuscript received by the ASME Applied Mechanics Division, Aug. 27, 1997; final revision, Feb. 19, 1998. Associate Technical Editor: R. C. Benson.

To integrate Eq. (7), we first rewrite the product of Bessel functions $J_1(\xi r)J_1(\xi r')$ as

$$J_1(\xi r)J_1(\xi r') = J_1\left(\xi\sqrt{r^2+r'^2}\cdot\frac{r}{\sqrt{r^2+r'^2}}\right)J_1\left(\xi\sqrt{r^2+r'^2}\,\frac{r'}{\sqrt{r^2+r'^2}}\right). \quad (9)$$

We can then write (Bailey, 1936; Erdélyi et al., 1953):

$$J_1(\xi r)J_1(\xi r') = \sum_{n=0}^{\infty}\frac{1}{n!(n+1)!}\left(\frac{\xi}{2}\frac{rr'}{\sqrt{r^2+r'^2}}\right)^{2n+1}J_{2n+1}(\xi\sqrt{r^2+r'^2}). \quad (10)$$

Substituting Eq. (10) into Eq. (7), utilizing Eq. (8), and noticing that the integral variable in Eq. (7) is ξ, we obtain

$$G_\theta(r,z;r',z') = \frac{1}{2\mu}\sum_{n=0}^{\infty}\frac{1}{n!(n+1)!}\left(\frac{1}{2}\frac{rr'}{\sqrt{r^2+r'^2}}\right)^{2n+1} \times\int_0^\infty\frac{e^{-|z-z'|\sqrt{\xi^2-k_T^2}}}{\sqrt{\xi^2-k_T^2}}\,\xi^{2n+2}\cdot J_{2n+1}(\xi\sqrt{r^2+r'^2})d\xi. \quad (11)$$

To evaluate the integral in Eq. (11) we let $z=-iy$, then the identity (Watson, 1952)

$$\int_0^\infty J_n(bt)\frac{K_m(a\sqrt{t^2+z^2})}{(t^2+z^2)^{m/2}}t^{n+1}dt = \frac{b^n}{a^m}\left(\frac{\sqrt{a^2+b^2}}{z}\right)^{m-n-1}K_{m-n-1}(z\sqrt{a^2+b^2})$$

becomes

$$\int_0^\infty J_n(bt)\frac{K_m(a\sqrt{t^2-y^2})}{(t^2-y^2)^{m/2}}t^{n+1}dt = \frac{b^n}{a^m}\left(i\frac{\sqrt{a^2+b^2}}{y}\right)^{m-n-1}K_{m-n-1}(-iy\sqrt{a^2+b^2}), \quad (12)$$

where $K_m(z)$ is the modified Bessel function of order m of the second kind. In Eq. (12), a and b are arbitrary constants.

Since (Lebedev, 1972)

$$K_v(z) = \frac{\pi i}{2}e^{v(\pi i/2)}H_v^{(1)}(ze^{(\pi i/2)}), \quad -\pi < \arg z < \frac{\pi}{2}, \quad (13)$$

where $H_v^{(1)}$ is the Bessel function of the third kind,

$$H_{-v}^{(1)}(z) = e^{v\pi i}H_v^{(1)}(z) \quad (14)$$

$$K_{1/2}(z) = \sqrt{\frac{\pi}{2z}}\,e^{-z} \quad (15)$$

if we let $m=\frac{1}{2}$, then

$$\int_0^\infty J_n(bt)\frac{e^{-a\sqrt{t^2-y^2}}}{\sqrt{t^2-y^2}}t^{n+1}dt = i\sqrt{\frac{\pi}{2}}\,b^n\left(\frac{y}{\sqrt{a^2+b^2}}\right)^{n+1/2}H_{n+1/2}^{(1)}(y\sqrt{a^2+b^2}). \quad (16)$$

Using Eq. (16) and letting $a=|z-z'|$, $b=\sqrt{r^2+r'^2}$, $t=\xi$, $y=k_T$, Eq. (11) can now be integrated to yield

$$G_\theta(r,z;r',z') = \frac{i}{2\mu}\sqrt{\frac{\pi}{rr'}}\sum_{n=0}^{\infty}\frac{1}{n!(n+1)!} \times\left(\frac{k_Trr'}{2\sqrt{|z-z'|^2+r^2+r'^2}}\right)^{2n+3/2} \cdot H_{2n+3/2}^{(1)}(k_T\sqrt{|z-z'|^2+r^2+r'^2}). \quad (17)$$

The Green's function, as expressed by Eq. (17), can now be evaluated as accurately as numerical algorithms permit, but it is still not satisfactory for two reasons: It is difficult to see whether the function is singular at $r=r'$, $z=z'$. If it is, it is still difficult to see what kind of singularity it possesses. In order to arrive at a better expression for the Green's function, we use the identity (Abramovitz and Stegun, 1972)

$$\sqrt{\frac{\pi}{2z}}H_{n+1/2}^{(1)}(z) = \frac{e^{iz}}{iz}i^{-n}\sum_{k=0}^{n}\frac{(n+k)!}{k!(n-k)!}\left(\frac{i}{2z}\right)^k. \quad (18)$$

Substituting Eq. (18) into Eq. (17) then yields

$$\begin{aligned}
G_q(r,z;r',z') &= \frac{1}{2\mu}\frac{e^{ik_T\sqrt{|z-z'|^2+r^2+r'^2}}}{\sqrt{|z-z'|^2+r^2+r'^2}}\sum_{n=0}^{\infty}\frac{1}{n!(n+1)!}\left(\frac{k_Trr'}{2i\sqrt{|z-z'|^2+r^2+r'^2}}\right)^{2n+1} \\
&\quad\cdot\sum_{k=0}^{2n+1}\frac{(2n+1+k)!}{k!(2n+1-k)!}\left(\frac{i}{2k_T\sqrt{|z-z'|^2+r^2+r'^2}}\right)^k \\
&= \frac{1}{2\mu}\frac{e^{ik_T\sqrt{|z-z'|^2+r^2+r'^2}}}{\sqrt{|z-z'|^2+r^2+r'^2}}\sum_{n=0}^{\infty}\frac{(4n+2)!}{n!(n+1)!(2n+1)!}\frac{1}{2^{2n+1}\cdot 2^{2n+1}}\left(\frac{rr'}{|z-z'|^2+r^2+r'^2}\right)^{2n+1} \\
&\quad+\frac{1}{2\mu}\frac{e^{ik_T\sqrt{|z-z'|^2+r^2+r'^2}}}{\sqrt{|z-z'|^2+r^2+r'^2}}\sum_{n=0}^{\infty}\frac{1}{n!(n+1)!}\left(\frac{k_Trr'}{2i\sqrt{|z-z'|^2+r^2+r'^2}}\right)^{2n+1} \\
&\quad\cdot\sum_{k=0}^{2n}\frac{(2n+1+k)!}{k!(2n+1-k)!}\left(\frac{i}{2k_T\sqrt{|z-z'|^2+r^2+r'^2}}\right)^k. \quad (19)
\end{aligned}$$

We observe that for elastodynamic problems, the singular term of a Green's function must be independent of the wave number. An inspection of Eq. (19) reveals that the summation in the first term on the right side of the equation is independent of the wave number k_T.

Using mathematical induction, we can prove that

$$\frac{(4n+2)!}{2^{2n+1}(2n+1)!} = \{1\cdot 5\cdot 9\ldots (4n+1)\}\{3\cdot 7\ldots (4n-1)\},\ n = 0, 1, 2, \ldots. \quad (20)$$

But (Lebedev, 1972)

$$Q_{1/2}(x) = \frac{\sqrt{\pi}\,\Gamma(1+\frac{1}{2})}{\Gamma(2)(2x)^{3/2}} F\left(\frac{5}{4}, \frac{3}{4}; 2; \frac{1}{x^2}\right) = \pi \sum_{n=0}^{\infty} \frac{\{1\cdot 5\cdot 9\ldots (4n+1)\}\{3\cdot 7\cdot 11\ldots (4n-1)\}}{n!(n+1)!2^{2n+1}} \left(\frac{1}{2x}\right)^{2n+1+1/2} \quad (21)$$

where $Q_{1/2}(z)$ is the Legendre function of degree $\frac{1}{2}$ of the second kind and $F(\alpha, \beta; \gamma; z)$ is the hypergeometric function. Therefore, we can decompose the Green's function into a singular term, $G_\theta^s(r, z; r', z')$, and a regular term, $G_\theta^r(r, z; r', z')$, as

$$G_\theta(r, z; r', z') = G_\theta^s(r, z; r', z') + G_\theta^r(r, z; r', z'), \quad (22)$$

where

$$G_\theta^s(r, z; r', z') = \frac{e^{ik_T\sqrt{|z-z'|^2+r^2+r'^2}}}{2\pi\mu\sqrt{rr'}} \cdot Q_{1/2}\left(\frac{|z-z'|^2+r^2+r'^2}{2rr'}\right) \quad (22a)$$

$$G_\theta^r(r, z; r', z') = \frac{1}{2\mu} \frac{e^{ik_T\sqrt{|z-z'|^2+r^2+r'^2}}}{\sqrt{|z-z'|^2+r^2+r'^2}} \sum_{n=0}^{\infty} \frac{1}{n!(n+1)!} \left(\frac{k_T r r'}{2i\sqrt{|z-z'|^2+r^2+r'^2}}\right)^{2n+1} \cdot \sum_{k=0}^{2n} \frac{(2n+1+k)!}{k!(2n+1-k)!} \left(\frac{i}{2k_T\sqrt{|z-z'|^2+r^2+r'^2}}\right)^k. \quad (22b)$$

The term $G_\theta^r(r, z; r', z',)$ is regular. Since $Q_{1/2}(z)$ can be expressed in terms of the complete elliptic integrals of the first and the second kinds, $K(z)$ and $E(z)$ as

$$Q_{1/2}(z) = z\sqrt{\frac{2}{1+z}}\, K\left(\sqrt{\frac{2}{1+z}}\right) - \sqrt{2(1+z)}\, E\left(\sqrt{\frac{2}{1+z}}\right), \quad (23)$$

and $K(z)$ has a logarithmic singularity at $z = 1$ while $E(z)$ is regular (Cayley, 1961), it follows that $G_\theta^s(r, z; r', z',)$, and therefore $G_\theta(r, z; r', z',)$, has a logarithmic singularity at $r = r'$, $z = z'$. Equation (22) is the desired expression for the Green's function.

Conclusion

The elastodynamic Green's function for a torsional ring source is derived using the Fourier-Hankel transform. The singular term of the Green's function can be expressed as a function of Legendre function of half-degree of the second kind.

Acknowledgment

This work is supported by the Advisory Committee for Research, Southwest Research Institute. The author wishes to thank Mr. Jerry L. Jackson and Dr. Robert E. Beissner for helpful suggestions and discussions.

References

Bailey, W. N., 1936, "On the Product of Two Legendre Polynomials with Different Arguments," *Proceedings of the London Mathematical Society, Series 2*, Vol. 41, pp. 215–220.

Cayley, A., 1961, *An Elementary Treatise on Elliptic Functions*, Dover, New York.

Cruse, T. A., Snow, D. W., and Wilson, R. B., 1977, "Numerical Solutions in Axisymmetric Elasticity," *Computers & Structures*, Vol. 7, pp. 445–451.

Cullity, B. D., 1972, *Introduction to Magnetic Materials, Reading*, Addison-Wesley, MA.

Erdélyi, A., Magnus, W., Oberhettinger, F., and Tricomi, F. G., 1953, *Higher Transcendental Functions*, McGraw-Hill, New York (there is a typo in Eq. (11), page 100, Vol. II).

Hartmann, F., 1989, *Introduction to Boundary Elements, Theory and Applications*, Springer-Verlag, Berlin.

Kermanidis, T., 1975, "A Numerical Solution for Axially Symmetrical Elasticity Problems," *International Journal of Solids and Structures*, Vol. 11, pp. 493–500.

Kwun, H., and Teller, C. M., 1994, "Magnetostrictive Generation and Detection of Longitudinal, Torsional, and Flexural Waves in a Steel Rod," *Journal of the Acoustical Society of America*, Vol. 96, pp. 1202–1204.

Lebedev, N. N., 1972, *Special Functions and Their Applications*, Dover, New York.

Mayr, M., Drexler, W., and Kuhn, G., 1980, "A Semianalytical Boundary Integral Approach for Axisymmetric Elastic Bodies with Arbitrary Boundary Conditions," *International Journal of Solids and Structures*, Vol. 16, pp. 863–871.

Mohr, W., and Höller, P., 1976, "On Inspection of Thin-Walled Tubes for Transverse and Longitudinal Flaws by Guided Ultrasonic Waves," *IEEE Transactions*, Vol. SU-23, No. 5, pp. 369–374.

Watson, G. N., 1952, *A Treatise on the Theory of Bessel Functions*, Cambridge University Press, Cambridge, UK.

V. P. W. Shim
Associate Professor,
Department of Mechanical and
Production Engineering,
National University of Singapore,
10, Kent Ridge Crescent,
Singapore 119260
Mem. ASME

S. E. Quah
Research Engineer,
Motorola Electronics Pte., Ltd.
12, Ang Mo Kio St. 64,
Singapore 569088

Solution of Impact-Induced Flexural Waves in a Circular Ring by the Method of Characteristics

A study of elastic wave propagation in a curved beam (circular ring) is presented. The governing equations of motion are formulated in two forms based on Timoshenko beam theory. Solutions are obtained using the method of characteristics, whereby a numerical scheme employing higher-order interpolation is proposed for the finite difference equations. Results obtained are verified by experiments; it is found that use of the higher-order numerical scheme improves correlation with experimental results. Comparison of the relative accuracy between the two mathematical formulations—one in terms of generalized forces and velocities and the other in terms of generalized displacements—shows the former to be mathematically simpler and to yield more accurate results.

Introduction

Unlike solid continua, transmission of elastic stresses through cellular structures such as honeycombs and tightly packed tube and ring arrays, is effected by propagation along the walls of constituent cells. One simple two-dimensional idealization of a cellular material is an array of rings, which Stronge and Shim (1987) subjected to impact deformation. In seeking to understand how impact stresses are transmitted through such arrays, it is instructive to examine the types of stresses generated in a single ring and their propagation characteristics.

General two or three-dimensional theory for the analysis of wave propagation in beams—e.g., that by Pochhammer-Chree (Abramson et al., 1958)—is mathematically too complex for most practical applications. It has been demonstrated that one-dimensional Timoshenko beam analysis (Graff, 1975) is suitable for the study of stress propagation in straight beams (Goland et al., 1955; Kuo, 1961; Aprahamian et al. 1971; Ripperger and Abramson, 1957; Shim et al., 1992). Application of Timoshenko-type theory to wave propagation in curved beams has been undertaken by Morley (1961) and Graff (1970). The difference between their analyses was the reference axis chosen—Morley selected the neutral axis whereas Graff used the centroidal axis. This results in different forms of the governing equations and the predicted velocities also differ slightly because of this. Both analyses predicted three modes of wave propagation—radial shearing, longitudinal extension, and flexure. Radial shearing has the highest wave speed while the flexural mode is slowest.

The validity of Morley's approach to curved beams has been verified by Phillips and Crowley (1972) and Crowley et al. (1974), who conducted photoelasticity experiments on wave propagation in 90-deg elbows of rectangular cross section and constant curvature. Axial force and bending moment pulses were applied at one end of the elbow and bending moment, axial and shear force distributions along the elbow at different times studied. However, the response to radial loads was not examined.

Contributed by the Applied Mechanics Division of THE AMERICAN SOCIETY OF MECHANICAL ENGINEERS for publication in the ASME JOURNAL OF APPLIED MECHANICS.

Discussion on the paper should be addressed to the Technical Editor, Professor Lewis T. Wheeler, Department of Mechanical Engineering, University of Houston, Houston, TX 77204-4792, and will be accepted until four months after final publication of the paper itself in the ASME JOURNAL OF APPLIED MECHANICS.

Manuscript received by the ASME Applied Mechanics Division, Sept. 12, 1997; final revision, Dec. 26, 1997. Associate Technical Editor: R. C. Benson.

This study investigates the use of classical Timoshenko analysis and solution by the method of characteristics to radial impact on curved beams. The application of a concentrated load (bending moment, axial, or radial force) introduces discontinuities in gradients of the displacements—axial extension (u), radial displacement (w), and cross-sectional rotation (ϕ). Discontinuities in the displacement gradients propagate along characteristic lines which may or may not coincide with lines defining the mesh network normally employed for solution by the method of characteristics (Chou and Mortimer, 1967; Mortimer and Hoburg, 1969). Treatment of discontinuities along lines not conforming to the standard characteristic network is complicated. A radial load modeled as a concentrated shear force produces a discontinuity in the radial displacement gradient which propagates along a characteristic not coincident with the standard network. For situations involving three different wave propagation modes, as in the present study, the numerical solution procedure is significantly more complex. The present investigation overcomes this difficulty by approximating the concentrated shear force by distributing a force linearly over a small segment of the beam to eliminate all displacement gradient discontinuities. This study utilizes a one-dimensional theory based on Morley's (1961), with spatial location as the independent variable, to examine the response of circular rings to radial impact.

Assumptions and Governing Equations

Figure 1 illustrates an element in a curved beam; the circumferential and radial displacements ($\bar{u}$ and $\bar{w}$) are described by

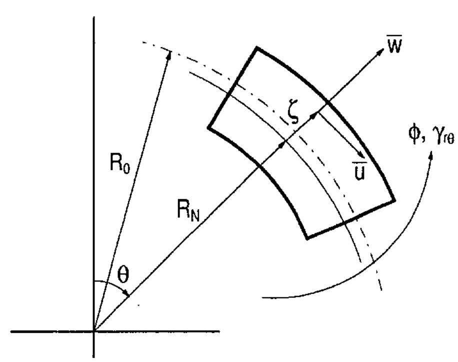

Fig. 1 Displacements in a curved beam segment

$$\bar{u}(\theta, t, r) = u(\theta, t, R_N) - \zeta\phi(\theta, t) \quad (1a)$$

$$\bar{w}(\theta, t, r) = w(\theta, t, R_N) \quad (1b)$$

where u and w are the circumferential and radial displacements, respectively, at the neutral axis

ζ is the radial distance from the neutral axis (i.e., $r = R_N + \zeta$),
R_N is the radius of curvature of the neutral axis of the curved beam,
ϕ is the rotation of the cross section.

The strain-displacement relations in polar coordinates are

$$\epsilon_{\theta\theta} = \frac{1}{r}\frac{\partial \bar{u}}{\partial \theta} + \frac{\bar{w}}{r} \quad (2a)$$

$$\gamma_{r\theta} = \frac{1}{r}\frac{\partial \bar{w}}{\partial \theta} + \frac{\partial \bar{u}}{\partial r} - \frac{\bar{u}}{r}. \quad (2b)$$

Substitution of the kinematic relations (1) into Eq. (2) yields the following strains:

$$\epsilon_{\theta\theta} = \frac{1}{R_N + \zeta}\left(\frac{\partial u}{\partial \theta} - \zeta\frac{\partial \phi}{\partial \theta} + w\right) \quad (3a)$$

$$\gamma_{r\theta} = \frac{1}{R_N + \zeta}\left(\frac{\partial w}{\partial \theta} - u + \zeta\phi\right) - \phi. \quad (3b)$$

Assuming the plane stress ($\sigma_{rr} = \sigma_{zz} = 0$), Hooke's law results in

$$\sigma_{\theta\theta} = E\epsilon_{\theta\theta} \quad (4a)$$

$$\tau_{r\theta} = \kappa G\gamma_{r\theta} \quad (4b)$$

where κ is the shear correction factor.

With respect to a beam cross section, Eqs. (4a) and (3a) combine to yield the axial force in a cross section:

$$N = \int_A \sigma_{\theta\theta}dA = \frac{EA}{R_N}\left(\frac{\partial u}{\partial \theta} + w\right). \quad (5)$$

Equations (4b) and (3b) provide the shear force

$$V = \int_A \tau_{r\theta}dA = \kappa GA\left[\frac{1}{R_N}\left(\frac{\partial w}{\partial \theta} - u\right) - \phi\right]. \quad (6)$$

Similarly, the bending moment is obtained from Eqs. (4a) and (3a):

$$M = \int_A \sigma_{\theta\theta}\zeta dA = EAe\frac{\partial \phi}{\partial \theta}. \quad (7)$$

The above expressions are obtained based on the following identities for curved beams (Boresi et al., 1993):

$$\int_A \frac{dA}{R_N + \zeta} = \frac{A}{R_N} \quad \text{and} \quad \int_A \frac{\zeta dA}{R_N + \zeta} = 0.$$

With reference to Fig. 2, the resulting equations of motion are

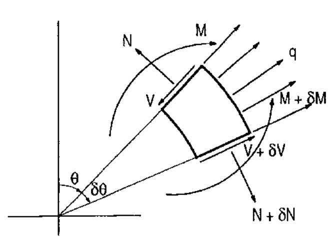

Fig. 2 Forces acting on a curved beam segment

$$R_o\frac{\partial N}{\partial s} + V = \rho A\{\ddot{u}(R_N + e) - \ddot{\phi}[e(R_N + e) + \bar{h}^2]\} \quad (8a)$$

$$R_o\frac{\partial V}{\partial s} - N + R_N q = \rho\ddot{w}A(R_N + e) \quad (8b)$$

$$R_o\frac{\partial M}{\partial s} + R_N V = \rho\{\ddot{u}A[e(R_N + e) + \bar{h}^2] - \ddot{\phi}A[R_N(e^2 + \bar{h}^2) + e(3\bar{h}^2 + e^2)]\} \quad (8c)$$

where

e is the distance between the neutral axis and the centroid of the cross section,
R_o is the radius of curvature of the centroidal axis,
$\bar{h}$ is the radius of gyration of the beam cross section about the centroid,

$$s = R_o\theta; \quad \int_A \zeta dA = eA; \quad \int_A \zeta^2 dA = A(\bar{h}^2 + e^2),$$

and

$$\int_A \zeta^3 dA = eA(3\bar{h}^2 + e^2)$$

for cross sections that are symmetrical about the vertical through the centroid.

The variables are nondimensionalized according to

$$s^* = \frac{s}{\bar{h}}, \quad u^* = \frac{u}{\bar{h}}, \quad w^* = \frac{w}{\bar{h}}, \quad N^* = \frac{N}{EA},$$

$$V^* = \frac{V}{EA}, \quad M^* = \frac{M}{EA\bar{h}}$$

$$\beta = \frac{\bar{h}}{R_o}, \quad \alpha = \frac{R_N}{R_o}, \quad t^* = \frac{ct}{\bar{h}}, \quad q^* = \frac{q\bar{h}}{EA},$$

$$k = \frac{E}{\kappa G}, \quad c = \sqrt{\frac{E}{\rho}}.$$

The governing equations can thus be expressed in terms of *generalized forces* N^*, V^*, M^* (axial and shear forces and bending moment):

$$\frac{1}{\alpha}\frac{\partial N^*}{\partial s^*} + \frac{\beta}{\alpha}V^* = \frac{1}{\alpha}\ddot{u}^* - \ddot{\phi}^*\left(\frac{\beta}{\alpha} + \frac{1}{\alpha\beta} - \frac{1}{\beta}\right) \quad (9a)$$

$$\frac{1}{\alpha}\frac{\partial V^*}{\partial s^*} - \frac{\beta}{\alpha}N^* + q^* = \frac{1}{\alpha}\ddot{w}^* \quad (9b)$$

$$\frac{\beta}{\alpha}\frac{\partial M^*}{\partial s^*} + \beta V^* = -\ddot{u}^*\left(\frac{\beta}{\alpha} + \frac{1}{\alpha\beta} - \frac{1}{\beta}\right)\beta + \ddot{\phi}^*\left(3\frac{\beta}{\alpha} + \frac{1}{\alpha\beta} + \frac{\alpha}{\beta} - 2\beta - \frac{2}{\beta}\right) \quad (9c)$$

$$N^* = \frac{1}{\alpha}\frac{\partial u^*}{\partial s^*} + \frac{\beta}{\alpha}w^* \quad (9d)$$

$$V^* = \frac{1}{k}\left(\frac{1}{\alpha}\frac{\partial w^*}{\partial s^*} - \frac{\beta}{\alpha}u^* - \phi^*\right) \quad (9e)$$

$$M^* = \frac{1}{\beta^2}(1 - \alpha)\frac{\partial \phi^*}{\partial s^*}. \quad (9f)$$

An alternative set of governing equations can be formulated in terms of the *generalized displacements* u^*, w^*, and ϕ^*, by eliminating N^*, V^*, and M^*:

$$\frac{1}{\alpha^2}\frac{\partial^2 u^*}{\partial s^{*2}} - \frac{1}{\alpha}\frac{\partial^2 u^*}{\partial t^{*2}} + \left(\frac{\beta}{\alpha} + \frac{1}{\alpha\beta} - \frac{1}{\beta}\right)\frac{\partial^2 \phi^*}{\partial t^{*2}} + \frac{\beta}{\alpha^2}\left(1 + \frac{1}{k}\right)\frac{\partial w^*}{\partial s^*} - \frac{\beta^2}{\alpha^2 k}u^* - \frac{\beta}{\alpha k}\phi^* = 0 \quad (10a)$$

$$\frac{1}{\alpha^2 k}\frac{\partial^2 w^*}{\partial s^{*2}} - \frac{1}{\alpha}\frac{\partial^2 w^*}{\partial t^{*2}} - \frac{\beta}{\alpha^2}\left(1 + \frac{1}{k}\right)\frac{\partial u^*}{\partial s^*} - \frac{1}{\alpha k}\frac{\partial \phi^*}{\partial s^*} - \frac{\beta^2}{\alpha^2}w^* = -q^* \quad (10b)$$

$$\frac{(1-\alpha)}{\alpha\beta}\frac{\partial^2 \phi^*}{\partial s^{*2}} - \left(3\frac{\beta}{\alpha} + \frac{1}{\alpha\beta} + \frac{\alpha}{\beta} - 2\beta - \frac{2}{\beta}\right)\frac{\partial^2 \phi^*}{\partial t^{*2}} + \left(\frac{\beta}{\alpha} + \frac{1}{\alpha\beta} - \frac{1}{\beta}\right)\beta\frac{\partial^2 u}{\partial t^{*2}} + \frac{\beta}{\alpha k}\frac{\partial w^*}{\partial s^*} - \frac{\beta^2}{\alpha k}u^* - \frac{\beta}{k}\phi = 0. \quad (10c)$$

Both nondimensionalized sets of governing equations contain two parameters, β and α, which influence wave propagation in circular rings. β quantifies curvature, which increases with the value of β; a zero value corresponds to a straight beam. The parameter α defines the offset between the neutral and centroidal axes of the cross section; the larger the curvature, the larger the offset, while $\alpha = 1$ corresponds to a straight beam, in which the neutral and centroidal axes coincide. The value of α also depends on cross-sectional shape and on β. Rings of identical curvature (β) but different cross section have different values of α.

$$c_1^* = \left\{\frac{(1 - 2\alpha\beta^2 - \alpha + 3\beta^2) + \sqrt{(1 - 2\alpha\beta^2 - \alpha + 3\beta^2)^2 - 4\alpha\beta^2(1-\beta^2)(1-\alpha)}}{2(1-\alpha)}\right\}^{1/2} \quad (11a)$$

$$c_2^* = \left\{\frac{(1 - 2\alpha\beta^2 - \alpha + 3\beta^2) - \sqrt{(1 - 2\alpha\beta^2 - \alpha + 3\beta^2)^2 - 4\alpha\beta^2(1-\beta^2)(1-\alpha)}}{2(1-\alpha)}\right\}^{1/2} \quad (11b)$$

$$c_3^* = \sqrt{\frac{1}{\alpha k}} \quad (11c)$$

For a rectangular cross section,

$$\alpha = \beta\sqrt{12}/\ln\left(\frac{1 + \beta\sqrt{3}}{1 - \beta\sqrt{3}}\right).$$

For a circular cross section,

$$\alpha = \tfrac{1}{2} + \sqrt{\tfrac{1}{4} - \beta^2}.$$

The parameter k is defined as $E/(\kappa G)$, with the shear correction factor κ relating the cross-sectional shear force to the shear strain at the neutral axis.

For a rectangular cross section,

$$\kappa = \frac{2\alpha(1-\alpha)}{3\beta^2 + 2\alpha - \alpha^2 - 1}.$$

For a circular cross section,

$$\kappa = \frac{3\alpha(1-\alpha)}{4\beta^2 - \alpha^2 + 2\alpha - 1}.$$

For isotropic materials, the corresponding values of k are

$$k = \frac{(3\beta^2 + 2\alpha - \alpha^2 - 1)(1 + \upsilon)}{\alpha(1-\alpha)}$$

for a rectangular cross section

and

$$k = \frac{2(4\beta^2 - \alpha^2 + 2\alpha - 1)(1 + \upsilon)}{3\alpha(1-\alpha)}$$

for a circular cross section.

Solution by the Method of Characteristics

The systems of Eqs. ($9a$–f) and ($10a$–c) are solved numerically using the method of characteristics. The general approach adopted is similar to that used by Chou and Mortimer (1967) and Plass (1958). However, the present numerical solution scheme differs in several aspects, a major one being the use of higher-order interpolation, which is found to yield better correlation with experimental results. Both forms of the governing equations are solved, because although they are mathematically equivalent, they generate differences in the numerical results obtained.

Generalized Force-Velocity Formulation. Derivation of the characteristic lines and equations in this formulation is achieved through matrix diagonalization and manipulation of the equations of motion, the details of which are described by Quah (1994). Three pairs of characteristic lines are obtained, each pair corresponding to a mode of wave propagation. These characteristic lines and their accompanying characteristic equations are defined by the nondimensionalized wave speeds:

where $c_1^* > c_2^* > c_3^*$.

Along the characteristics $ds^*/dt^* = \pm c_1^*$,

$$\alpha\left(\frac{\beta}{\alpha} + \frac{1}{\alpha\beta} - \frac{1}{\beta}\right)c_1^{*2}dN^* + \left(c_1^{*2} - \frac{1}{\alpha}\right)dM^* \mp \left(\frac{\beta}{\alpha} + \frac{1}{\alpha\beta} - \frac{1}{\beta}\right)c_1^* d\dot{u}^* \mp \frac{(1-\alpha)}{\beta^2 c_1^*}\left(c_1^{*2} - \frac{1}{\alpha}\right)d\dot{\phi}^* \pm \alpha\left[\beta\left(\frac{\beta}{\alpha} + \frac{1}{\alpha\beta} - \frac{1}{\beta}\right)c_1^{*2} + \left(c_1^{*2} - \frac{1}{\alpha}\right)\right]c_1^* V^* dt^* - \beta\left(\frac{\beta}{\alpha} + \frac{1}{\alpha\beta} - \frac{1}{\beta}\right)c_1^{*2}\dot{w}^* dt^* = 0. \quad (12a)$$

Along the characteristics $ds^*/dt^* = \pm c_2^*$

$$\alpha\left(\frac{\beta}{\alpha}+\frac{1}{\alpha\beta}-\frac{1}{\beta}\right)c_2^{*2}dN^*+\left(c_2^{*2}-\frac{1}{\alpha}\right)dM^*$$

$$\mp\left(\frac{\beta}{\alpha}+\frac{1}{\alpha\beta}-\frac{1}{\beta}\right)c_2^*d\dot{u}^*\mp\frac{(1-\alpha)}{\beta^2c_2^*}\left(c_2^{*2}-\frac{1}{\alpha}\right)d\dot{\phi}^*$$

$$\pm\alpha\left[\beta\left(\frac{\beta}{\alpha}+\frac{1}{\alpha\beta}-\frac{1}{\beta}\right)c_2^{*2}+\left(c_2^{*2}-\frac{1}{\alpha}\right)\right]c_2^*V^*dt^*$$

$$-\beta\left(\frac{\beta}{\alpha}+\frac{1}{\alpha\beta}-\frac{1}{\beta}\right)c_2^{*2}\dot{w}^*dt^*=0. \quad (12b)$$

Along the characteristics $ds^*/dt^*=\pm c_3^*$

$$dV^*\mp c_3^*d\dot{w}^*\mp\beta c_3^*N^*dt^*+\frac{\beta}{\alpha k}\dot{u}^*dt^*$$

$$+\frac{1}{k}\dot{\phi}^*dt^*\pm c_3^*q^*dt^*=0. \quad (12c)$$

These three pairs of coupled equations can be written in finite difference form along their respective characteristics. Figure 3 shows a characteristic mesh in the t^*-s^* plane. The intersections of the characteristics, $ds^*/dt^*=\pm c_1^*$, define the nodes of the mesh. Figure 4(a) shows a typical element in the mesh on which the computation scheme is based. The quantities, N^*, V^*, M^*, $\dot{u}^*$, $\dot{w}^*$, and $\dot{\phi}^*$ at points A, B, C, A_2, B_2, C_2, A_3, B_3, and C_3 are identified by their respective subscripts. All the quantities at point P are unknown and have to be computed from known values at the neighboring points A, B, and C. The solution thus requires the evaluation of the following system of simultaneous equations:

$$\begin{bmatrix}
\alpha\left(\frac{\beta}{\alpha}+\frac{1}{\alpha\beta}-\frac{1}{\beta}\right)c_1^{*2} & \frac{\alpha\delta t^*}{2}\left[\beta\left(\frac{\beta}{\alpha}+\frac{1}{\alpha\beta}-\frac{1}{\beta}\right)c_1^{*2}+c_1^{*2}-\frac{1}{\alpha}\right]c_1^* & c_1^{*2}-\frac{1}{\alpha} & -\left(\frac{\beta}{\alpha}+\frac{1}{\alpha\beta}-\frac{1}{\beta}\right)c_1^* & -\frac{\beta\delta t^*}{2}\left(\frac{\beta}{\alpha}+\frac{1}{\alpha\beta}-\frac{1}{\beta}\right)c_1^{*2} & -\frac{(1-\alpha)}{\beta^2c_1^*}\left(c_1^{*2}-\frac{1}{\alpha}\right)\\
\alpha\left(\frac{\beta}{\alpha}+\frac{1}{\alpha\beta}-\frac{1}{\beta}\right)c_1^{*2} & -\frac{\alpha\delta t^*}{2}\left[\beta\left(\frac{\beta}{\alpha}+\frac{1}{\alpha\beta}-\frac{1}{\beta}\right)c_1^{*2}+c_1^{*2}-\frac{1}{\alpha}\right]c_1^* & c_1^{*2}-\frac{1}{\alpha} & \left(\frac{\beta}{\alpha}+\frac{1}{\alpha\beta}-\frac{1}{\beta}\right)c_1^* & -\frac{\beta\delta t^*}{2}\left(\frac{\beta}{\alpha}+\frac{1}{\alpha\beta}-\frac{1}{\beta}\right)c_1^{*2} & \frac{(1-\alpha)}{\beta^2c_1^*}\left(c_1^{*2}-\frac{1}{\alpha}\right)\\
\alpha\left(\frac{\beta}{\alpha}+\frac{1}{\alpha\beta}-\frac{1}{\beta}\right)c_2^{*2} & \frac{\alpha\delta t_2^*}{2}\left[\beta\left(\frac{\beta}{\alpha}+\frac{1}{\alpha\beta}-\frac{1}{\beta}\right)c_2^{*2}+c_2^{*2}-\frac{1}{\alpha}\right]c_2^* & c_2^{*2}-\frac{1}{\alpha} & -\left(\frac{\beta}{\alpha}+\frac{1}{\alpha\beta}-\frac{1}{\beta}\right)c_2^* & -\frac{\beta\delta t_2^*}{2}\left(\frac{\beta}{\alpha}+\frac{1}{\alpha\beta}-\frac{1}{\beta}\right)c_2^{*2} & -\frac{(1-\alpha)}{\beta^2c_2^*}\left(c_2^{*2}-\frac{1}{\alpha}\right)\\
\alpha\left(\frac{\beta}{\alpha}+\frac{1}{\alpha\beta}-\frac{1}{\beta}\right)c_2^{*2} & -\frac{\alpha\delta t_2^*}{2}\left[\beta\left(\frac{\beta}{\alpha}+\frac{1}{\alpha\beta}-\frac{1}{\beta}\right)c_2^{*2}+c_2^{*2}-\frac{1}{\alpha}\right]c_2^* & c_2^{*2}-\frac{1}{\alpha} & \left(\frac{\beta}{\alpha}+\frac{1}{\alpha\beta}-\frac{1}{\beta}\right)c_2^* & -\frac{\beta\delta t_2^*}{2}\left(\frac{\beta}{\alpha}+\frac{1}{\alpha\beta}-\frac{1}{\beta}\right)c_2^{*2} & \frac{(1-\alpha)}{\beta^2c_2^*}\left(c_2^{*2}-\frac{1}{\alpha}\right)\\
-\frac{\beta\delta t_3^*}{2}c_3^* & 1 & 0 & \frac{\beta\delta t_3^*}{2\alpha k} & -c_3^* & \frac{\delta t_3^*}{2k}\\
\frac{\beta\delta t_3^*}{2}c_3^* & 1 & 0 & \frac{\beta\delta t_3^*}{2\alpha k} & c_3^* & \frac{\delta t_3^*}{2k}
\end{bmatrix}
\begin{bmatrix} N_P^*\\ V_P^*\\ M_P^*\\ \dot{u}_P^*\\ \dot{w}_P^*\\ \dot{\phi}_P^*\end{bmatrix}$$

$$=\begin{bmatrix}
\alpha\left(\frac{\beta}{\alpha}+\frac{1}{\alpha\beta}-\frac{1}{\beta}\right)c_1^{*2}N_A^*-\frac{\alpha\delta t^*}{2}\left[\beta\left(\frac{\beta}{\alpha}+\frac{1}{\alpha\beta}-\frac{1}{\beta}\right)c_1^{*2}+c_1^{*2}-\frac{1}{\alpha}\right]c_1^*V_A^*+\left(c_1^{*2}-\frac{1}{\alpha}\right)M_A^*-\left(\frac{\beta}{\alpha}+\frac{1}{\alpha\beta}-\frac{1}{\beta}\right)c_1^*\dot{u}_A^*+\frac{\beta\delta t^*}{2}\left(\frac{\beta}{\alpha}+\frac{1}{\alpha\beta}-\frac{1}{\beta}\right)c_1^{*2}\dot{w}_A^*-\frac{(1-\alpha)}{\beta^2c_1^*}\left(c_1^{*2}-\frac{1}{\alpha}\right)\dot{\phi}_A^*\\
\alpha\left(\frac{\beta}{\alpha}+\frac{1}{\alpha\beta}-\frac{1}{\beta}\right)c_1^{*2}N_C^*+\frac{\alpha\delta t^*}{2}\left[\beta\left(\frac{\beta}{\alpha}+\frac{1}{\alpha\beta}-\frac{1}{\beta}\right)c_1^{*2}+c_1^{*2}-\frac{1}{\alpha}\right]c_1^*V_C^*+\left(c_1^{*2}-\frac{1}{\alpha}\right)M_C^*+\left(\frac{\beta}{\alpha}+\frac{1}{\alpha\beta}-\frac{1}{\beta}\right)c_1^*\dot{u}_C^*+\frac{\beta\delta t^*}{2}\left(\frac{\beta}{\alpha}+\frac{1}{\alpha\beta}-\frac{1}{\beta}\right)c_1^{*2}\dot{w}_C^*+\frac{(1-\alpha)}{\beta^2c_1^*}\left(c_1^{*2}-\frac{1}{\alpha}\right)\dot{\phi}_C^*\\
\alpha\left(\frac{\beta}{\alpha}+\frac{1}{\alpha\beta}-\frac{1}{\beta}\right)c_2^{*2}N_{A_2}^*-\frac{\alpha\delta t_2^*}{2}\left[\beta\left(\frac{\beta}{\alpha}+\frac{1}{\alpha\beta}-\frac{1}{\beta}\right)c_2^{*2}+c_2^{*2}-\frac{1}{\alpha}\right]c_2^*V_{A_2}^*+\left(c_2^{*2}-\frac{1}{\alpha}\right)M_{A_2}^*-\left(\frac{\beta}{\alpha}+\frac{1}{\alpha\beta}-\frac{1}{\beta}\right)c_2^*\dot{u}_{A_2}^*+\frac{\beta\delta t_2^*}{2}\left(\frac{\beta}{\alpha}+\frac{1}{\alpha\beta}-\frac{1}{\beta}\right)c_2^{*2}\dot{w}_{A_2}^*-\frac{(1-\alpha)}{\beta^2c_2^*}\left(c_2^{*2}-\frac{1}{\alpha}\right)\dot{\phi}_{A_2}^*\\
\alpha\left(\frac{\beta}{\alpha}+\frac{1}{\alpha\beta}-\frac{1}{\beta}\right)c_2^{*2}N_{C_2}^*+\frac{\alpha\delta t_2^*}{2}\left[\beta\left(\frac{\beta}{\alpha}+\frac{1}{\alpha\beta}-\frac{1}{\beta}\right)c_2^{*2}+c_2^{*2}-\frac{1}{\alpha}\right]c_2^*V_{C_2}^*+\left(c_2^{*2}-\frac{1}{\alpha}\right)M_{C_2}^*+\left(\frac{\beta}{\alpha}+\frac{1}{\alpha\beta}-\frac{1}{\beta}\right)c_2^*\dot{u}_{C_2}^*+\frac{\beta\delta t_2^*}{2}\left(\frac{\beta}{\alpha}+\frac{1}{\alpha\beta}-\frac{1}{\beta}\right)c_2^{*2}\dot{w}_{C_2}^*+\frac{(1-\alpha)}{\beta^2c_2^*}\left(c_2^{*2}-\frac{1}{\alpha}\right)\dot{\phi}_{C_2}^*\\
\frac{\beta\delta t_3^*}{2}c_3^*N_{A_3}^*+V_{A_3}^*-\frac{\beta\delta t_3^*}{2\alpha k}\dot{u}_{A_3}^*-c_3^*\dot{w}_{A_3}^*-\frac{\delta t_3^*}{2k}\dot{\phi}_{A_3}^*-\frac{\alpha c_3^*\delta t_3^*}{2}\left(q_P^*+q_A^*\right)\\
-\frac{\beta\delta t_3^*}{2}c_3^*N_{C_3}^*+V_{C_3}^*-\frac{\beta\delta t_3^*}{2\alpha k}\dot{u}_{C_3}^*+c_3^*\dot{w}_{A_3}^*-\frac{\delta t_3^*}{2k}\dot{\phi}_{C_3}^*+\frac{\alpha c_3^*\delta t_3^*}{2}\left(q_P^*+q_{C_3}^*\right)
\end{bmatrix}. \quad (13)$$

The values of quantities $q_{A_2}^*$, $q_{A_3}^*$, $q_{C_2}^*$, and $q_{C_3}^*$ can be interpolated from q_A^*, q_B^* and q_C^*; for linear interpolation, this is effected using

$$\left.\begin{aligned} q_{A_3}^* &= q_B^*+\frac{2c_3^*}{c_1^*+c_3^*}(q_A^*-q_B^*)\\ q_{C_3}^* &= q_B^*+\frac{2c_3^*}{c_1^*+c_3^*}(q_C^*-q_B^*)\end{aligned}\right\}. \quad (14)$$

Quantities such as $\dot{u}_{A_2}^*$, $\dot{u}_{A_3}^*$, $\dot{w}_{A_2}^*$, $\dot{w}_{A_3}^*$, $\dot{\phi}_{A_2}^*$, $\dot{\phi}_{A_3}^*$, $N_{A_2}^*$, $N_{A_3}^*$, $M_{A_2}^*$, $M_{A_3}^*$, $\dot{u}_{C_2}^*$, $\dot{u}_{C_3}^*$, $\dot{w}_{C_2}^*$, $\dot{w}_{C_3}^*$, $\dot{\phi}_{C_2}^*$, $\dot{\phi}_{C_3}^*$, $N_{C_2}^*$, $N_{C_3}^*$, $V_{C_2}^*$, $V_{C_3}^*$, $M_{C_2}^*$, and $M_{C_3}^*$ are evaluated in the same manner. Figures 4(b) and 4(c) show generic elements adjacent to the t^*-axis and the line RS (Fig. 3), respectively. For an element adjacent to the t^*-axis, only the equations for the negative characteristics are needed for the computation of values. Similarly, an element adjacent to the line RS requires the equations for the positive characteristics. In both these cases there are insufficient equations to solve for the six unknowns N_P^*, V_P^*, M_P^*, $\dot{u}_P^*$, $\dot{w}_P^*$, and $\dot{\phi}_P^*$. Three more independent equations are needed for each of the two cases. These additional equations are obtained from boundary conditions; e.g., a free boundary has $N_P^*=V_P^*=M_P^*=0$. For a circular ring subjected to radial impact, symmetry boundary conditions are formulated to reduce the problem to that of half the ring, whereby $V_P^*=\dot{u}_P^*=\dot{\phi}_P^*=0$. For initial conditions with a point load at O (Fig. 3), the solution process commences with computation of the unknowns in the lowermost element OUV and proceeds progressively upwards to adjoining elements. This procedure is utilized with the boundary and loading conditions shown in Fig. 5, in which a point load pulse is approximated by a linearly distributed force applied over a small ring segment of length δs^* (Fig. 5) and which has a triangular time variation. Displacements are computed by integrating the velocities; e.g., u^* is evaluated from (Fig. 4(a)):

$$u_P^*=u_B^*+\delta t^*(\dot{u}_B^*+\dot{u}_P^*) \quad (15)$$

Generalized Displacement Formulation. The equations along the characteristic lines can also be expressed in terms of generalized displacements and their derivatives: u'^*, $\dot{u}^*$, u^*,

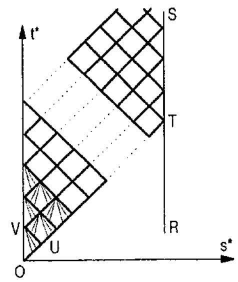

Fig. 3 Characteristics mesh in the $s^* - t^*$ plane

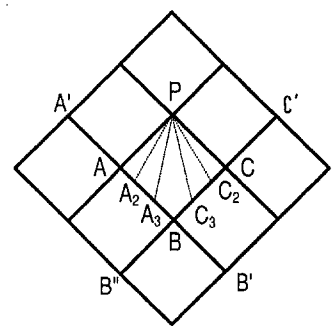

Fig. 6 Grid points used in higher-order interpolation scheme

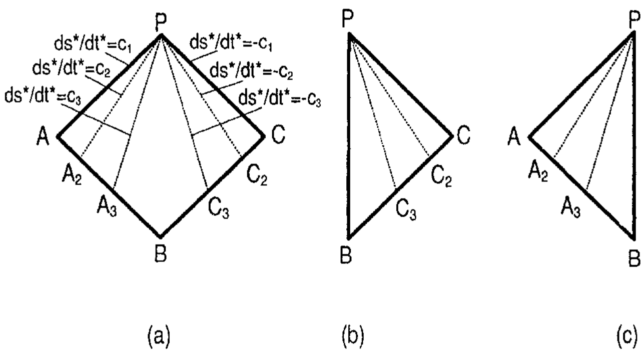

Fig. 4 Typical elements for solution of finite difference equations

w'^*, $\dot{w}^*$, w^*, ϕ'^*, $\dot{\phi}^*$, and ϕ^*. This entails elimination of the second-order terms u''^*, $\ddot{u}^*$, w''^*, $\ddot{w}^*$, ϕ''^*, and $\ddot{\phi}^*$ from Eq. (10), with the assumption that displacement derivatives of u^*, w^*, and ϕ^* are continuous in the $s^* - t^*$ plane. In this approach, the characteristic equations are more complicated than those in the generalized force-velocity formulation.

Along the characteristics $ds^*/dt^* = \pm c_1^*$:

$$F_1 c_1^{*2} du'^* \mp -F_1 c_1^* d\dot{u}^* \pm \frac{F_2 \beta^2 c_1^* dt^*}{\alpha} u^* \pm \left(F_1 F_6 c_1^{*2} + \frac{F_7}{k}\right)\beta c_1^* dt^* w'^* + \frac{(1-\alpha)F_7}{\beta} d\phi'^* \pm F_4 c_1^* d\dot{\phi}^* \pm F_2 \beta c_1^* dt^* \phi^* = 0. \quad (16a)$$

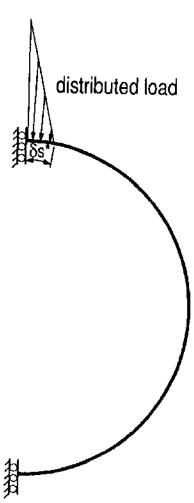

Fig. 5 Load idealization for a half ring

Along the characteristics $ds^*/dt^* = \pm c_2^*$:

$$F_1 c_2^{*2} du'^* \mp -F_1 c_2^* d\dot{u}^* \pm \frac{F_3 \beta^2 c_2^* dt^*}{\alpha} u^* \pm \left(F_1 F_6 c_2^{*2} + \frac{F_8}{k}\right)\beta c_2^* dt^* w'^* + \frac{(1-\alpha)F_8}{\beta} d\phi'^* \pm F_5 c_2^* d\dot{\phi}^* \pm F_3 \beta c_2^* dt^* \phi^* = 0. \quad (16b)$$

Along the characteristics $ds^*/dt^* = \pm c_3^*$:

$$\mp \frac{F_6 \beta c_3^* dt^*}{\alpha^2} u'^* + \frac{1}{\alpha^2 k} dw'^* \mp \frac{c_3^*}{\alpha} d\dot{w}^* \mp \frac{\beta^2 c_3^* dt^*}{\alpha^2} w^* \mp \frac{c_3^* dt^*}{\alpha k} \phi'^* = \mp c_3^* dt^* q^* \quad (16c)$$

where

$$F_1 = \frac{1 - \alpha + \beta^2}{\alpha^3}, \quad F_2 = \frac{1 - c_1^{*2} - \beta^2 c_1^{*2}}{\alpha^2 k},$$

$$F_3 = \frac{1 - c_2^{*2} - \beta^2 c_2^{*2}}{\alpha^2 k},$$

$$F_4 = \frac{1 - 2\alpha + \alpha^2 + 3\beta^2 - 2\alpha\beta^2 - \alpha\beta^2 c_1^{*2} + \alpha\beta^4 c_1^{*2}}{\alpha^3 \beta},$$

$$F_5 = \frac{1 - 2\alpha + \alpha^2 + 3\beta^2 - 2\alpha\beta^2 - \alpha\beta^2 c_2^{*2} + \alpha\beta^4 c_2^{*2}}{\alpha^3 \beta},$$

$$F_6 = 1 + \frac{1}{k}, \quad F_7 = \frac{\alpha c_1^{*2} - 1}{\alpha^3} \quad \text{and} \quad F_8 = \frac{\alpha c_2^{*2} - 1}{\alpha^3},$$

and c_1^*, c_2^*, and c_3^* are defined previously in Eq. (11).

The solution procedure is similar to that for the generalized force-velocity formulation. However, there are now nine quantities to be evaluated from only six characteristic equations. Three

Table 1 Comparison of errors in the generalized force-velocity and generalized displacement formulations

Time*	0.5	1	1.4
Absolute percent error in momentum value (generalized force-velocity formulation)	0.38	2.3	4.4
Absolute percent error in momentum value (generalized displacement formulation)	3.0	4.3	20.0

Note: time* refers to the ratio: time elapsed after q^* acts/time for stress wave (speed c_1) to travel through half the ring.

other independent equations are obtained from continuity considerations:

$$\left.\begin{aligned} du^* &= \dot{u}^* dt^* + u'^* ds^* \\ dw^* &= \dot{w}^* dt^* + w'^* ds^* \\ d\phi^* &= \dot{\phi}^* dt^* + \phi'^* ds^* \end{aligned}\right\} . \tag{17}$$

The finite difference form of the characteristic and continuity equations as applied to a typical element shown in Fig. $4(a)$ are

$$\begin{bmatrix}
F_1c_1^{*2} & -F_1c_1^* & \frac{F_2\beta^2c_1^*\delta t^*}{2\alpha} & \left(F_1F_6c_1^{*2}+\frac{F_7}{k}\right)\frac{\beta c_1^*\delta t^*}{2} & 0 & 0 & \frac{(1-\alpha)F_7}{\beta} & F_4c_1^* & \frac{F_2\beta c_1^*\delta t^*}{2} \\
F_1c_1^{*2} & F_1c_1^* & -\frac{F_2\beta^2c_1^*\delta t^*}{2\alpha} & -\left(F_1F_6c_1^{*2}+\frac{F_7}{k}\right)\frac{\beta c_1^*\delta t^*}{2} & 0 & 0 & \frac{(1-\alpha)F_7}{\beta} & -F_4c_1^* & -\frac{F_2\beta c_1^*\delta t^*}{2} \\
F_1c_2^{*2} & -F_1c_2^* & \frac{F_3\beta^2c_2^*\delta t_2^*}{2\alpha} & \left(F_1F_6c_2^{*2}+\frac{F_8}{k}\right)\frac{\beta c_2^*\delta t_2^*}{2} & 0 & 0 & \frac{(1-\alpha)F_8}{\beta} & F_5c_2^* & \frac{F_3\beta c_2^*\delta t_2^*}{2} \\
F_1c_2^{*2} & F_1c_2^* & -\frac{F_3\beta^2c_2^*\delta t_2^*}{2\alpha} & -\left(F_1F_6c_2^{*2}+\frac{F_8}{k}\right)\frac{\beta c_2^*\delta t_2^*}{2} & 0 & 0 & \frac{(1-\alpha)F_8}{\beta} & -F_5c_2^* & -\frac{F_3\beta c_2^*\delta t_2^*}{2} \\
-\frac{F_6\beta c_3^*\delta t_3^*}{2\alpha^2} & 0 & 0 & \frac{1}{\alpha^2k} & -\frac{c_3^*}{\alpha} & -\frac{\beta^2c_3^*\delta t_3^*}{2\alpha^2} & -\frac{c_3^*\delta t_3^*}{2\alpha k} & 0 & 0 \\
\frac{F_6\beta c_3^*\delta t_3^*}{2\alpha^2} & 0 & 0 & \frac{1}{\alpha^2k} & \frac{c_3^*}{\alpha} & \frac{\beta^2c_3^*\delta t_3^*}{2\alpha^2} & \frac{c_3^*\delta t_3^*}{2\alpha k} & 0 & 0 \\
-\frac{c_1^*\delta t^*}{2} & -\frac{\delta t^*}{2} & 1 & 0 & 0 & 0 & 0 & 0 & 0 \\
0 & 0 & 0 & -\frac{c_1^*\delta t^*}{2} & -\frac{\delta t^*}{2} & 1 & 0 & 0 & 0 \\
0 & 0 & 0 & 0 & 0 & 0 & -\frac{c_1^*\delta t^*}{2} & -\frac{\delta t^*}{2} & 1
\end{bmatrix}
\begin{bmatrix} u_P'^* \\ \dot{u}_P^* \\ u_P^* \\ w_P'^* \\ \dot{w}_P^* \\ w_P^* \\ \phi_P'^* \\ \dot{\phi}_P^* \\ \phi_P^* \end{bmatrix}$$

$$= \begin{bmatrix}
F_1c_1^{*2}u_A'^* - F_1c_1^*\dot{u}_A^* - \frac{F_2\beta^2c_1^*\delta t^*}{2\alpha}u_A^* - \left(F_1F_6c_1^{*2}+\frac{F_7}{k}\right)\frac{\beta c_1^*\delta t^*}{2}w_A'^* + \frac{(1-\alpha)F_7}{\beta}\phi_A'^* + F_4c_1^*\dot{\phi}_A^* - \frac{F_2\beta c_1^*\delta t^*}{2}\phi_A^* \\
F_1c_1^{*2}u_C'^* + F_1c_1^*\dot{u}_C^* + \frac{F_2\beta^2c_1^*\delta t^*}{2\alpha}u_C^* + \left(F_1F_6c_1^{*2}+\frac{F_7}{k}\right)\frac{\beta c_1^*\delta t^*}{2}w_C'^* + \frac{(1-\alpha)F_7}{\beta}\phi_C'^* - F_4c_1^*\dot{\phi}_C^* + \frac{F_2\beta c_1^*\delta t^*}{2}\phi_C^* \\
F_1c_2^{*2}u_{A_2}'^* - F_1c_2^*\dot{u}_{A_2}^* - \frac{F_3\beta^2c_2^*\delta t_2^*}{2\alpha}u_{A_2}^* - \left(F_1F_6c_2^{*2}+\frac{F_8}{k}\right)\frac{\beta c_2^*\delta t_2^*}{2}w_{A_2}'^* + \frac{(1-\alpha)F_8}{\beta}\phi_{A_2}'^* + F_5c_2^*\dot{\phi}_{A_2}^* - \frac{F_3\beta c_2^*\delta t_2^*}{2}\phi_{A_2}^* \\
F_1c_2^{*2}u_{C_2}'^* + F_1c_2^*\dot{u}_{C_2}^* + \frac{F_3\beta^2c_2^*\delta t_2^*}{2\alpha}u_{C_2}^* + \left(F_1F_6c_2^{*2}+\frac{F_8}{k}\right)\frac{\beta c_2^*\delta t_2^*}{2}w_{C_2}'^* + \frac{(1-\alpha)F_8}{\beta}\phi_{C_2}'^* - F_5c_2^*\dot{\phi}_{C_2}^* + \frac{F_3\beta c_2^*\delta t_2^*}{2}\phi_{C_2}^* \\
\frac{F_6\beta c_3^*\delta t_3^*}{2\alpha^2}u_{A_3}'^* + \frac{1}{\alpha^2k}w_{A_3}'^* - \frac{c_3^*}{\alpha}\dot{w}_{A_3}^* + \frac{\beta^2c_3^*\delta t_3^*}{2\alpha^2}w_{A_3}^* + \frac{c_3^*\delta t_3^*}{2\alpha k}\phi_{A_3}'^* - \frac{c_3^*\delta t_3^*}{2}\left(q_P^* + q_{A_3}^*\right) \\
-\frac{F_6\beta c_3^*\delta t_3^*}{2\alpha^2}u_{C_3}'^* + \frac{1}{\alpha^2k}w_{C_3}'^* + \frac{c_3^*}{\alpha}\dot{w}_{C_3}^* - \frac{\beta^2c_3^*\delta t_3^*}{2\alpha^2}w_{C_3}^* - \frac{c_3^*\delta t_3^*}{2\alpha k}\phi_{C_3}'^* + \frac{c_3^*\delta t_3^*}{2}\left(q_P^* + q_{C_3}^*\right) \\
\frac{c_1^*\delta t^*}{2}u_A'^* + \frac{\delta t^*}{2}\dot{u}_A^* + u_A^* \\
\frac{c_1^*\delta t^*}{2}w_A'^* + \frac{\delta t^*}{2}\dot{w}_A^* + w_A^* \\
\frac{c_1^*\delta t^*}{2}\phi_A'^* + \frac{\delta t^*}{2}\dot{\phi}_A^* + \phi_A^*
\end{bmatrix} . \tag{18}$$

For elements adjacent to the t^*-axis and the line RS (Fig. 3), the boundary conditions for a circular ring under radial loading are $\dot{u}_P^* = u_P^* = w_P'^* = \dot{\phi}_P^* = \phi_P^* = 0$. The finite difference equations for solution of the unknowns for these two types of elements are subsets of Eq. (18). Generalized forces cannot be obtained directly from solutions of the equations in the generalized displacement formulation. They are obtained from the generalized displacements and their derivatives using Eqn. $(9(d-f))$:

Higher-Order Interpolation. Numerical solution of the governing finite difference equations necessitates use of the characteristic mesh shown in Fig. 3. Grid points are defined by intersections of the characteristic lines $ds^*/dt^* = \pm c_1^*$; these are referred to as "standard grid points" of the "standard mesh" depicted. Figures 3 and $4(a)$ show that there are other characteristic lines (dashed) that do not intersect standard grid points. Figure $4(a)$ shows a typical element with characteristic lines $ds^*/dt^* = \pm c_2^*$ and $ds^*/dt^* = \pm c_3^*$ intersecting the standard mesh at points A_2, A_3, C_2, and C_3. Values of the generalized forces, velocities, and displacements at these points can be interpolated from those at standard grid points. The simplest method to do so is described by Eq. (14)—linear interpolation based on two neighboring standard grid points (e.g., for A_2, the neighboring standard grid points are A and B). This approach has been used by Plass (1958) in his study of wave propagation in straight beams. It is also initially used in the present investigation, but a higher-order interpolation scheme is formulated and results of both compared with experiments to ascertain superiority of the latter. With reference to Fig. 6, the proposed higher-order scheme interpolates values of the unknowns at A_2 and A_3 based on values at A', A, B, and B', which are fitted by a cubic polynomial. For C_2 and C_3, the value at C' is still unknown; hence, interpolation is based on three points, C, B, and B'', which are fitted by a quadratic polynomial. Polynomials of higher order (e.g., quartic) are not used because of greater computational cost.

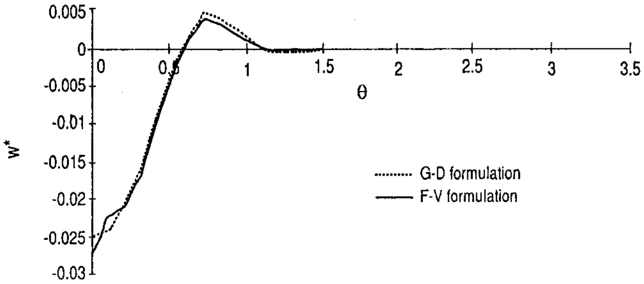

Fig. 7(a)

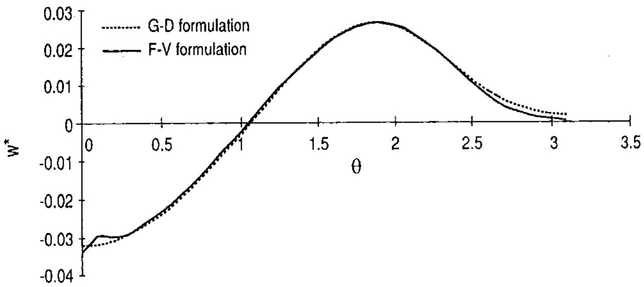

Fig. 7(b)

Fig. 7 Radial displacement (a) $\beta = 0.1$, $\hat{t} = 0.5$; (b) $= 0.1$, $\hat{t} = 2$

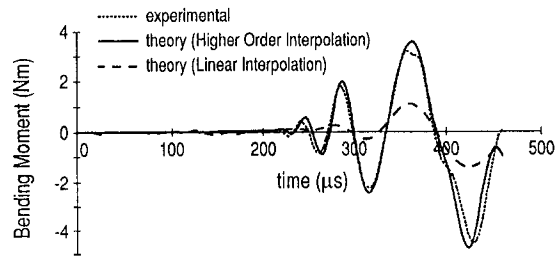

Fig. 9(a) $\theta = 140$ deg

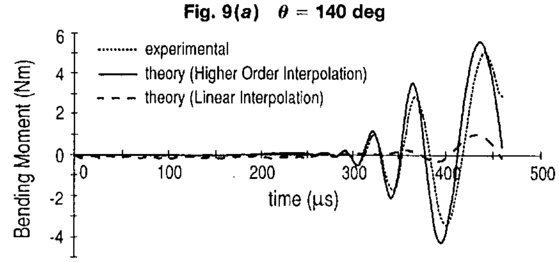

Fig. 9(b) $\theta = 180$ deg

Fig. 9 Comparison of higher-order and linear interpolation methods with experimental data—bending moment history for the brass ring

Comparison Between Force-Velocity and Displacement Formulations

Although the generalized force-velocity and generalized displacement formulations are mathematically equivalent, there are differences in numerical evaluation of their solutions. These arise from discretization and truncation errors. Discretization error results from expression of the differential equations in finite difference form and from assumptions about how quantities vary between grid points. Consider the following:

$$du^* = \dot{u}^* dt^* + u'^* ds^*.$$

In finite difference form (Fig. 4(a)),

$$u_P^* - u_A^* = \frac{\delta t^*}{2}(\dot{u}_P^* + \dot{u}_A^*) + \frac{\delta s^*}{2}(u_P'^* + u_A'^*).$$

The above corresponds to an assumption that variation of $\dot{u}^*$ and u'^* between grid points is linear and thus average values of $\dot{u}^*$ and u'^* between points A and P are used. The two formulations involve different quantities which may vary differently between grid points. The more frequently terms which require an average value between two grid points are used, the less accurate the results. A comparison between the generalized force-velocity and generalized displacement formulations shows that the former has fewer such terms. Hence, the generalized force-velocity formulation is less susceptible to discretization error. An impulse-momentum check substantiates this—the impulse-momentum balance exhibits better agreement for results obtained with a generalized force-velocity formulation. This deviation between impulse and momentum increases as computation proceeds from one grid to the next. Table 1 shows the percentage deviation for a typical simulation, whereby a ring of curvature $\beta = 0.05$ is subjected to an impact (triangular force-time pulse of four units of nondimensional time, acting over one grid length, $\delta s^* = 1$). The percentage error is larger and ultimately grows more rapidly with the generalized displacement formulation. Truncation error is related to the number of computations required in the solution process. The generalized force-velocity formulation involves six quantities and manipulation of six simultaneous equations, whereas the generalized displacement formulation involves nine quantities and nine equations. Hence, the latter is also prone to higher truncation error.

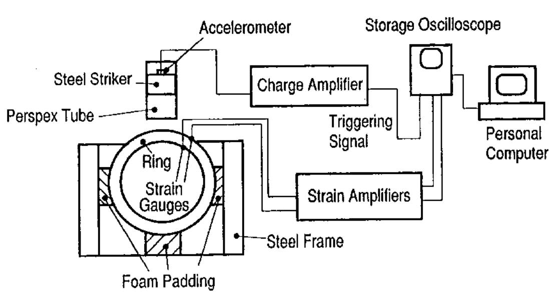

Fig. 8 Schematic diagram of experimental arrangement

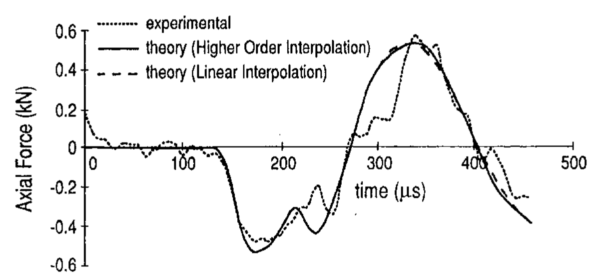

Fig. 10(a) $\theta = 140$ deg

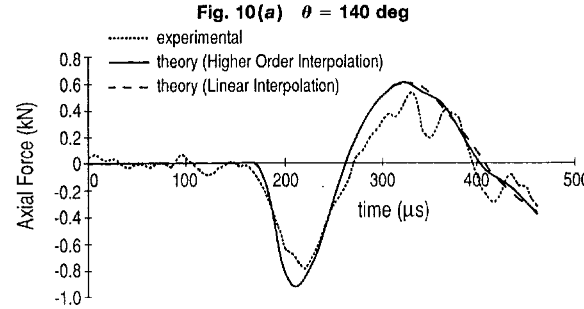

Fig. 10(b) $\theta = 180$ deg

Fig. 10 Comparison of higher order and linear interpolation methods with experimental data—axial force history for the brass ring

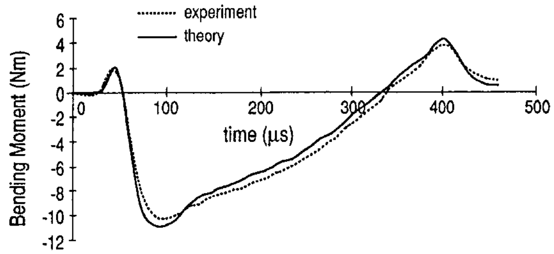

Fig. 11(*a*) θ = 20 deg

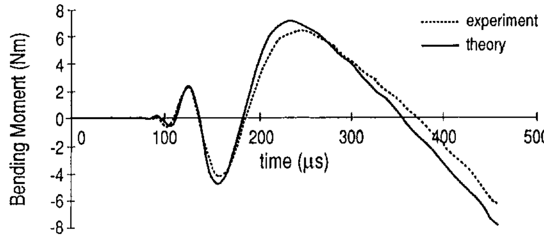

Fig. 11(*b*) θ = 60 deg

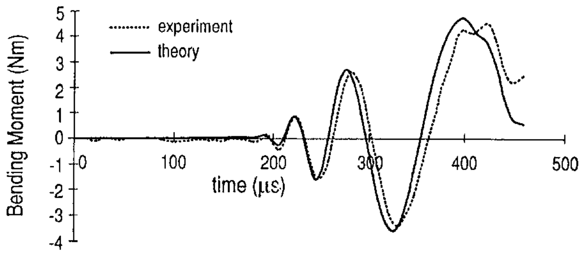

Fig. 11(*c*) θ = 120 deg

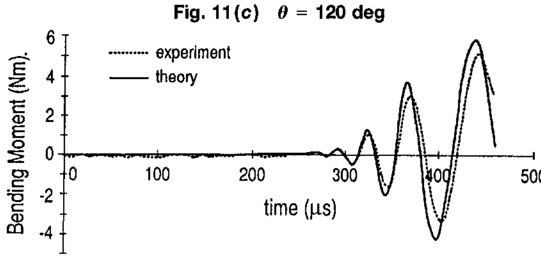

Fig. 11(*d*) θ = 180 deg

Fig. 11 Experimental and theoretical bending moment history for the brass ring

The preceding discussion points to the conclusion that a generalized force-velocity formulation produces better accuracy in terms of an impulse-momentum balance. However, this approach does not yield generalized displacements directly from solution of the characteristic equations. Numerical integration of forces and velocities is required in determining displacements. This does not ensure continuity of displacement gradients (which is satisfied in the generalized displacement formulation) and may give rise to error in displacement values. Figure 7 illustrates this by comparing results from the two formulations. From symmetry, the slope $dw^*/d\theta^*$ at $\theta = 0$ deg should be zero. The generalized displacement formulation uses this as a boundary conditions and therefore w^* satisfies this. However, the generalized force-velocity formulation produces a steep nonzero slope at $\theta = 0$ deg which is unrealistic. Nevertheless, Fig. 7 shows that agreement between the two formulations is good at angular positions away from the vicinity of impact ($\theta = 0$ deg).

In terms of computing time and accuracy of results (i.e., for N^*, V^*, M^*, $\dot{u}^*$, $\dot{w}^*$, and $\dot{\phi}^*$), the generalized force-velocity formulation is preferred because it involves a smaller number of equations. Also, its results show a better impulse-momentum balance. Its main inaccuracy lies in prediction of radial displacements near the point of impact. However, elsewhere it yields w^* values which are very close to those from the generalized displacement formulation. Therefore, the generalized force-velocity approach is preferred.

Impact Experiments

Experiments were conducted to measure the time history of generalized forces (bending moment and axial force) at selected points on a ring subjected to impact for comparison with theoretical results. A brass and an aluminum ring of identical dimensions, external diameter of 400 mm, internal diameter of 380 mm, and a width of 10 mm, were subjected to radial impact by a falling 0.412 kg cylindrical steel striker. Figure 8 shows the test arrangement. Circumferential strains at selected angular locations around the ring were determined by pairs of strain gauges, one on the outer and the other on the inner surface of the ring, measuring ϵ_o and ϵ_i, respectively. This facilitated computation of the axial force and bending moment from

$$N = \frac{Elh}{2}(\epsilon_o + \epsilon_i) \tag{19}$$

$$M = \frac{Elh^2}{12}(\epsilon_o - \epsilon_i) \tag{20}$$

where

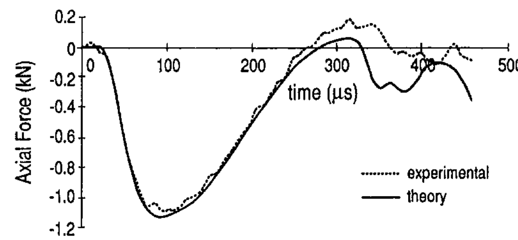

Fig. 12(*a*) θ = 20 deg

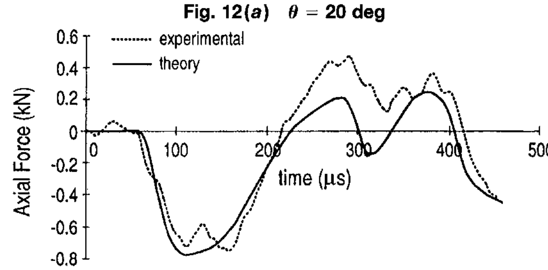

Fig. 12(*b*) θ = 60 deg

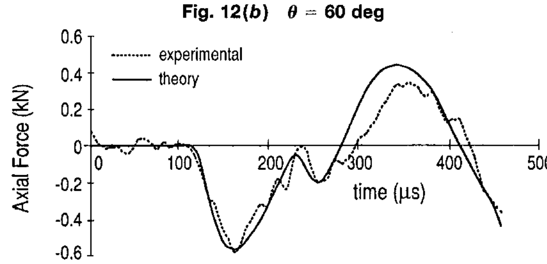

Fig. 12(*c*) θ = 120 deg

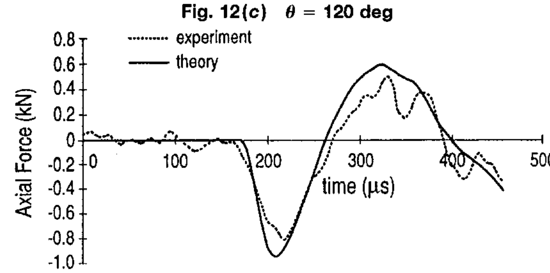

Fig. 12(*d*) θ = 180 deg

Fig. 12 Experimental and theoretical axial force history of the brass ring

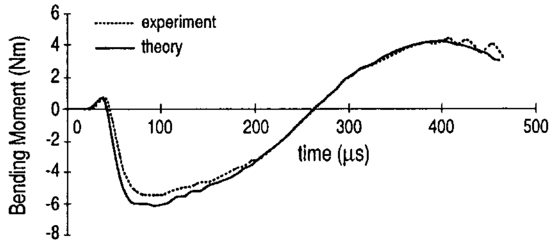

Fig. 13(*a*) $\theta = 20$ **deg**

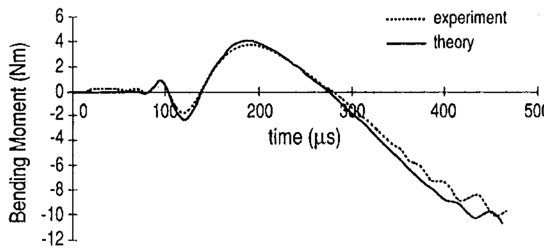

Fig. 13(*b*) $\theta = 60$ **deg**

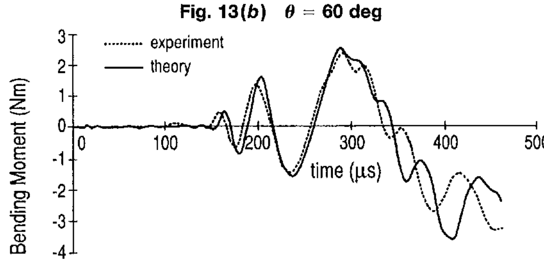

Fig. 13(*c*) $\theta = 120$ **deg**

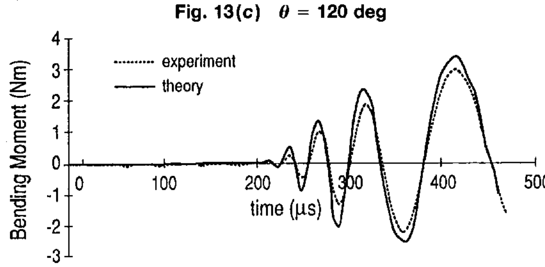

Fig. 13(*d*) $\theta = 180$ **deg**

Fig. 13 Experimental and theoretical bending moment history for the aluminum ring

h is the ring thickness = 10 mm
l is the ring width = 25.4 mm
$E_{\text{aluminum}} = 70$ GPa; $E_{\text{brass}} = 114$ GPa.

The force exerted by the striker during impact was measured by an attached accelerometer. Tests were repeated several times for each specimen to ensure consistency and repeatability of results.

To facilitate comparison, the experimental impact force history was used as a basis to define the load input for calculations based on the theoretical analysis. The numerical solution procedure requires the load to be in the form of a force intensity-time input (i.e., force per unit length of ring circumference), but experimental data represent impact as a force-time history. This can be expressed as a force intensity-time pulse by assuming that the force acts over a small circumferential segment of the ring on which the striker makes contact. The distribution of the impact force on the segment δs^* is assumed to be linear as shown in Fig. 5. However, the contact length is unknown and difficult to determine in practice. To estimate a suitable segment length over which the force may be assumed to act, a preliminary investigation of the sensitivity of numerical results to segment length was performed. Two different segment lengths, 2.89 mm and 5.77 mm, corresponding to nondimensional lengths of $s^* = 0.5$ and $s^* = 1$ were selected for study. Numerical results for the bending moment and axial force histories using these two values were compared the difference found to be insignificant. The assumption of a segment length over which the impact force acts required a finite difference grid size that was either equal to or smaller than this length. A segment length of $s^* = 1$ was used because this value required less storage space and computing time.

Comparison Between Theoretical and Experimental Results

Experimental results of the bending moment and axial force histories at various angular positions along the ring specimens were compared. First, a comparison was made between test data, and results generated by linear and higher-order interpolation schemes to determine which scheme is superior. Figures 9 and 10 show comparisons between results generated by the two schemes and experimental bending moment and axial force histories at $\theta = 140$ deg and $\theta = 180$ deg for the brass specimen. The difference between the experimental bending moment data and theoretical results based on linear interpolation is large (Fig. 9). Agreement is significantly better with higher-order interpolation. Deviation between the two interpolation methods

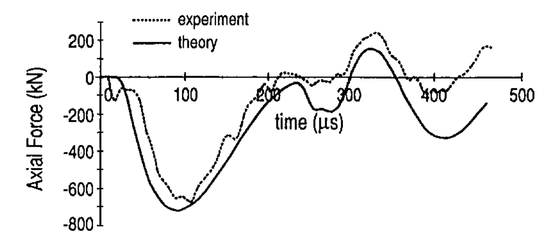

Fig. 14(*a*) $\theta = 20$ **deg**

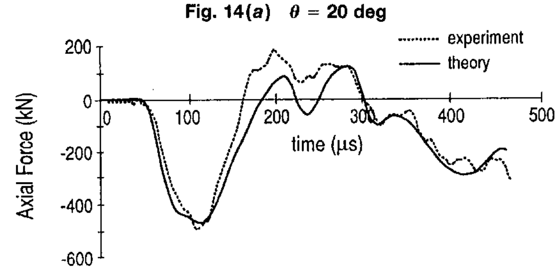

Fig. 14(*b*) $\theta = 60$ **deg**

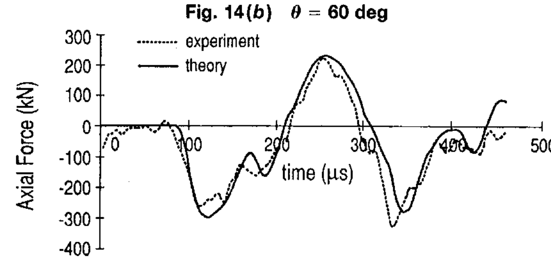

Fig. 14(*c*) $\theta = 120$ **deg**

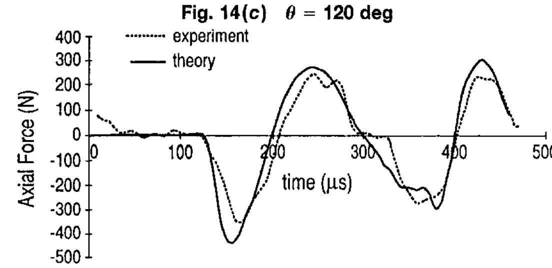

Fig. 14(*d*) $\theta = 180$ **deg**

Fig. 14 Experimental and theoretical axial force history for aluminum ring

Table 2(*a*) Wave speeds in the brass ring

	Arrival times (μs)		Speed (m/s) = *distance measured along centroid of cross section/arrival time*	
Angular positions	Bending moment	Axial force	Bending moment	Axial force
θ = 60 deg	89	81	2290	2521
θ = 120 deg	183	111	2230	3680
θ = 180 deg	277	164	2210	3740

Table 2(*b*) Wave speeds in the aluminum ring

	Arrival times (μs)		Speed (m/s) = *distance measured along centroid of cross section/arrival time*	
Angular positions	Bending moment	Axial force	Bending moment	Axial force
θ = 60 deg	75	51	2720	4000
θ = 120 deg	148	80	2760	5110
θ = 180 deg	218	122	2810	5021

is negligible for axial force predictions (Fig. 10). Based on this comparison, the higher-order interpolation scheme was utilized in the rest of this study.

Figures 11–14 show, respectively, comparisons between experimental and theoretical bending moment and axial force histories at locations 20 deg, 60 deg, 120 deg, and 180 deg from the point of impact for the brass and aluminum rings. Overall agreement is good and correlation is excellent immediately following commencement of impact. Deviation between theory and experiment tends to increase with time. This may be the result of frictional losses or damping, which are not accounted for in the equations of motion. A second possible cause of the experimental deviation are the lateral constraints imposed by the steel frame via foam pads (Fig. 8); these additional forces are also not accounted for in the analysis. However, these two factors appear minimal in their influence.

The experimental results confirm several typical characteristics of wave propagation predicted by the governing equations. First, finite wave speeds; Figs. 11 to 14 show distinct arrival times at which the bending moment and axial force are detected at different angular positions along the rings. Secondly, the dependence of wave speeds on material properties. Flexural, longitudinal, and radial shearing wave speeds increase with the bar velocity c ($= \sqrt{E/\rho}$) of a material. The bar velocities of aluminum and brass are 5040 m/s and 3670 m/s, respectively. A comparison of the arrival times of the bending moment and axial force in the ring specimens for common angular positions (Figs. 11 and 13, Figs. 12 and 14), shows an earlier occurrence for the aluminum ring. Thirdly, the governing theory predicts that axial stress waves travel faster than flexural waves. Comparison between the arrival times of the bending moment and axial force for identical positions in the brass and aluminum rings (Figs. 11 and 12) confirms this. Tables 2(a–b) show the bending moment and axial force wave speeds derived from experimental data. These values indicate that the axial force propagates at a higher speed. They also show that the flexural wave speed measured at the various positions exhibit a smaller variation than the speed of axial force propagation. This is because it is experimentally easier to detect the arrival time of a flexural wave. Bending generates a larger and more easily detected circumferential strain $\epsilon_{\theta\theta}$ at the ring surface than an axial force does.

Comparisons between the experimental and theoretical results confirm that the numerical scheme proposed in this study is capable of predicting the transient response of a ring with good accuracy. Figures 11 to 14 show that correlation between theory and experiment is good for at least 460 μs after initiation of impact. An estimate of the time for the fastest wave (radial shear) to travel from the top to the bottom of an aluminum ring is 120 μs. Hence, 460 μs after impact, this mode of disturbance would have traveled completely around the ring more than once. Yet, correlation between theory and experiment remains good, implying that the proposed solution scheme is capable of predicting the response even after the stress waves reach the bottom of the ring. Strictly speaking, numerical computation of the response before and after the waves reach the bottom should differ. Application of the governing equations to radial impact on circular rings requires assumption of physically valid boundary conditions, i.e., $V^* = \dot{u}^* = \dot{\phi}^* = 0$, at both ends of a half ring. Computation of the response before the stress waves reach the bottom of the ring is based on boundary conditions imposed at the location of impact (i.e., the top end of a half ring), while computation of the response after the stresses reach the bottom is based on boundary conditions imposed at both the impact point and the bottom of the ring (i.e., at both ends of a half ring). Truncation error in the numerical solution process is cumulative. Hence, results generated after the stress waves reach the bottom of a ring would contain an accumulation of truncation error. However, this error is still relatively small compared to the actual magnitudes of bending moment and axial force and therefore correlation between the experimental and numerical results remains good.

Conclusions

Morley's (1961) adaptation of Timoshenko beam theory for elastic wave propagation in curved rods was applied to stress wave propagation in circular rings subjected to short-duration radial impact. The governing partial differential equations were solved numerically using the method of characteristics. An improvement of the solution procedure used by Chou and Mortimer (1967) and Phillips and Crowley (1972) was proposed, whereby a higher-order interpolation scheme was employed. Results in terms of generalized forces were verified by impact experiments on metal rings. They showed that the higher order scheme yielded better correlation with experimental data and substantiated the validity of the theoretical formulation and solution process.

The governing equations could be solved via either a generalized force velocity or a generalized displacement formulation, the difference being the quantities selected as the variables. It was found that that the former yielded better results with respect to an impulse-momentum balance. A comparison of both formulations also showed that the generalized force-velocity formulation is mathematically simpler and therefore incurs smaller truncation errors during computation. Its finite difference equations also have smaller inherent discretization errors, because of fewer terms involving average values between grid points. However, computations based on the generalized force-velocity formulation do not yield displacements directly and require subsequent integration of velocities. This generated steep variations in the distribution of radial displacement near the impact point. Nevertheless, in view of the smaller truncation and discretization errors involved, it is the preferred approach.

References

Abramson, H. N., Plass, H. J., and Ripperger, E. A., 1958, "Stress Wave Propagation in Rods and Beams," *Advances in Applied Mechanics*, Vol. 5, H. L. Dryden, ed., Academic Press, New York, pp. 111–194.

Aprahamian, R., Evensen, D. A., Mixson, J. S., and Wright J. E., 1971, "Application of Pulsed Holographic Interferometry to the Measurement of Propagating Transverse Waves in Beams," *Experimental Mechanics*, Vol. 11, pp. 309–314.

Boresi, A. P., Schmidt, R. J., and Sidebottom, O. M., 1993, *Advanced Mechanics of Materials,* John Wiley and Sons, New York.

Chou, P. C., and Mortimer, R. W., 1967, "Solution of One-Dimensional Elastic Wave Problems by the Method of Characteristics," ASME JOURNAL OF APPLIED MECHANICS, Vol. 34, pp. 745–750.

Crowley, III, F. B., Phillips, J. W., and Taylor C. E., 1974, "Pulse Propagation in Straight and Curved Beams: Theory and Experiment," ASME JOURNAL OF APPLIED MECHANICS, Vol. 41, pp. 71–76.

Goland, M., Wickersham, P. D., and Dengler, M. A., 1955, "Propagation of Elastic Impact in Beams in Bending," ASME JOURNAL OF APPLIED MECHANICS, Vol. 22, pp. 1–7.

Graff, Karl F., 1970, "Elastic Wave Propagation in a Curved Sonic Transmission Line," *IEEE Transactions on Sonics and Ultrasonics,* Vol. 41, pp. 1–6.

Graff, K. F., 1975, *Wave Motion in Elastic Solids,* Clarendon Press, Oxford, UK.

Kuo, S. S., 1961, "Beam Subjected to Eccentric Longitudinal Impact," *Experimental Mechanics,* Vol. 1, pp. 102–108.

Morley, L. S. D., 1961, "Elastic Waves in a Naturally Curved Rod," *Quarterly Journal of Mechanics and Applied Mathematics,* Vol. 14, pp. 155–172.

Mortimer, R. W., and Hoburg, James F., 1969, "MCDIT 21: A Computer-Code for One-Dimensional Elastic Wave Problems," NASA CR-1306, Apr., pp. 33–64.

Phillips, J. W., and Crowley, III, F. B., 1972, "On the Theory of Pulse Propagation in Curved Beams," *Journal of Sound and Vibration,* Vol. 24, pp. 247–258.

Plass, H. J., Jr., 1958, "Some Solutions of the Timoshenko Beam Equations for Short Pulse-Type Loading," ASME JOURNAL OF APPLIED MECHANICS, Vol. 25, pp. 379–385.

Quah, S. E., 1994, "Impact Stress Wave Propagation in Curved and Periodic Structures," Masters of Engineering thesis, National University of Singapore.

Ripperger, E. A., and Abramson, N. H., 1957, "A Study of the Propagation of Flexural Waves in Elastic Beams," ASME JOURNAL OF APPLIED MECHANICS, Vol. 24, pp. 431–434.

Shim, V. P. W., Toh, S. L., and Quah, S. E., 1992, "Impact-Induced Flexural Waves in a Timoshenko Beam—Shearographic Detection and Analysis," *Proceedings of the VII International Congress on Experimental Mechanics,* pp. 679–685.

Stronge, W. J., and Shim, V. P. W., 1987, "Dynamic Crushing of a Ductile Cellular Array," *International Journal of Mechanical Sciences,* Vol. 29, pp. 381–406.

Contact Problems of Two Dissimilar Anisotropic Elastic Bodies

Chyanbin Hwu

C. W. Fan

Institute of Aeronautics and Astronautics,
National Cheng Kung University,
Tainan, Taiwan, R.O.C.

In this paper, a two-dimensional contact problem of two dissimilar anisotropic elastic bodies is studied. The shapes of the boundaries of these two elastic bodies have been assumed to be approximately straight, but the contact region is not necessary to be small and the contact surface can be nonsmooth. Base upon these assumptions, three different boundary conditions are considered and solved. They are: the contact in the presence of friction, the contact in the absence of friction, and the contact in complete adhesion. By applying the Stroh's formalism for anisotropic elasticity and the method of analytical continuation for complex function manipulation, general solutions satisfying these different boundary conditions are obtained in analytical forms. When one of the elastic bodies is rigid and the boundary shape of the other elastic body is considered to be flat, the reduced solutions can be proved to be identical to those presented in the literature for the problems of rigid punches indenting into (or sliding along) the anisotropic elastic half-plane. For the purpose of illustration, examples are also given when the shapes of the boundaries of the elastic bodies are approximated by the parabolic curves.

1 Introduction

Due to mathematical infeasibility, three-dimensional contact problems were usually formulated and solved under several restrictive assumptions. For example, the contact region is very small and the equations of the undeformed surfaces near the contact region could be approximated sufficiently accurately by functions of the form $z = ax^2 + 2bxy + cy^2$. For isotropic bodies, the problem was first solved by Hertz (1882) considering only frictionless surfaces and perfectly elastic solids. Following his work, the progress in contact mechanics has been associated largely with the removal of these restrictions. Extensive references can be found in the books by Shtaerman (1949), Galin (1953), Gladwell (1980), and Johnson (1985). For the contact of anisotropic bodies, an important result has been demonstrated by Willis (1966). Practical examples of the analysis of a transversely isotropic half-space may be found in Conway (1956), Fabrikant (1971), Dahan and Zarka (1977), etc.

As to the two-dimensional contact problems, the contact region has not been assumed to be small and no assumption regarding the shapes of the boundaries has been made, except the condition that they should be approximate to straight lines. For isotropic elastic bodies, the solutions can be found in Muskhelishvili (1954) for smooth surfaces, and in Glagolev (1945) for nonsmooth surfaces. Two-dimensional anisotropic contact problems were discussed by Galin (1953) and the indentation of an anisotropic half-plane by a rigid punch is solved in Green and Zerna (1954). Recently, by employing the Stroh's formalism (Stroh, 1958; Ting, 1996), we solved a series of punch problems (Fan and Hwu, 1996; Hwu and Fan, 1998a). In that series, only one elastic medium (i.e., the half-plane) is considered and the punch indenting into (or sliding along) the half-plane is assumed to be rigid. By carefully reviewing these solutions, we find that the punch problem is just a counterpart of the interface crack problem, with one of the materials being rigid (Hwu and Fan, 1998b). This observation stimulates us to study the contact problems of two anisotropic elastic bodies, since its possible counterpart (the problem of the interface cracks between two dissimilar anisotropic elastic media) has been solved long ago (Gotoh, 1970; Willis, 1971).

2 Problem Formulation

Consider two dissimilar anisotropic elastic bodies S_1 and S_2 which are in contact along a segment L of their boundaries (Fig. 1). If these two elastic bodies satisfy the basic laws for two-dimensional linear anisotropic elasticity, by using the Stroh's formalism (Stroh, 1958; Ting, 1996; also see Appendix A for a brief introduction) the displacement vector $\mathbf{u} = (u_1, u_2, u_3)$ and the stress function vector $\boldsymbol{\phi} = (\phi_1, \phi_2, \phi_3)$ of these two bodies may be expressed in a fixed rectangular coordinate system x_i, $i = 1, 2, 3$ as (the symbols x_1 and x_2 will be replaced by x and y for the convenience of presentation)

$$\left.\begin{aligned}\mathbf{u}_1 &= \mathbf{A}_1\mathbf{f}_1(z) + \bar{\mathbf{A}}_1\overline{\mathbf{f}_1(z)},\\ \boldsymbol{\phi}_1 &= \mathbf{B}_1\mathbf{f}_1(z) + \bar{\mathbf{B}}_1\overline{\mathbf{f}_1(z)},\end{aligned}\right\}, \quad z \in S_1 \qquad (2.1a)$$

and

$$\left.\begin{aligned}\mathbf{u}_2 &= \mathbf{A}_2\mathbf{f}_2(z) + \bar{\mathbf{A}}_2\overline{\mathbf{f}_2(z)},\\ \boldsymbol{\phi}_2 &= \mathbf{B}_2\mathbf{f}_2(z) + \bar{\mathbf{B}}_2\overline{\mathbf{f}_2(z)},\end{aligned}\right\}, \quad z \in S_2 \qquad (2.1b)$$

where the subscripts 1 and 2 are used to denote the quantities pertaining to the bodies S_1 and S_2, respectively. The overbar represents the conjugate of a complex number. The stresses σ_{ij} are related to the stress function vector $\boldsymbol{\phi}$ by

$$\sigma_{i1} = -\phi_{i,2}, \quad \sigma_{i2} = \phi_{i,1}. \qquad (2.1c)$$

$\mathbf{f}(z) = [f_1(z_1)\ f_2(z_2)\ f_3(z_3)]^T$ is a function vector composed of three holomorphic complex function $f_\alpha(z_\alpha)$, $\alpha = 1, 2, 3$, which will be determined by satisfying the boundary conditions of the problems. The argument z_α of each component function $f_\alpha(z_\alpha)$ is written as $z_\alpha = x + p_\alpha y$ in which p_α is the material

---

Contributed by the Applied Mechanics Division of THE AMERICAN SOCIETY OF MECHANICAL ENGINEERS for publication in the ASME JOURNAL OF APPLIED MECHANICS.

Discussion on the paper should be addressed to the Technical Editor, Professor Lewis T. Wheeler, Department of Mechanical Engineering, University of Houston, Houston, TX 77204-4792, and will be accepted until four months after final publication of the paper itself in the ASME JOURNAL OF APPLIED MECHANICS.

Manuscript received by the ASME Applied Mechanics Division, June 3, 1997; final revision, Dec. 10, 1998. Associate Technical Editor: J. T. Jenkins.

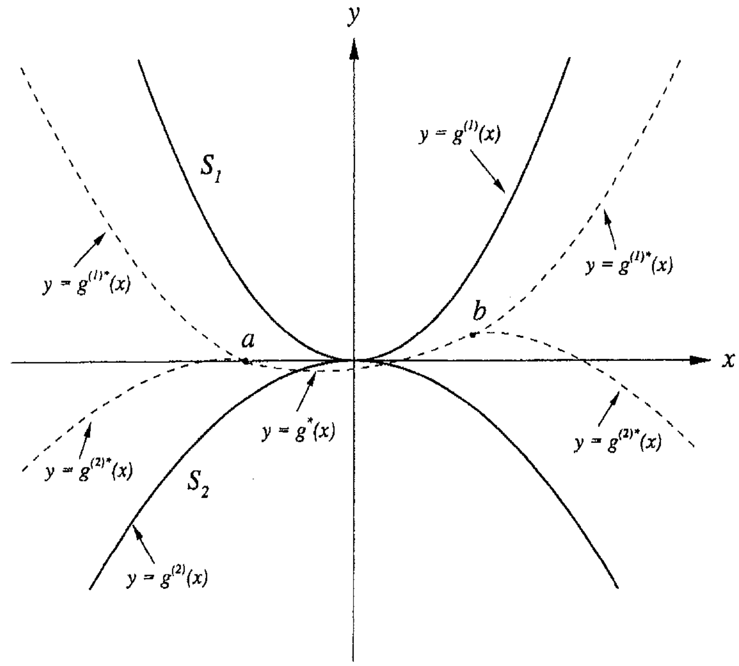

Fig. 1 Contact of two dissimilar anisotropic elastic bodies. (Solid line: before deformation; dot line: after deformation.)

eigenvalue whose imaginary part has been arranged to be positive. $\mathbf{A} = [\mathbf{a}_1, \mathbf{a}_2, \mathbf{a}_3]$ and $\mathbf{B} = [\mathbf{b}_1, \mathbf{b}_2, \mathbf{b}_3]$ are 3×3 complex matrices of which $(\mathbf{a}_\alpha, \mathbf{b}_\alpha)$, $\alpha = 1, 2, 3$, are the material eigenvectors associated with p_α.

Equation (2.1) does not consider the physical conditions of the contact problems. It is just a solution set for any two anisotropic elastic bodies. In this solution set, the material properties of these two elastic bodies may be reflected by the eigenvalues p_α and eigenvector matrices $\mathbf{A}$ and $\mathbf{B}$. In order to have a complete knowledge about the contact behavior from (2.1), the unknown function vectors $\mathbf{f}_1(z)$ and $\mathbf{f}_2(z)$ should be determined through the satisfaction of the boundary conditions. For a contact problem, many different boundary conditions may be considered to suit for a real situation. In this paper, three commonly encountered boundary conditions will be formulated and solved. They are: contact in the presence of friction, contact in the absence of friction, and contact in complete adhesion. Before we write down the mathematical expressions for these three different boundary conditions, a few common physical assumptions will be discussed and formulated as follows.

If $y = g^{(1)}(x)$ and $y = g^{(2)}(x)$ are, respectively, the equations of the boundaries of the bodies S_1 and S_2 before deformation, and $y = g^*(x)$ is the equation of the line of contact after deformation (Fig. 1), the contact in the x_2-direction can be expressed as

$$g^{(1)}(x) + u_2^{(1)}(x) = g^*(x + u_1^{(1)}),$$
$$g^{(2)}(x) + u_2^{(2)}(x) = g^*(x + u_1^{(2)}), \quad x \in L, \qquad (2.2a)$$

where the superscripts (1) and (2) are used to denote the quantities pertaining to the bodies S_1 and S_2, respectively. In the cases of small deformation, $g^*(x + u_1^{(1)})$ can be represented by its Taylor series $g^*(x) + u_1^{(1)} g^{*\prime}(x) + \ldots$. Similarly, $g^*(x + u_1^{(2)}) = g^*(x) + u_1^{(2)} g^{*\prime}(x) + \ldots$. Subtracting $(2.2a)_2$ from $(2.2a)_1$, we have

$$g^{(1)}(x) + u_2^{(1)}(x) - g^{(2)}(x) - u_2^{(2)}(x)$$
$$= (u_1^{(1)} - u_1^{(2)}) g^{*\prime}(x) + \ldots \qquad (2.2b)$$

If the line of contact after deformation is approximate to a straight line, i.e., $g^{*\prime}(x) \cong 0$, (2.2) may then be replaced by a simple expression as

$$u_2^{(2)}(x) - u_2^{(1)}(x) = g(x), \quad x \in L, \qquad (2.3a)$$

where

$$g(x) = g^{(1)}(x) - g^{(2)}(x). \qquad (2.3b)$$

In addition to the consideration of deformation in x_2-direction, the traction continuity across the contact region and the traction-free condition along the uncontact region should also be considered. If the shapes of the boundaries are approximate to straight lines, the stresses normal and tangent to the boundaries may be approximated by σ_{22}, σ_{12}, and σ_{32}. The mathematical expressions for the traction conditions may then be written as

$$\sigma_{12}^{(1)} = \sigma_{12}^{(2)}, \quad \sigma_{22}^{(1)} = \sigma_{22}^{(2)}, \quad \sigma_{32}^{(1)} = \sigma_{32}^{(2)}, \quad x \in L,$$
$$\sigma_{12}^{(1)} = \sigma_{12}^{(2)} = \sigma_{22}^{(1)} = \sigma_{22}^{(2)} = \sigma_{32}^{(1)} = \sigma_{32}^{(2)} = 0, \quad x \notin L. \qquad (2.4)$$

Equations (2.3) and (2.4) are written based upon the assumptions of small deformation and small boundary slopes, and are common conditions for the three different boundary conditions described below. On the basis of these two conditions, we may now write down the boundary conditions for three different cases as follows.

Contact in the Presence of Friction:

$$\left.\begin{aligned} \sigma_{12}^{(1)}(x) = \sigma_{12}^{(2)}(x) &= \eta_1 \sigma_{22}(x) \\ \sigma_{32}^{(1)}(x) = \sigma_{32}^{(2)}(x) &= \eta_3 \sigma_{22}(x) \\ \sigma_{22}^{(1)}(x) = \sigma_{22}^{(2)}(x) &= \sigma_{22}(x) \\ u_2^{(2)}(x) - u_2^{(1)}(x) &= g(x) \end{aligned}\right\}, \quad x \in L, \qquad (2.5a)$$

$$\sigma_{12}^{(1)}(x) = \sigma_{12}^{(2)}(x) = \sigma_{22}^{(1)}(x) = \sigma_{22}^{(2)}(x)$$
$$= \sigma_{32}^{(1)}(x) = \sigma_{32}^{(2)}(x) = 0, \quad x \notin L, \qquad (2.5b)$$

where η_1 and η_3 are, respectively, the load ratios of the normal force to the horizontal forces in x_1 and x_3 directions. The limit values of these two load ratios will be the coefficients of static friction in the x_1 and x_3 directions.

Contact in the Absence of Friction:

$$\left.\begin{aligned}\sigma_{12}^{(1)}(x) = \sigma_{12}^{(2)}(x) &= 0\\ \sigma_{32}^{(1)}(x) = \sigma_{32}^{(2)}(x) &= 0\\ \sigma_{22}^{(1)}(x) &= \sigma_{22}^{(2)}(x)\\ u_2^{(2)}(x) - u_2^{(1)}(x) &= g(x)\end{aligned}\right\}, \quad x \in L, \tag{2.6a}$$

$$\begin{aligned}\sigma_{12}^{(1)}(x) &= \sigma_{12}^{(2)}(x) = \sigma_{22}^{(1)}(x) = \sigma_{22}^{(2)}(x)\\ &= \sigma_{32}^{(1)}(x) = \sigma_{32}^{(2)}(x) = 0, \quad x \notin L.\end{aligned} \tag{2.6b}$$

Contact in Complete Adhesion:

$$\left.\begin{aligned}u_1^{(1)}(x) = u_1^{(2)}(x), \quad \sigma_{12}^{(1)}(x) &= \sigma_{12}^{(2)}(x)\\ u_3^{(1)}(x) = u_3^{(2)}(x), \quad \sigma_{32}^{(1)}(x) &= \sigma_{32}^{(2)}(x)\\ u_2^{(2)}(x) - u_2^{(1)}(x) &= g(x),\\ \sigma_{22}^{(1)}(x) &= \sigma_{22}^{(2)}(x)\end{aligned}\right\}, \quad x \in L, \tag{2.7a}$$

$$\begin{aligned}\sigma_{12}^{(1)}(x) &= \sigma_{12}^{(2)}(x) = \sigma_{22}^{(1)}(x) = \sigma_{22}^{(2)}(x)\\ &= \sigma_{32}^{(1)}(x) = \sigma_{32}^{(2)}(x) = 0, \quad x \notin L.\end{aligned} \tag{2.7b}$$

3 The Method of Analytical Continuation

The common conditions for the three different boundary conditions given in (2.5)–(2.7) are the traction continuity across the contact region and the traction free along the uncontact region, which are expressed by (2.4). By using the relations (2.1c), these common conditions may be rewritten in terms of $\boldsymbol{\phi}_1'$ and $\boldsymbol{\phi}_2'$ as

$$\boldsymbol{\phi}_1' = \boldsymbol{\phi}_2', \quad \forall x,$$

$$\boldsymbol{\phi}_1' = \boldsymbol{\phi}_2' = \mathbf{0}, \quad x \notin L. \tag{3.1}$$

By applying the general solutions given in (2.1), the traction continuity condition $(3.1)_1$ leads to

$$\mathbf{B}_1\mathbf{f}_1(x^+) - \bar{\mathbf{B}}_2\overline{\mathbf{f}_2(x^-)} = \mathbf{B}_2\mathbf{f}_2(x^-) - \bar{\mathbf{B}}_1\overline{\mathbf{f}_1(x^+)}, \tag{3.2}$$

where $x^+ = x + i0^+$ and $x^- = x + i0^-$. One of the important properties of holomorphic functions used in the method of analytical continuation is that if $\mathbf{f}(z)$ is holomorphic in S_1 (or S_2), then $\overline{\mathbf{f}(\bar{z})}$ is holomorphic in S_2 (or S_1). From this property and Eq. (3.2), we may introduce a function which is holomorphic in the entire domain including the axis $y = 0$, i.e.,

$$\boldsymbol{\theta}^*(z) = \begin{cases}\mathbf{B}_1\mathbf{f}_1(z) - \bar{\mathbf{B}}_2\overline{\mathbf{f}_2(\bar{z})}, & z \in S_1,\\ \mathbf{B}_2\mathbf{f}_2(z) - \bar{\mathbf{B}}_2\overline{\mathbf{f}_1(\bar{z})}, & z \in S_2.\end{cases} \tag{3.3}$$

Since $\boldsymbol{\theta}^*(z)$ is now holomorphic and single-valued in the whole plane including the point at infinity, by Liouville's Theorem we have $\boldsymbol{\theta}^*(z) \equiv$ constant. However, constant function vector $\mathbf{f}$ corresponds to rigid-body motion which may be neglected. Therefore,

$$\boldsymbol{\theta}^*(z) \equiv 0. \tag{3.4}$$

Combining (3.3) and (3.4), we have

$$\bar{\mathbf{f}}_2(z) = \bar{\mathbf{B}}_2^{-1}\mathbf{B}_1\mathbf{f}_1(z), \quad z \in S_1,$$

$$\bar{\mathbf{f}}_1(z) = \bar{\mathbf{B}}_1^{-1}\mathbf{B}_2\mathbf{f}_2(z), \quad z \in S_2. \tag{3.5}$$

By employing (3.5) into the traction-free condition $(3.1)_2$, we get $\mathbf{B}_1\mathbf{f}_1'(x^+) + \mathbf{B}_2\mathbf{f}_2'(x^-) = \mathbf{0}$. Based upon this relation, we now introduce a new function vector

$$\boldsymbol{\theta}(z) = \begin{cases}-\mathbf{B}_1\mathbf{f}_1(z), & z \in S_1,\\ \mathbf{B}_2\mathbf{f}_2(z), & z \in S_2.\end{cases} \tag{3.6}$$

Applying (3.5) and (3.6) to (2.1) for the points above and below the x-axis, we may derive the following expressions:

$$\begin{aligned}\boldsymbol{\phi}_1'(x^+) &= \boldsymbol{\phi}_2'(x^-) = \boldsymbol{\theta}'(x^-) - \boldsymbol{\theta}'(x^+),\\ \mathbf{u}_1(x^+) &= i\mathbf{M}_1^{-1}\boldsymbol{\theta}(x^+) + i\bar{\mathbf{M}}_1^{-1}\boldsymbol{\theta}(x^-),\\ \mathbf{u}_2(x^-) &= -i\mathbf{M}_2^{-1}\boldsymbol{\theta}(x^-) - i\bar{\mathbf{M}}_2^{-1}\boldsymbol{\theta}(x^+),\end{aligned} \tag{3.7}$$

where $\mathbf{M}_k$, $k = 1, 2$, are the impedance tensors defined as

$$\mathbf{M}_k = -i\mathbf{B}_k\mathbf{A}_k^{-1}, \quad k = 1, 2. \tag{3.8a}$$

It has been shown that (Ting, 1988) $\mathbf{M}_k^{-1}$, $k = 1, 2$, are Hermitian matrices ($\mathbf{M}_k^{-1} = \bar{\mathbf{M}}_k^{-T}$) and

$$\mathbf{M}_k^{-1} = \mathbf{L}_k^{-1}(\mathbf{I} + i\mathbf{S}_k^T) = (\mathbf{I} - i\mathbf{S}_k)\mathbf{L}_k^{-1}, \tag{3.8b}$$

where $\mathbf{S}$ and $\mathbf{L}$ are two real matrices defined as

$$\mathbf{S} = i(2\mathbf{A}\mathbf{B}^T - \mathbf{I}), \quad \mathbf{L} = -2i\mathbf{B}\mathbf{B}^T. \tag{3.9}$$

Moreover, $\mathbf{L}$ is positive definite if the strain energy is positive. Explicit expressions of $\mathbf{S}$ and $\mathbf{L}$ for general anisotropic materials and, in particular, for monoclinic materials have been presented by Ting (1992) and Wei and Ting (1994). For orthotropic materials, the explicit expressions of $\mathbf{S}$ and $\mathbf{L}$ have been found in (Dongye and Ting, 1989; Hwu, 1993a) and are shown in Appendix B.

Subtracting $(3.7)_2$ from $(3.7)_3$, we have

$$\mathbf{u}_2(x^-) - \mathbf{u}_1(x^+) = -i\{\mathbf{M}^*\boldsymbol{\theta}(x^+) + \bar{\mathbf{M}}^*\boldsymbol{\theta}(x^-)\}, \tag{3.10}$$

where $\mathbf{M}^*$ is a 3×3 bimaterial matrix defined as

$$\mathbf{M}^* = \mathbf{M}_1^{-1} + \bar{\mathbf{M}}_2^{-1}. \tag{3.11}$$

Note that $\mathbf{M}^*$ is not a newly defined matrix. Actually it plays an important role in the problems of interface cracks. By (3.8b), we can prove that $\mathbf{M}^*$ is also a Hermitian matrix ($\mathbf{M}^* = \bar{\mathbf{M}}^{*T}$) which may be expressed as

$$\mathbf{M}^* = \mathbf{D} - i\mathbf{W}, \tag{3.12a}$$

where $\mathbf{D}$ is a real symmetric and positive definite matrix, and $\mathbf{W}$ is a real antisymmetric marix. They are related to the real matrices $\mathbf{S}_1$, $\mathbf{S}_2$, $\mathbf{L}_1$, and $\mathbf{L}_2$ by

$$\mathbf{D} = \mathbf{L}_1^{-1} + \mathbf{L}_2^{-1}, \quad \mathbf{W} = \mathbf{S}_1\mathbf{L}_1^{-1} - \mathbf{S}_2\mathbf{L}_2^{-1}. \tag{3.12b}$$

With the solutions provided in Appendix B, it can easily be shown that $\mathbf{M}^*$ of the orthotropic bimaterials has the following simple structure:

$$\mathbf{M}^* = \begin{bmatrix}\dfrac{1}{L_{11}^{(1)}} + \dfrac{1}{L_{11}^{(2)}} & -i\left(\dfrac{S_{12}^{(1)}}{L_{22}^{(1)}} - \dfrac{S_{12}^{(2)}}{L_{22}^{(2)}}\right) & 0\\ i\left(\dfrac{S_{12}^{(1)}}{L_{22}^{(1)}} - \dfrac{S_{12}^{(2)}}{L_{22}^{(2)}}\right) & \dfrac{1}{L_{22}^{(1)}} + \dfrac{1}{L_{22}^{(2)}} & 0\\ 0 & 0 & \dfrac{1}{L_{33}^{(1)}} + \dfrac{1}{L_{33}^{(2)}}\end{bmatrix}. \tag{3.13}$$

4 Contact in the Presence of Friction

By using the function vector $\boldsymbol{\theta}$ defined in Section 3, the boundary conditions given in (2.5) may now be written as

$$\theta_1'(x^-) - \theta_1'(x^+) = \eta_1[\theta_2'(x^-) - \theta_2'(x^+)],$$

$$\theta_3'(x^-) - \theta_3'(x^+) = \eta_3[\theta_2'(x^-) - \theta_2'(x^+)],$$

$$m_{21}^*\theta_1(x^+) + m_{22}^*\theta_2(x^+) + m_{23}^*\theta_3(x^+) + \bar{m}_{21}^*\theta_1(x^-) + \bar{m}_{22}^*\theta_2(x^-) + \bar{m}_{23}^*\theta_3(x^-) = ig(x), \quad (4.1)$$

where θ_i, $i = 1, 2, 3$, are the components of the function vector $\boldsymbol{\theta}$, and m_{ij}^*, $i, j = 1, 2, 3$, are the components of the matrix $\mathbf{M}^*$. Rearrangement of the first and second equations of (4.1) gives

$$\lim_{y\to 0^+} [\theta_i'(z) - \eta_i\theta_2'(z)] = \lim_{y\to 0^-} [\theta_i'(z) - \eta_i\theta_2'(z)], \quad i = 1, 3. \quad (4.2)$$

Thus the function $\theta_i'(z) - \eta_i\theta_2'(z)$, $i = 1, 3$, is holomorphic in the whole plane including the points at infinity and it tends to zero as $|z| \to \infty$ since the stresses vanish at infinity, hence by Liouville's theorem one can conclude that

$$\theta_i'(z) - \eta_i\theta_2'(z) = 0, \quad i = 1, 3. \quad (4.3)$$

Employing this result into $(4.1)_3$, the displacement boundary conditions may now be expressed in terms of θ_2 as

$$\theta_2'(x^+) + \frac{\bar{\beta}}{\beta}\theta_2'(x^-) = \frac{i}{\beta}g'(x), \quad x \in L, \quad (4.4a)$$

where

$$\beta = m_{22}^* + \eta_1 m_{21}^* + \eta_3 m_{23}^*. \quad (4.4b)$$

Equation (4.4) is a standard Hilbert problem, the solution to it is (Muskhelishvili, 1954)

$$\theta_2'(z) = \frac{X(z)}{2\pi}\left\{\int_L \frac{g'(t)}{\beta X^+(t)(t-z)}\,dt + iN\right\}, \quad (4.5a)$$

where

$$X(z) = (z-a)^{-\delta}(z-b)^{\delta-1},$$
$$\delta = \frac{1}{2\pi}\arg\left(-\frac{\bar{\beta}}{\beta}\right), \quad 0 \le \delta < 1. \quad (4.5b)$$

N is the resultant normal force applied by the body S_1 (or S_2) to the body S_2 (or S_1). arg stands for the argument of a complex number. Note that δ is a real number and hence there are no oscillatory singularities in the solution. a and b are the ends of the contact region L, which should be determined by assuming the stresses vanish at $x = a$ and $x = b$, i.e., $\sigma_{22}(a) = \sigma_{22}(b) = 0$.

For a contact problem, it is always interesting to know the contact pressure and the surface deformation of these two elastic bodies. From (3.7), (2.1c), and (4.3), we have

$$\sigma_{22}(x) = \theta_2'(x^-) - \theta_2'(x^+),$$
$$u_2^{(1)} = i\beta^{(1)}\theta_2'(x^+) + i\bar{\beta}^{(1)}\theta_2'(x^-),$$
$$u_2^{(2)} = -i\bar{\beta}^{(2)}\theta_2'(x^+) - i\beta^{(2)}\theta_2'(x^-), \quad (4.6a)$$

where

$$\beta^{(k)} = m_{22}^{(k)} + \eta_1 m_{21}^{(k)} + \eta_3 m_{23}^{(k)}, \quad k = 1, 2, \quad (4.6b)$$

and $m_{ij}^{(k)}$, $i, j = 1, 2, 3$ are the components of the matrices $\mathbf{M}_k^{-1}$, $k = 1, 2$. Also, from (3.11), (4.4b), and (4.6b), we have $\beta^{(1)} + \bar{\beta}^{(2)} = \beta$. By (4.4$a$), we may express $\theta_2(x^+)$ (or $\theta_2(x^-)$) in terms of $\theta_2(x^-)$ (or $\theta_2(x^+)$) for the contact region. As to the noncontact region, $\theta_2(x^+) = \theta_2(x^-)$, which is obtained from the traction-free conditions given in $(3.1)_2$ and $(3.7)_1$. By these relations, the contact pressure and the surface deformation may be completely determined by $\theta_2(x^-)$ (or $\theta_2(x^+)$). Through the assumption $g^{*\prime}(x) \cong 0$, the surface after deformation in the x_2-direction may be expressed, by (2.2a), as $g^{(1)*}(x) = g^{(1)}(x) + u_2^{(1)}(x)$ for the body S_1, and $g^{(2)*}(x) = g^{(2)}(x) + u_2^{(2)}(x)$ for the body S_2. Along the contact line $g^{(1)*}(x) = g^{(2)*}(x) = g^*(x)$, where $x \in L$. Following the above statements, we may now derive a simplified expression for the contact pressure and surface deformation. The result is

$$\left.\begin{aligned} \sigma_{22}(x) &= \frac{1}{\beta}\{(\beta+\bar{\beta})\theta_2'(x^-) - ig'(x)\}, \\ g^*(x) &= \frac{1}{\beta}\{\bar{\beta}^{(2)}g^{(1)}(x) + \beta^{(1)}g^{(2)}(x) \\ &\quad + i(\bar{\beta}^{(1)}\bar{\beta}^{(2)} - \beta^{(1)}\beta^{(2)})\theta_2(x^-)\} \end{aligned}\right\}, \quad x \in L \quad (4.7a)$$

and

$$\left.\begin{aligned} g^{(1)*}(x) &= g^{(1)}(x) + i(\beta^{(1)} + \bar{\beta}^{(1)})\theta_2(x^-), \\ g^{(2)*}(x) &= g^{(2)}(x) - i(\beta^{(2)} + \bar{\beta}^{(2)})\theta_2(x^-), \end{aligned}\right\}, \quad x \notin L. \quad (4.7b)$$

The problem now is solved in principle. Since no analytical solution has been found for such a general case, the verification was done by specializing the present problem to a problem of which the analytical solution exists. The most recent one should be the problem considering a rigid punch sliding along the half-plane surface. By letting $\mathbf{M}_1 = \mathbf{0}$ (from the condition that S_1 is rigid) and $g^{(2)\prime}(x) = 0$ (from the condition that the half-plane surface is flat), it can easily be proved that our present solutions (4.5) and (4.7) agree with the solutions presented in Fan and Hwu (1996) and Hwu and Fan (1998a) for the case of a rigid punch sliding along the half-plane surface.

From the solutions obtained in (4.5), we observed that the anisotropic effects are reflected through the parameter β. For the contact of two orthotropic elastic bodies, the explicit expression of β may be obtained by substituting (3.13) into (4.4b). The result is

$$\beta = \frac{1}{L_{22}^{(1)}L_{22}^{(2)}}\{L_{22}^{(1)} + L_{22}^{(2)} + i\eta_1(S_{12}^{(1)}L_{22}^{(2)} - S_{12}^{(2)}L_{22}^{(1)})\}. \quad (4.8)$$

For two contacted isotropic elastic bodies, (4.8) may be further reduced by employing the relations given in (B5). The result is

$$\beta = \frac{1}{4\mu_1\mu_2}\{\mu_1(1+\kappa_2) + \mu_2(1+\kappa_1) + i\eta_1[\mu_2(1-\kappa_1) - \mu_1(1-\kappa_2)]\}. \quad (4.9)$$

Contact of Two Parabolic Elastic Bodies. Consider the case of contact between two anisotropic elastic bodies bounded by surfaces $g^{(1)}(x) = x^2/2R_1$ and $g^{(2)}(x) = -(x^2/2R_2)$ where R_1 and R_2 are the radii of the curvatures and should be large enough to approximate to straight lines. The resultant vector of the external force applied by the body S_1 (or S_2) to the body S_2 (or S_1) is $(N, F, 0)$, from which $\eta_1 = F/N$ and $\eta_3 = 0$. By (2.3b), we have

$$g(x) = \frac{x^2}{2}\left(\frac{1}{R_1} + \frac{1}{R_2}\right). \quad (4.10)$$

Substituting (4.10) into (4.5), and evaluating the line integral with the aid of residue theory (Muskhelishvili, 1954), we obtain

$$\theta_2'(z) = \frac{i(R_1+R_2)}{(\beta+\bar{\beta})R_1R_2}\{z - X(z)j_2(z)\} + \frac{iN}{2\pi}X(z), \quad (4.11a)$$

where

$$j_2(z) = z^2 - [\delta(a-b) + b]z - \tfrac{1}{2}\delta(1-\delta)(a-b)^2. \quad (4.11b)$$

The normal pressure $\sigma_{22}(x)$ along the contact region can then be calculated by substituting (4.11) into $(4.7a)_1$. The result is

$$\sigma_{22}(x) = \frac{-iX(x^-)(R_1+R_2)}{\beta R_1 R_2}\left\{ j_2(x) - \frac{(\beta+\bar{\beta})R_1R_2N}{2\pi(R_1+R_2)} \right\}, \quad a < x < b, \quad (4.12a)$$

where

$$X(x^-) = -(x-a)^{-\delta}(b-x)^{\delta-1}e^{-i\pi\delta}, \; a < x < b. \quad (4.12b)$$

The contact region (a, b) can now be determined by assuming the stresses vanish at the ends $x = a$ and $x = b$. Substituting (4.12) into $\sigma_{22}(a) = \sigma_{22}(b) = 0$, we obtain

$$a^2 = \frac{\delta(\beta+\bar{\beta})R_1R_2N}{\pi(1-\delta)(R_1+R_2)},$$

$$b^2 = \frac{(1-\delta)(\beta+\bar{\beta})R_1R_2N}{\pi\delta(R_1+R_2)}. \quad (4.13)$$

Corresponding to these values, (4.12) can be further simplified to

$$\sigma_{22}(x) = -\frac{2(R_1+R_2)\sin\pi\delta}{(\beta+\bar{\beta})R_1R_2}(x-a)^{1-\delta}(b-x)^{\delta}, \quad a < x < b. \quad (4.14)$$

The solution (4.14) shows clearly how the parameters R_1, R_2, a, b, β, δ influence the contact pressure. With the aid of $(4.4b)$, $(4.5b)_2$, (4.8), (4.9), and (4.13), it can be easily understood how these parameters relate to the geometry, loading, and material properties of the contact bodies.

To find the solution for the surface deformation, one may use $(3.7)_{2,3}$ in which $\boldsymbol{\theta}(x^{\pm}) = \{\theta_1(x^{\pm}), \theta_2(x^{\pm}), \theta_3(x^{\pm})\}^T$ where $\theta_2(z)$ are obtained from (4.11) by integration with respective to z, and $\theta_1(z)$ and $\theta_3(z)$ are related to $\theta_2(z)$ by (4.3). If one is only concerned about the deformation in the x_2-direction, a simplified result has been provided in $(4.7a, b)$.

Numerical Example. Consider two orthotropic elastic bodies whose material properties are

$$E_1 = 114.8 \text{ Gpa}, \quad E_2 = 48.0 \text{ Gpa}, \quad G_{12} = 24.0 \text{ Gpa}, \quad \nu_{12} = 0.21, \quad \text{for } S_1,$$

$$E_1 = 60.7 \text{ Gpa}, \quad E_2 = 24.8 \text{ Gpa}, \quad G_{12} = 12.0 \text{ Gpa}, \quad \nu_{12} = 0.23, \quad \text{for } S_2,$$

where E, G, and ν are, respectively, the Young's modulus, shear modulus, and the Poisson's ratio. The subscripts 1 and 2 denote the x and y directions. The radii of the curvatures for the boundaries of the elastic bodies are $R_1 = 100$ m and $R_2 = 200$ m. The coefficient of static friction is $\mu_s = 0.5$. We now consider the contact of these two elastic bodies suppressed by the normal force $N = 1$ kN and the horizontal force $F = 0.4$ kN, which is less than the maximum friction force so that these two bodies are in the equilibrium condition. From these data we obtained $\eta_1 = 0.4$, $\beta = (10.85 + 0.41i) \times 10^{-11}$ m^2/N, $\beta^{(1)} = (3.68 - 0.47i) \times 10^{-11}$ m^2/N, $\beta^{(2)} = (7.17 - 0.88i) \times 10^{-11}$ m^2/N, $\delta = 0.488$, $a = -2.09 \times 10^{-3}$ m, $b = 2.20 \times 10^{-3}$ m. The contact pressure and surface deformation can then be calculated by using (4.14) and (4.7). The results are shown in Fig. 2 which seems to be symmetric with respect to the contact center. It looks unreasonable since the friction is considered in this case. However, the numerical data of a, b, and δ calculated above show that they are really unsymmetric but nearly symmetric. A more clear unsymmetric deformation is shown in Fig. 1 in which $\eta_1 = 0.8$. Note that the surface deformation plotted in Figs. 1 and 2 has been magnified 10^5 times to see clearly how they deform.

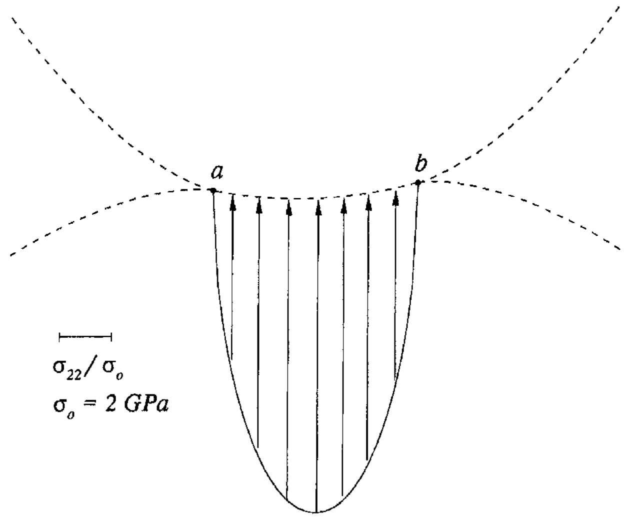

Fig. 2 Contact pressure and surface deformation for the contact between two parabolic orthotropic elastic bodies

5 Contact in the Absence of Friction

In the case that the surface between two contact bodies is frictionless, the load ratios η_1 and η_3 cannot exceed zero, because no horizontal forces can be applied on these two bodies in order to have an equilibrium state. Thus, the contact problems in the absence of friction can easily be solved by substituting $\eta_1 = \eta_3 = 0$ into the results obtained in Section 4.

From $(4.4b)$ and $(4.6b)$ with $\eta_1 = \eta_3 = 0$, we have $\beta = m^*_{22}$ and $\beta^{(k)} = m^{(k)}_{22}$ which are positive nonzero real numbers by (3.12) and $(3.8b)$. Thus, δ defined in $(4.5b)_2$ will be equal to $\frac{1}{2}$ for the frictionless contact surface. Hence, by substituting $\beta = \bar{\beta} = m^*_{22}$, $\delta = \frac{1}{2}$ and $\eta_1 = \eta_3 = 0$ into (4.5)–(4.9), the solutions to the contact problems in the absence of friction can be obtained. For the case of two parabolic elastic bodies, simplification of (4.11), (4.13), and (4.14) leads to

$$\theta_2'(z) = \frac{i(R_1+R_2)}{2m^*_{22}R_1R_2}\left\{ z - \frac{z^2 - (b^2/2)}{\sqrt{z^2-b^2}} \right\} + \frac{iN}{2\pi\sqrt{z^2-b^2}}, \quad (5.1)$$

$$\sigma_{22}(x) = -\frac{R_1+R_2}{m^*_{22}R_1R_2}\sqrt{b^2-x^2}, \quad |x| < b, \quad (5.2)$$

where

$$-a = b = \sqrt{\frac{2m^*_{22}R_1R_2N}{\pi(R_1+R_2)}}. \quad (5.3)$$

From (5.2) and (5.3), we see that the maximum contact pressure $(\sigma_{22})_{\max}$ occurs at the middle of the contact region. That is, when $x = 0$, we have

$$|\sigma_{22}|_{\max} = \frac{(R_1+R_2)b}{m^*_{22}R_1R_2} = \frac{2N}{\pi b}, \quad (5.4)$$

in which the second equation is obtained by using the relation given in (5.3).

Knowing that $\beta^{(1)}$ $(=m_{22}^{(1)})$ and $\beta^{(2)}$ $(=m_{22}^{(2)})$ are real numbers for the bodies with frictionless surfaces, the surface deformation in the x_2-direction given in (4.7) can now be simplified by integrating (5.1) with respective to z and letting $z = x^-$. The result is

$$g^*(x) = \frac{R_2 m_{22}^{(2)} - R_1 m_{22}^{(1)}}{2m_{22}^* R_1 R_2} x^2, \quad -b < x < b,$$

$$g^{(1)*}(x) = \frac{x^2}{2R_1} + 2im_{22}^{(1)}\theta_2(x^-),$$

$$g^{(2)*}(x) = -\frac{x^2}{2R_2} - 2im_{22}^{(2)}\theta_2(x^-), \tag{5.5a}$$

where

$$\theta_2(x^-) = \begin{cases} \dfrac{iN}{2\pi}[(x^2 - x\sqrt{x^2-b^2})/b^2 \\ \quad + \log(x + \sqrt{x^2-b^2})], \quad x > b, \\ \dfrac{iN}{2\pi}[(x^2 + x\sqrt{x^2-b^2})/b^2 \\ + \log|x - \sqrt{x^2-b^2}|], \quad x < -b. \end{cases} \tag{5.5b}$$

By comparing our solutions for anisotropic elastic bodies with the solutions provided in Rekach (1979) for isotropic elastic bodies, it is surprising to find that they are quite similar in the solution form and the anisotropy is reflected only through the parameter m_{22}^*. When we substitute m_{22}^* by its corresponding isotropic value (given by (4.9) with $\eta_1 = 0$), we find that our solution is identical to that given in Rekach (1979) in which the problem was solved by employing the concept of superposition of surface Green's function. It is also possible to apply this concept to anisotropic media. In the following, we like to double check our solution by employing this concept.

An Alternative Approach. Because the problem we discuss in this section is the contact in the absence of friction, we assume the state of surface tractions between the contact region have only σ_{22} component and $\sigma_{12} = \sigma_{32} = 0$. Let the compressive stress σ_{22} be expressed by the unknown distributed forces of intensity $p(x)$ whose resultant N is given, i.e.,

$$\int_L p(x)dx = N.$$

The stress and displacement field of a half-plane subjected to this distributed forces may be found by integrating the solutions associated with the point forces. The solution to the anisotropic half-plane subjected to a point force applied on the half-plane surface can be found in Ting (1996). If the point force $p(\xi)d\xi$ is located on $(\xi, 0)$, the surface deformation in the x_2-direction may be expressed by Ting (1996)

$$du_2(x) = -\frac{1}{\pi}\ln|x-\xi|L_{22}^{-1}p(\xi)d\xi,$$

$$\text{along the half-plane surface.} \tag{5.6}$$

Knowing that the forces applied on the bodies S_1 and S_2 have the same value but opposite direction, by integration of (5.6) for bodies S_1 and S_2, the boundary condition shown in $(2.6a)_4$ may now be written as

$$\frac{m_{22}^*}{\pi}\int_L \ln|x-\xi|p(\xi)d\xi = g(x), \tag{5.7}$$

in which the relation given in (3.13) for m_{22}^* has been used. For the case of two parabolic elastic bodies, substitution of (4.10) into (5.7) and differentiation of (5.7) with respect to x may lead to

$$\frac{m_{22}^*}{\pi}\int_{-a}^{a}\frac{p(\xi)}{x-\xi}d\xi = x\left(\frac{1}{R_1} + \frac{1}{R_2}\right). \tag{5.8}$$

The form of the integral Eq. (5.8) is identical to that of the corresponding isotropic integral equation (Rekach, 1979). Thus, by comparison one may easily prove that the solution of the unknown intensity $p(x)$ is exactly the same as that presented in (5.2) and (5.3).

6 Contact in Complete Adhesion

By the method of analytical continuation presented in Section 3, we show that the tractions and displacements can be expressed in terms of a single sectionally holomorphic function vector $\boldsymbol{\theta}$. Through the use of $(3.7)_1$ and (3.10), the boundary conditions (2.7) for the contact in complete adhesion may now be written as

$$\boldsymbol{\theta}'(x^-) - \boldsymbol{\theta}'(x^+) = \mathbf{0}, \quad x \notin L,$$

$$-i\{\mathbf{M}^*\boldsymbol{\theta}(x^+) + \bar{\mathbf{M}}^*\boldsymbol{\theta}(x^-)\} = \mathbf{g}(x), \quad x \in L, \tag{6.1a}$$

where

$$\mathbf{g}(x) = \begin{Bmatrix} 0 \\ g(x) \\ 0 \end{Bmatrix}. \tag{6.1b}$$

To solve $\boldsymbol{\theta}(z)$ from (6.1), we rewrite $(6.1a)_2$ into a standard vector form of the Hilbert problem as

$$\boldsymbol{\theta}'(x^+) + \mathbf{M}^{*-1}\bar{\mathbf{M}}^*\boldsymbol{\theta}'(x^-) = i\mathbf{M}^{*-1}\mathbf{g}'(x), \quad x \in L. \tag{6.2}$$

The solution to this Hilbert problem of the vector form is (Hwu, 1992; Fan and Hwu, 1996)

$$\boldsymbol{\theta}'(z) = \frac{1}{2\pi}\mathbf{X}_0(z)\int_L \frac{1}{t-z}[\mathbf{X}_0^+(t)]^{-1}\mathbf{M}^{*-1}\mathbf{g}'(t)dt + \mathbf{X}_0(z)\mathbf{d}_0. \tag{6.3}$$

$\mathbf{X}_0(z)$ is the basic Plemelj function satisfying

$$\mathbf{X}_0^+(x) = \mathbf{X}_0^-(x), \quad x \notin L,$$

$$\mathbf{X}_0^+(x) + \mathbf{M}^{*-1}\bar{\mathbf{M}}^*\mathbf{X}_0^-(x) = \mathbf{0}, \quad x \in L, \tag{6.4a}$$

whose solution is

$$\mathbf{X}_0(z) = \frac{1}{\sqrt{(z-a)(z-b)}}\boldsymbol{\Lambda}\left\langle\left\langle\left(\frac{z-a}{z-b}\right)^{i\epsilon_\alpha}\right\rangle\right\rangle, \tag{6.4b}$$

where the angular bracket $\langle\langle\ \rangle\rangle$ denotes the diagonal matrix in which each component is varied according to the Greek index α. $\boldsymbol{\Lambda} = [\boldsymbol{\lambda}_1, \boldsymbol{\lambda}_2, \boldsymbol{\lambda}_3]$. ϵ_α and $\boldsymbol{\lambda}_\alpha$, $\alpha = 1, 2, 3$ of $(6.3d)$ are the eigenvalues and eigenvectors of $(\bar{\mathbf{M}}^* - e^{2\pi\epsilon_\alpha}\mathbf{M}^*)\boldsymbol{\lambda}_\alpha = \mathbf{0}$. The explicit solutions for the eigenvalues ϵ_α are $\epsilon_1 = -\epsilon_2 = \epsilon$, $\epsilon_3 = 0$, and

$$\epsilon = \frac{1}{2\pi}\ln\frac{1+\gamma}{1-\gamma}, \quad \gamma = \left[-\frac{1}{2}\operatorname{tr}(\mathbf{W}\mathbf{D}^{-1})^2\right]^{1/2}, \tag{6.5}$$

where tr stands for the trace of matrix. To get a unique eigenvector, the normalization $\frac{1}{2}\bar{\boldsymbol{\Lambda}}^T(\mathbf{M}^* + \bar{\mathbf{M}}^*)\boldsymbol{\Lambda} = \mathbf{I}$ is used (Hwu, 1993b).

To determine the constant vector $\mathbf{d}_0$ in (6.3), the force equilibrium condition may be applied. With reference to the problems of half-plane indentation, one may prove that

$$\mathbf{d}_0 = \frac{1}{2\pi i}\boldsymbol{\Lambda}^{-1}\mathbf{q}, \tag{6.6}$$

where $\mathbf{q}$ is the resultant force vector applied on the elastic body S_1 (or S_2). The contact pressure can now be obtained by substituting the result of (6.3) into $(3.7)_1$. The contact region is then determined by assuming that the stresses vanish at its ends. The verification can also be done by specializing the present problem to a problem of which the analytical solution exists. Similar to the problem discussed in Section 4, by letting $\mathbf{M}_1 = \mathbf{0}$ and $\mathbf{g}^{(2)'}(x) = 0$ one may prove that our present solutions are identical to those presented in Fan and Hwu (1996) for the case of a rigid punch indenting into a half-plane.

7 Concluding Remarks

Note that during the derivation through the method of analytical continuation, the argument of each component function of $\boldsymbol{\theta}(z)$ is written as $z = x + py$ without referring to its associated eigenvalues p_α. So are the function vectors $\mathbf{f}_1(z)$ and $\mathbf{f}_2(z)$ calculated from $\boldsymbol{\theta}(z)$ by the relations given in (3.6). However, the general solutions presented in (2.1) show that $\mathbf{f}_1(z)$ or $\mathbf{f}_2(z)$ should be in the form of $[f_1(z_1)\ f_2(z_2)\ f_3(z_3)]^T$ where the argument of each component function is written as $z_\alpha = x + p_\alpha y$, $\alpha = 1, 2, 3$, in which p_α are the eigenvalues of material 1 or 2. With this understanding, we know that the replacement of z_1, z_2, or z_3 for each component function of $\mathbf{f}_1(z)$ and $\mathbf{f}_2(z)$ is necessary for any problem found in this paper. For example, when we obtain the solution of $\theta_2'(z)$ from (4.5) for the contact problems in the presence of friction, we may find $\theta_1'(z)$ and $\theta_3'(z)$ by (4.3). Then, by using (3.6), we have $\mathbf{f}_1(z) = -\mathbf{B}_1^{-1}\boldsymbol{\theta}(z)$ and $\mathbf{f}_2(z) = \mathbf{B}_2^{-1}\boldsymbol{\theta}(z)$ in which $\boldsymbol{\theta}(z) = [\theta_1(z), \theta_2(z), \theta_3(z)]^T$. After getting $\mathbf{f}_1(z)$ and $\mathbf{f}_2(z)$, a replacement of $z_1^{(i)}$, $z_2^{(i)}$, or $z_3^{(i)}$ for each component function of $\mathbf{f}_i(z)$, $i = 1, 2$ should be made in order to calculate the field solutions for the stresses and displacements from (2.1).

Acknowledgments

The authors would like to thank the support by National Science Council, Republic of China, through Grant No. NSC 86-2212-E006-056 and NSC 88-2212-E006-066.

References

Conway, H. D., 1956, "The Indentation of a Transversely Isotropic Half-Space by a Rigid Punch," *J. Applied Mathematics and Physics (ZAMP)*, Vol. 7, pp. 80–85.

Dahan, M., and Zarka, J., 1977, "Elastic Contact Between a Sphere and a Semi-Infinite Transversely Isotropic Body," *International Journal of Solids and Structures*, Vol. 13, pp. 229–238.

Dongye, C., and Ting, T. C. T., 1989, "Explicit Expressions of Barnett-Lothe Tensors and Their Associated Tensors for Orthotropic Materials," *Q. Appl. Math.*, Vol. 47, pp. 723–734.

Eshelby, J. D., Read, W. T., and Shockley, W., 1953, "Anisotropic Elasticity with Application to Dislocation Theory," *Act. Met.*, Vol. 1, pp. 251–259.

Fabrikant, V. I., 1971, "Effect of Shearing Force and Tilting Moment on a Cylindrical Punch Attached to a Transversely Isotropic Half-Space," *Journal of Applied Mathematics and Mechanics*, Vol. 35, pp. 178–182.

Fan, C. W., and Hwu, C., 1996, "Punch Problems for an Anisotropic Elastic Half-Plane," ASME Journal of Applied Mechanics, Vol. 63, pp. 69–76.

Galin, L. A., 1953, *Contact Problems of the Theory of Elasticity*, Gostekhteoretizdat, Moscow (in Russian); English Translation by I. N. Sneddon, ed., 1961, Department of Mathematics, North Carolina State College, Raleigh, NC.

Glagolev, N. I., 1945, "Resistance to Rotation of Cylindrical Bodies," *Journal of Applied Mathematics and Mechanics*, Vol. 9, No. 4, pp. 318–333.

Gladwell, G. M. L., 1980, *Contact Problems in the Classical Theory of Elasticity*, Sithoff and Noordhoff, Alpen aan den Rijn, The Netherlands.

Gotoh, M., 1967, "Some Problems of Bonded Anisotropic Plates with Crack along the Bond," *Int. J. of Fracture Mechanics*, Vol. 3, pp. 253–265.

Green, A. E., and Zerna, W., 1968, *Theoretical Elasticity*, Oxford University Press, London.

Hertz, H., 1882, "On the Contact of Elastic Solids," *J. reine und angewandte Mathematik*, Vol. 92, pp. 156–171.

Hwu, C., 1992, "Thermoelastic Interface Crack Problems in Dissimilar Anisotropic Media," *International Journal of Solids and Structures*, Vol. 29, pp. 2077–2090.

Hwu, C., 1993a, "Fracture Parameters for Orthotropic Bimaterial Interface Cracks," *Engineering Fracture Mechanics*, Vol. 45, No. 1, pp. 89–97.

Hwu, C., 1993b, "Explicit Solutions for the Collinear Interface Crack Problems," *International Journal of Solids and Structures*, Vol. 30, pp. 301–312.

Hwu, C., and Fan, C. W., 1998a, "Sliding Punches with/without Friction Along the Surface of the Anisotropic Elastic Half-Plane," *Q. J. Mech. Appl. Math.*, Vol. 51, Pt. 1, pp. 159–177.

Hwu, C., and Fan, C. W., 1998b, "Solving the Punch Problems by Analogy with the Collinear Interface Crack Problems," *International Journal of Solids and Structures*, in press.

Johnson, K. L., 1985, *Contact Mechanics*, Cambridge University Press, Cambridge, UK.

Muskhelishvili, N. I., 1954, *Some Basic Problems of the Mathematical Theory of Elasticity*, Noordhoff, Groningen, The Netherlands.

Rekach, V. G., 1979, *Manual of the Theory of Elasticity*, Mir Publishers, Moscow.

Shtaeman, A. Ia, 1949, *Contact Problems of the Theory of Elasticity*, Gostekhteoretizdat, Moscow (in Russian).

Stroh, A. N., 1958, "Dislocations and Cracks in Anisotropic Elasticity," *Phil. Mag.*, Vol. 7, pp. 625–646.

Ting, T. C. T., 1988, "Some Identities and the Structure of Ni in the Stroh Formalism of Anisotropic Elasticity," *Q. Appl. Math.*, Vol. 46, pp. 109–120.

Ting, T. C. T., 1992, "Barnett-Lothe Tensors and Their Associated Tensors for Monoclinic Materials with the Symmetry Plane at $x_3 = 0$," *J. Elasticity*, Vol. 27, pp. 143–165.

Ting, T. C. T., 1996, *Anisotropic Elasticity—Theory and Applications*, Oxford Science Publications, New York.

Wei, L., and Ting, T. C. T., 1994, "Explicit Expressions of Barnett-Lothe Tensors for Anisotropic Materials," *J. Elasticity*, Vol. 36, pp. 67–83.

Willis, J. R., 1966, "Hertzian Contact of Anisotropic Bodies," *J. Mech. Phys. Solids*, Vol. 14, pp. 163–176.

Willis, J. R., 1971, "Fracture Mechanics of Interfacial Cracks," *J. of Mechanics and Physics of Solids*, Vol. 19, pp. 353–368.

APPENDIX A

Stroh's Formalism

In a fixed rectangular coordinate system x_i, $i = 1, 2, 3$, let u_i, σ_{ij}, ϵ_{ij} be, respectively, the displacement, stress, and strain. The strain-displacement equations, the stress-strain laws, and the equations of equilibrium for anisotropic elasticity are

$$\epsilon_{ij} = \tfrac{1}{2}(u_{i,j} + u_{j,i}), \quad \sigma_{ij} = C_{ijks}\epsilon_{ks}, \quad \sigma_{ij,j} = 0, \qquad \text{(A1)}$$

where repeated indices imply summation, a comma stands for differentiation, and C_{ijks} are the elastic constants which are assumed to be fully symmetric and positive definite. Consider a two-dimensional deformation in which u_i, $i = 1, 2, 3$, depend on x_1 and x_2 only, the general solution to (A1) can be written as

$$\mathbf{u} = \sum_{\alpha=1}^{6} \mathbf{a}_\alpha f_\alpha(z_\alpha), \quad z_\alpha = x_1 + p_\alpha x_2, \qquad \text{(A2)}$$

in which f_α, $\alpha = 1, 2, \ldots, 6$ are arbitrary functions of their arguments and p_α and $\mathbf{a}_\alpha$ are the eigenvalues and eigenvectors of the following eigenrelation:

$$\{\mathbf{Q} + p(\mathbf{R} + \mathbf{R}^T) + p^2\mathbf{T}\}\mathbf{a} = \mathbf{0}. \qquad \text{(A3)}$$

In (A3) the superscript T stands for the transpose and $\mathbf{Q}$, $\mathbf{R}$, $\mathbf{T}$ are the 3×3 real matrices given by

$$Q_{ik} = C_{i1k1}, \quad R_{ik} = C_{i1k2}, \quad T_{ik} = C_{i2k2}. \qquad \text{(A4)}$$

Since p_α cannot be real if the strain energy is positive (Eshelby, et. al., 1953), p_α occurs as three pairs of complex conjugates. We let $p_{\alpha+3} = \bar{p}_\alpha$, $\mathrm{Im}(p_\alpha) > 0$, $\alpha = 1, 2, 3$, where an overbar denotes the complex conjugate and Im stands for the imaginary part. We then have $\mathbf{a}_{\alpha+3} = \bar{\mathbf{a}}_\alpha$, $\alpha = 1, 2, 3$. For the displacement $\mathbf{u}$ to be real, we let $f_{\alpha+3} = \bar{f}_\alpha$, $\alpha = 1, 2, 3$, and (A2) becomes

$$\mathbf{u} = 2\,\mathrm{Re}\{\sum_{\alpha=1}^{3} \mathbf{a}_\alpha f_\alpha(z_\alpha)\}, \qquad \text{(A5)}$$

in which Re stands for the real part. Introducing the vector

$$\mathbf{b} = (\mathbf{R}^T + p\mathbf{T})\mathbf{a} = -\frac{1}{p}(\mathbf{Q} + p\mathbf{R})\mathbf{a}, \qquad \text{(A6)}$$

where the second equality comes from (A3), the stresses σ_{ij} obtained by substituting (A2) into $(\mathrm{A1})_1$ and $(\mathrm{A1})_2$ can be written as

$$\sigma_{i1} = -\phi_{i,2}, \quad \sigma_{i2} = \phi_{i,1}, \tag{A7}$$

where $\boldsymbol{\phi}$ is the stress function

$$\boldsymbol{\phi} = 2\,\mathrm{Re}\{\sum_{\alpha=1}^{3} \mathbf{b}_\alpha f_\alpha(z_\alpha)\}. \tag{A8}$$

If we introduce a 3×1 column vector $\mathbf{f}(z)$ and two 3×3 complex matrices $\mathbf{A}$ and $\mathbf{B}$ by

$$\mathbf{f}(z) = \{f_1(z_1),\ f_2(z_2),\ f_3(z_3)\}^T,$$
$$\mathbf{A} = [\mathbf{a}_1 \quad \mathbf{a}_2 \quad \mathbf{a}_3], \quad \mathbf{B} = [\mathbf{b}_1 \quad \mathbf{b}_2 \quad \mathbf{b}_3], \tag{A9}$$

Eqs. (A5) and (A8) can be written as

$$\mathbf{u} = 2\,\mathrm{Re}\{\mathbf{A}\mathbf{f}(z)\}, \quad \boldsymbol{\phi} = 2\,\mathrm{Re}\{\mathbf{B}\mathbf{f}(z)\}. \tag{A10}$$

APPENDIX B

The Explicit Expressions of S and L

For orthotropic materials, the explicit expressions for **S** and **L** have been found by Dongye and Ting (1989). Their solutions are written in terms of the elastic constants C_{ij} as follows:

$$S_{21} = \left[\frac{C_{66}(\sqrt{C_{11}C_{22}} - C_{12})}{C_{22}(C_{12} + 2C_{66} + \sqrt{C_{11}C_{22}})}\right]^{1/2}, \quad S_{12} = -\sqrt{\frac{C_{22}}{C_{11}}}\,S_{21},$$

$$L_{11} = (C_{12} + \sqrt{C_{11}C_{22}})S_{21}, \quad L_{22} = \sqrt{\frac{C_{22}}{C_{11}}}\,L_{11},$$

$$L_{33} = (C_{44}C_{55})^{1/2}, \tag{B1}$$

and all the other components of S_{ij} and L_{ij} are equal to zero.

Following the solutions provided in (B1), Hwu (1993a) derived a more convenient formulae for **S** and **L**. They wrote the explicit solutions in terms of the Young's moduli E_1, E_2, E_3, the Poisson's ratios ν_{ij}, and the shear moduli G_{23}, G_{31}, G_{12}. Their results are

$$S_{12} = -s\kappa_1\alpha_2, \quad S_{21} = s\kappa_2\alpha_1,$$
$$L_{11} = \kappa_1\alpha_1E_1, \quad L_{22} = \kappa_2\alpha_2E_2, \quad L_{33} = \sqrt{G_{23}G_{31}}, \tag{B2}$$

where

$$\kappa_1 = (E_1/G_{12} + 2s\sqrt{E_1/E_2})^{-1/2},$$
$$\kappa_2 = (E_2/G_{12} + 2s\sqrt{E_2/E_1})^{-1/2}. \tag{B3}$$

In the case of generalized plane strain

$$\alpha_1 = (1 - \nu_{13}\nu_{31})^{-1/2}, \quad \alpha_2 = (1 - \nu_{23}\nu_{32})^{-1/2},$$
$$s = \sqrt{(1 - \nu_{13}\nu_{31})(1 - \nu_{23}\nu_{32})} - \sqrt{(\nu_{21} + \nu_{31}\nu_{23})(\nu_{12} + \nu_{32}\nu_{13})}, \tag{B4a}$$

whereas in the case of generalized plane stress

$$\alpha_1 = \alpha_2 = 1, \quad s = 1 - \sqrt{\nu_{12}\nu_{21}}. \tag{B4b}$$

For isotropic materials, $E_1 = E_2 = E$, $G_{12} = G_{23} = G_{31} = \mu = E/[2(1 + \nu)]$, $\nu_{23} = \nu_{32} = \nu_{13} = \nu_{31} = \nu_{12} = \nu_{21} = \nu$, (B2) may then be specialized as

$$S_{21} = -S_{12} = \frac{\kappa - 1}{\kappa + 1},$$
$$L_{11} = L_{22} = \frac{4\mu}{1 + \kappa}, \quad L_{33} = \mu. \tag{B5}$$

where $\kappa = 3 - 4\nu$ for plane-strain conditions and $\kappa = (3 - \nu)/(1 + \nu)$ for the generalized plane-stress condition.

Dispersion of Waves in Composite Laminates With Transverse Matrix Cracks, Finite Element and Plate Theory Computations

M. Åberg

P. Gudmundson
Mem. ASME

Department of Solid Mechanics,
Royal Institute of Technology, KTH,
100 44 Stockholm, Sweden

Dispersion relations for laminated composite plates with transverse matrix cracks have been computed using two methods. In the first approach it is assumed that the matrix cracks appear periodically and hence it is possible to consider a periodic cell of the structure using Bloch-type boundary conditions. This problem was formulated in complex notation and solved in a standard finite element program (ABAQUS) using two identical finite element meshes, one for the real part and one for the imaginary part of the displacements. The two meshes were coupled by the boundary conditions on the cell. The code then computed the eigenfrequencies of the system for a given wave vector. It was then possible to compute the phase velocities. The second approach used may be viewed as a two step homogenization. First the cracked layers are homogenized and replaced by weaker uncracked layers and then the standard first-order shear-deformation laminate theory is used to compute dispersion relations. Dispersion relations were computed using both methods for three glass-fiber/epoxy laminates ($[0/90]_2$, $[0/90]_S$ and $[0/45/-45]_S$ with cracks in the 90 and ± 45 deg plies). For the lowest flexural mode the difference in phase velocity between the methods was less then five percent for wavelengths longer than two times the plate thickness. For the extensional mode a wavelength of ten plate thicknesses gave a five percent difference.

1 Introduction

If a composite laminate is strained the first damage which appears is often transverse matrix cracking. Other damage types, such as fiber fracture and delaminations, will also start to develop before the laminate finally fails (Eggers et al., 1994; Ogihara and Takeda, 1995; Jamison and Reifsnider, 1982). The theories developed to describe the laminate during this process, especially regarding the evolution of damage, should be validated by experiments (Adolfsson and Gudmundson, 1996; Hahn et al., 1988; Xu, 1996).

One possible technique for monitoring the evolution of damage is acoustic emission. The basic idea behind acoustic emission is that any damage process within the material will emit sound (stress waves) and by measuring and analyzing the waves one can localize and characterize the process. In a classical acoustic emission experiment a resonant transducer is used to measure the values of certain preset parameters, but there is also the possibility of using a broadband transducer and looking at the signal in time-domain instead. For a fairly recent example see Gorman and Ziola (1991) or Prosser et al. (1995). A prerequisite for either scheme to be successful, however, is that one has a detailed knowledge of how waves propagate in the material. A complication with a composite laminate is that the velocity of the waves will depend on the frequency (dispersion). This dependence can, of course, be measured but there is also a need for a theoretical understanding of how waves behave in the material, and it is desirable to know on beforehand what velocity to expect at a given frequency.

Wave dispersion in infinite uncracked anisotropic elastic laminated plates has previously been studied thoroughly using at least two different approaches. In the first approach the full three-dimensional equations are solved. One example of this approach is the so-called stiffness method by Dong and Nelson (1972). The stiffness method, which essentially is a semi-one-dimensional finite element method, has been extended and refined by Datta and co-workers (1988, 1991a, b) to the point where it is possible to compute dispersion curves for arbitrary laminates and wave propagation directions. Also, a method with which standard finite element codes can be used to compute dispersion relations has recently been proposed by Åberg and Gudmundson (1997). The second approach is to use a plate theory, which may be viewed as a homogenization in the thickness direction. It is well known that the classical laminated plate theory is too stiff when the wavelength approaches the thickness of the laminate, and as a remedy a theory including first-order shear deformation and rotational inertia is often used (Yang et al., 1966; Whitney and Pagano, 1970). In conjunction with the first-order shear-deformation theory, shear correction factors are often utilized to take the variation of shear stress through the cross section of the laminate into account. Whitney (1973) has shown one possible way to arrive at shear correction factors. The choice of shear correction factor is somewhat arbitrary and consequently there has been work on plate theories that do not include a shear correction factor. One way to get around the need for a shear correction factor is to use higher-order displacement fields. The drawback is that more displacement parameters have to be introduced, and hence the more refined methods,

Contributed by the Applied Mechanics Division of THE AMERICAN SOCIETY OF MECHANICAL ENGINEERS for publication in the ASME JOURNAL OF APPLIED MECHANICS.

Discussion on the paper should be addressed to the Technical Editor, Professor Lewis T. Wheeler, Department of Mechanical Engineering, University of Houston, Houston, TX 77204-4792, and will be accepted until four months after final publication of the paper itself in the ASME JOURNAL OF APPLIED MECHANICS.

Manuscript received by the ASME Applied Mechanics Division, June 6, 1997; final revision, Feb. 16, 1998. Associate Technical Editor: V. K. Kinra.

like the discrete layer theory, approach a finite element formulation as far as degrees-of-freedom are concerned. A comparison between different order plate theories may be found in the paper by Noor and Burton (1990), and one of their conclusions is that a first-order shear-deformation theory with shear correction factors according to Whitney provides a fair prediction of the gross response for a wide variety of laminates. In conclusion, wave propagation in uncracked laminates seems to be fairly well understood and there are good tools available for prediction of dispersion curves.

Analyses of laminates with transverse matrix cracks have so far mainly been focused on static properties such as loss of stiffness due to cracks. For a review see Abrate (1991). A closed-form estimate of the loss of stiffness of a general laminate with periodic cracks was proposed by Gudmundson and Zang (1993) and has since been extended and validated in a series of works by Adolfsson and Gudmundson (1994, 1995, 1996, 1997). They have, among other things, proposed a way to take the loss of stiffness into account in classical laminate theory (Adolfsson and Gudmundson, 1997).

Dispersion in solids with several cracks has received attention in the literature (Smyshlyaev and Willis, 1993; Achenbach and Li, 1986), but to the authors' knowledge there are few works that focus on dispersion in laminates with transverse matrix cracks. One exception is Aboudi (1988), where Legendre polynomials are used to describe the local deformation in a subcell of a composite material with imperfect bonding (cracks). Curves are presented showing the transient behavior of a wave traveling through the material, but unfortunately dispersion curves are not given for this case.

The present work will focus on dispersion in laminated plates with transverse matrix cracks. The work is divided into two basic parts. In the first part it is assumed that the cracked laminate can be approximated by a linear elastic laminate containing a periodic distribution of cracks and the effects of crack closure will be ignored. Thus the problem is linear. Ignoring the effects of crack closure seems justifiable in laminates because residual stresses will usually keep the cracks open and the displacements due to wave motion are usually small. The periodicity assumption is based on the observation that transverse matrix cracks most often appear fairly evenly spaced. Having made those assumptions the laminate is modeled by a periodic unit-cell and the procedure using finite elements described by Åberg and Gudmundson (1997) is used to compute dispersion relations for glass fiber reinforced epoxy laminates. In the second part the stiffness estimations by Gudmundson and Zang (1993) and the first-order shear-deformation laminated plate theory with shear correction factors according to Whitney (1973) are used in conjunction to arrive at a first-order shear laminate theory for transversely cracked laminates. This is then applied to the same laminates as the finite element computations and the results are compared.

2 Periodic Distribution of Cracks

The scheme outlined and derived in this section is applicable to the general problem of harmonic wave propagation in linear elastic materials with a periodic geometry. It is the same procedure as used in an earlier work by the authors, and it is presented here for sake of clarity.

2.1 Governing Elastic Equations. A periodic structure made of one or several linear elastic materials is considered. By a periodic structure it is meant that the structure can be divided into identical finite-sized periodic cells, and therefore one single cell can be used to describe the whole structure (see Fig. 1). The governing equations at a point in the structure are

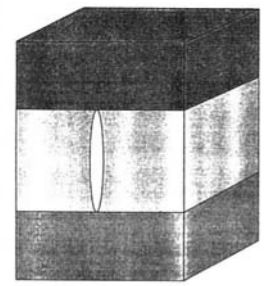

Periodic cell

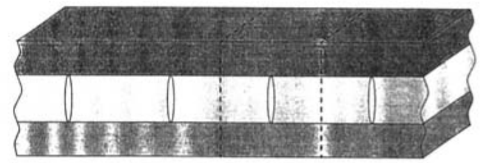

Periodic structure

Fig. 1 Example of a periodic structure and a corresponding periodic cell

$$\sigma_{ij,j} = \rho \frac{\partial^2 u_i}{\partial t^2}, \tag{1}$$

$$\sigma_{ij} = C_{ijkl}\epsilon_{kl} \tag{2}$$

where

$$\epsilon_{kl} = \tfrac{1}{2}(u_{k,l} + u_{l,k}). \tag{3}$$

Here σ_{ij} is the stress tensor, ϵ_{kl} the strain tensor, u_i the displacement vector, C_{ijkl} the stiffness tensor, and ρ the density. In all tensor equations the usual summation convention is assumed and differentiation with respect to a Cartesian coordinate is denoted by a comma. Note that the stiffness and the density depend on position periodically. Now consider solutions of the form

$$u_m(x_n, t) = U_m(x_n)e^{-i\omega t}, \tag{4}$$

where $U_m(x_n)$ is complex valued and x_n is the position vector. As a consequence the stresses and the strains will be given by

$$\sigma_{ij}(x_n, t) = \Sigma_{ij}(x_n)e^{-i\omega t} \tag{5}$$

and

$$\epsilon_{ij}(x_n, t) = E_{ij}(x_n)e^{-i\omega t}. \tag{6}$$

The equations of motion may now be written as

$$\Sigma_{ij,j} + \rho\omega^2 U_i = 0, \tag{7}$$

$$\Sigma_{ij} = C_{ijkl}E_{kl} \tag{8}$$

and

$$E_{kl} = \tfrac{1}{2}(U_{k,l} + U_{l,k}). \tag{9}$$

The periodic structure is divided into periodic cells. Due to the periodicity in C_{ijkl} and ρ the displacement at equivalent points in different periodic cells are related through

$$U_m(x_n) = U_m(x_n + l_n)e^{-ikn_j l_j}, \tag{10}$$

where k denotes the wave number, n_j the direction cosines of wave propagation, and l_j is the vector connecting equivalent points in the periodic cells. From Eqs. (8) and (9) it follows that the stresses in the points under consideration satisfy an equivalent periodicity relation, thus

$$\Sigma_{ij}(x_n) = \Sigma_{ij}(x_n + l_n)e^{-ikn_jl_j}. \tag{11}$$

A single periodic cell is now considered. For each point on the boundary of the cell there exists an equivalent periodic point for which the relations (10) and (11) are valid. For corner points of the cell, in particular, there exists more than one equivalent periodic point. Excluding for a moment the corner points, the pair of equivalent points on the boundary of the periodic cell have outward normal vectors in opposite directions. Hence the traction vector components, S_m, defined by

$$S_m(x_n) = \Sigma_{mj}(x_n)v_j, \tag{12}$$

where v_j denotes the outward normal vector, satisfy the following periodicity equation.

$$S_m(x_n) = -S_m(x_n + l_n)e^{-ikn_jl_j} \tag{13}$$

Equations (10) and (13) give the boundary conditions on the periodic cell. Because very few of the standard finite element programs in solid mechanics handle complex valued fields, the displacement and other fields are split into real and imaginary parts. That is

$$U_m(x_n) = U_m^{\mathrm{Re}}(x_n) + iU_m^{\mathrm{Im}}(x_n), \tag{14}$$

$$S_m(x_n) = S_m^{\mathrm{Re}}(x_n) + iS_m^{\mathrm{Im}}(x_n). \tag{15}$$

In doing this, Eq. (7) separates into the equations

$$\begin{cases} \Sigma_{ij,j}^{\mathrm{Re}} + \rho\omega^2 U_i^{\mathrm{Re}} = 0 \\ \Sigma_{ij,j}^{\mathrm{Im}} + \rho\omega^2 U_i^{\mathrm{Im}} = 0, \end{cases} \tag{16}$$

for the real and imaginary parts, respectively. The boundary conditions (10) and (13) split into

$$\begin{cases} U_m^{\mathrm{Re}}(x_n) = U_m^{\mathrm{Re}}(x_n + l_n)\cos(kn_jl_j) + U_m^{\mathrm{Im}}(x_n + l_n)\sin(kn_jl_j) \\ U_m^{\mathrm{Im}}(x_n) = U_m^{\mathrm{Im}}(x_n + l_n)\cos(kn_jl_j) - U_m^{\mathrm{Re}}(x_n + l_n)\sin(kn_jl_j) \end{cases} \tag{17}$$

and

$$\begin{cases} S_m^{\mathrm{Re}}(x_n + l_n) = -S_m^{\mathrm{Re}}(x_n)\cos(kn_jl_j) + S_m^{\mathrm{Im}}(x_n)\sin(kn_jl_j) \\ S_m^{\mathrm{Im}}(x_n + l_n) = -S_m^{\mathrm{Im}}(x_n)\cos(kn_jl_j) - S_m^{\mathrm{Re}}(x_n)\sin(kn_jl_j). \end{cases} \tag{18}$$

2.2 Finite Element Formulation. It is now observed that the real and imaginary parts are uncoupled in Eq. (16), and therefore it is possible to solve the eigenvalue problem defined by Eqs. (16), (17), and (18) using two identical, unit cell shaped, finite element meshes, one for the real part and one for the imaginary part. If the boundaries of the two meshes are coupled by the displacement boundary conditions in (17) the boundary conditions for the tractions are fulfilled automatically due to the way that most standard finite element codes implement condition (17).

In order to highlight this, consider the two identical, for clarity two-dimensional meshes in Fig. 2 representing a quadratic unit cell. The finite element formulation of (16) is

$$\left(\begin{bmatrix} [K] & 0 \\ 0 & [K] \end{bmatrix} - \omega^2 \begin{bmatrix} [M] & 0 \\ 0 & [M] \end{bmatrix}\right) \begin{bmatrix} \mathbf{u}_i^{\mathrm{Re}} \\ \mathbf{u}_1^{\mathrm{Re}} \\ \mathbf{u}_2^{\mathrm{Re}} \\ \mathbf{u}_i^{\mathrm{Im}} \\ \mathbf{u}_1^{\mathrm{Im}} \\ \mathbf{u}_2^{\mathrm{Im}} \end{bmatrix} = \begin{bmatrix} \mathbf{P}_i^{\mathrm{Re}} \\ \mathbf{P}_1^{\mathrm{Re}} \\ \mathbf{P}_2^{\mathrm{Re}} \\ \mathbf{P}_i^{\mathrm{Im}} \\ \mathbf{P}_1^{\mathrm{Im}} \\ \mathbf{P}_2^{\mathrm{Im}} \end{bmatrix}. \tag{19}$$

Here the vector $\mathbf{u}^{\mathrm{Re}}$, the real part of the displacement, is parti-

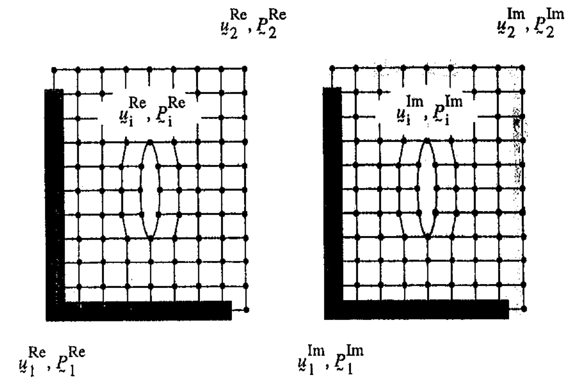

Fig. 2 Principle of the division and labeling of nodal displacements and nodal forces

tioned into $\mathbf{u}_i^{\mathrm{Re}}$, $\mathbf{u}_1^{\mathrm{Re}}$ and $\mathbf{u}_2^{\mathrm{Re}}$ denoting the internal nodes, the nodes of set 1 and the nodes of set 2, respectively. The real parts of the corresponding nodal forces are labeled $\mathbf{P}_i^{\mathrm{Re}}$, $\mathbf{P}_1^{\mathrm{Re}}$ and $\mathbf{P}_2^{\mathrm{Re}}$. The imaginary counterparts have the superscript "Im" instead of "Re." The submatrices $[K]$ and $[M]$ are the stiffness and mass matrices, of a single mesh, respectively. The boundary conditions (17) have the following appearance:

$$\begin{bmatrix} \mathbf{u}_i^{\mathrm{Re}} \\ \mathbf{u}_1^{\mathrm{Re}} \\ \mathbf{u}_2^{\mathrm{Re}} \\ \mathbf{u}_i^{\mathrm{Im}} \\ \mathbf{u}_1^{\mathrm{Im}} \\ \mathbf{u}_2^{\mathrm{Im}} \end{bmatrix} = [Q] \begin{bmatrix} \mathbf{u}_i^{\mathrm{Re}} \\ \mathbf{u}_2^{\mathrm{Re}} \\ \mathbf{u}_i^{\mathrm{Im}} \\ \mathbf{u}_2^{\mathrm{Im}} \end{bmatrix}. \tag{20}$$

The constraint matrix $[Q]$ can be schematically written as

$$[Q] = \begin{bmatrix} [I] & 0 & 0 & 0 \\ 0 & [C] & 0 & [S] \\ 0 & [I] & 0 & 0 \\ 0 & 0 & [I] & 0 \\ 0 & -[S] & 0 & [C] \\ 0 & 0 & 0 & [I] \end{bmatrix}, \tag{21}$$

where $[C]$ and $[S]$ are diagonal block matrices containing the cosine and sine factors of (17) and $[I]$ is the identity matrix. Substitution of (20) into (19) and premultiplication by $[Q]^T$ yields the following system of equations:

$$[Q]^T\left(\begin{bmatrix} [K] & 0 \\ 0 & [K] \end{bmatrix} - \omega^2 \begin{bmatrix} [M] & 0 \\ 0 & [M] \end{bmatrix}\right)[Q] \begin{bmatrix} \mathbf{u}_i^{\mathrm{Re}} \\ \mathbf{u}_2^{\mathrm{Re}} \\ \mathbf{u}_i^{\mathrm{Im}} \\ \mathbf{u}_2^{\mathrm{Im}} \end{bmatrix} = \begin{bmatrix} \mathbf{P}_i^{\mathrm{Re}} \\ [C]\mathbf{P}_1^{\mathrm{Re}} + \mathbf{P}_2^{\mathrm{Re}} - [S]\mathbf{P}_1^{\mathrm{Im}} \\ \mathbf{P}_i^{\mathrm{Im}} \\ [C]\mathbf{P}_1^{\mathrm{Im}} + \mathbf{P}_2^{\mathrm{Im}} + [S]\mathbf{P}_1^{\mathrm{Re}} \end{bmatrix}. \tag{22}$$

When a standard finite element code computes the eigenfrequencies and eigenmodes the vector on the right side of Eq. (22) is set to zero. In (22) this corresponds to an absence of body forces on the internal node set and the fulfillment of the traction boundary conditions in Eq. (18). In other words, the boundary conditions of Eq. (18) are automatically fulfilled if Eq. (17) is fulfilled.

Thus, by having two identical finite element meshes and implementing the constraints of Eq. (17), the eigenfrequencies ω, which can be shown to be double eigenvalues, can be computed for any given wave number, k, and wave direction, n_j. This procedure makes it possible to compute the dispersion relation for the periodic structure.

In the case of a plate the vertical boundaries of the cell (see Fig. 1) will be connected through Eqs. (17) and (18), and the horizontal boundaries will be free.

3 Laminated Plate Theory

The finite element computations have limitations. The fact that each ply must be modeled with a fair amount of nodes puts a practical limit on the number of possible plies in the studied laminate. There are also limitations due to the periodicity assumption. If Eq. (10) is studied it is seen that there is no point in increasing k beyond the value $\pi/n_i l_i$ because of the periodic nature of the boundary condition and the symmetry of the cell regarding propagation direction. Since the cracked laminates in reality are not perfectly periodic, this puts a lower limit on the wavelength.

Dispersion computations based on first-order shear-deformation laminate theories, on the other hand, are very inexpensive. Also, since there is no structural periodicity in the equations, there is no lower limit to the wavelength. The trade-off is that the stiffness variation in the thickness direction is smeared out, and thus the influence of the layer nature of the laminate and the geometry of the cracks on wave propagation is lost.

3.1 Dispersion Calculations by Laminate Theory. The details concerning the equations below may be found in the work of Whitney and Pagano (1970) and Whitney (1973). Here an infinitely large laminated plate in the x-y plane without external loads is considered. The displacements are assumed to be

$$u = u^0(x, y, t) + z\psi_x(x, y, t)$$
$$v = v^0(x, y, t) + z\psi_y(x, y, t)$$
$$w = w^0(x, y, t). \tag{23}$$

The in-plane stress resultants (N_x, N_y, and N_{xy}) and bending moments (M_x, M_y, and M_{xy}) are defined in the usual manner and are given the notation

$$\mathbf{N} = \begin{bmatrix} N_x \\ N_y \\ N_{xy} \end{bmatrix} \quad \text{and} \quad \mathbf{M} = \begin{bmatrix} M_x \\ M_y \\ M_{xy} \end{bmatrix}. \tag{24}$$

The assumed displacement fields result in the following in-plane strains (ϵ_x, ϵ_y and γ_{xy}) and curvatures (κ_x, κ_y, and κ_{xy}):

$$\epsilon_x = \frac{\partial u^0}{\partial x} \quad \epsilon_y = \frac{\partial v^0}{\partial y} \quad \gamma_{xy} = \frac{\partial u^0}{\partial y} + \frac{\partial v^0}{\partial x}$$
$$\kappa_x = \frac{\partial \psi_x}{\partial x} \quad \kappa_y = \frac{\partial \psi_y}{\partial y} \quad \kappa_{xy} = \frac{\partial \psi_x}{\partial y} + \frac{\partial \psi_y}{\partial x}, \tag{25}$$

which are also collected in vectors according to

$$\boldsymbol{\epsilon} = \begin{bmatrix} \epsilon_x \\ \epsilon_y \\ \gamma_{xy} \end{bmatrix} \quad \text{and} \quad \boldsymbol{\kappa} = \begin{bmatrix} \kappa_x \\ \kappa_y \\ \kappa_{xy} \end{bmatrix}. \tag{26}$$

The stress and moment resultants are connected to the strains and curvatures through the usual stiffness matrix in laminate theory

$$\begin{bmatrix} \mathbf{N} \\ \mathbf{M} \end{bmatrix} = \begin{bmatrix} \mathbf{A} & \mathbf{B} \\ \mathbf{B} & \mathbf{D} \end{bmatrix} \begin{bmatrix} \boldsymbol{\epsilon} \\ \boldsymbol{\kappa} \end{bmatrix}, \tag{27}$$

where the submatrices $\mathbf{A}$, $\mathbf{B}$, and $\mathbf{D}$ are defined as

$$\mathbf{A} = \begin{bmatrix} A_{11} & A_{12} & A_{16} \\ A_{12} & A_{22} & A_{26} \\ A_{16} & A_{26} & A_{66} \end{bmatrix} \quad \mathbf{B} = \begin{bmatrix} B_{11} & B_{12} & B_{16} \\ B_{12} & B_{22} & B_{26} \\ B_{16} & B_{26} & B_{66} \end{bmatrix}$$
$$\mathbf{D} = \begin{bmatrix} D_{11} & D_{12} & D_{16} \\ D_{12} & D_{22} & D_{26} \\ D_{16} & D_{26} & D_{66} \end{bmatrix}. \tag{28}$$

In the first-order shear-deformation theory according to Whitney (1973), out-of-plane shear forces (Q_{yz} and Q_{xz}) and strains (γ_{yz} and γ_{xz}) are related according to

$$\begin{bmatrix} Q_{yz} \\ Q_{xz} \end{bmatrix} = \begin{bmatrix} k_2^2 A_{44} & k_2 k_1 A_{45} \\ k_2 k_1 A_{45} & k_1^2 A_{55} \end{bmatrix} \begin{bmatrix} \gamma_{yz} \\ \gamma_{xz} \end{bmatrix}, \tag{29}$$

where

$$\gamma_{yz} = \frac{\partial w^0}{\partial y} + \frac{\partial \psi_y}{\partial y} \quad \text{and} \quad \gamma_{xz} = \frac{\partial w^0}{\partial x} + \frac{\partial \psi_x}{\partial x}. \tag{30}$$

The expressions for the stiffnesses (A_{44}, A_{45}, and A_{55}) and the shear-correction factors (k_2 and k_1) are found in Whitney (1973) (there are misprints in Eq. (6) and the equation below it).

In the case of harmonic wave propagation, it is further assumed that the displacement functions take the form

$$(u^0, v^0, w^0, \psi_x, \psi_y) = (U, V, W, \Psi_x, \Psi_y)e^{i(k_x x + k_y y - \omega t)}, \tag{31}$$

where the capital letters are complex-valued constants, k_x and k_y are the x and y-components of the wave vector and ω is the circular frequency. Substituting Eq. (31) into the equations of motion for the laminate yields the following generalized eigenvalue problem

$$\left(\begin{bmatrix} K_{11} & K_{12} & K_{13} & K_{14} & K_{15} \\ K_{12} & K_{22} & K_{23} & K_{24} & K_{25} \\ K_{13} & K_{23} & K_{33} & K_{34} & K_{35} \\ K_{14} & K_{24} & -K_{34} & K_{44} & K_{45} \\ K_{15} & K_{25} & -K_{35} & K_{45} & K_{55} \end{bmatrix} - \omega^2 \begin{bmatrix} \rho h & 0 & 0 & 0 & 0 \\ 0 & \rho h & 0 & 0 & 0 \\ 0 & 0 & \rho h & 0 & 0 \\ 0 & 0 & 0 & \frac{\rho h^3}{12} & 0 \\ 0 & 0 & 0 & 0 & \frac{\rho h^3}{12} \end{bmatrix} \right) \begin{bmatrix} U \\ V \\ W \\ \Psi_x \\ \Psi_y \end{bmatrix} = \begin{bmatrix} 0 \\ 0 \\ 0 \\ 0 \\ 0 \end{bmatrix}, \tag{32}$$

where ρ is the density, which is assumed to be the same in all plies, and h is the thickness of the laminate. The K_{ij}s, which depend on the wave vector and laminate stiffnesses, are given by

$$K_{11} = A_{11}k_x^2 + 2A_{16}k_x k_y + A_{66}k_y^2,$$
$$K_{12} = A_{16}k_x^2 + (A_{12} + A_{66})k_x k_y + A_{26}k_y^2$$
$$K_{13} = 0, \quad K_{14} = B_{11}k_x^2 + 2B_{16}k_x k_y + B_{66}k_y^2,$$
$$K_{15} = B_{16}k_x^2 + (B_{12} + B_{66})k_x k_y + B_{26}k_y^2$$

$$K_{22} = A_{66}k_x^2 + 2A_{26}k_xk_y + A_{22}k_y^2, \quad K_{23} = 0,$$

$$K_{24} = B_{16}k_x^2 + (B_{66} + B_{12})k_xk_y + B_{26}k_y^2$$

$$K_{25} = B_{66}k_x^2 + 2B_{26}k_xk_y + B_{22}k_y^2,$$

$$K_{33} = A_{55}k_1^2k_x^2 + 2A_{45}k_1k_2k_xk_y + A_{44}k_2^2k_y^2$$

$$K_{34} = -i(A_{55}k_1^2k_x + A_{45}k_1k_2k_y),$$

$$K_{35} = -i(A_{44}k_2^2k_y + A_{45}k_1k_2k_x)$$

$$K_{44} = D_{11}k_x^2 + 2D_{16}k_xk_y + D_{66}k_y^2 + A_{55}k_1^2,$$

$$K_{45} = D_{16}k_x^2 + (D_{12} + D_{66})k_xk_y + D_{26}k_y^2 + A_{45}k_1k_2$$

$$K_{55} = D_{66}k_x^2 + 2D_{26}k_xk_y + D_{22}k_y^2 + A_{44}k_2^2. \tag{33}$$

For given wave vector components, k_x and k_y, the generalized eigenvalue problem of equation (32) gives five real-valued eigenfrequencies (note that K is Hermitian), ω, corresponding to five dispersion curves.

3.2 Stiffness Reduction due to Cracks. The presence of transverse matrix cracks will reduce the stiffness of the laminate. Gudmundson and Zang (1993) have given closed-form approximate expressions for the effective stiffnesses (three-dimensional and plane-stress stiffnesses) of such laminates. The method may briefly be described as follows: First exact formulas for the reduced effective stiffness of a cracked laminate are derived based on the difference in global strain of a cracked and an uncracked laminate when subjected to a constant stress. The difference in global strain can be expressed in terms of average crack-opening displacements in the cracked laminate. An approximation regarding the crack-opening displacements is then introduced. The crack-opening displacements are taken from the known case of an infinite row of vertical cracks, each subjected to constant traction on the crack surface. Thus, the main approximation is that there is no interaction between neighboring plies as far as the cracks are concerned. The expressions of Gudmundson and Zang (1993) are applicable to any laminate lay-up and to laminates with both internal and surface cracks. Adolfsson and Gudmundson (1995) have investigated the accuracy of the model by finite element computations and experiments and found that it provides good estimates of the effective stiffness.

Adolfsson and Gudmundson (1997) have also taken bending into account and developed a version of the classical laminate theory including the effects of transverse matrix cracking. This is done by extending the scheme of Gudmundson and Zang (1993) and take linearly varying stresses on the crack surfaces into account also. This approach will give the same **A** matrix (see Eq. (27)) as the two-step homogenization outlined below, and will yield better values for the **B** and **D** matrices than the two-step homogenization, but it does not give the crucial shear stiffnesses of Eq. (29).

The effective stiffnesses of Gudmundson and Zang (1993) can be used to develop a first-order shear-deformation laminate theory with shear correction factors. The idea is quite simple. Since the expressions by Gudmundson and Zang (1993) are applicable to any laminate and there is no interaction between neighboring plies it is also applicable to the special case of a single cracked ply, whether it is a surface ply or an internal ply. Therefore one can first calculate the stiffnesses of the cracked layers one by one, using the expressions of Gudmundson and Zang (1993), and then use those stiffnesses and the stiffnesses of the eventual uncracked layers to calculate plate properties. Thus, it may be viewed as a two-step homogenization. This is shown schematically in Fig. 3. In the first step the cracked layers with material stiffness C_{ijkl} are homogenized and replaced by uncracked layers with material stiffness $C_{ijkl}^{\text{cracked}}$, and in the second step the regular homogenization of the first-order shear-deformation laminate theory (Whitney and Pagano, 1970; Whitney, 1973) is employed.

There is one problem with this scheme. The out-of-plane shear stiffness for a single surface layer with cracks (such as the top layer in Fig. 3) are not possible to compute using the method of Gudmundson and Zang (1993). To keep things simple the out-of-plane shear stiffnesses of a surface cracked ply are estimated by out-of-plane shear stiffnesses of an internally cracked ply with twice the thickness. It should be noted, however, that the largest transverse shear stresses appear in the middle of the laminate and hence the approximations related to the surface layers regarding transverse shear should not be too crucial.

Once the laminated plate stiffnesses are known for the cracked laminate Eq. (32) is used to find dispersion relations.

4 Results

In this section results of both methods for three different lay-ups ($[0/90]_S$, $[0/90]_2$ and $[0/+45/-45]_S$) of glass-fiber laminae are presented. The material parameters of the plies may be found in Table 1. The results are presented in the form of diagrams displaying dimensionless phase velocities versus dimensionless wave numbers. The dimensionless parameters are defined as

$$\hat{c} = \frac{\omega}{k}\sqrt{\frac{\rho}{E_L}} \tag{34}$$

and

$$\hat{k} = \frac{kh}{2\pi}, \tag{35}$$

where ω is the eigenfrequency and k is the wave number, as defined earlier. The thickness of the plate is h, and ρ and E_L are the density and elastic modulus in the fiber direction, respectively.

For each lay-up different degrees of cracking was considered. The crack density, δ_k, in a ply (k) is here defined as

$$\delta_k = \frac{t_k}{d_k}, \tag{36}$$

where t_k is the thickness of ply k and d_k is the average distance between cracks in the ply. Thus, for an uncracked ply δ_k is zero.

For all laminates considered, the direction of wave propagation was the 0 deg direction (i.e., the fiber-direction of the top layer) and the three so-called acoustical modes are presented. The methods presented set no restriction to the direction of wave propagation. Due to space limitations, however, only some representative results are presented here. For low frequencies the lowest acoustical mode corresponds to a flexural wave, the next lowest to an in-plane shear wave, and the highest to an extensional wave. In some cases the dispersion curves of the so-called optical modes cross the curve of one or more of the acoustical modes, but for clarity reasons the crossing optical modes are not presented here.

4.1 Crossply Laminates. Two crossply laminates were considered; $[0/90]_s$ and $[0/90]_2$ with cracks in the 90 deg plies.

4.1.1 The $[0/90]_s$ Laminate. In Fig. 4 the results of the laminate theory (dashed) and the finite element computations (solid) are compared for different crack densities, δ_k. In diagrams a, b, and c the crack densities in the 90 deg ply are 0, 0.5, and 1, respectively. The reason for abruptly ending the solid finite element curves in diagrams b and c can be understood in view of the periodicity of Eq. (10) and the discussion of it in the beginning of Section 3. In diagram a the dashed and the solid curve are on top of each other for the in-plane shear mode.

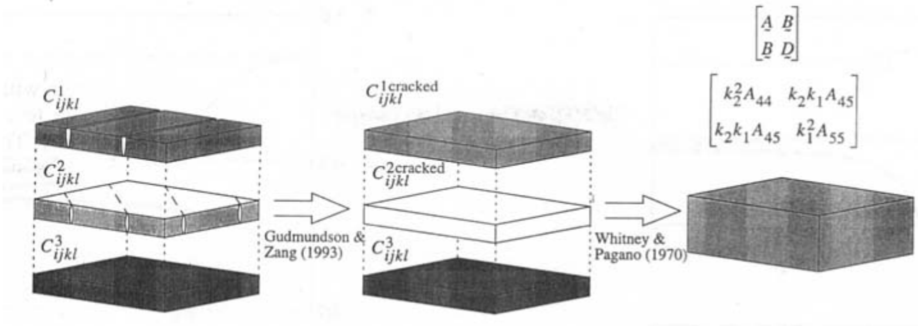

Fig. 3 A schematic picture of the two-step homogenization

Table 1 Properties of the glass fiber reinforced epoxy ply

E_L (GPa)	E_T (GPa)	υ_{LT}	υ_{TT}	G_{LT} (GPa)	ρ (kg/m^3)
46	18	0.29	0.42	7.9	1930.16

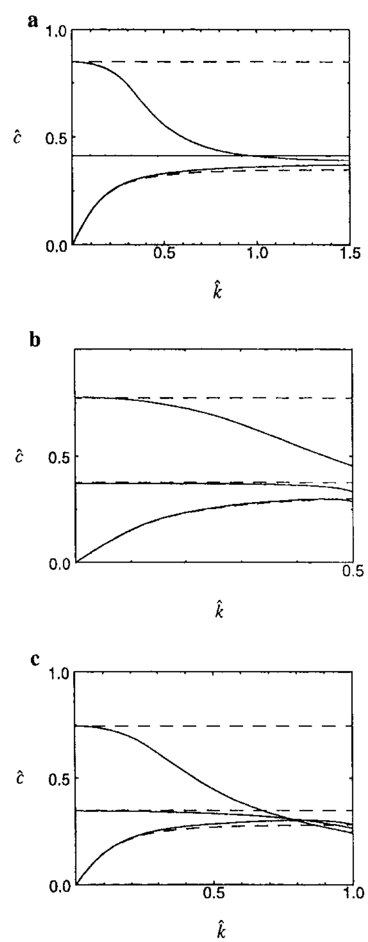

Fig. 4 Results for the $[0/90]_S$ laminate with cracks in the 90 deg plies. A comparison between the laminate theory (dashed) and finite element computations (solid) for different crack densities (a: $\delta = 0$, b: $\delta = 0.5$ and c: $\delta = 1$).

Figure 5 shows the finite element results for the three different crack densities in the same diagram. The solid, dashed, and dotted line correspond to δ_k equal to 0, 0.5, and 1, respectively.

4.1.2 The $[0/90]_2$ Laminate. Figure 6 shows the results of the laminated plate theory (dashed) and the finite element computations (solid). In diagrams a, b, and c the crack densities in the 90 deg plies are 0, 0.5, and 1, respectively. In diagram a the dashed and the solid curves are on top of each other for the in-plane shear mode.

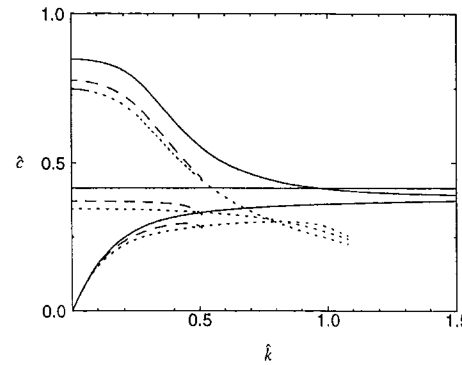

Fig. 5 Results for the $[0/90]_S$ laminate with cracks in the 90 deg plies. Finite element computations for crack densities of 0 (solid), 0.5 (dashed), and 1 (dotted).

In Fig. 7 the finite element results for the three different crack densities are shown. The solid dashed and dotted line correspond to δ_k equal to 0, 0.5, and 1, respectively.

4.2 $[0/+45/-45]_S$ Laminate. A $[0/+45/-45]_S$ laminate with cracks in the ± 45 deg plies was also analyzed. The average distance between the cracks was the same in both types of plies, and therefore according to definition (36) the crack density in the -45 deg ply was twice the density in the $+45$ deg plies.

Figure 8 shows finite element (solid) and laminate theory (dashed) results. The crack densities in the -45 deg ply was 0 in diagram a and 1 in diagram b.

The results of the finite element computations for crack densities in the -45 deg of 0 (solid) and 1 (dashed) are shown in Fig. 9.

5 Discussion

An interesting question is if the cracks themselves influence the dispersion relations directly or if their only effect is seen as a reduction in global stiffness. Figures 5, 7, and 9 indicate that at the studied wave lengths the cracks mainly reduce stiffness, because at higher crack densities there is a downward shift of the curve due to less global stiffness, but the shape of the curve is kept.

Looking at the general shape of the dispersion curves in Figs. 5, 7, and 9 it is seen that the flexural mode curve basically looks like the dispersion curve of a homogeneous plate. The in-plane shear mode shows very little or no dispersion. This is not surprising because the traction boundary conditions between neighboring plies and on the surface are trivially fulfilled in this case, and hence the wave is not affected by the differing shear stiffnesses or the free surface.

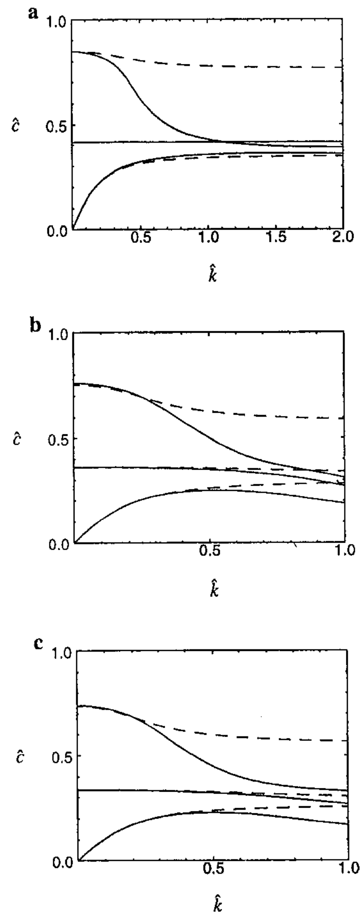

Fig. 6 Results for the $[0/90]_S$ laminate with cracks in the 90 deg plies. A comparison between the laminate theory (dashed) and finite element computations (solid) for different crack densities (a: $\delta = 0$, b: $\delta = 0.5$ and c: $\delta = 1$).

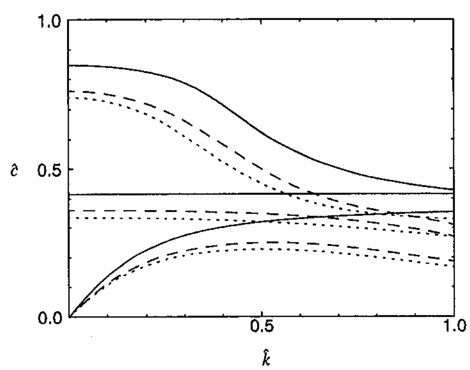

Fig. 7 Results for the $[0/90]_S$ laminate with cracks in the 90 deg plies. Finite element computations for crack densities of 0 (solid), 0.5 (dashed), and 1 (dotted).

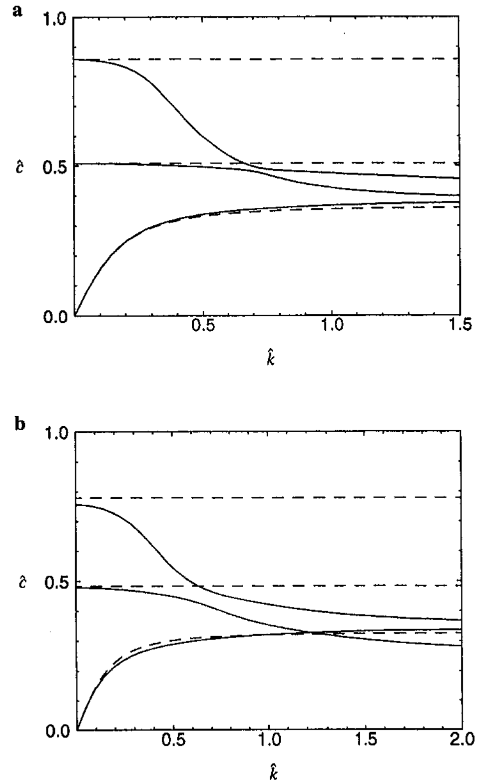

Fig. 8 Results for the $[0/+45/-45]_2$ laminate with cracks in the ± 45 deg plies. A comparison between the laminate theory (dashed) and finite element computations (solid) for uncracked (a) and cracked laminate (b: $\delta = 1$ in the -45 deg ply). The crack density in the $+45$ deg plies is half the crack density in the -45 deg ply.

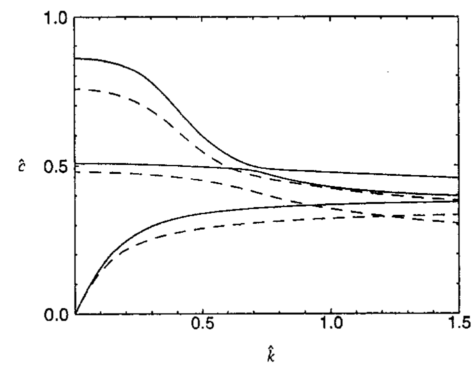

Fig. 9 Results for the $[0/+45/-45]_S$ laminate with cracks in the ± 45 deg plies. Finite element computations for uncracked (solid) and cracked laminate (dashed).

The most striking feature of the extensional wave dispersion curves in Figs. 5, 7, and 9 is that they show a drop at wavelengths, $\lambda = 3.5h$ (h is the thickness of the laminate). For small wavelengths the plate nature of the structure is not felt by the wave, and it will then move as a slower surface or a Stoneley-type wave. A possibility to better capture the drop in the dispersion curve for the extensional mode would be to apply a higher-order theory for extensional motion; for example, the model presented by Kane and Mindlin (1956).

The laminated plate theory may be viewed as an approximation of the finite element solution, at least down to moderate wavelengths. Figures 4, 6, and 8 show comparisons between the laminated plate theory results and the finite element computations. In all cases the flexural wave phase velocities are estimated rather well by the laminated plate results (with the exception mentioned earlier) even at relatively short wavelengths. In diagram c in Fig. 4, for example, there is less than five percent difference in phase velocity at $\lambda = 2h$.

The phase velocity of the in-plane shear wave is estimated well by the laminated plate theory, at least for the crossplies. For the cracked $[0/+45/-45]_S$ laminate there is less five percent difference in phase velocity at $\lambda = 3h$.

For the extensional mode the laminated plate theory predicts no dispersion for the symmetric laminates and slight dispersion for the $[0/90]_2$ laminate. This estimate breaks down when the extensional wave dispersion curves of the finite element computations start to drop. For the symmetric laminate there is less than five percent difference at $\lambda = 7h$. The situation for the $[0/90]_2$ laminate is somewhat better.

6 Conclusions

Dispersion relations for three types of laminates with transverse matrix cracks have been calculated using two different methods. The first method approximates the cracked laminate with a periodically cracked laminate and then a periodic cell is analyzed using finite elements. The second method may be viewed as a two-step homogenization. First the cracked plies are replaced by plies without cracks but with less stiffness, and then a regular first-order shear-deformation plate theory is used to arrive at dispersion relations.

Based on the finite element computations it is concluded that there is a noticeable drop in phase velocity with increasing crack density. Also, for a given crack density, there is a rather sharp drop in phase velocity for the extensional wave as the frequency increases.

The laminate theory resulting from the two-step homogenization provides good estimates for different crack densities for the phase velocity of the important flexural wave and the in-plane shear wave. The estimation of phase velocities of the extensional wave is poor from the point where the curve drops. If one deals with wave propagation in finite-sized cracked laminates, for example in an acoustic emission experiment, it seems unrealistic to model the cracks and the laminate in detail and hence some kind of homogenization is needed. The laminate theory presented here is one such homogenization, and it could be used to model finite-sized cracked laminates.

The results presented here will ultimately have to be checked against experiments. It is possible that crack closure, which is neglected here, plays an important role. A second important aspect is that real laminates are not periodically cracked, and hence some of the results of the finite element computations could be artificial.

Acknowledgments

The financial support from the Swedish Research Council for Engineering Sciences (TFR) is gratefully acknowledged. The authors are also thankful for the assistance provided by Dr. Erik Adolfsson during the course of the work.

References

Åberg, M., and Gudmundson, P., 1997, "The usage of standard finite element codes for computations of dispersion relations in materials with periodic microstructure," *Journal of the Acoustical Society of America*, Vol. 102, pp. 2007–2013.

Aboudi, J., 1988, "Wave propagation in damaged composite materials," *International Journal of Solids and Structures*, Vol. 24, pp. 117–138.

Abrate, S., 1991, "Matrix cracking in laminated composites: a review," *Composites Engineering*, Vol. 1, pp. 337–353.

Achenbach, J. D., and Li, Z. L., 1986, "Propagation of horizontally polarized transverse waves in a solid with a periodic distribution of cracks," *Wave Motion*, Vol. 8, pp. 371–379.

Adolfsson, E., and Gudmundson, P., 1994, "Matrix crack closure effects on thermoelastic properties of $[(0_m/90_n/+\theta_p/-\theta_q)_s]_M$ composite laminates," *Failure Mechanics in Advanced Polymeric Composites, AMD-Vol. 196*, G. A. Kardomateas and Y. D. S. Rajapakse, eds., ASME, New York, pp. 125–140.

Adolfsson, E., and Gudmundson, P., 1995, "Matrix crack induced stiffness reductions in $[(0_m/90_n/+\theta_p/-\theta_q)_s]_M$ composite laminates," *Composites Engineering*, Vol. 5, pp. 107–123.

Adolfsson, E., and Gudmundson, P., 1996, "Matrix crack initiation and progression in composite laminates subjected to bending and extension," Department Solid Mechanics, KTH, Report 195, ISRN KTH/HFL/R–96/10–SE, TRITA HFL-195 ISSN 0281-1502.

Adolfsson, E., 1996, "Modelling of translaminar cracks in cross-ply composite laminates," *Journal of Composite Materials*, Vol. 30, pp. 1683–1709.

Adolfsson, E., and Gudmundson, P., 1997, "Thermoelastic properties in combined bending and extension of thin composite laminates with transverse matrix cracks," *International Journal of Solids and Structures*, Vol. 34, pp. 2035–2060.

Datta, S. K., Shah, A. H., Bratton, R. L., and Chakraborty, T., 1988, "Wave propagation in laminated composite plates," *Journal of the Acoustical Society of America*, Vol. 83, No. 6, pp. 2020–2026.

Dong, S. B., and Nelson, R. B., 1972, "On Natural Vibrations and Waves in Laminated Orthotropic Plates," ASME Journal of Applied Mechanics, Vol. 39, pp. 739–745.

Eggers, H., Goetting, H. C., and Bäumel, H., 1994, "Synergism between layer cracking and delaminations in multidirectional laminates of carbon-fibre-reinforced epoxy," *Composites Science and Technology*, Vol. 50, pp. 343–354.

Gorman, M. R., and Ziola, S. M., 1991, "Plate waves produced by transverse matrix cracking," *Ultrasonics*, Vol. 29, pp. 245–251.

Gudmundson, P., and Zang, W., 1993, "An analytic model for thermoelastic properties of composite laminates containing transverse matrix cracks," *International Journal of Solids and Structures*, Vol. 30, pp. 3211–3231.

Hahn, R. D., Han, Y. M., and Kim, R. Y., 1988, "Resistance curves for ply cracking in composite laminates," *Proceedings of the 33rd International SAMPE Symposium*, Mar. 7–10, pp. 1101–1108.

Jamison, R. D., and Reifsnider, K. L., 1982, "Advanced fatigue damage development in graphite epoxy laminates," Report AFWAL TR-82-3103, Virginia Polytechnic Institute and State University, Blacksburg, VA.

Kane, T. R., and Mindlin, R. D., 1956, "High-Frequency Extensional Vibrations of Plates," ASME Journal of Applied Mechanics, Vol. 23, pp. 277–283.

Karunasena, W. M., Bratton, R. L., Datta, S. K., and Shah, A. H., 1991, "Elastic Wave Propagation in Laminated Composite Plates," ASME *Journal of Engineering Materials and Technology*, Vol. 113, pp. 411–418.

Karunasena, W. M., Shah, A. H., and Datta, S. K., 1991, "Wave Propagation in a Multilayered Laminated Cross-Ply Composite Plate," ASME Journal of Applied Mechanics, Vol. 58, pp. 1028–1032.

Noor, A. K., and Burton, S., 1990, "Assessment of computational models for multilayered anisotropic plates," *Composite Structures*, Vol. 14, pp. 233–265.

Ogihara, S., and Takeda, N., 1995, "Interaction between transverse cracks and delamination during damage progress in CFRP cross-ply laminates," *Composites Science and Technology*, Vol. 54, pp. 395–404.

Prosser, W. H., Jackson, K. E., Kellas, S., Smith, B. T., McKeon, J., and Friedman, A., 1995, "Advanced waveform-based acoustic emission detection of matrix cracking in composites," *Materials Evaluation*, Sept. pp. 1052–1058.

Smyshlyaev, V. P., and Willis, J. R., 1993, "Self-consistent analysis of waves in a matrix-inclusion composite-III. A matrix containing cracks," *Journal of the Mechanics and Physics of Solids*, Vol. 41, pp. 1809–1824.

Whitney, J. M., and Pagano, N. J., 1970, "Shear Deformation in Heterogeneous Anisotropic Plates," ASME Journal of Applied Mechanics, Vol. 37, pp. 1031–1036.

Whitney, J. M., 1973, "Shear Correction Factors for Orthotropic Laminates Under Static Load," ASME Journal of Applied Mechanics, Vol. 40, pp. 302–304.

Xu, L.-Y., 1996, "On the law of the transverse matrix cracks growth in brittle polymeric matrix composites under static loadings," *Journal of Composite Materials*, Vol. 30, pp. 384–405.

Yang, P. C., Norris, C. H., and Stavsky, Y., 1966, "Elastic wave propagation in heterogeneous plates," *International Journal of Solids and Structures*, Vol. 2, pp. 665–684.

Plasticity of Particle-Reinforced Composites With a Ductile Interphase

K. Ding
Graduate Student.

G. J. Weng
Professor,
Fellow ASME.

Department of Mechanical and
Aerospace Engineering,
Rutgers University,
New Brunswick, NJ 08903

A homogenization theory is developed to determine the overall elastoplastic behavior of a particle-reinforced composite with a ductile interphase. Unlike most existing homogenization theories which are primarily concerned with the ordinary two-phase composites, the present one is confronted with two ductile phases, with one enclosing the other. The theory is developed with the aid of a linear comparison composite using a field-fluctuation method to calculate an energy-based effective stress of the ductile phases. In order to examine its accuracy, an exact elastic-plastic analysis under dilatational loading is also developed, and it was found that, despite its simplicity, the theory could provide plausible estimates for the overall behavior of the three-phase composite. The theory is applicable to a composite system regardless whether the interphase is more ductile or stiffer than the matrix, and when the interphase is more ductile, it is shown that even the presence of a thin layer can have a very significant effect on the plasticity of the overall composite.

1 Introduction

There has been some progress in the development of homogenization methods to estimate the nonlinear elastoplastic behavior of two-phase composites. Most notable among these contributions are perhaps the variational approaches of Talbot and Willis (1985), Willis (1991, 1992), and Ponte Castañeda (1991, 1992). The former approach was developed from Hashin and Shtrikman's (1963) variational principle in elasticity, while the latter was built from a linear comparison composite. These approaches have been further refined—though with some added complexities—to a higher accuracy with the introduction of a nonlinear comparison material or pushed to a higher-order range (Talbot and Willis, 1994, 1997; Ponte Castañeda, 1996). Most problems which they have specifically examined are of the inclusion/matrix type, notwithstanding that their theories are applicable to other microgeometries as well. The direct secant-moduli method as suggested by Tandon and Weng (1988) and Weng (1990), and later improved by Qiu and Weng (1992), has also been primarily concerned with the inclusion/matrix type where Eshelby's (1957) solution plays a prominent role. Such is also the case with the pairwise-interaction approximation developed by Ju and Chen (1994), and the generalized self-consistent scheme of Herve and Zaoui (1990) and multilayered formulation of Bornert et al. (1994).

Despite these and other developments, it is evident that the influence of a ductile interphase on the overall elastoplastic response of the composite has never been addressed before. This issue is of some practical importance as the property of the matrix near the interface may change significantly due to diffusion or oxidation. Such a distinct interfacial zone may also be intentionally introduced to improve the strength or toughness of the composite. Motivated by this observation, the objective here is to develop a homogenization scheme for the overall elastoplastic behavior of such a layered system.

The direct secant-moduli approach makes use of a linear comparison matrix whose elastic moduli are set equal to the homogenized secant moduli of the ductile matrix at every stage of deformation. The values of the secant moduli of a ductile phase depend on its homogenized effective stress. Qiu and Weng (1992) defined this quantity based on the equivalence of the *distortional* energy between the homogenized medium and the heterogeneously deformed phase. This "energy-based" definition—in contrast to the "mean-stress" approach based on the mean deviatoric stress—has been called an "energy approach." At present there exist two methods to evaluated this quantity. The first one is the global energy equivalence between the composite system and its constituent phases as also suggested by Qiu and Weng, and the second one is the "field-fluctuation method" recently advanced by Hu (1996). The former method can only apply to a two-phase composite, and the evaluation is complete only when the matrix is incompressible. Hu's method is a better one; it is applicable to a multiphase composite regardless of the compressibility of the ductile phase, and the evaluation is always complete. With an incompressible matrix, Qiu and Weng (1992, 1995) have proved that their approach provided results which are identical to Ponte Castañeda's bounds or estimates, but with a compressible matrix it was after Hu has completely evaluated the effective stress that such a connection was also established. In a separate development, Suquet (1995, 1996) has introduced a "modified secant moduli" theory and established a direct link with Ponte Castañeda's variational procedure. Suquet's effective stress was based on the "second moment" of the stress field which is identical to the energy-based definition of Qiu and Weng, and it was evaluated by a method identical to Hu's. In essence, when the effective stress of a ductile phase is defined by the energy-based approach and is evaluated by Hu's or Suquet's method, the direct secant-moduli approach is exactly equivalent to Ponte Castañeda's variational procedure.

In this study both the matrix and the interphase will be allowed to have their independent elastoplastic properties. The theoretical development was motivated by the work of Qiu and Weng (1992) and Hu (1996), but as stated above it turned out to be identical to Ponte Castañeda's variational procedure and

Contributed by the Applied Mechanics Division of The American Society of Mechanical Engineers for publication in the ASME Journal of Applied Mechanics.

Discussion on the paper should be addressed to the Technical Editor, Professor Lewis T. Wheeler, Department of Mechanical Engineering, University of Houston, Houston, TX 77204-4792, and will be accepted until four months after final publication of the paper itself in the ASME Journal of Applied Mechanics.

Manuscript received by the ASME Applied Mechanics Division, June 24, 1997; final revision, Dec. 3, 1997. Associate Technical Editor: I. M. Daniel.

Suquet's modified secant moduli method. The developed theory will be applied to uncover the effect of the ductile interphase on the overall response of the three-phase system.

2 Constitutive Equations of the Ductile Phases

The representative volume element of the three-phase composite is taken to be of the concentrated sphere model, where the spherical particle is referred to as phase 1, the interphase as phase 2, and the regular matrix as phase 3. The volume concentration of the rth phase is denoted by c_r and, with a_r further representing its outer radius, one has

$$c_1 = (a_1/a_3)^3, \quad c_2 = (a_2^3 - a_1^3)/a_3^3,$$
$$c_3 = 1 - (c_1 + c_2). \qquad (1)$$

All constituent phases will be taken to be isotropic, with the bulk and shear moduli denoted by κ_r and μ_r for the rth phase. The plastic stress-strain relations of the ductile interphase and matrix are represented by the modified Ludwik equation as

$$\sigma_e^{(r)} = \sigma_y^{(r)} + h_r \cdot (\epsilon_e^{p(r)})^{n_r}, \quad r = 2, 3 \qquad (2)$$

where $\sigma_y^{(r)}$, h_r and $n_r (0 \le n_r \le 1)$ are the tensile yield stress, strength coefficient, and work-hardening exponent, in turn, of the rth phase. The effective stress and plastic strain are defined as usual

$$\sigma_e^{(r)} = [\tfrac{3}{2}\sigma_{ij}^{\prime(r)}\sigma_{ij}^{\prime(r)}]^{1/2}, \quad \epsilon_e^{p(r)} = [\tfrac{2}{3}\epsilon_{ij}^{p(r)}\epsilon_{ij}^{p(r)}]^{1/2}, \qquad (3)$$

in terms of its deviatoric stress $\sigma_{ij}^{\prime(r)}$ and plastic strain $\epsilon_{ij}^{p(r)}$.

The stress-strain relation of the composite with a ductile interphase will be calculated using the secant moduli approach originally used by Berveiller and Zaoui (1979) and Weng (1982) for polycrystal plasticity and by Tandon and Weng (1988) for particle-reinforced plasticity. In this regard, the secant Young's modulus of the rth phase is given by

$$E_r^s = \frac{\sigma_e^{(r)}}{\dfrac{\sigma_e^{(r)}}{E_r} + \left(\dfrac{\sigma_e^{(r)} - \sigma_y^{(r)}}{h_r}\right)^{1/n_r}}, \qquad (4)$$

in terms of its elastic Young's modulus, E_r. The secant shear modulus and the secant Poisson's ratio follow as

$$\mu_r^s = \frac{E_r^s}{2(1 + \nu_r^s)}, \quad \nu_r^s = \frac{1}{2} - \left(\frac{1}{2} - \nu_r\right)\frac{E_r^s}{E_r}, \qquad (5)$$

from the isotropic relations and plastic incompressibility, ν_r being the elastic Poisson's ratio.

3 The Linear Comparison Composite

In order to evaluate the effective elastoplastic properties of the three-phase solid, a linear comparison composite bearing an identical microgeometry as the nonlinear one will be used. The inclusion phase in the comparison composite is taken to have the same elastic properties as the original inclusions, and so are the bulk moduli of the interphase and matrix. The shear moduli of the interphase and matrix in the comparison composite, however, are set equal to the homogenized secant shear moduli of their corresponding phases in the original nonlinear composite. These secant moduli are calculated from their respective constitutive equations at a given homogenized effective stress. In section 4, the effective stress of both interphase and ductile matrix will be determined by a field-fluctuation method. Once the secant moduli of both ductile phases are known, the overall secant moduli of the nonlinear composite at the applied level of stress can be evaluated. Then, by increasing the level of the applied stress, the entire stress-strain curve of the composite with a ductile interphase can be obtained.

Thus it is useful to recall the effective bulk and shear moduli of the three-phase comparison composite first. Such information is also needed for the application of the field-fluctuation method. For the isotropic system, the effective moduli tensor L_s and compliances tensor M_s can be written as

$$L_s = (3\kappa_s, 2\mu_s), \quad M_s = (1/3\kappa_s, 1/2\mu_s), \qquad (6)$$

where the subscript s signifies the "secant" state of the constituent phases. Once κ_s and μ_s are known, the effective Young modulus E_s will follow from the isotropic relation $E_s = 9\kappa_s\mu_s/(3\kappa_s + \mu_s)$.

Based on Hashin's (1962) composite sphere model, the overall bulk modulus has been derived by Qiu and Weng (1991), as

$$\begin{aligned}\kappa_s = \kappa_3 &+ (3\kappa_3 + 4\mu_3^s)[c_1(3\kappa_2 + 4\mu_2^s)(\kappa_1 - \kappa_3) \\ &+ c_2(3\kappa_1 + 4\mu_2^s)(\kappa_2 - \kappa_3)]/\{(3\kappa_1 + 4\mu_2^s)[(3\kappa_2 + 4\mu_3^s) \\ &+ 3(c_1 + c_2)(\kappa_3 - \kappa_2)] + 3c_1(\kappa_2 - \kappa_1) \\ &\times [4(\mu_3^s - \mu_2^s)/(c_1 + c_2) + (3\kappa_3 + 4\mu_2^s)]\}. \qquad (7)\end{aligned}$$

The overall shear modulus can be derived also by means of Christensen and Lo's generalized self-consistent scheme by embedding the three-phase concentrated sphere in the infinite effective medium. After standard but elaborate analysis the shear modulus μ_s of the composite can be determined by setting the determinant of the 12×12 matrix in Appendix A equal to zero (where for brevity the subscript s reflecting the secant state has been omitted). As for the ordinary two-phase composite, the effective shear modulus of the three-phase system can also be cast in a second-order algebraic form in terms of μ_s.

4 Determination of the Homogenized Effective Stress of the Ductile Phases

The effective stress defined in Qiu and Weng (1992) is based on the equivalence of the distortional energy between a homogenized phase and the heterogeneously deformed phase in the composite, as

$$\frac{1}{6\mu_r^s}\sigma_e^{2(r)} = \frac{1}{V_r}\int_{V_r}\frac{1}{4\mu_r^s}\sigma_{ij}^{\prime(r)}(x)\sigma_{ij}^{\prime(r)}(x)dV,$$
$$\text{or} \quad \sigma_e^{2(r)} = \langle\sigma_e^{2(r)}(x)\rangle, \qquad (8)$$

where V_r represents the volume of the rth phase and the angle brackets $\langle . \rangle$ signify the volume average over the said phase. To evaluate this quantity for both the ductile interphase and the matrix the field-fluctuation method originally developed by Bobeth and Diener (1986) in elasticity and recently extended to plasticity by Suquet (1995, 1996) and Hu (1996) will be invoked here. As in Qiu and Weng, this method also starts out from the total elastic energy equivalence between the homogenized global system and the local constituent phases, but it takes the advantage of the field-fluctuation due to the variation of shear modulus in the ductile phase. In symbolic notations, the elastic energy U_s of the composite with a unit volume of an appropriate scale can be written as

$$2U_s = \bar{\boldsymbol{\sigma}}M_s\bar{\boldsymbol{\sigma}} = \sum\langle\boldsymbol{\sigma}_r M_r^s \boldsymbol{\sigma}_r\rangle, \qquad (9)$$

where the boldfaced $\bar{\boldsymbol{\sigma}}$ is the stress tensor of the composite, M_r^s is the compliances tensor of the rth phase, and the summation Σ extends to all three phases. Then a variation in the shear modulus of the rth phase from μ_r^s to $\mu_r^s + \delta\mu_r^s$ will result in a variation for the overall compliance tensor from M_s to $M_s + \delta M_s$ and a stress field from $\boldsymbol{\sigma}_r(x)$ to $\boldsymbol{\sigma}_r(x) + \delta\boldsymbol{\sigma}_r(x)$. Under the same boundary traction, Hill's relation (1963) implies that the contribution from the variation of the stress field $\delta\boldsymbol{\sigma}_r(x)$ on the overall energy vanishes due to the vanishing outer traction. As a consequence the following relation can be established:

$$c_r\langle\boldsymbol{\sigma}'_r\boldsymbol{\sigma}'_r\rangle\delta\left(\frac{1}{2\mu_r^s}\right) = \bar{\boldsymbol{\sigma}}\delta M_s\bar{\boldsymbol{\sigma}}, \qquad (10)$$

and this leads to the homogenized effective stress for the rth phase

$$\sigma_e^{2(r)} = \bar{\boldsymbol{\sigma}}\left(\frac{-3\mu_r^{s2}}{c_r}\frac{\delta M_s}{\delta\mu_r^s}\right)\bar{\boldsymbol{\sigma}}. \qquad (11)$$

This general relation provides the effective stress under the following three specific loadings:

(i) pure dilatation

$$\sigma_e^{2(r)} = \frac{\mu_r^{s2}\bar{\sigma}_{kk}^2}{3c_r\kappa_s^2}\frac{\delta\kappa_s}{\delta\mu_r^s}; \qquad (12)$$

(ii) pure shear

$$\sigma_e^{2(r)} = \frac{3\mu_r^{s2}\bar{\sigma}_{12}^2}{c_r\mu_s^2}\frac{\delta\mu_s}{\delta\mu_r^s}; \qquad (13)$$

(iii) pure tension

$$\sigma_e^{2(r)} = \frac{3\mu_r^{s2}\bar{\sigma}_{11}^2}{c_rE_s^2}\frac{\delta E_s}{\delta\mu_r^s}, \qquad (14)$$

which will be used later in the calculations.

The computational procedure goes as follows. At a given applied $\bar{\boldsymbol{\sigma}}$, the aim is to find the overall secant compliances tensor M_s in (6), or κ_s and μ_s, which are given in (7) and Appendix A, respectively, in terms of μ_2^s and μ_3^s of the interphase and the matrix. One may start out with some trial values for both and calculate the $\sigma_e^{(r)}$ by (11), and then substitute the calculated values into the constitutive Eqs. (4) and (5) to find the corresponding μ_r^s. If these values are identical—or very close—to the originally assumed ones, the solution is found. If not, a new set of μ_2^s and μ_3^s reflecting the calculated values should be assumed until the solution is found. Once M_s is known, the overall strain follows from $\bar{\boldsymbol{\epsilon}} = M_s\bar{\boldsymbol{\sigma}}$. By increasing the magnitude of $\bar{\boldsymbol{\sigma}}$ the entire stress-strain curve at a given concentration of interphase can be determined.

5 An Exact Local Analysis

It is desirable to assess the accuracy of the theory first before we proceed to use it to examine the influence of the interphase on the overall behavior of the composite. To this end we now carry out an exact analysis under a hydrostatic loading. Care must be exercised, however, that there are more than one possibility for the yielding process. Depending on the relative yield strength and elastic moduli of the two ductile phases, yielding may commence from the inclusion/interphase interface, or from the matrix side of the interphase/matrix interface. Furthermore, two partial yielding may simultaneously take place, or one may first reach the fully plastic state while the other yields progressively. The constants which appear in the following field equations are detailed in Appendix B.

First in the elastic state, the radial displacements in the inclusion, interphase, and matrix are given by

$$u_r^{(1)} = A_1r, \quad u_r^{(i)} = B_1^{(i)}r + B_2^{(i)}\frac{a_2^3}{r^2}, \quad i = 2, 3 \qquad (15)$$

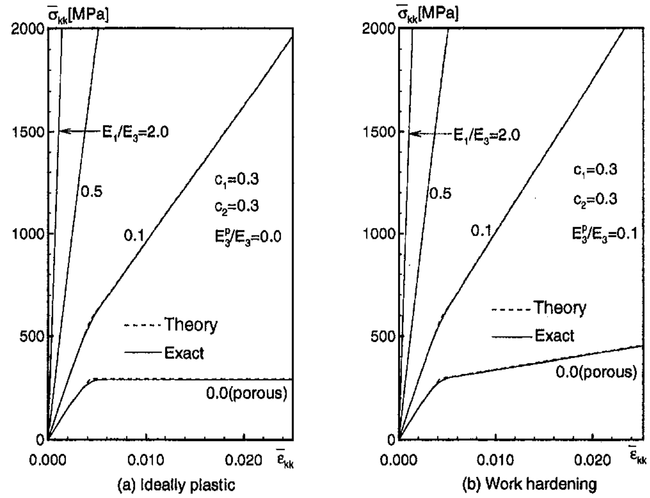

Fig. 1 Examination of the homogenization theory in light of an exact solution with a soft interphase: (*a*) ideally plastic matrix and interphase and (*b*) linearly work-hardening matrix and interphase

in a spherical coordinate system, and these result in the strain components

$$\epsilon_{rr}^{(1)} = \epsilon_{\theta\theta}^{(1)} = \epsilon_{\phi\phi}^{(1)} = A_1,$$

$$\epsilon_{rr}^{(i)} = B_1^{(i)} - B_2^{(i)}\frac{a_2^3}{r^3},$$

$$\epsilon_{\theta\theta}^{(i)} = \epsilon_{\phi\phi}^{(i)} = B_1^{(i)} + B_2^{(i)}\frac{a_2^3}{r^3}, \quad i = 2, 3 \qquad (16)$$

and stress fields

$$\sigma_{rr}^{(1)} = \sigma_{\theta\theta}^{(1)} = \sigma_{\phi\phi}^{(1)} = 3\kappa^{(1)}A_1,$$

$$\sigma_{rr}^{(i)} = 3\kappa_iB_1^{(i)} - 4\mu_iB_2^{(i)}\frac{a_2^3}{r^3},$$

$$\sigma_{\theta\theta}^{(i)} = \sigma_{\phi\phi}^{(i)} = 3\kappa_iB_1^{(i)} + 2\mu_iB_2^{(i)}\frac{a_2^3}{r^3}, \quad i = 2, 3. \qquad (17)$$

The constants A_1, $B_1^{(i)}$, and $B_2^{(i)}$ can be determined from the continuity conditions and the boundary condition; they are given in Appendix B.

Now to reduce the number of many yielding possibilities to a more tractable state, both the interphase and the ductile matrix will be taken to be elastically incompressible as well (Qiu and Weng (1992) have carried out an exact analysis for both compressible and incompressible matrix in a two-phase composite, and the results show that there is no difference in the evaluation process for the energy approach). The effective stress under a hydrostatic tension is then given by

$$\sigma_e^{(i)} = \sigma_{\theta\theta}^{(i)} - \sigma_{rr}^{(i)}. \qquad (18)$$

After plastic deformation commences in one phase, there are two possibilities: The plastic zone will spread while the other phase remains elastic, or partial plastic deformation will occur in both phases. Eventually both phases will enter into fully plastic state. A full analysis for a two-phase composite with a linearly work-hardening matrix ($n = 1$) has been given in Qiu and Weng (1992). Extending that procedure to the three-phase solid with incompressible, linearly work-hardening interphase

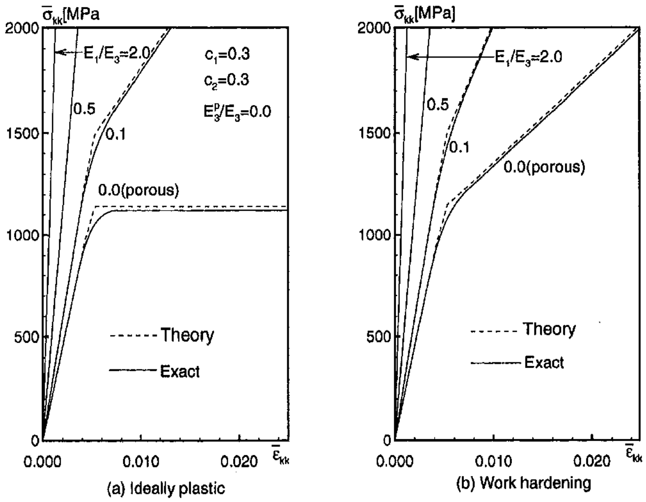

Fig. 2 Examination of the homogenization theory in light of an exact solution with a hard interphase: (*a*) ideally plastic matrix and interphase and (*b*) linearly work-hardening matrix and interphase

and matrix, one arrives at the following displacement, radial plastic strain, and stress fields in the plastic zone

$$u_r^{(i)} = -\frac{h_i + E_i}{2E_i}\frac{D_i}{r^2},$$

$$\epsilon_{rr}^{p(i)} = \frac{D_i}{r^3} + \frac{\sigma_y^{(i)}}{h_i + E_i},$$

$$\sigma_{rr}^{(i)} = \frac{2\sigma_y^{(i)}E_i}{h_i + E_i}\log r + \frac{2}{3}D_i h_i \frac{1}{r^3} + C_i. \tag{19}$$

When the ith phase is in a partial-yielding state, constant D_i can be further expressed in terms of the elastic-plastic boundary $r_p^{(i)}$

$$D_i = -\frac{\sigma_y^{(i)}}{h_i + E_i} r_p^{(i)3}. \tag{20}$$

In addition, the circumferential stress in the plastic state satisfies

$$\sigma_{\theta\theta}^{(i)} - \sigma_{rr}^{(i)} = \sigma_y^{(i)} - h_i\epsilon_{rr}^{p(i)}, \tag{21}$$

noting that $\epsilon_{rr}^{p(i)}$ is a negative value. Constants C_i, A_1, $B_1^{(i)}$, and $B_2^{(i)}$ can also be determined from the continuity conditions at the interfaces and the boundary traction. After some lengthy analysis, the end results are also recapitulated in Appendix B. Once these constants are determined, the overall dilatational strain follows as

$$\bar{\epsilon}_{kk} = 3c_1A_1, \tag{22}$$

due to the incompressibility assumption of both ductile phases.

Comparisons between the exact analysis and the theory for the overall dilatational behavior of the three-phase system are shown in Figs. 1 and 2. The results in Fig. 1 are for the condition that the interphase is more ductile than the matrix, with a property only $\frac{1}{10}$th of that of the latter

$$E_2 = E_3/10, \quad \sigma_y^{(2)} = \sigma_y^{(3)}/10, \quad E_2^p = E_3^p/10, \tag{23}$$

where E_i^p is the tangent modulus in the bilinear stress-strain curve of the ith phase, with $E_i^p = (E_i^{-1} + h_i^{-1})^{-1}$. On the other hand in Fig. 2 the interphase is taken to be stiffer than the matrix with

$$E_2 = 1.1E_3, \quad \sigma_y^{(2)} = 2.5\sigma_y^{(3)}, \quad E_2^p = 2.5E_3^p. \tag{24}$$

These values have been chosen to represent the two distinct yielding processes discussed in Appendix B: interphase yielding first and matrix yielding first, respectively. It must be noted that a harder interphase will not guarantee that the matrix will yield first, as the elastic moduli, yield stress and tangent moduli can all influence the onset of yielding and subsequent plastic deformation. For instance in (24) if the coefficients were replaced by 2 in all three terms, yielding would still commence from the interphase even though its yield stress is twice as high as that of the matrix, as in this case its higher Young's modulus will result in a higher elastic stress and cause it to yield first.

Parts (*a*) and (*b*) in both figures correspond to an ideally plastic matrix (and interphase) and a linearly work-hardening matrix (and interphase), respectively. These figures reveal how the nonlinearity of the three-phase system develops as the stiffness of the inclusions decreases from being harder ($E_1/E_3 = 2$) than the matrix to being softer, and eventually becoming a porous material with a ductile interfacial zone ($E_1/E_3 = 0$). When the inclusions are stiffer than the matrix, the dilatational response of the system is practically linear, but as the inclusions become softer than the matrix, a hydrostatic tension will induce a nonlinear volume change. When the inclusions turn into voids,

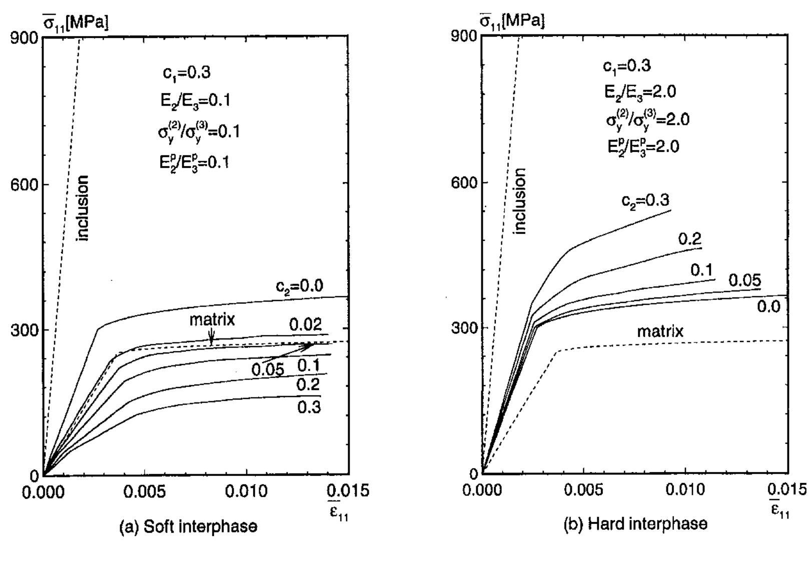

Fig. 3 Influence of the ductile interphase on the tensile behavior of a particle-reinforced composite: (*a*) soft interphase and (*b*) hard interphase

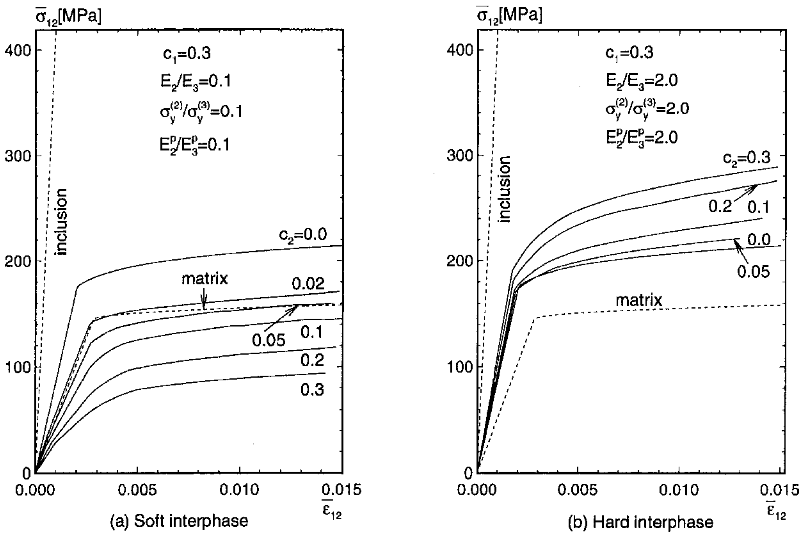

Fig. 4 Influence of the ductile interphase on the shear behavior of a particle-reinforced composite: (*a*) soft interphase and (*b*) hard interphase

the material as a whole displays a strong pressure sensitivity even both outer phases are individually rigid.

Now let us take a closer look at the predictions by the homogenization theory in light of the exact local analysis. For the case with a more ductile interphase, the results in both Fig. 1(*a*) and Fig. 1(*b*) indicate that the two curves are practically indistinguishable, except for the initial onset of yielding at which the local analysis can capture the local yielding more precisely. The difference becomes more discernible in Figs. 2(*a*) and (*b*) when the interphase is stiffer than the matrix, but once again, the theory can provide plausible predictions for the overall response of the system.

6 The Influence of the Ductile Layer on the Stress-Strain Relations of the Composite

Now that the theory is shown to provide some reliable results under dilatational loading, it will be used to examine how the volume concentration of the ductile interphase affects the overall response of the composite.

Specifically we shall take silicon-carbide/6061-T6 aluminum matrix as the base material, and consider the following compositions

$$c_1 = 0.3, \quad c_2 + c_3 = 0.7, \tag{25}$$

and let c_2 varies from 0 to 0.3, so that the three-phase composite will start out as a regular two-phase SiC/Al composite and then becomes a three-phase solid with an interphase. The properties of the constituents are (Arsenault, 1984; Nieh and Chellman, 1984)

$$E_1 = 490 \text{ GPA}, \quad \nu_1 = 0.17,$$
$$E_3 = 68.3 \text{ GPA}, \quad \nu_3 = 0.33, \quad \sigma_y^{(3)} = 250 \text{ MPa},$$
$$h_3 = 173 \text{ MPa}, \quad n_3 = 0.455. \tag{26}$$

We shall first consider the condition when the interphase is more ductile than the matrix, and then when it is stiffer.

As in the dilatational case, the properties of the soft interphase are taken to be $\frac{1}{10}$th of the matrix for the soft case, but retaining the same Poisson's ratio and n. The tensile behavior of the three-phase solid are shown in Fig. 3(*a*) as the volume concentration of the soft interphase increases from $c_2 = 0$. The stress-strain curves of SiC particles and Al matrix are also plotted as dotted lines for comparison. The elastoplastic behavior of the composite is seen to be strongly dependent upon the interphase concentration, and can be weakened considerably with an increasing interphase. Indeed even with the presence of a thin layer ($c_2 = 0.05$), the three-phase system is already softer than the matrix.

When the interphase is twice as stiff as the matrix, the tensile behavior are shown in Fig. 3(*b*). The overall response is seen to be strengthened with an increasing amount of the interphase, as expected. The departure from the behavior of the two-phase SiC/Al composite at low concentration, however, is not as significant as in the soft case.

The corresponding shear behavior with a more ductile and a stiffer interphase are depicted in Figs. 4(*a*) and (*b*), respectively. With a soft interphase, the low-concentration effect again shows a remarkable reduction in the overall yield strength due to the poor stress transfer from the matrix to the particle. While the corresponding flow stress under pure shear is lower than that under pure tension, the composite as a whole displays an equally strong dependence upon the volume concentration of the interphase.

Acknowledgment

This work was supported by the National Science Foundation, under Grant CMS-9625304, and by the Office of Naval Research, under Grant N-00014-91-J-1937.

References

Arsenault, R. J., 1984, "The Strengthening of Aluminum Alloy 6061 by Fiber and Platelet Silicon Carbide," *Materials Science and Engineering,* Vol. 64, pp. 171–181.

Berveiller, M., and Zaoui, A., 1979, "An Extension of the Self-Consistent Scheme to Plastically-Flowing Polycrystals," *Journal of the Mechanics and Physics of Solids,* Vol. 26, pp. 325–344.

Bobeth, M., and Diener, G., 1986, "Field Fluctuations in Multicomponent Mixtures," *Journal of the Mechanics and Physics of Solids,* Vol. 34, pp. 1–17.

Bornert, M., Herve, E., Soltz, C., and Zaoui, A., 1994, "Self-Consistent Approaches and Strain Heterogeneities in Two-Phase Elastoplastic Materials," ASME *Applied Mechanics Reviews,* Vol. 47, pp. S66–S76.

Christensen, R. M., and Lo, K. H., 1979, "Solutions for Effective Shear Properties in Three Phase Sphere and Cylinder Models," *Journal of the Mechanics and Physics of Solids,* Vol. 27, pp. 315–330.

Eshelby, J. D., 1957, "The Determination of the Elastic Field of an Ellipsoidal Inclusion, and Related Problems," *Proceedings of the Royal Society, London,* Vol. A241, pp. 376–396.

Hashin, Z., 1962, "The Elastic Moduli of Heterogeneous Materials," ASME Journal of Applied Mechanics, Vol. 29, pp. 143–150.

Hashin, Z. and Shtrikman, S., 1963, "A Variational Approach to the Theory of the Elastic Behavior of Multiphase Materials," *Journal of the Mechanics and Physics of Solids,* Vol. 11, pp. 127–140.

Herve, E., and Zaoui, A., 1990, "Modeling the Effective Behavior of Nonlinear Matrix Inclusion Composites," *European Journal of Mechanics/Solids*, Vol. 9, pp. 505–515.

Hill, R., 1963, "Elastic Properties of Reinforced Solids: Some Theoretical Principles," *Journal of the Mechanics and Physics of Solids*, Vol. 11, pp. 357–372.

Hu, G., 1996, "A Method of Plasticity for General Aligned Spherical Void or Fiber-Reinforced Composites," *International Journal of Plasticity*, Vol. 12, pp. 439–449.

Ju, J. W., and Chen, T. M., 1994, "Micromechanics and Effective Elastoplastic Behavior of Two-Phase Metal Matrix Composites," ASME *Journal of Engineering Materials and Technology*, Vol. 116, pp. 310–318.

Nieh, T. G., and Chellman, D. J., 1984, "Modulus Measurements in Discontinuous Reinforced Aluminum Composites," *Scripta Metallurgica*, Vol. 8, pp. 925–928.

Ponte Castañeda, P., 1991, "The Effective Mechanical Properties of Nonlinear Isotropic Composites," *Journal of the Mechanics and Physics of Solids*, Vol. 39, pp. 45–71.

Ponte Castañeda, P., 1992, "New Variational Principles in Plasticity and Their Application to Composite Materials," *Journal of the Mechanics and Physics of Solids*, Vol. 40, pp. 1757–1788.

Ponte Castañeda, P., 1996, "Exact Second-Order Estimates for the Effective Mechanical Properties of Nonlinear Composite Materials," *Journal of the Mechanics and Physics of Solids*, Vol. 44, pp. 827–862.

Qiu, Y. P., and Weng, G. J., 1991, "Elastic Moduli of Thickly Coated Particle and Fiber-Reinforced Composites," ASME JOURNAL OF APPLIED MECHANICS, Vol. 58, pp. 388–398.

Qiu, Y. P., and Weng, G. J., 1992, "A Theory of Plasticity for Porous Materials and Particle-Reinforced Composites," ASME JOURNAL OF APPLIED MECHANICS, Vol. 59, pp. 261–268.

Qiu, Y. P., and Weng, G. J., 1995, "An Energy Approach to the Plasticity of a Two-Phase Composite Containing Aligned Inclusions," ASME JOURNAL OF APPLIED MECHANICS, Vol. 62, pp. 1039–1046.

Suquet, P., 1995, "Overall Properties of Nonlinear Composites: A Modified Secant Moduli Theory and Its Link with Ponte Castañeda's Nonlinear Variational Procedure," *C. R. Academie des Sciences*, Vol. 320, Series IIb, pp. 563–571.

Suquet, P., 1996, "Overall Properties of Nonlinear Composites: Remarks on Secant and Incremental Formulations," *IUTAM Symposium on Micromechanics of Plasticity and Damage of Multiphase Materials*, A. Pineau and A. Zaoui, eds., Kluwer, Amsterdam, pp. 149–156.

Talbot, D. R. S., and Willis, J. R., 1985, "Variational Principles for Inhomogeneous Nonlinear Media," *IMA Journal of Applied Mathematics*, Vol. 35, pp. 39–54.

Talbot, D. R. S., and Willis, J. R., 1994, "Upper and Lower Bounds for the Overall Properties of a Nonlinear Composite Dielectric. I. Random Microgeometry," *Proceedings of the Royal Society, London*, Vol. A447, pp. 365–384.

Talbot, D. R. S., and Willis, J. R., 1997, "Bounds of Third Order for the Overall Response of Nonlinear Composites," *Journal of the Mechanics and Physics of Solids*, Vol. 45, pp. 87–111.

Tandon, G. P., and Weng, G. J., 1988, "A Theory of Particle-Reinforced Plasticity," ASME JOURNAL OF APPLIED MECHANICS, Vol. 55, pp. 126–135.

Weng, G. J., 1982, "A Unified, Self-Consistent Theory for the Plastic-Creep Deformation of Metals," ASME JOURNAL OF APPLIED MECHANICS, Vol. 49, pp. 728–734.

Weng, G. J., 1990, "The Overall Elastoplastic Stress-Strain Relations of Dual-Phase Metals," *Journal of the Mechanics and Physics of Solids*, Vol. 38, pp. 419–441.

Willis, J. R., 1991, "On Methods for Bounding the Overall Properties of Nonlinear Composites," *Journal of the Mechanics and Physics of Solids*, Vol. 39, pp. 73–86.

Willis, J. R., 1992, "On Methods for Bounding the Overall Properties of Nonlinear Composites: Correction and Addition," *Journal of the Mechanics and Physics of Solids*, Vol. 40, pp. 441–445.

APPENDIX A

Components of the matrix for the effective shear modulus in the generalized self-consistent scheme

$$
\begin{bmatrix}
1 & -\frac{6\nu_1}{1-2\nu_1} & -1 & \frac{6\nu_2}{1-2\nu_2}c_1^{\frac{2}{3}} & -3\left(\frac{1}{c_1}\right)^{\frac{5}{3}} & -\frac{5-4\nu_2}{1-2\nu_2}\left(\frac{1}{c_1}\right) & 0 & 0 & 0 & 0 & 0 & 0 \\
1 & -\frac{7-4\nu_1}{1-2\nu_1} & -1 & \frac{7-4\nu_2}{1-2\nu_2}c_1^{\frac{2}{3}} & 2\left(\frac{1}{c_1}\right)^{\frac{5}{3}} & -\left(\frac{2}{c_1}\right) & 0 & 0 & 0 & 0 & 0 & 0 \\
\frac{2\mu_1}{\mu_s} & \left[\frac{21\lambda_1}{\mu_s}-\frac{36\nu_1}{1-2\nu_1}\frac{\mu_1}{\mu_s}\right] & -\frac{2\mu_2}{\mu_s} & -\left[\frac{21\lambda_2}{\mu_s}-\frac{36\nu_2}{1-2\nu_2}\frac{\mu_2}{\mu_s}\right]c_1^{\frac{2}{3}} & \frac{24\mu_2}{\mu_s}\left(\frac{1}{c_1}\right)^{\frac{5}{3}} & \left[\frac{6\lambda_2}{\mu_s}+\frac{4(5-4\nu_2)}{1-2\nu_2}\frac{\mu_2}{\mu_s}\right]\left(\frac{1}{c_1}\right) & 0 & 0 & 0 & 0 & 0 & 0 \\
\frac{\mu_1}{\mu_s} & -\frac{(7+2\nu_1)\mu_1}{(1-2\nu_1)\mu_s} & -\frac{\mu_2}{\mu_s} & \frac{(7+2\nu_2)\mu_2}{(1-2\nu_2)\mu_s}c_1^{\frac{2}{3}} & -\frac{8\mu_2}{\mu_s}\left(\frac{1}{c_1}\right)^{\frac{5}{3}} & -\frac{2(1+\nu_2)\mu_2}{(1-2\nu_2)\mu_s}\left(\frac{1}{c_1}\right) & 0 & 0 & 0 & 0 & 0 & 0 \\
0 & 0 & 1 & -\frac{6\nu_2}{1-2\nu_2}(c_1+c_2)^{\frac{2}{3}} & 3\left(\frac{1}{c_1+c_2}\right)^{\frac{5}{3}} & \frac{5-4\nu_2}{1-2\nu_2}\frac{1}{c_1+c_2} & -1 & \frac{6\nu_3}{1-2\nu_3}(c_1+c_2)^{\frac{2}{3}} & -3\left(\frac{1}{c_1+c_2}\right)^{\frac{5}{3}} & -\frac{5-4\nu_3}{1-2\nu_3}\frac{1}{c_1+c_2} & 0 & 0 \\
0 & 0 & 1 & -\frac{7-4\nu_2}{1-2\nu_2}(c_1+c_2)^{\frac{2}{3}} & -2\left(\frac{1}{c_1+c_2}\right)^{\frac{5}{3}} & \frac{2}{c_1+c_2} & -1 & \frac{7-4\nu_3}{1-2\nu_3}(c_1+c_2)^{\frac{2}{3}} & 2\left(\frac{1}{c_1+c_2}\right)^{\frac{5}{3}} & -\frac{2}{c_1+c_2} & 0 & 0 \\
0 & 0 & \frac{2\mu_2}{\mu_s} & \left[\frac{21\lambda_2}{\mu_s}-\frac{36\nu_2}{1-2\nu_2}\frac{\mu_2}{\mu_s}\right](c_1+c_2)^{\frac{2}{3}} & -\frac{24\mu_2}{\mu_s}\left(\frac{1}{c_1+c_2}\right)^{\frac{5}{3}} & -\left[\frac{6\lambda_2}{\mu_s}+\frac{4(5-4\nu_2)}{1-2\nu_2}\frac{\mu_2}{\mu_s}\right]\frac{1}{c_1+c_2} & -2 & -\left[\frac{21\lambda_3}{\mu_s}-\frac{36\nu_3}{1-2\nu_3}\frac{\mu_2}{\mu_s}\right](c_1+c_2)^{\frac{2}{3}} & 24\left(\frac{1}{c_1+c_2}\right)^{\frac{5}{3}} & \left[\frac{6\lambda_3}{\mu_s}+\frac{4(5-4\nu_3)}{1-2\nu_3}\right]\frac{1}{c_1+c_2} & 0 & 0 \\
0 & 0 & \frac{\mu_2}{\mu_s} & -\frac{7+2\nu_2}{1-2\nu_2}\frac{\mu_2}{\mu_s}(c_1+c_2)^{\frac{2}{3}} & \frac{8\mu_2}{\mu_s}\left(\frac{1}{c_1+c_2}\right)^{\frac{5}{3}} & \frac{2(1+\nu_2)}{1-2\nu_2}\frac{\mu_2}{\mu_s}\frac{1}{c_1+c_2} & -1 & \frac{7+2\nu_3}{1-2\nu_3}(c_1+c_2)^{\frac{2}{3}} & -8\left(\frac{1}{c_1+c_2}\right)^{\frac{5}{3}} & -\frac{2(1+\nu_3)}{1-2\nu_3}\frac{1}{c_1+c_2} & 0 & 0 \\
0 & 0 & 0 & 0 & 0 & 0 & 1 & -\frac{6\nu_3}{1-2\nu_3} & 3 & \frac{5-4\nu_3}{1-2\nu_3} & -3 & 1 \\
0 & 0 & 0 & 0 & 0 & 0 & 1 & -\frac{7-4\nu_3}{1-2\nu_3} & -2 & 2 & 2 & 1 \\
0 & 0 & 0 & 0 & 0 & 0 & 2 & \frac{21\lambda_3-36\nu_3}{(1-2\nu_3)} & -24 & -\frac{6\lambda_3}{\mu_s}+\frac{4(5-4\nu_3)}{1-2\nu_3} & \frac{24\mu}{\mu_s} & \frac{2\mu}{\mu_s} \\
0 & 0 & 0 & 0 & 0 & 0 & 1 & -\frac{7+2\nu_3}{1-2\nu_3} & 8 & \frac{2(1+\nu_3)}{1-2\nu_3} & -\frac{8\mu}{\mu_s} & \frac{\mu}{\mu_s}
\end{bmatrix}
$$

APPENDIX B

Exact Local Elastic-Plastic Analysis

There are many yielding processes for the composite, but the most common one starts from the interphase until it becomes fully plastic, then followed by the matrix yielding. Another distinct yielding process starts from the matrix until it becomes fully plastic, then followed by the interphase yielding. The following exact solutions are for these two processes and can be used to construct Figs. 1 and 2, respectively.

1 Yielding From the Interphase. When both the interphase and the matrix are in the elastic state, the coefficients A_1, $B_1^{(m)}$, and $B_2^{(m)}$ are

$$A_1 = \frac{\bar{\sigma}_{kk}}{4(c_2E_2 + c_1c_3E_3)/(c_1 + c_2) + 3E_1/(1 - 2\nu_1)},$$

$$B_1^{(1)} = 0, \quad B_1^{(2)} = 0,$$

$$B_2^{(1)} = \frac{c_1\bar{\sigma}_{kk}}{4(c_2E_2 + c_1c_3E_3)/(c_1 + c_2) + 3E_1/(1 - 2\nu_1)},$$

$$B_2^{(2)} = \frac{c_1\bar{\sigma}_{kk}}{4(c_2E_2 + c_1c_3E_3)/(c_1 + c_2) + 3E_1/(1 - 2\nu_1)}. \quad \text{(B1)}$$

When the interphase is partly plastic and partly elastic but the matrix remains elastic, we let $X = [A_1, C_2, B_1^{(2)}, B_2^{(2)}, B_1^{(3)}, B_2^{(3)}]$. Then these constants can be determined in terms of the elastic-plastic boundary $r_p^{(2)}$ from the matrix equation $SX = B$, with

$$S = \left\{\begin{array}{cccccc} 1 & 0 & 0 & 0 & 0 & 0 \\ \dfrac{E_1}{1-2\nu_1} & -1 & 0 & 0 & 0 & 0 \\ 0 & 0 & -1 & -\dfrac{1}{r_p^{3(2)}} & 0 & 0 \\ 0 & 1 & -\dfrac{E_2}{1-2\nu_2} & \dfrac{2E_2}{(1+\nu_2)r_p^{3(2)}} & 0 & 0 \\ 0 & 0 & 1 & \dfrac{1}{c_1+c_2} & -1 & -\dfrac{1}{c_1+c_2} \\ 0 & 0 & \dfrac{E_2}{1-2\nu_2} & -\dfrac{2E_2}{(1+\nu_2)(c_1+c_2)} & -\dfrac{E_3}{1-2\nu_3} & \dfrac{2E_3}{(1+\nu_3)(c_1+c_2)} \end{array}\right\}, \quad \text{(B2)}$$

and

$$B = \left\{\frac{1}{2}\frac{\sigma_y^{(2)} r_p^{3(2)}}{E_2c_1}, \frac{2}{3}\frac{\sigma_y^{(2)}}{h_2 + E_2}\left[E_2 \log c_1 - \frac{h_2r_p^{3(2)}}{c_1}\right],\right.$$

$$\left. -\frac{1}{2}\frac{\sigma_y^{(2)}}{E_2}, -\frac{2}{3}\frac{\sigma_y^{(2)}}{h_2 + E_2}[E_2 \log r_p^{(2)} - h_2], 0, 0\right\}^T. \quad \text{(B3)}$$

The boundary $r_p^{(2)}$ is in turn related to the applied stress $\bar{\sigma}_{kk}$ through

$$\bar{\sigma}_{kk} = \frac{3E_3}{1 - 2\nu_3}B_1^{(3)} - \frac{6E_3}{1 + \nu_3}B_2^{(3)}. \quad \text{(B4)}$$

Therefore, corresponding to each increment of $r_p^{(2)}$, one can find out the components of X and $\bar{\sigma}_{kk}$.

When the interphase is fully plastic but the matrix is partly plastic and partly elastic, we let $X = [A_1, C_2, D_2, C_3, B_1^{(3)}, B_2^{(3)}]$. The coefficients in the $SX = B$ equation are

$$S = \left\{\begin{array}{cccccc} 1 & 0 & \dfrac{1}{2}\dfrac{h_2 + E_2}{E_2(c_1)} & 0 & 0 & 0 \\ \dfrac{E_1}{1-2\nu_1} & -1 & -\dfrac{2}{3}\dfrac{h_2}{c_1} & 0 & 0 & 0 \\ 0 & 0 & -\dfrac{1}{2}\dfrac{h_2 + E_2}{E_2(c_1 + c_2)} & 0 & 0 & 0 \\ 0 & 1 & \dfrac{2}{3}\dfrac{h_2}{c_1 + c_2} & -1 & 0 & 0 \\ 0 & 0 & 0 & 0 & -1 & -\dfrac{1}{r_p^{3(3)}} \\ 0 & 0 & 0 & 1 & -\dfrac{E_3}{1-2\nu_3} & \dfrac{2E_3}{1+\nu_3}\dfrac{1}{r_p^{3(3)}} \end{array}\right\}, \quad \text{(B5)}$$

and

$$B = \left\{0, \frac{2}{3}\frac{\sigma_y^{(2)}E_2 \log c_1}{h_2 + E_2}, \frac{1}{2}\frac{\sigma_y^{(3)} r_p^{3(3)}}{E_3(c_1 + c_2)},\right.$$

$$\frac{2}{3}\frac{\sigma_y^{(3)}}{h_3 + E_3}\left(E_3 \log (c_1 + c_2) - \frac{h_3r_p^{3(3)}}{c_1 + c_2}\right)$$

$$-\frac{2}{3}\frac{\sigma_y^{(2)}E_2 \log (c_1 + c_2)}{h_2 + E_2}, -\frac{1}{2}\frac{\sigma_y^{(3)}}{E_3},$$

$$\left. -\frac{2\sigma_y^{(3)}}{h_3 + E_3}\left(E_3 \log r_p^{(3)} - \frac{h_3}{3}\right)\right\}. \quad \text{(B6)}$$

One can obtain X in terms of $r_p^{(3)}$, which is again related to the applied $\bar{\sigma}_{kk}$ through (B4). Then by increasing $r_p^{(3)}$, one can proceed in the same fashion.

When both the interphase and the matrix are in the fully plastic state, we let $X = [A_1, C_2, D_2, C_3, D_3]$. From $SX = B$, with

$$S = \begin{Bmatrix} 1 & 0 & \dfrac{h_2 + E_2}{2E_2 c_1} & 0 & 0 \\ \dfrac{E_1}{1 - 2\nu_1} & -1 & -\dfrac{2h_2}{3c_1} & 0 & 0 \\ 0 & 0 & -\dfrac{h_2 + E_2}{2E_2(c_1 + c_2)} & 0 & \dfrac{h_3 + E_3}{2E_3(c_1 + c_2)} \\ 0 & 1 & \dfrac{2h_2}{3(c_1 + c_2)} & -1 & -\dfrac{2h_3}{3(c_1 + c_2)} \\ 0 & 0 & 0 & 1 & \dfrac{2h_3}{3} \end{Bmatrix}, \tag{B7}$$

and

$$B = \left\{0, 0, 0, \frac{2}{3}\frac{\sigma_y^{(2)} E_2 \log c_1}{h_2 + E_2}, \; 2\left[\frac{\sigma_y^{(3)} E_3}{h_3 + E_3} - \frac{\sigma_y^{(2)} E_2}{h_2 + E_2}\right]\right\}^T, \tag{B8}$$

the final stage of the stress-strain curve can be calculated.

2 Yielding From the Matrix. For the construction of the exact solution with a hard interphase in Figs. 2(a) and (b), Eqs. (B1), (B7), and (B8) remain valid. However, Eqs. (B2) to (B6) must be modified.

When the matrix is partly plastic and partly elastic while the interphase remains elastic, we let $X = [A_1, B_1^{(2)}, B_2^{(2)}, C_3, B_1^{(3)}, B_2^{(3)}]$.

Then

$$S = \begin{Bmatrix} 1 & -1 & -\dfrac{1}{c_1} & 0 & 0 & 0 \\ \dfrac{E_1}{1 - 2\nu_1} & -\dfrac{E_2}{1 - 2\nu_2} & \dfrac{2E_2}{(1 + \nu_2)c_1} & 0 & 0 & 0 \\ 0 & 1 & \dfrac{1}{c_1 + c_2} & 0 & 0 & 0 \\ 0 & \dfrac{E_2}{1 - 2\nu_2} & -\dfrac{2E_2}{(1 + \nu_2)(c_1 + c_2)} & -1 & 0 & 0 \\ 0 & 0 & 0 & 0 & -1 & -\dfrac{1}{r_p^{3(3)}} \\ 0 & 0 & 0 & 1 & -\dfrac{E_3}{1 - 2\nu_3} & \dfrac{2E_3}{(1 + \nu_3) r_p^{3(3)}} \end{Bmatrix} \tag{B9}$$

and

$$B = \left\{0, 0, \frac{1}{2}\frac{\sigma_y^{(3)} r_p^{3(3)}}{E_3(c_1 + c_2)}, \; \frac{2}{3}\frac{\sigma^{(3)}}{h_3 + E_3}\left[E_3 \log (c_1 + c_2) - \frac{h_3 r_p^{3(3)}}{c_1 + c_2}\right], \; -\frac{1}{2}\frac{\sigma_y^{(3)}}{E_3}, -2\frac{\sigma_y^{(3)}}{h_3 + E_3}\left[E_3 \log r_p^{(3)} - \frac{1}{3}h_3\right]\right\}^T. \tag{B10}$$

When the matrix is fully plastic but the interphase is partly plastic and partly elastic, we let $X = [A_1, C_2, B_1^{(1)}, B_2^{(1)}, C_3, D_3]$. Then

$$S = \begin{Bmatrix} 1 & 0 & 0 & 0 & 0 & 0 \\ \dfrac{E_1}{1 - 2\nu_1} & -1 & 0 & 0 & 0 & 0 \\ 0 & 0 & -1 & -\dfrac{1}{r_p^{3(2)}} & 0 & 0 \\ 0 & 1 & -\dfrac{E_2}{1 - 2\nu_2} & \dfrac{2E_2}{(1 + \nu_2) r_p^{3(2)}} & 0 & 0 \\ 0 & 0 & 1 & \dfrac{1}{c_1 + c_2} & 0 & \dfrac{1}{2}\dfrac{h_3 + E_3}{E_3(c_1 + c_2)} \\ 0 & 0 & \dfrac{E_2}{1 - 2\nu_2} & -\dfrac{2E_2}{(1 + \nu_2)(c_1 + c_2)} & -1 & -\dfrac{2}{3}\dfrac{h_3}{c_1 + c_2} \end{Bmatrix}, \tag{B11}$$

and

$$B = \left\{\frac{1}{2}\frac{\sigma_y^{(2)} r_p^{3(2)}}{E_2 c_1}, \frac{2}{3}\frac{\sigma_y^{(2)}}{h_2 + E_2}\left[E_2 \log c_1 - \frac{h_2 r_p^{3(2)}}{c_1}\right], \; -\frac{1}{2}\frac{\sigma^{(2)}}{E_2}, -2\frac{\sigma_y^{(2)}}{h_2 + E_2}\left[E_2 \log r_p^{(2)} - \frac{1}{3}h_2\right], \; 0, \frac{2}{3}\frac{\sigma_y^{(3)} E_3 \log (c_1 + c_2)}{h_3 + E_3}\right\}^T. \tag{B12}$$

C. S. Suh[1]
Assoc. Mem. ASME

C. P. Burger
Professor,
Mem. ASME.

Mechanical Engineering Department,
Texas A&M University,
College Station, TX 77843-3123

Effects of Thermomechanical Coupling and Relaxation Times on Wave Spectrum in Dynamic Theory of Generalized Thermoelasticity

A spectral study is performed to gain insight into the effects of relaxation times and thermomechanical coupling on dynamic thermoelastic responses in generalized thermoelasticity. The hyperbolic thermoelastic theories of Lord and Schulman (LS) and Green and Lindsay (GL) are selected for the study. A generalized characteristic equation is derived to investigate dispersion behavior of thermoelastic waves as functions of thermomechanical coupling and relaxation time constants. Thermomechanical coupling is found to impose a significant influence on phase velocities. The GL model implicitly indicates that the order of magnitude of the thermomechanical relaxation time can never be greater than that of thermal relaxation time.

Introduction

Because it incorporates a parabolic-type heat transport equation, the classical theory of thermoelasticity views heat propagation as a diffusion phenomenon and thus allows instantaneous responses to be observed everywhere in the problem domain upon the immediate action of thermal excitation. This means that a thermal disturbance travels with infinite speed and that the effects of a disturbance will be experienced instantaneously at locations infinitely far. To remedy this physically unrealistic contradiction, new theories based on a modified Fourier law of heat conduction or the incorporation of either an entropy production inequality or temperature-rate-dependent constitutive variables were proposed (Chandrasekharaiah, 1986; Ignaczak, 1980; Jakubowska, 1984). By introducing thermal relaxation time constants into the heat equation, these new generalized theories impart a finite nature to disturbance propagation. Of all the nonclassical theories, the Lord and Schulman (LS) (Lord and Schulman, 1967) and the Green and Lindsay (GL) (Green and Lindsay, 1972) models are in popular use in engineering applications (Spicer, 1991, and Hetnarski and Ignaczak, 1993). The LS model introduces a single time constant to dictate the relaxation of thermal propagation, as well as the rate of change of strain rate and the rate of change of heat generation. In the GL model, on the other hand, the thermal and thermomechanical relaxations are governed by two different time constants. Thus the underlying physical interpretations as well as the assumptions of dynamic thermoelastic processes by LS and GL are distinctively different. Many studies explored this difference to quantify the implications of their differences in particular field problems (Sanderson, 1995). Unfortunately, the complexity of solving coupled temperature and displacement fields, together with the argument that thermomechanical coupling shows negligible impact on the solutions (Nowinski, 1978; Spicer, 1991), have led to the frequent use of the decoupled formulations (with coupling terms omitted) in numerical models of thermoelastic responses. Further, although the occurrence of finite thermal wave speed for small intervals of time has long been experimentally observed (Chandrasekharaiah, 1986), the determination of relaxation times are largely based on the assumption that thermal waves can never travel faster than mechanical waves. These anomalies raise three questions:

1 In what manner and to what extent do LS and GL describe thermoelastic processes differently?
2 What are the implications and justifications for not considering coupling terms?
3 Do relaxation times have any impact at all on the solution fields?

This paper attempts to answer these questions by using spectral analysis, because the solutions to waves are governed by spectral relations. First, a general characteristic equation applicable to both the LS and GL models and the classical theory is derived. Second, the roles of thermomechanical couplings and relaxation times in generalized thermoelasticity are examined through the consideration of phase velocity. Finally, their combined effects on spectral behavior are investigated and a rationale is presented that is pertinent to applications that are characterized by large thermal gradients and short transient scales.

Thermoelastic Theories

The basic equations of generalized thermoelastic theory are derived from the equations of motion and the energy balance equation

$$\sigma_{ij,j} + \rho \mathbf{b}_i = \rho \ddot{\mathbf{U}}_i$$
$$\rho T \dot{\boldsymbol{\eta}} = -\mathbf{q}_{k,k} + Q \tag{1}$$

plus the constitutive equations (Chen and Weng, 1988; Tao and Provost, 1984)

[1] To whom all correspondence should be addressed. Currently Post-Doctoral Fellow, Department of Mechanical Engineering, Auburn University, Auburn, AL 36849.

Contributed by the Applied Mechanics Division of THE AMERICAN SOCIETY OF MECHANICAL ENGINEERS for publication in the ASME JOURNAL OF APPLIED MECHANICS.

Discussion on the paper should be addressed to the Technical Editor, Professor Lewis T. Wheeler, Department of Mechanical Engineering, University of Houston, Houston, TX 77204-4792, and will be accepted until four months after final publication of the paper itself in the ASME JOURNAL OF APPLIED MECHANICS.

Manuscript received by the ASME Applied Mechanics Division, Apr. 3, 1997; final revision, Dec. 9, 1997. Associate Technical Editor: J. T. Jenkins.

Table 1 Phase velocities for LS model for different relaxation times, t_0, for an aluminum material

Relaxation Time t_0 (sec)	Phase Velocity c_1 (m/sec)	Phase Velocity c_2 (m/sec)
$1.8\cdot10^{-14}$	67,830	*5,935*
$1.8\cdot10^{-13}$	21,450	*5,935*
$1.8\cdot10^{-12}$	6,800	*5,935*
$1.8\cdot10^{-11}$	*5,935*	2,143
$1.8\cdot10^{-10}$	*5,935*	678
$1.8\cdot10^{-9}$	*5,935*	214

Table 2 Phase velocities for GL model for different relaxation time ratio, t_1/t_2, for an aluminum material

Relaxation Time t_2 (sec)	t_1/t_2	Phase Velocity c_1 (m/sec)	Phase Velocity c_2 (m/sec)
$1.8\cdot10^{-14}$	10	67,830	5,935
$1.8\cdot10^{-14}$	5	67,830	5,935
$1.8\cdot10^{-14}$	2	67,830	5,935
$1.8\cdot10^{-13}$	10	21,450	5,931
$1.8\cdot10^{-13}$	5	21,450	5,933
$1.8\cdot10^{-13}$	2	21,450	5,934
$1.8\cdot10^{-12}$	10	6,936	5,803
$1.8\cdot10^{-12}$	5	6,864	5864
$1.8\cdot10^{-12}$	2	6,817	5,905

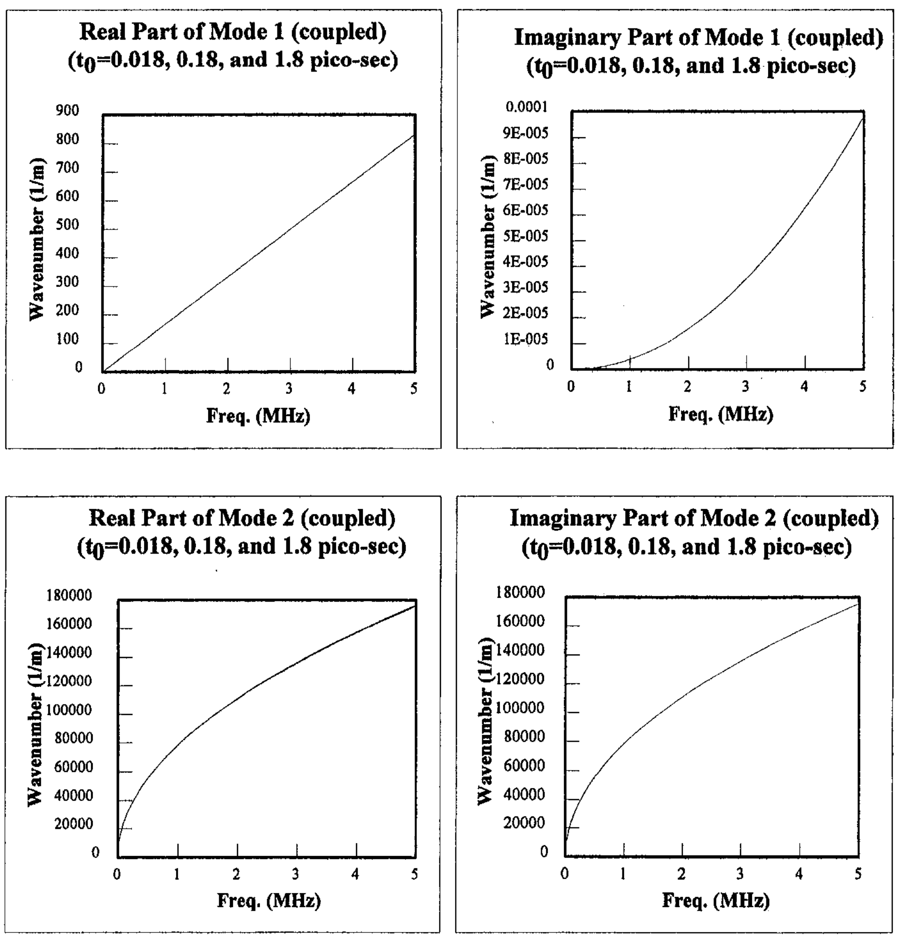

Fig. 1 Dispersion curves for the coupled case according to the LS model for different relaxation times (t_0 equals 0.018, 0.18, and 1.8 picoseconds)

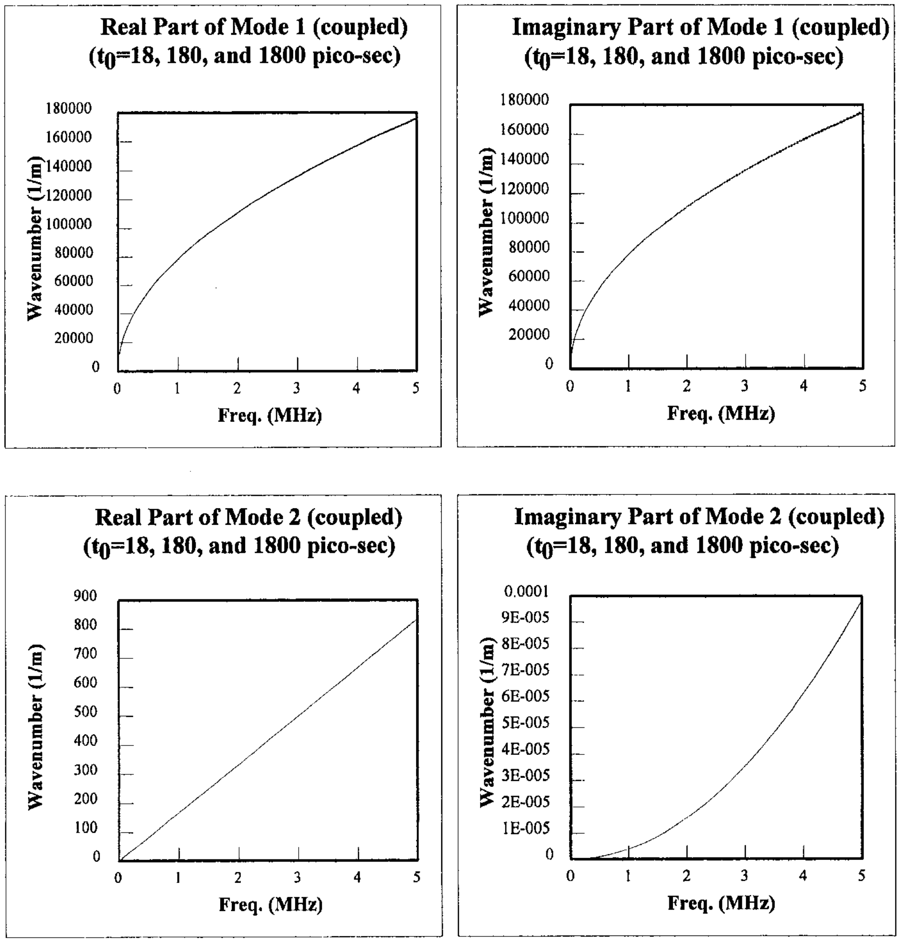

Fig. 2 Dispersion curves for the coupled case according to the LS model for different relaxation times (t_0 equals 18, 180, and 1800 picoseconds)

$$\sigma_{ij,j} = C_{ijkl}\epsilon_{kl,j} - \beta_{ij}(\theta + t_1\dot{\theta})$$

$$\mathbf{q}_i + t_0\dot{\mathbf{q}}_i = -k_{ij}\theta_{,j}$$

$$\boldsymbol{\eta} = \boldsymbol{\eta}_0 + c_v\theta + c_v t_2\dot{\theta} + \frac{1}{\rho}\beta_{ij}\epsilon_{ij} \qquad (2)$$

where σ_{ij} are the components of the stress tensor; C_{ijkl} the elastic moduli tensor; β_{ij} the thermal moduli tensor; ϵ_{ij} the strain tensor; k_{ij} the thermal conductivity tensor; $\mathbf{U}_i$ the displacement field components; ρ the density; $\mathbf{b}_i$ the body force vector; T the absolute temperature; θ the temperature increase, with $\theta = T - T_0$ and T_0 the reference temperature; $\boldsymbol{\eta}$ the entropy density, with $\boldsymbol{\eta}_0$ the entropy density at reference state; $\mathbf{q}_k$ the heat flux vector; c_v the specific heat; and Q the heat source. By substituting Eqs. (2) into Eqs. (1), the resulting generalized coupled field equations governing dynamic thermoelastic processes can be written as

$$\rho\ddot{\mathbf{U}}_i + (t_1\beta_{ij}\dot{\theta})_{,j} + (\beta_{ij}\theta - C_{ijkl}U_{k,l})_{,j} = \rho\mathbf{b}_i$$

$$\rho c_v(t_2 + t_0)\ddot{\theta} + \rho c_v\dot{\theta} + \beta_{ij}T_0(\dot{U}_{i,j} + t_0\ddot{U}_{i,j}) - (k_{ij}\theta_{,j})_{,i} = (Q + t_0\dot{Q}). \qquad (3)$$

The LS theory is obtained when $t_1 = t_2 = 0$, with t_0 the thermal relaxation time. In GL theory, $t_0 = 0$ and t_1 and t_2 are the thermal-mechanical relaxation time and the thermal relaxation time, respectively. When t_0, t_1, and t_2 all vanish, field Eqs. (3) reduce to the classical coupled formulations.

For homogenous isotropic materials and in the absence of body force and heat source, the equations of displacement motion and energy balance, Eqs. (3), can be expressed in terms of del operator (∇) and the Laplace operator (∇^2) as

$$\mu\nabla^2\mathbf{U} + (\lambda + \mu)\nabla\nabla\cdot\mathbf{U} - \beta\left(1 + t_1\frac{\partial}{\partial t}\right)\nabla\boldsymbol{\theta} = \rho\ddot{\mathbf{U}}$$

$$\rho c_v(t_2 + t_0)\ddot{\boldsymbol{\theta}} + \rho c_v\dot{\boldsymbol{\theta}} + \beta T_0(\nabla\dot{\mathbf{U}} + t_0\nabla\ddot{\mathbf{U}}) = k\nabla^2\boldsymbol{\theta} \quad (4)$$

in which

$$\beta = (3\lambda + 2\mu)\alpha \qquad (5)$$

is the thermoelastic coupling constant, with λ and μ the Lame's constants and α the coefficient of thermal expansion.

From Eqs. (3), the physical meaning of the time constant, t_0, may be interpreted as (1) a material property which dictates the finite nature of thermal waves, because the speed of thermal propagation can be explicitly determined to be $c_T = [k/(\rho c_v t_0)]^{1/2}$, and (2) the relaxation time required before the effect of rate of strain rate is experienced in the thermal field, as is evident in the fourth term on the left-hand side of Eqs. (3). Since t_0 does not appear in the equation of motion, it has no other physical implications on the mechanical field. However, although it is physically acceptable that t_0 may be an inherent property of the material, the concept of rate of strain rate is practically difficult to comprehend from the fundamental physics. Since the term of rate of strain rate cannot stand indepen-

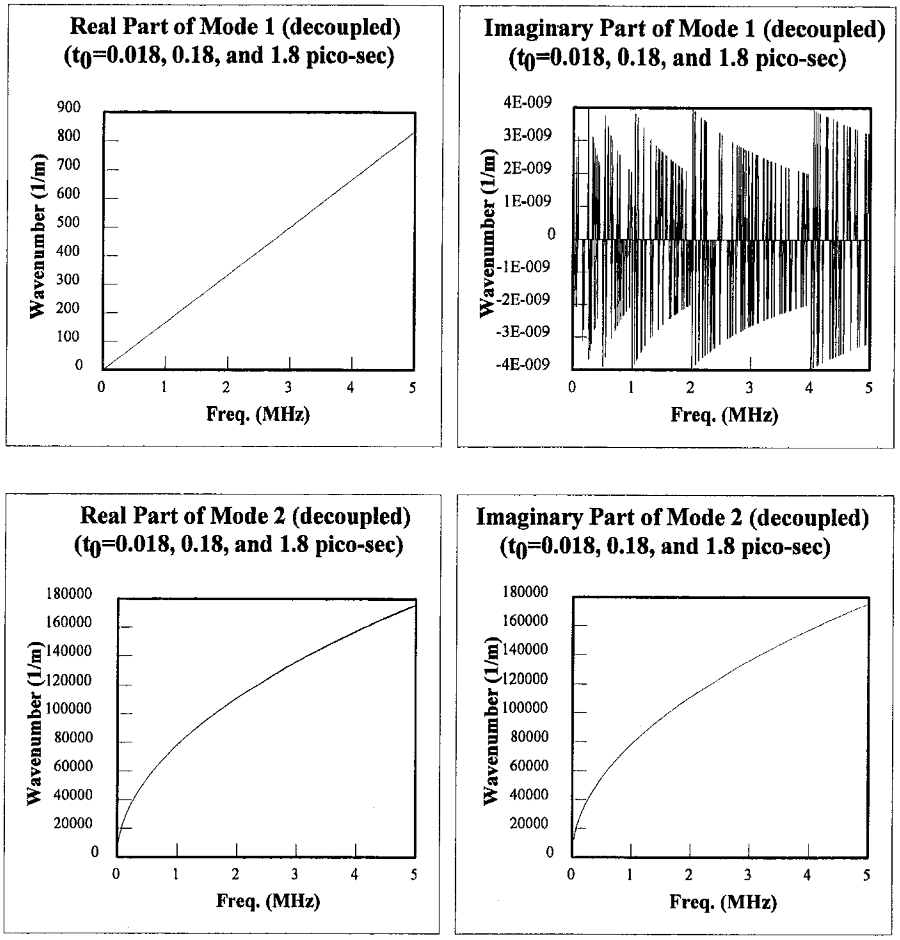

Fig. 3 Dispersion curves for the decoupled case according to the LS model for different relaxation times (t_0 equals 0.018, 0.18, and 1.8 picoseconds)

dently from t_0, or else the physical meaning they altogether represent—strain rate—cannot stand, a simultaneous co-existence of the two is implied. In other words, the variation of rate of strain rate can be quantified *if and only if* t_0 can be quantified.

Again, from Eqs. (3), with $t_0 = 0$, it is seen that the GL theory (1) admits finite energy transport speed and this speed is a function of the new material property t_2, (2) includes in the thermomechanical coupling term the rate of change of temperature gradient through a time constant t_1, and (3) exhibits strong interdependency (coupling) between the thermal and mechanical fields. As the effects of strain rate on the thermal field and temperature gradient on the mechanical field occur simultaneously, as described by the GL theory, the effects of rate of change of temperature gradient is not immediate. The time constant t_1 may be interpreted as the relaxation time required before the effect from thermal propagation is to be observed physically as displacements. However, it is difficult to quantify t_1, because the rate of change of thermal gradient has to be established first.

Spectral Analysis

A plane harmonic wave propagating with phase velocity c in a direction defined by the propagation vector $\mathbf{p}$ is represented by

$$\mathbf{U}(\mathbf{x}, t) = A\mathbf{d}e^{[i\gamma(\mathbf{x}\cdot\mathbf{p}-ct)]} \tag{6}$$

where $\mathbf{x}$ is the position vector, $\mathbf{d}$ is the unit vector defining the direction of particle motion, and $\gamma = 2\pi/\lambda$ is the wave number, where λ is the wavelength. A scalar temperature wave that accompanies a displacement wave may be assumed of the form (Achenbach, 1973)

$$\theta(\mathbf{x}, t) = Be^{[i\gamma(\mathbf{x}\cdot\mathbf{p}-ct)]}. \tag{7}$$

Substituting U and θ into Eq. (4) and eliminating B, gives

$$(\mu - \rho c^2)\mathbf{d} + (\lambda + \mu)(\mathbf{p}\cdot\mathbf{d})\mathbf{p} + \left(\frac{\beta^2 T_0 c}{\rho c_v}\right) \times \left[\frac{1 - i(t_0 + t_1)\gamma c + t_0 t_1 \gamma^2 c^2}{c + i[K_v\gamma - (t_0 + t_2)\gamma c^2]}\right](\mathbf{p}\cdot\mathbf{d})\mathbf{p} = 0 \tag{8}$$

where K_v is the thermal diffusivity. Since the direction of particle motion ($\mathbf{d}$) must either be parallel or perpendicular to the direction of wave propagation ($\mathbf{p}$), the cases of shear waves and longitudinal waves are investigated as follows.

For the case when $\mathbf{d} \neq \pm\mathbf{p}$, $\mathbf{p}\cdot\mathbf{d} = \mathbf{0}$ is implied and Eq. (8) becomes

$$c = \sqrt{\frac{\mu}{\rho}}, \tag{9}$$

Eq. (9) defines shear (transverse) waves. Two immediate observations are that shear waves are not functions of relaxation time constants nor thermal-mechanical coupling, and they do not interact with the temperature field.

When $\mathbf{d} = \pm\mathbf{p}$, so that $\mathbf{p}\cdot\mathbf{d} = \pm\mathbf{1}$, Eq. (8) becomes

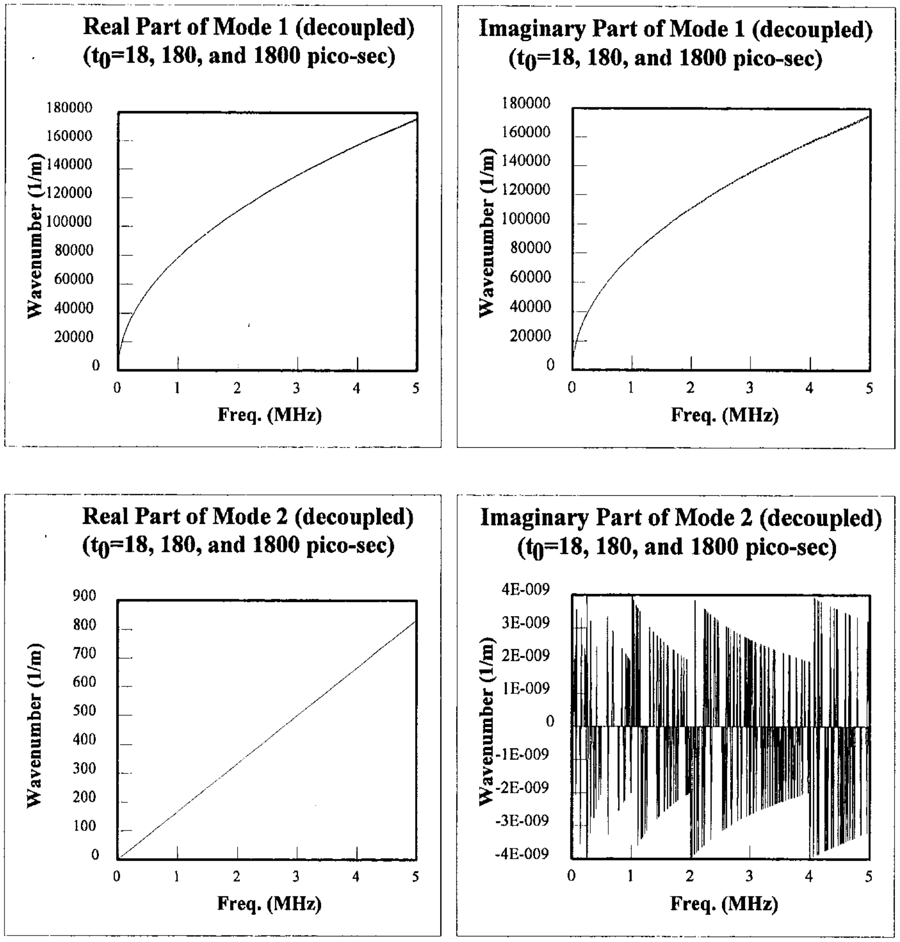

Fig. 4 Dispersion curves for the decoupled case according to the LS model for different relaxation times (t_0 equals 18, 180, and 1800 picoseconds)

$$(\lambda + 2\mu - \rho c^2) + \left(\frac{\beta^2 T_0 c}{\rho c_v}\right) \times \left[\frac{1 - i(t_0 + t_1)\gamma c + t_0 t_1 \gamma^2 c^2}{c + i[K_v \gamma - (t_0 + t_2)\gamma c^2]}\right] = 0. \quad (10)$$

This complex-valued characteristic equation shows that the phase velocity c depends on the wave number, γ, and the relaxation times (be it t_0 for the LS theory or t_1 and t_2 for the GL's), which indicates that thermoelastic waves are dispersive, attenuative, and closely related to the finite nature of the thermal waves. However, when the interactions between the thermal and mechanical fields are decoupled by setting $\beta = 0$, Eq. (10) reduces to the definition of longitudinal waves

$$c = c_L = \sqrt{\frac{\lambda + 2\mu}{\rho}}, \quad (11)$$

which implies that thermoelastic waves are nondispersive, nonattenuative, and independent of relaxation times. Since the classical uncoupled theory gives the identical results as Eq. (11), it can be concluded that the differences between the generalized and classical theories diminish in describing the phase velocities of uncoupled thermoelastic waves. Thus, the thermomechanical coupling effect is not always negligible. More physical insights into the thermoelastic processes can be revealed by considering the limitcases of γ. This is to be shown by first solving Eq. (10) for c. After rearranging and collecting terms and making $\gamma \to \infty$, we obtain two distinctive roots of c's

$$c_{1,2} = \pm \left[\frac{m \pm \sqrt{m^2 - 4K_v c_L^2 (t_0 + t_2)}}{2(t_0 + t_2)}\right]^{1/2}$$

where

$$m = (t_0 + t_2)c_L^2 + K_v + \frac{\beta^2 T_0}{\rho^2 c_v}(t_0 + t_1). \quad (12)$$

Table 1 gives the numerical values of c_1 and c_2 for different relaxation time t_0 for an aluminum material. The various properties of this material are given as follows:

Young's modulus:	70 GPa
Poisson ratio:	0.3
density:	2675 kg/m^3
specific heat:	921 J/kg°C
thermal conductivity:	204 W/m°C
expansion coefficient:	23 $\mu\epsilon$/°C

With t_1 and t_2 all being set to zero, this case corresponds to the LS theory. When the wavelength is small ($\gamma \to \infty$), the characteristic equation of LS always resolves two waves, with one approaching the longitudinal mechanical wave velocity (c_L = 5935 m/sec) and the other the thermal wave velocity ($c_T = [k/\rho c_v t_0]^{1/2}$). The resolution of mechanical waves is seen to be independent of the thermal relaxation, t_0 (and therefore the finite

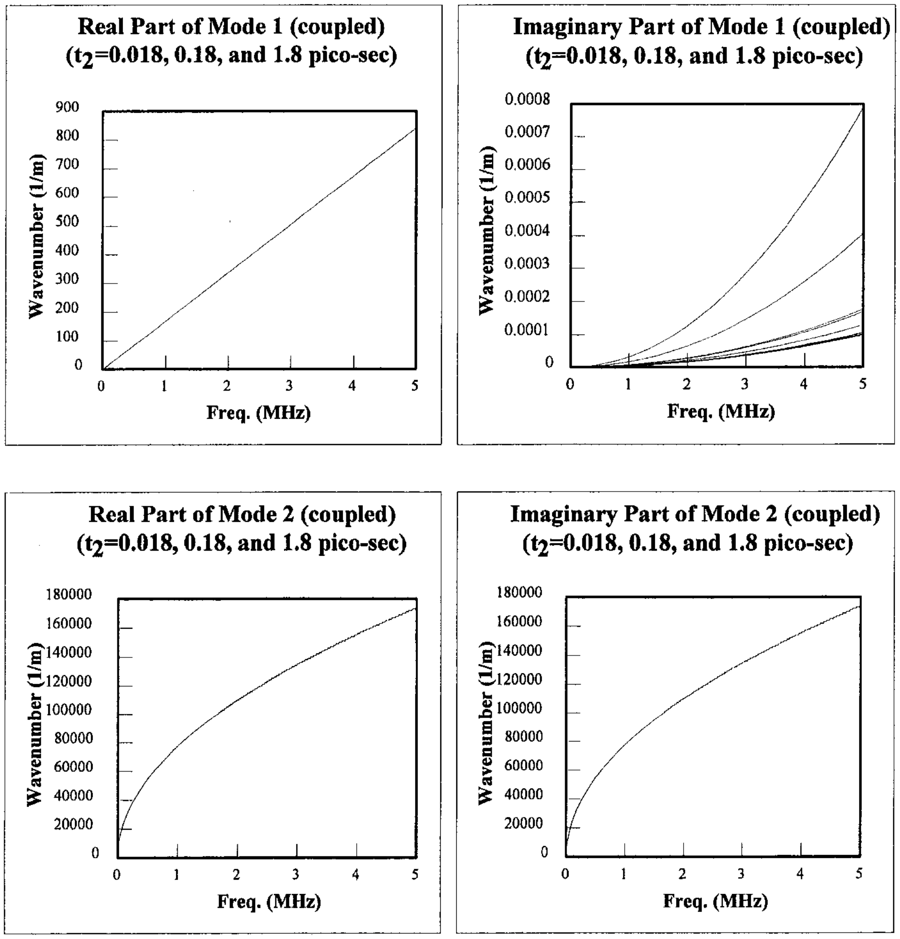

Fig. 5 Dispersion curves for the coupled case according to the GL model for different relaxation times and relaxation time ratios (t_2 equals 0.018, 0.18, and 1.8 picoseconds)

nature of thermal wave speed). This observation is not evident from the classical thermoelastic theory. However, when $\gamma \to 0$, the characteristic equation, Eq. (10), resolves only mechanical waves, no thermal waves, as is also the case with the classical theory (Doyle, 1988). Therefore, for applications that generate high-frequency thermoelastic waves due to large thermal gradients, the LS theory should provide significant insight not available from the classical theory.

Conclusions similar to the LS model can be obtained by the GL theory. In Table 2, phase velocities according to the GL model are tabulated against various t_1/t_2 ratios for the same aluminum material as in Table 1. Since t_2 is the thermal relaxation parameter for the GL model as t_0 is for the LS model, the cases when $t_2 = 1.8 \cdot 10^{-14}$ sec, $1.8 \cdot 10^{-13}$ sec, and $1.8 \cdot 10^{-12}$ sec are considered in Table 2. The most interesting observation from Table 2 is that steady resolution of mechanical waves can be maintained only when t_2 is less than 10^{-13} sec. When this is the case, the resolution is also independent of the relaxation ratio, t_1/t_2. For t_2 larger than 10^{-12} sec, the consistency of both the mechanical and thermal wave speeds deteriorate with increasing t_1/t_2 ratio. This makes applying GL theory rather difficult in engineering problems because thermal relaxation times of materials have to be somewhat accurately determined. However, when measured results are compared to the values in Table 2, GL theory implicitly indicates that the thermal relaxation time for aluminum is at least of the order of 0.1 picoseconds (10^{-13} sec). This marks the major attribute of the GL model which the LS model does not exhibit. As is seen from Table 1, the LS model always resolves two waves, one mechanical and one thermal waves, but gives no indications as to when fundamental physics is violated. It is noteworthy that the GL characteristic equation ($t_0 = 0$) is identical to the LS's ($t_1 = t_2 = 0$) if $t_1 = t_2 = t_0$, which means that both theories give the same descriptions of thermoelastic wave propagation only when the relaxation times for the thermal propagation and the thermal-mechanical interaction are of the same order of magnitude.

To numerically investigate the effects of coupling and relaxations on the spectral behavior of thermoelastic waves in the space-time domain, Eq. (10) is mathematically recast using $c = \omega/\gamma$, so that the wave number γ is represented as a function of radial frequency, ω, as follows:

$$K_v c_L^2 \gamma^4 - \left\{ i\left(c_L^2 + \frac{\beta^2 T_0}{\rho^2 c_v} \right)\omega + \left[(t_0 + t_2)c_L^2 + K_v + (t_0 + t_1)\frac{\beta^2 T_0}{\rho^2 c_v} \right]\omega \right\}\gamma^2 + [i + (t_0 + t_2)\omega]\omega^3 = 0. \quad (13)$$

The solutions to Eq. (13) are the spectrum relation for four different modes. Since Eq. (13) is a quadratic function of γ^2, there is always one pair of roots which is the negative images of the other pair. In the following figures, only the positive modes are shown for the same aluminum material as before.

Figure 1 shows the real and imaginary components of the two positive modes of the LS model for the cases when t_0 equals

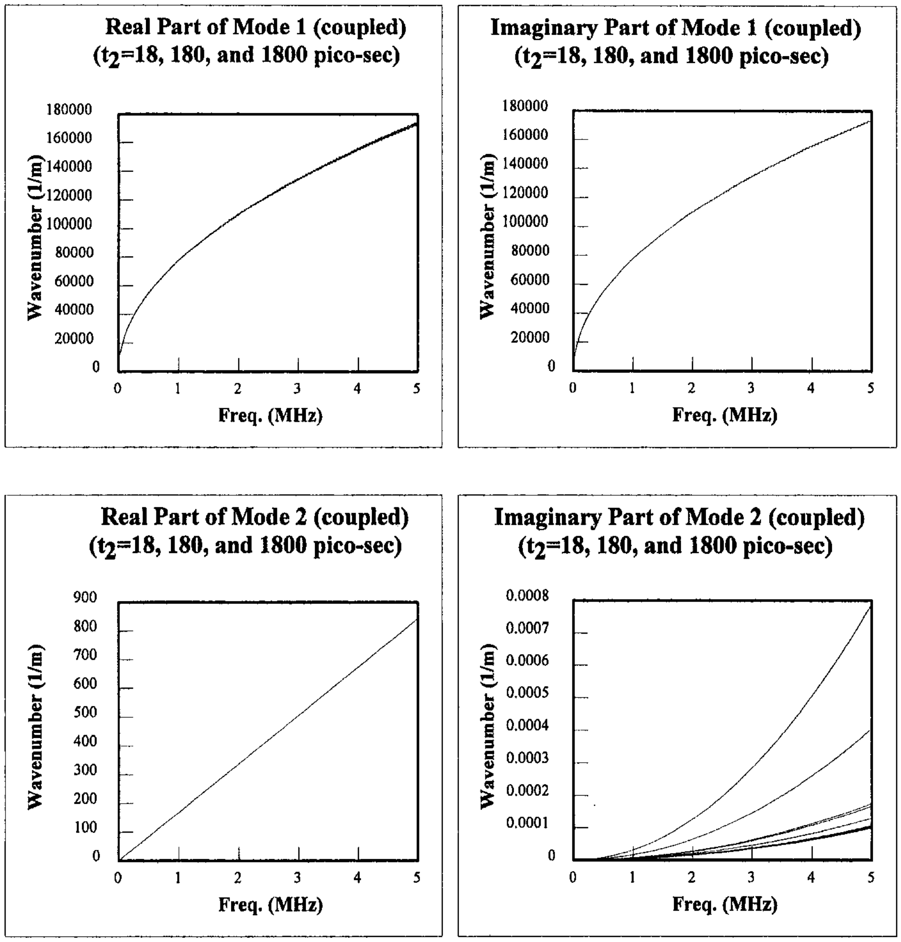

Fig. 6 Dispersion curves for the coupled case according to the GL model for different relaxation times and relaxation time ratios (t_2 equals 18, 180, and 1800 picoseconds)

$1.8 \cdot 10^{-14}$ sec, $1.8 \cdot 10^{-13}$ sec, and $1.8 \cdot 10^{-12}$ sec, as in Table 1. The mode 1 behavior exhibits a linear relation between frequency and the real part of the wave number, and a relatively negligible imaginary component. Since the real part gives rise to propagating wave trains and the imaginary part indicates attenuations in space, mode 1 represents that portion of the thermoelastic response suffers no attenuation and whose waveform remains unchanged in time. The mode 2 behavior shows nonlinear relations for both real and imaginary parts with significant magnitudes. Consequently, the ever-attenuating mode 2 is the portion of the response that propagates with much slower speed (than mode 1) and a changing waveform. It can be thus summarized that a propagating nondispersive thermoelastic response (mode 1) is always accompanied by a simultaneous effect (mode 2) which is highly localized in space. Also, relaxation times are seen to impose no perceivable effects on the dispersion curves in Fig. 1.

However, further increasing the order of t_0 does introduce significant changes in the behavior of modes 1 and 2. In Fig. 2, for the cases of $t_0 = 1.8 \cdot 10^{-11}$ sec, $1.8 \cdot 10^{-10}$ sec, and $1.8 \cdot 10^{-9}$ sec, the mode 1 behaves exactly as the mode 2 in Fig. 1, and the mode 2 as the mode 1 in Fig. 1. Except for the interchange of the modes, there is no noticeable difference between Figs. 1 and 2. Therefore, the same observations can be made with Fig. 2. Interestingly enough, although the thermomechanical coupling term β was shown to have a non-negligible influence on the phase velocity, it imposes no effects on the spectral relations. By setting β be zero (and therefore decoupling the field Eqs. (4)), the dispersion curves for all cases of t_0 considered in Figs. 1 and 2 are plotted in Figs. 3 and 4. Again, except for a much smaller imaginary part for the nondispersive propagating component, no noticeable difference is observed. It can thus be concluded that, regardless of the particular initial/boundary value problem, the spectral relations given by the LS model resolves two waves whose spectral behavior is insensitive to the effects of both relaxation times and coupling.

Figure 5 depicts the data for the GL model from Table 2. It shows the mode behavior of the GL model for the coupled cases when t_2 equals $1.8 \cdot 10^{-14}$ sec, $1.8 \cdot 10^{-13}$ sec, and $1.8 \cdot 10^{-12}$ sec with the ratio of the thermomechanical to thermal relaxation times, t_1/t_2, equal to 2, 5, and 10. The mode behavior with the same t_1/t_2 ratios while t_2 equals $1.8 \cdot 10^{-11}$ sec, $1.8 \cdot 10^{-10}$ sec, and $1.8 \cdot 10^{-9}$ sec is given in Fig. 6. The immediate observation is that all spectral relations identically resemble that of corresponding graphs in Figs. 1 and 2. Also, they exhibit no dependency on the relaxation time ratio t_1/t_2. The imaginary parts of mode 1 in Fig. 5 and of mode 2 in Fig. 6 are the only two that reveal some degree of sensitivity to the influence of relaxation ratios. Their magnitudes show a tendency to increase with increasing frequency; but they are so small compared to the corresponding real parts that they play a negligible role in attenuating the propagating nondispersive components. However, as the relaxation ratio becomes larger, the magnitude of the imaginary components also become non-negligibly large and therefore contribute to the attenuation of the wave. Since t_1 has been shown to be of the same order, or less, than t_2, an attenuating nondispersive wave can never physically exist. The spectral relations for the de-

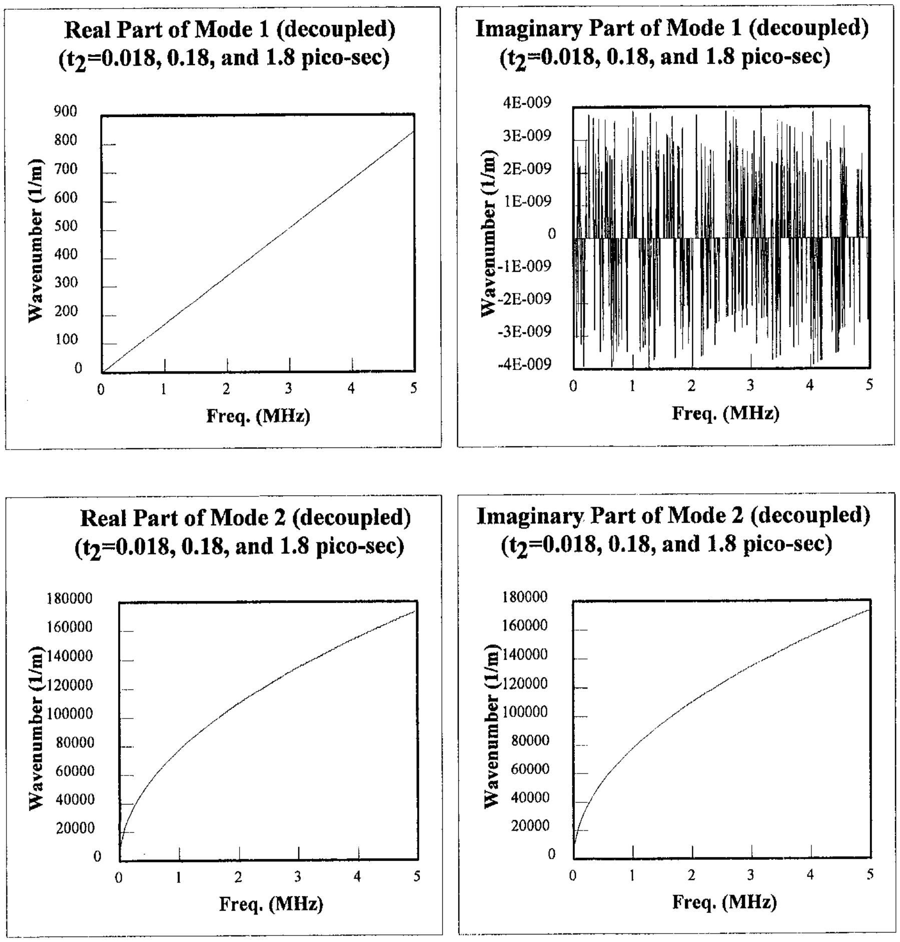

Fig. 7 Dispersion curves for the decoupled case according to the GL model for different relaxation times and relaxation time ratios (t_2 equals 0.018, 0.18, and 1.8 picoseconds)

coupled cases ($\beta = 0$) are given in Figs. 7 and 8. They show no discernable differences from the coupled cases in Figs. 5 and 6. By comparing Fig. 5 to Fig. 1, Fig. 6 to Fig. 2, and so forth, it is seen that the linearity/nonlinearity and the magnitudes of the dispersion curves for the GL and LS models are the same. Thus, the GL model resolves two waves that are spectrally and characteristically identical to that of LS.

Discussion and Conclusions

It is shown that, although the relaxation times t_1, t_2, and t_0 were derived from distinctively different physical assumptions and physical laws, the spectral behaviors described by LS and GL theories for thermoelastic responses are remarkably identical. Relaxation times and thermomechanical coupling terms are shown to have no influence on spectral relations. The capability of resolving two waves by both the LS and GL models is also demonstrated to be independent of the effects of relaxation time and coupling terms. However, it is also shown that coupling terms do have a non-negligible effect on the phase velocities of thermoelastic waves. It does not matter if generalized models or classical formulations should be used to analyze particular decoupled thermoelastic problems, because all of them give the same descriptions on fundamental wave characteristics such as phase velocities and spectral relations. It is also demonstrated that transverse waves are not functions of relaxation times nor thermomechanical coupling terms. Finally, the GL theory is shown to exhibit strong sensitivity to the choice of thermal relaxation time and it implicitly indicates the order of magnitude of the thermomechanical relaxation time constant.

The fact that the LS theory (1) does not indicate the order of magnitude of the thermal relaxation constant, so that fundamental physics is not violated, (2) introduces the rate of change of strain rate, a term physically difficult to comprehend, and (3) violates the Fourier conduction law at the fundamental level, raises questions concerning the feasibility as well as applicability of the theory in modeling thermoelastic problems. This concern was also addressed from the viewpoint of basic thermodynamics by Wegner and Haddow (1993). They show that the LS theory violates the entropy inequality when the thermal relaxation time constant is greater than a critical value. In other words, the LS theory may give results which are thermodynamically inadmissible. On the other hand, it has been demonstrated that the GL theory indicates, if the fundamental physics is to hold, the order of magnitude of the thermal relaxation time can be explicitly determined. Since it does not violate the Fourier conduction law, the GL theory has been shown, again, by Wegner and Haddow to follow the entropy inequality. In addition to all the major features which contribute to the feasibility of the GL theory, the applicability of it should include problems involving very short time intervals and very high heat influxes (Hetnarski and Ignaczak, 1994). This can be realized by re-examining again the physical meanings of t_1 and t_2. Because the extent of rate of change of the thermal gradient is resolved through t_1 and the effect of thermal loadings on the problem domain is governed by t_2, the GL theory

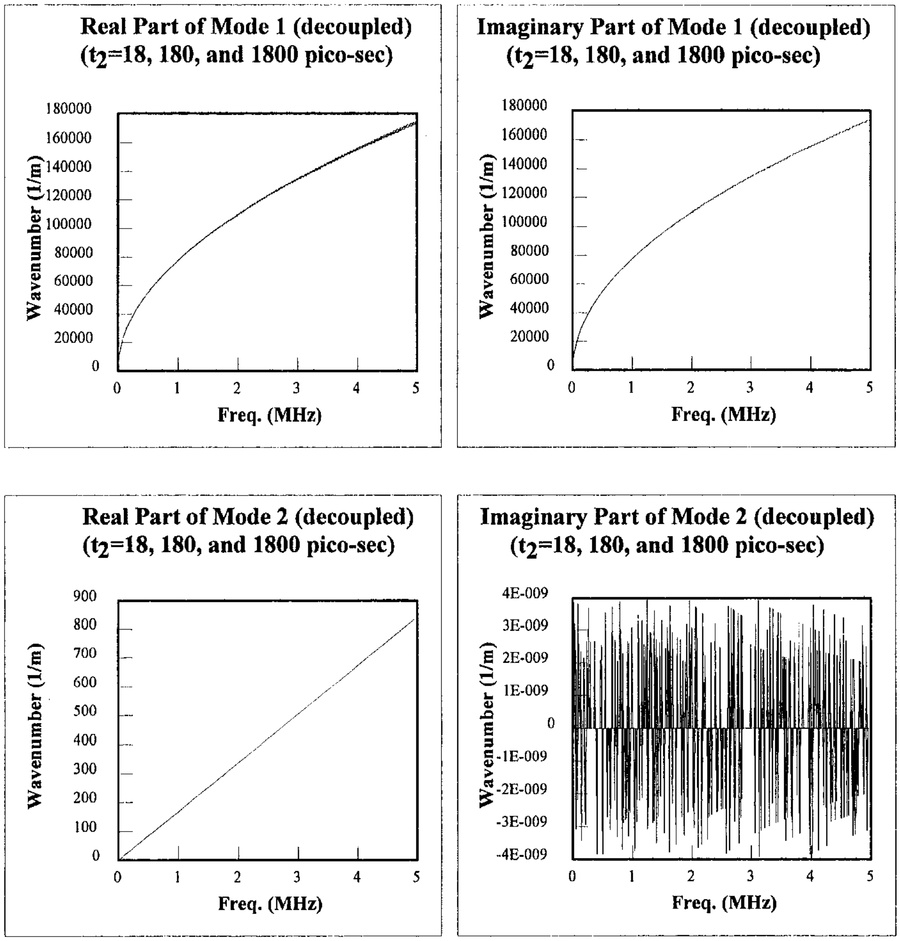

Fig. 8 Dispersion curves for the decoupled case according to the GL model for different relaxation times and relaxation time ratios (t_2 equals 18, 180, and 1800 picoseconds)

should provide significant insight into engineering applications such as laser-induced ultrasound modeling and plasma welding.

References

Achenbach, J. D., 1973, *Wave Propagation in Elastic Solids*, American Elsevier, New York.

Chandrasekharaiah, D. S., 1986, "Thermoelasticity With Second Sound: A Review," ASME *Appl. Mech. Review*, Vol. 39, pp. 355–376.

Chen, T.-C., and Weng, C.-I, 1988, "Generalized Coupled Transient Thermoelastic Plane Problems by Laplace Transform/Finite Element Method," ASME Journal of Applied Mechanics, Vol. 55, pp. 377–382.

Doyle, J. F., 1988, "Spectral Analysis of Coupled Thermoelastic Waves," *Journal Therm. Stresses*, Vol. 11, pp. 175–185.

Green, A. E., and Lindsay, K. E., 1972, "Thermoelasticity," *Journal Elasticity*, Vol. 2, pp. 1–7.

Hetnarski, R. B., and Ignaczak, J., 1993, "Generalized Thermoelasticity: Closed Form Solutions," *Journal Therm. Stresses*, Vol. 16, pp. 473–498.

Hetnarski, R. B., and Ignaczak, J., 1994, "Generalized Thermoelasticity: Response of Semi-Space to a Short Laser Pulse," *Journal Therm. Stresses*, Vol. 17, pp. 377–396.

Ignaczak, J., 1980, "Linear Dynamic Thermoelasticity—A Survey," *Shock Vib. Dig.*, Vol. 13, pp. 3–8.

Jakubowska, M., 1984, "Kirhchoff's Type Formula in Thermoelasticity with Finite Wave Speeds," *Journal Therm. Stresses*, Vol. 7, pp. 259–288.

Lord, H. W., and Schulman, Y., 1967, "A Generalized Dynamic Theory of Thermoelasticity," *Journal Mech. Phys. Solids*, Vol. 15, pp. 299–309.

Nowinski, J. L., 1978, *Theory of Thermoelasticity with Applications*, Sijthoff & Noordhoff International Publishers, Alpen aan den Rijn, The Netherlands.

Sanderson, T., Ume, C., and Jarzynski, J., 1995, "Hyperbolic Heat Equations in Laser Generated Ultrasound Models," *Ultrasonics*, Vol. 33, No. 6, pp. 415–421.

Spicer, J. B., 1991, "Laser Ultrasonics in Finite Structures: Comprehensive Modeling with Supporting Experiment," Ph.D. dissertation, Johns Hopkins University, Baltimore, MD.

Tao, D., and Provost, J. H., 1984, "Relaxation Effects on Generalized Thermoelasticity Wave," *Journal Therm. Stresses*, Vol. 7, pp. 79–89.

Wegner, J. L., and Haddow, J. B., 1993, "Linear Thermoelasticity, Second Sound and The Entropy Inequality," *Wave Motions*, Vol. 18, pp. 67–77.

Wensen Liu
Graduate Student,
Department of Applied Mechanics
and Engineering Sciences,
University of California, San Diego,
La Jolla, CA 92093
and
College of Engineering,
San Diego State University,
San Diego, CA 92182

X. Markenscoff
Professor,
Department of Applied Mechanics
and Engineering Sciences,
University of California, San Diego,
La Jolla, CA 92093
Fellow ASME

M. Paukshto
Professor,
Marine Technology University,
Saint Petersburg, Russia

The Cosserat Spectrum Theory in Thermoelasticity and Application to the Problem of Heat Flow Past a Rigid Spherical Inclusion

We apply the Cosserat Spectrum theory to boundary value problems in thermoelasticity and show the advantages of this method. The thermoelastic displacement field caused by a general heat flow around a spherical rigid inclusion is calculated and the results show that the discrete Cosserat eigenfunctions converge fast and thus provide a practical method for solving three-dimensional problems in thermoelasticity. In the case of uniform heat flow, the solution is obtained analytically in closed form and a variational principle within the frame of the Cosserat Spectrum theory shows that the solution maximizes the elastic energy.

Introduction

The Cosserat Spectrum theory was introduced by Cosserat and Cosserat (1898) and subsequently received rigorous mathematical attention by Mikhlin (1973). The subject of the Cosserat Spectrum theory is not widely known in the American applied mechanics community. Horgan and Knowles (1971) used similar equations as for the Cosserat eigenvalues in order to obtain the Korn constant for elastic bodies. Markenscoff and Paukshto (1998) have applied the Cosserat Spectrum theory to elasticity and thermoelasticity. They also established a new variational principle regarding the stationarity of the elastic energy in thermoelastic problems over all temperature distributions with constant thermal energy. Liu and Markenscoff (1997) applied the Papkovich-Neuber potential method to obtain the discrete Cosserat spectrum for the boundary value problems of displacement and traction for bodies of spherical geometry.

In this paper, we demonstrate the applicability of the Cosserat Spectrum theory to solve thermoelastic problems. We calculate the displacement field caused by a general heat flow around a spherical rigid inclusion. The results show that the discrete Cosserat eigenfunctions converge fast and provide a practical method for solving three-dimensional problems in thermoelasticity. We also solve the problem of uniform heat flow past a thermally insulated spherical rigid inclusion. Moreover, by applying the variational principle in the context of the Cosserat Spectrum theory (Markenscoff and Paukshto, 1998), we show that the elastic energy is maximized for a uniform heat flow past a thermally insulated spherical rigid inclusion. Of course, these problems might be solved by extending the methods of Sharma (1957) or McDowell and Sternberg (1957) (see also Nowacki, 1986). However, here we wish to demonstrate the applicability of the Cosserat Spectrum theory and its physical meaning. While for general geometry the Cosserat eigenvalues and eigenvectors are not known analytically, they can be obtained numerically, and due to the fast convergence only the first few terms are needed.

The Cosserat Spectrum theory could also be applied to the problems of a thermal inclusion (Erkman and Gurgoze, 1991; Dassios and Kostopoulos, 1994). The thermoelastic equations for a mixture are formally the same as the Navier equations in thermoelasticity (see Eq. (2.16) of Erkman and Gurgoze, 1991). Dassios and Kostopoulos studied the scattering of elastic waves by a spherical thermal inclusion. The leading low-frequency approximations are reduced to a sequence of static Navier problems for the exterior of the scatterer and to a sequence of static thermal stress problems for the interior (see Eq. (43) and Eq. (44) of Dassios and Kostopoulos, 1994). These equations can be solved readily by the Cosserat Spectrum representation theorems in the presence of thermal loading and body forces.

Application of the Cosserat Spectrum Theory to Thermoelasticity

The Cosserat Spectrum theory states that in a domain Ω the Navier equations of elasticity

$$\Delta u + \omega \nabla\nabla \cdot u = 0 \quad \text{in } \Omega \tag{1}$$

subjected to the displacement on the boundary $\partial\Omega$

$$u = 0 \quad \text{on } \partial\Omega \tag{2}$$

or traction

$$t = \sigma \cdot n = \mu[2\epsilon + (\omega - 1)\,\text{div}\, uI] \cdot n = 0 \quad \text{on } \partial\Omega \tag{3}$$

admit nontrivial solution when ω takes specific values $\tilde{\omega}_n$ in a set of points called the Cosserat eigenvalues. The nonzero solution $\tilde{u}_n$ is accordingly called the Cosserat eigenvector. In Eqs. (1)–(3), $\omega = (\lambda + \mu)/\mu$ is the spectrum parameter, λ and μ the Lame's constants, u the displacement vector, ϵ the strain tensor, σ the stress tensor, I the unit tensor, n the outward unit vector normal to $\partial\Omega$, and t the boundary traction.

Contributed by the Applied Mechanics Division of THE AMERICAN SOCIETY OF MECHANICAL ENGINEERS for publication in the ASME JOURNAL OF APPLIED MECHANICS.

Discussion on the paper should be addressed to the Technical Editor, Professor Lewis T. Wheeler, Department of Mechanical Engineering, University of Houston, Houston, TX 77204-4792, and will be accepted until four months after final publication of the paper itself in the ASME JOURNAL OF APPLIED MECHANICS.

Manuscript received by the ASME Applied Mechanics Division, Sept. 23, 1998; final revision, Jan. 12, 1998. Associate Technical Editor: J. R. Barber.

The Cosserat spectrum obviously lies outside the range of validity of the uniqueness theorem (Knops and Payne, 1971) in elasticity. The Cosserat eigenvectors are orthogonal and complete in the Sobolev space $H_1(\Omega)$ in three dimensions, namely for

$$\int (\nabla\cdot \tilde{u})^2 dV < \infty. \tag{4}$$

Therefore, the solution of the inhomogeneous equations, either in the differential equations as body force or in the boundary conditions, can be represented by superposition of the Cosserat eigenvectors (Mikhlin, 1973; Mikhlin et al., 1995). In the present paper, we consider a particular type of body force due to thermal effects, as follows:

$$F = -\mu(3\omega - 1)\alpha\nabla T \tag{5}$$

where α is the coefficient of thermal expansion, and T the temperature.

The first boundary value problem (boundary value problem of displacement) in thermoelasticity is described by

$$\Delta u + \omega\nabla\nabla\cdot u = (3\omega - 1)\alpha\nabla T \quad \text{in } \Omega \tag{6a}$$

$$u = 0 \quad \text{on } \partial\Omega \tag{6b}$$

Based on the representation theorem (Mikhlin, 1973), we show that the displacement field u caused by a general temperature field T (nonharmonic in presence of heat sources) admits the form

$$u = (3\omega - 1)\alpha \sum_n \left[\frac{\tilde{\omega}_n}{\tilde{\omega}_n - \omega} (T, \nabla\cdot\tilde{u}_n)\tilde{u}_n + \frac{1}{1+\omega}(T, \nabla\cdot\tilde{u}_n^{(-1)})\tilde{u}_n^{(-1)} \right] \tag{7a}$$

where $\tilde{\omega}_n$ and $\tilde{u}_n$ are the discrete Cosserat eigenvalues and eigenvectors for the first boundary problem, respectively; $\tilde{u}_n^{(-1)}$ are the Cosserat eigenvectors (forming an orthogonal subspace) corresponding to the eigenvalue $\tilde{\omega} = -1$ of infinite multiplicity; and we have defined

$$(T, \nabla\cdot\tilde{u}) \equiv \int T\nabla\cdot\tilde{u}dV. \tag{7b}$$

For a harmonic temperature field T, Eq. (7a) reduces to

$$u = (3\omega - 1)\alpha \sum_n \frac{\tilde{\omega}_n}{\tilde{\omega}_n - \omega}(T, \nabla\cdot\tilde{u}_n)\tilde{u}_n. \tag{8}$$

The second boundary value problem (boundary value problem of traction) in thermoelasticity is described by

$$\Delta u + \omega\nabla\nabla\cdot u = (3\omega - 1)\alpha\nabla T \quad \text{in } \Omega \tag{9a}$$

$$t = 0 \quad \text{on } \partial\Omega. \tag{9b}$$

The representation theorem for the displacement caused by any temperature field T (both harmonic and nonharmonic) takes the form

$$u = (3\omega - 1)\alpha \sum_n \left[\frac{1 - \tilde{\omega}_n}{\omega - \tilde{\omega}_n}(T, \operatorname{div}\tilde{u}_n)\tilde{u}_n + \frac{2}{\omega+1}(T, \operatorname{div}\tilde{u}_n^{(-1)})\tilde{u}_n^{(-1)} \right] \tag{10}$$

where $\tilde{\omega}_n$ and $\tilde{u}_n$ are the discrete Cosserat eigenvalues and eigenvectors for the second boundary problem, respectively, and $\tilde{u}_n^{(-1)}$ are the Cosserat eigenvectors (forming an orthogonal subspace) corresponding to the eigenvalue of infinite multiplicity $\tilde{\omega} = -1$.

Markenscoff and Paukshto (1998) developed a new variational principle in thermoelasticity within the framework of the Cosserat Spectrum theory. For a specific value of the total thermal energy $\int T^2 dV$, the elastic energy is minimized/maximized when $T = ((\omega - \tilde{\omega})/(3\omega - 1)\alpha) \operatorname{div}\tilde{u}$, where $\tilde{\omega}$ is the minimum/maximum eigenvalue of the Cosserat spectrum. This variational principle provides some physical understanding of the thermoelastic solution in terms of the stationarity of the elastic energy.

Heat Flow Past a Spherical Rigid Inclusion

We will provide two examples of heat flow past a spherical rigid inclusion to illustrate this solution technique for thermoelasticity and to examine the variational principle in terms of the Cosserat Spectrum theory.

For a spherical rigid inclusion in an infinite space, the discrete Cosserat eigenvalue $\tilde{\omega}_n$, the discrete eigenvector $\tilde{u}_n$, and their divergences $\nabla\cdot\tilde{u}_n$, for an axisymmetric problem are as follows (Liu and Markenscoff, 1997):

$$\tilde{\omega}_n = -\frac{2n+1}{n+1} \tag{11}$$

$$\tilde{u}_n = C_n(r^2 - r_0^2)\operatorname{grad} F_{-(n+1)} \tag{12}$$

$$\nabla\cdot\tilde{u}_n = -2(n+1)C_nF_{-(n+1)} \tag{13}$$

where

$$(C_n)^2 = \frac{2n-1}{16(n+1)\pi r_0^3} \tag{14}$$

$$F_{-(n+1)} = \left(\frac{r_0}{r}\right)^{n+1} P_n(\cos\theta) \tag{15}$$

and $P_n(\cos\theta)$ is the Legendre polynomial of degree n, and $n = 1, 2, 3 \ldots$.

General Heat Flow

In order to prove the fast convergence of the discrete Cosserat eigenfunctions and the advantage of the applicability of Eq. (8), we choose, as an example, a general enough temperature field, satisfying

$$\Delta T = 0 \quad r \geq r_0 \tag{16a}$$

$$T = \frac{\tau r_0 \sin\theta}{\theta} \quad r = r_0 \tag{16b}$$

where τ is a constant, r_0 the radius of the spherical rigid inclusion, and θ is the angle measured from the z-axis, as shown in Fig. 1. This temperature is axisymmetric in the azimuthal angle φ, which is not shown in the figure. The heat flow produces a sinc function type of temperature distribution on the boundary $r = r_0$.

This is an axisymmetric problem. The harmonic temperature field T is expanded in the form of a series of spherical harmonic functions

$$T(r, \theta) = \tau r_0 \sum_{n=0}^{\infty} T_n F_{-(n+1)} \tag{17}$$

where $F_{-(n+1)}$ is defined by Eq. (15) and $n = 0, 1, 2 \ldots, T_n$ is coefficients to be determined. Substituting Eq. (17) into the boundary condition Eq. (16b) yields

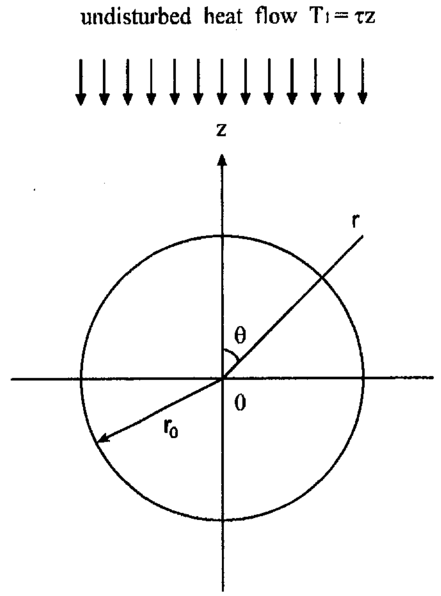

Fig. 1 Spherical coordinate system for a spherical rigid inclusion

$$\frac{\sin\theta}{\theta} = \sum_{n=0}^{\infty} T_n P_n(\cos\theta). \tag{18}$$

The orthogonality property of the Legendre polynomials allows T_n to be determined by

$$T_n = \frac{2n+1}{2}\int_0^{\pi}\frac{\sin\theta}{\theta}P_n(\cos\theta)\sin\theta\, d\theta. \tag{19}$$

We now study the displacement u caused by the temperature field Eq. (17). The current boundary value problem is posed as follows:

$$\Delta u + \omega\nabla\nabla\cdot u = (3\omega-1)\alpha\nabla T \quad r \geq r_0 \tag{20a}$$

$$u = 0 \quad r = r_0. \tag{20b}$$

The displacement $u = 0$ on the surface of the rigid inclusion $r = r_0$, while the traction vanishes at infinity.

We will study the current boundary value problem as follows. We consider first a boundary value problem of displacement for a spherical rigid inclusion in an infinite space at both $r = r_0$ and $r = \infty$, namely

$$\Delta u + \omega\nabla\nabla\cdot u = (3\omega-1)\alpha\nabla T \quad r \geq r_0 \tag{21a}$$

$$u = 0 \quad r = r_0, \infty. \tag{21b}$$

Substituting the temperature field Eq. (17) into the representation theorem for the first boundary value problem Eq. (8), we have

$$u = (3\omega-1)\alpha\tau r_0 \sum_{n=1}^{\infty}\sum_{m=0}^{\infty}\frac{\tilde{\omega}_n T_m}{\tilde{\omega}_n-\omega}(F_{-(m+1)}, \nabla\cdot\tilde{u}_n)\tilde{u}_n \tag{22a}$$

where

$$(F_{-(m+1)}, \nabla\cdot\tilde{u}_n) \equiv \int F_{-(m+1)}\nabla\cdot\tilde{u}_n dV. \tag{22b}$$

Substituting the Cosserat eigenvalues and eigenvectors given in Eqs. (11)–(15) into Eq. (22), we obtain the solution to Eq. (21) as follows:

$$u = \frac{(3\omega-1)\alpha\tau r_0^2}{2}\sum_{n=1}^{\infty}\frac{T_n}{(n+1)\omega+(2n+1)} \times \left[\left(\frac{r_0}{r}\right)^n - \left(\frac{r_0}{r}\right)^{n+2}\right]\left[(n+1)P_n e_r - \frac{dP_n}{d\theta}e_\theta\right]. \tag{23}$$

Equation (23) renders zero traction at infinity; it is also the displacement field caused by the temperature components $n \geq 1$ for the boundary value problem Eq. (20). By solving Eq. (20) directly, we calculate the displacement due to the component $n = 0$ of the temperature field, $\tau r_0 T_0 F_{-1} = \tau T_0(r_0^2/r)$, as follows:

$$u_0 = \frac{(3\omega-1)\alpha\tau r_0^2 T_0}{2(\omega+1)}\left(1-\frac{r_0^2}{r^2}\right)e_r. \tag{24}$$

Equation (24) is not a Cosserat eigenfunction for the first boundary value problem. The displacement remains a constant, while the traction vanishes at $r = \infty$. We can write the solution to Eq. (20) in a unified way, which includes the displacement given by Eq. (24), as follows:

$$u_r = \frac{(3\omega-1)\alpha\tau r_0^2}{2}\sum_{n=0}^{\infty}\frac{(n+1)T_n}{(n+1)\omega+(2n+1)} \times \left[\left(\frac{r_0}{r}\right)^n - \left(\frac{r_0}{r}\right)^{n+2}\right]P_n \tag{25a}$$

$$u_\theta = -\frac{(3\omega-1)\alpha\tau r_0^2}{2}\sum_{n=0}^{\infty}\frac{T_n}{(n+1)\omega+(2n+1)} \times \left[\left(\frac{r_0}{r}\right)^n - \left(\frac{r_0}{r}\right)^{n+2}\right]\frac{dP_n}{d\theta}. \tag{25b}$$

Using the first $N+1$ terms to approximate the dimensionless displacement fields $\bar{u}_r$ and $\bar{u}_\theta$, we have

$$\bar{u}_r = \frac{2u_r}{(3\omega-1)\alpha\tau r_0^2} \approx \sum_{n=0}^{N}\frac{(n+1)T_n}{(n+1)\omega+(2n+1)} \times \left[\left(\frac{r_0}{r}\right)^n - \left(\frac{r_0}{r}\right)^{n+2}\right]P_n \tag{26a}$$

$$\bar{u}_\theta = \frac{2u_\theta}{(3\omega-1)\alpha\tau r_0^2} \approx -\sum_{n=0}^{N}\frac{T_n}{(n+1)\omega+(2n+1)} \times \left[\left(\frac{r_0}{r}\right)^n - \left(\frac{r_0}{r}\right)^{n+2}\right]\frac{dP_n}{d\theta}. \tag{26b}$$

In order to study the convergence property of the discrete Cosserat eigenfunctions, we compute the dimensionless displacement fields $\bar{u}_r$ and $\bar{u}_\theta$. The Poisson's ratio $\nu = 0.26$ is used in the calculations.

Based on the computational results shown in Tables 1–2 in the Appendix for $r/r_0 = 1.1$, 2.0 and $\theta = 0$ deg, 45 deg, 90 deg, 135 deg, 180 deg, we see that, generally speaking, the series of the discrete Cosserat eigenfunctions converges very fast. Though the displacement fields are represented by a summation of infinite series of the discrete Cosserat eigenfunctions, we only need to calculate the first few terms. As an example, we choose a point where $r/r_0 = 1.1$ and $\theta = 90$ deg in Table 1. It only takes the first three terms (including $n = 0$ term) for $\bar{u}_r$ to converge within absolute error 10^{-3} and 11 terms to converge within 10^{-5}; it takes the first 2 terms for $\bar{u}_\theta$ to converge within 10^{-3} and 10 terms to converge within 10^{-5}.

Moreover, the convergence rate depends on field points. For the first boundary value problem of a spherical rigid inclusion in an infinite space, the farther a field point is away from the surface of the rigid inclusion, the faster the displacement field converges. To compare with the above-mentioned field point, we choose a point where $r/r_0 = 2.0$ and $\theta = 90$ deg in Table 2. It only takes the first three terms (including $n = 0$ term) for $\bar{u}_r$ to converge within absolute error 10^{-3} and five terms to converge within 10^{-5}; it takes the first two terms for $\bar{u}_\theta$ to converge within 10^{-3} and eight terms to converge within 10^{-5}.

Uniform Heat Flow

The problem of a uniform heat flow past a thermally insulated spherical cavity was solved by Florence and Goodier (1959). In the present paper, we solve the problem of a uniform heat flow past a spherical rigid inclusion and view the solution in the context of the variational principle in terms of the Cosserat Spectrum theory.

The harmonic temperature field due to a constant heat flux τ at infinity, disturbed by a spherical rigid inclusion as shown in Fig. 1, is given by

$$T = \tau\left(r + \frac{r_0^3}{2r^2}\right)\cos\theta. \tag{27}$$

This temperature is axisymmetric. It is decomposed into two parts $T_1 = \tau r \cos\theta$ and $T_2 = (\tau r_0^3/2r^2)\cos\theta$. The latter is caused by the disturbance of the spherical rigid inclusion.

The temperature field T_1 is a linear function of position $z = r\cos\theta$, the displacement field corresponding to T_1 is given by

$$u_r = \frac{1}{2}\alpha\tau r_0^2\left[\left(\frac{r}{r_0}\right)^2 + \frac{\omega+1}{2\omega+3}\left(\frac{r_0}{r}\right) - \frac{3\omega+4}{2\omega+3}\left(\frac{r_0}{r}\right)^3\right]\cos\theta \tag{28a}$$

$$u_\theta = \frac{1}{2}\alpha\tau r_0^2\left[\left(\frac{r}{r_0}\right)^2 - \frac{\omega+2}{2(2\omega+3)}\left(\frac{r_0}{r}\right) - \frac{3\omega+4}{2(2\omega+3)}\left(\frac{r_0}{r}\right)^3\right]\sin\theta \tag{28b}$$

with the corresponding stress

$$\frac{\sigma_{rr}}{\mu} = \frac{1}{2}\alpha\tau r_0\left[-\frac{\omega+3}{2\omega+3}\left(\frac{r_0}{r}\right)^2 + \frac{6(3\omega+4)}{2\omega+3}\left(\frac{r_0}{r}\right)^4\right]\cos\theta \tag{29a}$$

$$\frac{\sigma_{\theta\theta}}{\mu} = \frac{\sigma_{\varphi\varphi}}{\mu} = \frac{1}{2}\alpha\tau r_0\left[\frac{1}{2\omega+3}\left(\frac{r_0}{r}\right)^2 - \frac{3(3\omega+4)}{2\omega+3}\left(\frac{r_0}{r}\right)^4\right]\cos\theta \tag{29b}$$

$$\frac{\sigma_{r\theta}}{\mu} = \frac{1}{2}\alpha\tau r_0\left[\frac{1}{2\omega+3}\left(\frac{r_0}{r}\right)^2 + \frac{3(3\omega+4)}{2\omega+3}\left(\frac{r_0}{r}\right)^4\right]\sin\theta \tag{29c}$$

$$\sigma_{r\varphi} = \sigma_{\theta\varphi} = 0. \tag{29d}$$

It should be pointed out that, though the temperature $T_1 = \tau r\cos\theta = \tau z$ is a linear function of position, the free-expansion condition (Timoshenko and Goodier, 1970) cannot be satisfied at the boundary $r = r_0$ of the spherical rigid inclusion, and thus generates a stress field.

The temperature distribution $T_2 = (\tau r_0^3/2r^2)\cos\theta$ produces the displacement field

$$u_r = \frac{(3\omega-1)\alpha\tau r_0^2}{2(2\omega+3)}\left(\frac{r_0}{r} - \frac{r_0^3}{r^3}\right)\cos\theta \tag{30a}$$

$$u_\theta = \frac{(3\omega-1)\alpha\tau r_0^2}{4(2\omega+3)}\left(\frac{r_0}{r} - \frac{r_0^3}{r^3}\right)\sin\theta \tag{30b}$$

with corresponding stress

$$\frac{\sigma_{rr}}{\mu} = \frac{(3\omega-1)\alpha\tau r_0}{2(2\omega+3)}\left(-\frac{7r_0^2}{r^2} + \frac{6r_0^4}{r^4}\right)\cos\theta \tag{31a}$$

$$\frac{\sigma_{\theta\theta}}{\mu} = \frac{\sigma_{\varphi\varphi}}{\mu} = -\frac{(3\omega-1)\alpha\tau r_0}{2(2\omega+3)}\left(\frac{2r_0^2}{r^2} - \frac{3r_0^4}{r^4}\right)\cos\theta \tag{31b}$$

$$\frac{\sigma_{r\theta}}{\mu} = \frac{(3\omega-1)\alpha\tau r_0}{2(2\omega+3)}\left(-\frac{2r_0^2}{r^2} + \frac{3r_0^4}{r^4}\right)\sin\theta \tag{31c}$$

$$\sigma_{r\varphi} = \sigma_{\theta\varphi} = 0. \tag{31d}$$

We verify that the displacement field Eq. (30) is a Cosserat eigenfunction corresponding to the eigenvalue $\tilde{\omega} = -(3/2)$ and satisfies the additional condition Eq. (4). According to the representation theorem Eq. (8), for the first boundary value problem of a spherical rigid inclusion in an infinite space, the discrete Cosserat spectrum is given by Eq. (11) with $\tilde{\omega}_n$ lying in the interval $[-2, -3/2]$. Therefore, $\tilde{\omega} = -(3/2)$ is the maximum eigenvalue, rendering the elastic energy of this problem maximum among all temperature distributions with constant thermal energy.

Discussion

For general heat flow past a spherical rigid inclusion, computational results show that the infinite series of the discrete Cosserat eigenfunctions converges very fast. Though the displacement fields are represented by a summation of the discrete Cosserat eigenfunctions, we only need to calculate the first few terms. The convergence rate depends on field points.

For the uniform heat flow past a thermally insulated rigid inclusion, the temperature field is decomposed of two parts, $T = T_1 + T_2$, where T_1 is the undisturbed uniform temperature field with constant gradient, while T_2 is introduced by the presence of spherical rigid inclusion. The displacement field due to T_2 is a Cosserat eigenvector corresponding to the maximum eigenvalue for the spherical rigid inclusion, thus maximizing the elastic energy according to a variational thermoelastic principle for the Cosserat eigenfunctions. This stationarity of the elastic energy was not previously known.

References

Cosserat, E., and Cosserat, F., 1898, "Sur les Equations de la Theorie de l'Elasticite," *C. R. Acad. Sci. Paris,* Vol. 126, pp. 1089–1091.

Dassios, G., and Kostopoulos, V., 1994, "Scattering of Elastic Waves by a Small Thermoelastic Body," *Int. J. Engng Sci.,* Vol. 32, No. 10, pp. 1593–1603.

Erkman, C., and Gurgoze, I. T., 1991, "Thermostatics of an Infinite Mixture of an Elastic Solid and a Fluid Containing a Spherical Thermal Inclusion," *Int. J. Engng Sci.,* Vol. 29, No. 10, pp. 1269–1276.

Florence, A. L., and Goodier, J. N., 1959, "Thermal Stress at Spherical Cavities and Circular Holes in Uniform Heat Flow," ASME JOURNAL OF APPLIED MECHANICS, Vol. 26, pp. 293–294.

Horgan, C. O., and Knowles, J. K., 1971, "Eigenvalue Problems Associated with Korn's Inequalities," *Archive for Rational Mechanics and Analysis,* Vol. 40, pp. 384–402.

Knops, R. J., and Payne, L. E., 1971, *Uniqueness Theorems in Linear Elasticity,* Springer-Verlag, New York.

Liu, W., and Markenscoff, X., 1997, "The Discrete Cosserat Spectrum for a Spherical Shell," submitted for publication.

McDowell, E. L., and Sternberg, E., 1957, "Axisymmetric Thermal Stress in a Spherical Shell of Arbitrary Thickness," ASME JOURNAL OF APPLIED MECHANICS, Vol. 24, pp. 376–380.

Markenscoff, X., and Paukshto, M. V., 1998, "The Cosserat Spectrum in the Theory of Elasticity and Applications," *Proc. R. Soc. Lond.,* Vol. A454, pp. 631–643.

Mikhlin, S. G., 1973, "The Spectrum of a Family of Operators in the Theory of Elasticity," *Uspekhi Mat. Nauk* (in Russian), Vol. 28, No. 3, pp. 43–82; English translation: *Russian Math. Surveys,* Vol. 28, No. 3, pp. 45–88.

Mikhlin, S. G., Morozov, N. F., and Paukshto, M. V., 1995, *The Integral Equations of the Theory of Elasticity,* Teubner Verlagsgesellschaft, Stuttgart, Germany.

Nowacki, W., 1986, *Thermoelasticity,* Pergamon, Oxford, UK.

Sharma, B., 1957, "Stress Due to a Nucleus of Thermoelastic Strain in an Infinite Solid with Spherical Cavity and in a Solid Elastic Sphere," *Z. Angew. Math. Phys.,* Vol. 8, pp. 142–150.

Timoshenko, S. P., and Goodier, J. N., 1970, *Theory of Elasticity,* McGraw-Hill, New York.

APPENDIX

Computational Results of the Dimensionless Displacement Field due to a General Heat Flow Past a Spherical Rigid Inclusion

Table 1(*a*) The dimensionless displacement field $\bar{u}_r$ for $r/r_0 = 1.1$

N	$\theta = 0^0$	$\theta = 45^0$	$\theta = 90^0$	$\theta = 135^0$	$\theta = 180^0$
0	0.034302	0.034302	0.034302	0.034302	0.034302
1	0.053483	0.043893	0.034302	0.024712	0.015122
2	0.051048	0.044197	0.035520	0.025017	0.012686
3	0.052030	0.043767	0.035520	0.025446	0.011704
4	0.051519	0.043915	0.035329	0.025594	0.011193
5	0.051821	0.043942	0.035329	0.025567	0.010891
6	0.051628	0.043880	0.035389	0.025505	0.010698
7	0.051758	0.043909	0.035389	0.025476	0.010568
8	0.051667	0.043916	0.035364	0.025482	0.010477
9	0.051733	0.043898	0.035364	0.025500	0.010411
10	0.051684	0.043907	0.035376	0.025509	0.010362
15	0.051711	0.043905	0.035373	0.025500	0.010243
20	0.051703	0.043906	0.035372	0.025500	0.010206
25	0.051706	0.043906	0.035372	0.025500	0.010191
30	0.051705	0.043906	0.035372	0.025500	0.010185

Table 1(*b*) The dimensionless displacement field $\bar{u}_\theta$ for $r/r = 1.1$

N	$\theta = 0^0$	$\theta = 45^0$	$\theta = 90^0$	$\theta = 135^0$	$\theta = 180^0$
0	0	0	0	0	0
1	0	0.008305	0.009590	0.008305	0
2	0	0.007251	0.009590	0.009360	0
3	0	0.007331	0.009222	0.009440	0
4	0	0.007469	0.009222	0.009302	0
5	0	0.007372	0.009316	0.009205	0
6	0	0.007386	0.009316	0.009191	0
7	0	0.007413	0.009281	0.009219	0
8	0	0.007389	0.009281	0.009243	0
9	0	0.007393	0.009297	0.009247	0
10	0	0.007402	0.009297	0.009238	0
15	0	0.007396	0.009290	0.009236	0
20	0	0.007396	0.009291	0.009234	0
25	0	0.007396	0.009292	0.009234	0
30	0	0.007396	0.009291	0.009234	0

Table 2(*a*) The dimensionless displacement field $\bar{u}_r$ for $r/r_0 = 2.0$

N	$\theta = 0^0$	$\theta = 45^0$	$\theta = 90^0$	$\theta = 135^0$	$\theta = 180^0$
0	0.148236	0.148236	0.148236	0.148236	0.148236
1	0.193824	0.171030	0.148236	0.125441	0.102647
2	0.190640	0.171428	0.149828	0.125839	0.099463
3	0.191347	0.171119	0.149828	0.126149	0.098757
4	0.191145	0.171177	0.149752	0.126207	0.098555
5	0.191210	0.171183	0.149752	0.126201	0.098489
6	0.191187	0.171176	0.149759	0.126194	0.098466
7	0.191196	0.171178	0.149759	0.126192	0.098458
8	0.191192	0.171178	0.149758	0.126192	0.098454
9	0.191194	0.171177	0.149758	0.126192	0.098453
10	0.191193	0.171178	0.149758	0.126192	0.098453
15	0.191193	0.171178	0.149758	0.126192	0.098452
20	0.191193	0.171178	0.149758	0.126192	0.098452
25	0.191193	0.171178	0.149758	0.126192	0.098452
30	0.191193	0.171178	0.149758	0.126192	0.098452

Table 2(*b*) The dimensionless displacement field $\bar{u}_\theta$ for $r/r_0 = 2.0$

N	$\theta = 0^0$	$\theta = 45^0$	$\theta = 90^0$	$\theta = 135^0$	$\theta = 180^0$
0	0	0	0	0	0
1	0	0.019740	0.022794	0.019740	0
2	0	0.018362	0.022794	0.021119	0
3	0	0.018419	0.022529	0.021176	0
4	0	0.018474	0.022529	0.021122	0
5	0	0.018453	0.022550	0.021101	0
6	0	0.018454	0.022550	0.021099	0
7	0	0.018456	0.022547	0.021101	0
8	0	0.018455	0.022547	0.021102	0
9	0	0.018455	0.022548	0.021102	0
10	0	0.018455	0.022548	0.021102	0
15	0	0.018455	0.022548	0.021102	0
20	0	0.018455	0.022548	0.021102	0
25	0	0.018455	0.022548	0.021102	0
30	0	0.018455	0.022548	0.021102	0

Vibration of Thick Prismatic Structures With Three-Dimensional Flexibilities

K. M. Liew
Mem. ASME.

K. C. Hung

M. K. Lim

Division of Engineering Mechanics,
School of Mechanical and
Production Engineering,
Nanyang Technological University,
Singapore 639798

This paper presents an investigation on free vibration of thick prismatic structures (thick-walled open sections of L, T, C, and I shapes). The derivation of a linear frequency equation based on an exact three-dimensional small-strain linearly elastic principle is presented. This formulation uses one and two-dimensional polynomial series to approximate the spatial displacements of the thick-walled open sections in three dimension. The proposed technique is applicable to vibration of thick-walled open sections of different cross-sectional geometries and end support conditions. In this study, however, we focus primarily on the cantilevered case which has high value in practical applications. The perturbation of frequency responses due to the variations of cross-sectional geometries and wall thicknesses is investigated. First-known frequency parameters and three-dimensional deformed mode shapes of these thick-walled open sections are presented in vivid graphical forms. The new results may serve as a benchmark reference to future research into the refined beam and plate theories and also for checking the accuracy of new numerical techniques.

1 Introduction

The desirable static load-bearing capability of thin or thick-walled open sections has widened their applications in many branches of engineering. These open sections are commonly employed as supporting members and stiffeners in building structures and ship hull designs. Static analyses of these open sections are well established. Literature dealing with this subject abounds, and design charts detailing the important mechanical properties and selection criteria of open sections are covered in most engineering texts and design codes.

However, comprehensive studies on the free vibration of these open sections are relatively scarce. Due to the eccentricity of the thick-walled open sections, the transverse vibration modes of these structures are often complicated by the presence of coupled torsional motion. Garland (1940) investigated the simultaneous flexure and torsion vibration modes of a C-channel beam with a cantilevered end support. The general solutions of prismatic structures were obtained by Golley and Grice (1989) using the finite strip method, and Le Dret (1989) using a computational model via discrete mathematical procedures. Most of these works, however, are restricted to the analysis of thin-walled members. In other words, these models treat the constitutive panels as thin plate elements that obey the Kirchhoff-Love hypothesis. Special numerical treatments are usually necessary at the junctions between panels. At these junctions, the kinematic connectivities are achieved approximately at nodes distributed along the interfaces. A detailed mathematical treatment on the junctions between adjacent panels of these thin-walled open sections has been presented recently by Bernadou et al. (1989).

In some practical cases, it is often required that the constitutive panels of the open sections be of considerable thickness. In such cases, the numerical methods based on the thin-plate approximation are erroneous. It is expedient to develop a numerical model that represents more accurately the thickness effects (notably, the transverse shear deformation and rotary inertia) of the constitutive panels. The three-dimensional vibration analyses of elastic solids have been considered earlier (Fromme and Leissa, 1970; Hutchinson and Zillmer, 1983; Leissa and Zhang, 1983; Leissa and Jacob, 1986; Young and Dickinson, 1994, 1995; Liew and Hung, 1995; Liew et al., 1993, 1995a–c, 1997). This study is a complement to the earlier works by providing a three-dimensional linear elasticity approach to obtain the governing frequency determinant for a thick-walled open section of different combinations of end support conditions.

Starting from the linear small-strain three-dimensional elasticity theory, the integral expressions for strain and kinetic energies of the thick-walled open sections are formulated. These are expressed in terms of sets of one and two-dimensional polynomial functions which approximate the displacement variations of the thick-walled open sections in the longitudinal and lateral directions. The one-dimensional polynomial functions are uniquely constructed to account for the kinematic constraints at both ends. The two-dimensional functions, on the other hand, automatically satisfy the free-surface boundary conditions on the lateral surfaces. The three-dimensional energy functional is obtained directly by summing the resulting displacement-based energy expressions. Finally, the Ritz minimum energy principle is applied to derive the eigenvalue matrix of the thick-walled open sections. The resulting eigenvalue matrix is solved iteratively to furnish the three-dimensional frequency results. This method models the prismatic structures as a single element for the entirely formulation unlike the discrete element methods that require many elements for solution.

Finally, in order to provide new information to the existing literature, a set of first-known vibration results in terms of frequency parameters and mode shapes are presented for cantilevered thick-walled open sections of L, T, C, and I shapes with different lengths and cross-sectional dimensions. The accuracy and reliability of the eigenvalues are ascertained through comparison with the classical Bernoulli-Euler solutions for slender T and I-shaped sections.

2 Mathematical Formulation

2.1 Problem Definition. The geometric configuration of a homogeneous, isotropic, thick-walled open section is depicted

Contributed by the Applied Mechanics Division of THE AMERICAN SOCIETY OF MECHANICAL ENGINEERS for publication in the ASME JOURNAL OF APPLIED MECHANICS.

Discussion on the paper should be addressed to the Technical Editor, Professor Lewis T. Wheeler, Department of Mechanical Engineering, University of Houston, Houston, TX 77204-4792, and will be accepted until four months after final publication of the paper itself in the ASME JOURNAL OF APPLIED MECHANICS.

Manuscript received by the ASME Applied Mechanics Division, May 28, 1996; final revision, July 20, 1997. Associate Technical Editor: N. C. Perkins.

in Fig. 1. The thick-walled open section is defined in a Cartesian coordinate system (x_1, x_2, x_3) with its origin located at the left end as shown in Fig. 1. Except for the edge at $x_3 = 0$ which is built in, all other edges are assumed to be free from stresses. The vibration frequencies and mode shapes of these cantilevered thick-walled open sections are to be determined from a three-dimensional displacement-based energy method. In the three-dimensional setting, the displacement at a generic point can be resolved into three orthogonal components, u_1, u_2 (lateral surface) and u_3 (longitudinal) parallel to x_1, x_2 and x_3-axes, respectively.

2.2 Three-Dimensional Elastic Strain and Kinetic Energy Expressions. In a Cartesian coordinate system, the linear elastic strain energy component, V can be written in an integral form as

$$V = \frac{1}{2}\iint_R \int_0^L [\Delta\{(1-\nu)A_1 + 2\nu A_2 + (1-2\nu)A_3\}]dx_1dx_2dx_3 \quad (1)$$

where

$$A_1 = \epsilon_{11}^2 + \epsilon_{22}^2 + \epsilon_{33}^2 \quad (2a)$$

$$A_2 = \epsilon_{11}\epsilon_{22} + \epsilon_{11}\epsilon_{33} + \epsilon_{22}\epsilon_{33} \quad (2b)$$

$$A_3 = \epsilon_{12}^2 + \epsilon_{13}^2 + \epsilon_{23}^2 \quad (2c)$$

and

$$\Delta = \frac{E}{(1+\nu)(1-2\nu)} \quad (2d)$$

in which E is Young's modulus and ν is Poisson's ratio.

The strain-displacement relations in a rectangular coordinate for small deformation are

$$\epsilon_{ij} = \frac{1}{2}\left[\frac{\partial u_i}{\partial x_j} + \frac{\partial u_j}{\partial x_i}\right]; \quad i, j = 1, 2, 3. \quad (3)$$

The kinetic energy for free vibration is given by

$$T = \frac{\rho}{2}\iint_R \int_0^L \left[\left(\frac{\partial u_1}{\partial t}\right)^2 + \left(\frac{\partial u_2}{\partial t}\right)^2 + \left(\frac{\partial u_3}{\partial t}\right)^2\right] \times dx_1dx_2dx_3 \quad (4)$$

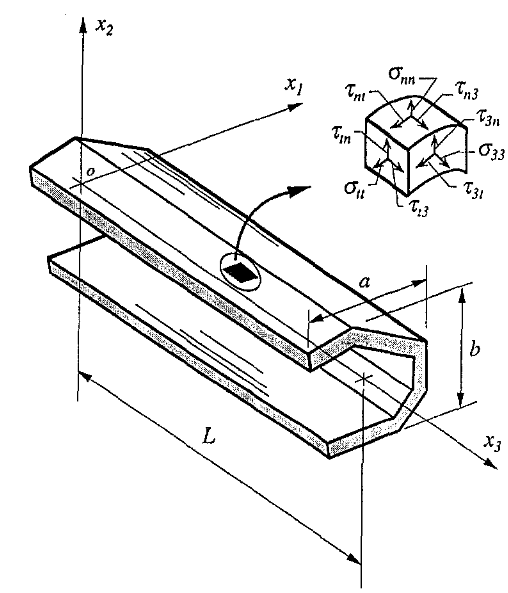

Fig. 1 Geometry and dimensions of a thick-walled open section

where ρ is the mass density per unit volume. The area integrals in Eqs. (1) and (4) are performed over the region, R, of the cross section.

For a linear small-strain simple harmonic motion, the displacement components assume the following forms:

$$\langle u_1(x_1, x_2, x_3, t);\ u_2(x_1, x_2, x_3, t);\ u_3(x_1, x_2, x_3, t)\rangle = \langle U_1(x_1, x_2, x_3);\ U_2(x_1, x_2, x_3);\ U_3(x_1, x_2, x_3)\rangle e^{i\omega t} \quad (5)$$

where ω denotes the frequency of vibration.

Introducing Eqs. (3) and (5) into the three-dimensional elastic strain and kinetic energy expressions and eliminating the periodic components of Eqs. (1) and (4), yields

$$V_{\max} = \frac{\Delta}{2}\iint_R \int_0^L \left[\left\{\nu(\sum_{i=1}^{3} U_{i,i})^2 + (1-2\nu)(\sum_{i=1}^{3} U_{i,i}^2) + \frac{1}{2}(1-2\nu)\{(U_{1,2}+U_{2,1})^2 + (U_{2,3}+U_{3,2})^2 + (U_{1,3}+U_{3,1})^2\}\right\}\right]dx_1dx_2dx_3 \quad (6a)$$

and

$$T_{\max} = \frac{\rho\omega^2}{2}\iint_R \int_0^L (\sum_{i=1}^{3} U_i^2)dx_1dx_2dx_3. \quad (6b)$$

The comma notation is adopted here to denote the partial differentiation.

The displacement amplitude functions, $U_i(x_1, x_2, x_3)$; $i = 1, 2, 3$, are approximated by sets of truncated double polynomial series in one and two dimensions as follows:

$$\langle U_1(x_1, x_2, x_3);\ U_2(x_1, x_2, x_3);\ U_3(x_1, x_2, x_3)\rangle = \langle \sum_{m=1}^{M}\sum_{n=1}^{N} C_{mn}^1\phi_m^1(x_1, x_2)\psi_n^1(x_3); \sum_{m=1}^{M}\sum_{n=1}^{N} C_{mn}^2\phi_m^2(x_1, x_2)\psi_n^2(x_3); \sum_{m=1}^{M}\sum_{n=1}^{N} C_{mn}^3\phi_m^3(x_1, x_2)\psi_n^3(x_3)\rangle \quad (7)$$

in which C_{mn}^1, C_{mn}^2, C_{mn}^3 are the unknown coefficients. The two-dimensional polynomials, ϕ_m^1, ϕ_m^2, ϕ_m^3, dictate the lateral surface variations of each displacement component. The one-dimensional polynomials, ψ_n^1, ψ_n^2, ψ_n^3, on the other hand, approximate the displacement variations in the longitudinal direction.

2.3 The Formation of Eigenvalue Matrix. Let Π be the energy functional given by

$$\Pi = V_{\max} - T_{\max}. \quad (8)$$

The minimization of this functional with respect to the coefficients

$$\left\langle \frac{\partial\Pi}{\partial C_{mn}^1}, \frac{\partial\Pi}{\partial C_{mn}^2}, \frac{\partial\Pi}{\partial C_{mn}^3}\right\rangle = \langle 0, 0, 0\rangle \quad (9)$$

leads to the governing eigenvalue equation of the form

$$\left(\begin{bmatrix} \mathbf{k}^{11} & \mathbf{k}^{12} & \mathbf{k}^{13} \\ & \mathbf{k}^{22} & \mathbf{k}^{23} \\ \text{Sym} & & \mathbf{k}^{33} \end{bmatrix} - \lambda^2 \begin{bmatrix} \mathbf{m}^{11} & 0 & 0 \\ & \mathbf{m}^{22} & 0 \\ \text{Sym} & & \mathbf{m}^{33} \end{bmatrix}\right)\begin{Bmatrix} \mathbf{C}^1 \\ \mathbf{C}^2 \\ \mathbf{C}^3 \end{Bmatrix} = \begin{Bmatrix} \mathbf{0} \\ \mathbf{0} \\ \mathbf{0} \end{Bmatrix}. \quad (10)$$

The explicit form of the respective elements in the stiffness submatrices $\mathbf{k}^{\alpha\beta}$ are given by

$$k_{mjnk}^{11}=\frac{1-\nu}{(1-2\nu)}(E_{mj}^{1010}F_{nk}^{00})_{11}+\frac{1}{2}\left\{\left(\frac{a}{b}\right)^2(E_{mj}^{0101}F_{nk}^{00})_{11}+\left(\frac{a}{L}\right)^2(E_{mj}^{0000}F_{nk}^{11})_{11}\right\} \quad (11a)$$

$$k_{mjnk}^{12}=\left(\frac{a}{b}\right)\left\{\frac{\nu}{(1-2\nu)}(E_{mj}^{1001}F_{nk}^{00})_{12}+\frac{1}{2}(E_{mj}^{0110}F_{nk}^{00})_{12}\right\} \quad (11b)$$

$$k_{mjnk}^{13}=\left(\frac{a}{L}\right)\left\{\frac{\nu}{(1-2\nu)}(E_{mj}^{1000}F_{nk}^{01})_{13}+\frac{1}{2}(E_{mj}^{0010}F_{nk}^{10})_{13}\right\} \quad (11c)$$

$$k_{mjnk}^{22}=\frac{1-\nu}{(1-2\nu)}\left(\frac{a}{b}\right)^2(E_{mj}^{0101}F_{nk}^{00})_{22}+\frac{1}{2}\left\{(E_{mj}^{1010}F_{nk}^{00})_{22}+\left(\frac{a}{L}\right)^2(E_{mj}^{0000}F_{nk}^{11})_{22}\right\} \quad (11d)$$

$$k_{mjnk}^{23}=\frac{\nu}{(1-2\nu)}\left(\frac{a}{L}\right)(E_{mj}^{0010}F_{nk}^{01})_{23}+\frac{1}{2}\left(\frac{a^2}{bL}\right)(E_{mj}^{0001}F_{nk}^{10})_{23} \quad (11e)$$

$$k_{mjnk}^{33}=\left(\frac{a}{L}\right)^2\frac{1-\nu}{(1-2\nu)}(E_{mj}^{0000}F_{nk}^{11})_{33}+\frac{1}{2}\left\{\left(\frac{a}{b}\right)^2(E_{mj}^{0101}F_{nk}^{00})_{33}+(E_{mj}^{1010}F_{nk}^{00})_{33}\right\} \quad (11f)$$

and the elements in the mass submatrix $\mathbf{m}^{\alpha\beta}$ are given by

$$m_{mjnk}^{11}=(1+\nu)(E_{mj}^{0000}F_{nk}^{00})_{11} \quad (11g)$$

$$m_{mjnk}^{22}=(1+\nu)(E_{mj}^{0000}F_{nk}^{00})_{22} \quad (11h)$$

$$m_{mjnk}^{33}=(1+\nu)(E_{mj}^{0000}F_{nk}^{00})_{33} \quad (11i)$$

where

$$(E_{mj}^{defg})_{\alpha\beta}=\iint_{\bar{R}}\frac{\partial^{d+e}\phi_m^{\alpha}(\bar{x}_1,\bar{x}_2)}{\partial\bar{x}_1\partial\bar{x}_2}\frac{\partial^{f+g}\phi_j^{\beta}(\bar{x}_1,\bar{x}_2)}{\partial\bar{x}_1\partial\bar{x}_2}d\bar{x}_1d\bar{x}_2 \quad (12a)$$

$$(F_{nk}^{rs})_{\alpha\beta}=\int_0^1\frac{\partial^r\psi_n^{\alpha}(\bar{x}_3)}{\partial\bar{x}_3}\frac{\partial^s\psi_k^{\beta}(\bar{x}_3)}{\partial\bar{x}_3}d\bar{x}_3 \quad (12b)$$

in which

$$\langle m;j\rangle=\langle 1,2,\ldots,(p+1)(p+2)/2;\,1,2,\ldots,(p+1)(p+2)/2\rangle \quad (12c)$$

$$\langle n;k\rangle=\langle 1,2,\ldots,q;\,1,2,\ldots,q\rangle \quad (12d)$$

$$\langle\alpha;\beta\rangle=\langle 1,2,3;\,1,2,3\rangle. \quad (12e)$$

The normalized variables, $\bar{x}_1$, $\bar{x}_2$, and $\bar{x}_3$ are defined as

$$\langle\bar{x}_1;\bar{x}_2;\bar{x}_3\rangle=\left\langle\frac{x_1}{a};\frac{x_2}{b};\frac{x_3}{L}\right\rangle. \quad (13)$$

The eigenvalue in Eq. (10) is expressed as

$$\lambda=\omega a\sqrt{\rho/E}\,. \quad (14)$$

2.4 The Truncated Double Series Polynomial-Based Shape Functions. The two-dimensional surface functions in Eq. (7) are intrinsically sets of admissible functions which are the product of a two-dimensional orthogonal polynomials space and a basic function, i.e.,

$${}^i\phi_j(x_1,x_2)=f_j(x_1,x_2)\{{}^i\phi_1(x_1,x_2)\}-\sum_{k=1}^{j-1}{}^i\Xi_{jk}\{{}^i\phi_k(x_1,x_2)\} \quad (15)$$

in which

$${}^i\Xi_{jk}=\frac{{}_1^i\Delta_{jk}}{{}_2^i\Delta_k} \quad (16a)$$

with

$${}_1^i\Delta_{jk}=\iint_R f_j(x_1,x_2)\{{}^i\phi_1(x_1,x_2)\}\times\{{}^i\phi_k(x_1,x_2)\}dx_1dx_2 \quad (16b)$$

$${}_2^i\Delta_k=\iint_R\{{}^i\phi_k^2(x_1,x_2)\}dx_1dx_2 \quad (16c)$$

and the index, $i=1,2,3$, denotes the respective displacement direction.

The two-dimensional generating function, $f_j(x_1,x_2)$, may be expressed as

$$f_j(x_1,x_2)=x_1^rx_2^s(\cos^2\pi\vartheta)+x_1^sx_2^r(\sin^2\pi\vartheta) \quad (17)$$

where

$$r=\lceil\sqrt{j-1}\rceil \quad (18a)$$

$$s=\vartheta(\cos^2\pi\vartheta)+(\vartheta-1/2)(\sin^2\pi\vartheta) \quad (18b)$$

$$\vartheta=(j-r^2-1)/2 \quad (18c)$$

and $\lceil\,\rceil$ is the greatest integer function, for example, $\lceil\sqrt{17}\rceil=4$.

2.5 Treatment of Free Wall Conditions and Symmetry Considerations. For a thick-walled open section with free-wall conditions, the following boundary conditions are to be satisfied;

$$\langle\sigma_{nn};\tau_{nt};\tau_{n3}\rangle=\langle 0;0;0\rangle \quad (19)$$

where n and t are the coordinates normal and tangent to the wall surface, σ_{nn} is the normal stress, and τ_{nt} and τ_{n3} are the shearing stresses. However, for the Ritz method, only the geometric boundary conditions need be satisfied in the numerical process.

The two-dimensional lateral surface functions, $\phi_m^1(x_1,x_2)$, $\phi_m^2(x_1,x_2)$, $\phi_m^3(x_1,x_2)$, adopted in this formulation are highly accommodative to a wide variety of cross-sectional geometries. For free-wall conditions, the basic functions, $\phi_1^{\alpha}(x_1,x_2)$; $\alpha=1,2,3$, of the two-dimensional polynomial shape functions assume the simplest form:

$$\langle\phi_1^1(x_1,x_2);\phi_1^2(x_1,x_2);\phi_1^3(x_1,x_2)\rangle=\langle 1;1;1\rangle. \quad (20)$$

Depending on the geometric symmetry inherent in the cross section, the vibration modes of the thick-walled open sections may be classified into distinct symmetry classes with respect to the x_1x_3 and x_2x_3-planes.

2.6 Treatment of Different End Supports. Thick-walled open sections can be supported in many ways. Depending on the kinematics constraints imposed at both ends, the boundary conditions take on a permutative combinations of free (F), hinged (S), and clamped (C) ends. The respective boundary conditions implied in each case are given as follows:

- *Stress-Free Condition (F).*

$$\langle \sigma_3; \tau_{13}; \tau_{23} \rangle = \langle 0; 0; 0 \rangle \tag{21a}$$

- *Hinged/Simply Supported Condition (S).*

$$\langle u_1; u_2; \sigma_3 \rangle = \langle 0; 0; 0 \rangle \tag{21b}$$

- *Clamped Condition (C).*

$$\langle u_1; u_2; u_3 \rangle = \langle 0; 0; 0 \rangle \tag{21c}$$

The one-dimensional longitudinal functions, $\psi_n^1(x_3)$, $\psi_n^2(x_3)$, $\psi_n^3(x_3)$, however, are constructed to satisfy only the essential geometric boundary conditions of the thick-walled section at both ends, i.e.,

$$\langle {}^1\psi_1; {}^2\psi_1; {}^3\psi_1 \rangle = \langle (x_3)^{{}^1\Omega_1}(x_3 - L)^{{}^1\Omega_2}; (x_3)^{{}^2\Omega_1}(x_3 - L)^{{}^2\Omega_2}; (x_3)^{{}^3\Omega_1}(x_3 - L)^{{}^3\Omega_2} \rangle \tag{22}$$

where ${}^i\Omega_\alpha$ ($i = 1, 2$ and 3; $\alpha = 1, 2$) are the basic powers of the boundary expression. The corresponding value of the basic power is chosen to satisfy the geometric boundary conditions at both ends of the thick-walled open section are given as follows:

- $${}^1\Omega_\alpha = \begin{cases} 0 \text{ if the } \alpha\text{th end is stress free;} \\ 1 \text{ if the } \alpha\text{th end is simply supported or clamped.} \end{cases} \tag{23a}$$

- $${}^2\Omega_\alpha = \begin{cases} 0 \text{ if the } \alpha\text{th end is stress free;} \\ 1 \text{ if the } \alpha\text{th end is simply supported or clamped.} \end{cases} \tag{23b}$$

- $${}^3\Omega_\alpha = \begin{cases} 0 \text{ if the } \alpha\text{th end is stress free or simply supported;} \\ 1 \text{ if the } \alpha\text{th end is clamped.} \end{cases} \tag{23c}$$

The subsequent one-dimensional polynomial functions in the longitudinal direction are constructed according to a recurrence formula.

For $P_k(x) \in \{{}^i\phi_k(x); i = 1, 2, 3\}$ and $x = x_3$, the recurrence process gives

$$P_{k+1}(x) = \{g(x) - \Theta_k^A\}P_k(x) - \Theta_k^B P_{k-1}(x); \quad k = 1, 2, 3, \ldots . \tag{24}$$

The polynomial $P_0(x)$ is defined as zero and the constants Θ_k^A and Θ_k^B are defined such that the set of polynomials generated maintain the orthogonality property:

$$\int_0^L P_j(x)P_k(x)dx = \delta_{jk} \tag{25}$$

in which δ_{jk} in the above equation is the Kronecker delta function.

From the recurrence relation of Eq. (24) and considering Eq. (25), we have

$$\langle \Theta_k^A; \Theta_k^B \rangle = \langle {}_3\Delta_k/{}_4\Delta_k; {}_4\Delta_k/{}_5\Delta_{k-1} \rangle \tag{26}$$

with

$$\langle {}_3\Delta_k; {}_4\Delta_k; {}_5\Delta_{k-1} \rangle = \left\langle \int_0^L g(x)P_k^2(x)dx; \int_0^L P_k^2(x)dx; \int_0^L P_{k-1}^2(x)dx \right\rangle . \tag{27}$$

3 Results and Discussion

The numerical formulation of the three-dimensional elasticity solution developed in the previous section has been applied to extract the vibration frequencies and mode shapes of the cantilevered thick-walled open sections of different cross-sectional geometries, lengths, and thicknesses. In this study, the L, C, T, and I cross sections are assumed to be inscribed within a rectangular domain of aspect ratio, $b/a = 2.0$. Uniform wall thicknesses of $h/a = 0.1$, 0.2, and 0.3 are assumed for all cases.

Convergence study was carried out carefully to establish the accuracy of the present method (Hung, 1995). It was found that different numbers of terms, q, and orders of polynomial, p, will be needed for each study case to ascertain the convergence of the frequency solutions. In this study, the results presented herein have been determined by very thorough convergence study. It was found that reasonably accurate frequency parameters were achieved with $p = 6$ (polynomial order of the two-dimensional surface functions) and $q = 10$ (number of terms in the one-dimensional longitudinal functions). Therefore $p = 6$ and $q = 10$ are used to compute the following results which can be used with confidence since their accuracy has been ascertain by the convergence study.

3.1 Comparison Study. The accuracies of the present three-dimensional elasticity solutions are further validated by comparing with the transverse bending modes obtained from the Bernoulli-Euler beam equation for slender beams of selected cross-sectional shapes. For the transverse vibration of slender beams, $L/a \geq 100$, the well-known Bernoulli-Euler equation is commonly used for solutions. The governing beam equation for sinusoidal transverse vibration has the following form (Tse et al., 1978):

$$\frac{d^4\varphi(x)}{dx^4} - \beta^4\varphi(x) = 0; \; \beta^4 = \frac{\rho A \omega^2}{EI} \tag{28}$$

Table 1 Comparison of three-dimensional elasticity solutions and the Bernoulli-Euler equation for slender open sections (h/a = 0.1, L/a = 100, a/b = 0.5, and ν = 0.3)

Source of results	Frequency Parameters			Multiplier
	$\beta_1 L$	$\beta_2 L$	$\beta_3 L$	$(L/a)[(a^2A)/I]^{1/4}$
T-shaped section				
• 3D CP†	1.8830	4.7073	7.8565	125.4
• 3D AP‡	1.8832	4.7074	7.8569	-
I-shaped section				
• 3D CP†	1.8797	4.6947	7.8277	116.3
• 3D AP‡	1.8797	4.6948	7.8279	-
Tse et al. (1978)	1.8751	4.6941	7.8548	-

†Solution by complete polynomials, ‡Solution by authors' polynomials

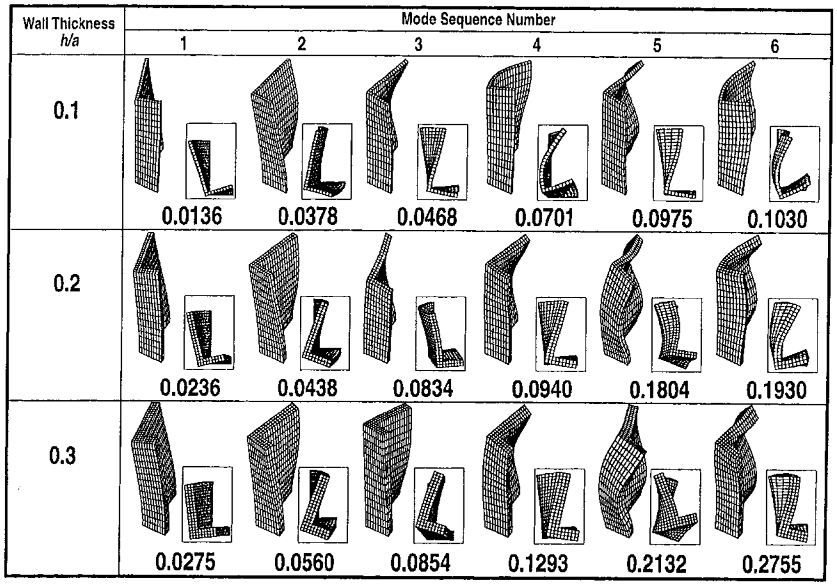

Fig. 2 Deformed mode shapes of a cantilevered L-shaped open section (b/a = 2.0 and L/a = 5.0)

where

$\varphi(x)$ = displacement amplitude function;
ρ = mass density per unit volume;
A = cross-sectional area;
E = Young's modulus;
I = moment of inertia.

The amplitude function has the general form

$$\varphi(x) = C_1 \sin \beta x + C_2 \cos \beta x + C_3 \sinh \beta x + C_4 \cosh \beta x. \quad (29)$$

Applying the cantilevered boundary conditions

$$\langle \varphi(0); \varphi'(0); \varphi''(L); \varphi'''(L) \rangle = \langle 0; 0; 0; 0 \rangle \quad (30)$$

leads to the following characteristic equation:

$$\cos \beta L \cosh \beta L + 1 = 0. \quad (31)$$

The relationship between the roots, βL, and the present frequency parameter, λ, is

$$(\beta L)^2 = \left(\frac{L}{a}\right)^2 \left(\frac{a^2 A}{I}\right)^{1/2} \lambda. \quad (32)$$

Table 1 shows the comparison of the first three roots computed from the Bernoulli-Euler beam equation and that obtained from the three-dimensional elasticity solutions. For the purpose of comparison, the three-dimensional elasticity solutions are calculated for T and I-shaped beams of length, $L/a = 100$, and thickness, $h/a = 0.1$, using the complete set polynomials (Leissa and Zhang, 1983) and the authors' polynomials. Both polynomials sets lead to convergent values which are less than 0.1 percent of discrepancy. To ensure that the three-dimensional

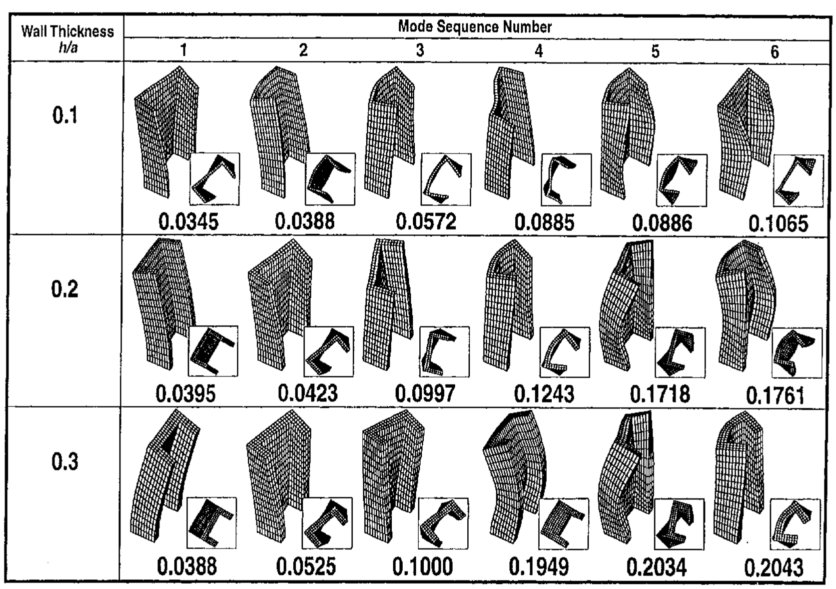

Fig. 3 Deformed mode shapes of a cantilevered C-shaped open section (b/a = 2.0 and L/a = 5.0)

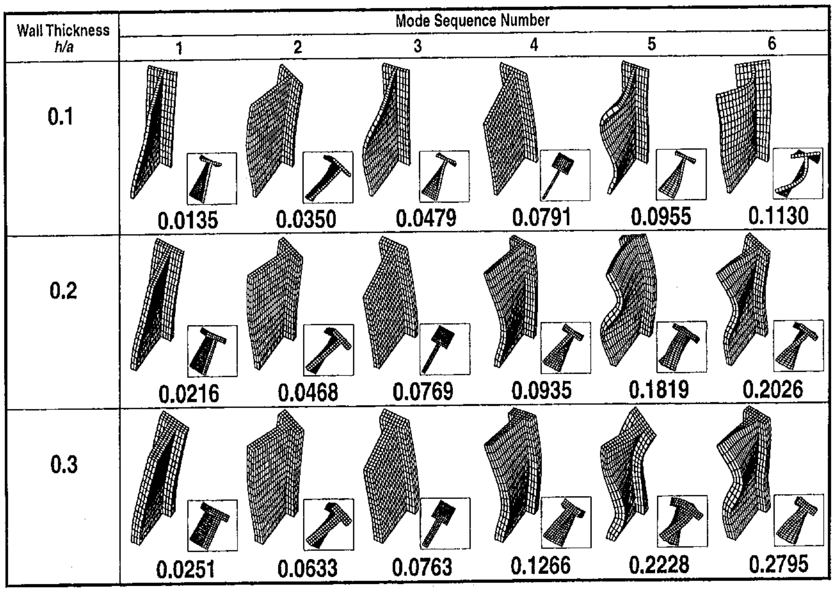

Fig. 4 Deformed mode shapes of a cantilevered T-shaped open section (b/a = 2.0 and L/a = 5.0)

elasticity solutions obtained are corresponding to the transverse bending modes, the respective deformed mode shapes have been examined beforehand. From Table 1, it is noted that the present three-dimensional solutions compared well with the Bernoulli-Euler beam solutions for the limiting case of a long slender beam.

3.2 Vibration Frequencies and Mode Shapes. The vibration frequencies and mode shapes of several thick-walled open sections have been computed. The thickness ratios, h/a, for this study are taken to be 0.2 and 0.3. Much information can be gathered from the three-dimensional vibration mode shapes presented in Figs. 2 to 5. The vibration mode shapes are computed for cantilevered sections with length-to-width ratio of L/a = 5.0, and b/a = 2.0.

Figure 2 shows the deformed geometries of the L-shaped section with different thickness ratios, h/a. The first (fundamental) mode in all cases exhibits simultaneous flexural and torsional motions. In higher modes, the coupling remains strong. Higher modes in this case are distinguished by the higher wave number in the longitudinal direction.

The three-dimensional deformed mode shapes of the C-shaped section are presented in Fig. 3. Due to the symmetry inherent in the cross section (about the x_1-axis), the deformed geometries are marked by the appearance of strong symmetry. At the thickness ratio of h/a = 0.1, the fundamental mode shows coupling between the torsional and transverse bending motions. This mode appears as the second normal mode for C-shaped sections with h/a = 0.2 and 0.3. Flange-wise motions are observed for the lowest modes with h/a = 0.1. At a higher thickness ratio, the flange-wise deformations are less obvious in the lower modes of vibration. The first and fourth modes of the C-shaped section with h/a = 0.3 are found to be the first and second pure transverse bending modes.

For the T-shaped section depicted in Fig. 4, it is noted that except for the first transverse bending mode about the x_1-axis

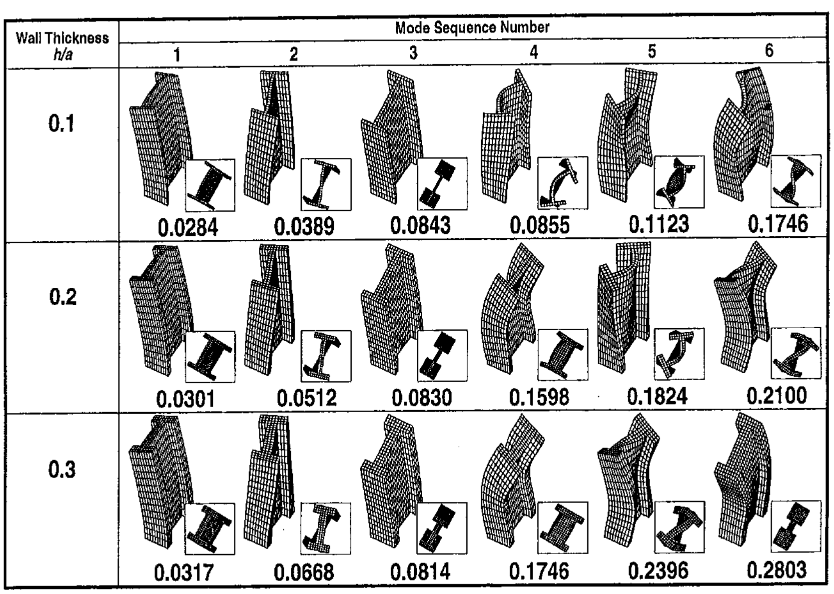

Fig. 5 Deformed mode shapes of a cantilevered I-shaped open section (b/a = 2.0 and L/a = 5.0)

(such as the fourth mode of $h/a = 0.1$; the third mode of $h/a = 0.2$ and 0.3), the other modes showing a strong coupling between the flexural and torsional vibration motions. It is observed that the thickness increases while the vibration frequency decreases. Mode switchings are also observed in this plot as the thickness ratio changes from 0.1 to 0.2.

Finally, the deformed mode shapes of an I-shaped section are presented in Fig. 5. This geometry possesses dual axes of symmetry. It is interesting to note that despite the different thickness ratios, the fundamental mode exhibits pure transverse bending motion about the x_2-axis. Pure torsional modes are observed in the second mode. And the third fundamental mode is a pure transverse bending motion about the x_1-axis. The higher modes involve torsional and transverse bending motions of higher order. Mode switchings are evident only in the higher modes. As the thickness ratio changes from 0.1 to 0.2, the fourth mode ($h/a = 0.1$) becomes the fifth mode ($h/a = 0.2$).

4 Conclusions

A three-dimensional elasticity model for the free vibration of thick-walled open sections with a built-in end is developed. The integral expressions for strain and kinetic energies of the thick-walled open sections are derived from the linear small-strain three-dimensional elasticity theory. The Ritz minimum energy principle is used to operate on the energy functional and culminated to a linear eigenvalue equation. The solution process made use of a set of uniquely constructed one and two-dimensional polynomial series. The orthogonality inherent in these polynomial series has led to a better computational efficiency. The versatility of the two-dimensional surface function to accommodate the thick prismatic structures of different cross-sectional geometries has been demonstrated for the thick-walled open sections of L, C, T, and I shapes. Based on the present model, the effects of wall thickness, effective length, and cross-sectional geometries on the natural frequencies of the thick-walled open sections are investigated and discussed. Vivid three-dimensional mode-shape plots are generated for selected dimensions. It is believed that the three-dimensional elasticity model could serve to enhance our understanding on the physics of vibration of this kind.

References

Bernadou, M., Fayolle, S., and Léné, F., 1989, "Numerical Analysis of Junctions Between Plates," *Computer Methods in Applied Mechanics and Engineering*, Vol. 74, pp. 307–326.

Fromme, J. A., and Leissa, A. W., 1970, "Free Vibration of the Rectangular Parallelepiped," *Journal of the Acoustical Society of America*, Vol. 48, pp. 290–298.

Garland, C. F., 1940, "The Normal Modes of Vibrations of Beams Having Nonlinear Elastic and Mass Axes," ASME JOURNAL OF APPLIED MECHANICS, Vol. 7, pp. 97–105.

Golley, B. W., and Grice, W. A., 1989, "Prismatic Folded Plate Analysis Using Finite Strip-Elements," *Computer Methods in Applied Mechanics and Engineering*, Vol. 76, pp. 101–118.

Hung, K. C., 1995, "A Treatise on Three-Dimensional Vibrations of a Class of Elastic Solids," Ph.D. thesis," Nanyang Technological University, Singapore.

Hutchinson, J. R., and Zillmer, S. D., 1983, "Vibrations of a Free Rectangular Parallelepiped," ASME JOURNAL OF APPLIED MECHANICS, Vol. 50, pp. 123–130.

Le Dret, H., 1989, "Folded Plates Revisited," *Computational Mechanics*, Vol. 5, pp. 345–365.

Leissa, A. W., and Zhang, Z., 1983, "On the three-dimensional vibrations of the cantilevered rectangular parallelepiped," *Journal of the Acoustical Society of America*, Vol. 73, pp. 2013–2021.

Leissa, A. W., and Jacob, K. I., 1986, "Three-Dimensional Vibrations of Twisted Cantilevered Parallelepipeds," ASME JOURNAL OF APPLIED MECHANICS, Vol. 53, pp. 614–618.

Liew, K. M., and Hung, K. C., 1995, "Three-Dimensional Vibratory Characteristics of Solid Cylinders and Some Remarks on Simplified Beam Theories," *International Journal of Solids and Structures*, Vol. 32, pp. 3499–3513.

Liew, K. M., Hung, K. C., and Lim, M. K., 1993, "A Continuum Three-Dimensional Vibration Analysis of Thick Rectangular Plates," *International Journal of Solids and Structures*, Vol. 30, pp. 3357–3379.

Liew, K. M., Hung, K. C., and Lim, M. K., 1995a, "Free-Vibration Studies on Stress-Free Three-Dimensional Elastic Solids," ASME JOURNAL OF APPLIED MECHANICS, Vol. 62, pp. 159–165.

Liew, K. M., Hung, K. C., and Lim, M. K., 1995b, "Vibration of Stress-Free Hollow Cylinders of Arbitrary Cross Section," ASME JOURNAL OF APPLIED MECHANICS, Vol. 62, pp. 718–724.

Liew, K. M., Hung, K. C., and Lim, M. K., 1995c, "Vibrotory Characteristics of Simply Supported Thick Skew Plates in Three-Dimensional Setting," ASME JOURNAL OF APPLIED MECHANICS, Vol. 62, pp. 880–886.

Liew, K. M., Hung, K. C., and Lim, M. K., 1997, "Three-Dimensional Vibration Analysis of Solid Cylinders of Polygonal Cross-Section Using the p-Ritz Method," *Journal of Sound and Vibration*, Vol. 200, pp. 505–518.

Tse, F. S., Morse, I. E., and Hinkle, R. T., 1978, *Mechanical Vibrations: Theory and Applications*, Boston: Allyn and Bacon, Boston, MA.

Young, P. G., and Dickinson, S. M., 1994, "Free Vibration of a Class of Solids With Cavities," *International Journal of Mechanical Sciences*, Vol. 36, pp. 1099–1107.

Young, P. G., and Dickinson, S. M., 1995, "Free Vibration of a Class of Homogeneous Isotropic Solids," ASME JOURNAL OF APPLIED MECHANICS, Vol. 62, pp. 706–708.

Yu-Tsung Chiu[1]
Graduate Student

Kuang-Chong Wu
Professor

Institute of Applied Mechanics,
National Taiwan University,
Taipei 106, Taiwan

Analysis for Elastic Strips Under Concentrated Loads

The problem of a general anisotropic elastic strip under concentrated loads is analyzed. By using the Stroh formalism for anisotropic elasticity in conjunction with the Fourier transform, the elastic fields for a concentrated load are expressed as integrals which can be evaluated by residue theory to give eigenfunction expansions. The eigenfunction expansions can be divided into two parts. The first part arises from the singularities at the origin of the integrands of the Fourier integrals and corresponds to classical beam bending and stretching solutions. The second part consists of the other terms in the eigenfunction expansions and corresponds to exponentially decaying self-equilibrium solutions. The solution for a concentrated load is used to investigate the problems of a pair of collinear compressive loads and three-point bending.

1 Introduction

With respect to a rectangular coordinate system (x_1, x_2, x_3) with base vectors $\{\mathbf{e}_1, \mathbf{e}_2, \mathbf{e}_3\}$, let an infinite strip occupy the region $-\infty < x_1 < \infty$, $-h/2 < x_2 < h/2$, h being the thickness of the strip. The paper is concerned with the solution for the strip in the presence of concentrated loads as shown in Fig. 1.

Filon (1903) used the Fourier series to obtain an approximate solution for a finite strip, $-L \le x_1 \le L$, $-h/2 \le x_2 \le h/2$. The approximate solution yields the exact tractions on the edges $x_2 = \pm h/2$ but gives only the correct traction resultants and moments at the ends $x_1 = \pm L$. In the case of infinite strip Filon's solution is expressed in terms of Fourier integral. Another related type of problem is that of a semi-infinite strip, $0 \le x_1 < \infty$, $-h/2 \le x_2 \le h/2$, subjected to end loads at $x_1 = 0$. The semi-infinite strip problem was considered by Papkovich (1941), Fadle (1941), and Johnson and Little (1965). For self-equilibrated end loads, the solution is expressed in terms of eigenfunction expansions which satisfy the traction-free conditions on $x_2 = \pm h/2$ and decay exponentially as x_1 increases. Buchwald (1964) showed that the singularities of the Fourier integrals for infinite strip at the origin give rise to the classical beam stretching and bending theories and that the Papkovich-Fadle functions are connected with other singularities of the Fourier integrals. An exact solution for finite plates with arbitrary edge forces were given by Baker et al. (1993). A general method for finite plate problem was discussed by Meleshko (1995). The aforementioned works are for isotropic elasticity.

Filon's approach was extended to orthotropic materials by Gerhardt and Liu (1983) and Whitney (1985) and to generally orthotropic materials by Sullivan and Van Oene (1986). Extensions of the Papkovich-Fadle functions to certain anisotropic elastic strips have been carried out by Horgan (1972), Choi and Horgan (1977), and Crafter et al. (1993) and to generally anisotropic strips by Wang et al. (1993). The symmetric state of stress caused by a pair of collinear compressive loads on opposite sides of an orthotropic strip were examined by Matemilola et al. (1995). Particular attention was focused on diffusion rates of stress. It was found that the first complex eigenvalue has a major influence on the exponential decay of normal stress at the middle surface. The Fourier integral for a dislocation in an infinite anisotropic strip was given by Wu and Chiu (1995). The main objective of the present paper is to generalize Buchwald's results (1964) to anisotropic material. The solution for a concentrated force on the surface of an infinite anisotropic strip is developed. The Fourier transform synthesized with Stroh's formalism (1958) developed by Wu and Chiu (1995) is followed. Although the Fourier transform of the present solution can also be obtained by the procedure in Wu and Chiu (1995), the expression so obtained involves functions which are not analytic in the transform variable. An analytic expression is derived here to yield eigenfunction expansions by residue theory. The concentrated load solution is used to investigate the problems of a pair of collinear compressive loads and three-point bending. In the case of three-point bending, an accurate approximate expression for the center deflection for a general anisotropic material was proposed based on the eigenfunction corresponding to the pole at the origin.

The plan of the paper is as follows. Basic equations are introduced in Section 2. The solution in the form of Fourier integrals for a concentrated load is discussed in Section 3. Eigenfunction expansions obtained from Fourier integrals are also derived in Section 3. The problems of a pair of collinear compressive loads and three-point bending are studied in Section 4.

2 Basic Equations

In the following discussion vectors or matrices are denoted by boldfaced letters. A subscript comma denotes partial differentiation and repeated Latin indices imply summation from 1 to 3, unless noted otherwise. Summation over Greek indices is indicated explicitly.

For a homogeneous anisotropic body, the generalized Hookes law and the equations of equilibrium are given as

$$\sigma_{ij} = C_{ijkl} u_{k,l} \tag{1}$$

$$\sigma_{ij,j} = 0 \tag{2}$$

where u_k and σ_{ij} is the displacement and stress component, respectively, and C_{ijkl} is the component of the elasticity tensor. If the displacement $\mathbf{u}$ depends only on x_1 and x_2, so does the corresponding stress tensor $\boldsymbol{\sigma}$. In view of Eq. (2), a stress function $\boldsymbol{\phi} = \phi_k \mathbf{e}_k$ can be introduced, such that

$$\sigma_{i1} = -\phi_{i,2}, \quad \sigma_{i2} = \phi_{i,1}, \quad i = 1, 2, 3. \tag{3}$$

[1] Currently at Industrial Technology Research Institute, Hsinshu, Taiwan.

Contributed by the Applied Mechanics Division of THE AMERICAN SOCIETY OF MECHANICAL ENGINEERS for publication in the ASME JOURNAL OF APPLIED MECHANICS.

Discussion on the paper should be addressed to the Technical Editor, Professor Lewis T. Wheeler, Department of Mechanical Engineering, University of Houston, Houston, TX 77204-4792, and will be accepted until four months after final publication of the paper itself in the ASME JOURNAL OF APPLIED MECHANICS.

Manuscript received by the ASME Applied Mechanics Division, Feb. 20, 1996; final revision, Oct. 2, 1997. Associate Technical Editor: J. W. Ju.

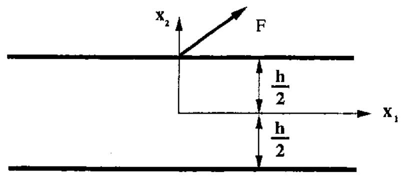

Fig. 1 An infinite strip under a concentrated load

Substitution of Eq. (3) into Eq. (1) yields

$$\mathbf{Q}\mathbf{u}_{,1} + \mathbf{R}\mathbf{u}_{,2} = -\boldsymbol{\phi}_{,2}$$

$$\mathbf{R}^T\mathbf{u}_{,1} + \mathbf{T}\mathbf{u}_{,2} = \boldsymbol{\phi}_{,1} \tag{4}$$

where the matrices $\mathbf{Q}$, $\mathbf{R}$, and $\mathbf{T}$ are defined as

$$Q_{ik} = C_{i1k1}$$

$$R_{ik} = C_{i1k2}$$

$$T_{ik} = C_{i2k2}.$$

Equation (4) can be rewritten as (Chadwick and Smith, 1977)

$$\mathbf{w}_{,2} = \mathbf{N}\mathbf{w}_{,1} \tag{5}$$

where

$$\mathbf{w} = \begin{bmatrix} \mathbf{u} \\ \boldsymbol{\phi} \end{bmatrix} \tag{6}$$

$$\mathbf{N} = \begin{bmatrix} \mathbf{N}_1 & \mathbf{N}_2 \\ \mathbf{N}_3 & \mathbf{N}_1^T \end{bmatrix}, \tag{7}$$

and

$$\mathbf{N}_1 = -\mathbf{T}^{-1}\mathbf{R}^T, \tag{8}$$

$$\mathbf{N}_2 = \mathbf{T}^{-1} = \mathbf{N}_2^T, \tag{9}$$

$$\mathbf{N}_3 = \mathbf{R}\mathbf{T}^{-1}\mathbf{R}^T - \mathbf{Q} = \mathbf{N}_3^T. \tag{10}$$

The Fourier transform of $\mathbf{w}$, $\tilde{\mathbf{w}}$, defined by

$$\tilde{\mathbf{w}}(\omega, x_2) = \int_{-\infty}^{\infty} \mathbf{w}(x_1, x_2) e^{-i\omega x_1} dx_1 \tag{11}$$

can be represented as (Wu and Chiu, 1995)

$$\tilde{\mathbf{w}}(\omega, x_2) = e^{i\omega(x_2 - y_0)\mathbf{N}} \tilde{\mathbf{w}}(\omega, y_0), \tag{12}$$

where y_0 is an arbitrary constant and $e^{i\omega x_2 \mathbf{N}}$ is a six-by-six matrix function given by

$$e^{i\omega x_2 \mathbf{N}} = \begin{bmatrix} \tilde{\mathbf{G}}_1(\omega, x_2) & \tilde{\mathbf{G}}_2(\omega, x_2) \\ \tilde{\mathbf{G}}_3(\omega, x_2) & \tilde{\mathbf{G}}_1^T(\omega, x_2) \end{bmatrix}, \tag{13}$$

and

$$\tilde{\mathbf{G}}_1(\omega, x_2) = \mathbf{A}\,\langle e^{i\omega p x_2}\rangle\,\mathbf{B}^T + \bar{\mathbf{A}}\,\langle e^{i\omega \bar{p} x_2}\rangle\,\bar{\mathbf{B}}^T,$$

$$\tilde{\mathbf{G}}_2(\omega, x_2) = \mathbf{A}\,\langle e^{i\omega p x_2}\rangle\,\mathbf{A}^T + \bar{\mathbf{A}}\,\langle e^{i\omega \bar{p} x_2}\rangle\,\bar{\mathbf{A}}^T,$$

$$\tilde{\mathbf{G}}_3(\omega, x_2) = \mathbf{B}\,\langle e^{i\omega p x_2}\rangle\,\mathbf{B}^T + \bar{\mathbf{B}}\,\langle e^{i\omega \bar{p} x_2}\rangle\,\bar{\mathbf{B}}^T.$$

Here $\mathbf{A} = [\mathbf{a}_1, \mathbf{a}_2, \mathbf{a}_3]$ and $\mathbf{B} = [\mathbf{b}_1, \mathbf{b}_2, \mathbf{b}_3]$ and $\langle e^{i\omega p x_2}\rangle$ and $\langle e^{i\omega \bar{p} x_2}\rangle$ stand for 3×3 diagonal matrices with $e^{i\omega p_\alpha x_2}$ and $e^{i\omega \bar{p}_\alpha x_2}\alpha = 1, 2, 3$, respectively, as the diagonal elements. The complex three-dimensional vectors $\mathbf{a}$ and $\mathbf{b}$ and the complex scalar p are Stroh's eigenvectors and eigenvalues related by

$$\mathbf{N}\begin{bmatrix} \mathbf{a} \\ \mathbf{b} \end{bmatrix} = p\begin{bmatrix} \mathbf{a} \\ \mathbf{b} \end{bmatrix}. \tag{14}$$

Equation (14) provides six roots, p_κ, $\kappa = 1, \ldots, 6$. Since p_κ are complex if the strain energy is positive definite (Eshelby et al., 1953), we can let

$$p_{\kappa+3} = \bar{p}_\kappa,\ \Im[p_\kappa] > 0$$

$$\boldsymbol{\xi}_{\kappa+3} = \bar{\boldsymbol{\xi}}_\kappa,\ \kappa = 1, 2, 3$$

where $\Im$ denotes imaginary part and overbar stands for complex conjugate.

The matrix function $e^{i\omega x_2 \mathbf{N}}$ possesses properties associated with the exponential function:

$$e^{i\omega x_2 \mathbf{N}} = \mathbf{I}, \text{ when } \omega x_2 = 0 \tag{15}$$

$$e^{i\omega x_2 \mathbf{N}} = e^{i\omega(x_2 - y_0)\mathbf{N}} e^{i\omega y_0 \mathbf{N}} \tag{16}$$

$$e^{-i\omega x_2 \mathbf{N}} = (e^{i\omega x_2 \mathbf{N}})^{-1}. \tag{17}$$

From Eqs. (15) and (13), we have

$$\tilde{\mathbf{G}}_1(\omega, 0) = \mathbf{I}, \quad \tilde{\mathbf{G}}_2(\omega, 0) = \tilde{\mathbf{G}}_3(\omega, 0) = \mathbf{0}. \tag{18}$$

Let the derivative of $\mathbf{w}$ with respect to x_1 be denoted by $\mathbf{v}$, i.e.,

$$\mathbf{v} = \mathbf{w}_{,1} = \begin{bmatrix} \mathbf{d} \\ \mathbf{t} \end{bmatrix} \tag{19}$$

where

$$\mathbf{d} = \mathbf{u}_{,1}, \quad \mathbf{t} = \boldsymbol{\phi}_{,1} = \sigma_{k2}\mathbf{e}_k. \tag{20}$$

From Eq. (12), the Fourier transform of $\mathbf{v}$, $\tilde{\mathbf{v}}$ can be expressed as

$$\tilde{\mathbf{v}}(\omega, x_2) = i\omega\tilde{\mathbf{w}} = e^{i\omega(x_2 - y_0)\mathbf{N}} \tilde{\mathbf{v}}(\omega, y_0) \tag{21}$$

where $\tilde{\mathbf{v}}(\omega, y_0) = i\omega\tilde{\mathbf{w}}(\omega, y_0)$.

In the above expressions, the complex constants p_α are assumed to be distinct. Consequently the formulation cannot be applied directly to isotropic materials for which $p = i$ is a double root for plane-strain deformation. However, in many problems, including the one considered in this paper, results for isotropic materials can be obtained by a limiting process discussed in (Wu, 1991).

3 Solution of a Concentrated Force

In this section, the elastic fields in an infinite strip of thickness $h = 2$ due to a concentrated load $\mathbf{F}$ on the surface are derived. The (x_1, x_3) plane is taken as the central plane of the strip. The configuration is shown in Fig. 1.

Without loss of generality let a concentrated force $\mathbf{F} = F_k\mathbf{e}_k$ be located at $x_1 = 0$, $x_2 = 1$. The boundary conditions are given by

$$\mathbf{t}(x_1, 1) = \delta(x_1)\mathbf{F} \tag{22}$$

$$\mathbf{t}(x_1, -1) = \mathbf{0} \tag{23}$$

where $\delta(x_1)$ is the Dirac delta function. The Fourier transforms of Eqs. (22) and (23) are given as

$$\tilde{\mathbf{t}}(x_1, 1) = \mathbf{F} \tag{24}$$

$$\tilde{\mathbf{t}}(x_1, -1) = \mathbf{0}. \tag{25}$$

Let $\tilde{\mathbf{v}}$ have the form given by Eq. (21) with $y_0 = -1$, i.e.,

Table 1 Stroh's eigenvalues p and the first two roots of Eq. (34) for isotropic material and the fiber-reinforced vinyl ester with various fiber orientations

	isotropic	$\theta = 45°$	$\psi = 0°$	$\psi = 45°$	$\psi = 90°$
p	i	$2.0618i$ $1.0238i$ $0.8471i$	$2.7389i$ $0.6597i$ $1.0470i$	$0.3935 + 0.9193i$ $-0.7648 + 0.6443i$ $-0.0459 + 0.9989i$	$0.3651i$ $1.5159i$ $0.9551i$
k_1	$2.1062 + 1.1253i$	1.6787	1.2388	$1.8745 + 0.1557i$	2.2382
k_2	$5.3563 + 1.5511i$	$2.252 + 0.9074i$	$2.3541 + 0.4430i$	$3.1640 + 0.2508i$	$4.2536 + 0.8004i$

$$\tilde{\mathbf{v}} = \tilde{\mathbf{f}}(\omega, x_2) = e^{i\omega(x_2+1)\mathbf{N}} \begin{bmatrix} \tilde{\mathbf{d}}_0 \\ \mathbf{0} \end{bmatrix}, \qquad (26)$$

where Eq. (25) at $x_2 = -1$ has been used. The vector $\tilde{\mathbf{d}}_0$ can be determined from Eq. (24) as

$$\tilde{\mathbf{d}}_0 = \tilde{\mathbf{G}}_3(\omega, 2)^{-1}\mathbf{F} \qquad (27)$$

where $\tilde{\mathbf{G}}_3$ is defined in Eq. (13).

The solution of $\mathbf{v}$ is obtained by inverting Eq. (26) with Eq. (27) as

$$\mathbf{v} = \frac{1}{2\pi} \int_{-\infty}^{\infty} e^{i\omega x_1} \tilde{\mathbf{v}} d\omega. \qquad (28)$$

Note that since $\mathbf{G}_3 = 0$ at $\omega = 0$ by Eq. (18), the principal values of Eq. (28) must be taken. By the standard Fourier transform inversion, $\mathbf{v}$ can be replaced by the sums of residues at the appropriate poles as follows:

$$\mathbf{v} = \sum_{n=0}^{\infty} \mathbf{v}^{(n)}, \qquad (29)$$

where

$$\mathbf{v}^{(n)} = \gamma_n i \ \mathrm{Res}\ [e^{i\omega x_1} \tilde{\mathbf{v}}(\omega, x_2)]|_{\omega=\omega_n}. \qquad (30)$$

Here $\gamma_0 = \frac{1}{2}$, $\gamma_n = 1$ otherwise and $\omega_0 = 0$, $\omega_n \neq 0$, $n = 1, 2, \ldots$, are the poles of $\tilde{\mathbf{v}}$ in the upper half complex ω-plane. Equation (29) converge for $x_1 + \alpha_{\max}(x_2 - 1)$ except $x_1 = 0$ and $x_2 = 1$. Here $\alpha_{\max}$ is the maximum of the real parts of p_1, p_2, and p_3 in Eq. (14).

Denote by Δ_i and $\mathbf{q}_i$, $i = 1, 2, 3$, the eigenvalues and eigenvectors of $\mathbf{G}_3(\omega, 2)$, i.e.,

$$\mathbf{G}_3(\omega, 2)\mathbf{q}_i = \Delta_i \mathbf{q}_i \quad \text{no sum on } i. \qquad (31)$$

As $\mathbf{G}_3$ is symmetric, the eigenvectors $\mathbf{q}_i\mathbf{q}_j$ can be normalized such that

$$\mathbf{q}_i^T \mathbf{q}_j = \delta_{ij}.$$

The matrix $[\tilde{\mathbf{G}}_3(\omega, 2)]^{-1}$ can be represented as

$$[\tilde{\mathbf{G}}_3(\omega, 2)]^{-1} = \sum_{i=1}^{3} \frac{1}{\Delta_i} \mathbf{q}_i \mathbf{q}_i^T. \qquad (32)$$

Substitution of Eq. (32) into Eq. (27) yields

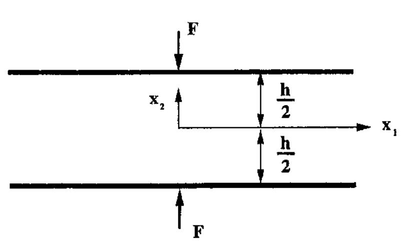

Fig. 2 An infinite strip under a pair of collinear compressive loads

$$\tilde{\mathbf{d}}_0 = \sum_{i=1}^{3} \frac{\mathbf{q}_i^T \mathbf{F}}{\Delta_i} \mathbf{q}_i. \qquad (33)$$

The poles of $\tilde{\mathbf{v}}$ are given by the roots of

$$|\tilde{\mathbf{G}}_3(\omega, 2)| = \Delta_1 \Delta_2 \Delta_3 = 0. \qquad (34)$$

If ω_n is a root, $-\omega_n$ as well as $-\bar{\omega}_n$ are also roots (Wang et al., 1993). If ω_n is a root of multiplicity m_i of $\Delta_i = 0$, Eq. (30) can be evaluated by the well-known residue formula as

$$\mathbf{v}^{(n)} = \gamma_n i \sum_i \frac{1}{(m_i - 1)!} \frac{\partial^{m_i - 1}}{\partial \omega^{m_i - 1}} \left((\omega - \omega_n)^{m_i} \frac{\mathbf{q}_i(\omega)^T \mathbf{F}}{\Delta_i(\omega)} \times e^{i\omega x_1} e^{i\omega(x_2+1)\mathbf{N}} \begin{bmatrix} \mathbf{q}_i(\omega) \\ \mathbf{0} \end{bmatrix} \right) \Bigg|_{\omega=\omega_n}. \qquad (35)$$

Each term given by Eq. (35) is an eigenfunction that satisfies traction-free conditions on the boundaries of the strip. For $\omega_n \neq 0$ the eigenfunctions decay exponentially as x_1 increases. Moreover, the corresponding stress functions $\boldsymbol{\phi}$ also vanish on the boundaries so that the stresses are self-equilibrated (Wang et al., 1993). The eigenfunctions derived by Wang et al. (1993) are special cases of Eq. (35) for $n \neq 0$ when all nonzero poles are simple ($m_i = 1$). The fact that the eigenfunctions due to opposed transverse forces are equivalent to the ones due to self-equilibrating end disturbance was noted by Durban and Stronge (1992).

The eigenfunction $\mathbf{v}^{(0)}$ corresponding to $\omega = 0$ is derived in the Appendix. The result can be expressed as

$$\mathbf{v}^{(0)} = \mathbf{v}_s^{(0)} + \mathbf{v}_b^{(0)} \qquad (36)$$

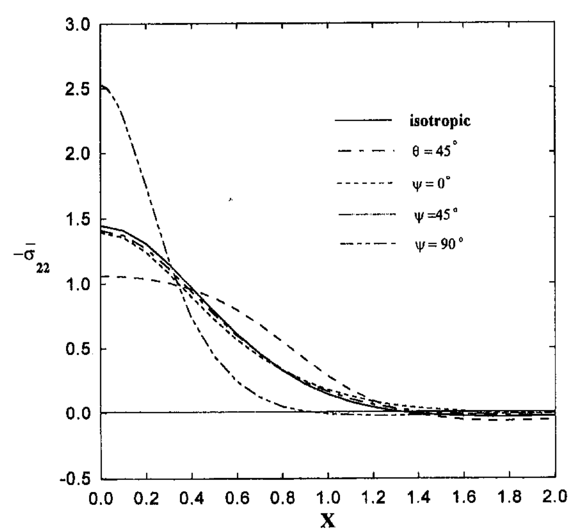

Fig. 3 $\bar{\sigma}_{22}$ as a function of X for collinear compressive loading

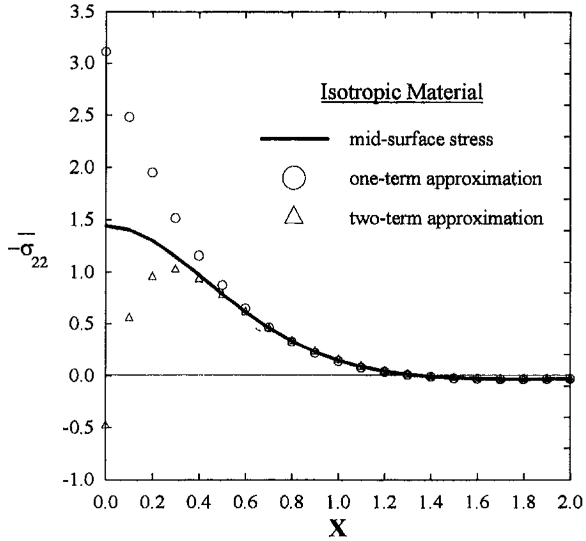

Fig. 4(*a*)

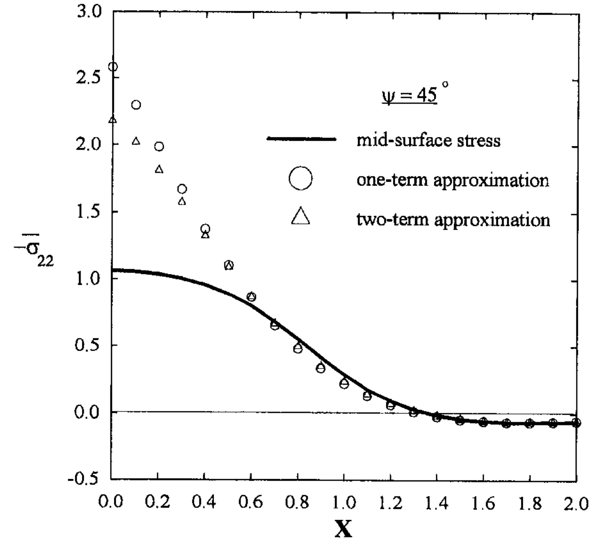

Fig. 4(*d*)

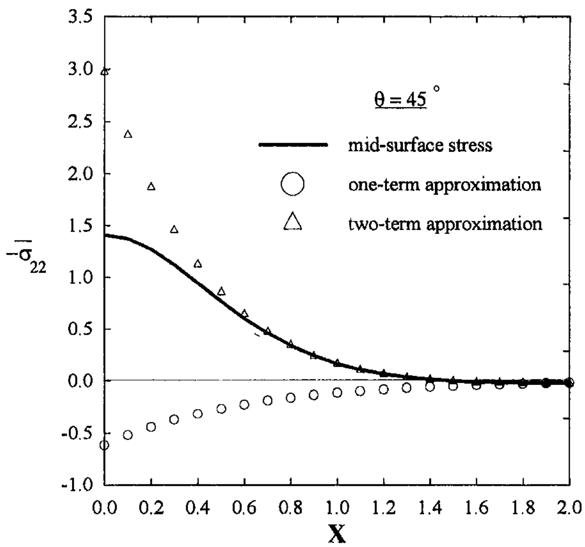

Fig. 4(*b*)

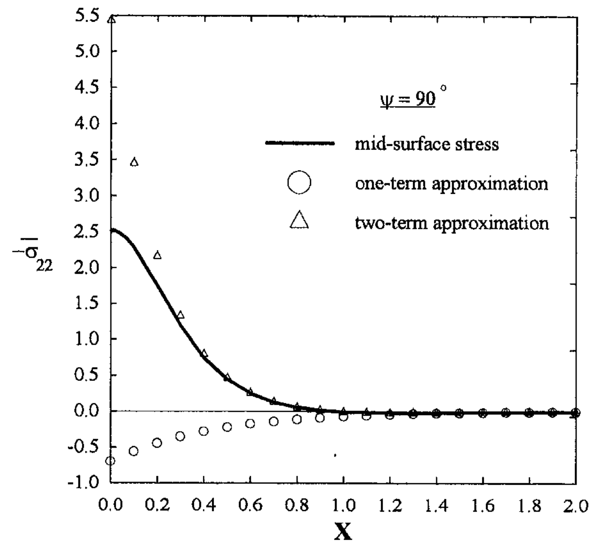

Fig. 4(*e*)

Fig. 4 comparison of the one-term and two-term approximations with the midplane stress, for (*a*) isotropic material, (*b*) composite with θ = 45 deg, (*c*) ψ = 0 deg, (*d*) ψ = 45 deg, (*e*) ψ = 90 deg

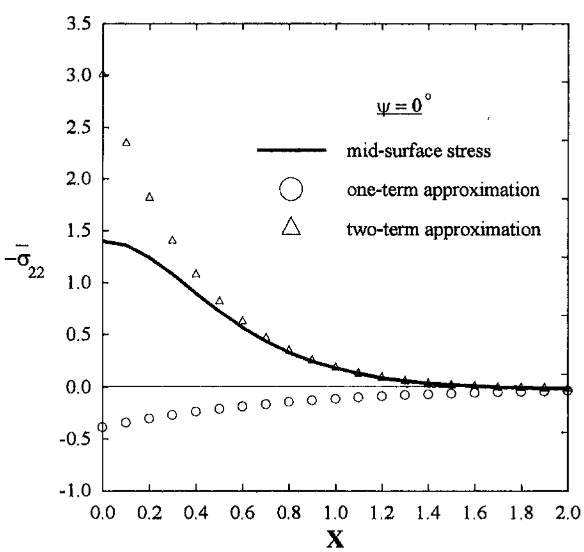

Fig. 4(*c*)

Here $\mathbf{v}_s^{(0)}$ is given by

$$\mathbf{v}_s^{(0)} = \frac{1}{4}\begin{bmatrix}\mathbf{N}_3^{(-1)}\mathbf{F}\\ \mathbf{0}\end{bmatrix}, \qquad (37)$$

where the matrix $\mathbf{N}_3^{(-1)}$ is the pseudo-inverse of $\mathbf{N}_3$ defined by

$$\mathbf{N}_3\mathbf{N}_3^{(-1)} = \mathbf{e}_1\mathbf{e}_1^T + \mathbf{e}_3\mathbf{e}_3^T.$$

$\mathbf{v}_b^{(0)}$ is given by

$$\mathbf{v}_b^{(0)} = \frac{3}{2\Delta_2'''(0)}\,\mathbf{g}_2''(0) - \frac{3\Delta_2^{(5)}(0)}{20\Delta_2'''(0)^2}\,\mathbf{g}_2(0) \qquad (38)$$

where

$$\mathbf{g}_2''(0) = (F_2x_1 + 2F_1)x_1\begin{bmatrix}\mathbf{e}_2\\ \mathbf{0}\end{bmatrix} - 2(F_2x_1 + F_1)x_2\begin{bmatrix}\mathbf{e}_1\\ \mathbf{0}\end{bmatrix}$$

$$+ F_2(1 - x_2^2)\mathbf{N}\begin{bmatrix}\mathbf{e}_1\\ \mathbf{0}\end{bmatrix} + \mathbf{q}_2''(0)^T\mathbf{F}\begin{bmatrix}\mathbf{e}_2\\ \mathbf{0}\end{bmatrix} + F_2\begin{bmatrix}\mathbf{q}_2''(0)\\ \mathbf{0}\end{bmatrix} \qquad (39)$$

$$\mathbf{g}_2(0) = F_2\begin{bmatrix} \mathbf{e}_2 \\ \mathbf{0} \end{bmatrix}. \tag{40}$$

$\Delta_2'''(0)$ and $\Delta_2^{(5)}(0)$ are given by Eq. (A11) and Eq. (A13), respectively, and $\mathbf{q}_2''(0)$ is given by Eq. (A14).

The stresses $\sigma_{11}^{(s)}$ and $\sigma_{31}^{(s)}$ obtained by substituting Eq. (37) into Eq. (5) are

$$\sigma_{11}^{(s)} = -\frac{F_1}{4}, \quad \sigma_{31}^{(s)} = -\frac{F_3}{4}. \tag{41}$$

Thus $\mathbf{v}_s^{(0)}$ describes a combined state of uniform compression and antiplane shearing. The stresses $\sigma_{i1}^{(b)}$, $i = 1, 3$, corresponding to $\mathbf{v}_b^{(0)}$ are obtained by substituting Eq. (38) into Eq. (5) as

$$\sigma_{11}^{(b)} = -\frac{3}{4}\left[(F_2x_1 + F_1)x_2 + \mathrm{F}_2\left(\frac{1}{3} - x_2^2\right)\left(r_6 - \frac{\hat{S}_{15}}{\hat{S}_{55}}r_4\right)\right] \tag{42}$$

$$\sigma_{13}^{(b)} = \frac{3F_2}{8}\left(x_2^2 - \frac{1}{3}\right)\left[s_6 + \frac{\hat{S}_{11}}{\hat{S}_{55}}r_4 - (s_4 + s_6)\frac{\hat{S}_{15}}{\hat{S}_{55}}\right] + \frac{3\hat{S}_{15}}{4\hat{S}_{55}}(F_2x_1 + F_1)x_2 \tag{43}$$

where r_i and s_i are defined by Eq. (A4). On the cross section normal to the x_1-axis, the traction resultants of $\sigma_{i1}^{(b)}$ are

$$\int_{-1}^{1}\sigma_{11}^{(b)}dx_2 = \int_{-1}^{1}\sigma_{13}^{(b)}dx_2 = 0, \quad \int_{-1}^{1}\sigma_{12}^{(b)}dx_2 = -\frac{F_2}{2} \tag{44}$$

and the moment produced by $\sigma_{11}^{(b)}$ is

$$-\int_{-1}^{1}\sigma_{11}^{(b)}x_2dx_2 = \tfrac{1}{2}(F_2x_1 + F_1). \tag{45}$$

Thus the stresses represents a classical solution for a cantilever beam of length x_1 subjected to a transverse force $F_2/2$ and a bending moment $F_1/2$ at $x_1 = 0$. Equation (42), when specialized for monoclinic material, recovers the result reported in (Lekhnitskii, 1968).

It is of interest to find the slope of the deflection curve of the centroidal axis $x_2 = 0$ due to F_2. The slope obtained from Eq. (38) is given by

$$\frac{\partial u_2}{\partial x_1} = \frac{3\Theta}{8\hat{S}_{55}}x_1^2F_2 - \Omega F_2 \tag{46}$$

where Θ is given by eqn (A4) and Ω by

$$\Omega = \frac{3}{2\Delta_2'''(0)}\left(r_2 + \frac{\Delta_2^{(5)}(0)}{10\Delta_2'''(0)} + 2\right), \tag{47}$$

with r_2 defined by Eq. (A4). The first term on the right-hand side of Eq. (46) results from flexural bending and the second term is the rotation due to shear deformation.

Equation (35) is the eigenfunction valid for $x_1 + \alpha_{\max}(x_2 - 1) \geq 0$ except $x_1 = 0$ and $x_2 = 1$ under a force $\mathbf{F}$ applied on $x_1 = 0$ and $x_2 = 1$. By considering a new coordinate x_i' obtained by rotating the x_i coordinates about the x_2-axis by π, the eigenfunctions valid for $x_1 + \alpha_{\min}(x_2 - 1) \leq 0$, except $x_1 = 0$ and $x_2 = 1$, can be derived. Here $\alpha_{\min}$ is the minimum of the real parts of p_1, p_2, and p_3 in Eq. (14). It is noted that for $\alpha_{\min} = \alpha_{\max} = 0$, $\mathbf{v}$ admits eigenfunction expansions in the entire strip except $x_1 = 0$, $x_2 = 1$. For nonzero $\alpha_{\min}$ and $\alpha_{\min}$, however, there is a triangular region, $\alpha_{\min}(1 - x_2) < x_1 < \alpha_{\max}(1 - x_2)$, where no eigenfunction expansions exist for $\mathbf{v}$. If the force is applied at the surface $x_2 = -1$, the corresponding eigenfunctions can be derived by considering a new reference coordinate x_i' obtained by rotating the x_i coordinates about the x_3-axis by π.

4 Numerical Examples

In this section the solution for a concentrated force is used to study the problems of a strip subjected to a pair of collinear compressive forces and three-point bending by the principle of superposition. The material considered is a vinyl ester reinforced by unidirectional glass fiber with the following properties with respect to the principal material coordinates (Sullivan and Van Oene, 1986):

$$\begin{aligned} E_1 &= 24.4 \text{ GPa} \\ E_2 &= 6.89 \text{ GPa} \\ G_{12} &= 2.85 \text{ GPa} \\ \nu_{12} &= \nu_{23} = 0.325 \end{aligned} \tag{48}$$

where 1-direction is parallel to the fibers, E_i are Young's moduli, G_{ij} are shear moduli, and ν_{ij} are Poisson's ratios. In the numerical examples considered, the material principal axes were obtained either by rotating an angle ψ about the x_3-axis or θ about the x_2-axis; Note that in the latter case the plane deformation and antiplane deformation are coupled. For comparison purposes, the results for an isotropic structural steel with Young's modulus $E = 204$ GPa and Poisson's ratio $\nu = 0.29$ were also considered.

In general, eigenfunction expansions were employed for numerical calculations when the series were convergent and only a few terms were needed to be included to ensure errors within 10^{-6}. In regions where the convergence was slow or the series diverged, the numerical results were obtained by evaluating the integral form of the solutions. The computations for glass fiber/vinyl ester were done with $\psi = 0$ deg, 45 deg, 90 deg and $\theta = 45$ deg. Stroh's eigenvalues p's for each case are listed in Table 1. The eigenvalues p are purely imaginary for all materials except $\psi = 45$ deg. Consequently, the eigenfunction expansions are uniformly convergent for all materials except $\psi = 45$ deg.

4.1 Collinear Compressive Loading. As shown in Fig. 2, an infinite strip of thickness h is subjected to a pair of collinear compressive loads of magnitude F at $x_1 = 0$, $x_2 = \pm h/2$. Since the resultant force and moment vanish on the cross sections, only the eigenfunctions corresponding to the nonzero poles need to be summed in the series solutions. Figure 3 shows the results of the dimensionless $\bar{\sigma}_{22} = \pi h\sigma_{22}/(4F)$ as a function of $X = 2x_1/h$ at $x_2 = 0$. The result for isotropic material was checked to agree with that reported by Filon (1903). The stress distributions for the fiber-reinforced vinyl ester with $\psi = 0$ deg and $\theta = 45$ deg are similar to that for isotropic material. For $\psi = 90$ deg, the stress exhibits a much higher peak value and decays more rapidly; whereas for $\psi = 45$ deg, the stress exhibits a lower peak value and decays more slowly.

The problem has been investigated by Matemilola et al. (1995) for orthotropic materials. It was found that at distances

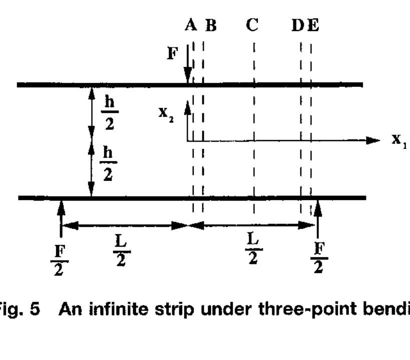

Fig. 5 An infinite strip under three-point bending

larger than one quarter of the thickness ($X > 0.5$), σ_{22} is closely represented by the sum of the eigenfunctions up to and including the first complex eigenfunction as well as its conjugate. The first two values of $k_n = -i\omega_n$, $n = 1, 2$ in the order of increasing real part for each case are given in Table 1. The eigenvalues that yield antisymmetric distributions of σ_{22} are not listed in Table 1. The first complex eigenvalue is k_1 for isotropic material and the composite material with $\psi = 45$ deg. In other cases the first complex eigenvalue is k_2. The approximations obtained by taking the first one or two terms in the eigenfunction expansions are given in Fig. 4(a)–4(e). Note that in the case of complex eigenvalue, the eigencomponent is twice the real part of the eigenfunction. Indeed for $X > 0.5$, the stress distribution is closely represented by the one-term approximation for isotropic material and the two-term approximation for orthotropic composites with $\psi = 0$ deg. For the orthotropic composite with $\psi = 90$ deg, the two-term eigenfunction expansion approximates the stress well even up to $X = 0.3$. Although the conclusion reached by Matemilola et al. (1995) is for orthotropic materials, it is found that the conclusion also holds for the composite with $\theta = 45$ deg. For the composite with $\psi = 45$ deg, the one-term approximation does not represent the stress as closely as in the other cases and the two-term approximation offers only slight improvement.

4.2 Three-Point Bending. A simply supported plate of thickness h and of span L subjected to a concentrated vertical force F is simulated by an infinite strip subjected to a vertical force F at $x_1 = 0$, $x_2 = h/2$ and $-F/2$ at $x_1 = \pm L/2$, $x_2 = -h/2$ as shown in Fig. 5. The problem for orthotropic beams and general orthotropic beams has been studied by Whitney (1985) and Sullivan and Van Oene (1986), respectively, by the Fourier series method. The concentrated load was represented by a distribution of uniform stress over a small area in either Whitney (1985) or Sullivan and Van Oene (1986).

The stresses on sections A to E as shown in Fig. 5 were calculated for $L = 5h$. Sections A and E are $0.05h$ from the applied load and the support, respectively. Sections B and D are $0.01575h$ from the applied load and the support, respectively. Section C is in the middle of the applied force and the support. Sections B, C, and D were also examined by Sullivan and Van Oene (1986). The results are expressed in terms of the following dimensionless quantities:

$$X = 2x_1/h, \quad \bar{\sigma}_{11} = 2h^2\sigma_{11}/3FL, \quad \bar{\tau}_{12} = 4h\sigma_{12}/3F,$$

$$Y = 2x_2/h, \quad \bar{\tau}_{13} = 2h^2\sigma_{13}/3FL, \quad \bar{\tau}_{23} = 4h\sigma_{23}/3F.$$

The distributions of $\bar{\sigma}_{11}$ on A to E are shown in Fig. 6. Note that for $\psi = 45$ deg, $\bar{\sigma}_{11}$ is asymmetric with respect to the x_2-

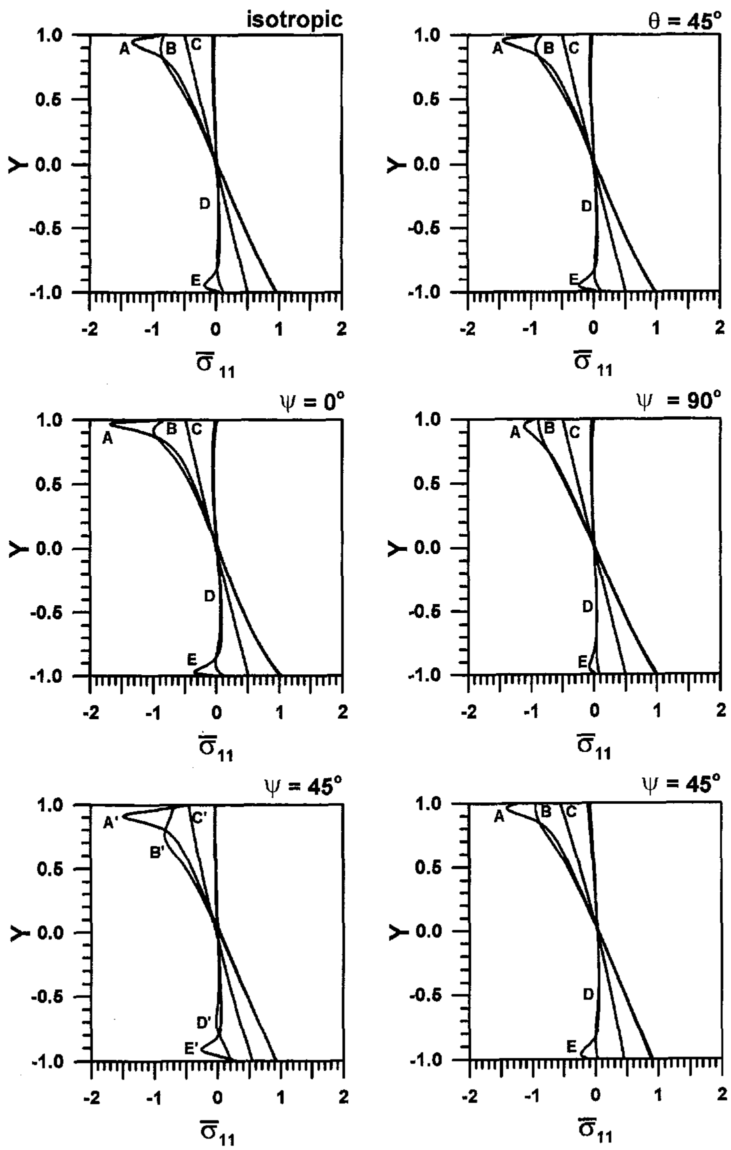

Fig. 6 Distributions of $\bar{\sigma}_{11}$ on the selected sections

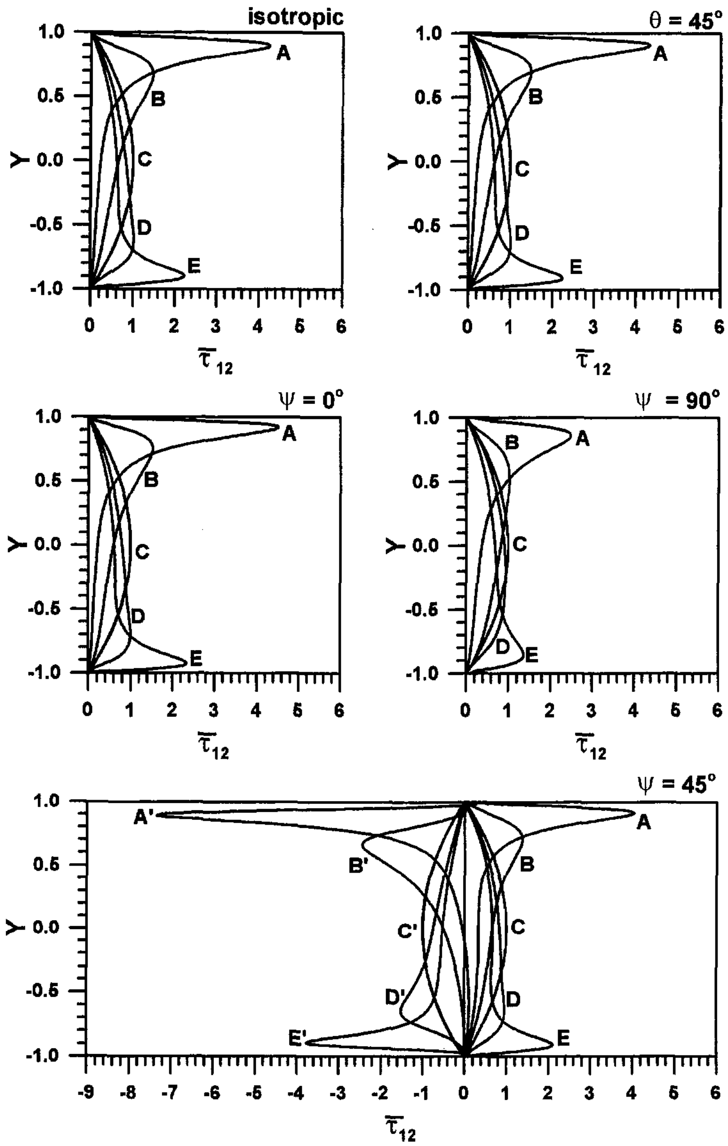

Fig. 7 Distributions of $\bar{\tau}_{12}$ on the selected sections

axis and the distributions are also shown in Fig. 6 for sections A′ to E′, which are symmetric to A to E with respect to the x_2-axis, respectively. The distributions for all the materials considered exhibit similar feature. They are essentially linear except at the points on the compression side near the applied load or the support, where the stress intensifies. For section C the result is indistinguishable from that given by classical beam bending solution. The distributions for $\bar{\tau}_{12}$ on A to E are shown in Fig. 7. The symmetric parabolic distribution with peak value $\bar{\tau}_{12} = 1$ as given by the classical bending solution only appears on section C. On other sections the distributions are asymmetric with respect to the centroidal axis and the peak values are greater than 1. The peak value increases as the applied loading or the support is approached. In particular, on section A the peak value is about 3 for $\psi = 90$ deg, and 5 for other materials. On section A′ the peak value exceeds 7 for $\psi = 45$. The stresses in the overhang were also calculated. The results show that on the section one thickness away from the support the maximum $\bar{\sigma}_{11}$ ranges from 0.0003 ($\psi = 90$ deg) to 0.007 ($\psi = 45$ deg) and maximum $\bar{\sigma}_{12}$ varies from 0.002 ($\psi = 90$ deg) to 0.03 ($\psi = 45$ deg). On the section, one and a half thickness away from the support, all stresses are within 0.002. Thus although the overhang considered here is infinite, the results may be regarded as good approximations for finite overhang longer than one thickness of the strip.

A quantity of interest in three-point bending tests is the center deflection. Here the center deflection v_c is defined as $v_c = -u_2(0, 0) + \frac{1}{2}(u_2(L/2, 0) + u_2(-L/2, 0))$. Based on Eq. (46), an approximate expression for v_c is given by

$$v_c = v_c^{(b)} + v_c^{(s)} \tag{49}$$

where

$$v_c^{(b)} = \frac{FL^3}{h^3 \Delta_2'''(0)}, \quad v_c^{(s)} = \frac{L}{h}\Omega F \tag{50}$$

and $\Delta_2'''(0)$ and Ω are given by Eq. (A11) and Eq. (47), respectively. The term $v_c^{(b)}$ in Eq. (49) is due to flexural bending and $v_c^{(s)}$ induced by shear deformation. For orthotropic materials Eq. (49) becomes

$$v_c = \frac{\hat{S}_{11} F L^3}{48 I}\left[1 + 1.2\left(\frac{h}{L}\right)^2\left(\frac{\hat{S}_{66}}{\hat{S}_{11}} + \frac{3\hat{S}_{12}}{4\hat{S}_{11}}\right)\right] \tag{51}$$

where $I = h^3/12$ is the moment of inertia of the section per

Table 2 Center deflections in mm for three-point bending

	isotropic	$\theta = 45°$	$\psi = 0°$	$\psi = 45°$	$\psi = 90°$
v_c	0.156	3.098	1.702	3.988	4.537
$v_c^{(b)}/v_c$	0.90	0.84	0.73	0.95	0.97
$(v_c^{(b)} + v_c^{(s)})/v_c$	1.00	1.02	1.03	1.01	1.00

unit length. Equation (51) is for plane-strain deformation. The corresponding expression for plane-stress condition, expressed in terms of the engineering constants, are

$$v_c = \frac{FL^3}{48E_1I}\left[1 + 1.2\left(\frac{h}{L}\right)^2\left(\frac{E_1}{G_{12}} - \frac{3}{4}\upsilon_{12}\right)\right]. \quad (52)$$

Equation (52) agrees with that given in Timoshenko and Goodier (1970) for isotropic material. Tarnopol'skii and Kincis (1985) reported an approximate formula containing the first two terms of Eq. (52). The exact values of the center deflection for $L = 100$ mm, $h = 20$ mm, $P = 1$ MN/m are given in Table 2. The values calculated by Eq. (49) with $v_c^{(b)}$ only and both $v_c^{(b)}$ and $v_c^{(s)}$ are also shown in Table 2. For comparison purposes the approximate values are expressed as fractions of the exact values. For all materials considered, the center deflections are underestimated by $v_c^{(b)}$. Indeed the value predicted by $v_c^{(b)}$ is 90 percent of the exact value for isotropic material and is only 73 percent for the composite with $\psi = 0$ deg. However, if $v_c^{(s)}$ is included, Eq. (49) yields very accurate approximations with errors within three percent higher than the exact values.

5 Concluding Remarks

An elasticity solution for a general anisotropic infinite strip under a concentrated load has been derived. It is shown that the solution in integral form can be expanded as eigenfunction series. However, for some anisotropic materials, the eigenfunction expansion is only valid outside certain triangular regions. The eigenfunction expansion consists of a part that is exponentially decaying and self-equilibrium and the other part corresponding to classical bending and stretching polynomial solutions. The solution for a concentrated load is used to study collinear compression and three-point bending problems. A highly accurate approximation is provided for the center deflection in the three-point bending problem.

Acknowledgments

The research was supported by National Science Council of the Republic of China under grant NSC-84-2212-E002-050.

References

Baker, G., Pavlovic, M. N., and Tahan, N., 1993, "An exact solution to the two-dimensional elasticity problem with rectangular boundaries under arbitrary edge forces," *Philosophical Transactions of the Royal Society of London*, Vol. A343, pp. 307–336.

Buchwald, V. T., 1964, "Eigenfunctions of plane elastostatics," *Proceedings of the Royal Society of London*, Vol. A227, pp. 385–400.

Chadwick, P., and Smith, G. D., 1977, "Foundations of the theory of surface waves in anisotropic elastic materials," *Advanced Applied Mechanics*, Vol. 17, pp. 303–376.

Choi, I., and Horgan, C. O., 1977, "Saint-Venant's Principle and End Effects in Anisotropic Elasticity," ASME JOURNAL OF APPLIED MECHANICS, Vol. 44, pp. 424–430.

Crafter, E. C., Heise, R. M., Horgan, C. O., and Simmonds, J. G., 1993, "The Eigenvalues for a Self-Equilibrated, Semi-Infinite, Anisotropic Elastic Strip," ASME JOURNAL OF APPLIED MECHANICS, Vol. 60, pp. 276–281.

Durban, D., and Stronge, W. J., 1992, "Diffusion of incremental loads in prestrained bars," *Proceedings of the Royal Society of London*, Vol. A439, pp. 583–600.

Eshelby, J. D., Read, W. T., and Shockley, W., 1953, "Anisotropic elasticity with applications to dislocation theory," *Acta Metallurgica*, Vol. 1, pp. 251–259.

Fadle, J., 1941, "Die Selbstspannungs-Eigenwertfuncktionen der quadratischen Scheibe," *Ingenieur-Arch.*, Vol. 11, pp. 125–148.

Filon, L. N. G., 1903, "On an approximate solution for the bending of a beam of rectangular cross-section under any system of load, with special reference to points of concentrated or discontinuous loading," *Transactions of the Royal Society of London*, Vol. A201, pp. 63–155.

Gerhardt, T. D., and Liu, J. Y., 1983, "Orthotropic beams under normal and shear loading," *ASCE Journal of Engineering Mechanics*, Vol. 109, No. 2, pp. 394–410.

Horgan, C. O., 1972, "On Saint-Venant's principle in plane anisotropic elasticity," *Journal of Elasticity*, Vol. 2, pp. 169–180.

Johnson, M. W., Jr., and Little, R. W., 1965, "The semi-infinite elastic strip," *Quarterly of Applied Mathematics*, Vol. 22, No. 4, pp. 335–344.

Lekhnitskii, S. G., 1968, *Anisotropic Plates*, translated from the second Russian edition by S. W. Tsai and T. Cheron, Gordon and Breach Science Publishers, New York.

Matemilola, S. A., Stronge, W. J., and Durban, D., 1995, "Diffusion rate for stress in orthotropic materials," ASME JOURNAL OF APPLIED MECHANICS, Vol. 62, pp. 654–661.

Meleshko, V. V., 1995, "Equilibrium of elastic rectangle: Mathieu-Inglis-Pickett Solution revisited," *Journal of Elasticity*, Vol. 40, pp. 207–238.

Papkovitch, P. F., 1941, "The questions of the theory of bending of thin elastic plates," *Prikl. Matematika i Mekhanika*, Vol. 5, pp. 359–374.

Stroh, A. N., 1958, "Dislocations and cracks in anisotropic elasticity," *Philosophical Magazine*, Vol. 3, pp. 625–646.

Sullivan, J. L. and Van Oene, H., 1986, "An elasticity analysis for the generally and specially orthotropic beams subjected to concentrated loads," *Composites Science and Technology*, Vol. 27, pp. 133–155.

Tarnopol'skii, Y. M., and Kincis, T., 1985, *Static Test Methods for Composites*, Van Nostrand Reinhold, New York (translated by G. Lubin).

Timoshenko, S. P., and Goodier, J. N., 1970, *Theory of Elasticity*, McGraw-Hill, New York.

Ting, T. C. T., 1988, "Some identities and the structure of $\mathbf{N}_i$ in the Stroh formalism of anisotropic elasticity," *Quarterly of Applied Mathematics*, Vol. 46, pp. 109–120.

Wang, M. Z., Ting, T. C. T., and Yan, G., 1993, "The anisotropic elastic semi-infinite strip," *Quarterly of Applied Mathematics*, Vol. 51, No. 2, pp. 283–297.

Whitney, J. M., 1985, "Elasticity analysis of orthotropic beams under concentrated loads," *Composites Science and technology*, Vol. 22, pp. 167–184.

Wu, K.-C., 1991, "Explicit crack-tip fields of an extending interface crack in an anisotropic bimaterial," *International Journal of Solids and Structures*, Vol. 27, pp. 455–466.

Wu, K.-C., and Chiu, Y.-T., 1995, "The Elastic Fields of A Dislocations in An Anisotropic Strip," *International Journal of Solids and Structures*, Vol. 32, pp. 543–552.

APPENDIX

In this Appendix $\mathbf{v}^{(0)}$ in Eq. (29) is derived.

The derivation to be followed requires the knowledge of the structures of some matrices discussed here. The matrices $\mathbf{N}_1$ and $\mathbf{N}_3$ defined by Eqs. (8) and (10), respectively, can be expressed explicitly in terms of the reduced elastic compliances $\hat{S}_{ij}$ given by

$$\hat{S}_{ij} = S_{ij} - \frac{S_{i3}S_{3j}}{S_{33}}, \quad (A1)$$

where S_{ij} are the contracted notation for the elastic compliances. The explicit expressions are (Ting, 1988)

$$\mathbf{N}_3 = -\frac{1}{\Theta}\begin{bmatrix} \hat{S}_{55} & 0 & -\hat{S}_{15} \\ 0 & 0 & 0 \\ -\hat{S}_{15} & 0 & \hat{S}_{11} \end{bmatrix}, \quad (A2)$$

$$\mathbf{N}_1 = -\begin{bmatrix} r_6 & 1 & s_6 \\ r_2 & 0 & s_2 \\ r_4 & 0 & s_4 \end{bmatrix}, \quad (A3)$$

$$\Theta = \hat{S}_{11}\hat{S}_{55} - (\hat{S}_{15})^2 > 0,$$
$$r_i = (-\hat{S}_{55}\hat{S}_{1i} + \hat{S}_{15}\hat{S}_{5i})/\Theta \quad (i = 6, 2, 4),$$
$$s_i = (\hat{S}_{15}\hat{S}_{1i} - \hat{S}_{11}\hat{S}_{5i})/\Theta \quad (i = 6, 2, 4). \quad (A4)$$

Let

$$\mathbf{N}_3^{(n)} = \mathbf{B}\mathbf{P}^n\mathbf{B}^T + \bar{\mathbf{B}}\bar{\mathbf{P}}^n\bar{\mathbf{B}}^T. \quad (A5)$$

where $n = 1, 2, \ldots$ and $\mathbf{P}$ is the diagonal matrix with p_1, p_2, and p_3 as the diagonal elements. By Eq. (A5) the nth-derivative of $\mathbf{G}_3(\omega, 2)$ with respect to ω at $\omega = 0$, denoted by $\mathbf{G}_3(0, 2)^{(n)}$, is related to $\mathbf{N}_3^{(n)}$ by

$$\mathbf{G}_3(0, 2)^{(n)}(0) = (2i)^n \mathbf{N}_3^{(n)}, \quad n = 1, 2, \ldots . \tag{A6}$$

Since by Eq. (18)

$$\mathbf{G}_3(0, 2) = \mathbf{0}, \tag{A7}$$

$\Delta_i(0) = 0$, $i = 1, 2, 3$. Differentiating Eq. (31) with respect to ω and setting $\omega = 0$ gives

$$2i\mathbf{N}_3\mathbf{q}_i(0) = \Delta_i'(0)\mathbf{q}_i(0) \quad i = 1, 2, 3. \tag{A8}$$

By Eq. (A2), Eq. (A8) yields $\Delta_1'(0) \neq 0$, $\Delta_2'(0) = 0$ and $\Delta_3'(0) \neq 0$ with the corresponding eigenvectors given by

$$\mathbf{q}_1(0) = \psi_1\mathbf{e}_1 + \psi_3\mathbf{e}_3,$$
$$\mathbf{q}_2(0) = \mathbf{e}_2,$$
$$\mathbf{q}_3(0) = \psi_1\mathbf{e}_3 - \psi_3\mathbf{e}_1, \tag{A9}$$

where ψ_1 and ψ_3 are constants such that $\psi_1^2 + \psi_3^2 = 1$. Equation (37) is given by the sum of the eigenfunctions associated with Δ_1 and Δ_2 as evaluated by Eq. (35) with $m = 1$. It can be shown that $\Delta_2''(0) = 0$ and

$$\mathbf{q}_2'(0) = i\mathbf{e}_1. \tag{A10}$$

Furthermore,

$$\Delta_2'''(0) = -i\,\frac{4\hat{S}_{55}}{\Theta} \tag{A11}$$

$$\Delta_2^{(4)}(0) = 0 \tag{A12}$$

$$\Delta_2^{(5)}(0) = 32i\left\{(\mathbf{N}_3^{(3)})_{11} - \frac{5}{2}\frac{\hat{S}_{55}}{\Theta} + \frac{5i}{6}\left[\hat{S}_{11}(\mathbf{N}_3^{(2)})_{11}^2 + \hat{S}_{55}(\mathbf{N}_3^{(2)})_{31}^2 + 2\hat{S}_{15}(\mathbf{N}_3^{(2)})_{11}(\mathbf{N}_3^{(2)})_{31}\right]\right\} \tag{A13}$$

and

$$\mathbf{q}_2''(0) = -\frac{2}{3\Theta}\begin{bmatrix} -2\hat{S}_{55}\hat{S}_{16} + \hat{S}_{15}\hat{S}_{56} + \hat{S}_{15}\hat{S}_{54} \\ -3\Theta/2 \\ 2\hat{S}_{15}\hat{S}_{54} - \hat{S}_{55}\hat{S}_{14} - \hat{S}_{55}\hat{S}_{56} \end{bmatrix}. \tag{A14}$$

The vector $\mathbf{v}_b^{(0)}$ give by Eq. (38) is obtained by Eq. (35) with $m = 3$.

D. N. Alleyne

M. J. S. Lowe

P. Cawley

Department of Mechanical Engineering,
Imperial College,
London SW7 2BX, U.K.

The Reflection of Guided Waves From Circumferential Notches in Pipes

The reflection of the $L(0, 2)$, axially symmetric guided elastic wave from notches in pipes is examined, using laboratory experiments and finite element simulations. The results show that the reflection coefficient of this mode is very close to a linear function of the circumferential extent of the notch, and is a stronger function of the through thickness depth of the notch. The motivation for the work was the development of a technique for inspecting chemical plant pipework, but the study addresses the nature of the reflection function and has general applicability.

1 Introduction

The authors are working on a project whose ultimate aim is to develop a guided wave testing technique for the inspection of pipework in chemical plant, the target being to detect any areas of corrosion larger than $3T \times 3T$ in area and $T/2$ deep where T is the pipe wall thickness. The technique is to work on insulated pipe in the 50–300 mm bore diameter (nominal 2–12 inch) range and an inspection range of at least 15 m from the transducer position is required.

Many researchers starting with Worlton (1957) have investigated the use of Lamb waves for the inspection of plate-like structures and there has also been a considerable amount of work on their use in the inspection of pipes and tubing (see, for example, Silk and Bainton, 1979; Böttger et al., 1987a, b; Ditri et al., 1992, Duncumb and Keighley, 1987; Brook et al., 1990; Mohr and Höller, 1976; Thompson et al., 1972; Alers, 1994). Unfortunately Lamb wave testing is complicated by the existence of at least two modes at any given frequency. In practice, it is difficult to generate a single, pure mode so the received signal generally contains more than one mode, and the proportions of the different modes present is modified by mode conversion at defects and other impedance changes. The modes are also generally dispersive, which means that the shape of a propagating wave changes with distance along the propagation path. This makes interpretation of the signals difficult and also leads to signal-to-noise problems since the peak amplitude in the signal envelope decreases rapidly with distance if the dispersion is strong. Long-range Lamb wave testing is most likely to be successful if a single mode is excited in a nondispersive region (Alleyne and Cawley, 1992a).

These problems are particularly acute in pipe testing since at a given frequency many more modes exist in a pipe than in a plate of similar thickness. Figure 1 shows the group velocity dispersion curves over the frequency range 0–100 kHz for a 152-mm bore diameter (nominal 6-inch schedule 40) steel pipe with a wall thickness of 7 mm. The curves were calculated using a general-purpose computer program which was developed by the authors (Lowe, 1995). It predicts the dispersion curves and mode shapes of flat or cylindrical structures with arbitrary numbers of layers. In cylindrical systems there may be an integer (n) number of wavelengths around the circumference, $n = 0, 1, 2, 3 \ldots,$. When $n = 0$ the system is axially symmetric and when $n > 0$ the propagating waves have components in both the circumferential and axial directions. The modes are labelled $L(0, m)$, $T(0, m)$, and $F(n, m)$ in accordance with, for example, Silk and Bainton (1979), where n and m are integers and L, T, and F relate to longitudinal, torsional, and flexural type modes, respectively. There are 50 modes in the frequency range up to 100 kHz: $-L(0, 1)$, $L(0, 2)$; $T(0, 1)$; $F(n, 1)$, $n \le 23$; $F(m, 2)$, $m \le 15$; $F(k, 3)$, $k \le 9$. Figure 1 shows all these modes, though the diagram is too crowded for them all to be labeled. The form of the dispersion diagram for a 76-mm bore diameter (nominal 3-inch) pipe with a wall thickness of 5.5 mm is very similar to that for the 152-mm (nominal 6-inch) pipe except that there are fewer $F(n, m)$ modes in the frequency range below 100 kHz; the velocities of the $L(0, 1)$ and $L(0, 2)$ modes in the frequency range around 70 kHz are almost identical in the two pipes.

The $L(0, 2)$ mode in the frequency range around 70 kHz is very attractive to use for long-range testing since it is practically nondispersive and is also the fastest mode, which means that it will be the first signal to arrive at the receiver and so can readily be separated by time-domain gating. Its mode shape is similar to that of the s_0 mode in plates at low-frequency-thickness products, the particle motion being predominantly axial and the strain being roughly uniform through the pipe wall. It is therefore well suited to the detection of corrosion which may initiate at either surface of the pipe.

Alleyne and Cawley (1996a) reported the development of a dry coupled piezoelectric transducer system for the excitation of the axially symmetric $L(0, m)$ modes in pipes. It comprises a ring of piezoelectric elements which are clamped individually to the pipe surface. Each transducer element has a dimension of 3.2 mm in the circumferential direction and the elements impart a force to the pipe wall in the axial direction. Each element is faced with a thin brass or steel shim to protect it from wear and is backed with tungsten loaded epoxy contained in a tufnol housing. The completed unit is coupled to the pipe by pressing down on the top of the tufnol housing. The number of elements in the ring should be greater than n where $F(n, 1)$ is the highest order flexural mode whose cut-off frequency is within the bandwidth of the excitation signal. The excitation signal used in the tests reported here was a 10-cycle 70 kHz toneburst modulated by a Hanning window. This has an upper 40 dB downpoint at 84 kHz so the highest order flexural mode at this frequency must be considered. In the 76-mm (nominal 3-inch) pipe, the highest order mode with a cutoff frequency below 84 kHz is $F(11, 1)$, while in the 152-mm (nominal 6-inch) pipe it is $F(20, 1)$. In the tests reported here, rings of 16

Contributed by the Applied Mechanics Division of THE AMERICAN SOCIETY OF MECHANICAL ENGINEERS for publication in the ASME JOURNAL OF APPLIED MECHANICS.

Discussion on the paper should be addressed to the Technical Editor, Professor Lewis T. Wheeler, Department of Mechanical Engineering, University of Houston, Houston, TX 77204-4792, and will be accepted until four months after final publication of the paper itself in the ASME JOURNAL OF APPLIED MECHANICS.

Manuscript received by the ASME Applied Mechanics Division, Sept. 11, 1996; final revision, May 6, 1998. Associate Technical Editor: V. K. Kinra.

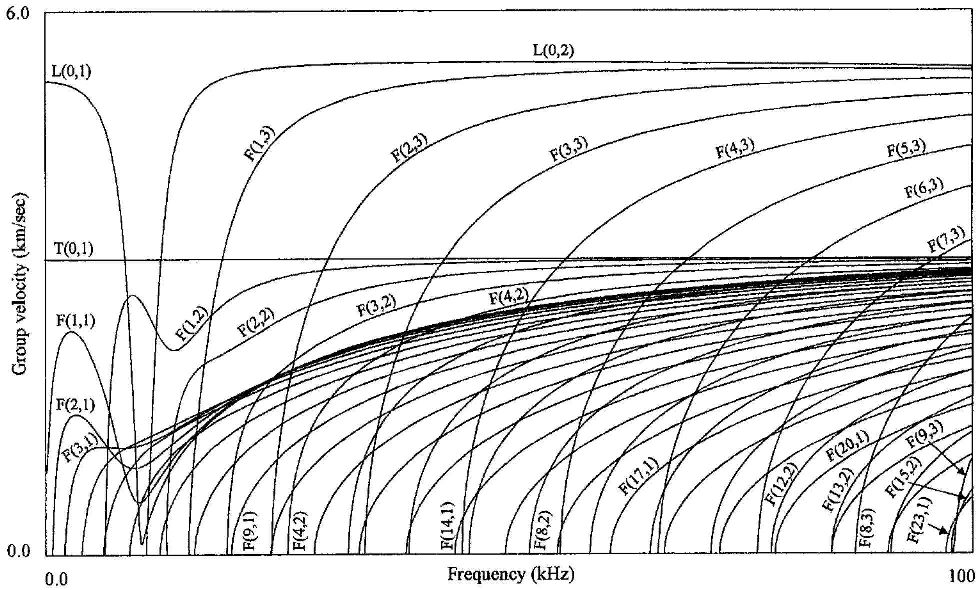

Fig. 1 Group velocity dispersion curves for 152-mm bore diameter (nominal 6-inch schedule 40), 7-mm wall thickness steel pipe

and 32 elements were used on the 76-mm and 152-mm pipes, respectively. This gave the possibility of operating at center frequencies higher than 70 kHz if this proved to be desirable.

Ideally, the transducer system would only excite and receive the $L(0, 2)$ mode. If the ring has enough elements and is perfectly symmetric, it will not generate or receive the flexural modes, and the direction of the stresses generated in the pipe is not appropriate for the excitation of torsional modes. However, the $L(0, 1)$ mode will be generated and received along with $L(0, 2)$. It may be possible to remove the $L(0, 1)$ mode by adjusting the length of the transducer elements and/or by employing multiple rings of transducers. However, Fig. 1 shows that the velocity of the $L(0, 2)$ mode is approximately twice that of the $L(0, 1)$ mode, so in a simple pipe system with a limited number of reflectors, it is straightforward to separate the signals corresponding to the two modes in the time domain.

This paper describes a quantitative study of the reflection of the $L(0, 2)$ mode from circumferential notches in pipes, using precise laboratory experiments and numerical simulations. The aim of the work was to investigate the nature of the reflection function. Therefore, while the motivation was the development of an inspection technique for industrial pipework, the work reported here has much wider relevance to the understanding of the scattering of guided waves in cylinders. Consideration of the specific practical issues for the exploitation of the technique for inspection of industrial pipework, together with the results of site trials, are reported elsewhere (Alleyne, Lowe, and Cawley, 1996).

The ultimate aim of the project is the detection of corrosion patches around three times the pipe wall thickness in diameter. In typical chemical plant pipework, this corresponds to a diameter of about 20 mm. The wavelength of the $L(0, 2)$ mode at a frequency of 70 kHz is approximately 80 mm. It was therefore decided to focus the study on defects whose axial extent is substantially smaller than the wavelength. A machined notch with an axial extent of only four percent of the $L(0, 2)$ wavelength was used for all of the experiments, so that the sensitivity of the reflections to the depth and circumferential extent could be studied without varying the axial extent. The use of a machined notch also allows for much better control of the dimensions than would be possible with simulated corrosion patches, thereby enabling a precise study of reflectivity to be undertaken.

The influence of the axial extent of a notch or corrosion patch on the strength of the reflection is not studied here but is worthy of brief discussion. Previous work on the transmission of the s_0 Lamb mode across a part-thickness notch (Alleyne and Cawley, 1992b) showed that the transmission coefficient is insensitive to the axial extent of the notch provided that this is much less than the wavelength. Alleyne and Cawley also found experimentally (1996b) that the strength of reflection of the $L(0, 2)$ mode from a part-thickness notch in a pipe is not altered much when the notch is ground out into a trough of the same depth, again provided that the axial extent is much smaller than the wavelength. This implied that results of studies using notches could be considered to be representative for small corrosion patches. However, recent modeling work has indicated that there is in fact some sensitivity of the reflection coefficient to the axial extent: the reflection of $L(0, 2)$ has been found to be sensitive to the axial extent of a part-through notch but has been found to be insensitive to the axial extent of a part-circumference through-wall notch. It is intended to present work on the influence of the axial extent of notches on the reflectivity in a future paper.

2 Test Setup

Tests were done on both 76-mm bore diameter (nominal 3-inch), 5.5-mm wall thickness and 152-mm bore diameter (nominal 6-inch), 7-mm wall thickness steel pipes to determine quantitatively the reflection sensitivity of the $L(0, 2)$ mode to a notch of constant depth as a function of circumferential extent, and a notch of constant circumferential extent as a function of its depth. The pipes which were used were 2.6 m long, a single ring of transducers being clamped to the pipe at one end as shown in Fig. 2. Notches were machined 0.9 m from the end remote from the transducer ring using a 3.2-mm diameter slot drill cutter. The cutter axis was aligned to lie on a radial axis of the pipe, and the notches were extended by rotating the pipe about its own axis. During tests the pipe was rested on steel "vee" blocks, earlier studies (Alleyne and Cawley, 1996b, 1997) having shown that the reflection from supports of this type was very small.

The instrumentation which was used is shown in Fig. 2. An arbitrary function generator (LeCroy 9101) delivered the excitation signal to an ENI 240L power amplifier whose output was sent to the transducer ring, the individual transducers in the ring being connected in parallel. The same transducers were used as receivers, a diode bridge circuit (Owens, 1980) being

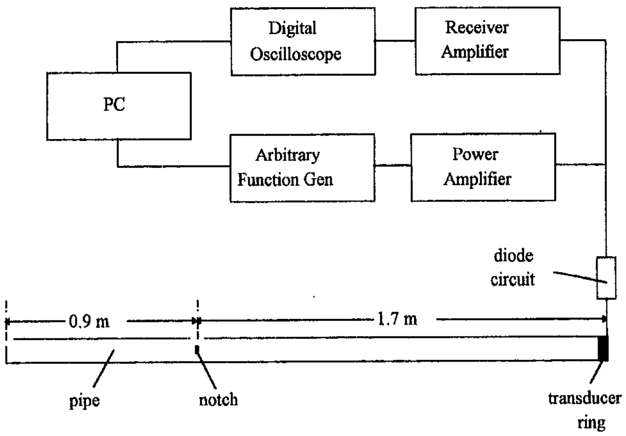

Fig. 2 Schematic diagram of equipment

connected between the ring and the power amplifier to isolate the receiver amplifier from the large-amplitude excitation signals. The received signal was amplified and transferred to a digital oscilloscope (LeCroy 9400) for digital capture, and then to a PC for processing and display. In order to improve the signal-to-noise ratio, 200 successive response signals were captured by the digital oscilloscope and averaged. In all cases, the signal output by the arbitrary function generator was a 10-cycle 70 kHz toneburst modulated by a Hanning window. The voltage output by the power amplifier was about 140 V peak-peak and the receiver amplifier gain was typically set to 20 dB.

Experiments were conducted on four separate pipes, using the following notches: (a) a notch of 50 percent depth with varying circumferential extent in a 76-mm (nominal 3-inch) pipe; (b) a through-thickness notch with varying circumferential extent in a 76-mm pipe; (c) a notch of short circumferential extent (11 percent) with varying depth in a 76-mm pipe; and (d) a notch of short circumferential extent (five percent) with varying depth in a 152-mm (nominal 6-inch) pipe. In each case the transducers remained fixed to the pipe throughout the experiment, including while the notch was being machined.

3 Experimental Results

Figures 3(a) and 3(b) show the time histories of the responses from the 76-mm (nominal 3-inch) pipe with a 2.75-mm deep notch (50 percent of the wall thickness) when the notch extended 18 mm (7.5 percent of the circumference) and half way around the pipe circumference, respectively. The duration of the test was sufficiently long to include the response of the pipe after the reflection of the $L(0, 2)$ mode from the notch and the end of the pipe. The initial signal in Fig. 3(a) is due to the response of the rudimentary diode bridge circuit to the excitation pulse; this has been gated out in Fig. 3(b) where only the reflected signals are shown. When $t < 1200$ μs the response is just that of the reflected $L(0, 2)$ mode from the notch and from the end of the pipe; the $L(0, 1)$ mode is produced on excitation and on reflection from the notch, but the time base is not sufficiently long for it to be seen.

The reflection coefficient for the notch was obtained by dividing the amplitude of the reflection from the notch by a reference measurement: the reflection from the end of the pipe when the notch was not present. For this experimental setup, only the $L(0, 2)$ and $L(0, 1)$ modes can exist when there is no notch. The deformation shape of the $L(0, 1)$ mode through the wall thickness is antisymmetric about the midwall (it consists of wall bending) whereas the shape of the $L(0, 2)$ mode is symmetric (axial extension). Conversion from one to the other can only occur at asymmetric features such as part-through notches and does not occur at the end of the pipe which was machined

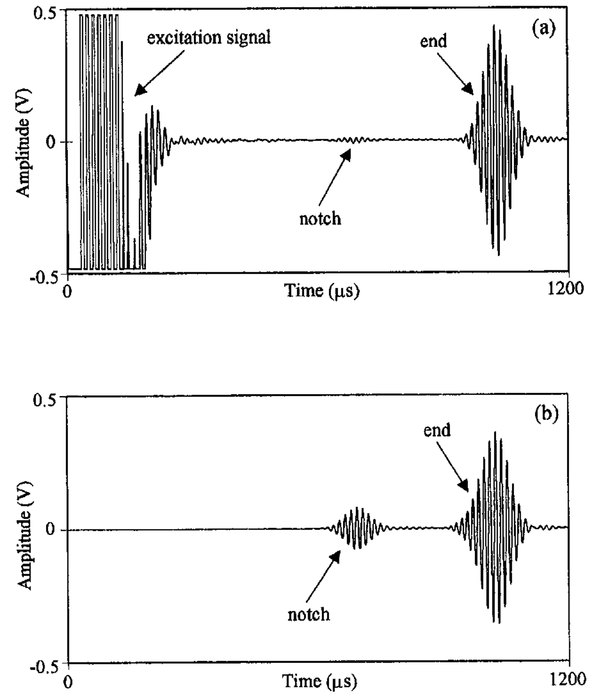

Fig. 3(a) Time history of the response measured at the end of the 76-mm (nominal 3-inch) pipe when a notch 2.7 mm deep extended over 18 mm (6.5 percent) of the circumference; (b) when the notch extended over half the circumference

square to the axis, so the reference measurement is in fact an $L(0, 2)$ signal of the same magnitude as the incident signal. This has also been confirmed experimentally. The reflection coefficients do therefore represent the division of the reflected $L(0, 2)$ mode by the incident $L(0, 2)$ mode. The division was carried out in the frequency domain.

Figure 4 shows the reflection coefficient from notches half the wall thickness deep which extended over 5, 10, 15, 20, 25, 30, 40, 50, 60, 70, 80, 90, and 100 percent (the symmetric case) around the circumference of the 76-mm (nominal 3-inch) pipe as a function of frequency. The results show that the amplitudes of the individual reflected signals are a weak function of frequency (the amplitude of the reflected signal increasing slightly with frequency) in the frequency range 60–85 kHz. There is a monotonic increase in the amplitude of the reflection coefficient with increasing notch extent, a notch 2.75 mm deep extending over the full circumference producing a reflection of about 34 percent of the amplitude of the incident $L(0, 2)$ mode.

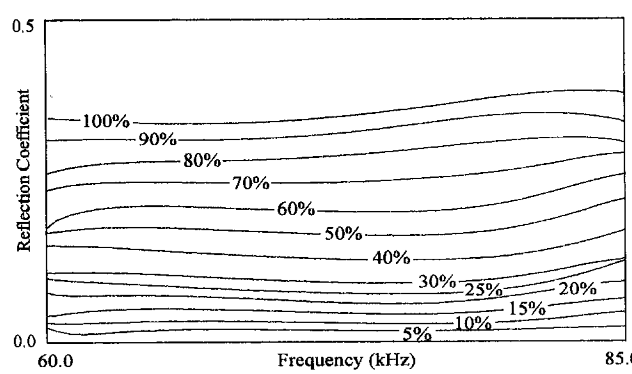

Fig. 4 The measured reflection coefficient of the $L(0, 2)$ mode for a half wall thickness deep notch in a 76-mm bore diameter (nominal 3-inch), 5.5-mm wall thickness pipe as a function of frequency. The different curves correspond to different notch circumferential extents which are expressed as a percentage of the total pipe circumference.

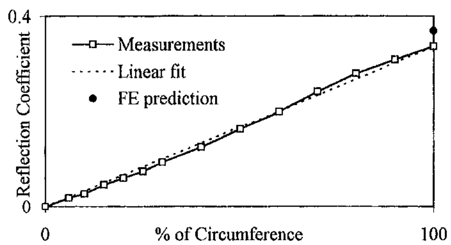

Fig. 5 Measured amplitude of the reflection coefficient for a half wall thickness deep notch in a 76-mm (nominal 3-inch) pipe at 70 kHz as a function of the percentage circumferential extent. Finite element prediction also shown for comparison.

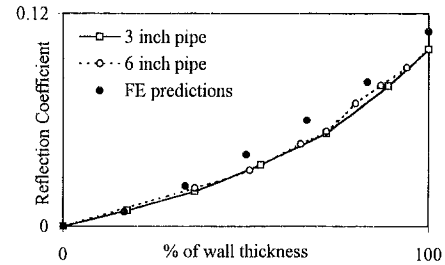

Fig. 7 Measured amplitude of the reflection coefficient at 70 kHz as a function of the notch depth on the 76-mm (nominal 3-inch) and 152-mm (nominal 6-inch) pipes for a notch extending over 11 percent of the circumference. The experimental results on the 76-mm pipe were done with a notch extending over 11 percent of the circumference; the notch in the 152-mm pipe extended over five percent of the circumference and the reflection coefficients shown have been scaled accordingly. Finite element predictions also shown for comparison.

Figure 5 shows the reflection coefficient of the $L(0, 2)$ mode at a frequency of 70 kHz as a function of the circumferential extent of the notch. This shows that the amplitude of the reflected signal is a roughly linear function of the circumferential extent of the notch. Figure 6 shows the corresponding result when the notch extended over the full pipe thickness. Again the reflection coefficient increases linearly with circumferential extent, and in this instance a notch extending over the full circumference (so detaching the section of pipe beyond the notch) gives 100 percent reflection.

Figure 7 shows the reflection coefficient of the $L(0, 2)$ mode for the notch covering 11 percent of the circumference of the 76-mm (nominal 3-inch) pipe as a function of notch depth (expressed as a percentage of wall thickness). Also shown are the corresponding results for the 152 mm (nominal 6-inch) pipe. The experiments on the 152-mm pipe were on a notch which extended over only five percent of the circumference, compared with 11 percent for the notch in the 76-mm pipe. The results of Figs. 5 and 6 show that the reflection coefficient from a notch of a given depth is directly proportional to its circumferential extent. Therefore, in order to compare the results of the 76-mm and 152-mm pipes, the reflection coefficients measured on the 152-mm pipe were multiplied by 11/5 (the ratio of the circumferential extents of the notches in the two pipes). Figure 7 shows that if this is done, the curves for the two pipe diameters are almost coincident, demonstrating that the factors affecting the reflection coefficient are the circumferential extent of the notch, expressed as a fraction of the total circumference, and its depth, expressed as a fraction of the wall thickness. The curves of Fig. 7 show that the reflectivity rises rapidly with depth when the depth is over 50 percent of the wall thickness, but that the rate of increase is modest at small depths.

The measurement accuracy in the experimental results is not easy to quantify but can be discussed briefly. With 8-bit analogue to digital conversion and 200 averages, the instrumentation error in the measurement of each received signal is expected to be better than one percent and is not of concern. More significant is the potential for errors due to variation of the pipe wall thickness around the circumference (by up to ten percent) and variation of the strength of coupling of the transducers to the pipe over the duration of the experiment. The latter is an important consideration because the reference measurement which was used in the calculation of each reflection coefficient could only be made at the start of the experiment, before starting to machine the notch. It should also be recognized that good results from a manual experiment involving large numbers of transducers and measurements relies on a great deal of experimental care, and a lot of time was spent on minimizing the sources of error and on checking the repeatability of measurements. It is therefore not possible to state numerical error bounds on the reported results, but in the judgement of the authors the error is likely always to be better than ten percent and typically very much better (two to three percent).

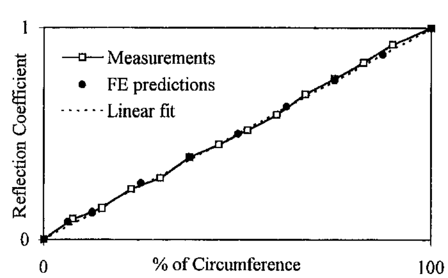

Fig. 6 Curves corresponding to Fig. 5 when notch extends over full wall thickness. Finite element predictions also shown for comparison.

4 Predictions

4.1 Finite Element Study. A full finite element analysis of the interaction of guided waves with discrete defects requires a three-dimensional solid model which, though possible, is computationally intensive. However, there are important cases of three-dimensional problems which are amenable to representative analysis using simplified spatial domains. For example, Alleyne and Cawley (1992b) have studied the interaction of Lamb waves with defects in flat plates using plane-strain models. These models represent sections through the plates and are relevant for long notches which are oriented normal to the direction of the incident waves. In the context of the notched pipes studied in this work it has been possible, using simplified yet accurate finite element models, to provide a clear demonstration of the relationships between reflection coefficient and notch extent. All of the modeling was performed using the program Finel, developed at Imperial College (Hitchings, 1994).

The relationship between the reflection coefficient and the circumferential extent of a through-thickness notch was studied using a three-dimensional membrane finite element model, illustrated schematically in Fig. 8(a). Membrane elements offer a very much simpler alternative to solid models, and their use in this circumstance can readily be justified. Around the frequency at which the experiments were performed, the $L(0, 2)$ mode has a plateau on its dispersion curve, the velocity being very close to that of the s_0 mode at very low frequency in a flat plate. Indeed, as discussed earlier, these two modes are extremely similar. The displacement mode shapes of $L(0, 2)$ in a 76-mm (nominal 3-inch) pipe at 70 kHz are shown in Fig. 9. They were calculated using the same program which was used to calculate the dispersion curves in Fig. 1. The axial displacement is almost constant through the wall thickness and the radial displacement varies almost linearly through the wall thickness. These displacement shapes are consistent with the shapes of a plate acting in plane stress and responding to a membrane stress, behavior which is described properly by membrane finite elements. The asymmetry of the radial displacement further indi-

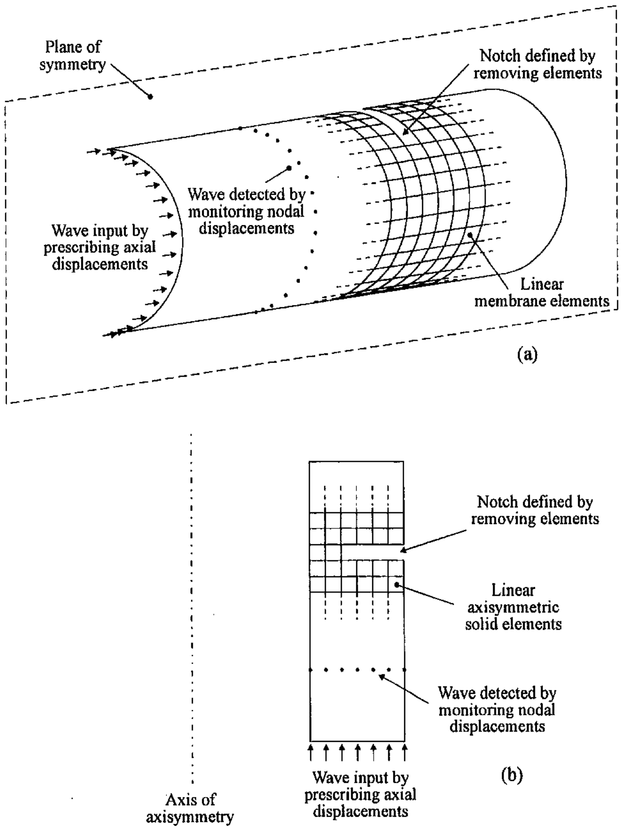

Fig. 8 Finite element spatial representation of notched pipes; (*a*) membrane model of through-thickness notch which extends over part of the circumference; (*b*) axisymmetric model of part-through notch which extends over full circumference

cates slight "breathing" motion in the pipe, and again this is adequately included in a membrane model by circumferential membrane action. The exclusion of bending behavior in the elements conveniently avoids the propagation of the unwanted $L(0, 1)$ mode which is characterized by local bending of the pipe wall. Additionally the computation time is reduced because of the absence of rotational degrees-of-freedom at the nodes. This simplification does not compromise the predictions of mode conversion at the notch because conversion from $L(0, 2)$ to $L(0, 1)$ is only expected where there is geometric asymmetry through the wall thickness (such as at a part-through notch); it should not occur at a through-thickness notch.

The model represented half of the circumferential extent of a 1.2-m length of pipe, assuming one plane of symmetry. A mesh of identically sized linear quadrilateral membrane elements was used, with 32 elements around the 180-deg circumference of the model. The element axial length was 3.2 mm, corresponding to about 25 elements per wavelength, well above the threshold of eight elements per wavelength which the authors have found from experience to be a good limit for accurate modeling. Material damping is minimal in practice and was ignored in the model. A 5-cycle 70 kHz toneburst in a Hanning window was chosen for the input. The toneburst was applied as a sequence of prescribed displacements in the axial direction of the pipe, the same sequence being applied concurrently at all of the nodes around the circumference at one end of the pipe. Explicit marching in the time domain was employed, assuming a diagonal mass matrix. The maximum time step which satisfies stability for an explicit marching scheme is given by L/C, where L is the element length and C is the wave speed of the fastest wave present (Bathe, 1982). In practice the authors have found a limit of 0.8 L/C to be sensible. This was satisfied here by choosing a constant time step of 0.4 μsec. The detection of the reflected waves was achieved simply by monitoring the axial displacements at all of the nodes around the circumference. As with the experiments, the summation of these signals ensured that the reflected $L(0, 2)$ mode was detected and any mode-converted flexural modes were ignored.

Initial tests without a notch demonstrated excellent agreement of the phase velocity predicted by the finite element model with that expected from the dispersion curve. A series of analyses incorporating through-thickness notches was then conducted. In order to satisfy the symmetry which was implied by modeling only half of the pipe, half of the circumferential extent of each notch was defined, starting from the plane of symmetry. The notches were introduced very simply by removing elements in the model, as shown in Fig. 8(*a*). Since the axial length of the notch was 3.2 mm, identical to the axial length of the elements, it was necessary only to remove one row of elements.

In fact, as discussed earlier, it has been found that the axial extent of through-wall notches has negligible influence on the strength of the reflections, provided that the axial length is short compared to the wavelength. Models incorporating notches of zero axial length, created simply by disconnecting adjacent elements, give almost the same results as those shown here. This is consistent with the findings of Owen and Fawkes (1983) that the manner in which the detail of a crack tip is modeled is unimportant in a global sense: a finite element model yields accurate global behaviour whether a crack is modeled using crack-tip elements or simply by disconnecting adjacent elements; inaccuracy only remains in the shape of the stress field very close to the notch roots. Therefore it is to be expected that when the notch width (the axial length) is small compared to the notch length (the circumferential length) then the precise shape of the notch will have little influence on the mode reflectivity. We therefore use the terms "notch" and "crack" synonymously here.

As with the experimental measurements, the reflection coefficient for the notched pipe was calculated by dividing the amplitude of the reflection from the notch by the amplitude of the reflection from the free end of the unnotched pipe. The results are shown in Fig. 6 for comparison with the experimental measurements. They demonstrate excellent agreement between the predictions and the experiments, and confirm once again a linear relationship between reflection coefficient and circumferential extent of the notch.

A second series of finite element analyses was conducted using an axisymmetric model to predict the reflection coefficient from a part-through notch which extended over the full circumference of the pipe. The model is illustrated schematically in Fig. 8(*b*). A mesh of identically sized linear quadrilateral axisymmetric solid elements was used, with six elements through the wall thickness of the pipe, and an axial element length of 1.6 mm. This model was therefore capable of predicting the propagation and mode conversion of any axially symmetric modes whose displacements are in the radial-axial plane, includ-

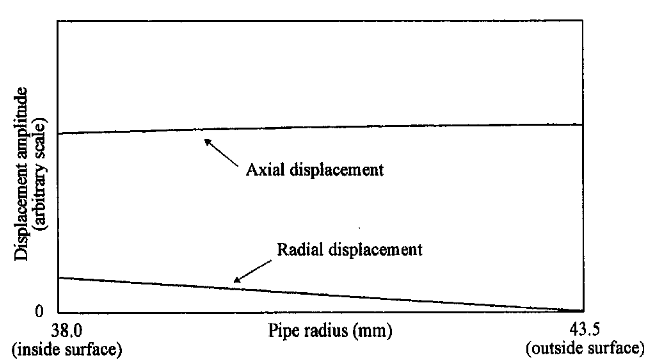

Fig. 9 Predicted displacement mode shapes of $L(0, 2)$ mode at 70 kHz

ing both $L(0, 1)$ and $L(0, 2)$. The $L(0, 1)$ mode involves local bending of the pipe wall and is described by displacements which are antisymmetric about the midwall. The excitation was limited to the $L(0, 2)$ mode by applying the tone-burst equally at all of the nodes through the thickness at one end of the pipe. The solution was obtained using the same time marching scheme as for the membrane model, this time with a time-step size of 0.125 μsec. Then on reception the $L(0, 2)$ mode was detected without any other mode-converted modes by summing the axial displacements at all of the nodes through the thickness. A range of depths of a circumferential notch on the outside of the pipe was studied, again by removing elements, and the reflection coefficient was calculated in the manner described for the membrane model. As discussed earlier, it was found that strength of reflection is sensitive to the axial length of the part-through notch: the results obtained by disconnecting adjacent elements differ, though not greatly, from those obtained by removing elements. Unlike the through-wall part-circumference notch, in which the axial length is much smaller than the notch length (the circumferential length), in this case the axial length is comparable to the notch length (the radial length).

The results of the axisymmetric analysis can only be compared directly with experiment for the single case of a 50 percent depth notch around the full circumference of the pipe, shown in Fig. 5. The predicted value of 0.37 agrees reasonably well with the experimental point but is some eight percent higher. One possible reason for this is circumferential variation of the pipe wall thickness: since the reflection function is not linear with the notch depth, this would affect the strength of the reflection even if the average thickness was correct. Another reason for the difference could be an error in the measurement of the reference signal from the end of the pipe which was taken before machining the notch. Unfortunately, after machining the notch, it was not possible to repeat the reference measurement and so this error could not be investigated further without repeating the whole experiment. An error in the reference signal would have a linear influence on all of the reflection coefficients. Thus the experimental measurements in Fig. 5 would still lie on a straight line, but would all be scaled down by a constant.

Although the finite element models could not include a notch which extends for only part of the circumference at the same time as only part of the thickness, there is a very reasonable argument to infer the reflection coefficients for any such cases from the predictions which have been reported. Since the reflection coefficient is linear with respect to the circumferential extent, both for a full-thickness notch and a half-thickness notch, it is reasonable to assume that it is linear with circumference for any depth of notch. The reflection coefficient for a notch of any depth and any circumferential extent is then found simply by scaling the results of the axisymmetric models according to the circumferential extent of the notch. Thus, taking the case of the experimental measurements for the part-through notch covering 11 percent of the circumference of a 76-mm (nominal 3-inch) pipe, the reflection coefficients are predicted simply by scaling the axisymmetric values by the factor 0.11. These scaled results are presented in Fig. 7, together with the experimental measurements, showing a good match to the experimental trend of nonlinear variation with notch depth and reasonable quantitative agreement. It is not known why the experimental values are a little lower than the predictions but it seems to be due to a factor which affects all of the measurements. When the notch is completely through the wall (100 percent depth) the experimental reflection coefficient is about ten percent lower than expected both from the finite element results and from the experimental findings in Fig. 6. A possible reason for this could be variation of the thickness of the pipe wall around the circumference of the pipe.

4.2 Fracture Mechanics Approach. In a recent publication, Ditri (1994) presented a thorough theoretical derivation of reflection and transmission at a circumferential through-thickness crack in a pipe, based on the S-parameter technique due to Auld (1990). An example which he discussed in order to illustrate the technique used a pipe which was similar in proportions to the 76-mm (nominal 3-inch) pipe considered here, and he concluded that the reflection coefficient of $L(0, 2)$ was related to the circumferential extent of the crack in a cubic manner. This conclusion differs markedly from the present findings of a linear relationship, and it is important to explain it. It is also interesting to examine why the relationship should be found in practice to be approximately linear rather than a more complicated function.

It is the belief of the authors that the technique which was derived by Ditri is correct in principle: if the crack-opening profile is known, then the method should yield the correct reflections and transmissions. However, it is believed that the example which was discussed was erroneous because it was assumed incorrectly that the wavelength of the incident wave was long enough for the quasistatic approximation. This led to an inaccurate function for the crack-opening profile. There are two aspects to consider.

First, the function which was presented for the crack-opening profile showed the maximum opening displacement to be proportional to the square of the crack length (Yoo and Pan, 1992). This is a stronger relationship than that for a crack in a flat plate (Tada et al., 1985) because it takes into account the additional opening of the crack due to bending of the pipe: A tensile load applied at a long distance from the crack causes a lateral movement of the whole pipe in the vicinity of the crack so that the line of action of the force passes through the remaining ligament, and thus the pipe bends near the crack even though the remote load is purely tensile. However, the bending of the pipe can only take place in combination with lateral body movement (movement of the whole pipe in the direction normal to its axis) near the location of the crack. Such lateral movement could not be significant in the case of the $L(0, 2)$ mode under consideration because of the short duration and wavelength of the passing wave cycle. This was demonstrated by performing a finite element study of a flat plate, modeled using membrane elements, with a centrally positioned through-thickness notch. The s_0 Lamb mode was excited such that it was normally incident at the notch. The reflection of s_0 from such notches is closely representative of the behaviour which is studied in the pipe, except that there is no possibility of bending, yet the reflection coefficient showed the same linear relationship as that which was found from the pipe models. Therefore the extent of any pipe bending with lateral body motion of the pipe is insignificant. Furthermore, the restriction of body movement at the test frequency is well illustrated by the severely limited extent of "breathing" of the pipe wall. "Breathing" is the radial movement of a pipe wall due to circumferential strain when the pipe is subjected to axial load. If the pipe was breathing freely then the circumferential stress would be zero, so the circumferential strain would be equal to the radial strain. Consequently the radial motion of the midwall of the pipe would be about seven times (i.e., the ratio of radius to thickness) larger than the change in the wall thickness. Referring to the mode shape for radial displacements, in Fig. 9, the displacement varies linearly through the wall thickness and is approximately zero at the outside surface. Therefore the motion of the midwall is only half of the change in the wall thickness.

The second difficulty with the function for the crack-opening profile is that the wavelength is not long enough with respect to the notch circumferential length in either the present example of the 76-mm (nominal 3-inch) pipe or in the example presented by Ditri (1994). The static crack-opening profile is valid only for a remote stress which remains constant as the crack opens. In the case of the 76-mm pipe, the 70 kHz wave has a wavelength of about 80 mm, equal to one diameter of the pipe. The axial stress varies over the wavelength and only has the same sign in a 40-mm length, equal to the pipe radius. Clearly, there-

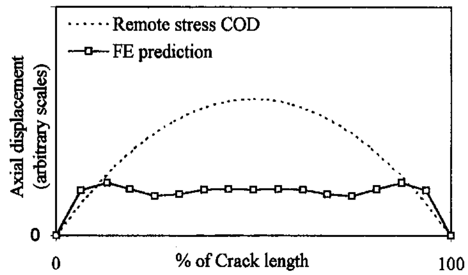

Fig. 10 Crack-opening displacement shape for a full-thickness notch extending over 50 percent of the circumference of a 76-mm (nominal 3-inch) pipe. Comparison of shape in finite element prediction with shape given by remote-stress fracture mechanics analysis.

fore, the wavelength is rather short with respect to all but the shortest circumferential notches and the stress state cannot be approximated as a remote stress.

A better approximation to the problem may be to consider it as if the wavelength was very much smaller than the notch length. Thus the majority of the wavefront which is incident at the notch sees the notch simply as a free surface from which it reflects totally. This approach is supported by predicted notch opening profiles which were monitored during the finite element analyses using the membrane models. The opening profile for the notch which extends over 50 percent of the circumference is shown in Fig. 10. The profile is of the axial opening displacements of the nodes along the notch face just at the moment when a peak of a wave is reflecting from the notch. Since the finite element model exploited symmetry about the center of the notch, the plotted displacements are perfectly symmetric in this respect. For comparison, the crack-opening profile for a pipe with a circumferential crack and remote static load (Ditri, 1994; Yoo and Pan, 1992) is also plotted, showing its markedly different shape. The finite element profile can be seen to approximate to a constant value for most of the length of the notch, as would be expected for reflection from a free surface. The reflection amplitude of the $L(0, 2)$ mode is given by the axially symmetric part of the reflected field, that is the average of the axial displacement around the circumference of the pipe (the remainder of the displacement field makes up the mode conversion to other modes). Thus the assumption of perfect reflection from a free surface at the notch would lead to the observed linear relationship between reflection coefficient and notch length.

5 Conclusions

A quantitative study of the reflection of the $L(0, 2)$ mode from notches in pipes has been carried out. It has been shown that the reflection coefficient of this mode is very close to a linear function of the ratio of the circumferential extent of the notch to the pipe circumference, and is a stronger function of the ratio of the through thickness depth of the notch to the pipe wall thickness, detectability increasing rapidly as the depth increases beyond 50 percent of the wall thickness. Good agreement has been obtained between the results on the 76-mm bore diameter (nominal 3 inch), 5.5-mm wall thickness and 152-mm bore diameter (nominal 6-inch), 7-mm wall thickness pipes, indicating that the defect detectability on one pipe size may readily be inferred from results on other sizes.

Good agreement between finite element predictions and the experimental results has been obtained, and the need for care in choosing crack-opening displacement functions if a fracture mechanics approach is to be used to predict the reflection coefficients has been discussed.

Acknowledgment

This experimental investigation was carried out under the U.K. government Industrial Measurement Systems LINK Initiative. The industrial collaborators were The Welding Institute, ICI, Esso Engineering and Phoenix Inspection Systems.

References

Alers, G. A., 1994, "Application of special wave modes to industrial inspection problems," *Proc. 1994 ASME Winter Meeting*, Symposium on Wave Propagation and Emerging Technologies, Chicago, IL.

Alleyne, D. N., and Cawley, P., 1992a, "Optimisation of Lamb wave inspection techniques," *NDT&E International*, Vol. 25, pp. 11–22.

Alleyne, D. N., and Cawley, P., 1992b, "The interaction of Lamb waves with defects," *IEEE Trans Ultrasonics, Ferroelectrics and Frequency Control*, Vol. 39, pp. 381–397.

Alleyne, D. N., and Cawley, P., 1996a, "The excitation of Lamb waves in pipes using dry coupled piezoelectric transducers," *J. NDE*, Vol. 15, pp. 11–20.

Alleyne, D. N., and Cawley, P., 1996b, "The effect of discontinuities on the long range propagation of Lamb waves in pipes," *J. Process Mechanical Engineering, Proc I Mech E*, Part E, Vol. 210, pp. 217–226.

Alleyne, D. N., and Cawley, P., 1997, "Long range propagation of Lamb waves in chemical plant pipework," *Materials Evaluation*, Vol. 55, pp. 504–508.

Alleyne, D. N., Lowe, M. J. S., and Cawley, P., 1996, "The inspection of chemical plant pipework using Lamb waves: defect sensitivity and field experience," *Review of Progress in Quantitative NDE*, Vol. 15, D. O. Thompson and D. E. Chimenti, eds., Plenum Press, New York, pp. 1859–1866.

Auld, B. A., 1990, "Acoustic fields and waves in solids," Edition 2, Robert E. Krieger, Malabar, FL.

Bathe, K.-J., 1982, *Finite Element Procedures in Engineering Analysis*, Prentice-Hall, Englewood Cliffs, NJ.

Böttger, W., Schneider, H., and Weingarten, W., 1987a, "Prototype EMAT system for tube inspection with guided ultrasonic waves," *Nuclear Eng. and Design*, Vol. 102, pp. 356–376.

Böttger, W., Schneider, H., and Weingarten, W., 1987b, "Tube inspection with an EMAT using guided ultrasonic waves," *Proc 4th European NDT Conference*, Vol. 4, Pergamon Press, Tarrytown, NY, pp. 2305–2313.

Brook, M. V., Ngoc, T. D. K., and Eder, J. E., 1990, "Ultrasonic inspection of steam generator tubing by cylindrical guided waves," *Review of Progress in Quantitative NDE*, Vol. 9, D. O. Thompson and D. E. Chimenti, eds., Plenum Press, New York, pp. 243–249.

Ditri, J., 1994, "Utilization of guided elastic waves for the characterization of circumferential cracks in hollow cylinders," *J. Acoust. Soc. Am.*, Vol. 96, pp. 3769–3775.

Ditri, J. J., Rose, J. L., McNight, W. J., and Carr, F. T., 1992, "A guided wave inspection technique for nuclear steam generator tubing," *13th World Conf. on NDT*, Brazil, pp. 191–195.

Duncumb, A. C., and Keighley, D. M., 1987, "Inspection of titanium tubing using ultrasonic Lamb waves generated by an electromagnetic acoustic transducer," *Proc 4th European NDT Conference*, Vol. 4, Pergamon Press, Tarrytown, NY, pp. 2228–2236.

Hitchings, D., 1994, *FE77 User manual*, Imperial College, London.

Lowe, M. J. S., 1995, "Matrix techniques for modelling ultrasonic waves in multilayered media," *IEEE Trans Ultrasonics, Ferroelectrics and Frequency Control*, Vol. 42, pp. 525–542.

Mohr, W., and Höller, P., 1976, "On inspection of thin walled tubes for transverse and longitudinal flaws by guided ultrasonic waves," *IEEE Trans Sonics and Ultrasonics*, Vol. SU-23, pp. 369–374.

Owen, D. R. J., and Fawkes, A. J., 1983, *Engineering fracture mechanics: Numerical methods and applications*, Pineridge Press, Swansea, UK.

Owens, E. J., 1980, "Automatic transmit-receive switch uses no relays but handles high power," *J. Acoust. Soc. Am.*, Vol. 68, pp. 712–713.

Silk, M. G., and Bainton, K. F., 1979, "The propagation in metal tubing of ultrasonic wave modes equivalent to Lamb waves," *Ultrasonics*, Vol. 17, pp. 11–19.

Tada, H., Paris, P. C., and Irwin, G. R., 1985, *The stress analysis of cracks handbook*, Edition 2, Paris Productions Inc. and Del Research Corp., St. Louis, MO.

Thompson, R. B., Alers, G. A., and Tennison, M. A., 1972, "Application of Direct Electromagnetic Lamb Wave Generation to Gas Pipeline Inspection," *Proc IEEE Ultrasonics Symposium*, Boston, Oct. 4–7, pp. 91–94.

Worlton, D. C., 1957, "Ultrasonic testing with Lamb waves," *Non-Destructive Testing*, Vol. 15, pp. 218–222.

Yoo, S. H., and Pan, J., 1992, "Approximate crack opening displacement solutions for long circumferential cracks in pipes subjected to bending and tension," ASME *Journal of Pressure Vessel Technology*, Vol. 114, pp. 178–180.

C. Semler
Mem. ASME

H. Alighanbari
Mem. ASME

M. P. Païdoussis[1]
Fellow ASME

Department of Mechanical Engineering,
McGill University,
817 Sherbrooke Street West,
Montreal, Quebec H3A 2K6,
Canada

A Physical Explanation of the Destabilizing Effect of Damping

In this paper, the destabilization due to small damping of the follower force system, known as Beck's problem, and of the cantilevered pipe conveying fluid system, two nonconservative systems, is considered. Instead of looking for a mathematical explanation, e.g., the evolution of the eigenvalues with different parameters, a more "physical" explanation is provided. It is shown that it is of particular interest to focus on the different modes of vibration and to understand how they evolve when damping is varied. Also, based on energy considerations, the key factors influencing stability are highlighted, e.g., the phase angles between the different coordinates. In the case of the pipe conveying fluid, the methodology developed and insight gained help explain the presence of "jumps" in the stability curves, that are known to play an important role in the linear and nonlinear dynamics of this system.

1 Introduction

Physical systems that exhibit paradoxical behavior have always fascinated the research community, and dissipation, or energy loss, which may make a stable system unstable belongs to that category. Phenomena involving destabilization due to damping have been observed for long time. For instance, fluid mechanicians know of Reynolds' two hypotheses, formulated in 1883, stating that (a) in some situations the inviscid fluid may be unstable, while the viscous one is stable, so that the effect of viscosity is purely stabilizing; and (b) in other situations the inviscid fluid may be stable while the viscous one unstable, indicating that viscosity is destabilizing (Drazin and Reid, 1981). Earlier still, in the general area of mechanics, Thomson and Tait (1879) showed that a statically unstable system which has been stabilized by gyroscopic forces could be destabilized by the introduction of small damping forces (Crandall, 1995). In aeronautics the destabilizing effect of damping has also been known for a long time, in relation to aircraft flutter, and has been carefully studied (Done, 1963; Nissim, 1965). In some cases, physical explanations have been provided, such as the emergence of frequency coalescence due to damping. Nevertheless, destabilization by dissipation is sufficiently perplexing to deserve further attention (Païdoussis, 1998).

An attempt to explain the phenomenon was made by Benjamin (1963) via an *activation energy* concept applied to a one-degree-of-freedom mechanical system subject to fluid flow. However, this concept is not acceptable for a real one-degree-of-freedom system and is not easily applicable to the problem of a cantilevered pipe conveying fluid. Gregory and Païdoussis (1966) were among the first to demonstrate that damping can *destabilize* cantilevered pipes conveying fluid, and this was also discussed, in the context of Beck's problem, by Nemat-Nasser et al. (1966) and Bolotin and Zhinzher (1969), but no attempt was made to provide a physical explanation of the phenomenon. Recently, Seyranian (1990) and Seyranian and Pedersen (1995) tried to provide a mathematical explanation by looking at the asymptotic behaviour and the interaction between the eigenvalues, but again no physical insight was given. It is the main purpose of this paper to provide such insight.

In general terms, the destabilizing effect of damping is known to be due to the presence of "negative energy modes" in the undamped system, i.e., modes that extract energy from the energy reservoir of the system, and these modes need an energy sink in order to be excited; damping often plays the role of the sink, thus destabilizing the system. This has been described in terms of negative energy waves in plasma physics (Craik, 1985) and in hydrodynamics (Triantafyllou, 1992).

For cantilevered pipes conveying fluid, Païdoussis and Li (1993) and Païdoussis (1996, 1998) have noted the importance of the "S-shaped" discontinuities or "jumps" in the stability curves of flow velocity (u) versus mass parameter (β), showing that the critical values of β at which these discontinuities occur are frequently associated with, or are seperatrices for, distinctly different dynamical behavior. An attempt to explain these discontinuities will be made here.

The paper is divided into two parts: in the first one, a detailed analysis of a two-degree-of-freedom articulated system subjected to a follower force is undertaken, to explain the possible destabilizing effect of damping of a nonconservative system, and to develop a methodology easily applicable to the problem of a pipe conveying fluid, which is considered in the second part of the paper.

2 Follower Force System

2.1 Physical System. The system consists of two masses, $2m$ and m, interconnected by massless rigid bars of length L (Fig. 1(a)), the lower one of which is subjected to a follower force, P. The upper bar is supported through a torsional spring of stiffness k and a "rotational" dashpot of damping coefficient c_1. The two bars are interconnected through a spring of the same stiffness, k, and a dashpot defined by c_2. Motion is in a horizontal plane. Introducing the nondimensional time $\tau = t\sqrt{k/(mL^2)}$ and the following nondimensional parameters

$$\gamma_1 = c_1/\sqrt{kmL^2}\,, \quad \gamma_2 = c_2/\sqrt{kmL^2}\,, \quad p = PL/k, \qquad (1)$$

it can be shown that the nondimensional equation of motion is given by

$$\mathbf{M}\{\ddot{\phi}\} + \mathbf{C}\{\dot{\phi}\} + \mathbf{K}\{\phi\} = \mathbf{0},$$

$$\mathbf{M} = \begin{bmatrix} 3 & 1 \\ 1 & 1 \end{bmatrix}, \quad \mathbf{C} = \begin{bmatrix} \gamma_1 + \gamma_2 & -\gamma_2 \\ -\gamma_2 & \gamma_2 \end{bmatrix},$$

[1] To whom correspondence should be addressed.

Contributed by the Applied Mechanics Division of THE AMERICAN SOCIETY OF MECHANICAL ENGINEERS for publication in the ASME JOURNAL OF APPLIED MECHANICS.

Discussion on the paper should be addressed to the Technical Editor, Professor Lewis T. Wheeler, Department of Mechanical Engineering, University of Houston, Houston, TX 77204-4792, and will be accepted until four months after final publication of the paper itself in the ASME JOURNAL OF APPLIED MECHANICS.

Manuscript received by the ASME Applied Mechanics Division, Dec. 17, 1996; final revision, Feb. 11, 1998. Associate Technical Editor: J. T. Jenkins.

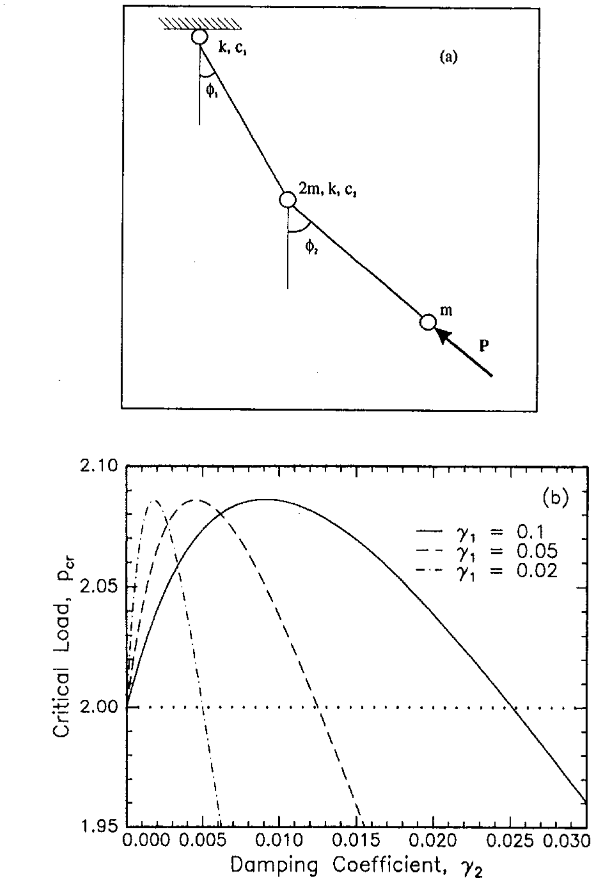

Fig. 1 (*a*) **Schematic of the articulated system and** (*b*) **variation of the critical load p_{cr} with γ_2 for three values of γ_1**

$$\mathbf{K} = \begin{bmatrix} 2-p & p-1 \\ -1 & 1 \end{bmatrix}. \tag{2}$$

Consequently, the system is completely defined by three parameters: the two nondimensional damping coefficients, γ_1 and γ_2, and the nondimensional follower force, p.

2.2 Dynamic Instability. It is well known that this system becomes unstable through a Hopf bifurcation if the follower force p exceeds a critical value p_{cr} that depends on both γ_1 and γ_2. This is due to the fact that the follower force renders the system *nonconservative,* since the direction of the force depends on the system response, which implies that the work done by p depends on the actual motion. In the absence of damping, the instability is due to the positive work done by the follower force during a cycle of oscillation. When damping is present, this work must be greater than the energy dissipated by the dashpots.

The critical value p_{cr} can be obtained by performing the eigenvalue analysis of Eq. (2), but for a two-degree-of-freedom system it can be found more easily via Routh's criteria; it can be shown that, in the presence of damping,

$$p_{cr} = \frac{4\gamma_1^2 + 33\gamma_1\gamma_2 + 4\gamma_2^2}{2(\gamma_1^2 + 7\gamma_1\gamma_2 + 6\gamma_2^2)} + \frac{1}{2}\gamma_1\gamma_2. \tag{3}$$

Figure 1(*b*) shows the variation of p_{cr} with γ_2 for three values of γ_1. It can be seen that the three curves are qualitatively similar: with increasing γ_2, p_{cr} first increases, reaches a maximum, and then decreases. This second, decreasing part of the curves illustrates the possible "destabilizing" effect of damping, discussed in the following section.

2.3 Effect of Damping. Since the stability behavior of the system is qualitatively similar for different values of γ_1, it is possible to focus on just one to explain the effect of damping. Thus, considering $\gamma_1 = 0.1$, it is seen that increasing γ_2 stabilizes the system when $\gamma_2 < 0.0095$, while destabilizing it for $\gamma_2 > 0.0095$; it should be mentioned that the stabilizing/destabilizing effect is *not* here defined vis-à-vis the critical value $p_{cr} = 2$ found for $\gamma_2 = 0$, but in a broader sense: Given a certain damping coefficient γ_2, if p_{cr} increases when γ_2 is increased, the damping is said to be "stabilizing," and if it decreases, it is said to be "destabilizing."

Consequently, the effect of damping for large values of γ_2 does not follow the usual pattern, which is to stabilize mechanical systems by dissipating energy. To explain this paradox, it is important to mention that damping not only dissipates energy but also plays an important role in defining the system response. Therefore, even though the energy dissipated in the dashpot increases as γ_2 is increased, the ability of the system to gain energy from the follower force may either be increased or decreased by altering the modal form of the oscillation. Finally, to clarify why sustained oscillations are possible even if dissipation of energy occurs, it is recalled that an "infinite" source of energy is available to maintain the follower force.

To illustrate the effect of damping on the vibration form let us consider the two modes of vibration for a particular set of parameters. Figure 2(*a*) shows the amplitude of the two articulations for the mode of vibration that is able to gain energy from the follower force. It can be seen that the amplitude of ϕ_2 is larger than that of ϕ_1, and that the phase angle between the two is very small. Figure 2(*b*) shows ϕ_1 and ϕ_2 for the mode that is not able to extract energy from p. In this case, the phase angle is much larger. It will be shown that if $\gamma_2 > 0.025$, this phase angle is even larger than $\pi/2$, the two angles thus appearing "out of phase." The mode displayed in Figs. 2(*a*), (*c*) that is able to extract energy from p will be referred to as the "unstable" mode, while that in Figs. 2(*b*), (*d*) represents the "stable" one. As will be seen in the next section, in the "unstable" mode, the configuration is such that the follower force p can do positive work on the system, while in the "stable" one, p does negative work. Furthermore, from the mode shapes shown in Figs. 2(*c*), (*d*), it is obvious that the motion in the stable mode is dominated by the angle between the two bars, $\phi_2 - \phi_1$, which is highly dependent on the damping coefficient γ_2. As will be seen, this is of major importance.

2.4 Energy Considerations. To quantify the energy dissipated by the dashpots and the work done by the follower force it is necessary to know the response of the system for any time τ, since the forces due to both dashpots and p are nonconservative. It is well known that for a *linear* two-degree-of-freedom system, the response for any initial condition can be computed if the response of the system is known in the two modes of vibration. Consequently, it is necessary to focus on these two modes. To find them, Eq. (2) is first transformed into first-order form by introducing the generalized vector, $\mathbf{x} = \{\phi_1, \phi_2, \dot{\phi}_1, \dot{\phi}_2\}^T$ such that $\dot{\mathbf{x}} = [A]\mathbf{x}$. Calculating the eigenvalues and the eigenvectors of $[A]$ and constructing an appropriate modal matrix $[P]$, it is possible to compute ϕ_1 and ϕ_2 at any time, in each mode of vibration (Païdoussis et al., 1997).

Of particular interest is the work done by the external force p on the system in each mode of vibration during a time interval $(0, \bar{\tau})$. It can be shown that this work is

$$W(\bar{\tau}) = \int_0^{\bar{\tau}} p\dot{\phi}_1 \sin(\phi_1 - \phi_2)d\tau. \tag{4}$$

Similarly, the energy dissipated by the two dashpots can be shown to be

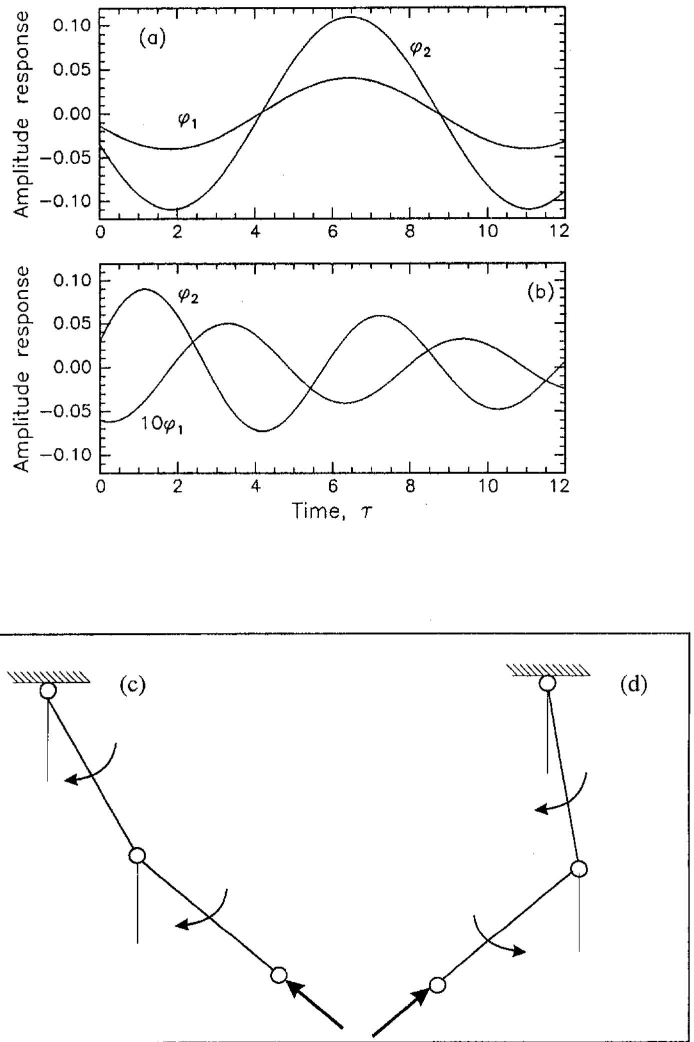

Fig. 2 Mode content of vibration for $\gamma_1 = 0.1$ and $\gamma_2 = 0.03$: (*a*) first mode, able to extract energy; (*b*) second mode of vibration (ϕ_1 has been multiplied by 10); (*c*), (*d*) shapes representing the system in (*a*) and (*b*), respectively

$$D(\bar{T}) = \int_0^{\bar{T}} [\gamma_1\dot{\phi}_1^2 + \gamma_2(\dot{\phi}_2 - \dot{\phi}_1)^2]d\tau. \qquad (5)$$

Then, the net energy gained by the system during a period T of the not necessarily neutrally stable oscillation is

$$\Delta E = W(T) - D(T). \qquad (6)$$

If $\Delta E > 0$ in one of the modes, the system gains energy in each cycle of oscillation and is unstable. The variation of ΔE, normalized with respect to the initial energy of the system, is shown in Fig. 3 for $p = 2$, as a function of γ_2. It is seen that $\Delta E > 0$ for $\gamma_2 > 0.025$, in agreement with the critical p, p_{cr}, in Fig. 1(*b*).

To gain a better understanding of the stability behavior, let us consider the system at its *neutrally stable state,* when $\Delta E = 0$, and both ϕ_1 and ϕ_2 are *purely periodic:*

$$\phi_1 = \sin(\omega\tau), \quad \phi_2 - \phi_1 = A\sin(\omega\tau - \theta). \qquad (7)$$

A represents the "amplitude ratio" between ϕ_1 and $\phi_2 - \phi_1$ and is assumed to be positive, and θ represents the phase difference. The reason for utilizing $\phi_2 - \phi_1$ is that, in view of Eqs. (4) and (5), it is a "natural" choice, resulting in simpler analysis. In order to obtain an analytical expression for $W(T)$, it is further assumed that ϕ_1 and ϕ_2 are small, so that $\sin(\phi_1 - \phi_2) \simeq \phi_1 - \phi_2$. This is possible since the problem is linear, so that only the relative amplitude is of importance. With this assumption, one obtains $\Delta E = pA\sin\theta - \omega(\gamma_1 + A^2\gamma_2) = 0$. Since the system is neutrally stable, necessarily $p = p_{cr}$ so that

$$p_{cr}\sin\theta = \omega(\gamma_1 + A^2\gamma_2)/A. \qquad (8)$$

Therefore, the right-hand side of Eq. (8) is positive, and it is clear that the existence of a *positive* p_{cr} is directly related to the sign of $\sin\theta$. However, the actual value of p_{cr} is related to different factors: the frequency of oscillation, ω, the phase angle, θ, the amplitude ratio, A, and the two damping coefficients γ_1 and γ_2. Therefore, for a constant γ_1, it is necessary to know the variation of these parameters with γ_2 in order to understand how p_{cr} varies with γ_2. Here, because of space limitations, only the evolution of the amplitude is shown; the variation of other key factors may be found in Païdoussis et al. (1997). It can be shown that, for the mode that becomes unstable, the phase angle is very small ($\theta \simeq 0.02$ deg) and varies almost linearly with γ_2. On the other hand, the variations of the amplitude ratio and of ω are not linear, but have parabolic shapes. This is also the case for the phase angle in the stable mode, which varies nonlinearly from 0.5 to 2.2 rad. Consequently, it is difficult to know a priori how p_{cr} varies with γ_2.

It is particularly interesting to examine the evolution of the right-hand side (rhs) of Eq. (8) with varying θ, since both terms play an important role in the stabilizing/destabilizing effect of

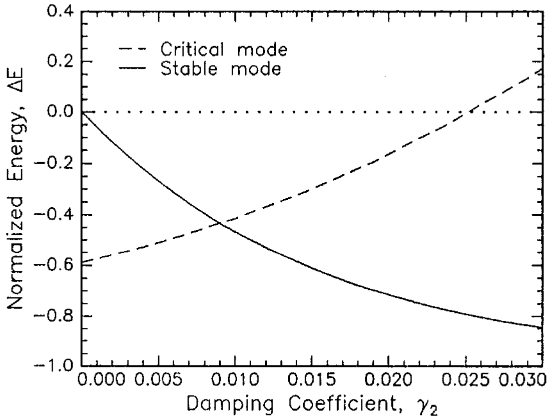

Fig. 3 Variation of the energy gained by the system in the two modes of vibration, normalized with respect to the initial energy, as a function of γ_2, for $\gamma_1 = 0.1$

γ_2. It can be shown (Païdoussis et al., 1997) that when γ_2 is small, rhs increases fast while the increase in θ is slow, implying that p_{cr} increases; for larger values of γ_2 ($\gamma_2 > 0.0095$), the increase of rhs becomes much slower, while the increase of θ remains the same, implying a decrease of p_{cr}.

It thus becomes clear that the phase angle θ plays an important role in the stability of the system, by having a large effect (i) on the value of p_{cr} and (ii) on its very existence. For example, despite the fact that the two modes of vibration for $\gamma_2 = 0.0095$ have the same frequency and the same generalized-coordinate amplitude ratio A, being therefore very similar, one of them is able to extract energy from p while the other one is not, simply because of the difference in phase angle. On the other hand, it is well known that damping has a big influence on the phase angle, which explains why it has such an important effect on stability.

For later comparison with the pipe problem, it is of interest to consider the form of Eq. (4) for small angles, when the integrand may be written as $p(\dot{\phi}_1\phi_1 - \dot{\phi}_1\phi_2)d\tau$. The first term is a complete differential and, for purely periodic motions, it vanishes when integrated over $(0, T)$; hence,

$$W(T) \simeq -\int_0^T p\phi_2\dot{\phi}_1 d\tau, \tag{9}$$

correct to third order in small angles. This shows that it is the lateral component of the follower force which does the nonconservative work.

Finally, the stabilizing/destabilizing effect of γ_2 can also be explained by looking at the relative amplitudes of motion of the two masses in the two modes of vibration, normalized with respect to the maximum amplitude of ϕ_2, $B = (\phi_2 - \phi_1)/\phi_2$. As shown in Fig. 4, when $0 \le \gamma_2 \le 0.0095$, B is greater in the unstable mode than in the stable one. But by its nature, γ_2 has a major effect when B is large, thus tending to reduce B. Therefore, in this region, by increasing γ_2 and keeping p constant, the unstable mode is reduced or suppressed, which means that γ_2 has a *stabilizing* effect. When $\gamma_2 > 0.0095$, B is larger in the stable mode, so that an increase of damping means a suppression of the *stable* mode, therefore leading to the opposite conclusion: More damping is *destabilizing.* Consequently, consideration of the relative amplitudes in the different modes is particularly useful in explaining the effects of damping on stability.

2.5 Conclusion. Despite the simplicity of the physical system, its stability characteristics proved to be rather complex; yet, the simplicity of the mathematical model allowed us to develop a general methodology for showing and explaining why damping can actually *destabilize* a stable system. It will be seen in the next section how this methodology can be used to examine the stability behavior of a pipe conveying fluid.

3 Pipe Conveying Fluid

3.1 Physical System. The system under consideration consists of a tubular cantilever of length L, mass per unit length m, flexural rigidity EI, and coefficient of Kelvin-Voigt damping a, conveying fluid of mass M per unit length, flowing in the pipe with axial velocity U. The pipe is clamped at its upstream end and free at the other, and it is assumed to oscillate in a horizontal plane.

For the linear system, the nondimensional equation of motion takes the particularly simple form

$$L(\eta) \equiv \alpha\dot{\eta}'''' + \eta'''' + u^2\eta'' + 2u\sqrt{\beta}\,\dot{\eta}' + \ddot{\eta} = 0, \tag{10}$$

where $(\ )^{\cdot} = \partial(\ )/\partial\tau$ and $(\ )' = \partial(\ )/\partial\xi$; $\eta(\xi, \tau)$ represents the lateral deflection of the pipe, u the nondimensional flow velocity, β a mass parameter, and α the coefficient of viscoelastic dissipation, all nondimensional, as defined below:

$$\xi = x/L, \quad \eta = y/L, \quad u = (M/EI)^{1/2}UL,$$

$$\tau = \left(\frac{EI}{m+M}\right)^{1/2}\frac{t}{L^2}, \quad \alpha = \left(\frac{EI}{m+M}\right)^{1/2}\frac{a}{L^2},$$

$$\beta = \frac{M}{m+M}. \tag{11}$$

Physically, in order of appearance, the terms in (10) are related to dissipation, flexural restoring forces, ''centrifugal'' or follower compressive forces proportional to u^2 ($MU^2(\partial^2 y/\partial x^2)$ in dimensional terms), Coriolis effects ($MU(\partial^2 y/\partial x\partial t)$ in dimensional terms), and inertia.

If there is no damping, the critical flow velocity can be obtained directly from the partial differential equation, but for convenience, the infinite-dimensional model is discretized by Galerkin's technique, with the cantilever beam eigenfunctions, $\phi_r(\xi)$, being used as a suitable set of base functions, and $q_r(\tau)$ representing the corresponding generalized coordinates; thus, $\eta(\xi, \tau) = \Sigma_{r=1}^{N} \phi_r(\xi)q_r(\tau)$, where N represents the number of modes used. Introducing $\{\mathbf{x}\} = \{\mathbf{q}, \dot{\mathbf{q}}\}^T$ of dimension $2N$, Eq. (10) can be transformed into a set of first-order ordinary differential equations,

$$\dot{\mathbf{x}} = [A]\mathbf{x} = \begin{bmatrix} 0 & [I] \\ -[K] & -[C] \end{bmatrix}\mathbf{x}, \tag{12}$$

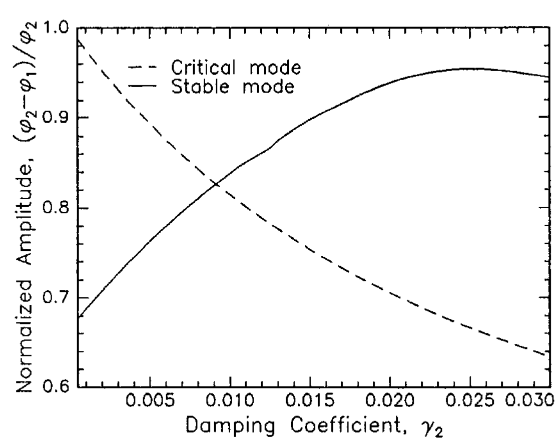

Fig. 4 Normalized amplitude $(\phi_2 - \phi_1)/\phi_2$ versus γ_2

where $[I]$, $[K]$, and $[C]$ are, respectively, the $N \times N$ identity, stiffness, and damping matrices. The stability of the system is determined by looking at the eigenvalues of $[A]$.

3.2 Dynamic Instability. As the follower force system, the *cantilevered* pipe conveying fluid is a nonconservative system that loses stability through a Hopf bifurcation if the flow velocity exceeds a critical value, u_{cr} (Benjamin, 1961; Gregory and Païdoussis, 1996). This instability is characterized by a pair of complex conjugate eigenvalues with a *zero* real part. The physical similarity to the follower force system is that the emerging jet at the free end of the cantilever gives rise to a follower-type reaction of magnitude MU^2, equivalent to P in Fig. 1(a). On the other hand, the pipe system is also subject to Coriolis-related damping. The instability occurs when the work done by the former overcomes that absorbed by both Coriolis and viscoelastic damping.

Typical stability boundaries representing the critical flow velocity as a function of the mass parameter β are shown in Fig. 5 for different values of damping and $N = 10$, which is sufficient to represent adequately the original system (Païdoussis, 1970). From this figure, two interesting remarks may be made.

Remark 1: Comparing the stability boundaries for $\alpha = 0$ and $\alpha \neq 0$, it is seen that damping stabilizes the system for $\beta < 0.29$, while it has a *destabilizing* effect for $\beta > 0.29$. The qualitative behavior of the pipe conveying fluid is thus very similar to the case of the follower force system described in Section 2.

Remark 2: A number of "jumps" can be observed when $\alpha = 0$; as will be seen, they are related to the emergence of successive modes, in a different sense to that envisaged in a previous investigation (Païdoussis, 1970).

3.3 Analysis. To prove that damping can be destabilizing, the effects of both α and β are considered, giving a measure of dissipative and Coriolis damping effects, respectively. Following the methodology developed previously, the amplitudes of the generalized coordinates $q_1, q_2, \ldots, q_N$ in the "critical" or "unstable" mode are computed. The reason for not considering the other modes is that they are highly damped, because of Coriolis effects. It should be mentioned that "modes" here signify *the modes of vibration* as usually defined in the literature; they are different from the zero-u "modes" of the cantilevered beam, i.e., the comparison functions, ϕ_r; in fact each mode of vibration involves a combination of the comparison functions.

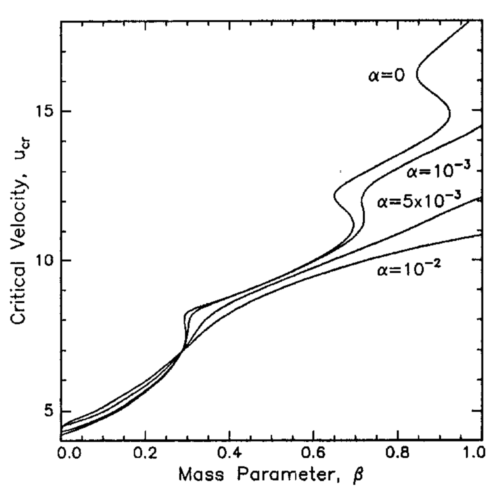

Fig. 5 Critical flow velocity u_{cr} versus the mass parameter β, for different values of α

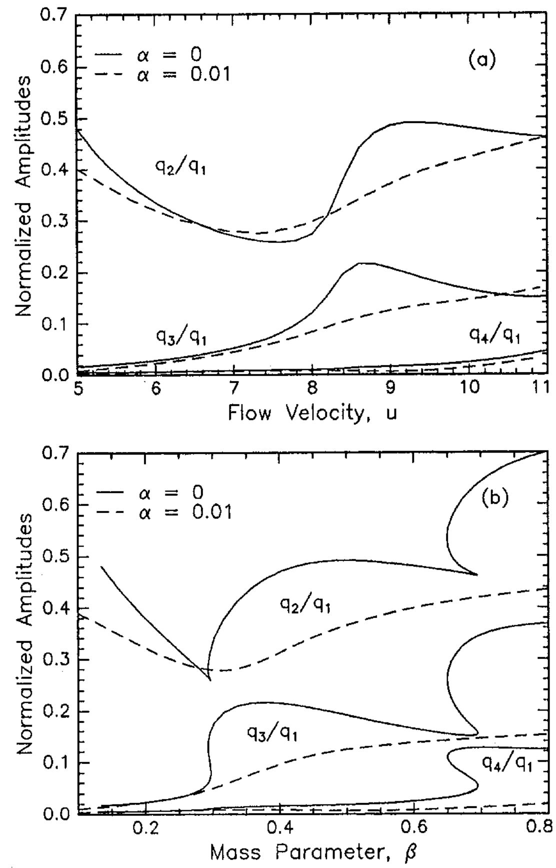

Fig. 6 Maximum amplitudes, q_2, q_3 and q_4, normalized with respect to q_{1max}, as a function of u and β, for two damping values

Introducing again an appropriate modal matrix $[P]$ and the change of variable $\mathbf{x} = [P]\mathbf{y}$ leads to N decoupled equations of the form

$$\begin{Bmatrix} \dot{y}_{p,1} \\ \dot{y}_{p,2} \end{Bmatrix} = \begin{bmatrix} \sigma_p & -\omega_p \\ \omega_p & \sigma_p \end{bmatrix} \begin{Bmatrix} y_{p,1} \\ y_{p,2} \end{Bmatrix}. \tag{13}$$

It is clear again that each set of equations represents a one-degree-of-freedom oscillator, σ_p and ω_p representing, respectively, the damping and frequency in each mode of vibration. Concentrating only on the mode for which $\sigma_p = 0$, the corresponding Eq. (13) can be solved easily, yielding the time response in the original coordinates. Then, the maximum amplitude of each coordinate q_r may be found for different parameters. Figure 6 shows the normalized amplitudes q_2, q_3, q_4 with and without damping as a function of u and β. It is seen that around $u \simeq 7.5$, the amplitude of q_2 reaches a minimum, while the amplitude of q_3 starts to increase sharply. It is noted that these variations with u are smooth, but when plotted versus β, as in Fig. 6(b), they become much more violent, generating "jumps." Moreover, when $\beta < \beta_{\text{jump1}}$, the third coordinate q_3 is very small, while it is significant after the jump. Therefore, the first conclusion drawn is that the third coordinate q_3 after the jump becomes more and more important when u and/or β increase.

Referring to Figs. 5 and 6, it is clear that q_3 has a "stabilizing" effect, since critical velocities increase very rapidly when q_3 starts to become effective. On the other hand, the damping coefficient α has a strong effect on the higher modes. This is reasonable from both physical and mathematical points of view, since the viscoelastic damping gives rise to a term $\alpha\lambda_i^4\dot{q}_i$ in the discretized equation, with λ_i representing the ith eigenvalue of the cantilevered beam. Consequently, because λ_i increases with the mode number, and because of the presence of the fourth power, damping tends to reduce the effect of the higher modes, while these higher modes become progressively more important as the mass parameter β is increased. Therefore, α and β have opposite effects on stability and it becomes obvious that α, suppressing the emergence of the third coordinate q_3 that stabilizes the system, can have a *destabilizing* effect.

Figure 6 also provides an explanation for the presence of the successive jumps observed in Fig. 5: These jumps are related to the emergence of substantial contributions of successive generalized coordinates q_r. For example, for $\alpha = 0$, the first jump around $\beta = 0.3$ is related to the emergence of q_3: q_3 is very small for smaller values of β and becomes increasingly more important after $\beta = 0.3$. To illustrate the effect of the number of modes, stability diagrams are constructed with a progressively higher number of modes in the Galerkin discretization. The results are shown in Fig. 7. It may be seen that, not only does the first jump around $\beta = 0.3$ not materialize with $N = 2$, while doing so with $N = 3$ or higher, but also $N = 4$ is required to obtain the second jump around $\beta = 0.7$, $N = 5$ to obtain the third one, and so on. This shows that the jumps are associated each time with the emergence of a new generalized coordinate.

From the discussion in the previous paragraph about damping, it is clear that damping tends to "kill" or annihilate the emergence of the higher q_i. In fact, by choosing appropriately the damping coefficient α, it is possible to eliminate the emergence of the successive generalized coordinates, and thereby to suppress the different jumps, as seen in Fig. 5. It has hence been proved again that the jumps are related to the emergence of higher modes that tend to stabilize the system (similarly to q_3 around the first jump). Therefore, if the damping is sufficiently high, e.g., $\alpha = 0.01$, because the higher mode cannot contribute, this "stabilization" cannot occur, which explains why the critical velocity u_{cr} is much smaller.

As a first conclusion, one might say that, similarly to the follower force system, the investigation of the relative amplitudes of the different generalized coordinates is particularly useful in understanding the effects of damping; this approach can also furnish an explanation for the appearance of the jumps. But again, energy considerations will help us illucidate other interesting characteristics. This is investigated next.

3.4 Energy Considerations. The dimensionless work done on the system by the forces contributing to Eq. (10) over a time interval $\overline{\tau}$ is

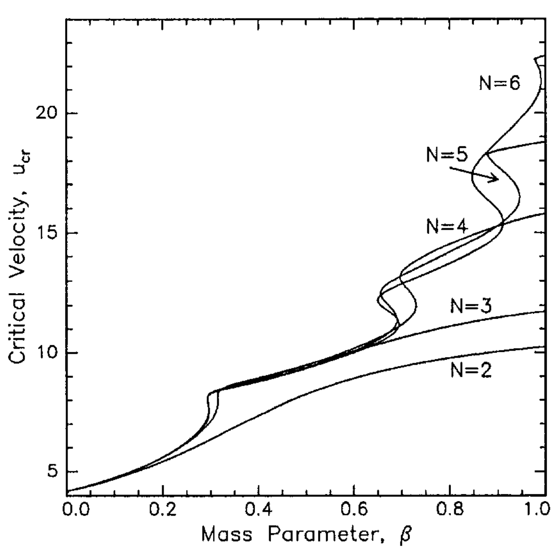

Fig. 7 Stability diagram u_{cr} versus β for Galerkin solutions with an increasing number of comparison functions, N

$$W(\overline{\tau}) = -\int_0^{\overline{\tau}}\int_0^1 L(\eta)\dot{\eta}\,d\xi d\tau = -\int_0^{\overline{\tau}} (u^2\dot{\eta}\eta' + u\sqrt{\beta}\dot{\eta}^2)|_0^1 d\tau$$
$$-\tfrac{1}{2}\int_0^1 (\eta''^2 - u^2\dot{\eta}'^2 + \dot{\eta}^2)|_0^{\overline{\tau}} d\xi - \int_0^{\overline{\tau}}\int_0^1 \alpha\dot{\eta}''^2 d\xi d\tau. \quad (14)$$

Henceforth, in contrast to the analysis of the follower force system, we shall consider the system to be in a *neutrally stable state* exclusively, when the motions are periodic. Then $\overline{\tau} = T$, where T is the period, the second integral on the right-hand side vanishes, and $\Delta E \equiv W(T) = 0$. Thus, we obtain

$$\Delta E = -\int_0^T u^2\dot{\eta}(1,\tau)\eta'(1,\tau)d\tau - \int_0^T u\sqrt{\beta}\dot{\eta}^2(1,\tau)d\tau$$
$$-\int_0^T\int_0^1 \alpha\dot{\eta}''^2(\xi,\tau)d\xi d\tau = 0, \quad (15)$$

or

$$W_{\text{centrif}}(T) - D_{\text{Coriolis}}(T) - D_{\text{damp}}(T) = 0, \quad (16)$$

where in the definition of the last two it was recognized that the corresponding integrals in (15) can only be positive, i.e., the Coriolis and viscoelastic terms can only dissipate energy. The first integral, however, can be negative if $\eta'(1,\tau)$ and $\dot{\eta}(1,\tau)$ have opposite signs over most of the period; hence, $W_{\text{centrif}}(T)$ can be positive, and the "centrifugal" or compressive tangential follower-force can supply energy to the pipe.

It is noted that Eq. (15) may also be obtained directly from Benjamin's (1961) statement of Hamilton's principle, in which case it is clear that $W_{\text{centrif}} - D_{\text{Coriolis}}$ is associated with the total nonconservative component of the reaction related to the exiting jet at the end of the cantilever.

Drawing a parallel with the work in Section 2.4, W_{centrif} is remarkably similar to the work done by p in Eq. (9), where again it is the *lateral* component of u^2, $u^2\eta'$, which does the nonconservative work; D_{Coriolis} corresponds to the work done by the dashpot γ_1 in Eq. (5) and D_{damp} to that by γ_2 in the same equation, in all cases only for the neutrally stable system.

Now, since the motion is periodic, similarly to Eq. (7), we take

$$q_r = A_r \sin(\omega\tau - \theta_r), \quad 1 \le r \le N. \quad (17)$$

Evaluating the different components in Eq. (15) using (17), a complicated expression relating the frequency ω, the relative amplitudes, A_r, and phases, θ_r, and the different parameters can be obtained. For example, when $N = 3$, it can be shown that $D_{\text{Coriolis}}/(4\pi u\sqrt{\beta}) = (A_1\cos\theta_1 - A_2\cos\theta_2 + A_3\cos\theta_3)^2 + (A_1\sin\theta_1 - A_2\sin\theta_2 + A_3\sin\theta_3)^2$ and $W_{\text{centrif}}/\pi u^2 = 13.6A_1A_2 \times \sin(\theta_1 - \theta_2) + 25.9A_1A_3\sin(\theta_3 - \theta_1) + 12.3A_2A_3 \times \sin(\theta_2 - \theta_3)$.

From these expressions and the computation of the different sources of energy, the following conclusions may be drawn: (i) even by considering only three modes of vibration ($N = 3$), it is difficult to estimate, even qualitatively, the effects of the different parameters, because of the complexity of the expressions involved; (ii) by increasing α, the energy dissipated increases, which is satisfactory from a physical point of view; (iii) the energy dissipated by damping is much smaller than the energy lost by the Coriolis forces, of the order of three percent to ten percent approximately; (iv) as in the follower force system, the critical velocity u_{cr} is sensitive to the phase differences, θ_r, which are highly dependent on damping. In particular, the phase differences between q_1 and q_2, and q_2 and q_3 are important in the neighborhood of the first jump; as seen in Fig. 8, very abrupt changes in $\sin(\theta_1 - \theta_2)$ and $\sin(\theta_2 - \theta_3)$ occur when $\beta \simeq 0.3$.

All these points explain that the destabilizing effect is *not* related to a decrease of energy dissipated (as may erroneously be thought) and that damping, even if it only dissipates a small amount of energy, can change the ability of the system to gain

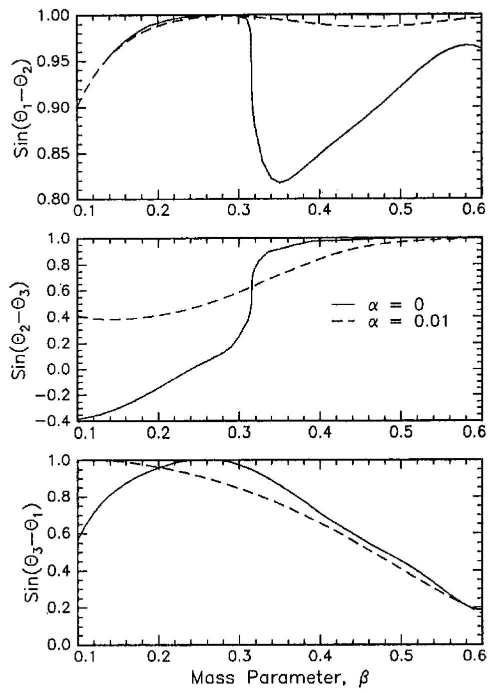

Fig. 8 Variation with β of the relative phase angles, sin $(\theta_r - \theta_s)$ for two damping values

energy from the fluid by modifying the system response. In particular, the phase differences between the different generalized coordinates q_r are important.

4 Conclusion

In this paper, the destabilization due to small damping in two nonconservative systems has been considered, and some physical insights have been gained.

In the case of Beck's problem, it has been shown that damping can *destabilize* the system if the configuration is such that the addition of damping decreases or suppresses the "stable" mode of vibration, which was then predominant. This is particularly evident in Fig. 4 where the relative amplitudes of the two modes of vibration clearly show which of the two modes is the largest. Hence, when the amplitude of the stable mode is smaller than that of the unstable one, damping *stabilizes* the system, and conversely. It has also been shown that the phase between the two angles, and its variation with damping, are very important in determining the stability of the system: at one point ($\gamma_2 = 0.0095$), the two modes have the same amplitude and the same frequency, but one of the modes is able to extract energy from the follower force while the other one is not.

The two-degree-of-freedom articulated system, despite its simplicity, displayed very interesting dynamical behavior, and helped develop a methodology to elucidate the dynamical behavior of the pipe conveying fluid. In this case again, the relative amplitude of the different generalized coordinates was of major importance. In particular, after the first "jump" occurring around $\beta \simeq 0.3$, it was shown that the third coordinate q_3 grew abruptly, and that it had a stabilizing effect. On the contrary, by its nature, viscoelastic damping had the tendency to annihilate the higher coordinates, so that the addition of damping had a *destabilizing* effect after the first jump. In that perspective, the explanation now seems rather straightforward.

The investigation on the effect of damping also helped explain the presence of the "jumps" in the stability diagram, Fig. 5: each jump is associated with the emergence of a new coordinate that is necessary to maintain the "right shape" that enables the pipe to extract energy from the fluid. Indeed, with the number of modes progressively increased, corresponding jumps could be observed. Furthermore, if damping is chosen such that the normally emergent mode is suppressed, the jump itself is suppressed. However, the reason for multiple solutions for certain values of β is not fully understood, mainly because of the complexity of the interaction between so many parameters. Nevertheless, it could be seen in the calculations that the phase angle plays a very important role in the emergence of the different coordinates; indeed, a very definite sequence occurs: prior to the first jump, $\theta_2 - \theta_3 \simeq \pi$; prior to the second, $\theta_3 - \theta_4 \simeq \pi$; and prior to the third one, it is $\theta_4 - \theta_5 \simeq \pi$—which is probably very important, see the expressions for W_{centrif} and D_{Coriolis}. Physically, once a new coordinate emerges, the other ones have to adjust themselves so that the pipe can still extract energy. Consequently, in the neighborhood of the jumps, if multiple solutions exist, it is to allow smooth changes in the modal shape of the pipe and because different combinations of the different generalized coordinates are possible to give the proper shape.

Acknowledgments

The authors express their appreciation to the Natural Sciences and Engineering Research Council of Canada and Le Fonds FCAR of Québec for their support; also to the two anonymous referees for bringing some additional and very useful references to their attention—and especially to one who forced us to think deeper about some aspects, greatly improving the paper.

References

Benjamin, T. B., 1961, "Dynamics of a System of Articulated Pipes Conveying Fluid. I. Theory. II. Experiments," *Proceedings of the Royal Society, London*, Vol. A261, pp. 457–499.

Benjamin, T. B., 1963, "The Three-fold Classification of Unstable Disturbances in Flexible Surfaces Bounding Inviscid Flows," *Journal of Fluid Mechanics*, Vol. 16, pp. 436–450.

Bolotin, V. V., and Zhinzher, N. I., 1969, "Effects of Damping on Stability of Elastic Systems Subjected to Non-conservative Forces," *International Journal of Solids and Structures*, Vol. 5, pp. 965–989.

Craik, A. D. D., 1985, *Wave Interaction and Fluid Flows*, Cambridge University Press, Cambridge, UK.

Crandall, S. H., 1995, "The effect of Damping on the Stability of Gyroscopic Pendulums," *Zeitschrift für angewandte Mathematik und Physik*, Vol. 46, special issue, pp. S762–S780.

Done, G. T. S., 1963, "The Effect of Linear Damping on Flutter Speed," *Aeronautical Research Council R&M*, No. 3396.

Drazin, P. G., and Reid, W. H., 1981, *Hydrodynamic Stability*, Cambrige University Press, Cambridge, UK.

Gregory, R. W., and Païdoussis, M. P., 1966, "Unstable Oscillation of Tubular Cantilevers Conveying Fluid. I. Theory; II. Experiments," *Proceedings of the Royal Society, London*, Vol. 293, pp. 512–542.

Nemat-Nasser, S., Prasad, S. N., and Herrmann, G., 1966, "Destabilizing Effect of Velocity-dependent Forces in Non-conservative Continuous Systems," *AIAA Journal*, Vol. 4, pp. 1276–1280.

Nissim, E., 1965, "Effect of Linear Damping on Flutter Speed. Part I: Binary Systems," *The Aeronautical Quaterly*, Vol. 16, pp. 159–178.

Païdoussis, M. P., 1970, "Dynamics of Tubular Cantilevers Conveying Fluid," *I. Mech. E. Journal of Mechanical Engineering Science*, Vol. 12, pp. 85–103.

Païdoussis, M. P., 1996, "Fluid-Structure Interactions between Axial Flows and Slender Structures," Sectional Lecture, XIXth ICTAM, Kyoto, Japan.

Païdoussis, M. P., 1998, *Fluid-Structure Interactions: Slender Structures and Axial Flow*, Vol. I, Academic Press, London.

Païdoussis, M. P., and Li, G. X., 1993, "Pipes Conveying Fluid: A Model Dynamical Problem," *Journal of Fluids and Structures*, Vol. 7, pp. 137–204.

Païdoussis, M. P., Semler, C., and Alighanbari, H., 1997, "A Physical Explanation of the Destabilizing Effect of Damping," *Proceedings International Symposium on FSI, AE&FIV + N*, Dallas, TX, Vol. I, ASME, New York, pp. 29–38.

Seyranian, A. P., 1990, "Destabilization Paradox in Stability Problems of Non-conservative Systems," *Advances in Mechanics* (Warszawa), Vol. 13, pp. 89–124.

Seyranian, A. P., and Pedersen, P., 1995, "On Two Effects in Fluid/Structure Interaction Theory," *Flow-Induced Vibration*, Bearman, ed., Balkema, Rotterdam, pp. 565–576.

Thomson, W., and Tait, P. G., 1879, *A Treatise on Natural Philosophy*, Vol 1, Part I, New Ed., Cambrige University Press, Cambridge, UK, pp. 387–391.

Triantafyllou, G. S., 1992, "Physical Condition for Absolute Instability in Inviscid Hydroelastic Coupling," *Physics of Fluids A*, Vol. 3, pp. 544–552.

The Mode Conversion of a Guided Wave by a Part-Circumferential Notch in a Pipe

M. J. S. Lowe

D. N. Alleyne

P. Cawley

Department of Mechanical Engineering,
Imperial College,
London SW7 2BX, U.K.

A study of the reflection of mode-converted guided waves from notches in pipes has been carried out. Measurements were made on a 76-mm bore diameter (nominal 3-inch), 5.5-mm wall thickness pipe with circumferentially oriented through-thickness notches of various lengths. In parallel, a finite element model was used to simulate the experiments. The axially symmetric L(0, 2) mode was incident on the notches and the L(0, 2), F(1, 3), and F(2, 3) modes were received in reflection. The results showed excellent agreement between the measurements and the predictions for all three modes. They also showed that the F(1, 3) mode reflects as strongly as the L(0, 2) mode when the notch length is short. Finally, it has been shown that a very simple analysis based on an assumed crack-opening profile may be used to make accurate predictions of the mode conversion.

1 Introduction

The corrosion of pipework is a major problem for the oil and gas and petrochemical industries. General wall-thinning and localized pitting corrosion can occur both from the inside and the outside of pipe walls. A high proportion of pipes are insulated, so that even the external defects cannot be detected by conventional NDE techniques without the expense of removing the insulation.

The authors are developing an ultrasonic guided-wave testing technique for the inspection of such industrial pipework. The testing scheme employs a pulse-echo arrangement from a single location on a pipe, using waves which are guided along the pipe wall. The presence and axial location of defects in the pipe wall are determined by any reflections and their arrival times. The scheme offers rapid inspection of long sections of pipe with the major advantage that the insulation need only be removed at the location where the transducers are attached. The original objective of the project was to detect any areas of corrosion larger than $3T \times 3T$ in area and $T/2$ deep where T is the pipe wall thickness. The scope is for insulated pipe in the 2–12 inch (51–305 mm) nominal bore diameter range and an inspection range of at least 15 m from the transducer position.

A number of researchers have studied the use of Lamb waves for the detection of defects in plate structures. Of particular note, Worlton (1957) studied their interaction with laminar flaws in a plate and was thus the first to identify their potential for rapid inspection. More recently, and of direct relevance to the work reported here, Alleyne and Cawley have studied the interaction of Lamb waves with notches in plates. They identified the mode conversion behavior (1992a) and recommended criteria for mode selection and inspection strategies (1992b).

Guided waves in tubular structures are similar in nature to Lamb waves in plates but considerably more complicated. Nevertheless a significant amount of work has previously been reported on their use for defect detection. An important need is the inspection of tubes in boilers and heat exchangers, motivating research by Silk and Bainton (1979), Böttger, Schneider, and Weingarten (1987a, 1987b), Duncumb and Keighley (1987), Brook, Ngoc, and Eder (1990), Ditri et al. (1992), Rose, Cho, and Ditri (1994), Ditri et al. (1994), and Ditri (1994). In the context of larger tubular structures, Thompson, Alers, and Tennison (1972) and Alers (1994) have addressed the inspection of gas pipelines using circumferential-traveling waves.

The authors' present project has already achieved considerable success. Alleyne and Cawley (1996a) have reported on the development of dry-coupled piezoelectric transducers for the excitation and detection of the guided waves. Alleyne and Cawley (1995) and Alleyne, Lowe, and Cawley (1998) have studied the reflection of the L(0,2) axially symmetric mode from notches in pipes. Alleyne and Cawley (1996b) measured reflections of the same mode from welds, flanges and pipe supports, and demonstrated that the mode can be propagated under wet or dry insulation. A commercial instrument under development is being used in field trials on industrial pipelines. Reports of the findings from the field trials of defect sensitivity, and of the influence of welds, flanges and pipe supports have been made by Alleyne and Cawley (1997), Alleyne, Lowe, and Cawley (1996) and Alleyne, Cawley, Lank, and Mudge (1997).

A key element of the inspection system is the selection and exploitation of a single mode. The large number of possible wave modes in a pipe is illustrated in the group velocity dispersion curves for a 76-mm (nominal 3-inch) bore, 5.5-mm wall thickness pipe, in Fig. 1. The curves were calculated using a general purpose computer program which was developed by the authors (Lowe, 1995). The modes are labeled after the convention of Silk and Bainton (1979); they include modes of longitudinal ("L"), flexural ("F"), and torsional ("T") motion of the pipe wall, with axial symmetry or integer harmonics of variation around the circumference. The first integer of the integer pair in each mode label gives the harmonic order of circumferential variation and the second integer is simply a sequential list of the modes of each type. Thus all modes whose first integer is zero are axially symmetric, all modes whose first integer is one have one wave cycle of variation of displacements and stresses around the circumference, and so on. The L(0,2) mode at approximately 70 kHz, as indicated by the dashed line on the figure, was identified as a particularly attractive choice. It is almost nondispersive—that is to say its group velocity is essentially constant with frequency so that there is minimal distortion of the wave packet over long propagation distances. Also, its mode shape consists predominantly of uniform axial

Contributed by the Applied Mechanics Division of THE AMERICAN SOCIETY OF MECHANICAL ENGINEERS for publication in the ASME JOURNAL OF APPLIED MECHANICS.

Discussion on the paper should be addressed to the Technical Editor, Professor Lewis T. Wheeler, Department of Mechanical Engineering, University of Houston, Houston, TX 77204-4792, and will be accepted until four months after final publication of the paper itself in the ASME JOURNAL OF APPLIED MECHANICS.

Manuscript received by the ASME Applied Mechanics Division, Dec. 17, 1996; final revision, Feb. 17, 1997. Associate Technical Editor: V. K. Kinra.

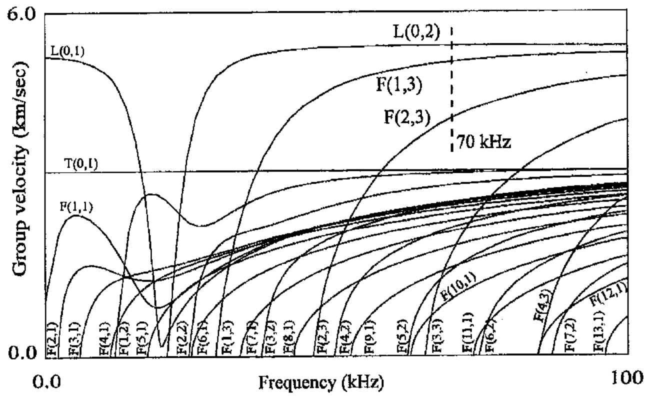

Fig. 1 Group velocity dispersion curves for 76-mm (nominal 3-inch) diameter, 5.5 mm wall thickness, schedule 40 steel pipe

motion throughout the wall thickness, like the s_0 plate mode at low frequency, which makes it equally sensitive to internal or external defects.

Excitation is achieved by using a ring transducer which is made up of mechanically independent dry-coupled piezoelectric elements distributed around the circumference (Alleyne and Cawley, 1996a). Each element has a dimension of 3.2 mm in the circumferential direction and the elements impart a force to the pipe wall in the axial direction. By exciting all of the elements equally and concurrently, the axially symmetric L(0,2) mode is launched. A narrow band signal is used, consisting of five or ten cycles at 70 kHz modulated by a Hanning window. Despite the fact that the transducers are relatively narrow, the use of 16 elements around the circumference avoids the excitation of any of the modes within the frequency bandwidth which are not axially symmetric (Alleyne and Cawley, 1996a). Excitation of the remaining unwanted mode at this frequency, the L(0,1) mode (whose deformation shape consists of wall bending), is minimized by transducer design. As an extra control, the use of more than one ring of transducers, spaced a quarter of a wavelength apart and with $\pi/2$ phase separation of their signals, allows the excitation of forward-traveling waves with insignificant excitation in the backward direction (Alleyne and Cawley, 1997). The same principle may also be used in reception in order to detect waves traveling in one direction while suppressing the detection of waves travelling in the other direction.

A previous study of mode reflection at notches (Alleyne, Lowe, and Cawley, 1998) examined the relationship between the amplitude of the reflected L(0,2) mode and the circumferential and through-thickness extents of notches. It was found that the reflection amplitude varied linearly with the circumferential extent and by a stronger than linear function with the depth of the notch. The results of the study supported the encouraging degree of sensitivity found in practice, and the reflected L(0,2) mode remains the principal choice for the majority of testing.

The aim of the work presented in this paper is to study the strengths of mode-converted reflections, principally of the F(1,3) mode, when the L(0,2) mode is incident. The motivation of the study was to improve the detection capabilities of the inspection technique for some specific occurrences of defects. The problem arises when attempting to detect defects at locations where there are circumferential welds. The change in geometry at a circumferential weld is such that a large part of the test signal is reflected. The reflection from a defect is superimposed on the reflection from the weld but is much smaller and therefore cannot be identified (Alleyne and Cawley, 1996b). The idea is to exploit the fact that the weld is approximately axially symmetric but a defect is almost invariably located at one side of the pipe and so is not axially symmetric. Therefore, for an incident L(0,2) mode, the weld will reflect only L(0,2) and L(0,1), but at the same time, because a defect is not axially symmetric, it will additionally reflect energy in nonzero-order mode-converted modes. Thus a measurement of reflected higher-order modes could be used to indicate the presence of a defect at a weld.

The paper describes a fundamental study using both a laboratory experiment and a finite element simulation. Although the motivation was for the industrial inspection task, the investigation has broad relevance to the understanding of the scattering of guided waves in cylinders. The study examined the mode conversion behavior from an incident L(0,2) 70 kHz narrowband signal to reflected F(1,3) and F(2,3) modes (indicated on Fig. 1) due to a part-circumference through-thickness notch. The F(1,3) and F(2,3) modes have practically the same profile of displacements and stresses through the wall thickness as the L(0,2) mode, the only difference being in the order of cyclic variation around the circumference. Thus, for example, the F(1,3) mode has the distribution of axial stress which would be found if the pipe was subjected to gross bending. A fourth mode with this through-thickness profile, F(3,3), may also be reflected but it is extremely dispersive at this frequency and is therefore omitted from the study. Conversion to modes other than these is not expected in this study. This is because the other modes which can exist at this frequency all have nonuniform profiles of axial displacement and stress through the wall thickness and therefore could only be excited if the notch geometry is nonuniform through the wall thickness, for example in the case of a part-through notch. In fact the reflection from part-through notches is of great practical interest; this study is limited to through-thickness notches for initial simplicity.

Following the mode conversion study, the utility of the findings for developing a means of discriminating between fully circumferential and part circumferential features is demonstrated using a second laboratory experiment with a welded pipe. Finally it is shown that a very simple analysis based on an assumed crack-opening profile may be used to make accurate predictions of the mode conversion.

2 Experimental Setup

The laboratory experiments for the mode conversion study were performed on a 2.6-m length of nominal 3-inch Schedule 40 steel pipe (internal diameter 76 mm, wall thickness 5.5 mm), illustrated in Fig. 2. The aim was to measure the reflected wave modes from a through-thickness circumferentially oriented notch for a range of lengths of the notch. Three rings of 16 transducers each were clamped to the pipe near end ''A'' as shown and were configured to excite the L(0,2) mode in the direction towards end ''B.'' An arbitrary function generator and power amplifier were used to generate a five-cycle 70 kHz toneburst modulated by a Hanning window, as input, and all of the elements on each transmitting ring were excited equally. The output signal from the power amplifier was approximately 100 V peak to peak. The same rings were used for receiving, a diode bridge circuit protecting the receiver amplifier during the excitation period (Owens, 1980). The signals were amplified and recorded independently for each of the 16 angular

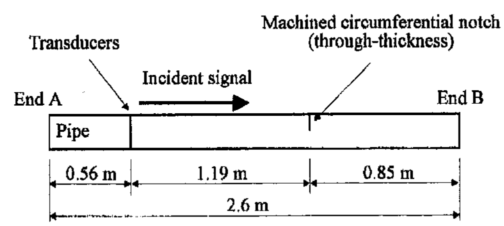

Fig. 2 Arrangement of pipe and transducers for experimental measurements of wave reflections from a through-thickness part-circumferential notch

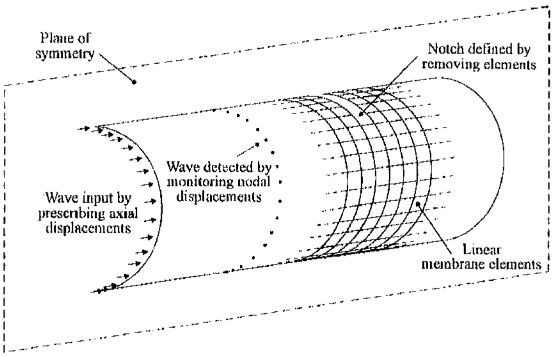

Fig. 3 Finite element spatial representation of the experiments, using a membrane model and exploiting the half-symmetry of the geometry

positions around the circumference of each ring. The amplification gain was about 20 dB. The signals were captured on a digital oscilloscope, taking 200 averages for each measurement, and then stored on a computer. The signals from the three rings were then processed to remove any of the L(0,1) mode and also the L(0,2) mode echoes from end A.

In order to obtain a reference measurement, reflections from end B were recorded before introducing any notch to the pipe. A through-thickness circumferential notch was then machined 0.85 m from end B, using a 3.2-mm diameter slot drill cutter. For practical interest, such a notch could reasonably represent a circumferential crack because the axial dimension of the notch is unimportant when it is much shorter than both the wavelength and the circumferential dimension (Alleyne, Lowe, and Cawley, 1996). Similarly, it could also represent a region of wall loss due to corrosion whose axial extent is much less than the 80-mm wavelength. Furthermore, it may be possible to infer the behavior due to part-through corrosion, by using the relationships which were established for reflection of the L(0,2) mode from part-through notches (Alleyne, Lowe, and Cawley, 1998). However, the reflections have been found to be sensitive to the axial extent of part-through notches, so that predictions for corrosion patches must be approximate at this stage. This issue will be addressed in a future paper. Measurements of the reflections from the notch were recorded for a range of eight different lengths of the notch, up to a maximum length of 50 percent of the circumference.

3 Finite Element Model

A full finite element analysis of the interaction of guided waves in a pipe with discrete defects requires a three-dimensional solid model which, though possible, is computationally intensive. However, it is often possible to perform meaningful analyses of three-dimensional problems using reduced spatial domains. In this case it was possible to model the pipe accurately using a three-dimensional membrane finite element model. The basis for such a simplification is the simple nature of the mode shapes of the incident L(0,2) mode and the reflected F(1,3) and F(2,3) modes at 70 kHz. All three modes are described accurately by membrane stresses and strains of the pipe wall. The three-dimensional membrane element models these membrane stresses within its plane and also has a mass matrix which has coefficients relating to all three directions. It is therefore capable of representing both the membrane action and any radial motion corresponding to pipe breathing. It follows also that the L(0,1) mode, which is characterized by local wall bending, does not propagate in the membrane model. The justification for the membrane modeling domain was examined thoroughly in the context of the previous study on the reflection of the L(0,2) mode (Alleyne, Lowe, and Cawley, 1998).

The model is illustrated schematically in Fig. 3. Half of the circumferential extent of a length of pipe was modeled, assuming one plane of symmetry. The full length of the pipe was modeled in some cases, so that the predicted time record could be compared directly with the experimental measurements. However, in the majority of cases a shortened length of 1.2 m was sufficient in order to reduce the computing time whilst still having enough time separation between the outgoing and reflected signals to enable calculation of the reflection coefficients. Comparisons between the two lengths of models confirmed that the shorter models gave the same reflection coefficients as the full-length models provided that the peak-to-peak amplitudes of the reflected signals were scaled to account for dispersion. In fact the signal reduction due to dispersion is negligible for the L(0,2) and F(1,3) modes and only needs to be considered for the F(2,3) mode. The peak-to-peak amplitude of the F(2,3) mode reduces by about 31 percent in 1 m of propagation. Meshes of identically sized linear quadrilateral membrane elements were used, with 32 elements around the 180-deg circumference of the model. The element axial length was 3.2 mm, corresponding to about 25 elements per wavelength, well above the threshold of eight elements per wavelength which the authors have found from experience to be a good limit for accurate modeling. Material damping is minimal in practice and was ignored in the model.

A five-cycle 70 kHz toneburst in a Hanning window was chosen for the input, thus matching the experimental signal. The toneburst was applied as a sequence of prescribed displacements in the axial direction of the pipe, the same sequence being applied concurrently at all of the nodes around the circumference at one end of the pipe. Explicit marching was employed in the time domain, assuming a diagonal mass matrix. The maximum time-step which satisfies stability for an explicit marching scheme is given by L/C, where L is the element length and C is the wave speed of the fastest wave present (Bathe, 1982). In practice the authors have found a limit of 0.8 L/C to be sensible. This was satisfied here by choosing a constant time-step of 0.4 μsec.

The detection of the reflected waves was achieved simply by monitoring the axial displacements at a ring of nodes around the circumference, as indicated. For direct comparison of the predicted time domain records with the measurements, the distance between the monitoring nodes and the notch in the full-length analyses was 1.19 m. This matches the distance between the transducers and the notch in the experiment (Fig. 2). Also, the distance between the notch and the remote end of the pipe was 0.85 m, again matching the experimental dimension. Thus the finite element time-domain results which are presented here can be compared directly with the measurements, provided that the time for the finite element results is taken to start at the moment the incident signal arrives at the monitoring nodes. This time shift has been incorporated in the results which are presented here.

A series of analyses including through-thickness notches of various circumferential lengths was conducted. In order to satisfy the symmetry which was implied by modeling only half of the pipe, half of the circumferential extent of each notch was defined, starting from the plane of symmetry. The notches were introduced very simply by removing elements in the model, as shown in the figure. Since the axial length of the notch was 3.2 mm, identical to the axial length of the elements, it was necessary only to remove one row of elements. In fact, earlier work (Alleyne, Lowe, and Cawley, 1998) has shown that the reflection coefficient of the L(0,2) mode is not influenced significantly if a through-thickness notch is modeled simply by disconnecting adjacent elements, thereby creating a notch of zero axial length, rather than by removing the row of elements (but this is not the case for a part-through notch, when the reflection coefficient is sensitive to the axial length). Further comparison in the present work showed that this is still true when considering the mode converted reflections.

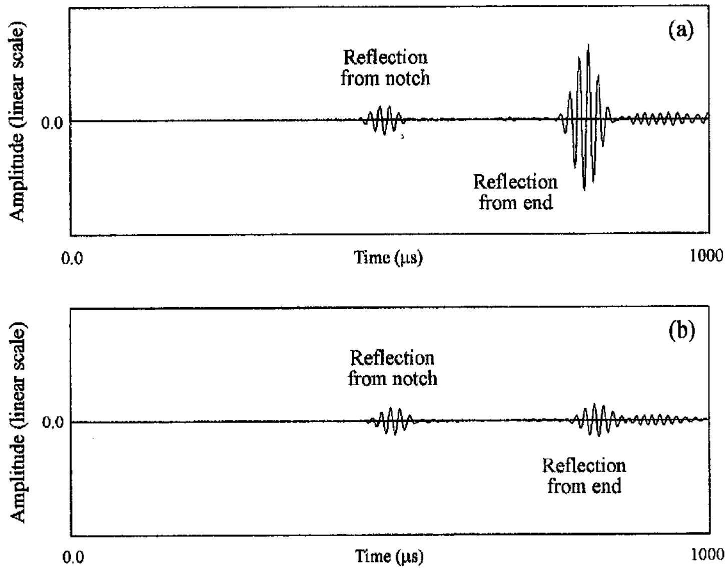

Fig. 4 Typical processed reflected signals from the experiments, shown for a notch which extends around one-eighth of the circumference; (*a*) with processing to extract order 0 (axisymmetric) signals; (*b*) with processing to extract order 1 (one wave cycle around the circumference) signals

4 Results of Reflection Study

Some simple signal processing was necessary in order to determine the amplitude of each of the reflected modes. An identical methodology was applied to both the experimental and the finite element results. For the reflection of the axially symmetric L(0,2) mode, the 16 individual signals from the transducers (or 32 signals from the nodes) were simply added. The resulting signal was thus exactly as if the transducers were wired together, as reported in previous studies of L(0,2) reflection. For the other two modes, a phase delay of $N\theta/2\pi$ was added to each signal before summing them. N is the circumferential order number and θ is the angular distance from the centre of the notch. Thus a separate processing calculation was performed in order to extract the amplitude of each of the three modes from the multiple transducer (or node) records. Since the signals were rather narrow band, the processing could reasonably have been performed directly on the raw time records. However, for better accuracy, the calculations were performed in the frequency domain, and then inverted to give a processed time-domain record for each mode.

Typical results, for the notch which extends around one-eighth of the circumference, are shown in Figs. 4 and 5 for experimental measurements and finite element predictions, respectively. Each figure shows the time record for order-0 processing (axisymmetric) in part (*a*) and for order-1 processing in part (*b*). The finite element results for order 0 show the incident signal as it passes the monitoring location (Fig. 3) before arriving at the notch. The incident signal does not appear in this way in the experimental measurements because the receiver ring is immediately adjacent to the transmitter ring and is isolated by the diode bridge circuit at the time of transmission. Some electrical noise is present at that time but has been gated out from the signal. As should be expected, the finite element incident signal also vanishes when the order-1 processing is performed. The predictions clearly agree very well with the measurements. Both show a moderate reflection from the notch, with amplitude approximately the same for both order-0 and order-1 processing. Both also show the strong reflection from end B for order 0 processing and a much reduced reflection for order 1 processing. The slight delay of the order 1 signals with respect to the order 0 signals is consistent with the slower speed of the F(1,3) mode compared to the L(0,2) mode (Fig. 1). Similarly good agreement was found for the other notch sizes and for order-2 processing.

To present the full set of results, a reflection coefficient was calculated from each processed time record. The reflection coefficient was defined as the ratio of the amplitude of the reflected signal to the amplitude of the L(0,2) reference signal which was taken from the end of the pipe before introducing the notch. The amplitudes were taken simply as peak-to-peak measurements in the time domain.

The reflection coefficient results are shown in Fig. 6. Good agreement can be seen between the experimental measurements and the finite element predictions for all three modes. The reflection coefficient for the L(0,2) mode is evidently rather linear with respect to the circumferential extent of the notch, exactly as reported previously (Alleyne and Cawley, 1995; Alleyne, Lowe, and Cawley, 1996, 1998). The reflection coefficients for the F(1,3) and F(2,3) modes approximate to the shapes of rectified half-sine and sine waves, respectively. The limiting values are intuitive: Zero reflections of F(1,3) and F(2,3) should be expected for no notch or for a full-circumference notch; maximum reflection of F(1,3) should be expected for a 50 percent notch. It is interesting, and of great significance, to observe that the reflections of F(1,3) are comparable to those of L(0,2) for short notches. This is the most important part of the graph for practical testing, and it appears that there is no loss in sensitivity here in using F(1,3) as an alternative to L(0,2). F(2,3), as well as being less sensitive than F(1,3) throughout the range of notch size, has the disadvantage of being rather dispersive at this frequency (Fig. 1). F(1,3) is therefore the clear choice for practical exploitation.

An alternative, though closely related methodology for extracting the reflection strengths of the different modes would be to use a two-dimensional Fourier transform (Alleyne and Cawley, 1991), choosing the circumference of the pipe with its 16 transducer signals as the spatial domain. Since the circumference is continuous, it would not be necessary to apply a spatial window. The time-domain signals would be gated to leave just the reflection from the notch. After performing the transform, the strengths of the modes would be given by the amplitudes at wave numbers corresponding to integer numbers of wavelengths around the circumference. In principle this methodology would reveal the strengths of conversion to all possible modes with a

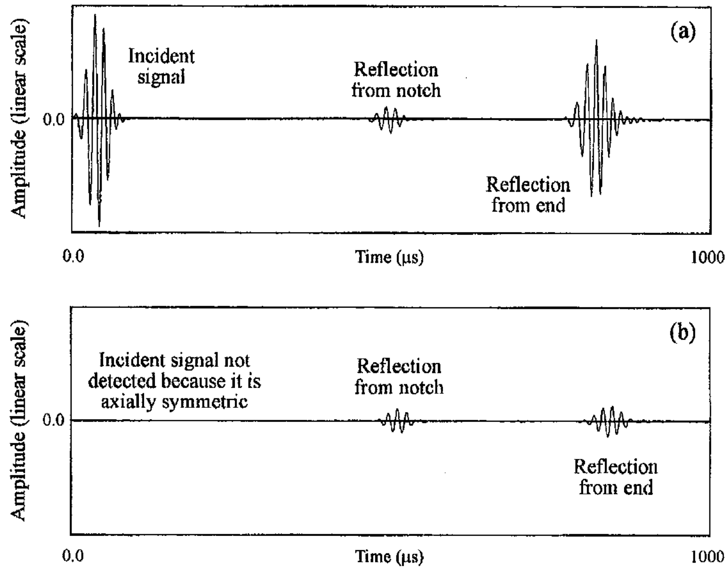

Fig. 5 Typical processed reflected signals from the finite element predictions, shown for the same notch and processing as in Fig. 4. Additional early signal is incident wave passing monitoring location before arriving at notch.

single calculation. However, in practice it is troublesome. A wide gate has to be set in order to capture the reflected modes which are traveling at different speeds, yet parts of the signal other than the reflection from the notch must be avoided. Therefore this approach has not been pursued.

5 Discussion

The motivation for the reflection coefficient study was the identification of a mode which could be used to detect part-circumferential defects at the same locations as axially symmetric features. The results suggest that the F(1,3) mode is a promising choice, particularly for the key need for the detection of defects whose circumferential extent is short. A second experiment was therefore performed in order to demonstrate its discrimination on a typical geometry. The second experiment was very similar to the first, except that the specimen consisted of two pipes joined end to end by a (typical) circumferential butt-weld. The average height of the weld profile above the pipe surface was 3 mm and the weld cap width was about 12 mm. The notch was machined at the axial location of the center of the weld. The specimen length and the axial distances between

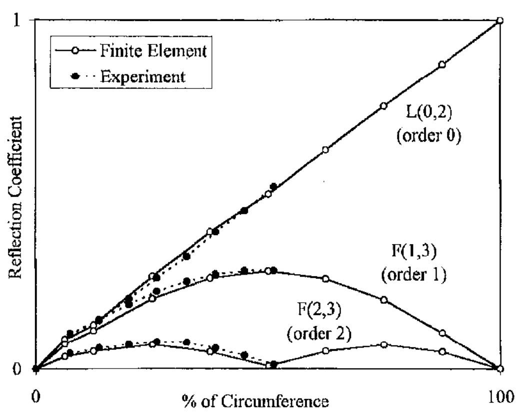

Fig. 6 Measured and predicted reflection coefficients for a through-thickness notch in a 76-mm (nominal 3-inch) diameter, 5.5-mm wall thickness pipe at 70 kHz as a function of the percentage circumferential extent of the notch

transducers and notch were approximately the same as those in the initial experiment. Reference measurements were taken before machining the notch, then reflection measurements were taken for a range of notch lengths. Finite element simulations were conducted in parallel.

Typical experimental results are shown in Figs. 7 and 8. All of the results are plotted on the same linear amplitude scale, for ease of comparison.

Figure 7 shows the reflections which were measured before introducing the notch. Figure 7(*a*) shows the signal after processing for order 0; it therefore shows the axially symmetric component of the reflections. A strong reflection from the weld is evident, as should be expected because of its axial symmetry. Figure 7(*b*) shows the signal after processing for order 1. Here it can be seen that there is almost no reflection from the weld, indicating as expected that there is very little mode conversion to the F(1,3) mode. However, some signal arrives later, suggesting that some order-1 energy is reflected from the end of the pipe. It is believed that this signal is due to differences between the strengths of coupling of the different transducer elements, introducing errors in the processing. Thus in this case there is "leakage" from order 0 to order 1. This leakage is only pronounced when (as here) the axially symmetric signal is strong.

Figure 8 shows the reflections which were measured when a notch extending around one-eighth of the circumference of the pipe was cut into the weld. Again Fig. 8(*a*) shows the signal after processing for order 0 and Fig. 8(*b*) shows the signal after processing for order 1. The reflection from the notch and weld in Fig. 8(*a*) is similar in magnitude to that from the weld alone, in Fig. 7(*a*), illustrating clearly that the order-0 mode cannot be used to discriminate between the two features. However, a clear reflection from the notch can now be seen, in part (*b*), when the order-1 processing is performed.

The same characteristics were observed in the results for other short lengths of the notch (up to a quarter of the circumference); the results are therefore omitted here for brevity. Similarly, the finite element predictions again matched the measurements very closely and are not shown. The demonstration clearly shows that the measurement of F(1,3) mode-converted reflections is an appropriate technique for the detection of non-axiallysymmetric defects at locations where there are axially symmetric reflectors such as circumferential welds.

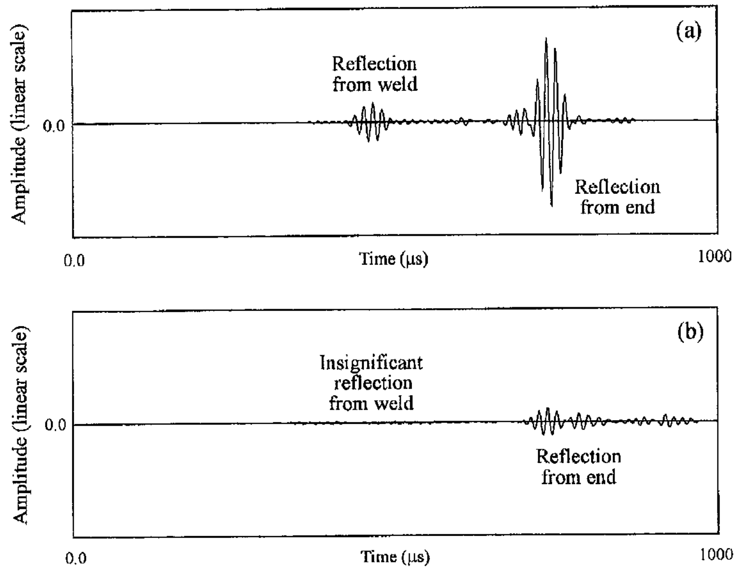

Fig. 7 Processed reflected measurements from circumferential weld without notch; (*a*) with processing to extract order 0 signals; (*b*) with processing to extract order 1 signals

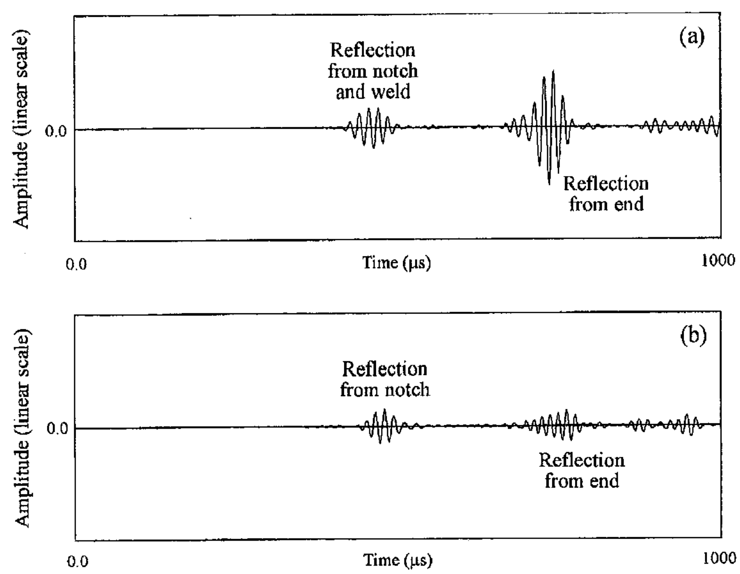

Fig. 8 Processed reflected measurements from circumferential weld with notch which extends around one eighth of the circumference. Parts (*a*) and (*b*) as in Fig. 7, for comparison.

In practice the measurement of mode converted signals will require some minor changes to the inspection instrument. However, the signal processing is straightforward and can be performed very quickly on the portable computer which is already part of the instrument.

Another issue to be tackled will be the identification of the angular position of the center of the defect. This has no influence on the existing L(0,2) measurements, but must be known for the extraction of the F(1,3) signals. In the experimental work and the finite element predictions which are reported here, the notch location was known; however, in general this information will not be available. It will be necessary to determine the angular location from the multichannel records, probably by performing the extraction of the F(1,3) for a range of angles. In practice the search will be aided by field experience, for example the likelihood of corrosion initiating at the lowest point on the pipe.

Differences in the strength of coupling of the transducers must also be minimized. It was possible in the laboratory to achieve good coupling but may be more difficult in the field. As discussed above, the result of uneven strengths of the transducers is that some energy is put into the F(1,3) mode when exciting L(0,2). This results in the detection of F(1,3) in reflection from axially symmetric features. This was seen in the end reflection in Fig. 7(*b*). Fortunately, strong leakage can only occur when the L(0,2) mode is reflected strongly. Thus in Fig. 7(*b*) the leakage is seen in the end reflection but not in the reflection from the weld.

Having completed the mode conversion experiments and finite element predictions, a calculation was performed in order to discover whether the reflection coefficients could be estimated from a simple assumption of the opening profile of the notch. The idea for the calculation came from the observation (Alleyne, Lowe, and Cawley, 1998) that the axial movement

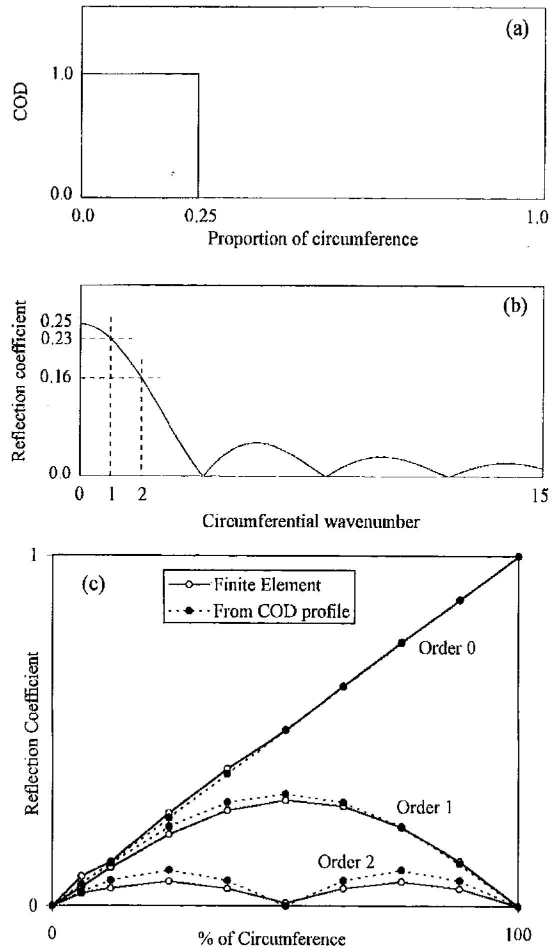

Fig. 9 Prediction of reflection coefficients from simple assumption of constant COD profile; (*a*) COD profile, shown for a notch which extends around one quarter of the circumference; (*b*) spatial Fourier transform of profile, showing amplitudes of modes of circumferential order 0, 1, 2, respectively; (c) predicted reflection coefficients from COD profile, with finite element curves for comparison.

of the face of the notch is approximately constant over the whole length of the notch, when the L(0,2) mode is incident and the frequency and geometry are as discussed here. Following the analysis of Ditri (1994), based on the S-parameter technique due to Auld (1990), the strength of conversion to each mode by a circumferential crack may be determined from the degree to which the crack-opening profile matches the stress mode shape of the mode.

In this work we are concerned with modes whose mode shapes consist of approximately constant axial stress through the wall thickness, together with integer harmonic orders of variation around the circumference. A spatial Fourier decomposition of the axial displacements around the circumference at the location of the notch therefore gives the excitation strengths of the mode-converted waves. The simple calculation is illustrated in Figs. 9(a) and (b). Figure 9(a) shows an assumed crack-opening displacement profile for a notch which extends around a quarter of the circumference. The crack-opening displacement has unit amplitude for a quarter of the circumference, corresponding to the extent of the notch, then zero amplitude. Figure 9(b) shows the spatial Fourier transform of the profile for circumferential orders up to 15. The dashed lines and the numbers next to the Y-axis illustrate the evaluation of the strengths of the reflections of modes of orders 0, 1, and 2.

Reflection coefficient functions for the three modes were found by repeating the calculation for a range of notch lengths. The results are plotted in Fig. 9(c) together with the finite element results from Fig. 6 for comparison. For like comparison in the figure, the crack-opening displacement predictions for order 2 were multiplied by the factor 0.65. This is the factor by which the peak-to-peak amplitude of the F(2,3) mode was found to reduce, due to dispersion, between the notch and the monitoring location in the finite element model. There is insignificant reduction of the L(0,2) and F(1,3) modes over this distance. The results show good agreement between the crack-opening displacement and the finite element predictions, supporting the simple assumption which was made for the crack-opening displacement profile. The true utility of this simple approach for more general application will depend critically on knowing the range of problem parameters for which the constant crack-opening displacement profile is valid. It is intended to address this in future work.

6 Conclusions

A series of experiments was conducted in which an axially symmetric mode was incident on a through-wall machined notch which extended over part of the circumference of a pipe. The reflections of the axially symmetric mode and of the mode-converted nonaxiallysymmetric modes were measured as the circumferential extent of the notch was increased. In parallel, finite element simulations of all of the experiments were performed. Excellent agreement was found between the experimental and the predicted results. In addition to the axially symmetric L(0,2) mode, significant reflections of the harmonic order 1 mode F(1,3) and the harmonic order-2 mode F(2,3) were detected. The results also showed that the F(1,3) mode reflects as strongly as the axially symmetric L(0,2) mode when the notch length is short.

The implications of the study are that mode-conversion in reflection from L(0,2) to F(1,3) can be used in pipeline NDE in order to discriminate between axially symmetric reflectors such as circumferential welds and any nonaxially symmetric defects. As a demonstration, it was shown that the presence or absence of a notch at the same axial location as a circumferential weld could be determined from the mode converted signal.

Finally, a very simple analysis was performed to estimate the mode conversion behavior using an assumed opening-displacement profile of the notch. Accurate predictions were made from the very simple assumption that the opening displacement is constant for all locations along the length of the notch. This simple approach has broad relevance to the scattering of guided modes in pipes when the wavelength is of similar size or smaller than the notch length, and when the axial extent of the notch is short.

Acknowledgment

This work was carried out under the European Commission THERMIE programme with financial support from a consortium of oil and chemical companies and the U.K. Health and Safety Executive.

References

Alers, G. A., 1994, "Application of special wave modes to industrial inspection problems," *Proc. 1994 ASME Winter Meeting*, Symposium on Wave Propagation and Emerging Technologies, Chicago, IL.

Alleyne, D. N., and Cawley, P., 1991, "A two-dimensional Fourier transform method for the measurement of propagating multimode signals," *J. Acoust. Soc. Am.*, Vol. 89, pp. 1159–1168.

Alleyne, D. N., and Cawley, P., 1992a, "The interaction of Lamb waves with defects," *IEEE Trans Ultrasonics, Ferroelectrics and Frequency Control*, Vol. 39, pp. 381–397.

Alleyne, D. N., and Cawley, P., 1992b, "Optimisation of Lamb wave inspection techniques," *NDT&E International*, Vol. 25, pp. 11–22.

Alleyne, D. N., and Cawley, P., 1995, "The long range detection of corrosion in pipes using Lamb waves," *Review of Progress in Quantitative NDE*, Vol. 14, D. O. Thompson and D. E. Chimenti, eds., Plenum Press, New York, pp. 2073–2080.

Alleyne, D. N., and Cawley, P., 1996a, "The excitation of Lamb waves in pipes using dry coupled piezoelectric transducers," *J. NDE*, Vol. 15, pp. 11–20.

Alleyne, D. N., and Cawley, P., 1996b, "The effect of discontinuities on the long range propagation of Lamb waves in pipes," *J. Process Mechanical Engineering*, Part E, Proc I Mech E, Vol. 210, pp. 217–226.

Alleyne, D. N., and Cawley, P., 1997, "Long range propagation of Lamb waves in chemical plant pipework," *Materials Evaluation*, Vol. 55, pp. 504–508.

Alleyne, D. N., Cawley, P., Lank, A. M., and Mudge, P. J., 1997, "The Lamb wave inspection of chemical plant pipework," *Review of Progress in Quantitative NDE*, Vol. 16, D. O. Thompson and D. E. Chimenti, eds., Plenum Press, New York, pp. 1269–1276.

Alleyne, D. N., Lowe, M. J. S., and Cawley, P., 1996, "The inspection of chemical plant pipework using Lamb waves: Defect sensitivity and field experience," *Review of Progress in Quantitative NDE*, Vol. 15, D. O. Thompson and D. E. Chimenti, eds., Plenum Press, New York, pp. 1859–1866.

Alleyne, D. N., Lowe, M. J. S., and Cawley, P., 1998, "The Reflection of Guided Waves from Circumferential Notches in Pipes," ASME JOURNAL OF APPLIED MECHANICS, Vol. 65, pp.

Auld, B. A., 1990, "Acoustic fields and waves in solids," Edition 2, Robert E. Krieger, Melbourne, FL.

Bathe, K.-J., 1982, "Finite Element Procedures in Engineering Analysis," Prentice-Hall, Englewood Cliffs, NJ.

Böttger, W., Schneider, H., and Weingarten, W., 1987a, "Prototype EMAT system for tube inspection with guided ultrasonic waves," *Nuclear Eng. and Design*, Vol. 102, pp. 356–376.

Böttger, W., Schneider, H., and Weingarten, W., 1987b, "Tube inspection with an EMAT using guided ultrasonic waves," *Proc. 4th European NDT Conference*, Vol. 4, Pergamon Press, Tarrytown, NY, pp. 2305–2313.

Brook, M. V., Ngoc, T. D. K., and Eder, J. E., 1990, "Ultrasonic inspection of steam generator tubing by cylindrical guided waves," *Review of Progress in Quantitative NDE*, Vol. 9, D. O. Thompson and D. E. Chimenti, eds., Plenum Press, New York, pp. 243–249.

Ditri, J. J., 1994, "Utilization of guided elastic waves for the characterization of circumferential cracks in hollow cylinders," *J. Acoust. Soc. Am.*, Vol. 96, pp. 3769–3775.

Ditri, J. J., Rose, J. L., McNight, W. J., and Carr, F. T., 1992, "A guided wave inspection technique for nuclear steam generator tubing," *13th World Conf on NDT*, Brazil, pp. 191–195.

Duncumb, A. C., and Keighley, D. M., 1987, "Inspection of titanium tubing using ultrasonic Lamb waves generated by an electromagnetic acoustic transducer," *Proc 4th European NDT Conference*, Vol. 4, Pergamon Press, Tarrytown, NY, pp. 2228–2236.

Lowe, M. J. S., 1995, "Matrix techniques for modelling ultrasonic waves in multilayered media," *IEEE Trans Ultrasonics, Ferroelectrics and Frequency Control*, Vol. 42, pp. 525–542.

Owens, E. J., 1980, "Automatic transmit-receive switch uses no relays but handles high power," *J. Acoust. Soc. Am.*, Vol. 68, pp. 712–713.

Rose, J. L., Cho, Y., and Ditri, J. J., 1994, "Cylindrical guided wave leakage due to liquid loading," *Review of Progress in Quantitative NDE*, Vol. 13, D. O. Thompson and D. E. Chimenti, eds., Plenum Press, New York, pp. 259–266.

Rose, J. L., Ditri, J. J., Pilarski, A., Rajana, K., and Carr, F., 1994, "A guided wave inspection technique for nuclear steam generator tubing," *NDT&E International*, Vol. 27, pp. 307–310.

Silk, M. G., and Bainton, K. F., 1979, "The propagation in metal tubing of ultrasonic wave modes equivalent to Lamb waves," *Ultrasonics*, Vol. 17, pp. 11–19.

Thompson, R. B., Alers, G. A., and Tennison, M. A., 1972, "Application of Direct Electromagnetic Lamb Wave Generation to Gas Pipeline Inspection," *Proc IEEE Ultrasonics Symposium*, Boston, Oct. 4–7, pp. 91–94.

Worlton, D. C., 1957, "Ultrasonic testing with Lamb waves," *Non-Destructive Testing*, Vol. 15, pp. 218–222.

Experimental Study of a Symmetrical Piecewise Base-Excited Oscillator

M. Wiercigroch
Mem. ASME

V. W. T. Sin

Department of Engineering,
University of Aberdeen,
King's College,
Aberdeen AB24 3UE, U.K.

This paper presents an experimental study on a base-excited piecewise linear oscillator with symmetrical flexible constrains of high stiffness ratio (above 20). The details of the adopted design of the oscillator, the experimental set-up, and calibration procedure are briefly discussed. The regions of chaotic motion predicted theoretically were confirmed by the experimental results arranged into bifurcation diagrams. Clearance, stiffness ratio, amplitude, and frequency of the external force were used as branching parameters. The discussion of the system dynamics is based on bifurcation diagrams and Lissajous curves. The investigated system tends to be periodic for large clearances and chaotic for small ones. This picture is reversed for the amplitude of the forcing changes, where periodic motion occurred for small values and chaos dominated for larger forcing. The same behavior is observed for increasing frequency ratio where, for values below the natural frequency, the most interesting dynamics occurs. For the investigated parameter values, the stiffness ratio variation produces only periodic motion.

1 Introduction

In a large number of mechanical engineering applications, excessive wear or operational conditions lead to collisions or intermittent contacts of the system components with motion restraining constrains such as clearances or backlashes. Nonlinear vibration absorbers, bearings, heat exchanges, gear boxes, percussive cutting, and impact print hammers are examples belonging into this category. One of the most common is a piecewise stiffness characteristic, which can be seen in many engineering applications such as rotating machinery, car suspension systems, and cutting processes, etc. The existence of these characteristics may result in an intermittent contact between the components; brining either detrimental or beneficial effects. Therefore, it is important from the point of view of the design and control of these systems to understand their complex behavior.

Recent years have seen considerable interest in single-degree-of-freedom piecewise oscillators subject to periodic external forcing, and which have been studied intensively via methods of nonlinear dynamics. The subject matter initiated nearly three decades ago by Kobrynskii (1969), has recently grown extensively, with many theoretical studies addressing specific problems. The investigations by Wanatabe (1978), Shaw and Holmes (1983), Natsiavas (1989), Nordmark (1991), Peterka and Vacik (1991), and Wiercigroch (1994a) are examples. Generalization of systems with discontinuities has been approached by Wiercigroch (1994b and 1996). These studies, based on bifurcation analysis, supplied evidence of complex dynamics, including subharmonic and chaotic motion. Although some experimental studies on piecewise systems have been carried out by Shaw (1985), Ehrich (1992), Stenson and Nordmark (1994), Blankeship and Kahraman (1995), and Gonsalves et al. (1995), there is a large disproportion between the quantity and quality of theoretical and experimental results. Therefore, in order to understand a law of motion for the investigated systems, it is essential to use appropriate models. This can be achieved by gathering convincing experimental data sets, which can be used for parameter estimation purposes and for verification of adopted models.

As a consequence, this paper will focus on an experimental study (supported by numerical simulation) of a simple discontinuous system, i.e., a piecewise linear base-excited oscillator undergoing nonlinear vibrations for higher stiffness ratios, above 20. The system responses have been scanned in a four-element parameter vector through a systematic construction of the experimental bifurcation diagrams. The obtained diagrams are used to discuss the system behavior and to conclude about the usefulness of piecewise models.

2 Experimental Setup

To chose an appropriate experimental model where the actual oscillator is capable of providing reliable data sets, an extensive design exercise has been carried out by considering many structurally different systems. The starting point for all designs was a linear system with a chosen a priori natural frequency to obtain values of parameters such as stiffness k_1, mass or inertia, and viscous damping coefficient. The linear oscillator was considered the worst case as the addition of the secondary stiffness in general reduces the amplitude of vibration; however, there is a possibility that a coexistence of super or subharmonic solutions could occur. A variety of designs using beams and coil springs were examined, with both translational and rotational motions. From all the designs, the beam-type system was selected for physical implementation due to its simplicity, the best flexibility in terms of parameter changes, ease of manufacturing, and cost effectiveness. As a consequence, the beam oscillator depicted in Fig. 1 was fully designed and manufactured.

The adopted design has two discontinuities, i.e., on the basis of contacts with the secondary stiffnesses. The beam system (Fig. 1) is comprised of the 1 kg block of mild steel which is held in position by two leaf springs with combined stiffness, k_1. These springs are mounted onto a stand which is bolted onto the base plate. The stiffness k_1 can be varied from 4.2 to 40.6 kN/m by changing the position of the stand along the slots on the base plate. This enables the natural frequency of the system to be varied between 10 and 32 Hz. A pneumatic damper is mounted on the

Contributed by the Applied Mechanics Division of The American Society of Mechanical Engineers for publication in the ASME Journal of Applied Mechanics.

Discussion on the paper should be addressed to the Technical Editor, Professor Lewis T. Wheeler, Department of Mechanical Engineering, University of Houston, Houston, TX 77204-4792, and will be accepted until four months after final publication of the paper itself in the ASME Journal of Applied Mechanics.

Manuscript received by the ASME Applied Mechanics Division, Nov. 6, 1996; final revision, Nov. 10, 1997. Associate Technical Editor: S. W. Shaw.

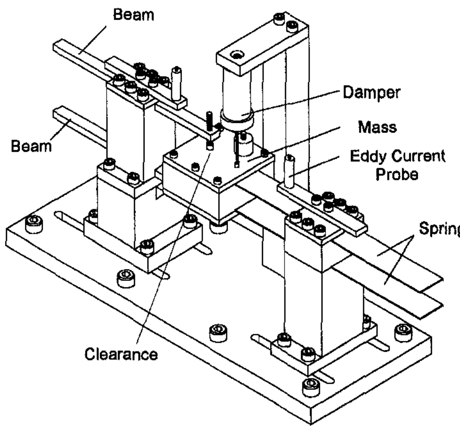

Fig. 1 Experimental oscillator

top bar with the other end fixed to the upper plate of the mass. The damper has two ball joints at the ends to compensate for misalignment. The secondary springs consist of two stainless steel beams mounted on a stand which is bolted onto the base plate. This enables a variation of the stiffness, k_2 by varying the length of the beams between 45 and 100 mm. The natural frequencies for these cantilever beams are 240 and 1194 Hz for the minimum and maximum stiffness respectively. The clearance, e, can be varied by adjusting the screws at the ends of the beams.

Figure 2(*a*) shows a schematic where the beam-type oscillator mounted on the dynamic system shaker together with the data measurement and acquisition system. A photograph of the beam-type system positioned on the shaker, along with the accelerometers and the eddy current probes, and other measuring equipment is depicted in Fig. 2(*b*).

The oscillator was mounted on the dynamic system shaker. The base excitation of the shaker was controlled by a arbitrary waveform generator with a sinusoidal output. The acceleration of the excitation, $\ddot{y}$, was measured using an accelerometer attached to the shaker table. This signal was passed through a charge amplifier and monitored by an oscilloscope before being captured on the data storage system (DSS). The relative displacement of the mass, z, was measured by sensing the deflection of the leaf spring based on the assumption of small angular displacements. Hence, the displacement of the mass had to be closely controlled by adjusting the excitation and the secondary stiffness. The measurement was carried out using an eddy current probe, mounted on the k_1 stand, and was passed through a low-pass filter to remove high-frequency noise prior to being captured on the DSS. The relative velocity of the mass, $\dot{z}$, was obtained by differentiating the signal tapped out of the low-pass filter and was also captured on the DSS. A second oscilloscope and a spectrum analyser were used to view the signals during the experiment. Another eddy current probe was used to measure the displacement, q, of the k_2 beam.

3 Mathematical Model

A physical model of the investigated oscillator is depicted in Fig. 3(*a*). A practical application of such a system could be as a limiter to prevent a mass from excessive displacement or a shaft with bearing clearances. As shown in Fig. 3(*a*), the model comprises a linear spring and a dashpot damper connected to the mass. In addition, two secondary linear springs are incorporated with clearances, e, at the top and bottom of the mass. The system is subjected to a harmonic base excitation in the form of $y = Y \sin \Omega t$. When the amplitude of oscillations is smaller than the clearances, the overall stiffness is equal to k_1 and is constant. When the amplitude of oscillation exceeds the clearances, the overall stiffness increases to the higher constant value of $k_1 + k_2$. This is only true by assuming small deflections of the both sets of springs; otherwise the systems should be regarded as piecewise nonlinear. The relationship between the restoring force in the spring(s) and the displacement of the mass is depicted in Fig. 3(*b*).

The equations of motion were derived in coordinates which are relative to the base excitation, assuming the gravitational force is compensated by the initial preloading of the primary spring. For this system, when the mass is oscillating, three conditions exist and they are as follows:

- The mass is not in contact with the secondary springs,

$$m\ddot{z} + c\dot{z} + k_1 z = mY\Omega^2 \sin \Omega t, \quad \text{for} \quad -e < z < e. \quad (1a)$$

- The mass is in contact with the secondary upper spring,

$$m\ddot{z} + c\dot{z} + k_1 z + k_2(z - e) = mY\Omega^2 \sin \Omega t, \quad \text{for} \quad z \geq e. \quad (1b)$$

- The mass is in contact with the secondary lower spring,

$$m\ddot{z} + c\dot{z} + k_1 z + k_2(z + e) = mY\Omega^2 \sin \Omega t, \quad \text{for} \quad z \leq -e. \quad (1c)$$

Equation (1) was nondimensionalized with respect to time and amplitude of motion, and the following simplified form was obtained:

$$Z'' + 2\xi Z' + Z + \beta\psi(Z) = F_0 \sin \nu\tau, \quad (2)$$

where

$$\psi(Z) = \begin{cases} 0, & |Z| < E \\ Z - E \operatorname{sign} Z, & |Z| \geq E \end{cases}, \quad (3)$$

$$Z = \frac{z}{y_0}, \quad \xi = \frac{c}{2m\omega_n}, \quad \tau = \omega_n t, \quad \nu = \frac{\Omega}{\omega_n},$$

$$F_0 = \frac{Yr^2}{y_0}, \quad \omega_n = \sqrt{\frac{k_1}{m}}$$

$$E = \frac{e}{y_0}, \quad \beta = \frac{k_2}{k_1}, \quad (') \equiv \frac{dZ}{d\tau}.$$

4 Bifurcation Analysis

Qualitative changes of dynamic behavior as a result of a change of one or more control parameters are named bifurcations. The

Nomenclature

- c = viscous damping
- e = gap
- E = dimentionless gap
- f_r = restoring force
- F_0 = modulus of external force
- k_1 = main stiffness
- k_2 = secondary stiffness
- m = mass
- t = time
- x = absolute displacement
- y = base displacement
- y_0 = reference base displacement assumed in this study to be of 1 mm
- Y = base amplitude
- z = relative displacement
- Z = dimentionless relative displacement
- β = stiffness ratio
- ξ = viscous damping ratio
- ω_n = natural frequency
- Ω = forcing frequency
- ψ = dicontinuous function
- τ = dimentionless time
- ν = frequency ratio

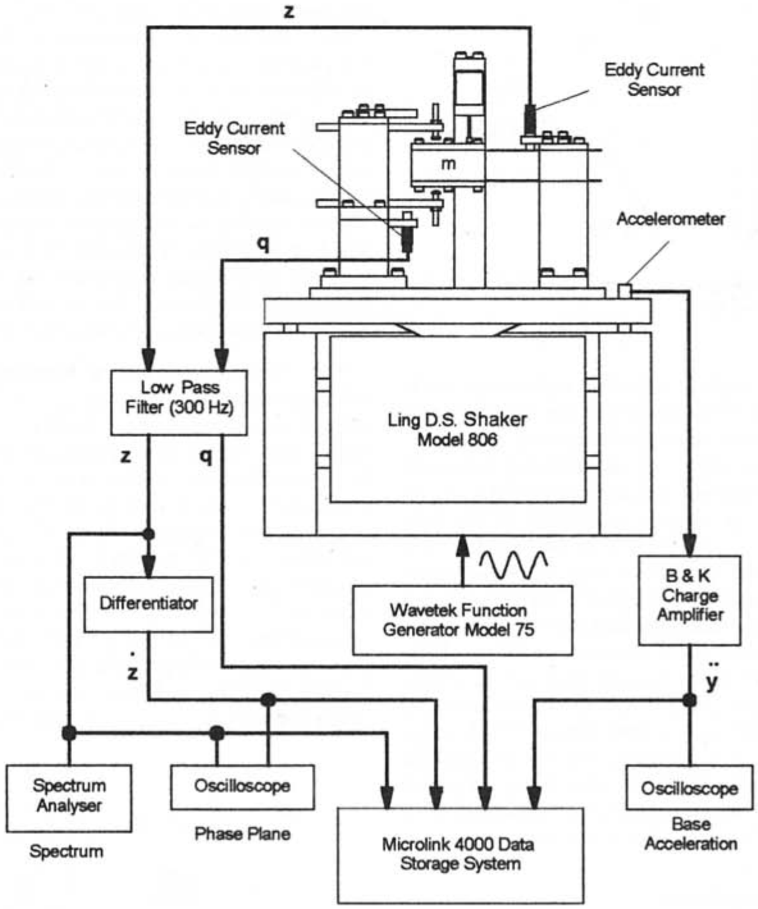

Fig. 2(*a*)

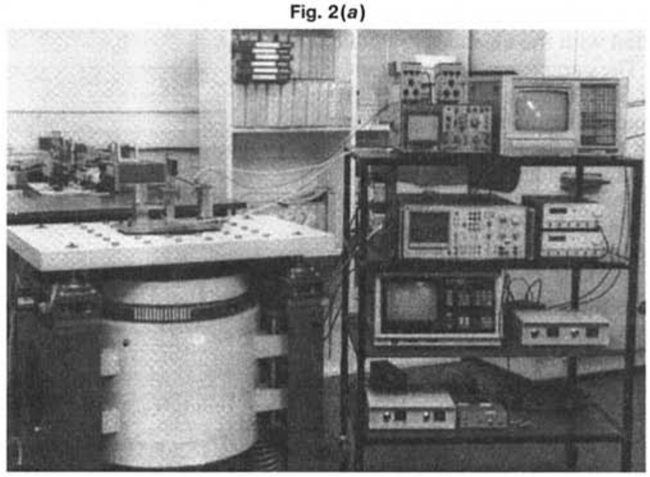

Fig. 2(*b*)

Fig. 2 Data acquisition system; (*a*) schematic layout of the instrumentation, (*b*) photograph of overall view

term was originally devised by Poincaré to describe splitting of equilibrium solutions of differential equations for certain values of the control parameter. This can be conveniently demonstrated for an autonomous system of differential equations as follows:

$$\mathbf{x}' = \mathbf{f}(\mathbf{x}, \mathbf{p}); \quad \mathbf{x} \in \Re^n, \quad \mathbf{p} \in \Re^k \tag{4}$$

where $\mathbf{x}$ is the n-dimensional solution vector, $\mathbf{p}$ is a k-dimensional parameter vector, and prime denotes $d/d\tau$. The equilibrium solutions of (4) are given by the solution of the equation $\mathbf{f}(\mathbf{x}, \mathbf{p}) = \mathbf{0}$. As $\mathbf{p}$ varies, the implicit function theorem implies that these equilibria are described by smooth functions of $\mathbf{p}$ away from those points, at which the Jacobian of $\mathbf{f}(\mathbf{x}, \mathbf{p})$ has its eigenvalues with respect to $\mathbf{x}$ (see Guckenheimer and Holmes, 1983). If the analysis is conducted when only one dimension of $\mathbf{p}$ is considered, one encounters local bifurcation, as will be used throughout this paper. In our case, the parameter vector has five dimensions, $\mathbf{p} = [E, F_0, \beta, \nu, \xi]^T$; however, in the present study a four parameter vector was investigated $\mathbf{p}^* = [E, F_0, \beta, \nu]^T$ by maintaining a constant value of the viscous damping, $\xi = 0.02$.

The experimental bifurcation diagrams were constructed in a similar way to numerical ones, i.e., by varying one of the

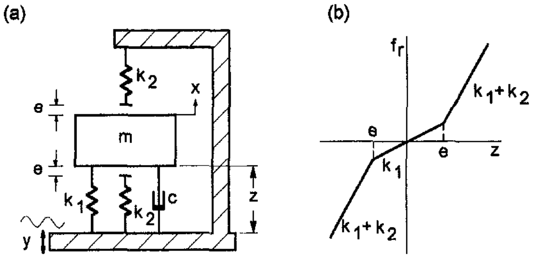

Fig. 3 System with clearance; (a) physical model, (b) relationship between displacement and restoring force

parameters while the others are kept constant, and then projecting the subsequent Poincaré maps on either the displacement or the velocity axis in the domain of the branching parameter. Before any experimental investigation, theoretical bifurcation diagrams were obtained numerically by integrating Eq. (2) and taking a special care about the precise evaluation of the time values when discontinuities occur (Wiercigroch, 1994b). All possible precautions were undertaken to ensure the same initial conditions for all experimentally constructed Poincaré sections; however, there is no absolute guarantee that this was achieved. The parameters varied include: the clearance, modulus of the excitation force, frequency of the excitation, and stiffness ratio. The natural frequency of the oscillator was held constant at 10 Hz throughout the experiment, and a time-step of 0.001 s was used to sample 4096 points for each data set, taken after the transients had died out. Due to the large data storage required to cover systematically the whole range of parameters, only data with major changes of motion were recorded.

5 Experimental Investigations

5.1 Clearance Variation. The experimental data set for the clearance variation was collected with the clearances, e, of 0.5, 0.7, 1.0, 1.3, 1.5, and 1.7 mm. The parameters held constant were Ω at 8 Hz, β at 40, ζ at 0.02, and $Y\Omega^2$ at 14.8 m/s^2. The experimental data was processed and bifurcation diagrams were constructed. As clearly seen in Fig. 4(*b*) the system exhibits a broad band of amplitudes at $e = 0.5$ mm, which gives an indication of possible chaotic motion. This was predicted theoretically, as depicted in the left portion of Fig. 4(*a*), where the phase plane coincides well with the experimental results. The broad range of amplitude obtained when $e = 0.5$ mm is the result of the irregular trajectories portrayed in the phase plane, so-called Lissajous curves. The disordered phase plane gave a broad spectrum of frequencies (Sin and Wiercigroch, 1996) and although additional checks are required to decide about the quality of motion, these three coinciding characteristics support the existence of chaotic motion. As the clearance, e, was increased, the behavior of the system changed, and distinct sets of points were obtained. These points, shown in the bifurcation diagram for clearance values between 0.7 to 1.7 mm (see Fig. 4(*b*)) manifest various periodic motions of the oscillator. For $e = 0.7$ mm, the trajectory creates a closed loop in the phase plane, and period 4 was observed. As the clearance was increased further, the response remained periodic, however, the quality of motion changed and the system went through subcritical bifurcations. Consequently, the system response for $e = 1.3$ has period 3 motion, as depicted in the theoretical (the middle part of Fig. 4(*a*)) and experimental (the middle part of Fig. 4(*b*)) diagrams. Above clearance of 1.3, only period 1 motion was observed, as shown in the right-hand portion of Fig. 4(*b*). However, the theoretical prediction (Fig. 4(*a*)) suggests at approximate clearance of 2 to have period 1, which differs from the experimental results.

The investigation on the clearance variation shows that for this particular set of parameters, chaotic motion was observed for small clearances, and periodic motion occurred for bigger values. An increase in clearance allows the mass to oscillate with a larger amplitude, and then a passage through the change of stiffness becomes smoother. At small clearances, the influence of the secondary stiffness is large, and this generates the rotated V shape of the bifurcation diagram. The mass can only travel a small distance before impacting the secondary spring which causes the irregular trajectories found in the phase plane. This is similar to the grazing effect, which was reported by Nordmark (1991). As the clearance is increased further, various periodic oscillations were obtained, which is mainly due to the decreased influence of the secondary stiffness, however none of the standard route to chaos has been recognised.

5.2 Modulus of Force Variation. For variation of the modulus of the excitation force, $Y\Omega^2$, the experiment was conducted with β set to 40, ξ at 0.02, e at 0.5 mm, and with Ω at 8 Hz. The experimental bifurcation diagram presented in Fig. 5(*b*) correlates reasonably well to its theoretical prediction depicted in Fig. 5(*a*), and which was prepared to cover the same range of the excitation force. Diagram 5(*b*) shows periodic solutions for $Y\Omega^2$ between 2.5 and 11.0 m/s^2, beyond that a broad band of amplitudes was obtained. A study of the phase plane at $Y\Omega^2 = 2.5$ m/s^2 shows the Lissajous curve in the form of an ellipse, indicating a simple periodic motion. Hence, the mass is oscillating periodically and is not in contact with the secondary stiffness. By increasing $Y\Omega^2$ from 3.0 to 3.6 m/s^2, again period 1 was detected, which is visible on the bifurcation

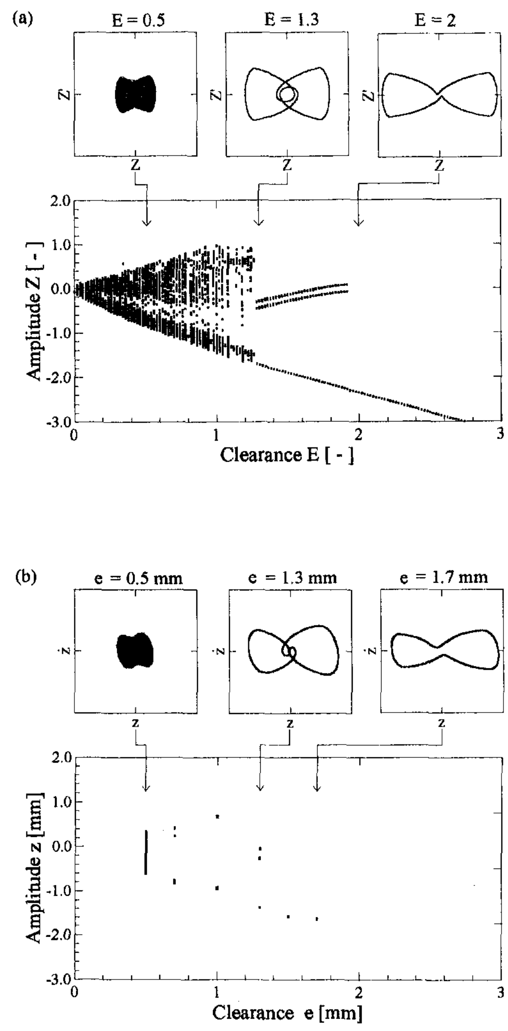

Fig. 4 Bifurcation diagrams, $z = f(e)$; (a) theoretical, (b) experimental

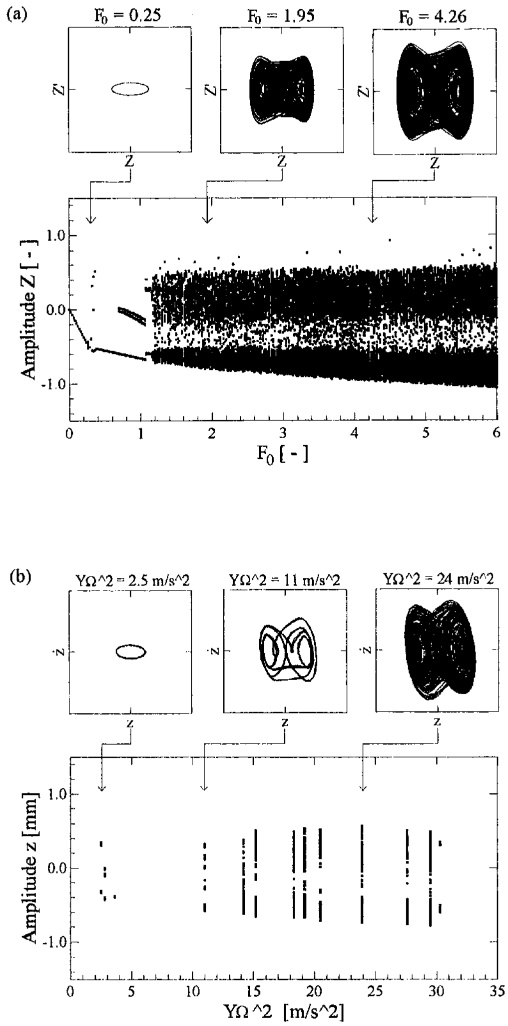

Fig. 5 Bifurcation diagrams, $z = f(Y\Omega^2)$; (*a*) theoretical, (*b*) experimental

diagram. When the excitation force is strong enough for the mass to be in contact with the secondary stiffness, more complex dynamics is revealed. At $Y\Omega^2$ at 11 m/s^2, the number of points in the bifurcation diagram increased. A study of the phase plane shows a period 7 motion, which was not found on the theoretical bifurcation diagram (Fig. 5(a)). This might be due to mismatch between theoretical and real damping in the system or coexistence of another stable solution. By increasing the modulus of excitation force even further, a sudden burst of a wide-band amplitudes occurs, which indicates the existence of chaotic motion. The phase plane corresponding to the cross section of the bifurcation diagram at $Y\Omega^2 = 24$ m/s^2 confirms such behavior.

Comparing the system responses for different values of the external force amplitude, it is clear from the bifurcation diagram and phase planes that periodic motion dominates at low, and chaotic at high, values of the forcing. At low modulus of the excitation force, the mass is insufficiently excited to be in contact with the secondary stiffness, which results in simple, single harmonic oscillations. As the forcing is increased, the oscillations rise in amplitude until the mass hits the secondary stiffnesses. This produces various harmonic and subharmonic motions. On further increasing of the forcing, the mass impacts onto the secondary stiffness generating chaotic motion; however, once again one cannot draw any conclusion about the bifurcation scenario.

5.3 Frequency Variation. The parameters kept constant for the forcing frequency variation were β at 20, ξ at 0.02, e at 0.5 mm and $Y\Omega^2$ at 7.5 m/s^2. The experimental data was processed and the bifurcation diagram illustrated in Fig. 6(b) was constructed. The diagram corresponds reasonably well with the theoretical prediction shown in Fig. 6(a) for the same frequency range as $f_n = 10$ Hz. The system exhibits a period 7 motion for $\Omega = 3$ Hz, which is clearly visible on the phase planes (theoretical and experimental). This is followed by a wide band of amplitudes when Ω is between 4 and 6 Hz. At 6 Hz, the broad band of amplitude is the result of the irregular trajectories portrayed in the phase planes, which indicates the existence of chaotic motion. Although the theoretical bifurcation diagram suggests a crisis type of onset to and from chaos, a specially dedicated theoretical study needs to be carried out. The frequency was increased further, the diagram again showing a set of distinct points indicating periodic motion.

The experimental results for the frequency variation correspond reasonably well with the numerical prediction. Both started off with subharmonic motions at low frequencies and are followed by a region of chaotic oscillations. At higher frequencies, harmonic motion was obtained again in both the experimental and numerical results.

5.4 Stiffness Ratio Variation. For the stiffness ratio variation, the parameters held constant were clearance, e, at 0.5 mm, forcing frequency, Ω, at 20 Hz, dimensionless damping ratio, ξ, at 0.02 and modulus of the forcing, $Y\Omega^2$, at 7.5 m/s^2. The experimental bifurcation diagram shown in Fig. 7(b) is compared with the theoretical prediction depicted in Fig. 7(a). The experimental phase plane when β was at 20 showed period

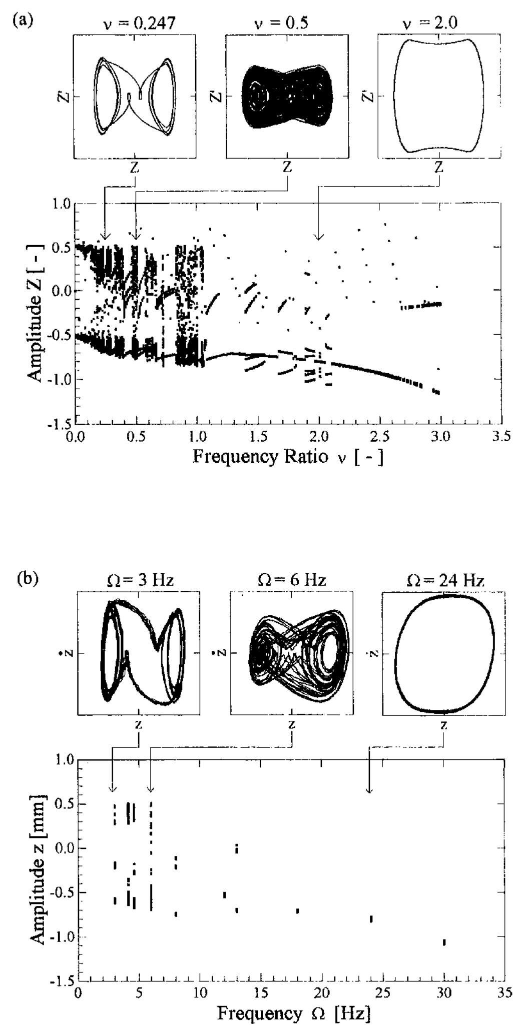

Fig. 6 Bifurcation diagrams, $z = f(\Omega)$; (*a*) theoretical, (*b*) experimental

2 motion, where the theoretical results suggest period 1. However, the differences in amplitudes and frequencies in these two motions are small. For β at 30, the response went through bifurcation and turned into period 5 motion, as depicted in the middle portion of Fig. 7(*b*). This differs from the theory suggesting period 3 as shown in Fig. 7(*a*). On the further increase of β to 50, strictly speaking period 10 is observed (the right-hand portion of Fig. 7(*b*)); however, again from practical stand point, it can be considered as period 5. Also, the differences could be a result of period of doubling bifurcations when phase trajectories split for small variation of the parameter values. Nevertheless, the obtained result coincides reasonably well with the theoretical prediction (Fig. 7(*a*)).

6 Concluding Remarks

The study looked into the behavior of a single-degree-of-freedom sinusoidal base-excited system with symmetrically piecewise linear stiffness characteristics.

A simple piecewise linear system with symmetrical flexible constraints was designed and manufactured to carry out a wide range of experimental dynamic analysis. The task undertaken is twofold; to provide reliable data and, ultimately, to validate the usefulness of widely used piecewise models. The design choice was made based on the criteria of accuracy representing the mathematical model, manufacturing simplicity, flexibility in terms of parameter changes, and cost effectiveness. The system chosen consists of a block mass supported by two leaf springs, whose stiffness can be easily varied by changing their length. The secondary stiffnesses in the form of cantilever beams can be widely varied in the same way. The clearance between the mass and secondary springs can also be varied by adjusting the screws at the ends of the beams. A pneumatic damper is mounted to the upper surface of the mass.

The experimental study was carried out by varying one of the parameters while others were kept constant. The regions of chaotic motion predicted theoretically were confirmed by the experimental results arranged into bifurcation diagrams. Clearance, stiffness ratio, amplitude, and frequency of the external force were used as branching parameters. The discussion of the system dynamics is based on bifurcation diagrams and Lissajous curves. The investigated system tended to be periodic for large clearances and chaotic for small ones. This picture is reversed for the amplitude of the forcing changes, where periodic motion occurred for small values and chaos dominated for larger forcing. The same behavior is observed for increasing frequency ratio, where for values below the natural frequency the most interesting dynamics occurs.

The onset to and from chaos are distinct for the variation of the excitation force amplitude, clearance and frequency; however, none of the typical bifurcation scenarios has been concluded. In case of the modulus of excitation force variation, the system starting from harmonic responses for the noncontacting cases goes through subharmonic motion and ends up with chaotic motion as the magnitude of force was increased. This scenario is reversed for the clearance variation, where the chaotic nature for small clearances died out for the larger ones. By varying the frequency a similar picture is observed, where the most interesting dynamics occurs up to the natural frequency of the system. For the investigated parameter values, the stiffness ratio variation produces only periodic motion.

Although it was not discussed in this paper, it is worth reporting the existence of quasi-periodic motion, noticed for the stiffness variation. However, quasi-periodic motion was only obtained in the experimental results. As this type of motion does not occur in a single-degree-of-freedom system with only stiffness nonlinearities, its appearance in the experimental result must be due to the impact effect, which has been shown by Peterka and Vacik (1992), or alternatively it is possible that the additional springs are behaving as extra degrees-of-freedom.

The experimental studies conducted confirmed the practical usefulness of piecewise models, which are widely used due to the simplicity and convenience of analysis. For some values of branching parameters the experimental results differ from the theoretical predictions, which can be caused by two different sources: coexistence of multiple stable solutions and (or) measurement errors. To eliminate the second source all necessary precautions need to be undertaken at the analysis and interpretation stages to avoid possible discrepancies. Nevertheless, the correlation between theory and experiment obtained, is encouraging and the piecewise models can be recommended for further investigations.

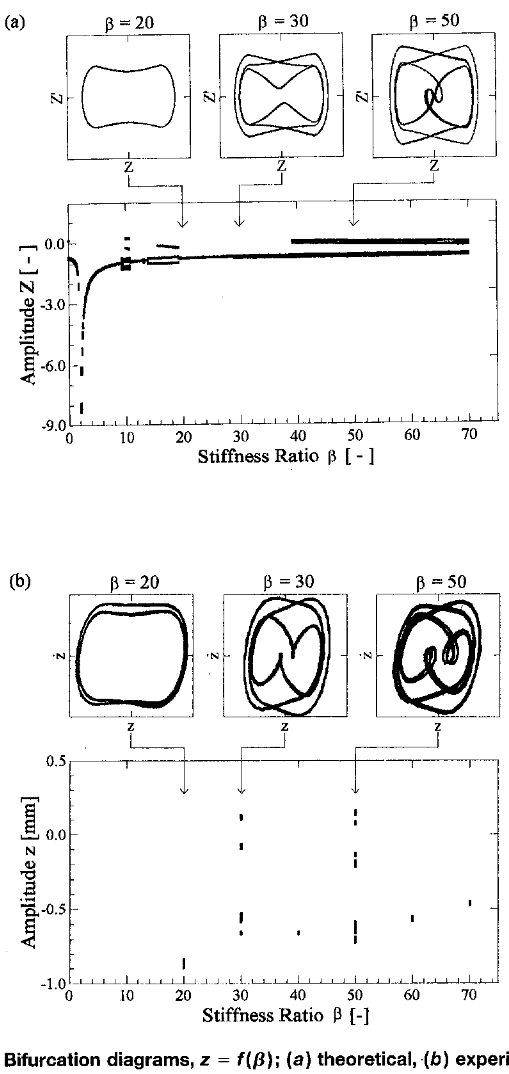

Fig. 7 Bifurcation diagrams, $z = f(\beta)$; (*a*) theoretical, (*b*) experimental

Acknowledgment

The support provided by University of Aberdeen Research Committee Grant No. 724 is gratefully acknowledged. The authors also would like to express their thanks to the anonymous reviewers, Prof. Matthew P. Cartmell, Glasgow University, and Dr. Jason M. Reese, Aberdeen University, for helpful comments on the manuscript.

References

Blankeship, P., and Kahraman, F. 1995, "Steady state forced response of a mechanical oscillator with combined parametric excitation and clearance type non-linearity," *J. Sound and Vibration*, Vol. 185, No. 5, pp. 743–765.

Ehrich, F. F., 1992, "Observations of Subcritical Superhamonic and Chaotic Responses," ASME *Journal of Vibration and Acoustics*, Vol. 114, pp. 93–100.

Gonsalves, H. D., Neilson, R. D., and Barr, A. D. S., 1995, "A study of the response of a discontinuously nonlinear rotor system," *Nonlinear Dynamics*, Vol. 7, pp. 451–470.

Guckenheimer, J., and Holmes, P., 1983, *Nonlinear Oscillations, Dynamical Systems, and Bifurcations of Vector Fields*, Springer-Verlag, New York.

Moon, F. C., and Shaw, S. W., 1983, "Chaotic vibrations of a beam with non-linear boundary conditions," *Int. J. Nonlinear Mechanics*, Vol. 18, pp. 465–477.

Natsiavas, S., 1989, "Periodic response and stability of oscillators with symmetric trilinear restoring force," *J. Sound and Vibration*, Vol. 134, No. 2, pp. 313–331.

Nordmark, A. B., 1991, "Non-periodic motion caused by grazing incidence in an impact oscillator," *J. Sound and Vibration*, Vol. 145, No. 2, pp. 279–287.

Peterka, F., and Vacik, J., 1992, "Transition to chaotic motion in mechanical systems with impacts," *J. Sound and Vibration*, Vol. 154, No. 1, pp. 95–115.

Shaw, S. W., and Holmes, P. J., 1983, "A periodically forced piecewise linear oscillator," *J. Sound and Vibration*, Vol. 90, No. 1, pp. 129–155.

Shaw, S. W., 1985, "Forced vibrations od a beam with one-sided amplitude constraint: Theory and experiment," *J. Sound and Vibration*, Vol. 99, No. 2, pp. 199–212.

Sin, W. T. V., and Wiercigroch, M., 1996, "Experimental and numerical study of a symmetrically piecewise linear oscillator," *Proc. ASME, Elasto-Impact and Friction in Dynamic Systems*, DE-Vol. 90, pp. 63–68.

Stenson, A., and Nordmark, A. B., 1994, "Experimental investigations of some consequences of low impacts in the chaotic dynamics of mechanical system," *Phil. Trans. R. Soc. Lond.*, Vol. A347, pp. 439–448.

Watanabe, T., 1974, "Forced Vibrations of Continuous System With Nonlinear Boundary Conditions," ASME *Journal of Mechanical Design*, Vol. 100, pp. 487–491.

Wiercigroch, M., 1994a, "Bifurcation analysis of harmonically excited linear oscillator with clearance," *Chaos, Solitons and Fractals*, Vol. 4, No. 2, pp. 297–303.

Wiercigroch, M., 1994b, *Dynamics of Discrete Mechanical Systems with Discontinuities*, Silesian University Press, Gliwice (in Polish).

Wiercigroch, M., 1996, "On modelling discontinuities in dynamic systems," *Machine Vibration*, Vol. 5, pp. 112–119.

J. Zhu
Integrated Engineering Software,
Winnipeg, Manitoba R3H 0X4
Canada

A. H. Shah
Professor,
Department of Civil and
Geological Engineering,
University of Manitoba,
Winnipeg R3T 5V6
Canada

S. K. Datta[1]
Professor and Chair,
Department of Mechanical Engineering,
University of Colorado,
CB 427,
Boulder, CO 80309-0427
Fellow ASME

Transient Response of a Composite Plate With Delamination

Transient response of a composite plate with a near-surface delamination has been studied in this paper. A new technique developed by the authors to evaluate the Cauchy Principal Value integrals and the weakly singular integrals involved in the boundary integral equations has been employed and modifided to treat the corner points on the boundary. The time harmonic Green's functions appearing in the boundary integral equation are evaluated by combining a stiffness method and the modal summation technique. To circumvent the difficulties associated with the evaluation of hypersingular integrals for cracks, the multidomain technique is employed. The accuracy and efficiency of the method are checked by comparing the displacements in a uniaxial graphite-epoxy plate containing a delamination with results obtained by a hybrid method. It is shown that the presence of the delamination significantly alters the surface response spectra of the plate. Results are presented in both time and frequency domains. The results show that the technique would be useful for ultrasonic nondestructive evaluation of defects in composite and anisotropic plates, and for studying dynamic response of such plates to impact.

Introduction

Wave propagation and scattering in laminated composite plates are of interest for ultrasonic nondestructive evaluation of defects, material characterization, and for dynamic response studies. In recent years, considerable progress has been made towards understanding wave propagation in composite plates (Datta, et al., 1988; Nayfeh and Chimenti, 1989; Zhu, et al., 1995a). Scattering of a single incident wave mode by a crack has been investigated by Al-Nassar et al. (1991) and Karunasena et al. (1991), who used a hybrid technique consisting of finite element and modal expansion methods. Datta et al. (1992) investigated scattering of Lamb waves, by combining the finite element discretization of the near-field with boundary integral representation of the field outside a contour completely enclosing the crack. Bond (1990) reviewed various applicable numerical techniques for a wave scattering problem, and recommended that the family of boundary methods is well suited for scattering by various defects.

The primary difficulty associated with the finite element method for crack problems stems from the stress field singularity at the crack tips. Accurate approximation of the singular behavior demands refined discretization, leading to a time-consuming computation. Moreover, a changing crack profile requires that the discretization be redone at each step. Working solely with function values on the domain boundary, a boundary integral formulation can circumvent the singularity and, therefore, avoid these difficulties. However, since the boundary integrals involve singular kernels, the integrations have to be performed with care and the overall accuracy of the boundary element methods is largely dependent on the precision with which the various integrals are evaluated. Also, as is well known, the direct boundary element method for a crack geometry fails: the discretization of the whole domain boundary, including both crack surfaces, yields a singular system of equations (Cruse, 1988). This follows from the observation that the integral equations generated by a pair of corresponding nodes on either side of the crack are identical. There have been many efforts devoted to evaluate the hypersingular integrals (Krishnasamy et al., 1990; Sladek et al., 1993) arising from the additional integral equation which expresses the boundary condition on the crack surface. Huang and Cruse (1993) gave a brief review of the techniques to treat the singular integrals involved in boundary integral equations. Most of the existing techniques are based on the explicit analytical expressions of the displacement and traction Green's functions as $\sim \ln r$ and $\sim r^{-1}$ in two dimensions, and as $\sim r^{-1}$ and $\sim r^{-2}$ in three-dimensional problems, respectively, where r is the distance between the source and field points. It may be noted that all these methods are valid only for smooth boundaries. Boundaries with corners pose considerable difficulties.

When the boundary element method is applied to the problem of wave propagation and scattering in composite laminates, the application of the infinite plane Green's function, if not impossible, is extremely difficult. It is not only because of the complexity in discretizing the interfaces between the different layers, but also because of the difficulty in deriving the explicit expression of the fundamental solution for infinite anisotropic media in time domain or in the transformed frequency domain.

Although the time harmonic Green's functions of layered media can be expressed as wave number integrals (Xu and Mal, 1987), the numerical evaluation of these integrals is quite a difficult task even for isotropic media. Also, when these Green's functions are employed in the boundary element analysis, the computations, which are very time-consuming (Datta et al., 1992), have to be repeated for any change in the location of the source or field point. To overcome this difficulty, the Green's functions in the present study are obtained through combining a stiffness method suggested by Dong and Huang (1985) and the modal summation technique. By solving the standard eigenvalue problem once, the eigenvalues and eigenvectors are obtained and stored, the Green's functions are computed in a discrete form through the thickness by the modal summation.

[1] To whom all correspondence should be addressed.

Contributed by the Applied Mechanics Division of THE AMERICAN SOCIETY OF MECHANICAL ENGINEERS for publication in the ASME JOURNAL OF APPLIED MECHANICS.

Discussion on the paper should be addressed to the Technical Editor, Professor Lewis T. Wheeler, Department of Mechanical Engineering, University of Houston, Houston, TX 77204-4792, and will be accepted until four months after final publication of the paper itself in the ASME JOURNAL OF APPLIED MECHANICS.

Manuscript received by the ASME Applied Mechanics Division, Dec. 5, 1996; final revision, Dec. 9, 1997. Associate Technical Editor: J. N. Reddy.

When the Green's functions for laminated composites (either in wave number integral form or discrete summation form) are used in the boundary element method, all the established techniques based on the analytical expressions of Green's functions to treat the singular integrals fail. Most recently, Zhu et al. (1996) established a new technique to evaluate the Cauchy Principal Value, singular and weakly singular integrals simultaneously by introducing the fictitious source concept. Numerical results have shown the accuracy and reliability of the technique.

In this paper, boundary element method is used to investigate the scattering of impact waves by delamination in a laminated composite plate. The new technique developed by the authors are employed and modifided to evaluate the Cauchy Principle Value and weakly singular integrals involved in the boundary integral equations. A double-node technique is incoporated to evaluate the singular integrals at corner points. In order to circumvent the difficulties associated with the evaluation of hypersingular integrals due to the presence of the delamination, the multidomain technique is adopted. Scattered wave fields for a uniaxial graphite-epoxy plate with a near-surface delamination have been computed and compared with the results from a hybrid method (Zhu, et al., 1995b). It is shown that the boundary element technique developed here is very accurate and efficient. It is demonstrated that the size and location of the delamination modifies the surface response spectra in the plate. Results for the time-domain response are obtained from the frequency-dependent response by employing inverse Fourier Transform. The transient response of top surface shows the effects of waves traveling and being scattered between the top surface and the crack surface. Numerical results indicate that the applications of this method to the ultrasonic nondestructive evaluation of defects and the study of dynamic response due to defects are very promising.

Formulation of the Problem

Consider a linearly elastic body of volume V, bounded by a regular surface S. The boundary integral equation in the Fourier transformed domain can be derived by combining the fundamental point-force solution with Betti's reciprocal theorem (Brebbia et al., 1984) as

$$c_{ij}(\xi)u_j(\xi) = \int_s [G_{ij}(\mathbf{x}, \xi)t_j(\mathbf{x}) - H_{ij}(\mathbf{x}, \xi)u_j(\mathbf{x})]dS + \int_v G_{ij}(\mathbf{x}, \xi)f_j(\mathbf{x})dV, \quad (1)$$

where u_i and t_i are the displacement and traction vectors, respectively; ξ and $\mathbf{x}$ are, respectively, the field and source points; and f_i is the body force vector. $G_{ij}(\mathbf{x}, \xi)$ is the displacement Green's function and represents the displacements at point ξ due to a unit harmonic point force of the form $e^{-j\omega t}$ ($j = \sqrt{-1}$) applied at point $\mathbf{x}$. $H_{ij}(\mathbf{x}, \xi)$ represents the tractions at point ξ due to the same load. The tensor c_{ij} is the well-known discontinuity term and ω the circular frequency.

Governing Equations. Dong and Huang (1985) presented a numerical technique applicable to plane wave propagation analysis in a layered anisotropic plate. The technique starts with dividing each lamina into several sublayers so that the total number of sublayers through the thickness ($2H$) of the plate is N (Fig. 1). Variations of the displacements through the thickness of each sublayer are approximated by quadratic functions of a thickness variable. The generalized coordinates in this representation are the displacements at the top, middle, and bottom of each sublayer.

For plane-strain condition, the relevant stress and strain components for the ith sublayer are related by

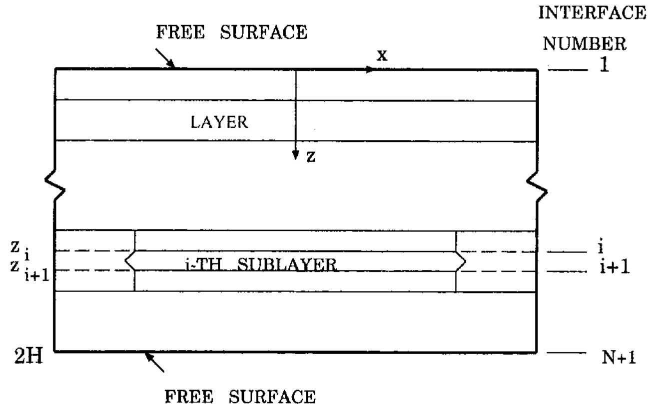

Fig. 1 Geometry of a laminated composite plate

$$\begin{Bmatrix} \sigma_{xx} \\ \sigma_{zz} \\ \sigma_{zx} \end{Bmatrix} = \begin{bmatrix} D_{11} & D_{13} & 0 \\ D_{13} & D_{33} & 0 \\ 0 & 0 & D_{55} \end{bmatrix} \begin{Bmatrix} \epsilon_{xx} \\ \epsilon_{zz} \\ 2\epsilon_{zx} \end{Bmatrix} \quad (2)$$

where σ_{ij} and ϵ_{ij} are the stress and strain components, and D_{ij} are the elements of the constitutive matrix for the sublayer. It is assumed here that each sublayer is orthotropic with symmetry axes paralled to the x and z-axes.

By applying the principle of virtual work to each sublayer, a set of approximate differential equations can be established. The governing equation for the entire plate is obtained by summation over all the sublayers (Karunasena et al., 1991) as

$$\mathbf{F} = \left(-\mathbf{K}_1 \frac{\partial^2}{\partial x^2} + \mathbf{K}_2 \frac{\partial}{\partial x} + \mathbf{K}_3 - \omega^2 \mathbf{M} \right) \mathbf{Q} \quad (3)$$

where the vectors $\mathbf{Q}$ and $\mathbf{F}$ represent the nodal displacements and tractions applied at the interfaces of the plate, respectively. The sizes of $\mathbf{Q}$ and $\mathbf{F}$ are $M \times 1$, and the sizes of matrices $\mathbf{M}$ and $\mathbf{K}_i$ ($i = 1, 2, 3$) are $M \times M$, where $M = 2 \times (2N + 1)$. Note that the matrices $\mathbf{M}$, $\mathbf{K}_1$, and $\mathbf{K}_3$ are real and symmetric, whereas $\mathbf{K}_2$ is real and antisymmetric.

Applying the Fourier transform with respect to x as

$$\tilde{f}(k) = \int_{-\infty}^{\infty} f(x)e^{-jkx}dx \quad (4)$$

to (3), the governing equation in the transformed domain is found to be

$$\tilde{\mathbf{F}} = (k^2\mathbf{K}_1 + jk\mathbf{K}_2 + \mathbf{K}_3^*)\tilde{\mathbf{Q}} \quad (5)$$

where k is the wave number in the x direction, $\tilde{\mathbf{F}}$ and $\tilde{\mathbf{Q}}$ are the Fourier transform of $\mathbf{F}$ and $\mathbf{Q}$, and $\mathbf{K}_3^* = \mathbf{K}_3 - \omega^2\mathbf{M}$.

Eigenvalue Problem. By setting $\tilde{\mathbf{F}} = \mathbf{0}$, the eigenvalue equation is obtained from Eq. (5) and can be arranged in the form

$$\mathbf{E}_1\mathbf{\Phi}_m^R = k_m\mathbf{\Phi}_m^R; \quad \mathbf{\Phi}_m^L\mathbf{E}_2 = k_m\mathbf{\Phi}_m^L \quad (6)$$

where

$$\mathbf{E}_1 = \begin{bmatrix} \mathbf{0} & \mathbf{I} \\ \mathbf{K}_1^{-1}\mathbf{K}_3^* & j\mathbf{K}_1^{-1}\mathbf{K}_2 \end{bmatrix};$$

$$\mathbf{E}_2 = \begin{bmatrix} \mathbf{0} & -\mathbf{K}_1^{-1} \\ \mathbf{K}_3^* & -j\mathbf{K}_2\mathbf{K}_1^{-1} \end{bmatrix} \quad (7)$$

$\mathbf{\Phi}_m^R$ and $\mathbf{\Phi}_m^L$ are right and left eigenvectors, respectively, and can be written in the partitioned forms as

$$\Phi_m^L = \langle \tilde{\mathbf{Q}}_m^L k_m \tilde{\mathbf{Q}}_m^L \rangle; \quad \Phi_m^R = \begin{Bmatrix} \tilde{\mathbf{Q}}_m^R \\ k_m \tilde{\mathbf{Q}}_m^R \end{Bmatrix} \tag{8}$$

in which $\tilde{\mathbf{Q}}_m^L$ and $\tilde{\mathbf{Q}}_m^R$ have sizes $1 \times M$ and $M \times 1$, respectively.

Green's Function in Frequency Domain. Following the modal summation technique (Liu and Achenbach, 1995) and making use of the orthogonality conditions of the left and right eigenvectors, we obtain the displacement in transformed domain as

$$\tilde{\mathbf{Q}} = \sum_{m=1}^{2M} \frac{k_m \tilde{\mathbf{Q}}_m^L \tilde{\mathbf{F}} \tilde{\mathbf{Q}}_m^R}{(k_m - k) B_m} \tag{9}$$

where

$$B_m = \tilde{\mathbf{Q}}_m^L \tilde{\mathbf{Q}}_m^R + k_m^2 \tilde{\mathbf{Q}}_m^L \mathbf{K}_1 \tilde{\mathbf{Q}}_m^R. \tag{10}$$

The displacement Green's functions along the thickness of the plate in the spatial domain due to a point load acting at point (x_0, z_0) can be obtained by applying the inverse Fourier transformation to Eq. (9) as

$$\mathbf{G}(x; x_0, z_0) = \frac{1}{2\pi} \int_{-\infty}^{\infty} \sum_{m=1}^{2M} \frac{k_m \tilde{\mathbf{Q}}_m^L \mathbf{F}_0 \tilde{\mathbf{Q}}_m^R}{(k_m - k) B_m} e^{jk(x-x_0)} dk \tag{11}$$

where $\mathbf{F}_0$ is a constant vector representing the amplitude of the external force. It is noted that in Eq. (11), $\tilde{\mathbf{Q}}_m^L$, $\tilde{\mathbf{Q}}_m^R$, $\mathbf{F}_0$, and B_m are independent of k. Also, of the $2M$ eigenvalues half of these (M) correspond to the waves traveling or decaying from source point toward infinity while the other half correspond to the waves traveling towards the source (Kausel and Peek, 1982). Applying Cauchy's Residue Theorem, choosing the M modes that decay with distance from the source or that propagate away from it, we obtain

$$\mathbf{G}(x; x_0, z_0) = -\sum_{m=1}^{M} \frac{jk_m \tilde{\mathbf{Q}}_m^L \mathbf{F}_0 \tilde{\mathbf{Q}}_m^R}{B_m} e^{jk_m(x-x_0)}. \tag{12}$$

The traction Green's functions can be obtained by using the constitutive equations.

Numerical Implementation

Equation (1) cannot, in general, be solved analytically and therefore resort must be taken to numerical methods of solution. For this purpose, the boundary is represented by a series of elements connected to boundary nodes. With the spatial discretization, writing Eq. (1) for each of the nodes, and allowing field point ξ to coincide sequentially with all the nodal points of the boundary, the global system of boundary element equations is obtained as (Brebbia et al., 1984)

$$\mathbf{H}\mathbf{u} = \mathbf{G}\mathbf{t} + \mathbf{b} \tag{13}$$

where matrix $\mathbf{H}$ contains the c_{ij} tensor and the traction kernel integrals, matrix $\mathbf{G}$ contains the displacement kernel integrals, and $\mathbf{u}$ and $\mathbf{t}$ are composed of the displacements and tractions at the nodes, respectively. $\mathbf{b}$ is due to the last integral in Eq. (1) containing the body force.

Evaluation of the Cauchy Principal Value and Weakly Singular Integrals. The diagonal 2×2 block of the assembled $\mathbf{H}$ matrix contains the tensor c_{ij} as well as the Cauchy Principle Value of the traction kernel integrals; also, the diagonal elements of the assembled $\mathbf{G}$ matrix contain the weakly singular displacement kernel integrals. An effective technique to evaluate these singular integrals is critical to the accuracy of the boundary element solution. As mentioned before, most of the existing methods to treat these singular integrals are based on the properties of full-plane/space Green's functions. They cannot be employed here. A new technique has been developed by the authors (Zhu et al., 1996). The technique starts with computing the displacement and traction Green's functions at the boundary nodes due to a point load inside the volume (artificial source). By applying these tractions back on the boundary, together with the artificial point load, we establish a well-posed boundary value problem. Assuming that this problem is solved by boundary element method with identical discretization, we expect that the same displacements at the boundary nodes will be obtained as computed before (i.e., the displacement Green's functions) provided that the Cauchy Principal Value and weakly singular integrals were evaluated accurately. Now, we invert the procedure. We assume that the diagonal 2×2 block elements of $\mathbf{H}$ ($h_{i,i}$, $h_{i,i+1}$, $h_{i+1,i}$ and $h_{i+1,i+1}$) and diagonal elements of $\mathbf{G}$ ($g_{i,i}$ and $g_{i+1,i+1}$) for each boundary node, I, are unknown, while the displacements, u_i, u_{i+1}, and tractions, t_i, t_{i+1}, are known (with i representing x direction components, $i+1$ representing z-direction components). Writing the boundary integral equations for each node I, we obtain

$$h_{i,i}u_i + h_{i,i+1}u_{i+1} - g_{i,i}t_i = \sum_{l \neq i,i+1} (-h_{i,l}u_l + g_{i,l}t_l) + g_{i,i+1}t_{i+1} + b_i \tag{14}$$

$$h_{i+1,i}u_i + h_{i+1,i+1}u_{i+1} - g_{i+1,i+1}t_{i+1} = \sum_{l \neq i,i+1} (-h_{i+1,l}u_l + g_{i+1,l}t_l) + g_{i+1,i}t_i + b_{i+1} \tag{15}$$

where u_l and t_l are the known displacements and tractions (Green's functions) due to the artificial source, $h_{i,l}$ and $g_{i,l}$ ($l \neq i$, $i+1$) on the right-hand side are the known elements of the matrices $\mathbf{H}$ and $\mathbf{G}$ in Eq. (13), and contain only regular integrals. From this concept, by choosing three independent artificial sources, we obtain sufficient number of equations to solve all the elements of the diagonal blocks in matrices $\mathbf{H}$ and $\mathbf{G}$. Details and numerical demonstration of the accuracy and the reliability of the technique can be found in Zhu et al. (1996).

Treatment of Corner Points. As is well known, the evaluation of the singular integrals around corner points of the boundary is complicated. A double nodes technique (Brebbia et al., 1984) is incorporated here. As shown in Fig. 2, two nodes, I and J, with the same coordinates are set on the adjacent sides of a corner point. Applying Eqs. (14) and (15) to point I, and noticing that one more off-diagonal 2×2 block of $\mathbf{H}$ and other two off-diagonal elements in $\mathbf{G}$ corresponding to node J contain singular integrals on the right-hand side of the Eqs. (14) and (15), we can manipulate these equations as

$$u_i(h_{i,i} + h_{i,j}) + u_{i+1}(h_{i,i+1} + h_{i,j+1}) - t_i g_{i,i} - t_j g_{i,j} = \sum_{l \neq i,i+1,j,j+1} (-h_{i,l}u_l + g_{i,l}t_l) + g_{i,i+1}t_{i+1} + g_{i,j+1}t_{j+1} + b_i \tag{16}$$

$$u_i(h_{i+1,i} + h_{i+1,j}) + u_{i+1}(h_{i+1,i+1} + h_{i+1,j+1}) - t_{i+1}g_{i+1,i+1} - t_{j+1}g_{i+1,j+1} = \sum_{l \neq i,i+1,j,j+1} (-h_{i+1,l}u_l + g_{i+1,l}t_l) + g_{i+1,i}t_i + g_{i+1,j}t_j + b_{i+1}. \tag{17}$$

In the above the continuity conditions

$$u_i = u_j, \quad u_{i+1} = u_{j+1} \tag{18}$$

are employed. Applying the concept of artificial source to each of the Eqs. (16) and (17) and choosing four artificial sources, we can establish the following two sets of linear equations:

$$\begin{bmatrix} u_i^1 & u_{i+1}^1 & -t_i^1 & -t_j^1 \\ u_i^2 & u_{i+1}^2 & -t_i^2 & -t_j^2 \\ u_i^3 & u_{i+1}^3 & -t_i^3 & -t_j^3 \\ u_i^4 & u_{i+1}^4 & -t_i^4 & -t_j^4 \end{bmatrix} \begin{Bmatrix} h_{i,i} + h_{i,j} \\ h_{i,i+1} + h_{i,j+1} \\ g_{i,i} \\ g_{i,j} \end{Bmatrix} = \begin{Bmatrix} r_i^1 \\ r_i^2 \\ r_i^3 \\ r_i^4 \end{Bmatrix} \tag{19}$$

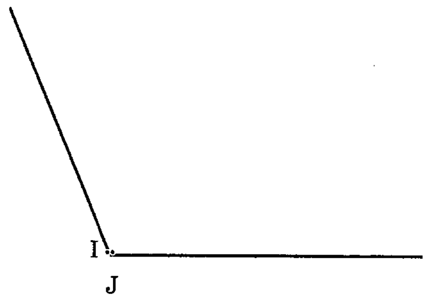

Fig. 2 Corner points

$$\begin{bmatrix} u_i^1 & u_{i+1}^1 & -t_{i+1}^1 & -t_{j+1}^1 \\ u_i^2 & u_{i+1}^2 & -t_{i+1}^2 & -t_{j+1}^2 \\ u_i^3 & u_{i+1}^3 & -t_{i+1}^3 & -t_{j+1}^3 \\ u_i^4 & u_{i+1}^4 & -t_{i+1}^4 & -t_{j+1}^4 \end{bmatrix} \begin{Bmatrix} h_{i+1,i} + h_{i+1,j} \\ h_{i+1,i+1} + h_{i+1,j+1} \\ g_{i+1,i+1} \\ g_{i+1,j+1} \end{Bmatrix} = \begin{Bmatrix} r_{i+1}^1 \\ r_{i+1}^2 \\ r_{i+1}^3 \\ r_{i+1}^4 \end{Bmatrix} \qquad (20)$$

where the superscript refers to the artificial source number, r_i represents the right-hand sides of Eqs. (16) and (17). Also, equations corresponding to nodes I and J in (13) are modified according to the continuity condition (18) so that the solutions from (19) and (20) can be applied.

Numerical Results. The method discussed above is employed to study the elastodynamic displacements in a uniaxial graphite-epoxy plate of thickness $2H$ (=5.08 mm) with a delamination, as shown in Fig. 3. The vertical load is applied on the top surface of the plate at a distance 3.5H to the left of the origin. The relevant elastic constants characterizing the plate material are D_{11} = 160.7 GPa, D_{33} = 13.92 GPa, D_{13} = 6.44 GPa, and D_{55} = 7.07 GPa, and the density is 1.8 g/cm^3. Thus, the longitudinal (c_p) and shear (c_s) wave speeds in the x-direction are 9.45 mm/μs and 1.98 mm/μs, respectively. The normalized cutoff frequencies, Ω (=$\omega H/c_s$), for the first two symmetric ($S1$, $S2$) and antisymmetric ($A1$, $A2$) modes are 2.20, 3.14, and 1.57, 4.4, respectively. This example is chosen purely for illustration. Multilayered plates (anisotropic) can be treated in the same manner.

In the first step, the plate is divided into sixteen sublayers to compute the eigenvalues and eigenvectors.

To overcome the difficulties associated with the evaluation of hypersingular integrals due to the presence of delamination, the multidomain technique (Blanford et al., 1981) is used. The essence of this technique is multidomain discretization and the use of the boundary integral equations for each domain. As shown in Fig. 3, the plate is divided into two domains by the delamination and the fictitious boundaries (dashed line). The displacement continuity condition and stress equilibrium condition are employed on the fictitious boundaries. Since the ultrasonic small displacements are of interest for the nondestructive evaluation purpose, we assume that the delamination is open. The stress-free condition is applied on the delamination surfaces. The boundary element mesh is composed of 124 quadratic elements and 204 nodes. Eight crack-tip singular elements (Blanford et al., 1981) are used.

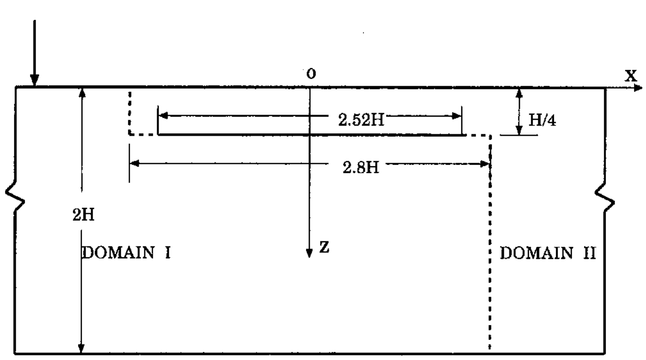

Fig. 3 Configuration of a composite plate with delamination

To illustrate the reliability and efficiency of the boundary element method, the problem is also solved by a hybrid method (Zhu, et al., 1995b), wherein the plate is divided into two regions: interior region bounded by two vertical boundaries at $x = -1.4H$ and $x = 1.4H$, and exterior region (outside the interior region). The interior region is modeled by the finite element method while the exterior region is represented by the modal summation formulation. The finite element mesh is composed of 392 quadratic elements and 1280 nodes.

The vertical displacements at two sections, $x = -1.4H$ and $x = 5H$, from the two methods are presented in Fig. 4 for Ω = 1 (the results from hybrid method are referred as the finite element method (FEM) in the figure). It is noted that due to a fairly large discretized region, the accuracy of the hybrid

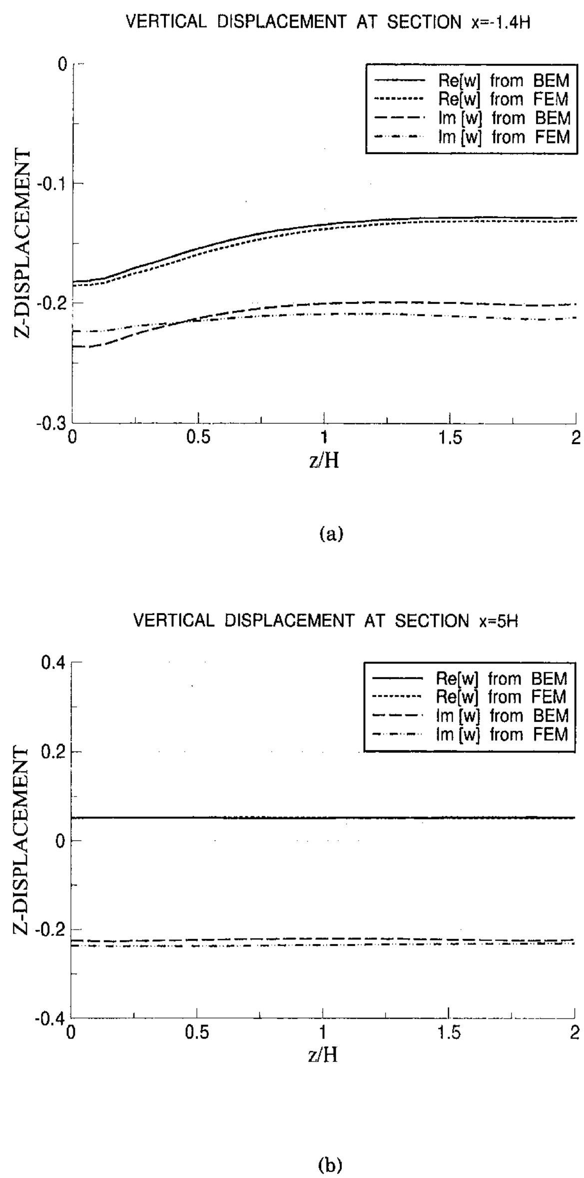

Fig. 4 Vertical displacements at two sections for Ω = 1; (*a*) $x = -1.4H$, (*b*) $x = 5H$

method degenerates especially in the near field. The results in the far field are in better agreements, as expected. The CPU time to solve this problem on a IBM RS6000/590 computer is 4 minutes and 20 seconds for the boundary element method and 20 minutes and 55 seconds for hybrid method.

Figures 5(a) and (b) show the frequency response of the top surface in the absence and presence of the delamination, respectively. The peaks at the cutoff frequencies for the first symmetric (2.20) and the second antisymmetric (4.40) are clearly seen in the absence of delamination in Fig. 5(a). In the presence of delamination, two significant features are observed which can be exploited to determine its size and location. First, the peaks at the cutoff frequency for the first antisymmetric mode (1.57) are prominent at the points between the ends of the delamination. Specifically, the surface response shows two pronounced maxima almost symmetrical about the origin above the center of delamination, as illustrated in Fig. 6. It is noted that each peak is at the point with $L/4$ distance from the origin (L is the crack length). This feature can be used to estimate

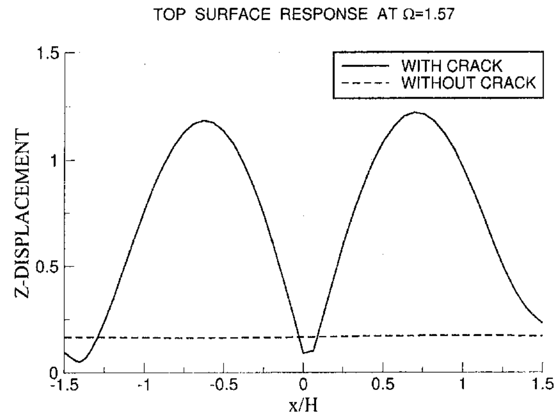

Fig. 6 Top surface response at Ω = 1.57

the crack length. For example, the left peak in Fig. 6 is at $-0.63H$, which gives the crack length to be $2.52H$. Secondly, there is a pronounced peak at $\Omega = 0.55$ (shown in Fig. 7). This peak is due to the resonance of the plate of finite length L above the delamination. This feature can be used to determine the depth of delamination. Since the ratio of delamination length ($2.52H$) to its depth ($H/4$) is large (>10), we can use locally the plate bending theory to determine the resonance frequency. The natural frequency of this plate is 0.54 for simply supported ends. The same results were observed by Datta et al. (1992). Similar conclusions were drawn by Keer et al. (1984) and Cawley and Theodorakopoulos (1989) that the resonance frequency for a defect may be predicted by using plate theory with length equal to delamination length and thickness equal to its depth. Figure 7 shows that the dynamic response of the plate above the delamination has several pronounced peaks at the resonance frequencies of the plate.

Transient response of the top surface, for the load acting at the same location as before, in the absence and presence of delamination is presented in Figs. 8(a) and (b), respectively. The time-dependence of the load was assumed as

$$f(\tau) = \frac{2}{\sqrt{2\pi}} e^{-(\tau-\tau_0)^2/2} \sin(\Omega_c \tau) \tag{21}$$

where normalized time $\tau = c_s t/H$. The time delay τ_0 was taken as 3.0, and the normalized central frequency Ω_c was taken as 3.14.

It is seen that the predominant response is due to the Rayleigh wave that is traveling at a speed, determined as about 1.8 mm/μs in the absence of crack. In the presence of a crack, however, the surface response is fairly complicated. Due to the diffraction

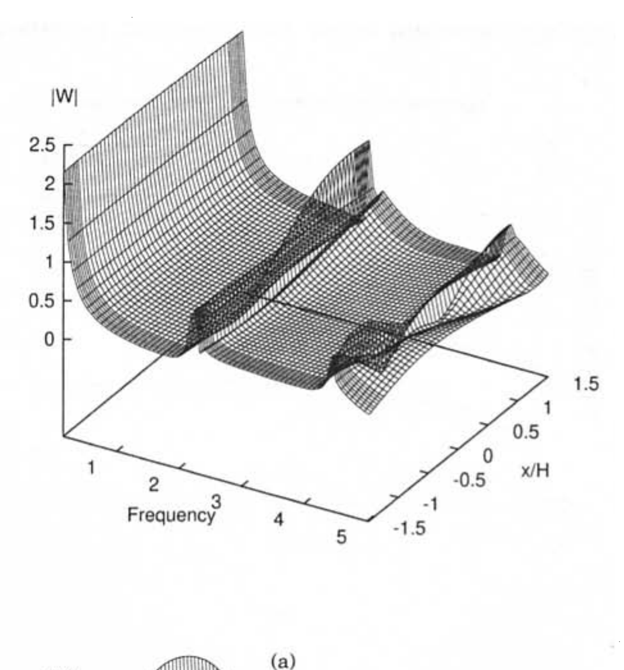

(b)

Fig. 5 Response spectra of top surface; (*a*) without delamination, (*b*) with delamination

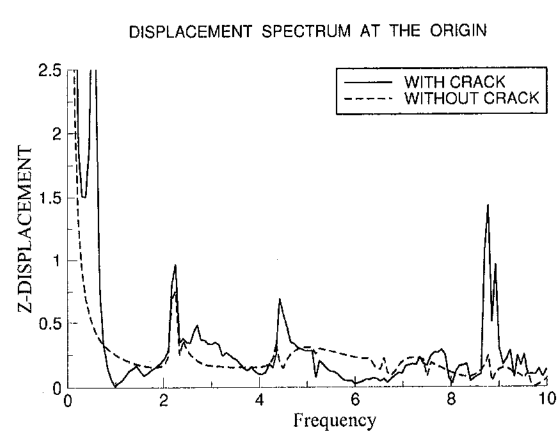

Fig. 7 Displacement spectrum at the origin

of Rayleigh waves by the left crack-tip, both dilatational and shear waves are generated. These waves, together with the Rayleigh waves, travel between the top surface of the plate and the new boundary-crack surface. Multiple reflections of waves between the boundary surfaces occur in this part with mode conversions. This is reflected in the complicated surface response at early time above the delamination (Fig. 8(*b*)). Figure 9 shows the response at the point above the right end of delamination. The presence of the delamination is seen to greatly modify the signal.

Conclusion

A general boundary element method for solving elastic wave scattering by a delamination in a laminated composite plate has been presented. The Green's function is obtained by combining a stiffness method and modal summation technique. A new method developed by the authors is applied here to evaluate the Cauchy Principal Value integrals and weakly singular integrals arising in the boundary integral equations. The response spectrum of the top surface has been analyzed and it is shown that this can be used to determine the size and location of the delamination. Numerical results show that application of the technique in nondestructive evaluation of defects is very promising. Since both near field and far field are calculated, results for the stress distribution close to delamination can be obtained. The stress concentration due to the presence of delamination can be calculated. This will be discussed in a later communication.

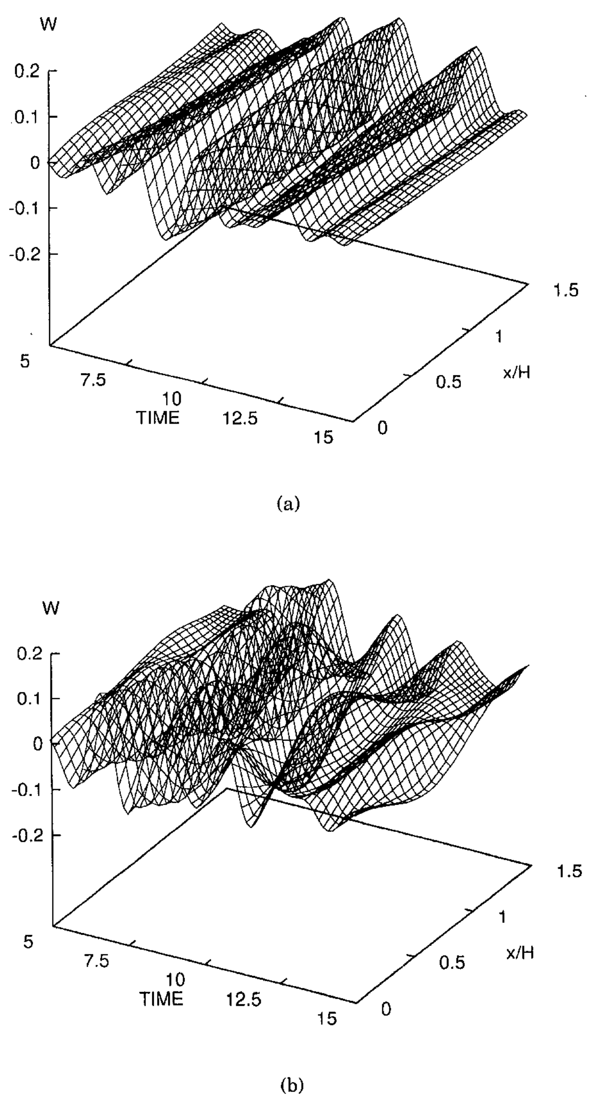

Fig. 8 Transient response of top surface; (*a*) without delamination, (*b*) with delamination

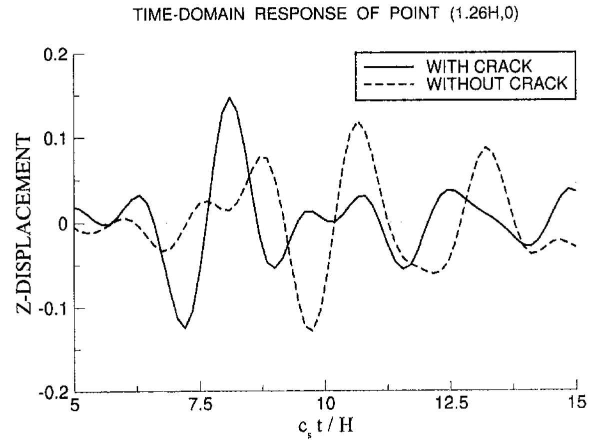

Fig. 9 Transient response of point (1.26*H*, 0)

Acknowledgment

The work reported here was supported in part by a grant from the Natural Science and Engineering Research Council of Canada (0GP-0007988). The first author would like to acknowledge the financial support from the University of Manitoba through Graduate Fellowship awards.

References

Al-Nassar, Y. N., Datta, S. K., and Shah, A. H., 1991, "Scattering of lamb waves by a normal rectangular strip weldment," *Ultrasonics*, Vol. 29, pp. 125–132.

Blanford, G. E., Ingraffea, A. R., and Liggett, J. A., 1981, "Two-dimensional stress intensity factor computations using the boundary element method," *Int. J. Numer. Methods Eng.*, Vol. 17, pp. 387–404.

Bond, L. J., 1990, "Numerical techniques and their use to study wave propagation and scattering—A review," *Proceedings of the IUTAM Symposium on Elastic Wave Propagation and Ultrasonic Evaluation*, pp. 17–27.

Brebbia, C. A., Telles, J. C. F., and Wrobel, L. C., 1984, *Boundary Element Techniques—Theory and Applications in Engineering*, Springer-Verlag, Berlin.

Cawley, P., and Theodorakopoulos, C., 1989, "The Membrane Resonance Method of Nondestructive Testing," *Journal of Sound and Vibration*, Vol. 130, No. 2, pp. 299–311.

Cruse, T. A., 1988, *Boundary Element analysis in Computational Fracture Mechanics*, Kluwer Academic Publishers, Boston.

Datta, S. K., Shah, A. H., Bratton, R. L., and Chakraborty, T., 1988, "Wave propagation in laminated composite plates," *J. Acoust. Soc. Am.*, Vol. 83, pp. 2020–2026.

Datta, S. K., Ju, T. H., and Shah, A. H., 1992, "Scattering of an Impact Wave by a Crack in a Composite Plate," ASME JOURNAL OF APPLIED MECHANICS, Vol. 59, pp. 596–603.

Dong, S. B., and Huang, K. H., 1985, "Edge vibrations in laminated composite plate," ASME JOURNAL OF APPLIED MECHANICS, Vol. 52, pp. 433–438.

Huang, Q., and Cruse, T. A., 1993, "Some notes on singular integral techniques in boundary element analysis," *Int. J. Numer. Methods Eng.*, Vol. 36, pp. 2643–2659.

Karunasena, W. M., Shah, A. H., and Datta, S. K., 1991, "Plane-strain-wave scattering by cracks in laminated composite plates," *J. Engng. Mech.*, Vol. 117, No. 8, pp. 1738–1754.

Kausel, E., and Peek, R., 1982, "Dynamic loads in the interior of a layered stratum: An explicit solution," *Bull. Seism. Soc. Am.*, Vol. 72, pp. 1459–1482.

Keer, L. M., Lin, W., and Achenbach, J. D., 1984, "Resonance Effects for a Crack Near a Free Surface," ASME JOURNAL OF APPLIED MECHANICS, Vol. 51, pp. 65–70.

Krishnasamy, G., Schmerr, L. W., Rudolphi, T. J., and Rizzo, F. J., 1990, "Hypersingular Boundary Integral Equations: Some Applications in Acoustic and Elastic Wave Scattering," ASME JOURNAL OF APPLIED MECHANICS, Vol. 57, pp. 404–414.

Liu, G. R., and Achenbach, J. D., 1995, "Strip Element Method to Analyze Wave Scattering by Cracks in Anisotropic Laminated Plates," ASME JOURNAL OF APPLIED MECHANICS, Vol. 62, pp. 607–613.

Nayfeh, A. H., and Chimenti, D. E., 1989, "Free Wave Propagation in Plates of General Anisotropic Media," ASME JOURNAL OF APPLIED MECHANICS, Vol. 56, pp. 881–886.

Sladek, V., Sladek, J., and Tanaka, M., 1993, "Regularization of hypersingular and nearly singular integrals in the potential theory and elasticity," *Int. J. Numer. Methods Eng.*, Vol. 36, pp. 1609–1628.

Xu, P. C., and Mal, A. K., 1987, "Calculation of the Green's functions for a layered viscoelastic solid," *Bull. Seism. Soc. Am.*, Vol. 77, pp. 1823–1837.

Zhu, J., Shah, A. H., and Datta, S. K., 1996, "The evaluations of Cauchy Principal Value integrals and weakly singular integrals in BEM and their applications," *Int. J. Numer. Methods Eng.*, Vol. 39, pp. 1017–1028.

Zhu, J., Shah, A. H., and Datta, S. K., 1995a, "Modal representation of two-dimensional elastodynamic Green's functions," *J. Eng. Mech.*, Vol. 121, pp. 26–36.

Zhu, J., Datta, S. K., and Shah, A. H., 1995b, "Modal representation of transient dynamics of laminated plates," *Composites Engineering*, Vol. 5, pp. 1477–1487.

F. Pourboghrat
Assistant Professor,
Department of Mechanical Engineering,
Michigan State University,
East Lansing, MI 48824-1226
Assoc. Mem. ASME

K. Chung
Department of Fiber and
Polymer Science,
Seoul National University,
Seoul, Korea
Assoc. Mem. ASME

O. Richmond
Alcoa Technical Center,
Alcoa Center, PA 15069-0001

A Hybrid Membrane/Shell Method for Rapid Estimation of Springback in Anisotropic Sheet Metals

A semi-analytical method to predict springback in sheet metal forming processes has been developed for the case of plane strain. In the proposed hybrid method, for each deformation increment, bending, and unbending stretches are analytically superposed on membrane stretches which are numerically obtained in advance from a membrane finite element code. Springback is then obtained by the unloading of a force and a bending moment at the boundary of each element treated as a shell. Hill's 1948 yield criterion with normal anisotropy is used in this theory along with kinematic and isotropic hardening laws during reverse loading. The method has been applied for the springback prediction of a 2008-T4 aluminum alloy in plane-strain draw-bending tests. The results indicate the necessity of including anisotropic hardening (especially Bauschinger effects) and elastoplastic unloading in order to achieve good agreement with experimental results.

1 Introduction

With the continuous advancement of computational methods, especially finite element methods the analysis of forming processes is now becoming a powerful indirect design tool, which may significantly reduce costly experimental trials. The numerical analysis methods, however, still need significant improvement in computational time to be widely useful for practical industrial applications. One popular scheme to reduce computational time in a sheet metal forming analysis is to treat the sheet as a membrane, neglecting the variation of deformation in the thickness direction. Thus, a thin sheet is computationally considered a two-dimensional material (Frey and Wenner, 1987; Sklad and Siekirk, 1990; Saran and Wagoner, 1991, Wenner, 1992). Strain localization during stretching is one of the important measures needed to evaluate formability of materials as well as to optimize forming processes. Numerical calculations based on membrane elements are cost-effective for analyzing strain localization, especially if the deformation gradient in the thickness direction is not so large.

When bending is dominant, however, the deformation gradient and therefore the stress gradient in the thickness direction become significant (Stoughton, 1985; Choudhry and Lee, 1994). In such cases, membrane calculations are not sufficient. When external forces and moments are unloaded after bending (and unbending), the parts undergo springback, which is a physical consequence of the through-thickness stress gradient. Thus, springback is another important measure to analyze for process optimization (Karafillis and Boyce, 1992).

In order to account for the bending property in sheet forming, shell elements have been developed by adding bending capability to membrane elements (Wang and Tang, 1988; Kubli et al., 1993; Lee et al. 1991; Sriram et al., 1996). Since a plane-stress condition is assumed in the shell element, the shell calculation is cost-effective compared to three-dimensional calculations. Another alternative to account for the bending is to superpose the effect onto the membrane calculations (Pourboghrat and Chandorkar, 1992; Pourboghrat and Chu, 1995). In this method, the bending effect is added analytically after membrane solutions are obtained separately: a sequential hybrid of numerical and analytical solution. In the shell calculations, solutions are obtained by iteratively solving nonlinear equilibrium conditions of forces and moment simultaneously, therefore, the sequential hybrid method is more cost-effective.

In the present work, the hybrid method is further developed for the case of plane strain. In stretch forming, the curved surfaces of a punch and die introduce bending at contact areas. In draw forming, however, bending is followed by unbending as material moves around the curved contact surfaces. The method described here can account for the bending and unbending in stretch/draw forming. In order to account for the bending, pure bending is superposed on stretches which are obtained from membrane calculations for each element, considering the curvatures of tools at contact. When reversely applied, the same bending algorithm can account for the unbending in draw forming, and also for springback during unloading after bending and unbending.

As for the superposition of the bending/unbending on membrane stretches, monotonic loading is assumed in which true (or logarithmic) strains are proportional: i.e., the principle values and directions are fixed. For such deformation, stress is obtained from the deformation theory of plasticity based on minimum plastic work paths (Chung and Richmond, 1993). Springback is then obtained by unloading an external force and moment. Details of the hybrid method are illustrated in Sections 2 through 8. In Section 9, the method is applied for the springback prediction of a 2008-T4 aluminum alloy and in Section 10, the predictions are compared with experimental results produced at Alcoa. The incorporation of unbending in draw forming along with anisotropic hardening are major differences between this work and similar previous works (Pourboghrat and Chandorkar, 1992; Pourboghrat and Chu, 1995).

2 Constitutive Equations

For elastic deformation, Hooke's law is used incrementally. Beyond the elastic limit, rigid-plasticity is used and further

Contributed by the Applied Mechanics Division of THE AMERICAN SOCIETY OF MECHANICAL ENGINEERS for publication in the ASME JOURNAL OF APPLIED MECHANICS.

Discussion on the paper should be addressed to the Technical Editor, Professor Lewis T. Wheeler, Department of Mechanical Engineering, University of Houston, Houston, TX 77204-4792, and will be accepted until four months after final publication of the paper itself in the ASME JOURNAL OF APPLIED MECHANICS.

Manuscript received by the ASME Applied Mechanics Division, Aug. 12, 1996; final revision, Nov. 5, 1997. Associate Technical Editor: J. L. Bassani.

elastic deformation in the plastic range is neglected for simplicity. In order to account for the Bauschinger effect during reverse loading, the kinematic hardening is incorporated as well as the isotropic hardening (the theoretical basis of the kinematic hardening is summarized in the Appendix). It is assumed that the material's effective stress-strain behavior, obtained from a uniaxial tensile test, can be expressed using the power law:

$$\bar{\sigma}_\alpha + \bar{\alpha} = K\cdot(\bar{\epsilon} + \bar{\epsilon}_o)^n \cdot \left(\frac{\dot{\bar{\epsilon}}}{\dot{\bar{\epsilon}}_o}\right)^m \tag{2.1}$$

where $\bar{\sigma}_\alpha$ is the effective stress which describes the size of the yield surface, while $\bar{\alpha}$ $(= \int d\bar{\alpha})$ is the effective back-stress which describes the translation distance of the yield surface. Also, $\bar{\epsilon}$ $(= \int d\bar{\epsilon})$ and $\dot{\bar{\epsilon}}$ are the effective strain and the effective strain rate, respectively. Besides, E is the modulus of elasticity, K is the strength coefficient, n is the strain-hardening exponent, m is the strain-rate sensitivity coefficient, $\bar{\epsilon}_o$ is a constant, and $\dot{\bar{\epsilon}}_o$ is a reference strain rate, all material constants.

Utilizing the yield criterion proposed by Hill (1948) for rigid plastic sheets with normal anisotropy, the following relationships are obtained for the combination type of isotropic and kinematic hardening; i.e.,

$$\bar{\sigma}_\alpha = \left[(\sigma_1 - \alpha_1)^2 + (\sigma_2 - \alpha_2)^2 - \frac{2R}{(R+1)}(\sigma_1 - \alpha_1)(\sigma_2 - \alpha_2)\right]^{1/2}, \tag{2.2}$$

$$\Delta\bar{\alpha} = \left[\Delta\alpha_1^2 + \Delta\alpha_2^2 - \frac{2R}{(R+1)}\Delta\alpha_1\Delta\alpha_2\right]^{1/2} \tag{2.3}$$

under the plane-stress condition ($\sigma_3 = 0$), where R is the normal anisotropy parameter. The conjugate effective strain is

$$\Delta\bar{\epsilon} = \sqrt{\frac{(R+1)}{(2R+1)}}\cdot[(R+1)\cdot(\Delta\epsilon_1^2 + \Delta\epsilon_2^2) + 2R\cdot\Delta\epsilon_1\cdot\Delta\epsilon_2]^{1/2}, \tag{2.4}$$

where $\Delta\bar{\alpha}$ and $\Delta\bar{\epsilon}$ are obtained from $d\bar{\alpha}$ and $d\bar{\epsilon}$ under the proportional true strain condition (see Appendix). In Eqs. (2.2)–(2.4), $\sigma_{i=1,2}$, $\alpha_{i=1,2}$, $\Delta\alpha_{i=1,2}$, and $\Delta\epsilon_{i=1,2}$ are principle stresses, back-stresses, back-stress increments, and plastic strain increments, respectively. When the normality rule is applied, the following relationship is obtained; i.e.,

$$\Delta\epsilon_1 = \frac{\Delta\bar{\epsilon}}{\bar{\sigma}_\alpha}\left\{(\sigma_1 - \alpha_1) - \frac{R}{R+1}(\sigma_2 - \alpha_2)\right\},$$

$$\Delta\epsilon_2 = \frac{\Delta\bar{\epsilon}}{\bar{\sigma}_\alpha}\left\{(\sigma_2 - \alpha_2) - \frac{R}{R+1}(\sigma_1 - \alpha_1)\right\} \tag{2.5}$$

and $\Delta\epsilon_3 = -(\Delta\epsilon_1 + \Delta\epsilon_2)$ from the plastic incompressibility condition.

3 Simplifications for Plane Strain

When the deformation is limited to the plane strain condition (i.e., $\Delta\epsilon_2 = 0$), the constitutive equations are further simplified; i.e.,

$$(\sigma_2 - \alpha_2) = \frac{R}{R+1}(\sigma_1 - \alpha_1), \quad \alpha_2 = \frac{R}{R+1}\alpha_1 \tag{3.1}$$

after considering Eq. (2.5) and the evolution law of the back-stress under the proportional loading condition (see Appendix). By substituting $\Delta\epsilon_2 = 0$ and Eq. (3.1) into Eqs. (2.2) and (2.3), the effective stress, effective back-stress, and effective strain become

$$\bar{\sigma}_\alpha = |(\sigma_1 - \alpha_1)|\,\frac{\sqrt{2R+1}}{R+1}, \quad \Delta\bar{\alpha} = |\Delta\alpha_1|\,\frac{\sqrt{2R+1}}{R+1} \tag{3.2}$$

$$\Delta\bar{\epsilon} = |\Delta\epsilon_1|\cdot\frac{R+1}{\sqrt{2R+1}}. \tag{3.3}$$

By substituting Eqs. (3.2) and (3.3) into Eq. (2.1) under monotonous loading and deformation conditions and by setting $\dot{\bar{\epsilon}}_o = \Delta\bar{\epsilon}_o/\Delta\tau$ and $\dot{\bar{\epsilon}} = \Delta\bar{\epsilon}/\Delta\tau$ ($\Delta\tau$ is the time increment), the following expression results relating the tangential stress ($\sigma_1 = \sigma$) to the tangential strain ($\epsilon_1 = \epsilon_p$) in the plastic range; i.e.,

$$\sigma = \alpha\cdot K\cdot(\epsilon_p + \epsilon_o)^n\cdot\left(\frac{\Delta\epsilon_p}{\Delta\epsilon_o}\right)^m \tag{3.4}$$

where

$$\alpha = \left(\frac{R+1}{\sqrt{2R+1}}\right)^{n+1} \tag{3.5}$$

and ϵ_o is a constant. This simplified constitutive relation allows the problem of plane-strain bending, unbending, and stretching of the sheet to be treated as one-dimensional.

4 Kinematics

Tangential Strains Caused by Bending, Unbending and Stretching: To calculate tangential strains caused by bending, unbending, and stretching, an element of the undeformed sheet with initial centerline length s_o, thickness t_o, and area A_o $(=s_o, t_o)$, is divided into N layers through the thickness, with each layer having a thickness Δz_o (i.e., $t_o = N\cdot\Delta z_o$), see Fig. 1(*a*). Tangential strains, ϵ, are then calculated under the plane-strain condition and the kinematic assumption that plane sections remain plane (Kirchhoff-Love) after the bending, unbending, and

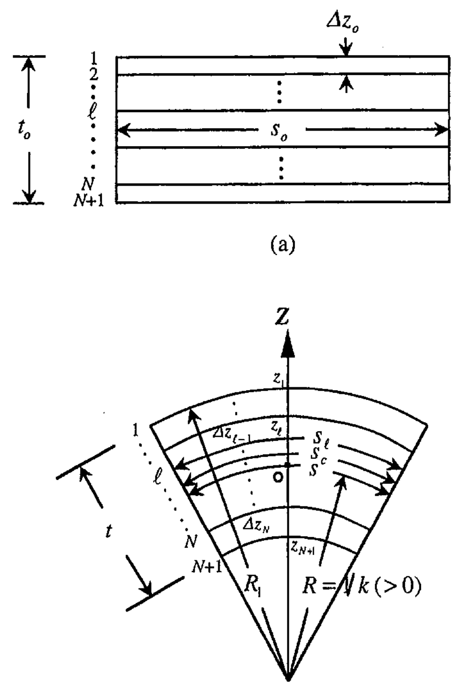

Fig. 1(*a*) An undeformed element of the sheet, and (*b*) an element of the bent sheet with *N* through-the-thickness layers

stretching. The latter assumption implies that through-the-thickness shear strains are small and can be neglected. The accuracy of this assumption was recently validated, even for cases where punch radius to thickness ratio is small and bending is dominant (Choudhry and Lee, 1994).

The current centerline curvature, k_c $(=1/R_c)$, is calculated by adding incremental changes in the centerline curvature, Δk_c, caused by bending and unbending the element, as

$$k_c = \sum_0 \Delta k_c . \tag{4.1}$$

The current thickness of the sheet is calculated, using the constancy of volume, as follows:

$$t = |R_c| \cdot \left\{ \sqrt{1.0 + \frac{A_o}{|R_c| \cdot s_c}} - \sqrt{1.0 - \frac{A_o}{|R_c| \cdot s_c}} \right\} \tag{4.2}$$

where in Eq. (4.2), s_c corresponds to the length of the original centerline fiber of the sheet. The radius of curvature and the length of the midsection of the sheet $(z = 0)$, R $(=1/k)$ and s, are related to R_c and s_c as follows:

$$|R| = \frac{|R_c|}{2} \cdot \left[\sqrt{1.0 + \frac{A_o}{|R_c| \cdot s_c}} + \sqrt{1.0 - \frac{A_o}{|R_c| \cdot s_c}} \right] \tag{4.3}$$

$$s = \frac{R}{R_c} \cdot s_c . \tag{4.4}$$

The current distance z_l of any fiber (l) from the midsection and the current thickness Δz_r of any through-the-thickness layer (r) is calculated from the following recursive equations when $z_1 = R/|R| \cdot t/2$ and $R_1 = |R| + z_1$:

$$\begin{cases} \Delta z_r = \dfrac{R}{|R|} \cdot \left\{ R_r - \sqrt{R_r^2 - 2 \cdot \dfrac{R}{s} \cdot \dfrac{A_o}{N}} \right\} \quad r = 1 \sim N \\[2ex] R_l = R_{l-1} - \dfrac{R}{|R|} \cdot \Delta z_{l-1} \quad l = 2 \sim (N+1). \\[2ex] z_l = z_{l-1} - \dfrac{R}{|R|} \cdot \Delta z_{l-1} \end{cases} \tag{4.5}$$

Then, the current length s_l of any fiber (l) through the thickness is calculated from s, using the incompressibility condition (see Fig. 1(*b*)) as follows:

$$s_l = (1 + k \cdot z_l) \cdot s \tag{4.6}$$

Finally, the incremental tangential strain for each through-the-thickness layer (l) is calculated from the incremental change in the length of the fiber,

$$\Delta\epsilon = \ln \left(\frac{s_l}{{}^o s_l} \right) \tag{4.7}$$

where ${}^o s_l$ is the length of the fiber at the previous deformation increment.

5 Stresses

Cyclic Loading: The bending, unbending, and stretching deformations cause some of the through-thickness material fibers to undergo unloading (or reverse loading by changing the direction of stress), that is, first unload elastically then unload further rigid-plastically. In order to calculate stress after the unloading, the history of deformation prior to unloading for that material fiber must be known. The information that need to be saved each time a material unloads are: (1) the strain and stress level from which the material unloaded; e.g., ϵ_{SU} and σ_{SU}, and (2) the "type" of stress-strain curve the material unloaded from; i.e., "type 1" or "type 2". In this paper, "type" refers to the shape of the stress-strain curve. The shape of a stress-strain curve is assumed to comprise of an origin, a linear (elastic) and a nonlinear (plastic) portion, see Fig. 2. A type 1 curve has the same shape as a typical stress-strain curve obtained from a uniaxial tensile test. A type 2 stress-strain curve is an inverted type 1 stress-strain curve. When a material fiber on a type 1 stress-strain curve unloads, it switches to a type 2 stress-strain curve with its origin at $(\sigma_{SU}, \epsilon_{SU})$, as shown in Fig. 2. After the elastic unloading, the stress-strain level at which the re-yielding occurs, i.e., $(\sigma_{SL}, \epsilon_{SL})$, is given by (see Fig. 2)

$$\begin{cases} \epsilon_{SL} = \epsilon_{SU} + \dfrac{\Delta\epsilon}{|\Delta\epsilon|} \cdot \beta \cdot \dfrac{|\sigma_{SU}|}{E'} \\[2ex] \sigma_{SL} = \sigma_{SU} + \dfrac{\Delta\epsilon}{|\Delta\epsilon|} \cdot \beta \cdot |\sigma_{SU}| \end{cases} \tag{5.1}$$

where $E' = E/(1 - \nu^2)$ is the plane-strain modulus and ν is the Poisson ratio. For an undeformed material, ϵ_{SL} and σ_{SL} are set equal to

$$\begin{cases} \epsilon_{SL} = \pm\epsilon_y \\ \sigma_{SL} = \pm\sigma_y \end{cases} \tag{5.2}$$

where (+) is used for type 1 and (−) is used for type 2 curves, respectively. The condition for an elastic unloading to occur is $\Delta\epsilon < 0$ (for a type 1 curve) and $\Delta\epsilon > 0$ (for a type 2 curve).

Figure 2 shows the assumed tangential stress-strain curve, $\sigma - \epsilon$, for a material with anisotropic hardening in reverse loading. The re-yielding stress in this anisotropic hardening case is determined by a positive constant parameter β. When $\beta \cdot |\sigma_{SU}|$ is twice the initial yield stress of the material; i.e., $2\sigma_y$, the re-yielding occurs according to pure kinematic hardening rule, and when $\beta = 2$, the re-yielding occurs according to isotropic hardening rule. Other values of β provide different re-yielding stress levels for the combination type of isotropic and kinematic hardening rule.

Tangential Stresses Caused by Bending, Unbending, and Stretching: In this section, the word "starts" or the phrase "starting point" refers to the stress-strain state at the *reference* configuration and the phrase "ends up" refers to the stress-strain state at the *current* configuration. It can be shown that there are a total of 20 possible locations on the $\sigma - \epsilon$ space (all four quadrants) where a material fiber can end up after experiencing an increment of deformation. Figures 3 and 4 show ten of these possible locations marked on the $\sigma - \epsilon$ curves. The other ten (out of 20) possible locations are not shown, but they correspond to the same ten cases in Figs. 3 and 4, except that the starting points are switched from a type 2 to a type 1 curve and vice versa.

Figure 3 shows six possible locations, where a material fiber ends up, if it starts from $({}^o\sigma, {}^o\epsilon)$ on the linear (elastic) portion of a type 1 curve. The exact location where the material fiber ends up depends on the magnitude and sign of the strain increment, $\Delta\epsilon$, experienced by the material fiber. Figure 4 shows the other four possible locations where a material ends up, if it starts from $({}^o\sigma, {}^o\epsilon)$ on the nonlinear (plastic) portion of a type 2 curve. It is worth mentioning that although the same expressions are used to calculate stresses for locations 5, 2, and 3 in Fig. 3 and for locations 8, 9, and 10 in Fig. 4, the reference states for these two sets are different. For the first set of locations the reference states are elastic while for the second set of locations the reference states are plastic.

In Fig. 2, ϵ_p is the strain on the nonlinear (plastic) portion of the stress-strain curve and $\Delta\sigma$ is the increase in stress due to ϵ_p, as measured from the origin of $\Delta\sigma(\epsilon_p) - \epsilon_p$ coordinate system. It is assumed that the nonlinear portion of the stress-

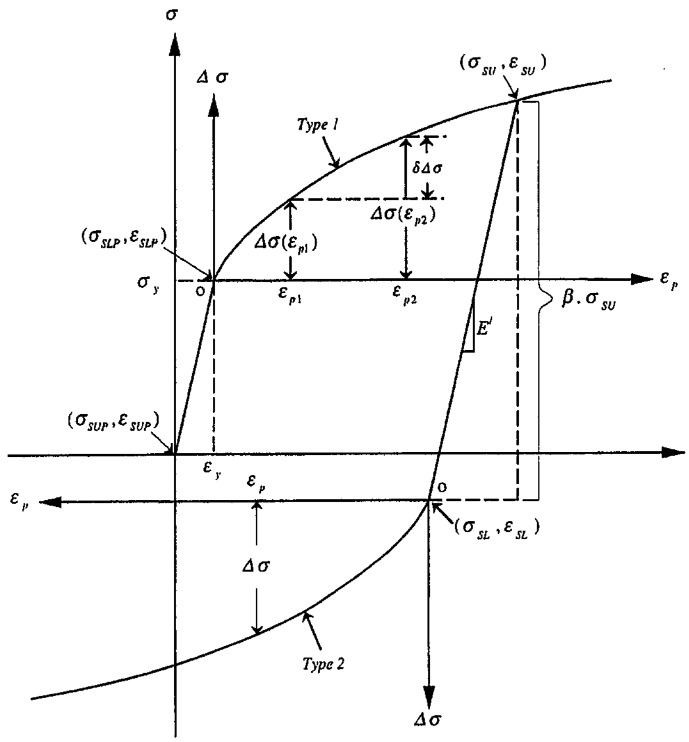

Fig. 2 Tangential stress-strain curve for a material with anisotropic hardening in reversed loading

strain curve is the same for all curves in the cyclic loading. Therefore, once an expression is found for $\Delta\sigma(\epsilon_p)$, using the original stress-strain curve of the material, it can be used for subsequent loading also. To calculate $\Delta\sigma(\epsilon_p)$, it is assumed that the stress and total strain can be written as (see Fig. 2)

$$\epsilon = \epsilon_y + \epsilon_p \tag{5.3}$$

$$\sigma = \sigma_y + \Delta\sigma(\epsilon_p) \tag{5.4}$$

where σ_y is the original tangential yield stress and $\epsilon_y = \sigma_y/E'$ is the original yield strain of the material. By substituting from Eqs. (5.3) and (5.4) into (3.4), the following expression for $\Delta\sigma(\epsilon_p)$ can be found:

$$\Delta\sigma(\epsilon_p) = \alpha \cdot K \cdot |\epsilon_p + \epsilon^*|^n \cdot \left|\frac{\Delta\epsilon_p}{\Delta\epsilon_o}\right|^m - \sigma^*. \tag{5.5}$$

In Eq. (5.5), ϵ^* and σ^* correspond to the origin (o in Fig.

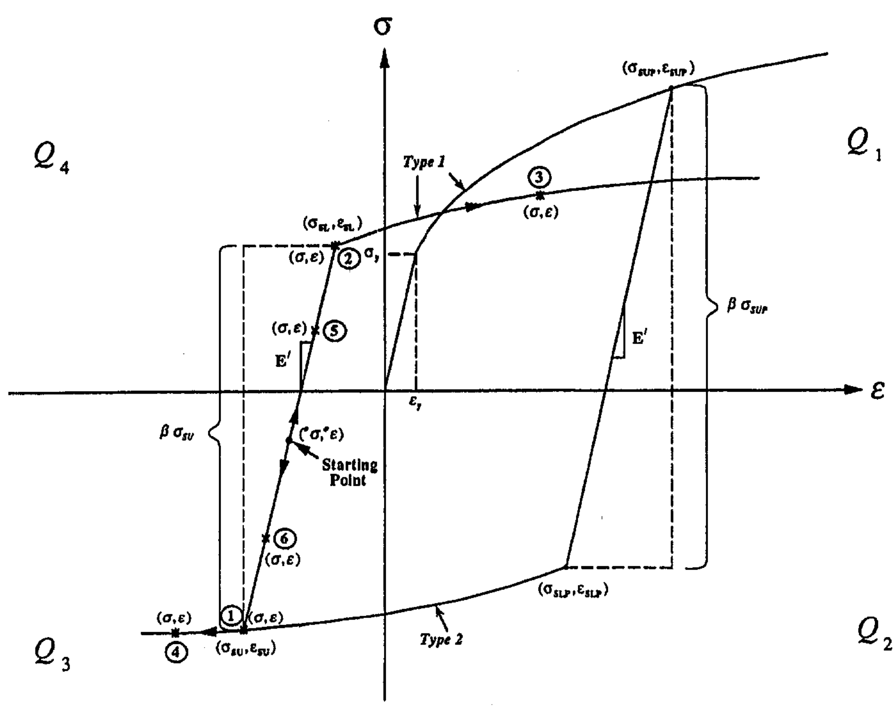

Fig. 3 Six possible locations is stress-strain space where a material fiber can fall during cyclic loading if it starts on the linear portion of a type 1 curve

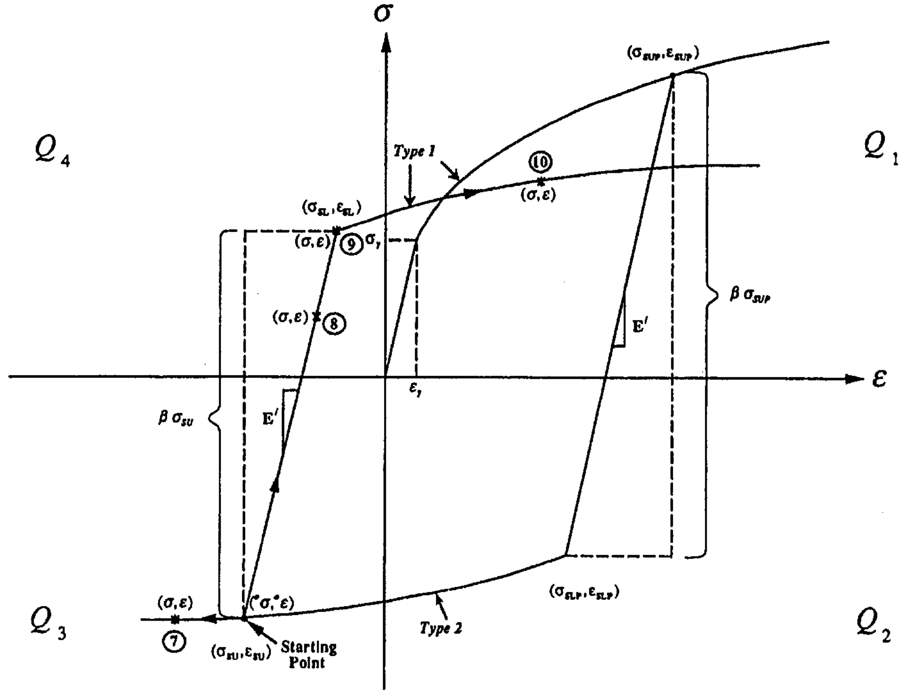

Fig. 4 Four possible locations in stress-strain space where a material fiber can fall during cyclic loading if it starts on the nonlinear portion of a type 2 curve

2) of the $\Delta\sigma(\epsilon_p) - \epsilon_p$ coordinate system. For an undeformed material, ϵ^* and σ^* are initially set equal to ϵ_y and σ_y, respectively. After each unloading, the origin of $\Delta\sigma(\epsilon_p) - \epsilon_p$ curve moves along the stress-strain curve, $\sigma - \epsilon$, to a new location calculated as following:

$$\begin{cases} \epsilon^* = \epsilon_P^* + |\epsilon_{SU} - \epsilon_{SLP}| \\ \sigma^* = \alpha \cdot K \cdot |\epsilon^*|^n \cdot \left|\dfrac{\Delta\epsilon_p}{\Delta\epsilon_o}\right|^m \end{cases} \tag{5.6}$$

where ϵ_P^* is the previous ϵ^* and ϵ_{SLP} is defined in Fig. 2. If ϵ^* and σ^* in Eq. (5.5) are replaced with the constants ϵ_y and σ_y, then it is implied that the origin of $\Delta\sigma(\epsilon_p) - \epsilon_p$ coordinate system is always fixed and that the entire nonlinear portion of the stress-strain curve is used to calculate $\Delta\sigma(\epsilon_p)$ after each unloading. But, if the updated values of ϵ^* and σ^* from Eq. (5.6) are used in Eq. (5.5), then only that portion which extends beyond the new origin will be used to calculate $\Delta\sigma(\epsilon_p)$ after each unloading.

The choice of an expression to be used to calculate stress at current configuration, σ, depends upon several conditions. In order to choose the correct expression, it should be determined if the starting (reference) stress, ${}^o\sigma$, is (1) on the linear (elastic) or nonlinear (plastic) portion of the stress-strain curve and (2) on a type 1 or type 2 curve. Based on these two information and the following additional conditions, the correct expression for calculating current stress, σ, can be decided. The flow charts shown in Tables 3 and 4, summarize the current stress calculation scheme to be described next.

Case I: Starting From the Linear (Elastic) Portion of $\boldsymbol{\sigma - \epsilon}$ Curve: For this case, the following parameters are calculated first:

$$\begin{cases} \Delta\epsilon_{TSU} = \epsilon_{SU} - \epsilon \\ \Delta\epsilon_{TSL} = \epsilon_{SL} - \epsilon \\ \Delta\epsilon_{UML} = \Delta\epsilon_{TSU} \cdot \Delta\epsilon_{TSL} \end{cases} \tag{5.7}$$

where $\epsilon\ (= \sum_0 \Delta\epsilon)$ is the total strain. Then, depending upon the sign of $\Delta\epsilon$ and the type of stress-strain curve (i.e., type 1 or 2, in Figs. 3 and 4), the correct expression to be used for calculating σ is decided based on the following additional conditions:

I.1. For curve type = 1 and $\Delta\epsilon < 0$ or curve type = 2 and $\Delta\epsilon > 0$, then:
if $\Delta\epsilon_{TSU} = 0$ (see location 1, Fig. 3), use

$$\sigma = \sigma_{SU}. \tag{5.8}$$

if $\Delta\epsilon_{UML} < 0$ (see location 6, Fig. 3), use

$$\sigma = {}^o\sigma + E' \cdot \Delta\epsilon. \tag{5.9}$$

if $\Delta\epsilon_{UML} > 0$ and $|\Delta\epsilon_{TSU}| < |\Delta\epsilon_{TSL}|$ (see location 4, Fig. 3), use

$$\begin{cases} \sigma = \sigma_{SU} + \dfrac{\Delta\epsilon}{|\Delta\epsilon|} \cdot \delta\Delta\sigma \\ \delta\Delta\sigma = \Delta\sigma(\epsilon_{p2}) - \Delta\sigma(\epsilon_{p1}) \\ \epsilon_{p1} = |\epsilon_{SU} - \epsilon_{SLP}| \\ \epsilon_{p2} = |\epsilon - \epsilon_{SLP}|. \end{cases} \tag{5.10}$$

In Eq. (5.10), ϵ_{SLP} is the previous ϵ_{SL} (see Fig. 2).

I.2. For curve type = 1 and $\Delta\epsilon > 0$ or curve type = 2 and $\Delta\epsilon < 0$, then:
if $\Delta\epsilon_{TSL} = 0$ (see location 2, Fig. 3), use

$$\sigma = \sigma_{SL}. \tag{5.11}$$

if $\Delta\epsilon_{UML} < 0$ (see location 5, Fig. 3), Eq. (5.9) should be used to calculate σ.
if $\Delta\epsilon_{UML} > 0$ and $|\Delta\epsilon_{TSU}| > |\Delta\epsilon_{TSL}|$ (see location 3, Fig. 3), use

$$\begin{cases} \sigma = \sigma_{SL} + \dfrac{\Delta\epsilon}{|\Delta\epsilon|} \cdot \Delta\sigma(\epsilon_p) \\ \epsilon_p = |\epsilon - \epsilon_{SL}|. \end{cases} \tag{5.12}$$

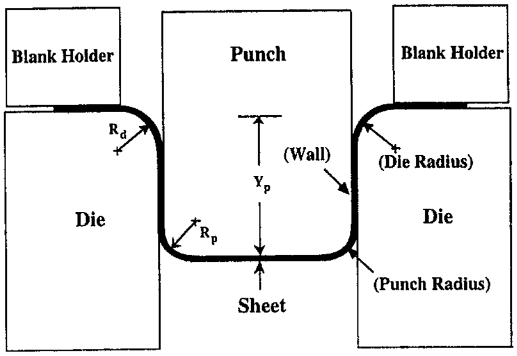

Fig. 5 A schematic of the two-dimensional draw bending operation

Case II: Starts From the Nonlinear (Plastic) Portion of $\sigma - \epsilon$ Curve:

II.1. For curve type = 1 and $\Delta\epsilon > 0$ or curve type = 2 and $\Delta\epsilon < 0$ (see location 7, Fig. 4), use

$$\begin{cases} \sigma = {}^o\sigma + \dfrac{\Delta\epsilon}{|\Delta\epsilon|} \cdot \delta\Delta\sigma \\ \delta\Delta\sigma = \Delta\sigma(\epsilon_{p2}) - \Delta\sigma(\epsilon_{p1}) \\ \epsilon_{p1} = |{}^o\epsilon - \epsilon_{SL}| \\ \epsilon_{p2} = |\epsilon - \epsilon_{SL}|. \end{cases} \tag{5.13}$$

It should be noted that since unloading does not occur in this case, ϵ_{SL} in Eq. (5.13) is the same as ϵ_{SLP} in Fig. 4.

II.2. For curve type = 1 and $\Delta\epsilon < 0$, first calculate

$$\begin{cases} \epsilon_{SL} = {}^o\epsilon - \beta \cdot \dfrac{|{}^o\sigma|}{E'} \\ \sigma_{SL} = {}^o\sigma - \beta \cdot |{}^o\sigma|. \end{cases} \tag{5.14}$$

II.3. For curve type = 2 and $\Delta\epsilon > 0$, first calculate

$$\begin{cases} \epsilon_{SL} = {}^o\epsilon + \beta \cdot \dfrac{|{}^o\sigma|}{E'} \\ \sigma_{SL} = {}^o\sigma + \beta \cdot |{}^o\sigma|. \end{cases} \tag{5.15}$$

Next, recalculate $\Delta\epsilon_{TSU}$, $\Delta\epsilon_{TSL}$, and $\Delta\epsilon_{UML}$ from Eq. (5.7). Then:
if $\Delta\epsilon_{UML} < 0$ (see location 8, Fig. 4), Eq. (5.9) should be used to calculate σ.
if $\Delta\epsilon_{TSL} = 0$ (see location 9, Fig. 4), Eq. (5.11) should be used to calculate σ.
if $\Delta\epsilon_{UML} > 0$ (see location 10, Fig. 4), Eq. (5.12) should be used to calculate σ.

6 Tension and Bending Moment

Once stresses are calculated according to Section 5, they are then integrated through the thickness to calculate tension and bending moment about the midsection for each element of the sheet, as follows:

$$T = \sum_{m=1}^{N} \hat{\sigma}(z_m) \cdot \Delta z_m \tag{6.1}$$

$$M = \sum_{m=1}^{N} \hat{\sigma}(z_m) \cdot \hat{z}_m \cdot \Delta z_m. \tag{6.2}$$

In Eqs. (6.1) and (6.2), N represents the number of layers assumed through the thickness and $\hat{\sigma}$ and $\hat{z}_m$ are defined as

$$\hat{\sigma}(z_m) = \frac{\sigma(z_m) + \sigma(z_{m+1})}{2} \tag{6.3}$$

and

$$\hat{z}_m = \frac{z_m + z_{m+1}}{2}. \tag{6.4}$$

7 Springback

Calculation of springback involves iterative procedure to calculate a new midsection curvature and length for each element, s and k, such that the resulting tension and bending moment about the midsection vanish everywhere in the sheet. In this iterative procedure, the Newton-Raphson method is used to calculate the updated values for s and k.

For comparison purposes, springback was also calculated using only the elastic and neglecting the plastic range at the last step. For such cases, the final unloaded midsection curvature and the length of each element, s and k, are calculated such that tension and bending moment calculated by the elastic deformation are equal to those calculated by the plastic deformation prior to the unloading:

$$\begin{cases} {}^oT + \Delta T_e = 0 \\ {}^oM + \Delta M_e = 0. \end{cases} \tag{7.1}$$

To obtain s and k after springback, consider the following tangential strain after tension and bending is applied to a flat element; i.e.,

$$\epsilon(z) = \frac{z + c}{R - c} \tag{7.2}$$

where c is the distance between the midsection and the neutral axis (where $\epsilon = 0$) caused by tension, and R is the radius of the midsection curvature. The tangential strain increment between before and after elastic unloading becomes

$$\Delta\epsilon(z) = \frac{z + c}{R_u - c} - \frac{z + {}^oc}{{}^oR - {}^oc} = \epsilon - {}^o\epsilon \tag{7.3}$$

where the superscript "o" indicates known values based on the geometry before the elastic unloading and R_u is the radius of curvature after the elastic unloading. Utilizing Eq. (7.3) to calculate the elastic tension and bending moment, and the relationships shown in Eq. (7.1) lead to

$$R_u = \frac{t^2 \cdot {}^oT \cdot (A - 1) + E' \cdot t^3}{12 \cdot {}^oM \cdot (A - 1)} \tag{7.4}$$

where A is a known constant defined as

Table 1 Mechanical properties of the 2008-T4 aluminum alloy

Material	K (MPa)	n	m	E (GPa)	R	σ_y (MPa)	ν	μ (Friction Coeff.)
AL 2008-T4	460.0	0.247	0.0	69.0	0.70	133.0	0.33	0.1

Table 2 Tooling geometry

Case	t (mm)	R_p (mm)	R_d (mm)	Die opening (mm)	Y_p (mm)	Clearance (mm)	Wall angle (Deg.)	BHF (KN)
a	1.0	3.175	3.175	66.68	45.0	8.0	89.0	89.0
b	1.0	6.35	6.35	80.31	50.0	15.4	78.0	97.0

$$A = \frac{E' \cdot {}^o t^3}{12 \cdot {}^o R \cdot {}^o M - {}^o T \cdot {}^o t^2}. \tag{7.5}$$

The unloaded length of each element of the sheet is also calculated as follows:

$$s = {}^o s \cdot \exp\left(\frac{c}{R_u - c} - \frac{{}^o c}{{}^o R - {}^o c}\right) \tag{7.6}$$

8 Unloaded Shape of the Sheet After Springback

Nodal coordinates of the unloaded elements, after springback, are calculated from the following expressions:

$$\begin{cases} \Delta x(i) = s(i) \cdot \cos\left[\sum_{j=1}^{i} k(j) \cdot s(j)\right] \\ \Delta y(i) = s(i) \cdot \sin\left[\sum_{j=1}^{i} k(j) \cdot s(j)\right] \end{cases} \tag{8.1}$$

with boundary conditions, $x(0) = x_o$; $y(0) = y_o$. In Eq. (8.1), $s(i)$ represents the midsection length of the ith element.

9 Verification Procedure

The theory described in this paper was tested using the plane-strain finite element membrane code SHEET-S (Saran and Wagoner, 1991). SHEET-S, a two-dimensional finite element analysis code, was originally developed at Ohio State University to simulate the stretch/draw forming operation of plane-strain sections using the incremental theory of plasticity with *membrane* line elements. Using the theory developed and membrane solutions obtained from the SHEET-S code, springback and formation of the side wall curl in two-dimensional draw bending operation, see Fig. 5, were predicted. To verify the accuracy, the predictions were compared with experimental results.

A two-dimensional draw bending experiment, shown in Fig. 5, was performed using the 2008-T4 aluminum alloy sheet of 1.0 mm thickness. Table 1 shows the mechanical properties of the 2008-T4 aluminum alloy. Table 2 shows two different punch and die radii, R_p and R_d, and clearances used for the experiments. It was observed from these experiments that after the unloading, curls were formed on the sidewall of the parts as shown in Figs. 6(a) and 6(b). Figure 6(a) shows that sidewall curls are more pronounced for parts formed with the sharper die radius and tighter clearance.

For the numerical prediction, the SHEET-S code was employed to simulate the draw bending experiment with forming conditions shown in Table 2. The updated shape of the sheet, that is nodal coordinates obtained from SHEET-S for every deformation increment, was used to calculate the updated midsection length and curvature of each element. Then, using the bending/unbending theory, tangential strains and stresses were calculated and integrated through the thickness to obtain tension and bending moment for each element.

Table 3 Flow chart for case I: starting point from the linear (elastic) portion of stress-strain curve

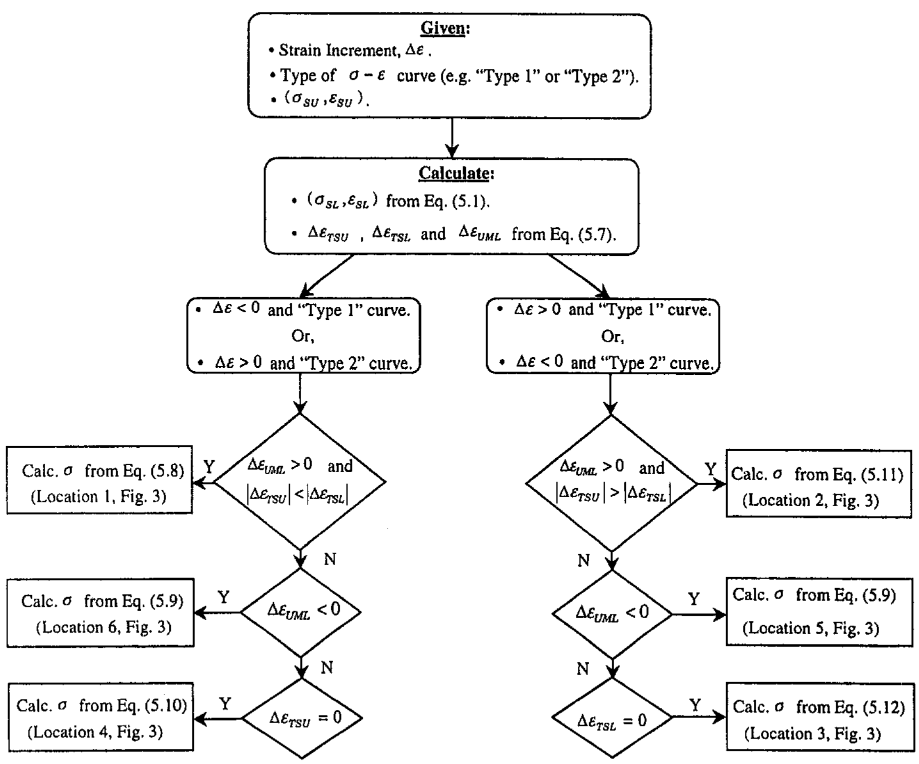

Table 4 Flow chart for case II: starting point from the nonlinear (plastic) portion of stress-strain curve

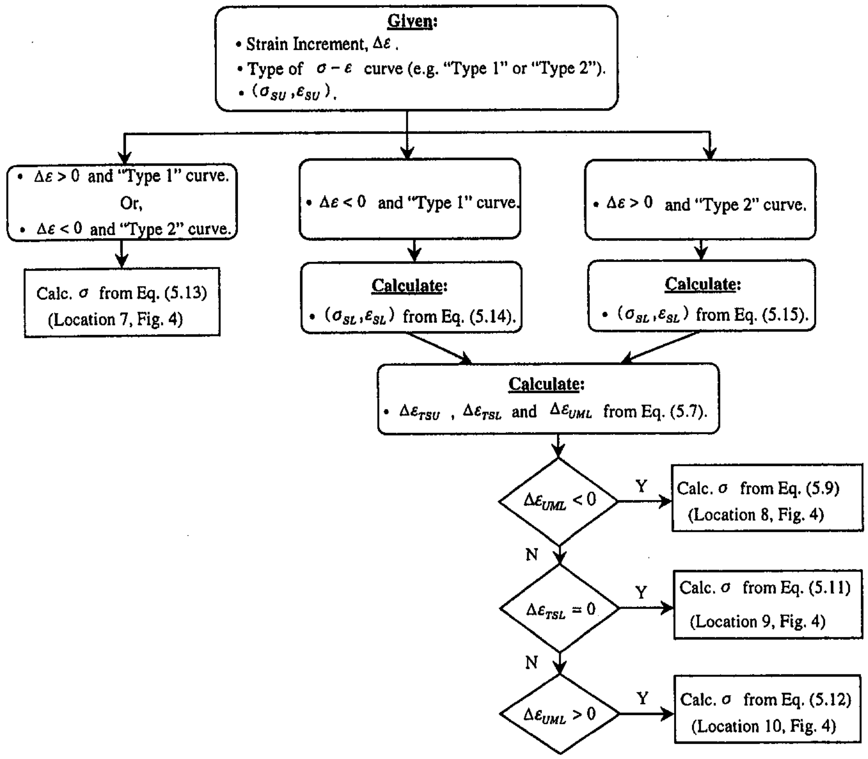

In this paper, for comparison purposes, both pure kinematic (KIN) as well as pure isotropic (ISO) hardening laws were employed. Springback was calculated using both elasto/rigid-plastic (EPUN) as well as elastic unloading (ELUN) methods. This provides four sets of predicted unloaded shape for each set of boundary conditions. Since predicted springback results using the elastic and elasto/rigid-plastic unloading theories were not significantly different under the isotropic hardening (ISO) condition, only the results of the elasto/rigid-plastic unloading are reported in this paper.

10 Results and Discussions

Figures $6(a)$ and $6(b)$ show that pure kinematic hardening law with the elasto/rigid-plastic unloading (KIN-EPUN) model predict the most accurate springback results for the 2008-T4 aluminum alloy in two-dimensional channel forming. The predicted results, i.e., KIN-EPUN, exactly match the experimental data for both cases (a) and (b). The other two results based on the kinematic hardening law with the elastic unloading (KIN-ELUN) and the isotropic hardening law with the elasto/rigid-plastic unloading (ISO-EPUN), do not predict the unloaded shape of the channel well.

The differences in the predictions stem from their differences in predicting the unloaded midsection curvature of the sheet at the three critical regions on the channel: the die radius, the wall, and the punch radius regions as shown in Fig. 5. The sheet in these three regions undergo different deformations with different amount of stretching, bending, and unbending. The two models, KIN-ELUN and ISO-EPUN, underestimate, compared with KIN-EPUN, the springback of the sheet at the punch region where the sheet only bends and slightly stretches over the punch radius but does not draw over it. However, all the three models predict almost the same springback in the die region where the sheet slides and stretches over the die radius but does not enter into the die cavity. Finally, both KIN-ELUN and ISO-EPUN underestimate, compared with KIN-EPUN, the springback for the sheet that bends, unbends, and stretches as it draws over the die radius and forms the wall region of the channel.

In order to better understand the cause of different results observed in Figs. $6(a)-(b)$, Figs. $7(a)-(c)$ are included. These figures show the evolution of the normalized moment-curvature ($M/M_y - k/k_y$) curves for the sheet that undergoes (1) a bending to a curvature k after an initial stretch to a tension T, followed by (2), an unbending under the same tension T, until the sheet is straightened ($k = 0$), and finally (3), an elasto/rigid-plastic unloading that causes both tension and bending moment vanish ($T = M = 0$). After the complete unloading, since the curvature of the element does not vanish ($k_u \neq 0$), k_u is used as a measure of springback. Figures $7(a)-(c)$ show the difference in ($M/M_y - k/k_y$) curves and springback after the unloading for both kinematic and isotropic hardening laws at different levels of applied tension (T/T_y). Here, M_y and k_y are the bending moment and curvature in pure bending when initial yield occurs at the outer fiber, while T_y is the initial uniaxial yield strength of the sheet:

$$\begin{cases} M_y = \dfrac{2\cdot\alpha\cdot K}{(2+n)}\cdot\left(\dfrac{t}{2}\right)^{n+2}\cdot k_y^n \\ k_y = \dfrac{2\cdot(1-\nu^2)\cdot\sigma_y}{t\cdot E} \\ T_y = \sigma_y\cdot t. \end{cases} \quad (10.1)$$

In Fig. $7(a)$ ($T/T_y = 0$), during the transition from step 1 to step 2, the magnitude of the normalized curvature, k/k_y, at $M = 0$ and normalized bending moment, $|M/M_y|$, at reyielding, are larger for the isotropic case (ISO) than for the kinematic hardening case (KIN). As tension increases toward the tension at yield ($T/T_y = 1.0$), the curvature k/k_y at $M = 0$ and bending moment, $|M/M_y|$, at re-yielding become almost the same for both the isotropic (ISO) and the kinematic hardening cases

(KIN) as shown in Fig. 7(b). Figure 7(c) shows that this trend reverses as tension increases beyond the initial yield (T/T_y = 1.25).

The magnitude of k/k_y at $M = 0$ determines the springback of the sheet at the die and punch radii of the channel. Figures 7(a)–(b), where $0.0 \leq T/T_y \leq 1.0$, represent the deformation and springback characteristics of the sheet at the punch radius, while Fig. 7(c), where $T/T_y > 1.0$, represent the deformation and springback characteristics of the sheet at the die radius where stretching is larger than at the punch radius region. The deformation and springback characteristics of the wall of the channel is represented by Fig. 7(c), after the unloading (step 3), where the sheet first straightens ($k/k_y = 0$) and then unloads elasto/rigid-plastically to a final curvature k_u at $M = 0$. As shown in Fig. 7(c), the curvature k_u is larger for the kinematic hardening case (KIN) with the elasto/rigid-plastic unloading than it is for the isotropic hardening case (ISO). In fact, the above analyses are consistent with the results shown in Figs. 6(a)–(b) at the wall and the die and punch radii regions.

Figures 8(a)–(b) show the $M/M_y - k/k_y$ curves at different tension levels T/T_y for kinematic and isotropic hardening laws, respectively. It is interesting to see that for the isotropic hardening case, as tension level increases, the magnitude of the bending moment in reversed loading and springback, as measured by k_u after the unloading, decreases. On the other hand, for the kinematic hardening case, the trend is reversed. Consequently, as tension level increases, the magnitude of the side wall curl increases for the kinematic hardening while it decreases for the isotropic hardening. Assuming that the real materials' stress-

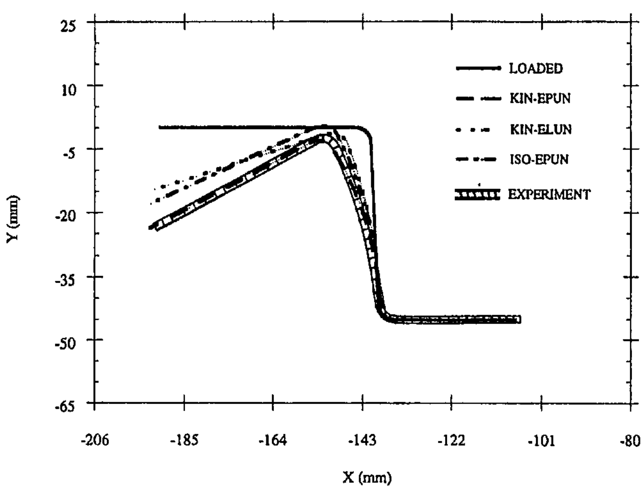

Fig. 6(a) Three predicted and the measured unloaded shape of the sheet for the 2008-T4 aluminum alloy (case a, Table 2)

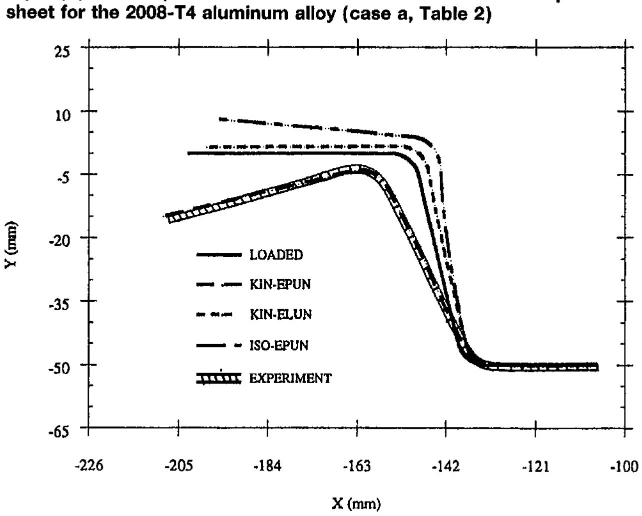

Fig. 6(b) Three predicted and the measured unloaded shape of the sheet for the 2008-T4 aluminum alloy (case b, Table 2)

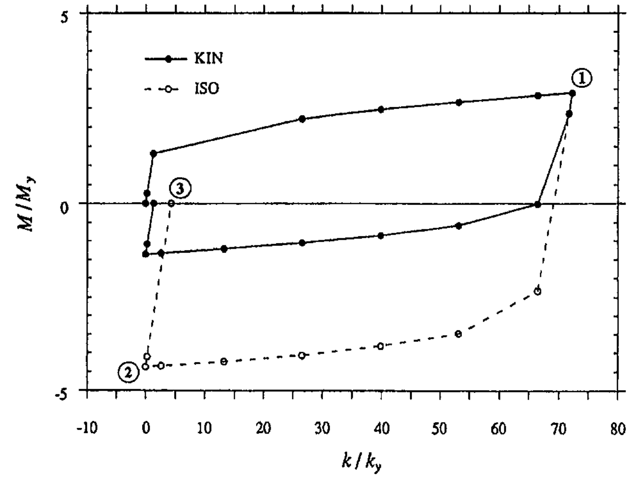

Fig. 7(a) Normalized moment and curvature in cyclic loading, for kinematic and isotropic hardening laws and tension T/T_y = 0. Unloading from step 2 to step 3 is done elasto/rigid-plastically.

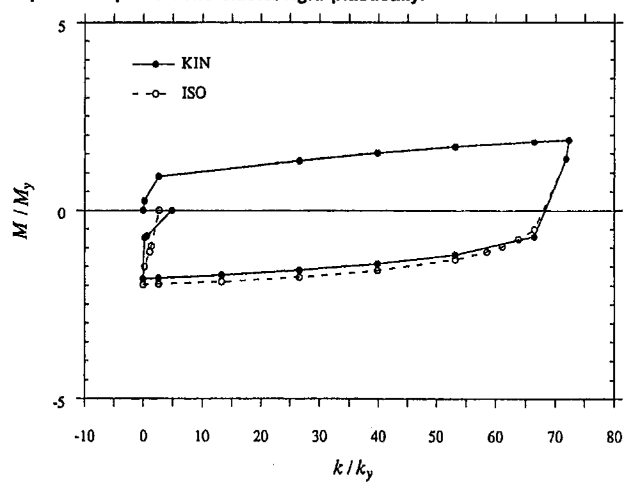

Fig. 7(b) Normalized moment and curvature in cyclic loading, for kinematic and isotropic hardening laws and tension T/T_y = 1.0. Unloading from step 2 to step 3 is done elasto/rigid-plastically.

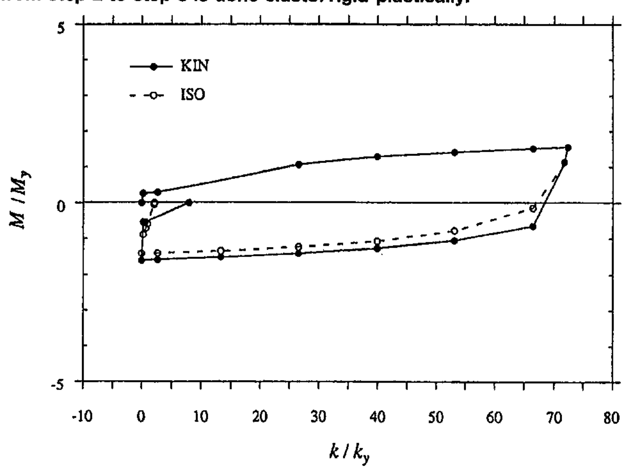

Fig. 7(c) Normalized moment and curvature in cyclic loading, for kinematic and isotropic hardening laws and tension T/T_y = 1.25. Unloading from step 2 to step 3 is done elasto/rigid-plastically.

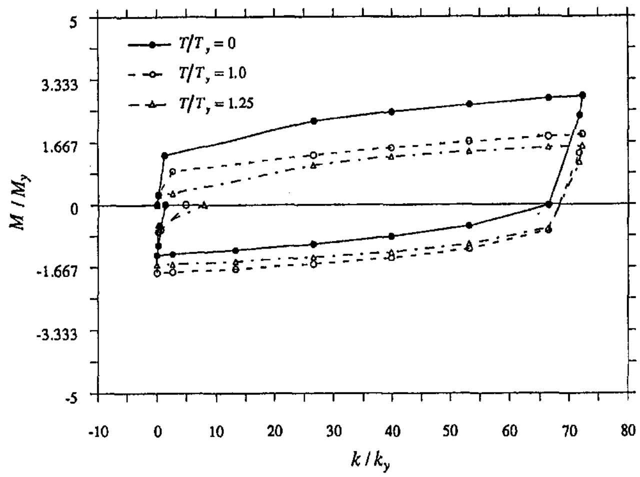

Fig. 8(*a*) Normalized moment and curvature in cyclic loading, for kinematic hardening law at tension levels: $T/T_y = 0$, $T/T_y = 1.0$ and $T/T_y = 1.25$. Unloading is done elasto/rigid-plastically.

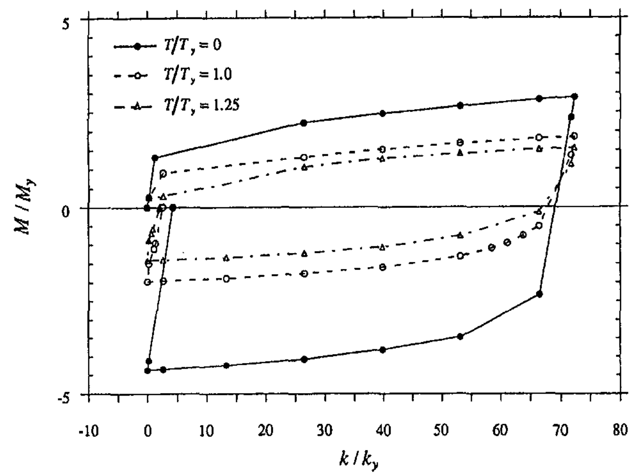

Fig. 8(*b*) Normalized moment and curvature in cyclic loading, for isotropic hardening law at tension levels: $T/T_y = 0$, $T/T_y = 1.0$ and $T/T_y = 1.25$. Unloading is done elasto/rigid-plastically.

strain curve falls somewhere between the isotropic and the kinematic hardening curves, shown in Figs. 3 and 4, then according to results of Figs. 8(*a*)–(*b*), applying more tension might not always work as a solution to reduce springback. Ayres (1984) showed that it is sometimes necessary to use multistamping operations, rather than single stamping operation with high tension, to reduce springback.

11 Summary and Conclusions

A semianalytical method was presented in this paper for calculating springback when a sheet metal undergoes multiple plane-strain bending, unbending, and stretching. In the proposed hybrid method, bending and unbending stretches are analytically superposed on membrane stretches which are numerically obtained in advance from a membrane finite element code. Springback is calculated using the elasto/rigid-plastic unloading of the force and bending moment at the boundary of each element treated as a shell. Hill's plane-stress yield function with normal anisotropy was used. For reverse loading, both kinematic and isotropic hardening laws were incorporated in this theory. This method due to its nature of post-processing bending correction, unlike nonlinear shell models, contribute very little to the overall computational time needed to analyze the sheet metal forming problem and therefore retains the efficiency advantage of the membrane code.

For verification purposes, several results for the unloaded shape of the sheet formed by the stretch/draw operation into a channel were obtained for the 2008-T4 aluminum and the results were compared with experimental results. For the 2008-T4 aluminum alloy, it was found that the kinematic hardening model with the elasto/rigid-plastic unloading (KIN-EPUN) well predicted the results measured experimentally.

It was further observed that, depending upon the hardening model in reversed loading, different unloaded shapes and sidewall curls were predicted. Since the accurate prediction of springback of stamped sheet metals are sensitive to mechanical properties of materials under the unloading condition, further experimental study to characterize appropriate material properties in reversed loading might be essential.

Acknowledgment

The authors would like to thank Mr. B. L. McCall and Mr. J. L. Morson at the Alcoa Technical Center for conducting the experiments.

References

Ayres, R. A., 1984, "SHAPESET: A Process to Reduce Sidewall Curl Springback in High-Strength Steel Rails," *J. Applied Metalworking*, Vol. 3, No. 2, p. 127.

Choudhry, S., and Lee, J. K., 1994, "Dynamic Plane-Strain Finite Element Simulation of Industrial Sheet-Metal Forming Processes," *Int. J. Mech. Sci.*, Vol. 36, No. 3, pp. 189–207.

Chung, K., and Richmond, O., 1992, "Ideal forming, Part I: Homogenous deformation with minimum plastic work," *Int. J. Mech. Sci.*, Vol. 34, pp. 617–633.

Chung, K., and Richmond, O., 1993, "A Deformation Theory of Plasticity Based on Minimum Work Path," *Int. J. Plasticity*, Vol. 9, pp. 907–920.

Frey, W. H., and Wenner, M. L., 1987, "Development and Application of a One-Dimensional Finite Element Code for Sheet Metal Forming Analysis," *Interdisciplinary Issues in Materials Processing and Manufacturing*, S. K. Samanta et al., eds., Vol. 1, pp. 307–320.

Hill, R., 1948, "A Theory of the yielding and Plastic Flow of Anisotropic Metals," *Royal Soc. London Proc.*, Vol. A193, p. 281.

Karafillis, A. P., and Boyce, M. C., 1992, "Tooling Design in Sheet Metal Forming Using Springback Calculations," *Int. J. Mech. Sci.*, Vol. 34, No. 2, pp. 113–131.

Kubli, W., and Reissner, J., 1993, "Optimization of Sheet Metal Forming Processes Using the Special-Purpose Program AUTOFORM," *Proceedings, 2nd International Conference, NUMISHEET '93*, A. Makinouchi et al., eds., Aug. 3–Sept. 2, Isehara, Japan, pp. 271–280.

Lee, J. K., Cho, U. Y., Hambrecht, J., and Choudhry, S., 1991, "Recent Advances in Sheet Metal Forming Analysis," *Advances in Finite Deformation Problems in Materials Processing and Structures*, Dec., 1–6, Atlanta, GA, ASME, New York, AMD-Vol. 125, pp. 119–130.

Pourboghrat, F., and Chandorkar, K., 1992, "Springback Calculation For Plane Strain Sheet Forming Using Finite Element Membrane Solution," *Symposium on Numerical Methods for Simulation of Industrial Metal Forming Processes*, Anaheim, CA, Nov. 8–13, ASME, New York, pp. 85–93.

Pourboghrat, F., and Chu, E., 1995, "Springback in Plane Strain Stretch/Draw Sheet Forming," *Int. J. Mech. Sci.*, Vol. 36, No. 3, pp. 327–341.

Prager, W., 1956, "A New Method of Analyzing Stresses and Strains in Work-Hardening Plastic Solids," ASME Journal of Applied Mechanics, Vol. 23, pp. 493–496.

Saran, M. J., and Wagoner, R. H., 1991, "A user's manual and verification examples for section form (Sheet-S/version 3), section analysis of sheet stampings," Ohio State University, Report No. ERC/NSM-S-91-17.

Sklad, M. P., and Siekirk, J. F., 1990, *Proc. 16th IDDRG Congress*, ASM International, Bolange, Sweden, pp. 295–303.

Stoughton, T. B., 1985, "Finite Element Modeling of 1008 AK Sheet Steel Stretched over a Rectangular Punch with Bending Effects," *Computer Modeling of Sheet Metal Forming Processes*, N. M. Wang and S. C. Tang, eds., The Metallurgical Society, Warrendale, PA, pp. 143–159.

Sriram, S., and Wagoner, R. H., 1996, "Simulating the LDH Test," *Proceedings, 3rd International Conference, NUMISHEET '96*, J. K. Lee et al., eds., Sept. 29–Oct. 3, Dearborn, MI, pp. 128–135.

Wang, N. M., and Tang, S. C., 1988, "Analysis of Bending Effects in Sheet Forming Operations," *Int. J. Numer. Methods Eng.*, Vol. 25, pp. 253–267.

Wenner, M. L., 1992, "Elementary Solutions and Process Sensitivities for Plane-Strain Sheet-Metal Forming," ASME Journal of Applied Mechanics, Vol. 59, pp. 23–28.

Ziegler, H., 1959, "A modification of Prager's hardening rule," *Q. Appl. Math.*, Vol. 17, pp. 55–65.

APPENDIX

Kinematic Hardening in Plasticity

1 Introduction. In the classical plasticity, the effective stress represents a convex yield stress surface in the stress field which limits the elastic deformation range of materials. The proper measurements and descriptions of the initial yield stress surface and its evolution are essential for the constitutive law in plasticity. Since the yield surface and, especially, its evolution are difficult to measure, the isotropic hardening of the initial yield surface is commonly assumed in the theoretical plasticity. Under such assumption, the initial yield surface expands radially (or proportionally) in the stress field during plastic deformation. The assumption is reasonably effective to predict plastic deformations, especially when the deformations of material elements are approximately monotonous and proportional.

If material elements undergo nonmonotonous deformations, the assumed isotropic hardening might not be so effective, even though deformations are approximately proportional. When sheet parts are removed from tools after forming, material elements experience elastic unloading and springback. During this reverse loading, material elements usually demonstrate the Bauschinger effect, which is caused by the translation of the yield stress surface. The isotropic hardening assumption therefore does not properly predict the Bauschinger effect and the springback. Assuming the initial yield stress surface to translate in the stress field without changing its shape and size during plastic deformation is another way to simplify the evolution of the yield stress surface: kinematic hardening. In order to describe the expansion and translation of the yield stress surface during plastic deformation, the combination type of isotropic and kinematic hardening is also commonly used.

In order to provide a theoretical basis for kinematic hardening (and also for the combination type), the definitions of effective stress, effective plastic strain increment, and effective back-stress increment are discussed here along with the evolution of the back-stress. The definitions are for any initial anisotropic yield stress surfaces, which are described as first-order homogenous functions. The flow theory is also derived by applying the normality rule. The deformation theory based on the minimum effective plastic strain path is then derived from the flow theory in order to provide a theoretical basis for computational methods. Discussions are for rigid-plasticity based on a materially embedded (or rotationless) coordinate system.

2 Effective Stress and Effective Plastic Strain Increment. When a current yield stress surface is translated from an initial position by a back-stress, $\boldsymbol{\alpha}$, the plastic work increment, dw, becomes

$$dw = \boldsymbol{\sigma}\cdot d\boldsymbol{\epsilon} = (\boldsymbol{\sigma} - \boldsymbol{\alpha})\cdot d\boldsymbol{\epsilon} + \boldsymbol{\alpha}\cdot d\boldsymbol{\epsilon} \qquad \text{(A1)}$$

where $\boldsymbol{\sigma}$ and $d\boldsymbol{\epsilon}$ are the Cauchy stress and the increment of plastic strain tensors, respectively. It should be noted that all parameters, set in boldface type, correspond to tensors. The effective quantities are now defined considering the following modified plastic work equivalence relationships, i.e.,

$$dw_{\sigma-\alpha} = (\boldsymbol{\sigma} - \boldsymbol{\alpha})\cdot d\boldsymbol{\epsilon} = \bar{\sigma}_\alpha d\bar{\epsilon} \qquad \text{(A2)}$$

where $\bar{\sigma}_\alpha$ and $d\bar{\epsilon}$ are the effective stress and effective plastic strain increment, respectively. Note that $\bar{\sigma}_\alpha$ is defined in Eq. (A2) for the stress translated by $\boldsymbol{\alpha}$. Therefore, $\bar{\sigma}_\alpha$ is obtained from the initial effective stress (which is relevant to the relationship, $\bar{\sigma}d\bar{\epsilon} = \boldsymbol{\sigma}\cdot d\boldsymbol{\epsilon}$) by replacing $\boldsymbol{\sigma}$ with $\boldsymbol{\sigma} - \boldsymbol{\alpha}$. Then, the effective plastic strain increment for the kinematic hardening in Eq. (A2) becomes equivalent to the initial effective strain increment, i.e., the effective plastic strain rate surface is stationary.

If $\bar{\sigma}_\alpha$ and $d\bar{\epsilon}$ are defined from the relationship of plastic work equivalence, $\bar{\sigma}d\bar{\epsilon} = \boldsymbol{\sigma}\cdot d\boldsymbol{\epsilon}$, the effective plastic strain increment evolves as the yield stress surface translates during kinematic hardening. The effective plastic strain increment then becomes singular when a stress on the yield stress surface reaches the origin of the stress field, which is a major drawback of this definition.

3 Evolution of Back-Stress and Effective Back-Stress Increment. As for the translation of the yield stress surface for kinematic hardening during plastic deformation, the following evolution law is assumed here for the back-stress (Ziegler, 1959), i.e.,

$$d\boldsymbol{\alpha} \sim (\boldsymbol{\sigma} - \boldsymbol{\alpha}) \qquad \text{(A3)}$$

where $d\boldsymbol{\alpha}$ is the Jaumann increment (the increment in the materially embedded coordinate system). When plastic deformation is incompressible, the yield stress surface is a cylinder aligned perpendicularly to the deviatoric plane. Therefore, its translation is effective only along the deviatoric plane. In the deviatoric stress field, Eq. (A3) becomes

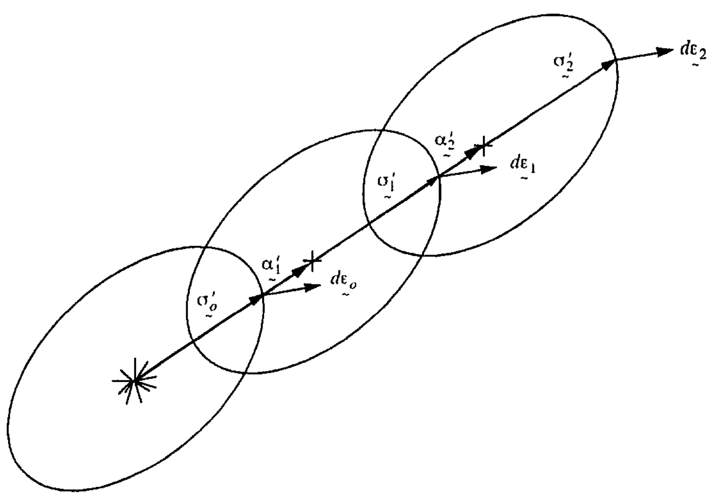

Fig. A1 Yield surface translates along the stress increment direction

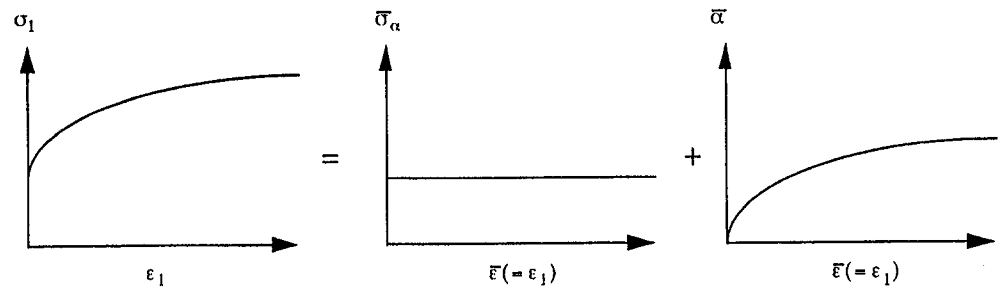

Fig. A2(*a*) Work hardening caused by translation of the yield surface but without size change

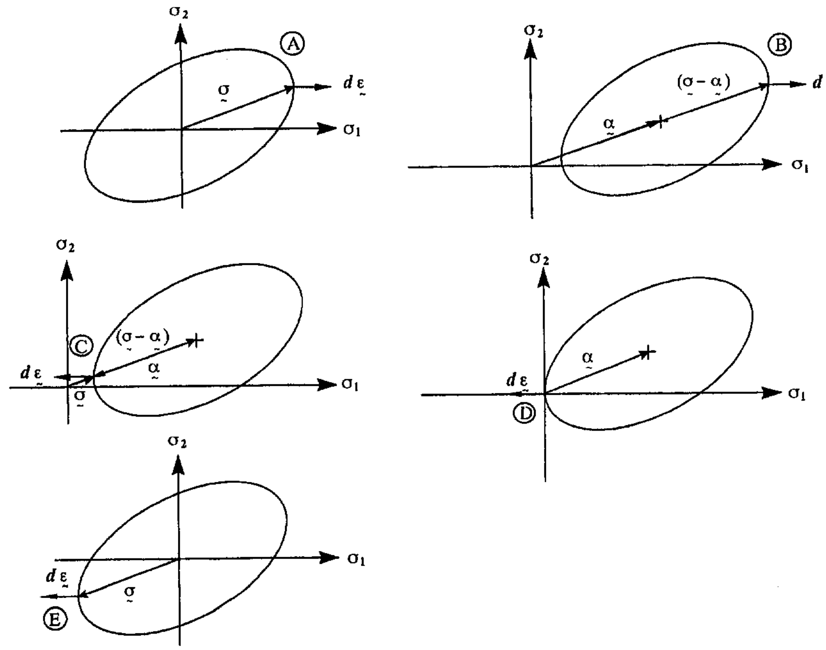

Fig. A2(*b*) Plane-strain loading and unloading, according to Fig. A1

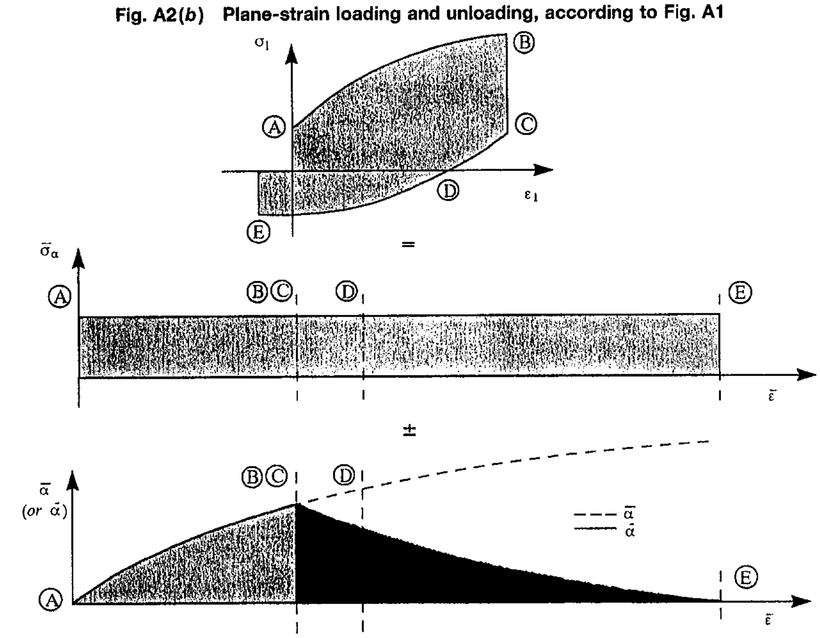

Fig. A2(*c*) Schematic representation of total stress during loading and unloading. The dark shaded area for back stress indicates the amount to be subtracted from the total stress during the unloading.

$$d\boldsymbol{\alpha}' \sim (\boldsymbol{\sigma}' - \boldsymbol{\alpha}') \qquad \text{(A4)}$$

where the superscript "′" represents quantities in the deviatoric space.

Another common assumption for the translation of the back-stress is along the plastic strain increment (Prager, 1956):

$$d\boldsymbol{\alpha}' \sim d\boldsymbol{\epsilon}. \qquad \text{(A5)}$$

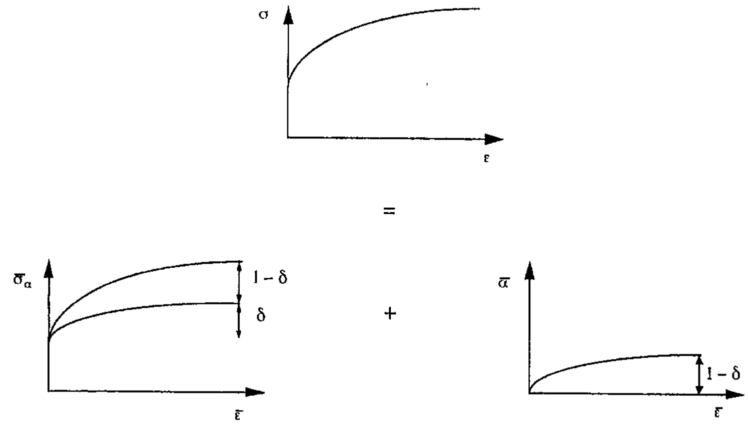

Fig. A3 Work hardening caused by translation and size change of the yield surface

Note that, for the evolution law in Eq. (A4), proportional plastic deformation is obtained for proportional loading (from an initial state) and vice versa as schematically illustrated in Fig. A1(a). However, for the evolution law in Eq. (A5), nonproportional plastic deformation is obtained for proportional loading (or nonproportional loading is obtained for proportional plastic deformation) as shown in Fig. A1(b). Only an exceptional case is found for the Mises yield stress surface, in which Eqs. (A4) and (A5) are equivalent, i.e., $(\boldsymbol{\sigma}' - \boldsymbol{\alpha}') \sim d\boldsymbol{\epsilon}$.

As for the effective back-stress increment, $d\bar{\alpha}$, the value is obtained from the initial effective stress by replacing $\boldsymbol{\sigma}$ with $d\boldsymbol{\alpha}$. The definitions of the effective quantities for stress, plastic strain increment, and back-stress increment are for any initial anisotropic yield stress surfaces, which are expressed as first-order homogenous functions. They are also applicable for the combination type of isotropic and kinematic hardening laws by properly relating work-hardening with the size increase and translation of yield stress surfaces, especially when loading and deformation are proportional.

When plastic deformation and loading are monotonously proportional (from an initial state) as shown in Fig. A1(a),

$$dw_\alpha = \boldsymbol{\alpha} \cdot d\boldsymbol{\epsilon} = \bar{\alpha} d\bar{\varepsilon} \tag{A6}$$

where $\bar{\alpha} = \int d\bar{\alpha}$. Therefore,

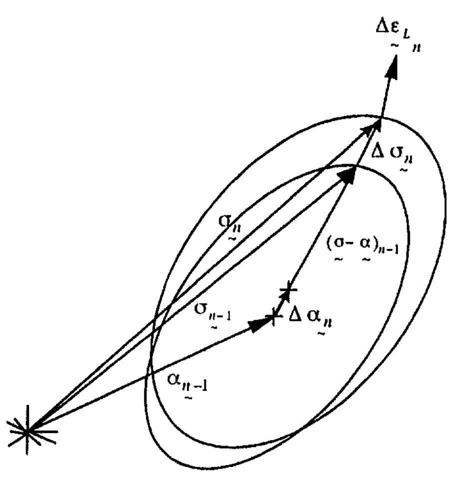

Fig. A4 A schematic representation of the yield surface is translating and changing size

$$dw = dw_{\sigma-\alpha} + dw_\alpha = \bar{\sigma}_\alpha d\bar{\varepsilon} + \bar{\alpha} d\bar{\varepsilon}. \tag{A7}$$

For general cases,

$$dw_\alpha = \boldsymbol{\alpha} \cdot d\boldsymbol{\epsilon} = \pm\tilde{\alpha} d\bar{\varepsilon} \tag{A8}$$

where the value $\tilde{\alpha}$ is obtained from the initial effective stress by replacing $\boldsymbol{\sigma}$ with $\boldsymbol{\alpha}$. In Eq. (A8), the negative sign is for the case, $\boldsymbol{\alpha} \cdot d\boldsymbol{\epsilon} < 0$. Therefore,

$$dw = dw_{\sigma-\alpha} + dw_\alpha = \bar{\sigma}_\alpha d\bar{\varepsilon} \pm \tilde{\alpha} d\bar{\varepsilon}. \tag{A9}$$

Equations (A7) and (A9) are also valid for the combination type.

For demonstration purposes, plastic energy dissipated during proportional loading/unloading under the plane-strain condition is schematically discussed in Fig. A2 for a planar isotropic material which hardens kinematically. Figure A2(a) shows that the measured work-hardening is caused by the translation of an initial yield surface without its size change. In Fig. A2(b), stress states are schematically illustrated for loading (A and B) and unloading (C, D, and E). In Fig. A2(c), the dark shaded area for $\tilde{\alpha}$ is to be subtracted since $\boldsymbol{\alpha} \cdot d\boldsymbol{\epsilon} < 0$ during unloading from C to D and E.

4 Flow-Type Constitutive Law and the Deformation Theory. According to the normality rule, the following relationships are obtained, i.e.,

$$d\boldsymbol{\epsilon} = d\lambda \frac{\partial \bar{\sigma}}{\partial \boldsymbol{\sigma}} = d\lambda \frac{\partial \bar{\sigma}_\alpha}{\partial(\boldsymbol{\sigma} - \boldsymbol{\alpha})}, \quad \boldsymbol{\sigma} - \boldsymbol{\alpha} = \kappa \frac{\partial d\bar{\varepsilon}}{\partial d\boldsymbol{\epsilon}} \tag{A10}$$

or

$$d\boldsymbol{\epsilon} = d\lambda \frac{\partial \bar{\sigma}'}{\partial \boldsymbol{\sigma}'} = d\lambda \frac{\partial \bar{\sigma}'_\alpha}{\partial(\boldsymbol{\sigma}' - \boldsymbol{\alpha}')}, \quad \boldsymbol{\sigma}' - \boldsymbol{\alpha}' = \kappa \frac{\partial d\bar{\varepsilon}'}{\partial d\boldsymbol{\epsilon}'} \tag{A11}$$

in the deviatoric space for incompressible plasticity. When the relationship in Eq. (A2) is applied for Eqs. (A10) and (A11), $d\lambda = d\bar{\varepsilon}$ and $\kappa = \bar{\sigma}_\alpha$ for the first-order homogenous effective functions. Equations (A3) and (A10) (or Eqs. (A4) and (A11)), along with work-hardening relationships associated with the size change $(\bar{\sigma}_\alpha - \bar{\varepsilon})$ and the translation $(\bar{\alpha} - \bar{\varepsilon})$ of the yield stress surfaces, make up the flow type of constitutive law (see Fig. A3).

For computational applications, in which assuming deformation paths during a small discrete step is inevitable, assuming the proportional true (or logarithmic) strain is convenient: incremental deformation theory. For materials which harden isotropically, the proportional true strain path is the minimum plastic work (or minimum effective strain) path (Chung and Richmond, 1992). For materials which harden kinematically (and also for the combination type), the proportional true strain path provides the minimum effective strain path since the effective plastic strain increment defined by Eq. (A2) does not evolve (stationary). Therefore, the quantity associated with a plastic work increment defined in Eq. (A2), $\Delta w_{\sigma-\alpha}$ $(= \int dw_{\sigma-\alpha})$, becomes minimum. The proportional true strain increment is obtained when the stress increment changes proportionally along $\boldsymbol{\sigma} - \boldsymbol{\alpha}$ (or $\boldsymbol{\sigma}' - \boldsymbol{\alpha}'$). Under the assumption of the proportional true strain path, deformation is completely separable from rotation. Therefore, the stress can be updated conveniently from the deformation only, using the constitutive law based on the materially embedded coordinate system.

Under the proportional true strain condition, the (minimum) effective strain is obtained from the (stationary) plastic strain increment simply by replacing the plastic deformation increment, $d\boldsymbol{\epsilon}$, with the logarithmic strain increment, $\Delta\boldsymbol{\epsilon}_L$, i.e.,

$$\Delta\bar{\epsilon}\left(=\int d\bar{\epsilon}\right) = d\bar{\epsilon}(\Delta\boldsymbol{\epsilon}_L). \tag{A12}$$

Also, Eqs. (A10) and (A11) become

$$\Delta\boldsymbol{\epsilon}_L = \Delta\bar{\epsilon}\frac{\partial\bar{\sigma}}{\partial\boldsymbol{\sigma}} = \Delta\bar{\epsilon}\frac{\partial\bar{\sigma}_\alpha}{\partial(\boldsymbol{\sigma}-\boldsymbol{\alpha})}, \quad \boldsymbol{\sigma}-\boldsymbol{\alpha} = \bar{\sigma}_\alpha\frac{\partial\Delta\bar{\epsilon}}{\partial\Delta\boldsymbol{\epsilon}_L} \tag{A13}$$

and

$$\Delta\boldsymbol{\epsilon}_L = \Delta\bar{\epsilon}\frac{\partial\bar{\sigma}'}{\partial\boldsymbol{\sigma}'} = \Delta\bar{\epsilon}\frac{\partial\bar{\sigma}'_\alpha}{\partial(\boldsymbol{\sigma}'-\boldsymbol{\alpha}')},$$

$$\boldsymbol{\sigma}'-\boldsymbol{\alpha}' = \bar{\sigma}'_\alpha\frac{\partial\Delta\bar{\epsilon}}{\partial\Delta\boldsymbol{\epsilon}_L}, \tag{A14}$$

respectively, while

$$\Delta\boldsymbol{\alpha} \sim \boldsymbol{\sigma} - \boldsymbol{\alpha} \text{ (or } \Delta\boldsymbol{\alpha}' \sim \boldsymbol{\sigma}' - \boldsymbol{\alpha}'). \tag{A15}$$

Equations (A13) and (A15) are applicable for the combination type of isotropic and kinematic hardening, in which the isotropic hardening and the kinematic hardening are two extreme cases. The discrete increment of the Cauchy stress is proportional along $\boldsymbol{\sigma} - \boldsymbol{\alpha}$ (or $\boldsymbol{\sigma}' - \boldsymbol{\alpha}'$), accounting for the size change and the translation of the yield stress surface as shown in Fig. A4. Detailed derivations are discussed elsewhere for isotropic hardening (Chung and Richmond, 1993). When the deformation is under proportional true strain condition for the whole process, the resulting stress and strain are equivalent for all the combination types of the isotropic and kinematic hardening.

ERRATUM

The paper "Contact Stresses in Cables due to Tension and Torsion," by K. Kumar, J. E. Cochran, Jr., and M. A. Cutchins, which was published in the December 1997 issue of the ASME *Journal of Applied Mechanics* (Vol. 64, pp. 935-939) incorrectly listed the third author as J. A. Cutchins.

A Geometrically Nonlinear Model for Laminated Composite Strips With Extension-Twist Coupling in the Presence of Delamination

A. Makeev
Post Doctoral Fellow

E. Armanios
Professor

School of Aerospace Engineering,
Georgia Institute of Technology,
Atlanta, GA 30332-0150

A geometrically nonlinear analysis for the extension-twist coupling in pretwisted laminated composite strips in the presence of delamination is developed. Closed-form solutions for strips with internal and edge delaminations are obtained. A parametric study is performed to investigate the influence of delamination length, material system, and stacking sequence on the extension-twist coupling in a class of hygrothermally stable laminates. The model predictions are in good agreement with test data. The results indicate that internal delamination has a negligible influence on the extension-twist coupling behavior while free-edge delamination could result in a significant drop in coupling.

Introduction

Elastic tailoring of laminated composites allows a unique flexibility to meet the design requirements efficiently and economically. Coupling of deformation modes, such as extension-twist and bending-twist, can be created in composite structures by an appropriate selection of material, geometry, and stacking sequence. Extension-twist coupling in laminated composite strips is provided by antisymmetric stacking sequences. Such laminates will twist when subjected to axial load. The test data show nonlinear axial force-twist dependence which is due to low torsional to extensional stiffness ratio.

A review of geometrically nonlinear models for coupled composite beams without damage is provided in Hodges (1990). Most of the approaches are numerically based. Among recent publications, the work of Cesnik and Hodges (1997) is worth noting. In this work the variational-asymptotical method is used to dimensionally reduce a three-dimensional elasticity problem for a beam of arbitrary geometry and material properties. A two-dimensional cross-sectional analysis and one-dimensional beam problem are extracted from a geometrically nonlinear elasticity formulation. A finite element code for cross-sectional modeling was developed. A geometrically nonlinear shell-type model for extension-twist coupled laminates was developed by Armanios et al. (1996). The closed-form solution was in good agreement with existing theoretical results and test data.

In order to implement elastically tailored composites in practical applications such as fixed wing and rotorcraft structures, their damage tolerance needs to be assessed. One of the primary damage modes observed in test and service is delamination or separation of layers. Most of the published geometrically nonlinear analytical models, taking into account delamination, are related to stability issues, and are based on Von Karman's kinematic approach. To cite a few works, delamination buckling and post-buckling are treated in Simitses et al. (1985) and Kardomateas (1989).

To the best of the authors' knowledge there is no published closed-form solution which takes into account the influence of delamination on the nonlinear extension-twist coupling behavior of antisymmetric laminates. To this end, a finite displacement model which accounts for delamination, is developed in this work. A closed-form solution for extension-twist coupling behavior of a pretwisted strip in the presence of an internal or an edge delamination is derived.

Analysis

Consider the laminated strip shown in Fig. 1. The thickness h of the laminate is small relative to the width $2b$ which is small compared to the length L. That is

$$h \ll 2b \ll L. \tag{1}$$

The strip has a pretwist about the longitudinal axis X. Assume that the strains are small (negligible compared to 1) and independent of the longitudinal direction; the pretwist rate θ_0 and the elastic twist rate θ are constant; and the material is linearly elastic.

The strip has a midsurface symmetric internal or free-edge delaminations shown in Figs. 2 and 3, respectively. Accordingly, the strip is divided into two sublaminates, groups of plies above and below the delamination interface, denoted by indices 1 and 2 in Fig. 1. The middle surface of each sublaminate is referred to the material coordinates x and y, the transverse material coordinate is denoted by z as shown for the group of plies above the internally delaminated interface in Fig. 2. If the strip is flat, the position vector of an arbitrary point of a sublaminate is defined as

$$\mathbf{r}_f = x\hat{\mathbf{i}} + y\hat{\mathbf{j}} + z\hat{\mathbf{k}}$$

$$0 \le x \le L, \quad -b \le y \le b, \quad -\frac{h}{4} \le z \le \frac{h}{4} \tag{2}$$

where $\hat{\mathbf{i}}, \hat{\mathbf{j}}, \hat{\mathbf{k}}$ are the unit base vectors of the reference Cartesian coordinate system shown in Fig. 1.

The position vector $\mathbf{r}_0$ of a material point in the initial state is derived in Armanios et al. (1996). The steps are discussed briefly in the following for convenience. First, a rigid cross section is rotated about the longitudinal axis of the strip. Second, the out-of-plane strains caused by the previous step are set to

Contributed by the Applied Mechanics Division of The American Society of Mechanical Engineers for publication in the ASME Journal of Applied Mechanics.

Discussion on the paper should be addressed to the Technical Editor, Professor Lewis T. Wheeler, Department of Mechanical Engineering, University of Houston, Houston, TX 77204-4792, and will be accepted until four months after final publication of the paper itself in the ASME Journal of Applied Mechanics.

Manuscript received by the ASME Applied Mechanics Division, Feb. 27, 1997; final revision, May 5, 1998. Associate Technical Editor: V. K. Kinra.

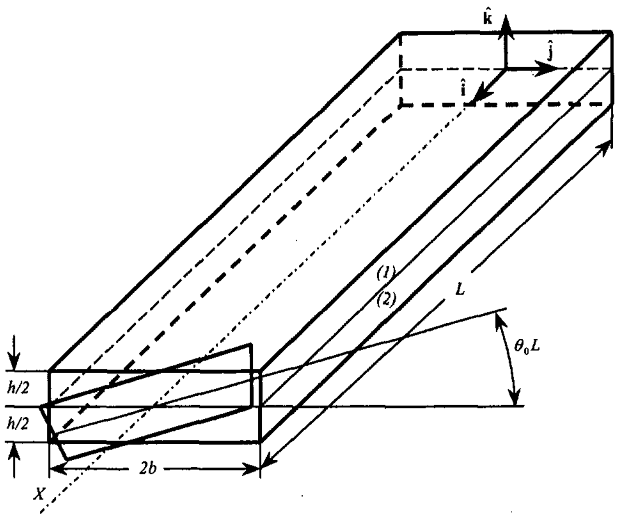

Fig. 1 Laminate geometry

zero by rotating a straight line element perpendicular to the middle surface of the flat strip. The result is

$$\mathbf{r}_0^{(1,2)} = \left(x - \frac{\theta_0 y}{\sqrt{1+(\theta_0 y)^2}}\left(z \pm \frac{h}{4}\right)\right)\hat{\mathbf{i}} + y\hat{\mathbf{e}}_{20} + \frac{1}{\sqrt{1+(\theta_0 y)^2}}\left(z \pm \frac{h}{4}\right)\hat{\mathbf{e}}_{30} \quad (3)$$

where

$$\hat{\mathbf{e}}_{20} = \cos\theta_0 x\hat{\mathbf{j}} + \sin\theta_0 x\hat{\mathbf{k}},\ \hat{\mathbf{e}}_{30} = -\sin\theta_0 x\hat{\mathbf{j}} + \cos\theta_0 x\hat{\mathbf{k}}. \quad (4)$$

The superscripts associated with $\mathbf{r}_0$ indicate the corresponding sublaminate. The plus and minus signs are associated with sublaminates 1 and 2, respectively. These conventions will be used for convenience in the subsequent development.

The position vector $\mathbf{r}$ of the material point in the deformed state is derived in the same way as in the initial state, except for a small displacement field which is added to account for all strain components

$$\mathbf{r}^{(1,2)} = \left(x - \frac{(\theta_0+\theta)y}{\sqrt{1+(\theta_0+\theta)^2 y^2}}\left(z \pm \frac{h}{4}\right) + u^{(1,2)}\right)\hat{\mathbf{i}} + (y + v^{(1,2)})\hat{\mathbf{e}}_2 + \left(\frac{1}{\sqrt{1+(\theta_0+\theta)^2 y^2}}\left(z \pm \frac{h}{4}\right) + w^{(1,2)}\right)\hat{\mathbf{e}}_3 \quad (5)$$

where

$$\hat{\mathbf{e}}_2 = \cos(\theta_0+\theta)x\hat{\mathbf{j}} + \sin(\theta_0+\theta)x\hat{\mathbf{k}}$$
$$\hat{\mathbf{e}}_3 = -\sin(\theta+\theta_0)x\hat{\mathbf{j}} + \cos(\theta_0+\theta)x\hat{\mathbf{k}} \quad (6)$$

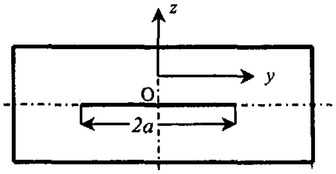

Fig. 2 Internal delamination and coordinate system

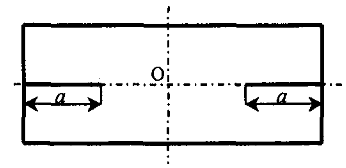

Fig. 3 Free-edge delamination

and

$$u^{(1,2)} = \epsilon_0 x + U^{(1,2)}(y,z),\quad v^{(1,2)} = V^{(1,2)}(y,z)$$
$$w^{(1,2)} = W^{(1,2)}(y,z) \quad (7)$$

are the small displacement vector components.

The Lagrangian strain tensor components are defined as (Sokolnikoff, 1964)

$$2\epsilon_{ij} = g_{ij} - h_{ij} \quad (8)$$

where g_{ij} and h_{ij} are the metric tensor components in the deformed and the initial states, respectively,

$$g_{ij} = \frac{\partial \mathbf{r}}{\partial x^i}\cdot\frac{\partial \mathbf{r}}{\partial x^j},\quad h_{ij} = \frac{\partial \mathbf{r}_0}{\partial x^i}\cdot\frac{\partial \mathbf{r}_0}{\partial x^j}$$
$$(x^1 = x,\ x^2 = y,\ x^3 = z). \quad (9)$$

The following limits are imposed on the maximum values of the kinematic parameters

$$\theta_0 h,\ \theta h = O(\epsilon)$$
$$(\theta_0 b)^2,\quad (\theta b)^2 = O(\epsilon)$$
$$\frac{\partial U}{\partial y},\frac{\partial U}{\partial z},\frac{\partial V}{\partial y},\frac{\partial V}{\partial z},\frac{\partial W}{\partial y},\frac{\partial W}{\partial z} = O(\epsilon)$$
$$\theta_0 V,\ \theta_0 W,\ \theta V,\ \theta W = O(\epsilon^{3/2}) \quad (10)$$

where ϵ is the maximum magnitude of strain. Terms of $O(\epsilon^{3/2})$ and higher will be neglected in the strain-displacement relations.

For a thin strip the out-of-plane shear strains are replaced by their average values with respect to thickness

$$\gamma_{yz} = \gamma_{yz}(y),\quad \gamma_{xz} = \gamma_{xz}(y). \quad (11)$$

Moreover, nondeformability in the z-material direction is assumed

$$\epsilon_{zz} = 0. \quad (12)$$

According to Eqs. (3)–(12), the small displacement field components in Eq. (7) can be expressed as

$$U^{(1,2)} = U_0^{(1,2)}(y) - zU_1^{(1,2)}(y)$$
$$V^{(1,2)} = V_0^{(1,2)}(y) - zV_1^{(1,2)}(y),\quad W^{(1,2)} = W_0^{(1,2)}(y) \quad (13)$$

and the engineering strain-displacement relationships become

$$\epsilon_{ij}^{(1,2)} = \epsilon_{ij}^{0(1,2)} - z\kappa_{ij}^{(1,2)},\quad (i,j = x,y)$$
$$\epsilon_{xx}^{0(1,2)} = \epsilon_0 + \tfrac{1}{2}(\theta^2 + 2\theta_0\theta)y^2,\quad \kappa_{xx}^{(1,2)} = 0$$
$$\epsilon_{yy}^{0(1,2)} = V_{0,y}^{(1,2)},\quad \kappa_{yy}^{(1,2)} = V_{1,y}^{(1,2)}$$
$$\epsilon_{zz}^{(1,2)} = 0$$
$$\gamma_{yz}^{(1,2)} = -V_1^{(1,2)} + W_{0,y}^{(1,2)}$$
$$\gamma_{xz}^{(1,2)} = -U_1^{(1,2)}$$
$$\gamma_{xy}^{0(1,2)} = U_{0,y}^{(1,2)} \mp \frac{\theta h}{2},\quad \kappa_{xy}^{(1,2)} = U_{1,y}^{(1,2)} + 2\theta \quad (14)$$

where partial derivatives are denoted by subscript commas.

Strips in the presence of a midplane symmetric internal delamination (Fig. 2) and a symmetric edge delamination (Fig. 3) are considered. If necessary, the delaminated and undamaged regions of the laminate will be identified in the equations by superscript (d) and (u), respectively. If the displacements in a delaminated region do not satisfy the following condition

$$W_0^{(1)(d)} \geq W_0^{(2)(d)}, \tag{15}$$

the identity

$$W_0^{(1)(d)} = W_0^{(2)(d)} \tag{16}$$

has to be enforced to avoid overlapping. Continuity of the displacements across the sublaminate interface in the undamaged regions is assumed. That is

$$\left[U_0^{(1)} + \frac{h}{4}U_1^{(1)}\right]^{(u)} = \left[U_0^{(2)} - \frac{h}{4}U_1^{(2)}\right]^{(u)}$$

$$\left[V_0^{(1)} + \frac{h}{4}V_1^{(1)}\right]^{(u)} = \left[V_0^{(2)} - \frac{h}{4}V_1^{(2)}\right]^{(u)}$$

$$W_0^{(1)(u)} = W_0^{(2)(u)}. \tag{17}$$

Continuity of the displacements in the sublaminates at the boundary

$$|y| = y_1 = \begin{cases} a, \text{ internal delamination} \\ b - a, \text{ edge delamination} \end{cases} \tag{18}$$

of the delaminated and the undamaged regions is also imposed. Use Eqs. (13) to write this condition as

$$|y| = y_1$$

$$[U_0, V_0, W_0, U_1, V_1]^{(1,2)(d)} = [U_0, V_0, W_0, U_1, V_1]^{(1,2)(u)}. \tag{19}$$

The equilibrium equations and boundary conditions for a cantilever strip subjected to an axial force F and a torque T are derived from the principle of virtual work. The following symmetry property considerably simplifies the analysis.

The stress state and the displacement field for an antisymmetric laminate loaded by the axial force and the torque are symmetric about the center O of the cross sections shown in Figs. 2 and 3. Using this symmetry property, the principle of virtual work can be written as

$$\int_0^{y_1} dy \sum_{k=1}^{2} \int_{-h/4}^{h/4} (\sigma^{ij}\delta\epsilon_{ij}\sqrt{g})^{(k)} dz + \int_{y_1}^{b} dy \sum_{k=1}^{2} \int_{-h/4}^{h/4} (\sigma^{ij}\delta\epsilon_{ij}\sqrt{g})^{(k)} dz - \frac{T\delta\theta}{2} - \frac{F\delta\epsilon_0}{2} - \frac{\delta W_m}{L} = 0$$

$$(i, j = x, y, z) \tag{20}$$

where σ^{ij} are the second Piola-Kirchhoff stress tensor components. Summation over the repeated indices is assumed. The Jacobian

$$\sqrt{g} = \frac{\partial \mathbf{r}_0}{\partial x} \cdot \left(\frac{\partial \mathbf{r}_0}{\partial y} \times \frac{\partial \mathbf{r}_0}{\partial z}\right) = 1 \tag{21}$$

if the terms of $O(\epsilon)$ are neglected compared to unity. The last term in Eq. (20) represents the work of the surface tractions at the boundary $y = 0$

$$\delta W_m = -\int_0^L dx \sum_{k=1}^{2} \int_{-h/4}^{h/4} [(\sigma^{xy}\hat{\mathbf{i}} + \sigma^{yy}\hat{\mathbf{e}}_2 + \sigma^{yz}\hat{\mathbf{e}}_3) \cdot \delta\mathbf{r}\sqrt{a}]^{(1,2)}|_{y=0} dz \tag{22}$$

where $\mathbf{r}$ is defined in Eq. (5), and the quantity

$$\sqrt{a} = \left|\frac{\partial \mathbf{r}_0}{\partial z} \times \frac{\partial \mathbf{r}_0}{\partial x}\right| = 1 \tag{23}$$

according to the small strain assumption. Substitute the following symmetry conditions

$$y = 0, \quad (u, v, w)^{(1)}|_z = (u, -v, -w)^{(2)}|_{-z}$$

$$(\sigma^{xy}, \sigma^{yy}, \sigma^{yz})^{(1)}|_z = (-\sigma^{xy}, \sigma^{yy}, \sigma^{yz})^{(2)}|_{-z} \tag{24}$$

into Eq. (22) to obtain

$$\delta W_m = 0. \tag{25}$$

Internal Delamination. Consider the case of a strip with internal delamination (Fig. 2). Denote the forces and moments per unit length of the middle surface by

$$(N_{xx}, N_{yy}, Q_y, Q_x, N_{xy}, M_{xx}, M_{yy}, M_{xy})^{(1,2)} = \int_{h/4}^{h/4} (\sigma^{xx}, \sigma^{yy}, \sigma^{yz}, \sigma^{xz}, \sigma^{xy}, z\sigma^{xx}, z\sigma^{yy}, z\sigma^{xy})^{(1,2)} dz \tag{26}$$

where the subscripts do not denote covariant tensor components. Substitute Eqs. (14)–(18), (21), (25), and (26) into the principle of virtual work (20), integrate by parts, use Eqs. (19) and (24), and reduce the resulting equilibrium equations and boundary conditions to

$$N_{xy}^{(1)(d)} = -N_{xy}^{(2)(d)} = \text{const}, \quad N_{yy}^{(1,2)(d)} = 0 \tag{27}$$

$$W_0^{(1,2)(d)} \text{ independent}, \; Q_y^{(1,2)(d)} = 0 \tag{28}$$

$$W_0^{(1)(d)} = W_0^{(2)(d)}, \quad Q_y^{(1)(d)} = -Q_y^{(2)(d)} \tag{29}$$

$$[M_{xy,y}^{(1,2)} - Q_x^{(1,2)}]^{(d)} = 0, \quad [M_{yy,y}^{(1,2)} \mp Q_y^{(1)}]^{(d)} = 0 \tag{30}$$

$$[N_{xy}, N_{yy}, Q_y]^{(1)(u)} = -[N_{xy}, N_{yy}, Q_y]^{(2)(u)} \tag{31}$$

$$\left[\left(M_{xy}^{(1,2)} + \frac{h}{4}N_{xy}^{(1)}\right)_{,y} - Q_x^{(1,2)}\right]^{(u)} = 0$$

$$\left[\left(M_{yy}^{(1,2)} + \frac{h}{4}N_{yy}^{(1)}\right)_{,y} \mp Q_y^{(1)}\right]^{(u)} = 0 \tag{32}$$

$$y = 0$$

$$[U_0, V_0, W_0, U_1, V_1]^{(1)(d)} = [U_0, -V_0, -W_0, -U_1, V_1]^{(2)(d)} \tag{33}$$

$$y = 0, \quad [M_{yy}, M_{xy}]^{(1)(d)} = [-M_{yy}, M_{xy}]^{(2)(d)} \tag{34}$$

$$y = a$$

$$[U_0, V_0, W_0, U_1, V_1]^{(1,2)(d)} = [U_0, V_0, W_0, U_1, V_1]^{(1,2)(u)} \tag{35}$$

$$y = a, \left[M_{xy}^{(1,2)} + \frac{h}{4}N_{xy}^{(1)}\right]^{(d)} = \left[M_{xy}^{(1,2)} + \frac{h}{4}N_{xy}^{(1)}\right]^{(u)}$$

$$\left[M_{yy}^{(1,2)} + \frac{h}{4}N_{yy}^{(1)}\right]^{(d)} = \left[M_{yy}^{(1,2)} + \frac{h}{4}N_{yy}^{(1)}\right]^{(u)} \tag{36}$$

$$y=b,\ \left[M_{xy}^{(1,2)}+\frac{h}{4}N_{xy}^{(1)}\right]^{(u)}=0,$$

$$\left[M_{yy}^{(1,2)}+\frac{h}{4}N_{yy}^{(1)}\right]^{(u)}=0 \tag{37}$$

$$2\left\{\int_0^a\sum_{k=1}^{2}N_{xx}^{(k)(d)}dy+\int_a^b\sum_{k=1}^{2}N_{xx}^{(k)(u)}dy\right\}=F \tag{38}$$

$$2\left\{\int_0^a\sum_{k=1}^{2}\left(N_{xx}^{(k)(d)}[\theta_0+\theta]y^2-2\left[M_{xy}^{(k)}+\frac{h}{4}N_{xy}^{(1)}\right]^{(d)}\right)dy\right.$$
$$+\int_a^b\sum_{k=1}^{2}\left(N_{xx}^{(k)(u)}[\theta_0+\theta]y^2\right.$$
$$\left.\left.-2\left[M_{xy}^{(k)}+\frac{h}{4}N_{xy}^{(1)}\right]^{(u)}\right)dy\right\}=T. \tag{39}$$

The first condition in Eq. (28) signifies that the transverse displacements $W_0^{(1)(d)}$ and $W_0^{(2)(d)}$ in the delaminated region are independent. If the nonoverlapping condition (15) is not satisfied, Eqs. (29) have to be used instead of Eq. (28).

Assume that the linear constitutive relations are given in local rectangular Cartesian coordinates. Although the base vectors

$$\frac{\partial\mathbf{r}_0}{\partial x},\quad\frac{\partial\mathbf{r}_0}{\partial y},\quad\frac{\partial\mathbf{r}_0}{\partial z} \tag{40}$$

of the material coordinate system (x, y, z) in the initial state are not orthogonal, transformation to the orthogonal coordinates would introduce correction of $O(\epsilon^2)$ to the strain field as shown in Armanios et al. (1996).

Equation (12) implies that for each lamina

$$E_{33}\rightarrow\infty,\quad\nu_{13}=\nu_{23}=0 \tag{41}$$

where E_{33}, ν_{13}, and ν_{23} are Young's modulus and Poisson's ratios associated with the transverse material direction. Indices 1, 2, 3 denote the principal material axes. Therefore, the in-plane components of the lamina stiffness matrix are the same as for the plane stress state.

Sublaminates with symmetric stacking sequences are considered. Since the middle surface strains and curvatures for a symmetric sublaminate are uncoupled, the constitutive relations can be written in the following form:

$$\begin{Bmatrix}N_{xx}\\N_{yy}\\N_{xy}\end{Bmatrix}^{(1,2)}=\begin{bmatrix}A_{11}&A_{12}&\pm A_{16}\\A_{12}&A_{22}&\pm A_{26}\\\pm A_{16}&\pm A_{26}&A_{66}\end{bmatrix}\begin{Bmatrix}\epsilon_{xx}^0\\\epsilon_{yy}^0\\\gamma_{xy}^0\end{Bmatrix}^{(1,2)}$$

$$\begin{Bmatrix}M_{xx}\\M_{yy}\\M_{xy}\end{Bmatrix}^{(1,2)}=\begin{bmatrix}D_{12}&D_{22}&\pm D_{16}\\D_{12}&D_{22}&\pm D_{26}\\\pm D_{16}&\pm D_{26}&D_{66}\end{bmatrix}\begin{Bmatrix}-\kappa_{xx}\\-\kappa_{yy}\\-\kappa_{xy}\end{Bmatrix}^{(1,2)}$$

$$\begin{Bmatrix}Q_y\\Q_x\end{Bmatrix}^{(1,2)}=\begin{bmatrix}A_{44}&\pm A_{45}\\\pm A_{45}&A_{55}\end{bmatrix}\begin{Bmatrix}\gamma_{yz}\\\gamma_{xz}\end{Bmatrix}^{(1,2)}. \tag{42}$$

The stiffness parameters are defined as

$$(A_{ij}, D_{ij})=\int_{-h/4}^{h/4}(\bar{Q}_{ij}, \bar{Q}_{ij}z^2)^{(1)}dz \tag{43}$$

where $\bar{Q}_{ij}$ are the components of the lamina stiffness matrix in the (x, y, z)-coordinates (Vinson and Sierakowski, 1986).

One can substitute Eqs. (14) into the constitutive relations (42), and finally write all differential equations and boundary conditions in terms of displacements. The system can be reduced to two uncoupled sets of differential equations and boundary conditions in terms of sum and difference of displacement parameters. The results of solving the system are provided below.

Introduce the following notation

$$(\ )^{(+)}=(\ )^{(1)}+(\ )^{(2)},\quad(\ )^{(-)}=(\ )^{(1)}-(\ )^{(2)}. \tag{44}$$

The axial strain ϵ_0 and the elastic twist rate θ can be determined from Eqs. (38) and (39) written as

$$2\left\{\int_0^a N_{xx}^{(+)(d)}dy+\int_a^b N_{xx}^{(+)(u)}dy\right\}=F \tag{45}$$

$$2\left\{\int_0^a\left(N_{xx}^{(+)(d)}[\theta_0+\theta]y^2-2\left[M_{xy}^{(+)}+\frac{h}{4}N_{xy}^{(-)}\right]^{(d)}\right)dy\right.$$
$$+\int_a^b\left(N_{xx}^{(+)(u)}[\theta_0+\theta]y^2\right.$$
$$\left.\left.-2\left[M_{xy}^{(+)}+\frac{h}{4}N_{xy}^{(-)}\right]^{(u)}\right)dy\right\}=T \tag{46}$$

where

$$N_{xx}^{(+)(d)}=\alpha_{11}[2\epsilon_0+(\theta^2+2\theta_0\theta)y^2]+\alpha_{12}\left[\frac{\alpha_{12}}{\alpha_{22}}\frac{1}{3}(\theta^2\right.$$
$$\left.+2\theta_0\theta)(a^2-3y^2)-\frac{h}{4}\left(\frac{U_1^{(+)(d)}|_a}{a}+4\theta\right)\right]$$

$$N_{xy}^{(-)(d)}=2N_{xy}^{(1)(d)}=\alpha_{12}\left[2\epsilon_0+\frac{1}{3}(\theta^2+2\theta_0\theta)a^2\right]$$
$$-\alpha_{22}\frac{h}{4}\left(\frac{U_1^{(+)(d)}|_a}{a}+4\theta\right) \tag{47}$$

$$\begin{Bmatrix}N_{xx}^{(+)}\\N_{xy}^{(-)}=2N_{xy}^{(1)}\end{Bmatrix}^{(u)}=\begin{bmatrix}\alpha_{11}&\alpha_{12}\\\alpha_{12}&\alpha_{22}\end{bmatrix}\begin{Bmatrix}2\epsilon_0+(\theta^2+2\theta_0\theta)y^2\\-\frac{h}{4}(U_{1,y}^{(+)(u)}+4\theta)\end{Bmatrix} \tag{48}$$

$$\begin{Bmatrix}M_{yy}^{(-)}\\M_{xy}^{(+)}\end{Bmatrix}^{(d),(u)}=\begin{bmatrix}D_{22}&D_{26}\\D_{26}&D_{66}\end{bmatrix}\begin{Bmatrix}-V_{1,y}^{(-)}\\-U_{1,y}^{(+)}-4\theta\end{Bmatrix}^{(d),(u)} \tag{49}$$

and

$$\alpha_{11}=A_{11}-\frac{A_{12}^2}{A_{22}},\quad\alpha_{12}=A_{16}-\frac{A_{12}A_{26}}{A_{22}}$$
$$\alpha_{22}=A_{66}-\frac{A_{26}^2}{A_{22}},\quad\beta=A_{55}-\frac{A_{45}^2}{A_{44}}. \tag{50}$$

The solution for the displacement parameters in the delaminated region is

$$U_1^{(+)(d)}=B_1\sinh\left(\sqrt{\frac{\beta}{D_{66}-D_{26}^2/D_{22}}}\,y\right)$$

$$V_1^{(-)(d)}=-B_1\frac{D_{26}}{D_{22}}\sinh\left(\sqrt{\frac{\beta}{D_{66}-D_{26}^2/D_{22}}}\,y\right)+B_2y \tag{51}$$

if the condition

$$W_0^{(-)(d)} = -\int_y^a \left(V_1^{(-)(d)} + \frac{A_{45}}{A_{44}} U_1^{(+)(d)} \right) dy \geq 0 \quad (52)$$

is satisfied in the delaminated region. Otherwise

$$\begin{Bmatrix} U_1^{(+)} \\ V_1^{(-)} \end{Bmatrix}^{(d)} = B_1 \begin{Bmatrix} 1 \\ -\dfrac{D_{26}\eta_1 - A_{45}}{D_{22}\eta_1 - A_{44}} \end{Bmatrix} \sinh \sqrt{\eta_1} y$$

$$+ \mathrm{B}_2 \begin{Bmatrix} 1 \\ -\dfrac{D_{26}\eta_2 - A_{45}}{D_{22}\eta_2 - A_{44}} \end{Bmatrix} \sinh \sqrt{\eta_2} y \quad (53)$$

where η_1 and η_2 are the roots of the following characteristic equation:

$$(D_{22}\eta - A_{44})(D_{66}\eta - A_{55}) - (D_{26}\eta - A_{45})^2 = 0. \quad (54)$$

The displacement parameters in the undamaged region are given by the following expression:

$$\begin{Bmatrix} U_1^{(+)} \\ V_1^{(-)} \end{Bmatrix}^{(u)} = \begin{Bmatrix} 1 \\ -\dfrac{D_{26}\eta_3 - A_{45}}{D_{22}\eta_3 - A_{44}} \end{Bmatrix} (B_3 \sinh \sqrt{\eta_3} y$$

$$+ B_4 \cosh \sqrt{\eta_3} y)$$

$$+ \begin{Bmatrix} 1 \\ -\dfrac{D_{26}\eta_4 - A_{45}}{D_{22}\eta_4 - A_{44}} \end{Bmatrix} (B_5 \sinh \sqrt{\eta_4} y$$

$$+ \mathrm{B}_6 \cosh \sqrt{\eta_4}\, y) + \begin{Bmatrix} -1 \\ \dfrac{A_{45}}{A_{44}} \end{Bmatrix} \frac{h}{2} \frac{\alpha_{12}}{\beta} (\theta^2 + 2\theta_0\theta) y \quad (55)$$

where η_3 and η_4 are the roots of

$$(D_{22}\eta - A_{44}) \left(\left[D_{66} + \left(\frac{h}{4} \right)^2 \alpha_{22} \right] \eta - A_{55} \right)$$

$$- (D_{26}\eta - A_{45})^2 = 0. \quad (56)$$

The constants B_i can be obtained from the following boundary conditions:

$$y = a,\ U_1^{(+)(d)} = U_1^{(+)(u)},\ V_1^{(-)(d)} = V_1^{(-)(u)}$$

$$\left(M_{xy}^{(+)} + \frac{h}{4} N_{xy}^{(-)} \right)^{(d)} = \left(M_{xy}^{(+)} + \frac{h}{4} N_{xy}^{(-)} \right)^{(u)}$$

$$M_{yy}^{(-)(d)} = M_{yy}^{(-)(u)} \quad (57)$$

$$y = b,\ \left(M_{xy}^{(+)} + \frac{h}{4} N_{xy}^{(-)} \right)^{(u)} = 0, \quad M_{yy}^{(-)(u)} = 0. \quad (58)$$

It is worth noting that for the case of no delamination ($a = 0$), the solution is represented by Eqs. (55) with constants B_4 and B_6 set to zero according to symmetry, and the remaining constants determined from Eqs. (58).

The only nonzero interlaminar shear stress is

$$t_{xz} = N_{xy,y}^{(1)(u)} = \alpha_{12}(\theta^2 + 2\theta_0\theta) y - \alpha_{22} \frac{h}{8} U_{1,yy}^{(+)(u)}. \quad (59)$$

If the applied torque T is equal to zero, the following axial force-twist relationship can be obtained

$$F(b_1 - \theta_0 - \theta)$$

$$= (b_2 + \tfrac{4}{3} b_3\theta_0 + 2b_4\theta_0^2)\theta + (b_3 + 3b_4\theta_0)\theta^2 + b_4\theta^3 \quad (60)$$

where the constants b_i are defined in terms of the cross section thickness, width, delamination length, and the stiffness parameters A_{ij} and D_{ij}. The influence of internal delamination on the axial force-twist relationship is negligible as shown in the Application section. On the other hand, the free-edge delamination has a significant effect on the extension-twist coupling. An explicit form of the coefficients in the axial force-twist relationship for the case of free-edge delamination is provided in the following section.

Free-Edge Delamination. The procedure for solving the problem for a strip with free-edge delamination (Fig. 3) is similar to the one provided in the previous section for internal delamination. However, the equilibrium equations and boundary conditions are modified according to the principle of virtual work. Equilibrium Eqs. (27) change to

$$N_{xy}^{(1,2)(d)} = N_{yy}^{(1,2)(d)} = 0 \quad (61)$$

and boundary conditions (36) and (37) become

$$y = b - a, \quad M_{xy}^{(1,2)(d)} = \left[M_{xy}^{(1,2)} + \frac{h}{4} N_{xy}^{(1)} \right]^{(u)}$$

$$M_{yy}^{(1,2)(d)} = \left[M_{yy}^{(1,2)} + \frac{h}{4} N_{yy}^{(1)} \right]^{(u)} \quad (62)$$

$$y = b, \quad M_{xy}^{(1,2)(d)} = M_{yy}^{(1,2)(d)} = 0. \quad (63)$$

The extension-twist relations (38) and (39) become

$$2 \left\{ \int_0^{b-a} N_{xx}^{(+)(u)} dy + \int_{b-a}^{b} N_{xx}^{(+)(d)} dy \right\} = F \quad (64)$$

$$2 \left\{ \int_0^{b-a} \left(N_{xx}^{(+)(u)} [\theta_0 + \theta] y^2 - 2 \left[M_{xy}^{(+)} + \frac{h}{4} N_{xy}^{(-)} \right]^{(u)} \right) dy \right.$$

$$\left. + \int_{b-a}^{b} (N_{xx}^{(+)(d)} [\theta_0 + \theta] y^2 - 2M_{xy}^{(+)(d)}) dy \right\} = T \quad (65)$$

where the constitutive relationships for the stress resultants are provided in Eqs. (47)–(49), except for $N_{xx}^{(+)(d)}$ which changes to

$$N_{xx}^{(+)(d)} = \left(\alpha_{11} - \frac{\alpha_{12}^2}{\alpha_{22}} \right) [2\epsilon_0 + (\theta^2 + 2\theta_0\theta) y^2]. \quad (66)$$

The following expressions represent the solution for the displacement parameters

$$\begin{Bmatrix} U_1^{(+)} \\ V_1^{(-)} \end{Bmatrix}^{(u)} = \begin{Bmatrix} 1 \\ -\dfrac{D_{26}\eta_3 - A_{45}}{D_{22}\eta_3 - A_{44}} \end{Bmatrix} C_1 \sinh \sqrt{\eta_3} y$$

$$+ \begin{Bmatrix} 1 \\ -\dfrac{D_{26}\eta_4 - A_{45}}{D_{22}\eta_4 - A_{44}} \end{Bmatrix} C_2 \sinh \sqrt{\eta_4} y$$

$$+ \begin{Bmatrix} -1 \\ \dfrac{A_{45}}{A_{44}} \end{Bmatrix} \frac{h}{2} \frac{\alpha_{12}}{\beta} (\theta^2 + 2\theta_0\theta) y \quad (67)$$

Table 1 Properties of T300/954-3 graphite/cyanate material system

$E_{11} = 135.6$ GPa, $E_{22} = 9.9$ GPa
$G_{12} = G_{13} = 4.2$ GPa, $G_{23} = 2.5$ GPa
$\nu_{12} = 0.3$

Table 2 Properties of S2/F584 glass/epoxy material system

$E_{11} = 44.1$ GPa, $E_{22} = 12.4$ GPa
$G_{12} = G_{13} = 4.46$ GPa, $G_{23} = 4.14$ GPa
$\nu_{12} = 0.29$

where η_3 and η_4 are the roots of Eq. (56). The solution for the delaminated region is

$$U_1^{(+)(d)} = C_3 \sinh\left(\sqrt{\frac{\beta}{D_{66} - D_{26}^2/D_{22}}}\, y\right) + C_4 \cosh\left(\sqrt{\frac{\beta}{D_{66} - D_{26}^2/D_{22}}}\, y\right)$$

$$V_1^{(-)(d)} = -\frac{D_{26}}{D_{22}}\left(C_3 \sinh\left[\sqrt{\frac{\beta}{D_{66} - D_{26}^2/D_{22}}}\, y\right] + C_4 \cosh\left[\sqrt{\frac{\beta}{D_{66} - D_{26}^2/D_{22}}}\, y\right]\right) + C_5 y + C_6 \quad (68)$$

if the condition

$$W_0^{(-)(d)} = \int_{b-a}^{y} \left(V_1^{(-)(d)} + \frac{A_{45}}{A_{44}} U_1^{(+)(d)}\right) dy \geq 0 \quad (69)$$

is satisfied. Otherwise

$$\left\{\begin{matrix} U_1^{(+)} \\ V_1^{(-)} \end{matrix}\right\}^{(d)} = \left\{\begin{matrix} 1 \\ -\dfrac{D_{26}\eta_1 - A_{45}}{D_{22}\eta_1 - A_{44}} \end{matrix}\right\} (C_3 \sinh \sqrt{\eta_1} y + C_4 \cosh \sqrt{\eta_1} y) + \left\{\begin{matrix} 1 \\ -\dfrac{D_{26}\eta_2 - A_{45}}{D_{22}\eta_2 - A_{44}} \end{matrix}\right\} (C_5 \sinh \sqrt{\eta_2} y + C_6 \cosh \sqrt{\eta_2} y) \quad (70)$$

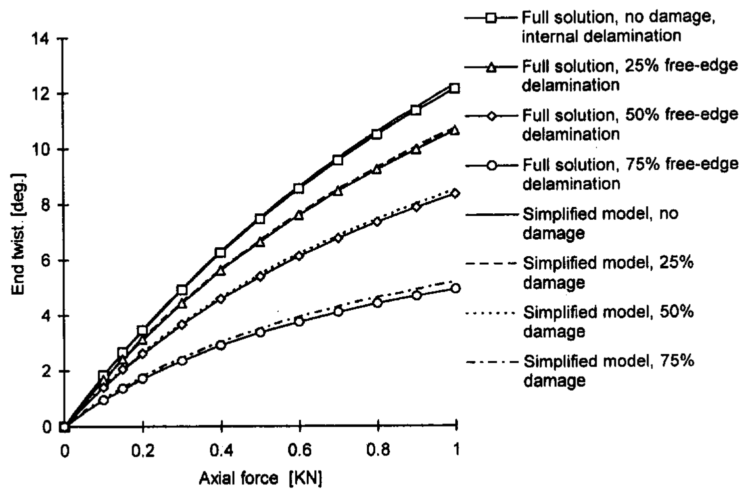

Fig. 4 Axial force-twist relationship for 20-deg glass/epoxy laminate

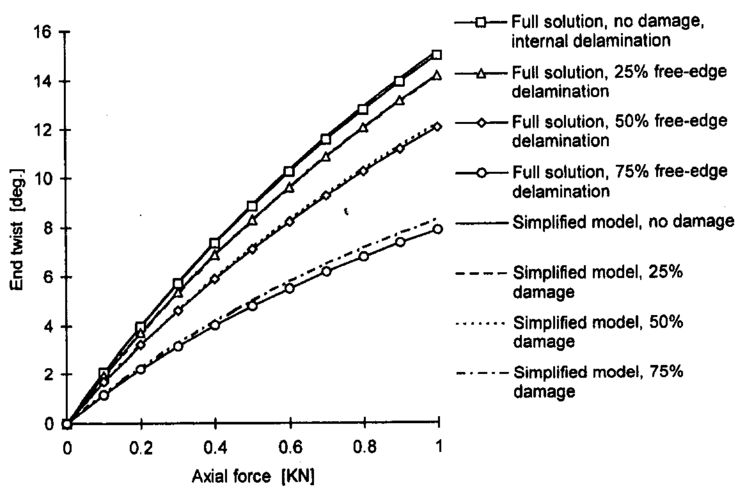

Fig. 5 Axial force-twist relationship for 20-deg graphite/cyanate laminate

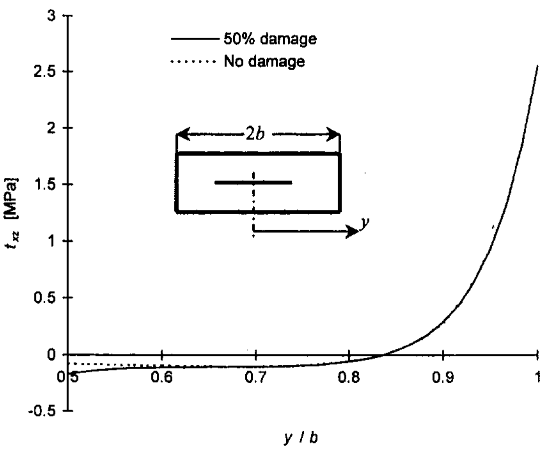

Fig. 6 Interlaminar stress t_{xz} distributions in 20-deg graphite/cyanate laminate at 1 KN axial force

where η_1 and η_2 are the roots of Eq. (54). The constants C_i can be determined from the following boundary conditions:

$$y = b - a, \quad U_1^{(+)(d)} = U_1^{(+)(u)}, \; V_1^{(-)(d)} = V_1^{(-)(u)}$$

$$M_{xy}^{(+)(d)} = \left(M_{xy}^{(+)} + \frac{h}{4} N_{xy}^{(-)} \right)^{(u)}, \quad M_{yy}^{(-)(d)} = M_{yy}^{(-)(u)} \tag{71}$$

$$y = b, \quad M_{xy}^{(+)(d)} = M_{yy}^{(-)(d)} = 0. \tag{72}$$

When the applied torque T is zero, the form of the axial force-twist relationship is still represented by Eq. (60). However, the coefficients b_i are different. The interlaminar shear stress in the undamaged region is given by Eq. (59).

The limiting case of full delamination, $(a = b)$, can be derived as follows. Substitute Eqs. (68) or (70) into the symmetry relations $U_1^{(+)}(0) = V_1^{(-)}(0) = 0$ and the boundary conditions (72) to obtain the solution for $U_1^{(+)}$ and $V_1^{(-)}$. The coefficient b_1 in Eq. (60) will vanish indicating absence of extension-twist coupling at zero pretwist.

The Kirchhoff-Love assumption of no transverse strains allows for extremely simple expressions for the coefficients b_i in the axial force-twist relationship (60). They are given by

$$b_1 = \frac{6\bar{\alpha}_{12}}{b^2 \alpha_{11(3)}}, \quad b_2 = \frac{48(\bar{\alpha}_{11}\bar{\alpha}_{22} - \bar{\alpha}_{12}^2)}{b\bar{\alpha}_{11(3)}}$$

$$b_3 = 12a\left(2 - \frac{a}{b}\right) \frac{\bar{\alpha}_{12}}{\bar{\alpha}_{11(3)}} \left(\alpha_{11} - \frac{\alpha_{12}^2}{\alpha_{22}} \right),$$

$$b_4 = \frac{2b^3}{15} \left(9 \frac{\bar{\alpha}_{11(5)}\bar{\alpha}_{11}}{\bar{\alpha}_{11(3)}} - 5\bar{\alpha}_{11(3)} \right) \tag{73}$$

where

$$\bar{\alpha}_{11} = \alpha_{11} - \frac{a}{b} \frac{\alpha_{12}^2}{\alpha_{22}}, \quad \bar{\alpha}_{12} = \left(1 - \frac{a}{b}\right) \frac{h}{4} \alpha_{12}$$

$$\bar{\alpha}_{22} = D_{66} + \left(1 - \frac{a}{b}\right)\left(\frac{h}{4}\right)^2 \alpha_{22}$$

$$\bar{\alpha}_{11(3)} = \alpha_{11} - \left(1 - \left[1 - \frac{a}{b}\right]^3\right) \frac{\alpha_{12}^2}{\alpha_{22}}$$

$$\bar{\alpha}_{11(5)} = \alpha_{11} - \left(1 - \left[1 - \frac{a}{b}\right]^5\right) \frac{\alpha_{12}^2}{\alpha_{22}} \tag{74}$$

and α_{ij} are defined in Eqs. (50). Although neglecting the transverse shear strains would result in violation of the boundary conditions at the free edges and the delamination front, the global behavior is modeled correctly even for large delamination as shown in the Application section.

Application

The influence of delamination on the extension-twist coupling is investigated for strips made of two practical material systems, S2/F584 glass/epoxy and T300/954-3 graphite/cyanate, with properties given in Table 1 and 2. The first material system provides a Young's modulus ratio E_{11}/E_{22} of 3.6 while the second, a value of 13.7. The length, the width, and the thickness of the laminates are 254 mm, 26 mm, and 1.2 mm, respectively. The hygrothermally stable antisymmetric stacking sequences, $[\alpha_2/(\alpha - 90)_4/\alpha_2/-\alpha_2/(90 - \alpha)_4/-\alpha_2]$, are considered. This class of laminates, proposed by Winckler (1985), will not warp as result of changes in temperature or moisture. If other antisymmetric lay-ups were used, the residual stresses associated with the curing cycle would have to be accounted for. The effect of curing stresses on the extension-twist coupling could be significant, it is discussed for undamaged strips in Makeev et al. (1998).

In applying the present analysis to the damaged strips it was found that assuming an opening mode with independent transverse displacements in the delaminated region or enforcing

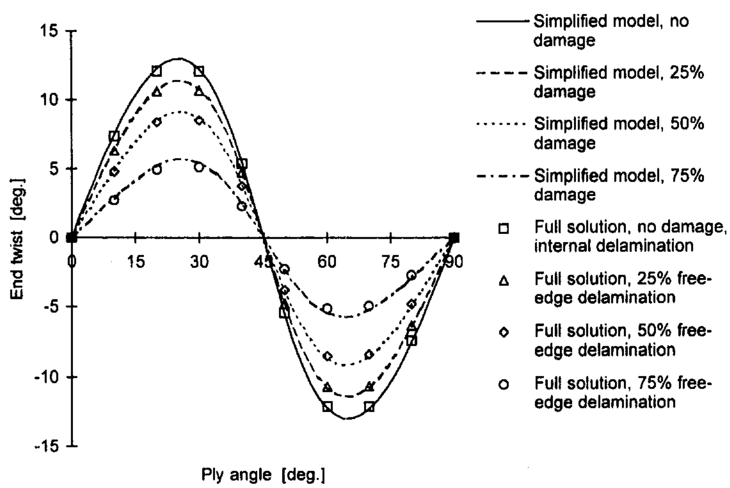

Fig. 7 Influence of delamination on coupling for glass/epoxy laminates at 1 KN axial force

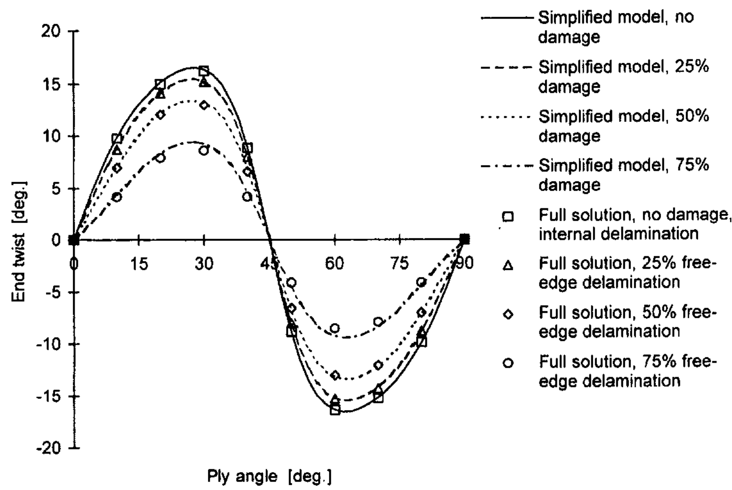

Fig. 8 Influence of delamination on coupling for graphite/cyanate laminates at 1 KN axial force

equal transverse displacements throughout the delaminated faces results in indistinguishable difference in predictions of the axial force-twist relationship and the interlaminar shear stresses.

The axial force-twist relationship (60) is plotted in Figs. 4 and 5 for internally and free-edge delaminated α = 20-deg strips ($[20_2/-70_4/20_2/-20_2/70_4/-20_2]$ stacking sequence). Predictions of the model based on the no-transverse-strains assumption, which results in expressions (73) for the coefficients in the axial force-twist relationship, are labeled as *Simplified model*. The following three observations are worth noting.

First, the axial force-twist relationship is clearly nonlinear. Second, the internal delamination does not affect the extension-twist coupling, the relative difference in predictions of the full solution between the undamaged and 75 percent internally delaminated strips is found to be less than 0.2 percent. Indeed, the interlaminar stress t_{xz} distribution, which controls the extension-twist coupling in the strip through the magnitude of the shear couple $N_{xy}^{(1)} = -N_{xy}^{(2)}$, is negligibly influenced by the internal delamination (as long as the thickness to width ratio of the undamaged regions remains small). This is shown in Fig. 6 where t_{xz} distributions are plotted ahead of the delamination front for an axial force of 1 KN in an undamaged and 50 percent internally delaminated α = 20-deg graphite/cyanate strips.

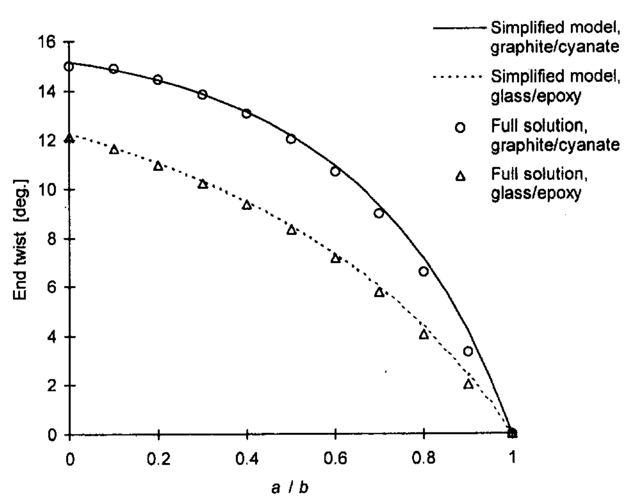

Fig. 9 Comparison of full and simplified solution predictions for 20-deg laminates with free-edge delamination at 1 KN axial force

Unlike internal delamination, the free-edge delamination results in a significant drop in coupling compared to the undamaged case. This is explained by observing that the solution for a strip with free-edge delamination can also be obtained from the equilibrium equations and boundary conditions for the undamaged strip if the delaminated region is characterized by zero in-plane shear forces $N_{xy}^{(1,2)}$, and continuity of the displacement parameters $U_1^{(+)}$, $V_1^{(-)}$, and the moments $M_{xy}^{(+)} + h/4N_{xy}^{(-)}$ and $M_{yy}^{(-)}$ per unit length of the middle surface of the strip is assumed throughout the laminate. Vanishing in-plane shear forces in the delaminated region reduces the extension-twist coupling compared to the undamaged case by affecting the distribution of the twisting moment and the axial force per unit length of the middle surface of the strip.

The second observation holds for strongly as well as weakly coupled laminates as shown in Figs. 7 and 8 where the absolute values of the end twist angle at an axial force of 1 KN are plotted versus the ply angle α for both material systems. Extension-twist coupling vanishes for α = 0, 45-deg and 90-deg angles, and is maximum for $\alpha = \pm 26$ deg for glass/epoxy and $\alpha = \pm 28$ deg for graphite/cyanate both damaged and undamaged laminates.

Third, Figs. 4, 5, 7, and 8 show that the full and the simplified solution predictions are in close agreement. The complete free-edge delamination range is considered in Fig. 9 where the absolute values of the end twist angle are plotted versus the free-edge delamination length normalized with respect to the cross section width for α = 20-deg strips subjected to a 1 KN axial force. Both models illustrate the same trend despite the fact that the simplified model does not accurately predict local effects such as interlaminar stress concentration at the delamination tip, and free-edge boundary conditions. Based on this observation, one can conclude that an accurate (singular) stress field at the delamination tip is not needed for a correct prediction of the global axial force-twist behavior.

The accuracy of the axial force-twist relationship (60) is assessed through comparison with test data for α = 20-deg strips made of T300/954-3 graphite/cyanate material system. Four undamaged specimens, four specimens with 50 percent internal delamination, and three specimens with 50 percent free-edge delamination were tested. The dimensions were 254 × 25.4 × 1.17 mm for the undamaged and internally delaminated strips, and 254 × 26.0 × 1.20 mm for the strips with free-edge delamination. The strips had an end pretwist angle of 5 deg. The manufacturing and testing programs for undamaged strips are described in Armanios et al. (1996). The damaged speci-

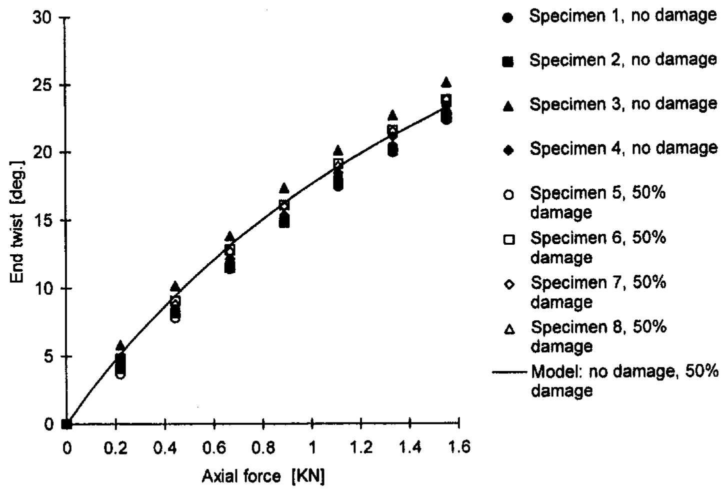

Fig. 10 Comparison of model predictions with test data for undamaged and 50 percent internally delaminated strips

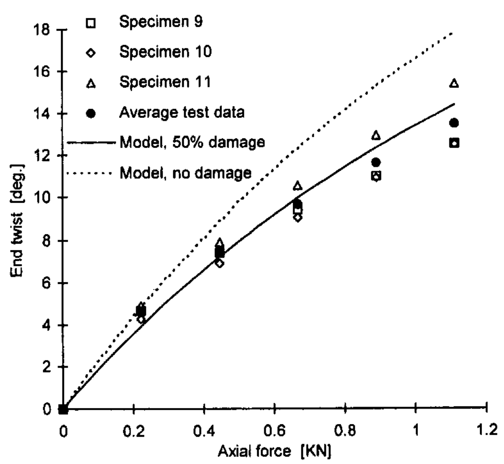

Fig. 11 Comparison of model predictions with test data for strips with 50 percent free-edge delamination

mens contained one 12.7-mm wide internal or two 6.5-mm wide free-edge midplane delaminations. Teflon FEP film was used to simulate the delamination and was placed along the full length of the specimens. The testing was performed in an Instron testing machine using the patented rotational displacement apparatus (Hooke and Armanios, 1997). This apparatus uses air as a bearing medium in order to allow for free end twist as the axial load is applied.

The test data and analytical predictions of the axial force-twist behavior are compared in Fig. 10 for the undamaged and internally delaminated strips, and in Fig. 11 for the strips with free-edge delamination. The maximum test load was kept low in order to avoid any delamination growth. The test data are labeled as *Specimen 1-Specimen 11* in the figures. As expected, the internal delamination does not affect the extension-twist coupling while the free-edge delamination results in significant drop in coupling compared to the undamaged case. For the free-edge delaminated strips the analysis predicts a 14.7-deg end-twist angle at the maximum test load of 1.112 KN, while the average test data is 13.5 deg. The correlation coefficient, r^2, for the closed-form solution is 0.989 with the free-edge delamination data. The end-twist angle corresponding to the undamaged laminate is 17.8 deg with a correlation coefficient of 0.995.

Conclusion

A geometrically nonlinear model for pretwisted laminated composite strips with extension-twist coupling in the presence of delamination is presented. A closed-form solution is obtained. The axial force-twist behavior is investigated for a class of antisymmetric hygrothermally stable laminates made of two material systems with various internal and free-edge delamination lengths. The results indicate that internal delamination has a negligible influence on the extension-twist coupling while free-edge delamination could result in a significant drop in coupling. The accuracy of the developed model is assessed through comparison of the axial force-twist relationship predictions with test data for strips made of a graphite/cyanate material system.

Acknowledgments

This work is sponsored by the National Rotorcraft Technology Center under Grant NCC2-945. This support is gratefully acknowledged.

References

Armanios, E. A., Makeev, A., and Hooke, D. A., 1996, "Finite Displacement Analysis of Laminated Composite Strips with Extension-twist Coupling," *ASCE Journal of Aerospace Engineering,* Vol. 9, No. 3, pp. 80–91.

Cesnik, C. E. S., and Hodges, D. H., 1997, "VABS: A New Concept for Composite Rotor Blade Modeling," *Journal of the American Helicopter Society,* Vol. 42, No. 1, pp. 27–38.

Hodges, D. H., 1990, "A Review of Composite Rotor Blade Modeling," *AIAA Journal,* Vol. 28, No. 3, pp. 561–565.

Hooke, D. A., and Armanios, E. A., 1997, "Rotational Displacement Apparatus with Ultra-low Torque and High Thrust Load Capability," U.S. Patent No. 5,661,247.

Kardomateas, G. A. 1989, "Geometric Nonlinearities in the Postbuckling Behavior of Delaminated Composites," *Key Engineering Materials, Vol. 37, Interlaminar Fracture of Composites,* E. A. Armanios, ed., Trans Tech Publications, pp. 269–284.

Makeev, A., Armanios, E. A., and Hooke, D. A., 1998, "The Influence of Curing Stresses on the Extension-twist Coupling in Pretwisted Composite Laminates," *Proceedings of the 39th Structures, Structural Dynamics and Materials Conference,* April 20–23, Long Beach, CA, pp. 972–982.

Simitses, G. J., Sallam, S., and Yin, W. L., 1985, "Effect of Delamination of Axially Loaded Homogeneous Laminated Plates," *AIAA Journal,* Vol. 23, No. 9, pp. 1437–1444.

Sokolnikoff, I. S. 1964, *Tensor Analysis, Theory and Applications to Geometry and Mechanics of Continua,* John Wiley and Sons, New York.

Vinson, J. R., and Sierakowski, R. L., 1986, *The Behavior of Structures Composed of Composite Materials,* Martinus Nijhoff, Dordrecht, The Netherlands.

Winckler, S. I., 1985, "Hygrothermally Curvature Stable Laminates with Tension-Torsion Coupling," *Journal of the American Helicopter Society,* Vol. 31, No. 7, pp. 56–58.

S. E. Bechtel
Department of Aerospace Engineering, Applied Mechanics, and Aviation, The Ohio State University, Columbus, OH 43210
Mem. ASME

M. G. Forest
Department of Mathematics, University of North Carolina, Chapel Hill, NC 27599-3250

N. T. Youssef
Department of Aerospace Engineering, Applied Mechanics, and Aviation, The Ohio State University, Columbus, OH 43210

H. Zhou
Department of Mathematics, University of North Carolina, Chapel Hill, NC 27599-3250

The Effect of Dynamic Surface Tension on the Oscillation of Slender Elliptical Newtonian Jets

We investigate free-surface oscillating jets with elliptical cross section, focusing on behavior associated with decaying surface tension. Previous one-dimensional equations for an oscillating jet are extended to allow variable surface tension on short space and time scales relevant for surfactant mixtures. We presume the decay of surface tension as a function of surface age, and derive the resulting jet behavior. Three plausible forms of decay are studied: an exponential decay, a diffusion model derived in Brazee et al. (1994), and an algebraic form due to Hua and Rosen (1991). Our simulations suggest both experimental regimes, and measurable jet features in these regimes, which may be exploited in an inverse formulation to deduce the unknown rapid surface tension decay of a given surfactant mixture. In particular, we establish numerical relationships between the amplitude and the wavelength of either a sustained far-field oscillation or oscillation at a fixed downstream location and the entire history of surface tension decay. These numerical relationships are ideal for the inverse formulation, in that the complete surface tension evolution may be deduced solely from far-field or downstream jet measurements, away from the confined part of the jet where the surface tension is rapidly changing.

1 Introduction

To model and understand agricultural and industrial processes such as spraying, fiber spinning, and film blowing, it is necessary to resolve the sizable and rapid change of material properties over small time and distance scales. The surface tension of pesticide solutions in air varies with surface age, from an initial value near that of pure water (72 dyne cm^{-1}) when the surface is created to an equilibrium value as low as 20 dyne cm^{-1} at 70 ms. Significant decay in surface tension occurs in the first 2–5 ms, which coincides with the timescale of drop formation and atomization (Thomas and Potter, 1975; Brazee et al., 1994; Reichard et al., 1997). Since surface tension dominates the hydrodynamic instability leading to droplets, accurate methods for the determination of surface tension on submillisecond timescales are necessary; slow or static techniques such as the Du-Nouy ring (Lunkenheimer and Wantke, 1981) yield only the equilibrium surface tension.

Measurements of oscillating free-surface jets have long been used in inverse problems to deduce surface tension (Rayleigh, 1879; Bohr, 1909; Hansen et al., 1958; Defay and Hommelen, 1958; Thomas and Potter, 1975; Bechtel et al., 1995). An experimentalist can prepare conditions (specified in the text below) under which a fluid exiting an elliptical orifice establishes a steady jet with a chain-like free surface fixed in space: the jet cross section oscillates in the downstream direction between perpendicular ellipses (Rayleigh, 1879). This jet flow is elongational. Features of the steady free-surface profile, such as the local wavelength of the oscillation, can be conveniently measured and are strongly tied to the local interfacial surface tension.

The oscillating jet technique is the only experimental tool for the measurement of dynamic surface tension both on the rapid time scales and in an elongational flow relevant to industrial and agricultural processes of spraying, fiber spinning, and film blowing. To exploit the technique, one combines measurements of the oscillating jet profile with an analytical model that governs the evolution of the jet cross section for prescribed material properties; material coefficients are then determined so that the model and experiment agree. Importantly, all previous models predict oscillating jet behavior under the assumption that surface tension and viscosity are constant in the spatial interval over which measurements are taken. These models quantify the decay of surface tension only on the resolution of a wavelength of oscillation; for typical flow rates and orifice sizes, this results in an averaging over a time interval of 1.5 to 2 ms, during which the surface tension can drop 20–30 percent (Brazee et al., 1994).

This paper provides the model formulation necessary to resolve dynamic surface tension within a wavelength and on submillisecond time scales. We assume a surface tension decay as a function of surface age is given; three different surface tension decay forms are studied. To implement the inverse formulation of the model in conjunction with oscillating jet experiments, one must (i) identify physical regimes and corresponding models specific to those experimental regimes, and (ii) establish features of the models which can be reliably measured and which can be inverted to characterize the surface tension form and decay parameters. To prepare for the inverse formulation, this paper identifies the regimes, thereby dictating how the experiment is to be designed, and further provides numerically generated relationships between the decay parameters and the free-surface profile of the oscillating jet. In particular we find that the complete evolution of surface tension, from its initial value at the nozzle exit to its stabilized equilibrium value, can be deduced solely from far-field wavelength and amplitude mea-

Contributed by the Applied Mechanics Division of THE AMERICAN SOCIETY OF MECHANICAL ENGINEERS for publication in the ASME JOURNAL OF APPLIED MECHANICS.

Discussion on the paper should be addressed to the Technical Editor, Professor Lewis T. Wheeler, Department of Mechanical Engineering, University of Houston, Houston, TX 77204-4792, and will be accepted until four months after final publication of the paper itself in the ASME JOURNAL OF APPLIED MECHANICS.

Manuscript received by the ASME Applied Mechanics Division, Dec. 18, 1996; final revision, Mar. 25, 1998. Associate Technical Editor: S. A. Berger.

surements, or measurements at a fixed downstream position. Although this is accomplished specifically for the three forms of surface tension, the methodology applies for any surface tension decay form that may emerge from fundamental studies.

2 One-Dimensional Models for the Oscillating Jet

The fluid is assumed incompressible, and flows in the direction of gravity $\mathbf{g}$. We define space-fixed (Eulerian) Cartesian coordinates $\mathbf{x} = (x_1, x_2, x_3)$ with corresponding unit base vectors $\mathbf{e}_1, \mathbf{e}_2, \mathbf{e}_3$ such that the $\mathbf{e}_3$ direction coincides with the centerline of the jet. We assume the jet cross section is elliptical for several oscillations; the free surface of the jet is therefore posited in the form

$$\frac{x_1^2}{\Phi_1^2(x_3, t)} + \frac{x_2^2}{\Phi_2^2(x_3, t)} - 1 = 0, \tag{1}$$

where $\Phi_1(x_3, t)$ and $\Phi_2(x_3, t)$ are the principal semi-axes, coincident with the x_1, x_2-axes. (An estimate for inviscid fluids of the inherent error in this assumption is given in Bechtel et al. (1995).)

Recall that the oscillating jet experiment we are modeling here is steady in the Eulerian sense. In the steady case Φ_1 and Φ_2 in (1) are functions only of x_3. However, in Eqs. (1) through (15) we retain time dependence in the problem formulation, in anticipation of future stability studies; after (15) we suppress time dependence to model the steady experiment at hand.

Also, this paper is part of an overall effort in material characterization which requires the ability to model non-Newtonian viscosity. Hence in this derivation we allow for variable viscosity,

$$\hat{\mathbf{T}} = 2\eta(\mathbf{x}, t)\mathbf{D}, \tag{2}$$

even though in this paper we only present solutions in the Newtonian special case. In (2) $\hat{\mathbf{T}}$ is the determinate part of the Cauchy stress tensor $\hat{\mathbf{T}} - p\mathbf{I}$, $\mathbf{D}$ is the symmetric part of the velocity gradient, and $\eta(\mathbf{x}, t)$ is the viscosity.

On the free surface (1) the kinematic boundary condition is

$$\left(\frac{\partial}{\partial t} + \mathbf{v}\cdot\nabla\right)\left(\frac{x_1^2}{\Phi_1^2(x_3, t)} + \frac{x_2^2}{\Phi_2^2(x_3, t)} - 1\right) = 0, \tag{3}$$

and the kinetic boundary condition modeling the surface tension (Edwards et al., 1991; Milliken et al., 1993) is

$$(\mathbf{T}_{\text{ambient}} - \hat{\mathbf{T}} + p\mathbf{I})\mathbf{n} = \sigma\kappa\mathbf{n} - \nabla_s\sigma. \tag{4}$$

In (3), $\mathbf{v}$ is the velocity and ∇ is the Eulerian gradient; in (4), $\mathbf{T}_{\text{ambient}}$ is the Cauchy stress tensor in the ambient atmosphere, $\mathbf{n}$ is the outward normal to the free surface, σ is the surface tension of the fluid/ambient interface (assumed to vary only with axial length x_3 and time t), κ is the mean curvature of the free surface, and $\nabla_s\sigma$ is the gradient operator on the free surface defined by (Stone and Leal, 1990),

$$\nabla_s\sigma = (\mathbf{I} - \mathbf{n}\otimes\mathbf{n})\nabla\sigma. \tag{5}$$

We assume the ambient is passive, so that the stress of the ambient atmosphere is

$$\mathbf{T}_{\text{ambient}} = -p_a\mathbf{I}, \tag{6}$$

where p_a is a constant pressure. As speeds increase in the experiment, assumption (6) becomes inadequate, and must be replaced with an empirically derived air drag model (e.g., Kase and Matsuo, 1967).

We employ the slender-filament perturbation theory described in Bechtel et al. (1995). We recall those features necessary to connect models with experiments. The small parameter is the slenderness ratio ϵ,

$$\epsilon = \frac{r_0}{z_0} \ll 1, \tag{7}$$

where r_0 and z_0 are typical length scales in the jet cross section and in the axial direction, specifically selected at the end of this section. The Eulerian coordinates x_1, x_2, x_3, t and transverse free-surface semi-axes Φ_1 and Φ_2 are scaled using the above characteristic length scales and a characteristic time scale t_0:

$$x_1 = r_0x, \quad x_2 = r_0y, \quad x_3 = z_0z, \quad t = t_0\tau,$$
$$\Phi_1(x_3, t) = r_0\phi_1(z, \tau), \quad \Phi_2(x_3, t) = r_0\phi_2(z, \tau), \tag{8}$$

where x, y, z, τ and ϕ_1, ϕ_2 are dimensionless. The velocity to leading order is assumed to be of the form

$$\mathbf{v} = \frac{z_0}{t_0}\{[\epsilon x\zeta_1(z, \tau) + O(\epsilon^3)]\mathbf{e}_1 + [\epsilon y\zeta_2(z, \tau) + O(\epsilon^3)]\mathbf{e}_2 + [v(z, \tau) + O(\epsilon^2)]\mathbf{e}_3\}, \tag{9}$$

where ζ_1, ζ_2, v are dimensionless $O(1)$ functions of axial coordinate z and time τ.

The kinematic boundary condition (3) and incompressibility constraint yield the leading-order equations

$$\phi_{1,\tau} + v\phi_{1,z} - \phi_1\zeta_1 = 0,$$
$$\phi_{2,\tau} + v\phi_{2,z} - \phi_2\zeta_2 = 0,$$
$$\zeta_1 + \zeta_2 + v_{,z} = 0, \tag{10}$$

where ",z" denotes differentiation with respect to z, and ",τ" with respect to τ.

The three-dimensional vector momentum equation

$$\rho\left(\frac{\partial\mathbf{v}}{\partial t} + \mathbf{v}\cdot\nabla\mathbf{v}\right) = \nabla\cdot\hat{\mathbf{T}} - \nabla p + \rho\mathbf{g}, \tag{11}$$

is reduced to one-dimensional scalar equations by integration over the jet cross section and use of the kinetic boundary condition (4). In nondimensional form these equations are

$$B(P - 2Z\phi_1\phi_2\zeta_1) + \frac{\phi_1\phi_2}{W}K_c - \epsilon^2\phi_1\phi_2\frac{W_{,z}}{W^2}Y_c + \epsilon^2B\frac{\phi_1^3\phi_2}{4}(Z_{,z}\zeta_{1,z} + \zeta_{1,zz}Z) = \frac{\phi_1^3\phi_2}{4}(\zeta_{1,\tau} + v\zeta_{1,z} + \zeta_1^2) + O(\epsilon^2),$$

$$B(P - 2Z\phi_1\phi_2\zeta_2) + \frac{\phi_1\phi_2}{W}K_s - \epsilon^2\phi_1\phi_2\frac{W_{,z}}{W^2}Y_s + \epsilon^2B\frac{\phi_1\phi_2^3}{4}(Z_{,z}\zeta_{2,z} + \zeta_{2,zz}Z) = \frac{\phi_2^3\phi_1}{4}(\zeta_{2,\tau} + v\zeta_{2,z} + \zeta_2^2) + O(\epsilon^2),$$

$$\epsilon^2\frac{1}{W}(\phi_1\phi_{2,z}K_s + \phi_2\phi_{1,z}K_c) - \epsilon^2\frac{W_{,z}}{W^2}\int_0^{2\pi}\frac{1}{\Delta}(\phi_2^2\cos^2\theta + \phi_1^2\sin^2\theta)d\theta + B\epsilon^2(2\phi_1\phi_2Z_{,z}v_{,z} + 2\phi_1\phi_2Zv_{,zz} - P) + \frac{1}{F}\phi_1\phi_2 = (v_{,\tau} + vv_{,z})\phi_1\phi_2. \tag{12}$$

The dimensionless parameters and functions in (12) are

$$B = \frac{t_0^2 f_0}{\rho r_0^4}, \quad \frac{1}{W}(z, \tau) = \frac{\sigma(z, \tau) t_0^2}{\rho r_0^3},$$

$$\frac{W_{,z}}{W^2}(z, \tau) = \frac{\sigma_{,z}(z, \tau) t_0^2}{\rho r_0^3},$$

$$\frac{1}{F} = \frac{g t_0^2}{z_0}, \quad Z(z, \tau) = \frac{\eta(z, \tau) r_0^2}{t_0 f_0},$$

$$Z_{,z}(z, \tau) = \frac{\eta_{,z}(z, \tau) r_0^2}{t_0 f_0}, \tag{13}$$

where f_0 is a characteristic force scale, to be made explicit along with the other characteristic scales later in this section. Note that

$$BZ = \frac{\eta(z, \tau) t_0}{\rho r_0^2} = \frac{1}{R}, \tag{14}$$

where R is the Reynolds number. The nondimensional pressure resultant P and functions K_c, K_s, Y_c, Y_s, and $\tilde{\Delta}$ are defined by

$$P = \frac{1}{\pi f_0} \int \int (p - p_a) dx_1 dx_2,$$

$$K_c = \frac{1}{\pi} \int_0^{2\pi} r_0 \kappa \cos^2 \theta d\theta$$

$$= -\frac{\phi_1 \phi_2}{\pi} \int_0^{2\pi} \frac{\cos^2 \theta}{(\phi_1^2 \sin^2 \theta + \phi_2^2 \cos^2 \theta)^{3/2}} d\theta + O(\epsilon^2),$$

$$K_s = \frac{1}{\pi} \int_0^{2\pi} r_0 \kappa \sin^2 \theta d\theta$$

$$= -\frac{\phi_1 \phi_2}{\pi} \int_0^{2\pi} \frac{\sin^2 \theta}{(\phi_1^2 \sin^2 \theta + \phi_2^2 \cos^2 \theta)^{3/2}} d\theta + O(\epsilon^2),$$

$$Y_c = \frac{1}{\pi} \int_0^{2\pi} \frac{(\phi_1 \phi_{2,z} \sin^2 \theta + \phi_2 \phi_{1,z} \cos^2 \theta)}{(\phi_1^2 \sin^2 \theta + \phi_2^2 \cos^2 \theta + O(\epsilon^2))^{1/2}} \cos^2 \theta d\theta,$$

$$Y_s = \frac{1}{\pi} \int_0^{2\pi} \frac{(\phi_1 \phi_{2,z} \sin^2 \theta + \phi_2 \phi_{1,z} \cos^2 \theta)}{(\phi_1^2 \sin^2 \theta + \phi_2^2 \cos^2 \theta + O(\epsilon^2))^{1/2}} \sin^2 \theta d\theta,$$

$$\tilde{\Delta} = (\phi_2^2 \cos^2 \theta + \phi_1^2 \sin^2 \theta + O(\epsilon^2))^{1/2}. \tag{15}$$

We now suppress the time dependence in the governing Eqs. (10) and (12), to model the oscillating jet experiment. In the steady problem we select the characteristic radial length scale r_0 to be the geometric mean of the initial principal radii of the elliptical cross section, and the characteristic axial velocity z_0/t_0 to be the axial nozzle velocity, dictated by the experiment. This translates to dimensionless upstream conditions

$$\phi_1(0)\phi_2(0) = 1, \quad v(0) = 1. \tag{16}$$

The steady forms of (10) imply

$$\zeta_1 = \frac{v \phi_{1,z}}{\phi_1}, \quad \zeta_2 = \frac{v \phi_{2,z}}{\phi_2}, \quad v \phi_1 \phi_2 = 1, \tag{17}$$

where the constant in Eq. $(17)_3$ is fixed by the upstream conditions (16).

The remaining leading-order equations follow from the steady forms of (12), in which we have retained the leading-order contributions within each physical effect, namely viscosity (BZ), viscosity gradient ($BZ_{,z}$), surface tension (W^{-1}), surface tension gradient ($W_{,z}/W^2$), constraint pressure (BP), inertia (1), and gravity (F^{-1}). In a particular experiment some subset of these effects will be dominant, and thus survive in the leading-order dominant-balance equations. A *regime* of jet behavior is determined by the order of the full set of nondimensional parameters (13), relative to the slenderness ratio ϵ, in the physical experiment being modeled. Once identified, each regime then specifies the dominant asymptotic balance in Eqs. (12).

In order to observe an oscillating jet in an experiment, one must design the experiment so that inertia and surface tension dominate to leading order in the transverse momentum Eqs. $(12)_{1,2}$. Viscosity must either balance surface tension and inertia (which leads to attenuation of the oscillations), or be a weak effect (so that the leading-order behavior is inviscid). The constraint pressure term plays a fundamental role in our asymptotic analysis; this term must balance the right-hand sides of $(12)_{1,2}$ (inertia terms) and the surface tension terms. Unless the dimensionless parameter $B = t_0^2 f_0 / \rho r_0^4$ is $O(1)$, we cannot deduce a consistent slender oscillating jet model. This constraint therefore *selects the characteristic force*, f_0, in terms of the radial scale (r_0), time scale (t_0), and density (ρ):

$$f_0 = \frac{\rho r_0^4}{t_0^2}, \tag{18}$$

or equivalently, we impose $B \equiv 1$.

From analysis of the transverse momentum Eqs. $(12)_{1,2}$ above, we impose $B = 1$ and the experiment must be such that W^{-1} is $O(1)$, while Z is at most $O(1)$. Note that in the slenderness scaling these conditions automatically imply that inertia dominates surface tension and viscosity in the axial component of momentum $(12)_3$. Hence, a jet cross section evolves downstream either with constant axial velocity ($v_{,z} = 0$) if F^{-1} is less than $O(1)$, or with the free fall velocity ($vv_{,z} = 1/F$) if F^{-1} is $O(1)$.

We now posit specific regimes of oscillating jet behavior, and investigate the effect of variable surface tension as predicted by the leading-order equations.

3 Oscillating Jets With Nonconstant Surface Tension

Recall there are a priori four independent scales r_0, z_0, t_0, and f_0 which characterize a given experiment. We have specified the force scale f_0 in terms of r_0, t_0 in (18) in order to insure that the regime is oscillatory, with the correct balance in transverse momentum. The remaining scales, which depend on the experimental conditions, dictate if viscosity, gravity, etc., join surface tension and inertia as leading-order effects in the oscillating jet.

Regime 1: Surface Tension and Inertia-Dominated Jets. We first model a fluid jet with the density, viscosity, and initial surface tension of water ($\rho = 0.997$ g cm^{-3}, $\eta = 1.00 \times 10^{-2}$ g cm^{-1} s^{-1}, initial surface tension $= \sigma(0) = 72.8$ dyne cm^{-1}), whose surface tension decays with surface age due to evaporation of volatile species, migration of surfactant molecules to the surface, or contamination of the surface with dust. The jet has volume flow rate $Q = 0.342$ cm^3 s^{-1}, and initial elliptical semi-axes $\Phi_1(0) = 0.0225$ cm, $\Phi_2(0) = 0.0100$ cm. These experimental conditions yield the scales

$$r_0 = \sqrt{\Phi_1(0)\Phi_2(0)} = 0.0147 \text{ cm}, \quad z_0 = \frac{r_0}{\epsilon} = 0.147 \text{ cm},$$

$$\frac{z_0}{t_0} = \frac{Q}{\pi r_0^2} = 506 \frac{\text{cm}}{\text{s}} \quad (\text{so that } t_0 = 2.89 \times 10^{-4} \text{ s}),$$

$$f_0 = \frac{\rho r_0^4}{t_0^2} = 0.549 \text{ dyne}, \tag{19}$$

where we have tentatively selected $\epsilon = 0.1$. That is, the characteristic length of axial variation, z_0, identified as the wavelength of oscillation of the jet cross section, is anticipated to be on the order of ten times that of the transverse dimensions; subsequent computations validate this guess.

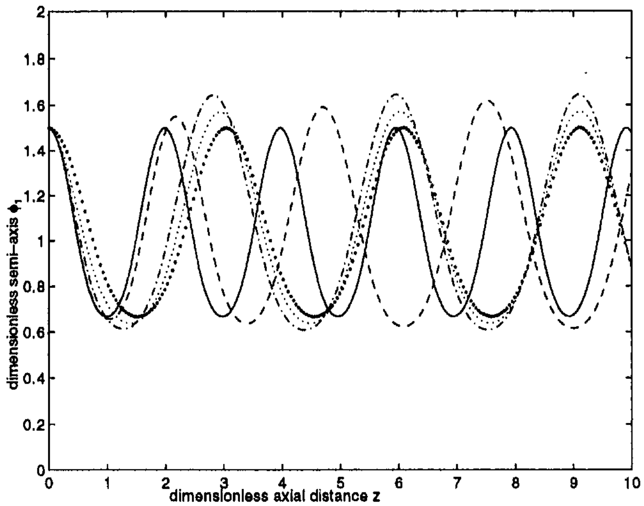

Fig. 1(*a*)

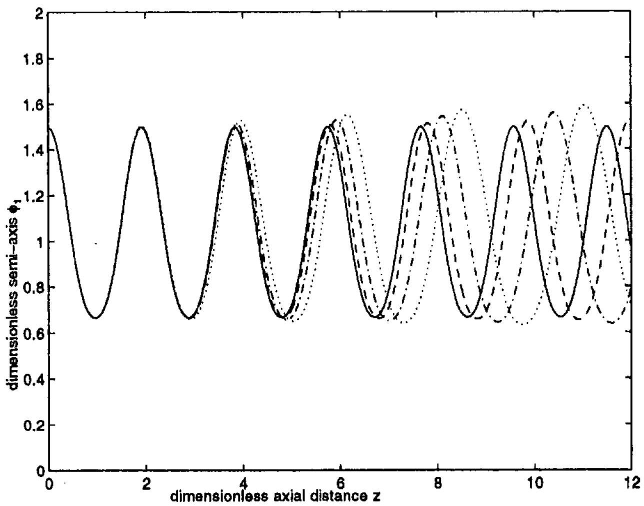

Fig. 1(*b*)

We assume that the surface age T at axial position $x_3 = 0$ is zero, i.e., the surface is created at the origin. For steady flows, surface age and axial position are related by

$$T = \int_0^{x_3} \frac{dx_3}{v_3(x_3)} = t_0 \int_0^z \frac{dz}{v(z)} . \qquad (20)$$

This allows surface tension, given as a function of surface age, to be expressed as a function of axial position,

$$\sigma = \sigma(T) = \sigma(x_3) = \sigma(z).$$

The dimensionless parameters (13) are expressed as an $O(1)$ number times a power of the slenderness ratio ϵ:

$$\frac{1}{F} = \frac{g t_0^2}{z_0} = 5.61 \times 10^{-4} = 5.61\epsilon^4,$$

$$\frac{1}{W(0)} = \frac{\sigma(0) t_0^2}{\rho r_0^3} = 1.92 = 1.92\epsilon^0,$$

$$Z = \frac{\eta r_0^2}{t_0 f_0} = 0.0135 = 1.35\epsilon^2, \quad Z_{,z} = 0. \qquad (21)$$

From these calculations we see that in this specific experiment W^{-1} is $O(1)$, at least upstream near the nozzle, and Z and F^{-1} are less than $O(1)$. Recalling the earlier discussion, this jet is in an oscillatory regime, at least upstream: the experimental design will result in an oscillating jet with no attenuation due to viscosity and no axial acceleration due to gravity, to leading order. In this section we wish to model experiments in which variable surface tension continues down the jet as a leading-order effect, but the surface tension gradient is not too large. Hence, the Weber number evolves down the jet subject to the restrictions

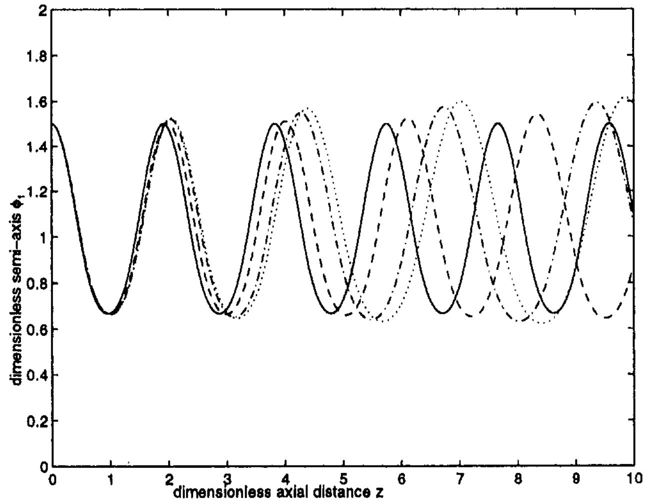

Fig. 1(*c*)

Fig. 1 Dimensionless nearfield free surface profiles $\phi_1(z)$ for inviscid jets with variable surface tension; for comparison, the profile with constant surface tension $\sigma = 72.8$ dyne cm^{-1} (——) is given. In all solutions the initial data is $\phi_1(0) = 1.5$, $\phi_{1,z}(0) = 0$. (Graphs can be converted to dimensional radius versus dimensional axial distance by multiplying the z-axis by 0.15 cm and the ϕ_1-axis by 0.015 cm). $\sigma(0) = 72.8$ dyne cm^{-1} and $\sigma_E = 31$ dyne cm^{-1}, so that $c_1 = 0.827$ and $c_2 = 1.115$. (*a*) Form 1: exponentially decaying form, with rate values $c_3 = 0.3$ (– – –), $c_3 = 2.1$ (– · – · –), $c_3 = 7.0$ (· · ·), $c_3 = 200$ (•••); (*b*) Form 2: Brazee et al. form, with rate values $c_4 = 2.16 \times 10^{-5}$ (– – –), $c_4 = 4.12 \times 10^{-5}$ (– · – · –), $c_4 = 6.07 \times 10^{-5}$ (· · ·); (*c*) Form 3: Hua and Rosen form, with parameter values $c_5 = 25.9$, $n = 3.839$ (– – –); $c_5 = 9.667$, $n = 2.328$ (– · – · ·); $c_5 = 4.58$, $n = 1.634$ (· · ·).

$$\epsilon < \frac{1}{W(z)} < \epsilon^{-1}, \quad \left| \epsilon^2 \frac{W_{,z}}{W^2(z)} \right| < \epsilon. \qquad (22)$$

For $\epsilon = 0.1$ this translates into the dimensional bounds

$$3.79 \,\frac{\text{dyne}}{\text{cm}} < \sigma(x_3) < 379 \,\frac{\text{dyne}}{\text{cm}} ,$$

$$|\sigma(x_3)_{,x_3}| < 2580 \,\frac{\text{dyne}}{\text{cm}^2} , \qquad (23)$$

which must be monitored during the experiment; note that the above value $\sigma(0) = 72.8$ dyne cm^{-1} is comfortably inside $(23)_1$. Within the bounds (23) the steady leading-order equations simplify to

$$v = 1, \quad \phi_1\phi_2 = 1, \quad (1 + \phi_1^4)\phi_{1,zz} - 2\,\frac{\phi_{1,z}^2}{\phi_1}$$

$$+ \frac{4}{\pi W(z)}\,\phi_1^3 \left(\int_0^{2\pi} \frac{(\cos^2\theta - \sin^2\theta)d\theta}{(\phi_1^2 \sin^2\theta + \phi_1^{-2}\cos^2\theta)^{3/2}} \right) = 0, \quad (24)$$

which we label Regime 1. Equation $(24)_3$ is the difference of the steady leading-order forms of Eqs. $(12)_1$ and $(12)_2$, with ζ_1 and ζ_2 eliminated using $(17)_{1,2}$. Since in Regime 1 gravity is not leading order and hence axial velocity is constant to leading order, surface age is proportional to axial location:

$$T = \frac{t_0}{z_0} x_3 = t_0 z. \tag{25}$$

Equations (24) were analyzed in Bechtel et al. (1988) and Bechtel (1989) for the special case of constant surface tension (W = constant), in which $(24)_3$ describes a conservative nonlinear oscillator and surface tension provides the restoring force. The total conserved energy per length is

$$h = \frac{1}{8}(1 + \phi_1^{-4})\phi_{1,z}^2 + \frac{4}{W}\left\{\frac{E(1-\phi_1^4)}{\pi\phi_1} - \frac{1}{2}\right\}, \tag{26}$$

where E is the complete elliptic integral of the second kind as defined in Abramowitz and Stegun (1964). The first term in (26) is the kinetic energy per length and the second term is potential energy per length, normalized so that it is non-negative.

When surface tension σ evolves, the energy per length h decays proportional to surface tension decay:

$$h_{,z} = -4\frac{W_{,z}}{W^2}\left\{\frac{E(1-\phi_1^4)}{\pi\phi_1} - \frac{1}{2}\right\}$$

$$= \frac{4t_0^2}{\rho r_0^3}\sigma_{,z}\left\{\frac{E(1-\phi_1^4)}{\pi\phi_1} - \frac{1}{2}\right\}. \tag{27}$$

To produce quantitative predictions of jets with nonconstant surface tension, we now invoke specific constitutive equations for the decay of surface tension with surface age. We investigate three functional forms: (i) exponential decay, (ii) the thin-film diffusion model derived by Brazee et al. (1994), and (iii) the algebraic form proposed by Hua and Rosen (1991). We do not address the fundamental issue of the physics and chemistry responsible for the evolution of surface tension.

For each posited surface tension form, we solve *the direct problem:* we numerically integrate the governing differential Eqs. (24) with the particular specified function $\sigma(z)$ to obtain the free-surface profile $\phi_1(z)$. Features of the jet profiles are then plotted. Looking ahead to an *inverse problem* based on experimental data and this model, we seek relationships between features of model solution behavior which can be reliably measured in an experiment and the surface tension functions, namely its form and coefficients within the form. For each of the three posited surface tension forms, we establish invertible relationships between decay rates and the far-field amplitude and wavelength of the oscillating free surface.

Form 1: Exponentially Decaying Surface Tension. First we assume an exponential decay of surface tension with surface age, equivalent in this regime to exponential decay of surface tension with axial position:

$$\sigma(x_3) = \sigma_E + (\sigma(0) - \sigma_E)e^{-\alpha x_3} \quad \text{or}$$

$$\frac{1}{W(z)} = c_1 + c_2 e^{-c_3 z}, \tag{28}$$

where the constant α is *the exponential decay rate parameter.* Note the relations $c_3 = z_0\alpha$, $c_2 = (t_0^2/\rho r_0^3)(\sigma(0) - \sigma_E)$, and $c_1 = (t_0^2/\rho r_0^3)\sigma_E$.

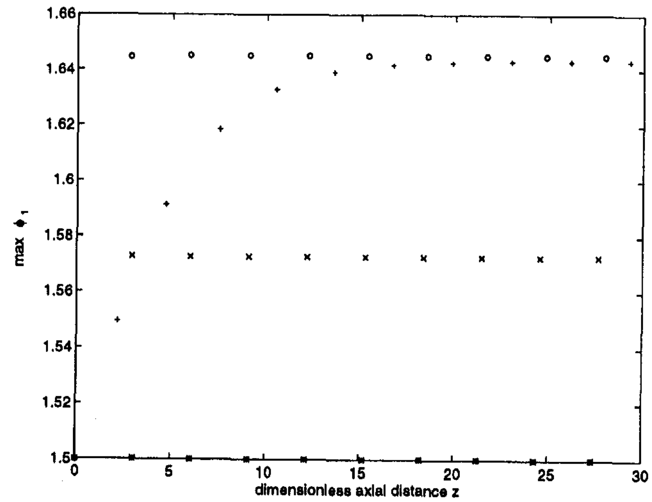

Fig. 2(a)

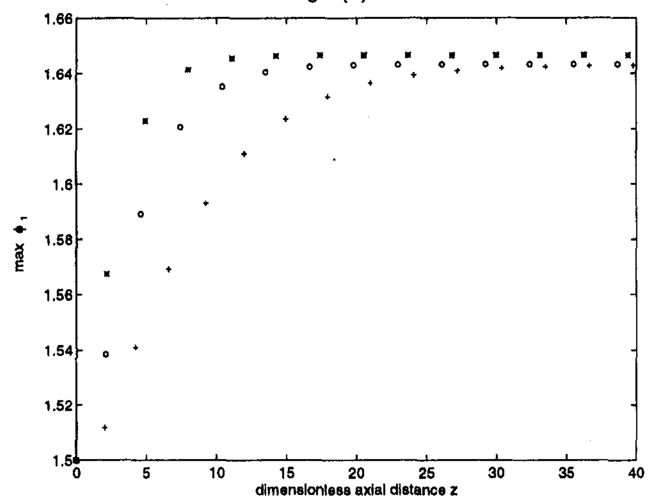

Fig. 2(b)

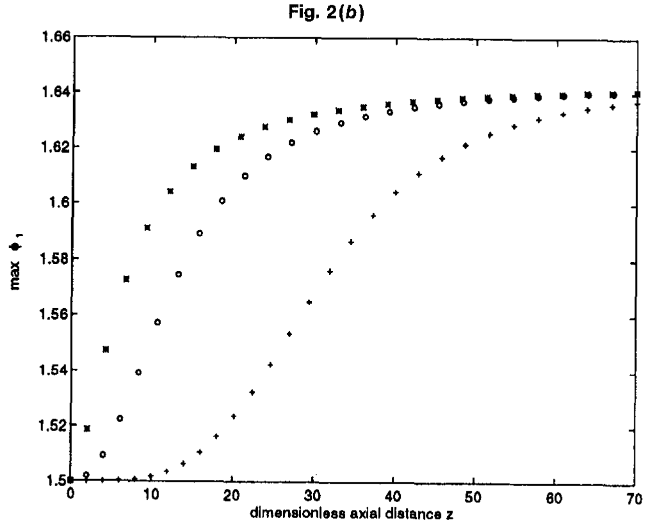

Fig. 2(c)

Fig. 2 Successive maximum amplitudes of each solution in Fig. 1, for a much larger axial domain (near-field and far-field). (a) Form 1: $c_3 = 0.3$ (+), $c_3 = 2.1$ (○), $c_3 = 7.0$ (×), $c_3 = 200$ (*); (b) Form 2: $c_4 = 2.16 \times 10^{-5}$ (+); $c_4 = 4.12 \times 10^{-5}$ (○); $c_4 = 6.07 \times 10^{-5}$ (*); (c) Form 3: $c_5 = 26.7241$, $n = 3.839$ (+); $c_5 = 9.975$, $n = 2.328$ (○); $c_5 = 4.725$, $n = 1.634$ (*).

Form 2: Thin-Film Diffusion Model of Brazee et al. Our second form is adopted from Brazee et al. (1994):

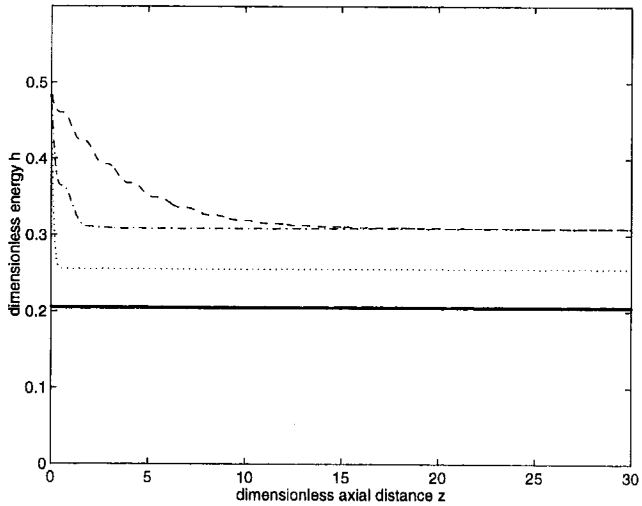

Fig. 3 The decay of energy per length (26) for the oscillating jets of Fig. 1(*a*) with exponentially decaying surface tension. c_3 = 0.3 (– – –), c_3 = 2.1 (– · – · –), c_3 = 7.0 (· · ·), c_3 = 200 (•••).

$$\sigma(T) = \sigma(0) + (\sigma_E - \sigma(0))\left\{1 - \frac{2}{\pi}\sum_{n=0}^{\infty}\frac{(-1)^n e^{-\pi^2 D(n+1/2)^2(T/a^2)}}{n+\frac{1}{2}}\right\}, \quad (29)$$

which follows from a thin-film diffusion model accounting for surface adsorption, where D is the diffusion coefficient and a is the apparent film thickness. Using the relation (25) between surface age T and axial location, we convert (29) to an expression for surface tension as a function of axial position x_3,

$$\sigma(x_3) = \sigma(0) + (\sigma_E - \sigma(0))\left\{1 - \frac{2}{\pi}\sum_{n=0}^{\infty}\frac{(-1)^n e^{-\pi^2 D(n+1/2)^2(t_0 x_3/z_0 a^2)}}{n+\frac{1}{2}}\right\},$$

$$\text{or}\quad \frac{1}{W(z)} = c_1 + c_2\frac{2}{\pi}\sum_{n=0}^{\infty}\frac{(-1)^n e^{-\pi^2(n+1/2)^2 c_4 z}}{n+\frac{1}{2}}, \quad (30)$$

where c_1 and c_2 have the same relations to $\sigma(0)$ and σ_E as in the exponential form (28), and $c_4 = t_0 Da^{-2}$. For three different agrochemical surfactants, each in varying concentrations, Brazee et al. (1994) provide an estimate of Da^{-2}. For all solutions they assume an initial surface tension of 72.8 dyne cm^{-1} and measure equilibrium surface tension values at a surface age of 70 ms, ranging between 30.4 and 42.9 dyne cm^{-1}. By matching with experimental measurements they deduce values of Da^{-2} between 0.02 and 0.2 s^{-1}.

Form 3: Algebraic Form Proposed by Hua and Rosen. The third form for dynamic surface tension is a power law proposed by Hua and Rosen (1991) and employed by Shavit and Chigier (1995),

$$\sigma(T) = \sigma_E + \frac{\sigma(0) - \sigma_E}{1 + \left(\frac{T}{t^*}\right)^n}, \quad (31)$$

where t^* and n are specified constants. This relation also predicts that surface tension σ decays smoothly from a specified initial value $\sigma(0)$ to a specified equilibrium value σ_E. Using the relation (25) between surface age T and axial location x_3, we have

$$\sigma(x_3) = \sigma_E + \frac{\sigma(0) - \sigma_E}{1 + \left(\frac{t_0 x_3}{z_0 t^*}\right)^n},$$

$$\frac{1}{W(z)} = c_1 + \frac{c_2}{1 + \left(\frac{z}{c_5}\right)^n}, \quad (32)$$

where $c_5 = t^*/t_0$.

Numerical Experiments. In all calculations we assume the initial surface tension to be that of water, $\sigma(0) = 72.8$ dyne cm^{-1}, and fix the equilibrium surface tension $\sigma_E = 31$ dyne cm^{-1}, consistent with common agrochemical surfactant solutions (Brazee et al., 1994); in the dimensionless forms, $c_1 = 0.827$ and $c_2 = 1.115$. We explore variations in the decay forms and associated decay parameters. In the inverse problem for surface tension characterization, σ_E will be measured with static techniques, such as the Du Nouy ring, and the remaining rate parameters (α in Form 1, Da^{-2} in Form 2, and t^* and n in Form 3) will be inferred from an inverse formulation of the

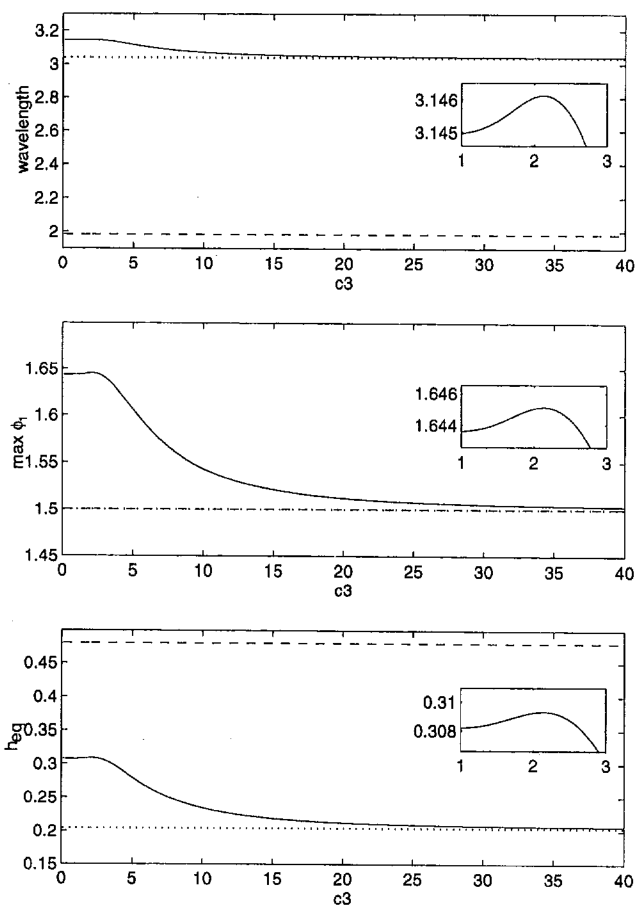

Fig. 4 Dependence of the sustained far-field oscillation on c_3 of a jet with exponentially decaying surface tension. The top, middle, and bottom graphs show the dependence of far-field wavelength, amplitude, and energy, respectively, for $c_3 > 0.1$. For comparison, the dashed and dotted lines indicate the values of these quantities when surface tension is constant: $\sigma \equiv \sigma(0) = 72.8$ dyne cm^{-1} (– – –) and $\sigma \equiv \sigma_E = 31$ dyne cm^{-1} (· · ·).

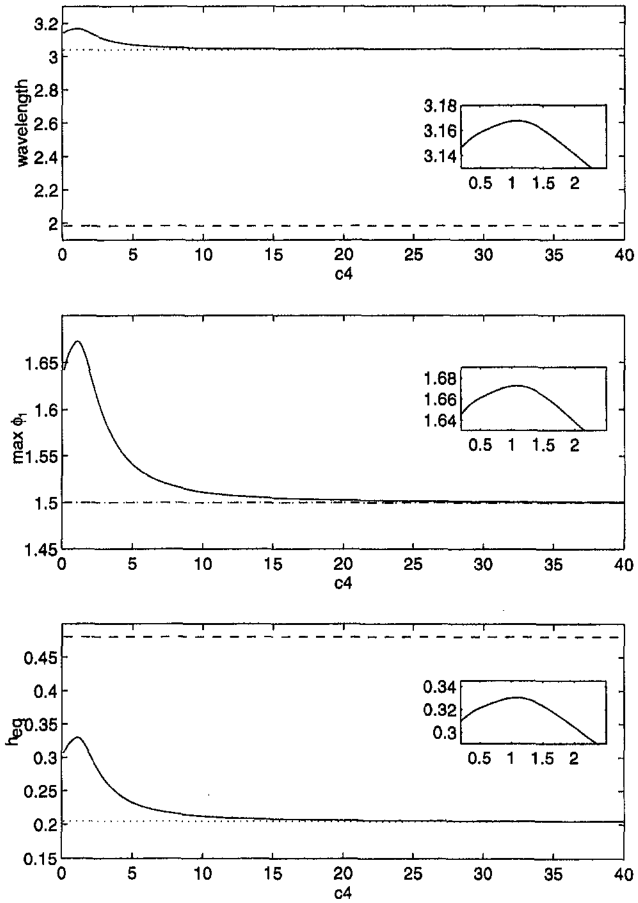

Fig. 5 Dependence of the sustained far-field oscillation on c_4 of a jet with decaying surface tension given by the Brazee et al. form. The top, middle, and bottom graphs show the dependence of far-field wavelength, amplitude, and energy, respectively, for $c_4 > 0.1$. The dashed and dotted lines indicate the values of these quantities when surface tension is constant: $\sigma \equiv \sigma(0) = 72.8$ dyne cm^{-1} (– – –) and $\sigma \equiv \sigma_E = 31$ dyne cm^{-1} (· · ·).

model coupled with experimental measurements of the oscillating jet profile.

In Fig. 1 we plot the *near-field free-surface profiles* for all three forms of surface tension decay. Figure 1(a) gives the profiles for exponential surface tension decay, Form 1. We note that the most rapid exponential decay ($c_3 = 200$) was purposefully chosen so that the condition $(22)_2$ on surface tension gradient is violated in a very short range (here $0 \le z \le 0.0015$). Therefore, the flow with $c_3 = 200$ is strictly not in Regime 1 very near the nozzle, but instead is in what we will call in the following Regime 2; see the next section. All other jets plotted in Fig. 1 satisfy conditions (22) everywhere along the jet, so that they are everywhere in Regime 1. Figure 1(b) depicts jet behavior under Form 2; we give the oscillating jet profiles for values of Da^{-2} ranging from 0.07 to 0.21 s^{-1}, consistent with the above values reported in Brazee et al. (1994). Figure 1(c) gives jet behavior for Form 3; the values of t^* and n we have chosen correspond to aqueous surfactant Tergitol NP-10 solutions with concentrations of 6 mM, 12 mM, and 60 mM (Shavit and Chigier, 1995). Figure 1 illustrates a complex dependence of amplitude and wavelength on the decay form and rate parameters. Observe that the wavelengths and amplitudes of the oscillating jets with decaying surface tension are consistently greater than those of the jet whose surface tension remains at the initial value; this is consistent with the behavior of a nonlinear mass/spring system with weakening spring constant.

To anticipate free-surface features which one might measure in experiments, in Fig. 2 we post-process from the solutions in Fig. 1 the locations and values of each maximum amplitude of the oscillation. We extend in Fig. 2 beyond the nearfield shown in Fig. 1 into the far-field. A careful inspection of Fig. 2 reveals that *the far-field amplitude of oscillation depends on the form and on the rate constants within a given form of surface tension.* This may be understood as follows: As surface tension decays to an equilibrium, so does energy. If one could infer the final (equilibrium) energy density h_{eq} from the surface tension decay alone, then the amplitude and wavelength of the far-field sustained oscillation could be deduced a priori, without integrating the equations of motion. However, from (27) we see

$$h_{eq} = h(0) + \frac{4t_0^2}{\rho r_0^3}\int_0^\infty \sigma_{,z}(z)\left\{\frac{E(1-\phi_1^4)}{\pi\phi_1} - \frac{1}{2}\right\}dz, \quad (33)$$

so that the equilibrium energy (and equivalently the farfield amplitude and wavelength) depends on the entire history of the oscillation, and cannot be inferred merely from $h(0)$ and $\sigma(z)$; h_{eq} must be numerically computed. In Fig. 3 we specialize to Form 1 and show the evolution of the energy density $h(z)$ for the solutions of Figs. 1(a), 2(a). The four jets each decay to different equilibrium energy per length values, $h_{eq} = 0.308063$, 0.309314, 0.255606, 0.204821 for $c_3 = 0.3$, 2.1, 7.0, 200, respectively, even though each decays to the same equilibrium surface tension. For comparison, the energies per length for the

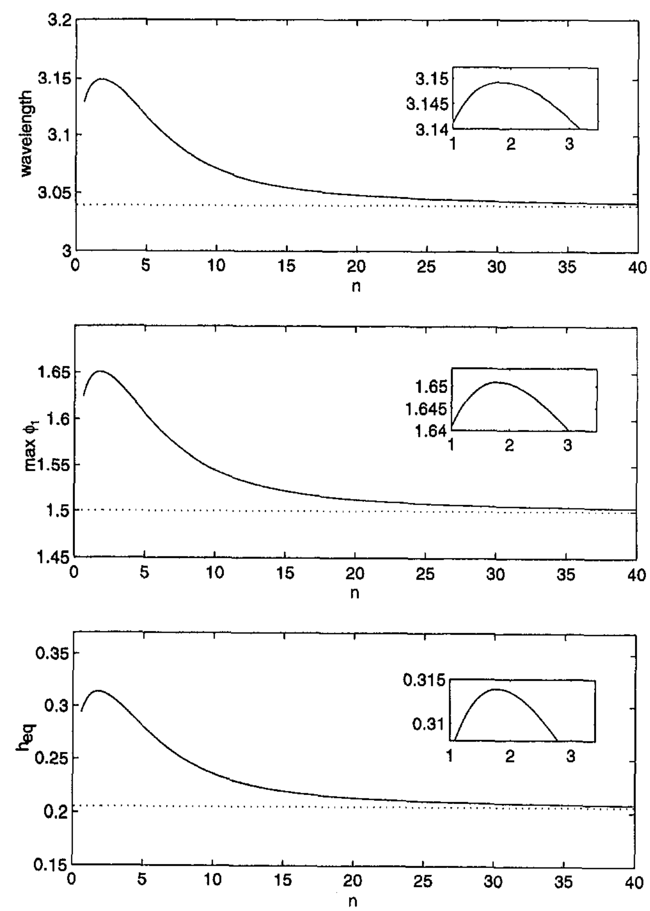

Fig. 6 Dependence of the sustained far-field oscillation on n of a jet with decaying surface tension given by the Hua and Rosen form when $c_6 = 1.0$. The top, middle, and bottom graphs show the dependence of far-field wavelength, amplitude, and energy, respectively, for $n > 0.6$.

oscillating jets with constant surface tensions 72.8 dyne cm^{-1} and 31 dyne cm^{-1} are the constants $h = 0.482$ and 0.2047, respectively.

The decay of surface tension is confined to the near-field, with the equilibrium value being reached typically at a fraction of the first wavelength, at its slowest before completion of the second oscillation. It would be difficult to make measurements of the jet free surface in this small domain with the necessary accuracy for the inverse problem. The discovery that far-field oscillatory jet behavior varies with the form of the surface tension decay and decay rate parameter(s), albeit in a nontrivial way, indicates that this is unnecessary. One can quantitatively infer the decay of surface tension, which happens very near the nozzle, with measurements far downstream of the nozzle, measurements that can be made much more reliably.

Figure 4 shows the dependence of equilibrium wavelength, amplitude, and energy on the exponential decay rate c_3 in Form 1. The relations are one to one except in a small range of c_3 inside of which the same wavelength occurs for two distinct values of c_3. The same behavior happens for amplitude. By inverting c_3 from amplitude *and* wavelength measurements, the multiplicity in the narrow band can be averted.

Figures 5–7 provide the analogous relationships for Form 2 and Form 3. *Figures 4–7 provide the basis for an inverse characterization of the surface tension decay forms and rate constants within those forms; experimental measurements provide the vertical axis information on amplitude and wavelength, which is then inverted using the figures to infer rate parameters.* A statistical procedure, e.g., least squares, could be implemented to find a best fit among these available surface tension decay forms.

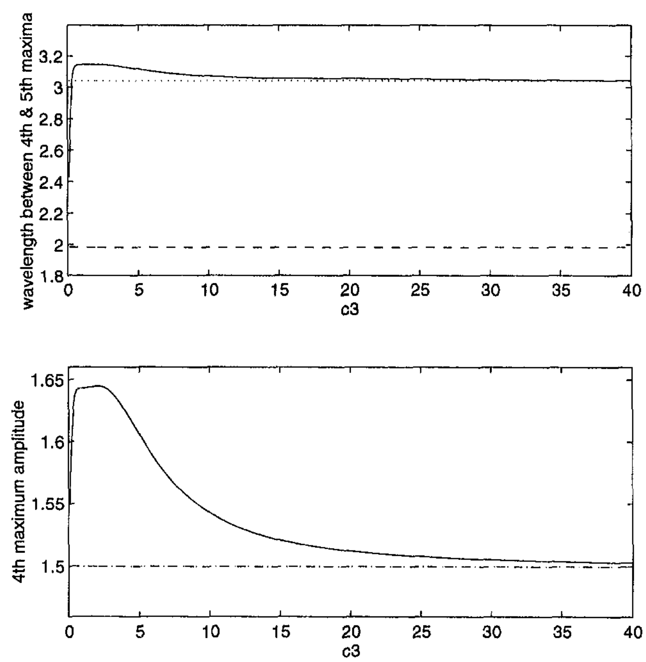

Fig. 8 Dependence of the oscillation after four cycles on c_3 of a jet with exponentially decaying surface tension. The top graph shows the dependence of the wavelength between the fourth and fifth maxima on c_3; the bottom graph shows the dependence of the fourth maximum amplitude on c_3. For comparison, the dashed and dotted lines indicate the values of these quantities when surface tension is constant: $\sigma \equiv \sigma(0) = 72.8$ dyne cm^{-1} (– – –) and $\sigma \equiv \sigma_E = 31$ dyne cm^{-1} (· · ·).

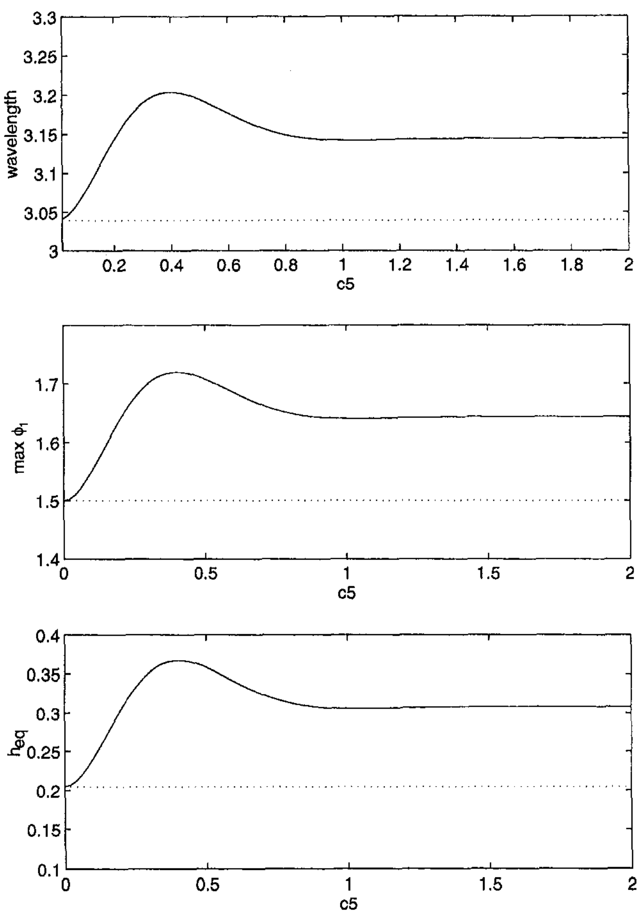

Fig. 7 Dependence of the sustained far-field oscillation on c_5 of a jet with decaying surface tension given by the Hua and Rosen form when $n = 3.0$. The top, middle, and bottom graphs show the dependence of far-field wavelength, amplitude, and energy, respectively.

As a practical matter, it is unnecessary to monitor that an equilibrium oscillation has been reached. Figures 8–11 show that the far-field relationships of Figs. 4–7 are duplicated if we focus on fixed downstream observations, chosen here as the fourth/fifth cycles of oscillation.

Regime 2: An Inviscid Jet With Dominant Surface Tension Gradient. As mentioned above, the jet in Fig. 1(a) with $c_3 = 200$ violates condition $(22)_2$ in the domain $0 \le z \le 0.0015$. In this narrow axial domain $1/W$ and B are $O(1)$, $W_{,z}/W^2$ is $O(\epsilon^{-2})$ and $1/F$, Z and $Z_{,z}$ are $O(\epsilon^2)$, so that the appropriate steady leading-order equations from (12) are

$$v_{,z} = -\epsilon^2 \frac{W_{,z}}{W^2} \int_0^{2\pi} (\phi_2^2 \cos^2\theta + \phi_1^2 \sin^2\theta)^{1/2} d\theta, \quad v\phi_1\phi_2 = 1,$$

$$\frac{1}{\phi_1}\left(\frac{1}{\phi_1^2} + \frac{1}{\phi_2^2}\right)\phi_{1,zz} - \frac{2}{\phi_1^4}\phi_{1,z}^2 + \left(\frac{1}{\phi_2^2} - \frac{1}{\phi_1^2}\right)\phi_2\phi_{1,z}v_{,z}$$

$$- \phi_2^2 v_{,z}^2 + \frac{\phi_2}{\phi_1} v_{,zz} + \frac{4}{W}(K_s - K_c)$$

$$- \epsilon^2 \frac{4W_{,z}}{W^2}(Y_s - Y_c) = 0, \quad (34)$$

rather than Eqs. (24). To compute the profile for $c_3 = 200$, one integrates Eqs. (34) in the domain $0 \le z \le 0.0015$ (in which $\epsilon^2 W_{,z}/W^2(z)$ is $O(1)$), and then integrates Eqs. (24) for $z >$

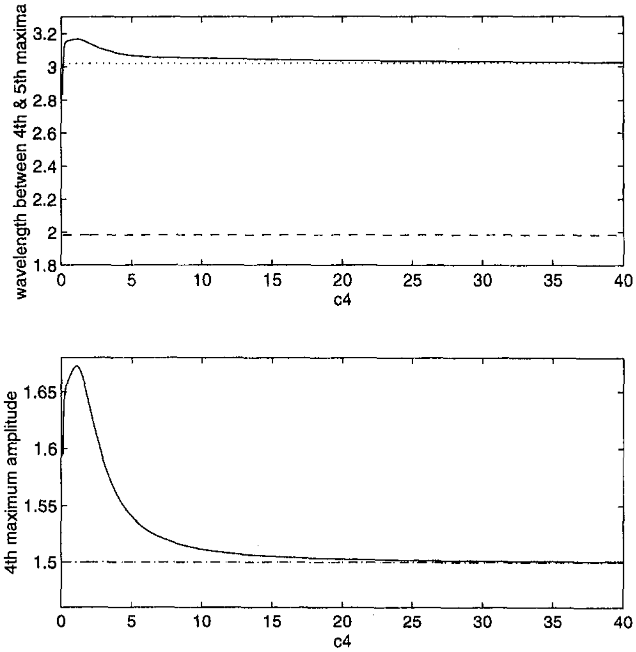

Fig. 9 Dependence of the oscillation after four cycles on c_4 of a jet with decaying surface tension given by the Brazee et al. form. The top graph shows the dependence of the wavelength between the fourth and fifth maxima on c_4; the bottom graph shows the dependence of the fourth maximum amplitude on c_4.

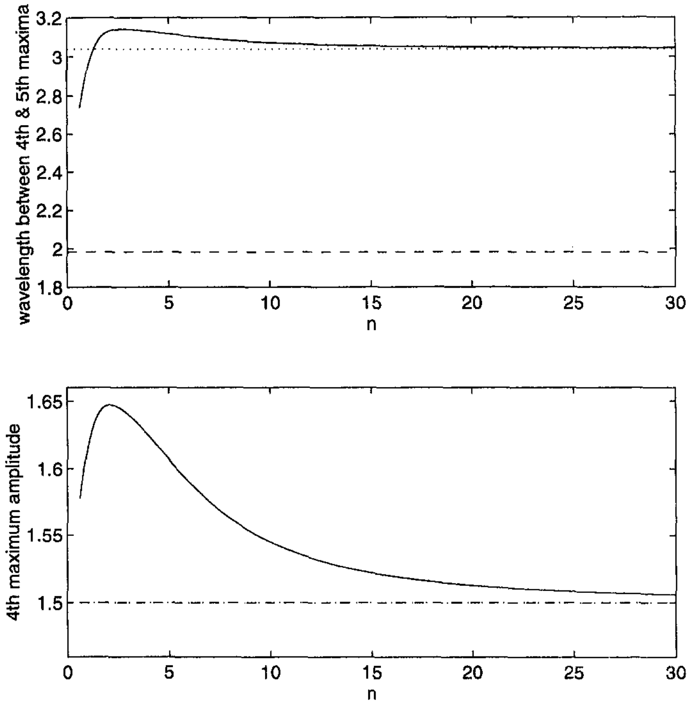

Fig. 10 Dependence of the oscillation after four cycles on n of a jet with decaying surface tension given by the Hua and Rosen form. The top graph shows the dependence of the wavelength between the fourth and fifth maxima on n; the bottom graph shows the dependence of the fourth maximum amplitude on n.

0.0015 (in which $\epsilon^2 W_{,z}/W^2(z)$ has decayed to below $O(1)$). For practical purposes, this effect is negligible.

Regime 3: Newtonian Jets in the Presence of Gravity. In this section we demonstrate that an experiment not much different than Regime 1 above can lead to a regime in which viscosity and gravity couple with inertia and surface tension as leading-order effects.

Consider a jet of the same fluid as above ($\rho = 0.997$ gm cm^{-3}, $\eta = 1.00 \times 10^{-2}$ g cm^{-1} s^{-1}, $\sigma(0) = 72.8$ dyne cm^{-1}) but with a larger aperture (semi-axes 1.5 and 0.97 cm) and greater volumetric flow rate ($Q = 240$ cm^3 s^{-1}). Retaining the slenderness ratio $\epsilon = 0.1$, we compute the dimensionless parameters

$$\frac{1}{F} = 0.5\epsilon^0, \quad \frac{1}{W(0)} = 1.0\epsilon^0, \quad \frac{1}{R} = BZ = 0.152\epsilon^0, \quad (35)$$

where R is the Reynolds number. Note that for this jet, $1/R$ and $1/F$ as well as B and $1/W$ are $O(1)$, and the steady leading-order equations are, from (12) and $(17)_3$,

$$vv_{,z} = \frac{1}{F}, \quad v\phi_1\phi_2 = 1,$$

$$v^2(\phi_1\phi_{1,zz} - \phi_2\phi_{2,zz}) + vv_{,z}(\phi_1\phi_{1,z} - \phi_2\phi_{2,z}) + \frac{8v}{R}\left(\frac{\phi_{1,z}}{\phi_1} - \frac{\phi_{2,z}}{\phi_2}\right) + \frac{4}{W(z)}(K_s - K_c) = 0. \quad (36)$$

With gravity as a leading-order effect, surface age is no longer proportional to axial distance, as in Eq. (25). Rather, combining (20) and $(36)_1$, we have

$$T(z) = t_0 \int_0^z \frac{dz}{\sqrt{\frac{2z}{F} + 1}} = t_0 F\left(\sqrt{\frac{2z}{F} + 1} - 1\right). \quad (37)$$

With (37), any form of surface tension as a function of surface age can be converted to a function of axial distance. For instance, the Brazee et al. form (29) becomes

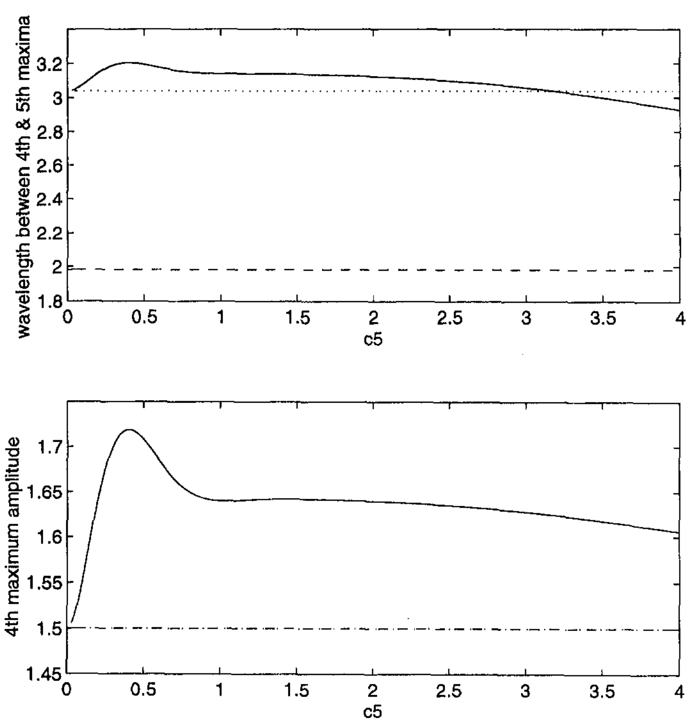

Fig. 11 Dependence of the oscillation after four cycles on c_5 of a jet with decaying surface tension given by the Hua and Rosen form. The top graph shows the dependence of the wavelength between the fourth and fifth maxima on c_5; the bottom graph shows the dependence of the fourth maximum amplitude on c_5. These values are the far-field values for amplitude, and energy for $c_5 > 0.03$.

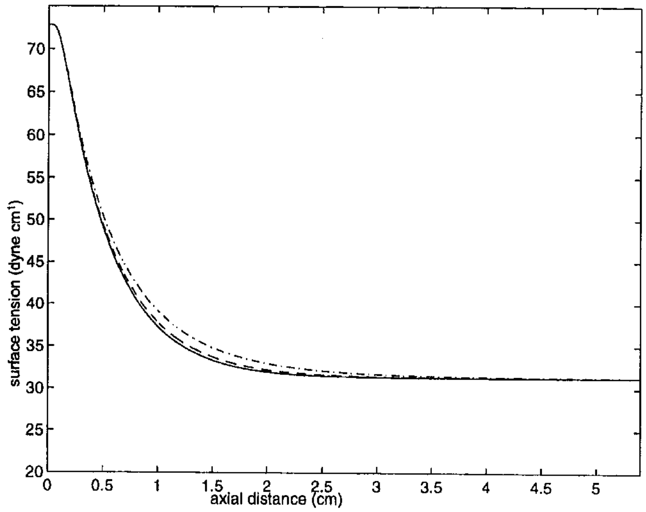

Fig. 12 The effect of gravity on surface tension as a function of axial distance. Surface tension as a function of surface age is given by the Brazee et al. form with $c_4 = 2.75 \times 10^{-5}$: $F^{-1} = 0$ (——), $F^{-1} = 0.5$ (- - -), $F^{-1} = 2$ (- · - · - ·).

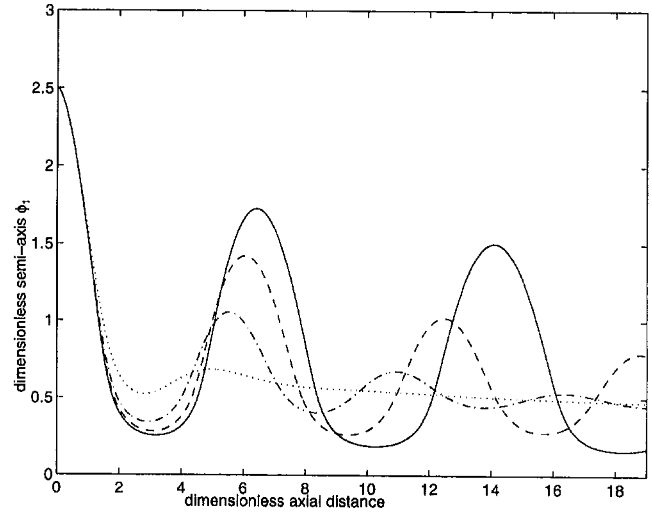

Fig. 14 The effect of viscosity on the oscillating jet profile with surface tension given by Fig. 12. $F^{-1} = 0.5$, $R^{-1} = 0$ (——), $R^{-1} = 0.0152$ (- - -), $R^{-1} = 0.045$ (- · - · - ·), $R^{-1} = 0.15$ (· · ·).

$$\sigma(x_3) = \sigma(0) + (\sigma_E - \sigma(0)) \left\{ 1 - \frac{2}{\pi} \sum_{n=0}^{\infty} \frac{(-1)^n e^{-\pi^2 D(n+1/2)^2 (t_0 F(\sqrt{2z/F+1}-1))/a^2}}{n + \frac{1}{2}} \right\}. \quad (38)$$

Figure 12 shows the effect of gravity to delay the decay of surface tension with axial distance; the specific form is the Brazee et al. form (Form 2) with $Da^{-2} = 0.095$ s^{-1}. Figure 13 shows how this delay, together with the underlying axial acceleration of the jet, continually stretches, decreases the amplitude, and decreases the mean surface of the free-surface oscillation. Figure 14 illustrates the damping effect of viscosity; the dotted line, with $F^{-1} = 0.5$ and $R^{-1} = 0.152$, is the predicted behavior of the experiment just described, with the decay of surface tension with surface age depicted in Fig. 12.

For more viscous fluids it might prove impossible to design an experiment in Regime 1; the viscosity-induced drag in the capillary upstream of the nozzle will likely force larger nozzles and flow rates, elevating (as was seen in the above experiment) gravity and/or viscosity to leading order. As is evident from Figs. 13 and 14, if either of gravity or viscosity is leading order, there is no equilibrium (sustained far-field oscillation), and hence there is no equivalent of Figs. 4–7 to be employed in the inverse problem for surface tension decay. In such regimes, one can focus the model and experiments at a fixed downstream location and reproduce the functional equivalents of Figs. 8–11.

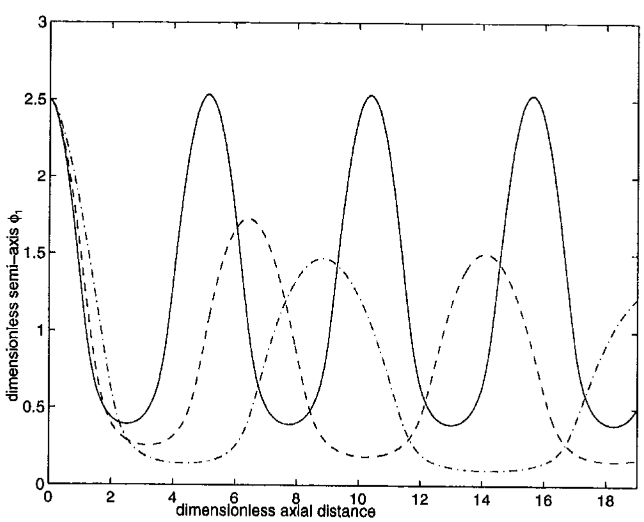

Fig. 13 The effect of gravity on the oscillating jet profile with surface tension given by Fig. 12. $\phi_1(0) = 2.5$, $\phi_{1,z}(0) = 0$, $R^{-1} = 0$, $F^{-1} = 0$ (——), $F^{-1} = 0.5$ (- - -), $F^{-1} = 2$ (- · - · - ·).

4 Conclusion

Previous equations for oscillating jets are extended to allow for surface tension to vary in space and time; the new models are used to investigate the effect of decaying surface tension on oscillating jet behavior. Three different functional forms for the decay of surface tension with surface age are studied: an exponential decay form, a diffusion model by Brazee et al. (1994), and an empirical form developed by Hua and Rosen (1991). In all forms we select initial and equilibrium values of surface tension, and decay rates consistent with experimental values reported in Thomas and Hall (1979), Hua and Rosen (1991), Brazee et al. (1994), and Shavit and Chigier (1995). The model behavior established here indicates that the rate and form of surface tension decay can be inferred from a combination of static and downstream measurements along with an inverse formulation of the model. This procedure avoids measurements of the jet profile near the nozzle where rapid surface tension decay takes place, and therefore appears to be practically attractive.

Acknowledgment

This work was funded in part by the National Science Foundation, under Grants CTS-9319128 and CTS-9711109, and the Air Force Office of Scientific Research, Air Force Materials Command, USAF, under Grants F49620-97-1-0001 and F49620-97-1-0003. The U.S. Government is authorized to reproduce and distribute reprints for governmental purposes notwithstanding any copyright notation thereon. The views and conclusions contained herein are those of the authors and should not be interpreted as necessarily representing the official policies or endorsements, either expressed or implied, of the Air Force Office of Scientific Research or the U.S. Government. SEB and MGF acknowledge valuable discussions with Robert Fox and Ross Brazee of the U.S. Department of Agriculture, Wooster, OH. All authors thank an anonymous referee for constructive suggestions.

References

Abramowitz, M., and Stegun, I. A., 1964, *Handbook of Mathematical Functions,* Dover, New York.

Bechtel, S. E., 1989, "The Oscillation of Slender Elliptical Inviscid and Newtonian Jets: Effects of Surface Tension, Inertia, Viscosity and Gravity," ASME JOURNAL OF APPLIED MECHANICS, Vol. 56, pp. 968–974.

Bechtel, S. E., Lin, K. J., and Forest, M. G., 1988, "On the behavior of viscoelastic free jets with elliptical cross-section," *Journal of Non-Newtonian Fluid Mechanics,* Vol. 27, pp. 87–126.

Bechtel, S. E., Cooper, J. A., Forest, M. G., Petersson, N. A., Reichard, D. L., Saleh, A., and Venkataramanan, V., 1995, "A new model to determine dynamic surface tension and elongational viscosity using oscillating jet measurements," *Journal of Fluid Mechanics,* Vol. 293, pp. 379–403.

Bohr, N., 1909, "Determination of dynamic surface tension by the method of jet vibration," *Transactions of the Royal Society, London,* Vol. A209, pp. 281–317.

Brazee, R. D., Bukovac, M. J., Cooper, J. A., Zhu, H., Reichard, D. L., and Fox, R. D., 1994, "Surfactant diffusion and dynamic surface tension in spray solutions," *Transactions of the ASAE,* Vol. 37, pp. 51–58.

Defay, R., and Hommelen, J., 1958, "Measurements of dynamic surface tensions of aqueous solutions by the oscillating jet method," *Journal of Colloid Science,* Vol. 13, pp. 553–564.

Edwards, D. A., Brenner, H., and Wasan, D. T., 1991, *Interfacial Transport Processes and Rheology,* Butterworth-Heinamann, Boston.

Hansen, R. S., Purchase, M. E., Wallace, T. C., and Woody, R. C., 1958, "Extension of the vibrating jet method for surface tension measurements to jets of non-uniform velocity profile," *Journal of Physical Chemistry,* Vol. 62, pp. 210–214.

Hua, X. Y., and Rosen, M. J., 1991, "Dynamic surface tension of aqueous surfactant solutions," *Journal of Colloid and Interface Science,* Vol. 141, pp. 180–189.

Kase, S., and Matsuo, T., 1967, "Studies on melt spinning, ii: Steady state and transient solutions of fundamental equations compared with experimental results," *Journal of Polymer Science,* Vol. 11, pp. 251–287.

Lunkenheimer, K., and Wantke, K. D., 1981, "Determination of the dynamic surface tension of surfactant solutions applying the method of Lecomte du Nouy (ring tensiometer)," *Coll. & Polymer Sci.,* Vol. 259, pp. 354–366.

Milliken, W. J., Stone, H. A., and Leal, L. G., 1993, "The effect of surfactant on the transient motion of Newtonian drops," *Physics of Fluids A,* Vol. 5, pp. 69–79.

Rayleigh, Lord, 1879, "On the capillary phenomena of jets," *Proceedings of the Royal Society, London,* Vol. 29A, pp. 71–97.

Reichard, D. L., Cooper, J. A., Bechtel, S. E., and Fox, R. D., 1997, "A system for determining dynamic surface tension using the oscillating jet technique," *Atomization and Sprays,* Vol. 7, pp. 219–233.

Shavit, U., and Chigier, N., 1995, "The role of dynamic surface tension in air assist atomization," *Physics of Fluids,* Vol. 7, pp. 24–33.

Stone, H. A., and Leal, L. G., 1990, "The effect of surfactants on drop deformation and breakup," *Journal of Fluid Mechanics,* Vol. 220, pp. 161–186.

Thomas, W. D. E., and Hall, D. J., 1979, "Dynamic surface tension of some non-ionic surfactant at the solution/air surface," *Surface Active Agents, Symposium, London: Soc. Chem. Ind,* Vol. 107–116.

Thomas, W. D. E., and Potter, L., 1975, "Solution/air interfaces 1. An oscillating jet relative method for determining dynamic surface tension," *Journal of Colloid and Interface Science,* Vol. 50, pp. 397–412.

F.-L. Liu[1]
Research Scholar,
CAD/CAM Laboratory

K. M. Liew
Senior Lecturer,
Division of Engineering Mechanics,
Mem. ASME

School of Mechanical and
Production Engineering,
Nanyang Technological University,
Singapore 639798

Static Analysis of Reissner-Mindlin Plates by Differential Quadrature Element Method

In this paper, a new numerical method, the differential quadrature element method has been developed for two-dimensional analysis of bending problems of Reissner-Mindlin plates. The basic idea of the differential quadrature element method is to divide the whole variable domain into several subdomains (elements) and to apply the differential quadrature method for each element. The detailed formulations for the differential quadrature element method and compatibility conditions between elements are presented. The convergent characteristics and accuracy of the differential quadrature element method are carefully investigated for the solution of the two-dimensional bending problems of Reissner-Mindlin plates. Finally, the differential quadrature element method is applied to analyze several bending problems of two-dimensional Reissner-Mindlin plates with different discontinuities including the discontinuous loading conditions, the mixed boundaries, and the plates with cutout. The accuracy and applicability of this method have been examined by comparing the differential quadrature element method solutions with the existing solutions obtained by other numerical methods and the finite element method solutions generated using ANSYS 5.3.

1 Introduction

The differential quadrature method has become increasingly popular in many engineering fields, especially in the structural mechanics field. Many researchers have shown that this method has the advantage of producing the highly accurate solutions with minimal computational effort and therefore has the potential to become an alternative to the conventional numerical methods in solving the structural problems (Bert et al., 1988, 1989; Pandya and Sherbourne, 1991; Bert and Malik, 1995; Liew et al., 1996; Bert and Malik, 1996). However, the further application of this new method has been greatly confined by the drawback that it can only be applicable directly to solve the problems which should satisfy the continuous conditions in the whole variable domain, including the geometry, boundary, material properties, and the loading conditions. To overcome this drawback, Striz, Chen, and Bert developed the quadrature element method to solve the bending of truss and beam (Striz et al., 1994) and free vibration of thin plate (Chen et al., 1997). Although the same idea had been used by Civan and Sliepcevich (1985) and by Shu and Richards (1992) to solve their respective problems, the works of Striz et al. (1994) are more comprehensive by considering the discontinuous loading and geometry as well, not just concerning the geometry domain of variables. However, for all the problems analyzed, Striz et al. (1994) introduced a δ-grid arrangement, which uses two points, separated by a small distance δ, to present one boundary point in order to satisfy the multiboundary conditions at one point. This is not convenient and accurate enough in solving the differential equations with four or higher orders.

In this paper, an improved differential quadrature method, or called the differential quadrature element method, is developed for the bending analysis of thick rectangular Reissner-Mindlin plates. The quadrature element of Reissner-Mindlin plate developed here has three degrees-of-freedom at each grid point and three boundary conditions are all exactly satisfied at every boundary point.

2 Differential Quadrature Element Method Formulation

Consider a rectangular Reissner-Mindlin plate with side lengths $a \times b$ as shown in Fig. 1. The plate is divided into N_E elements based on the discontinuities in the geometry, boundary constraints, and materials used. Each element consists of an isotropic material, has uniform thickness and continuous boundary constraints on each edge and is subjected to a continuously distributed load. For the lth element, the thickness of the plate, Young's modulus, shear modulus, Poisson's ratio, and the load intensity are represented by h_l, E_l, G_l, ν_l, and q_l, respectively.

2.1 Governing Equations and Constraint Conditions. For a given element l, the governing equations are given in terms of the displacement components as follows (Mindlin, 1951):

$$\frac{D_l}{2}\left[(1-\nu_l)\nabla^2\psi_x + (1+\nu_l)\frac{\partial\phi}{\partial x}\right] - \kappa G_l h_l\left(\frac{\partial w}{\partial x} + \psi_x\right) = 0 \quad (1a)$$

$$\frac{D_l}{2}\left[(1-\nu_l)\nabla^2\psi_y + (1+\nu_l)\frac{\partial\phi}{\partial y}\right] - \kappa G_l h_l\left(\frac{\partial w}{\partial y} + \psi_y\right) = 0 \quad (1b)$$

[1] To whom correspondence should be addressed.

Contributed by the Applied Mechanics Division of THE AMERICAN SOCIETY OF MECHANICAL ENGINEERS for publication in the ASME JOURNAL OF APPLIED MECHANICS.

Discussion on the paper should be addressed to the Technical Editor, Professor Lewis T. Wheeler, Department of Mechanical Engineering, University of Houston, Houston, TX 77204-4792, and will be accepted until four months after final publication of the paper itself in the ASME JOURNAL OF APPLIED MECHANICS.

Manuscript received by the ASME Applied Mechanics Division, Dec. 18, 1996; final revision, Mar. 25, 1998. Associate Technical Editor: J. N. Reddy.

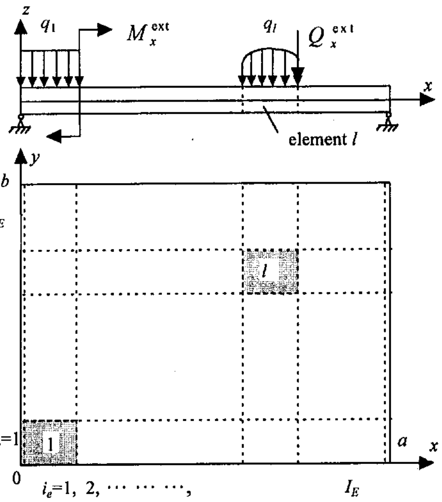

Fig. 1 A rectangular plate with side dimension $a \times b$

$$\kappa G_l h_l (\nabla^2 w + \phi) + q_l = 0 \tag{1c}$$

in which

$$\phi = \frac{\partial \psi_x}{\partial x} + \frac{\partial \psi_y}{\partial y} \tag{2}$$

$$\nabla^2 = \frac{\partial}{\partial x^2} + \frac{\partial}{\partial y^2} \tag{3}$$

$$D_l = \frac{E_l h_l^3}{12(1-\nu_l^2)}\,. \tag{4}$$

w is the transverse deflection; ψ_x and ψ_y are the rotations of the normal about the x-axis and y-axis, respectively; D_l is the plate flexural rigidity and κ is the shear correction factor, which is presently taken as $\frac{5}{6}$.

The moments and shear forces are expressed as

$$M_x = D_l\left(\frac{\partial \psi_x}{\partial x} + \nu_l \frac{\partial \psi_y}{\partial y}\right) \tag{5a}$$

$$M_y = D_l\left(\nu_l \frac{\partial \psi_x}{\partial x} + \frac{\partial \psi_y}{\partial y}\right) \tag{5b}$$

$$M_{xy} = \frac{1-\nu_l}{2} D_l\left(\frac{\partial \psi_x}{\partial y} + \frac{\partial \psi_y}{\partial x}\right) \tag{5c}$$

$$Q_x = \kappa G_l h_l\left(\frac{\partial w}{\partial x} + \psi_x\right) \tag{5d}$$

$$Q_y = \kappa G_l h_l\left(\frac{\partial w}{\partial y} + \psi_y\right)\,. \tag{5e}$$

The boundary conditions for the side of rectangular plate can be classified into four kinds. Taking side $x = 0$ for example, the boundary conditions are expressed as follows:

(*a*) *Generalized hard simply supported sides* (S):

$$w = 0,\ \psi_y = 0,\ M_x = (M_x^{\text{ext}})_1; \tag{6}$$

(*b*) *Generalized soft simply supported sides* (S'):

$$w = 0,\ M_{xy} = 0,\ M_x = (M_x^{\text{ext}})_1; \tag{7}$$

(*c*) *Clamped sides* (C):

$$w = 0,\ \psi_x = 0,\ \psi_y = 0; \tag{8}$$

(*d*) *Generalized free sides* (F):

$$Q_x = (Q_x^{\text{ext}})_1,\ M_x = (M_x^{\text{ext}})_1,\ M_{xy} = 0 \tag{9}$$

where $(M_x^{\text{ext}})_1$, $(M_y^{\text{ext}})_1$, $(Q_x^{\text{ext}})_1$, and $(Q_y^{\text{ext}})_1$ are the concentrated external line moments and loads at the side $x = 0$.

2.2 Rectangular Differential Quadrature Element Method Reissner-Mindlin Plate Element. The lth element is further divided into $N_x \times N_y$ grid points along the x and y-axis, respectively, and subjected to "external" concentrated line forces and moments, the combination action of the real external forces and moments applied at the four edges of element l, and the shear forces and moments produced by adjacent elements as shown in Fig. 2. By applying the differential quadrature method rule (Liew et al., 1996), the governing equations ($1a$–c) can be discretized at each discrete point on the inner grid of the element l as

$$\sum_{k=1}^{N_{lx}} C_{ik}^{(2)}(\psi_x)_{kj} + \frac{(1-\nu_l)}{2}\sum_{m=1}^{N_{ly}} \bar{C}_{jm}^{(2)}(\psi_x)_{im} - F_l(\psi_x)_{ij} + \frac{(1+\nu_l)}{2}\left[\sum_{k=1}^{N_{lx}} C_{ik}^{(1)} \sum_{m=1}^{N_{ly}} \bar{C}_{jm}^{(1)}(\psi_y)_{km}\right] - F_l \sum_{k=1}^{N_{lx}} C_{ik}^{(1)}(w)_{kj} = 0 \tag{10a}$$

$$\frac{(1+\nu_l)}{2}\left[\sum_{k=1}^{N_{lx}} C_{ik}^{(1)} \sum_{m=1}^{N_{ly}} \bar{C}_{jm}^{(1)}(\psi_x)_{km}\right] + \sum_{m=1}^{N_{ly}} \bar{C}_{jm}^{(2)}(\psi_y)_{im} + \frac{(1-\nu_l)}{2}\sum_{k=1}^{N_{lx}} C_{ik}^{(2)}(\psi_y)_{kj} - F_l(\psi_y)_{ij} - F_l \sum_{m=1}^{N_{ly}} \bar{C}_{jm}^{(1)}(w)_{im} = 0 \tag{10b}$$

$$\sum_{k=1}^{N_{lx}} C_{ik}^{(2)}(w)_{kj} + \sum_{m=1}^{N_{ly}} \bar{C}_{jm}^{(2)}(w)_{im} + \sum_{k=1}^{N_{lx}} C_{ik}^{(1)}(\psi_x)_{kj} + \sum_{m=1}^{N_{ly}} \bar{C}_{jm}^{(1)}(\psi_y)_{im} = -\frac{q_l}{\kappa G_l h_l}$$

$$i = 1, 2, 3, \ldots, N_x;\ j = 1, 2, 3, \ldots, N_y \text{ and } l = 1, 2, 3, \ldots, N_E \tag{10c}$$

where $C_{rs}^{(n)}$ and $\bar{C}_{rs}^{(n)}$ ($r = 1, 2, 3, \ldots, N_x$; $s = 1, 2, 3, \ldots, N_y$) are the weighting coefficients for the nth-order partial deriva-

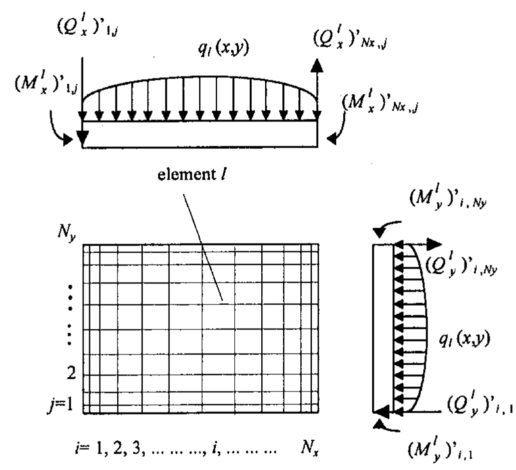

Fig. 2 Equilibrium and arrangement of grid points of element l

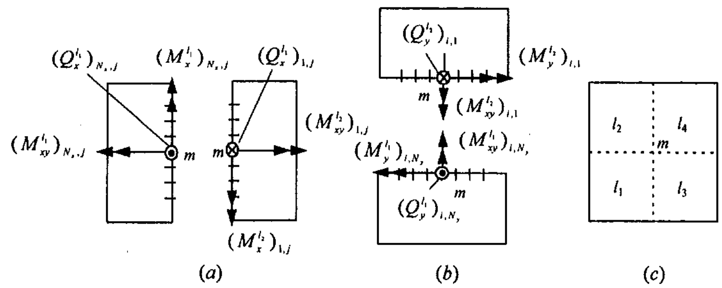

Fig. 3 Locations of the conjunction nodes on the interface boundaries of elements: (*a*) two elements are connected along *x*-axis; (*b*) two elements are connected along *y*-axis; (*c*) four elements are connected at point *m*

tives of w, ψ_x, and ψ_y with respect to the global coordinates x and y.

At the four edges of element l, the governing equations are replaced by the corresponding boundary conditions or compatibility conditions. If the edge is located at the sides of the plate, the boundary conditions (6) to (9) are used, otherwise, the compatibility conditions are employed.

The matrix form of Eqs. (10a–c) can be written as

$$\mathbf{K}^e\mathbf{d}^e = \mathbf{f}^e \tag{11}$$

in which $\mathbf{K}^e$, $\mathbf{d}^e$, and $\mathbf{f}^e$ are defined as the element weighting coefficient matrix, element displacement vector, and element force vector, respectively, and

$$\mathbf{d}^e = [w_{1,1}, \psi_{1,1}, \psi_{1,1}, w_{1,2}, \psi_{1,2}, \psi_{1,2}, \\ \ldots w_{N_x,N_y}, \psi_{N_x,N_y}, \psi_{N_x,N_y}]^T \tag{12}$$

$$\mathbf{f}^e = [(Q_x^l)'_{1,1}, (M_x^l)'_{1,1}, (M_{xy}^l)'_{1,1}, (Q_x^l)'_{1,2}, (M_x^l)'_{1,2}, \\ (M_{xy}^l)'_{1,2}, \ldots, (Q_x^l)'_{1,N_y}, (M_x^l)'_{1,N_y}, (M_{xy}^l)'_{1,N_y}, (Q_y^l)'_{2,1}, \\ (M_y^l)'_{2,1}, (M_{xy}^l)'_{2,1}, 0, 0, f_{2,2}, 0, 0, f_{2,3}, \ldots, 0, 0, f_{2,N_y-1}, \\ (Q_y^l)'_{2,N_y}, (M_y^l)'_{2,N_y}, (M_{xy}^l)'_{2,N_y}, \ldots\ldots, (Q_x^l)'_{N_x,1}, \\ (M_x^l)'_{N_x,1}, (M_{xy}^l)'_{N_x,1}, (Q_x^l)'_{N_x,2}, (M_x^l)'_{N_x,2}, (M_{xy}^l)'_{N_x,2}, \\ \ldots, (Q_x^l)'_{N_x,N_y}, (M_x^l)'_{N_x,N_y}, (M_{xy}^l)'_{N_x,N_y}]^T \tag{13}$$

where

$$f_{ij} = -\frac{q_{ij}^l}{\kappa G_l h_l}, \quad i = 2, 3, \ldots, N_x - 1; j = 2, 3, \ldots, N_y - 1.$$

$(Q_x^l)'_{1,j}$, $(M_x^l)'_{1,j}$, $(M_{xy}^l)'_{1,j}$, $(Q_x^l)'_{N_x j}$, $(M_x^l)'_{N_x j}$, $(M_{xy}^l)'_{N_x,j}$, $(Q_y^l)'_{i,1}$, $(M_y^l)'_{i,1}$, $(Q_y^l)'_{i,N_y}$, and $(M_y^l)'_{i,N_y}$ $(i = 2, 3, \ldots, N_x - 1; j = 1, 2, \ldots, N_y)$ are the combinations of the external forces and moments applied at the four edges of element l, and the shear forces and moments produced by adjacent elements. The expressions of these forces and moments are determined by the compatibility conditions given in Section 2.3. The coefficients in $\mathbf{K}^e$ are determined by Eqs. (10a–c).

2.3 Assembly of Plate Elements and Connection Conditions. To obtain a complete solution for the whole plate, a global system equations for all the nodal points of the plate labeled 1 to N should be constructed first. This is simply accomplished by assembling the weighting coefficient matrices, force and moment vectors, and displacement vectors of all elements. The final global matrix equation for the whole plate becomes

$$\mathbf{K}\mathbf{d} = \mathbf{F} \tag{14}$$

where $\mathbf{K}$, $\mathbf{d}$, and $\mathbf{F}$ represent the combined weighting coefficient matrix, global displacement vector and global force, and moment vector, respectively. The vector $\mathbf{d}$ is expressed as

$$\mathbf{d} = [w_1, (\psi_x)_1, (\psi_y)_1, w_2, (\psi_x)_2, \\ (\psi_y)_2, \ldots\ldots, w_N, (\psi_x)_N, (\psi_y)_N]^T. \tag{15}$$

The displacement compatibility and force/moment equilibrium conditions should also be built up for the conjunction nodes on the interface boundaries of the elements. Obviously, the displacement compatibility condition is automatically satisfied at all the interface conjunction nodes as the same global nodal number is used for each conjunction node. Only the equilibrium condition is needed to form the connection conditions for the differential quadrature element method plate elements. According to the locations of conjunction nodes and the number of the elements meeting at these nodes, the connection conditions are expressed as follows:

(1) For Nodes at Which Two Elements Meet: Suppose elements l_1 and l_2 are two adjacent elements as shown in Figs. 3(a) and (b). The connection conditions for the conjunction nodes at the interface edge of element l_1 and l_2 connected in the x direction can be written according to the equilibrium condition as

$$\left.\begin{aligned} (Q_x^{l_1})_{N_x,j} - (Q_x^{l_2})_{1,j} &= (Q_x^{\text{ext}})_m \\ (M_x^{l_1})_{N_x,j} - (M_x^{l_2})_{1,j} &= (M_x^{\text{ext}})_m \\ (M_{xy}^{l_1})_{N_x,j} - (M_{xy}^{l_2})_{1,j} &= (M_{xy}^{\text{ext}})_m \end{aligned}\right\} . \tag{16}$$

The connection conditions for the conjunction nodes of element l_1 and l_2 connected in the y-direction can be obtained similarly.

(2) For Nodes at Which Four Elements Meet. The connection conditions for the common node m of the four arbitrarily selected elements l_1, l_2, l_3, and l_4 as shown in Fig. 3(c) can be expressed as

$$\left.\begin{aligned} (Q_x^{l_1})_{N_x,N_y} + (Q_x^{l_2})_{N_x,1} - (Q_x^{l_3})_{1,N_y} - (Q_x^{l_4})_{1,1} &= (Q_x^{\text{ext}})_m \\ (M_x^{l_1})_{N_x,N_y} + (M_x^{l_2})_{N_x,1} - (M_x^{l_3})_{1,N_y} - (M_x^{l_4})_{1,1} &= (M_x^{\text{ext}})_m \\ (M_{xy}^{l_1})_{N_x,N_y} + (M_{xy}^{l_2})_{N_x,1} - (M_{xy}^{l_3})_{1,N_y} - (M_{xy}^{l_4})_{1,1} &= (M_{xy}^{\text{ext}})_m \end{aligned}\right\} \tag{17}$$

or expressed in terms of the y components of force/moments at node m of the four elements in the similar way.

(3) For Conjunction Nodes Located at the Boundaries of Plate. For the conjunction nodes located at the side boundaries of the plate, both the boundary conditions and the connection conditions should be considered. Take the side boundary $x = 0$ for example. The following modified boundary conditions should be used:

Table 1 Convergence of numerical results of a uniformly loaded CCCC square plate with refinement of elements (h/a = 0.01; grid points in each element 5 × 5)[a]

N_E	N	W_c	error (%)	$\overline{M}_{xc}$	error (%)	$\overline{M}_{yc}$	error (%)	$\overline{M}_{xm}$	error (%)
1	25	1.42256	12.90	2.95354	27.86	2.95354	27.86	-4.54390	-11.43
4	81	1.05050	-16.63	1.27193	-44.94	1.27193	-44.94	-4.06277	-20.80
9	169	1.13088	-10.25	2.02828	-12.20	2.02828	-12.20	-4.55796	-11.15
16	289	1.18772	-5.74	2.10737	-8.77	2.10737	-8.77	-4.80642	-6.31
25	441	1.21615	-3.48	2.19544	-4.96	2.19544	-4.96	-4.92359	-4.02
36	625	1.23245	-2.19	2.21919	-3.93	2.21919	-3.93	-4.99020	-2.73
49	841	1.24242	-1.40	2.24424	-2.85	2.24424	-2.85	-5.03055	-1.94
64	1089	1.24898	-0.87	2.25436	-2.41	2.25436	-2.41	-5.05706	-1.42
81	1369	1.25346	-0.52	2.26456	-1.97	2.26456	-1.97	-5.07513	-1.07
100	1681	1.25666	-0.27	2.26969	-1.75	2.26969	-1.75	-5.08798	-0.82
121	2025	1.25899	-0.08	2.27471	-1.53	2.27471	-1.53	-5.09733	-0.64
144	2401	1.26075	0.06	2.27759	-1.40	2.27759	-1.40	-5.10432	-0.50
exact[b]		1.26	—	2.31	—	2.31	—	-5.13	—

[a] $W_c = w_c D/(10^{-3} \times qa^4)$; $\overline{M}_{xc} = M_{xc}/(10^{-2} \times qa^2)$; $\overline{M}_{yc} = M_{yc}/(10^{-2} \times qa^2)$; $\overline{M}_{xm} = M_{xm}/(10^{-2} \times qa^2)$, where M_{xm} is the bending moment M_x at the mid-side of $x = 0$.

[b] Exact thin plate solution (Timoshenko and Woinowsky-Krieger 1959).

$$(a)\quad w_m = 0,\ \psi_{xm} = 0,\ \psi_{ym} = 0 \quad \text{(for clamped side)} \tag{18}$$

$$(b)\quad w_m = 0,\ \psi_{ym} = 0,\ (M_x^{l_1})_{1,N_y} + (M_x^{l_2})_{1,1} = (M_x^{\text{ext}})_m \quad \text{(for hard simply supported side)} \tag{19}$$

$$(c)\quad w_m = 0,\ (M_x^{l_1})_{1,N_y} + (M_x^{l_2})_{1,1} = (M_x^{\text{ext}})_m,\quad (M_{xy}^{l_1})_{1,N_y} + (M_{xy}^{l_2})_{1,1} = (M_{xy}^{\text{ext}})_m \quad \text{(for soft simply supported side)} \tag{20}$$

$$(d)\quad (Q_x^{l_1})_{1,N_y} + (Q_x^{l_2})_{1,1} = (Q_x^{\text{ext}})_m,\quad (M_x^{l_1})_{1,N_y} + (M_x^{l_2})_{1,1} = (M_x^{\text{ext}})_m,\quad (M_{xy}^{l_1})_{1,N_y} + (M_{xy}^{l_2})_{1,1} = (M_{xy}^{\text{ext}})_m \quad \text{(for free side)} \tag{21}$$

3 Convergence and Accuracy Studies

For all the computations in this paper, the Poisson's ratio has been taken as $\nu = 0.3$. The grid points are designated by

$$x_i = \frac{a}{2}\{1 - \cos[(i-1)\pi/(N_x - 1)]\};\quad i = 1, 2, 3, \ldots, N_x \tag{22}$$

$$y_j = \frac{b}{2}\{1 - \cos[(j-1)\pi/(N_y - 1)]\};\quad j = 1, 2, 3, \ldots, N_y. \tag{23}$$

To examine the validity of the differential quadrature element method in solution of the bending problems of Reissner-Mindlin plates, the uniformly loaded square plates with CCCC and SFSF boundary conditions, are chosen here for analysis. Since the mesh for the spaces of the grid points can be refined by either increasing the number of the discretized elements on plate or increasing the grid points in each element, the effects of both approaches on the convergence and accuracy of the differential quadrature element method results are investigated. The convergent properties and the relative percentage errors (error = $[(\text{Value})_{\text{DQEM}} - (\text{Value})_{\text{exact}}]/(\text{Value})_{\text{exact}} \times 100\%$) between the differential quadrature element method solutions and the exact thin plate solutions obtained by Timoshenko and Woinowsky-Krieger (1959) are shown in Tables 1 to 4. Based on the data of all these tables, the following conclusions can be made:

Table 2 Convergence of numerical results for a uniformly loaded SFSF square plate with refinement of elements (h/a = 0.01; grid points in each element: 5 × 5)[a]

N_E	N	W_c	error (%)	$\overline{M}_{xc}$	error (%)	$\overline{M}_{yc}$	error (%)
1	25	13.02505	-0.50	12.03526	-1.75	2.19724	-18.92
4	81	13.17772	0.67	12.52254	2.22	3.14739	16.14
9	169	13.16021	0.54	12.37831	1.05	2.93867	8.44
16	289	13.13406	0.34	12.32108	0.58	2.82683	4.31
25	441	13.12000	0.23	12.30284	0.43	2.80220	3.40
36	625	13.11224	0.17	12.29048	0.33	2.78318	2.70
49	841	13.10756	0.13	12.28240	0.26	2.77018	2.22
64	1089	13.10458	0.11	12.27651	0.22	2.75915	1.81
81	1369	13.10260	0.10	12.27226	0.18	2.75079	1.51
100	1681	13.10125	0.09	12.26893	0.15	2.74355	1.24
121	2025	13.10031	0.08	12.26634	0.13	2.73765	1.02
144	2401	13.09964	0.07	12.26422	0.12	2.73249	0.83
exact[b]		13.09	—	12.25	—	2.71	—

[a] $W_c = w_c D/(10^{-3} \times qa^4)$; $\overline{M}_{xc} = M_{xc}/(10^{-2} \times qa^2)$; $\overline{M}_{yc} = M_{yc}/(10^{-2} \times qa^2)$;

[b] Exact thin plate solution (Timoshenko and Woinowsky-Krieger 1959).

Table 3 Convergence of numerical results of a uniformly loaded CCCC square plate with grid point refinement in each element (h/a = 0.01; N_E = 2)[a]

$N_x \times N_y$	N	W_c	error (%)	$\overline{M}_{yc}$	error (%)	$\overline{M}_{xm}$	error (%)
5 × 5	45	1.23183	-2.24	2.31252	-24.69	-4.76129	-7.19
7 × 7	91	1.26610	0.48	2.27582	-1.43	-5.15036	0.40
9 × 9	153	1.26804	0.64	2.29156	-0.76	-5.11353	-0.32
11 × 11	231	1.26807	0.64	2.29182	-0.78	-5.13923	0.18
13 × 13	325	1.26805	0.64	2.29133	-0.79	-5.12936	-0.01
15 × 15	435	1.26802	0.64	2.29151	-0.80	-5.13209	0.04
exact[b]	—	1.26	—	2.31	—	-5.13	—

[a] $W_c = w_c D/(10^{-3} \times qa^4)$; $\overline{M}_{xc} = M_{xc}/(10^{-2} \times qa^2)$; $\overline{M}_{yc} = M_{yc}/(10^{-2} \times qa^2)$; $\overline{M}_{xm} = M_{xm}/(10^{-2} \times qa^2)$, where M_{xm} is the bending moment M_x at the mid-side of $x = 0$.

[b] Exact thin plate solution (Timoshenko and Woinowsky-Krieger 1959).

(1) Either to increase the number of the elements or to increase the grid points in each element will yield the converged numerical results to the corresponding exact solutions by using the differential quadrature element method.

(2) In comparison of two approaches to refine the mesh of the grid points on plate, increasing the grid points in each ele-

Table 4 Convergence of numerical results for a uniformly loaded SFSF square plate with increasing number of grid points in each element (h/a = 0.01, N_E = 2)[a]

$N_x \times N_y$	N	w_c	error(%)	$\overline{M}_{xc}$	error(%)	$\overline{M}_{yc}$	error(%)	W_m	error(%)
5 × 5	45	13.0498	-0.31	12.0780	-1.40	2.2038	-18.68	15.4917	2.66
7 × 7	91	13.1101	0.15	12.2651	0.12	2.7119	0.07	15.2413	1.00
9 × 9	153	13.0974	0.06	12.2169	-0.27	2.5765	-4.92	15.1563	0.44
11 × 11	231	13.1007	0.08	12.2508	0.007	2.6841	-0.95	15.1111	0.14
13 × 13	325	13.0991	0.07	12.2408	-0.08	2.6844	-0.94	15.0849	-0.03
15 × 15	435	13.0992	0.07	12.2509	0.01	2.6888	-0.78	15.0688	-0.14
exact[b]	—	13.09	—	12.25	—	2.71	—	15.09	—

[a] $W_c = w_c D/(10^{-3}\times qa^4)$; $\overline{M}_{xc} = M_{xc}/(10^{-2}\times qa^2)$; $\overline{M}_{yc} = M_{yc}/(10^{-2}\times qa^2)$; $W_m = w_m D/(10^{-3}\times qa^4)$, where w_m is the deflection at the mid-side of $y = 0$.
[b] Exact thin plate solution (Timoshenko and Woinowsky-Krieger 1959).

Table 5 Influences of relative thickness on convergence of the differential quadrature element method results of a uniformly loaded square plate with SFSF boundary conditions[a]

	W_c		$\overline{M}_{xc}$		$\overline{M}_{yc}$	
$N_x \times N_y$	h/a=0.01	h/a=0.2	h/a=0.01	h/a=0.2	h/a=0.01	h/a=0.2
5×5	13.17772	14.56199	12.52254	12.35869	3.14739	2.38639
7×7	13.13964	14.54131	12.39048	12.29873	3.00142	2.37625
9×9	13.12255	14.53939	12.32657	12.29294	2.86608	2.37247
11×11	13.11343	14.53927	12.29739	12.29255	2.80127	2.37224
13×13	13.10809	14.53926	12.28135	12.29253	2.76482	2.37223
15×15	13.10471	14.53926	12.27142	12.29253	2.74189	2.37223

[a] $W_c = w_c D/(10^{-3}\times qa^4)$; $\overline{M}_{xc} = M_{xc}/(10^{-2}\times qa^2)$; $\overline{M}_{yc} = M_{yc}/(10^{-2}\times qa^2)$.

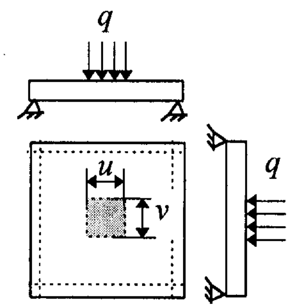

Fig. 4 A simply supported square plate subjected to a patch load

Table 6 Numerical results for a simply supported square plate under a patch load over a rectangle ($u = v$)[a]

v	h/a	W_c	$\overline{M}_{xc}$	$\overline{M}_{yc}$	$\overline{Q}_{xm}$	$\overline{M}_{xy1}$
0.2	0.01	0.43493	0.84964	0.84964	0.01667	-0.23875
0.2	exact[b]	0.43455	0.84697	0.84697	—	-0.23875
0.2	0.1	0.47191	0.84964	0.84964	0.01668	-0.23875
0.2	0.2	0.58395	0.84964	0.84964	0.01668	-0.23875
0.5	0.01	2.13348	2.94360	2.94360	0.10196	-1.33495
0.5	exact[b]	2.13219	2.94504	2.94504	—	-1.33495
0.5	0.1	2.26157	2.94360	2.94360	0.10196	-1.33495
0.5	0.2	2.64974	2.94360	2.94360	0.10196	-1.33495
0.8	0.01	3.70586	4.46838	4.46838	0.23808	-2.72893
0.8	exact[b]	3.70389	4.46731	4.46731	—	-2.72893
0.8	0.1	3.90031	4.46837	4.46837	0.23805	-2.72903
0.8	0.2	4.48954	4.46837	4.46837	0.23804	-2.72907

[a] $W_c = w_c D/(10^{-3}\times qa^4)$; $\overline{M}_{xc} = M_{xc}/(10^{-2}\times qa^2)$; $\overline{M}_{yc} = M_{yc}/(10^{-2}\times qa^2)$; $\overline{Q}_{xm} = Q_{xm}/(qa)$; $\overline{M}_{xy1} = M_{xy1}/(10^{-2}\times qa^2)$; where Q_{xm} and M_{xy1} are the shear force, Q_x, at the mid-side of $x = 0$ and the twisting moment at the corner $x = 0$, $y = 0$.
[b] Exact thin plate solution obtained using theoretical formulas (Pilkey 1994).

ment with fixed number of elements is much more effective than increasing the number of elements with fixed grid points in each elements to obtain a better accuracy and a higher convergent rate. Therefore, only the minimum number of elements enough to consider all the discontinuities on the plate is suggested to use in analysis.

To examine the influences of the relative thickness on the convergence and accuracy of the differential quadrature element method results, the SFSF rectangular plate is analyzed again. The numerical results solved by the differential quadrature element method for the square plate with different relative thicknesses are given in Table 5. It is found from Table 5 that the convergent rates of the differential quadrature element method results will be obviously improved as the relative thickness of the plate is increased.

4 Numerical Examples

Based on the convergence studies above, the differential quadrature element method is now applied to analyze several bending problems of Reissner-Mindlin plates with different discontinuities which otherwise can not be solved directly by the differential quadrature method. To ensure the accuracy of the computed results, 11 × 11 unevenly spaced cosine mesh pattern is used for each element. Some of the differential quadrature element method results, where possible, are compared with the exact analytical solutions or finite element method solutions to further verify the accuracy of the present method.

4.1 Example 1: A Simply Supported Square Plate Subjected to the Patch Load. The first example analyzed by the differential quadrature element method here is a simply supported square plate subjected to the patch load as shown in Fig. 4. The numerical results are presented in Table 6 and the comparison of the present solution for the thin plates (h/a = 0.01) with the exact solutions obtained using theoretical formulas (Pilkey, 1994) is also shown in this table. Excellent agreements have been achieved. It is observed that the values of all the normalized central deflections and moments, the shear forces at the midpoint of side $x = 0$, and the twisting moments at the corner $x = 0$, $y = 0$ increase with the dimensions of the loading area. The relative thickness seems to bear very slight influence on the moments and shear forces, but the value of the central deflection rises as the relative thickness increases.

4.2 Example 2: A Uniformly Loaded Square Plate With Mixed Boundaries. The second example analyzed is a uniformly loaded square plate with combination of clamped, simply supported, and free boundaries as shown in Fig. 5. The numerical results are given in Table 7 for different relative thickness. The finite element solutions generated by the computer software package ANSYS 5.3 are also tabulated for the purposes of comparison. One can see that the agreements are excellent for

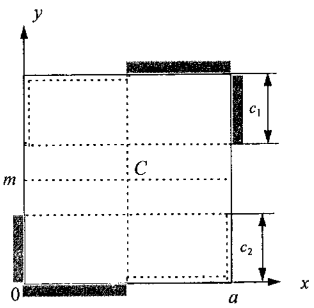

Fig. 5 A uniformly loaded square plate with mixed discontinuous boundaries

Table 7 Numerical results for a uniformly loaded square plate with mixture boundary conditions ($c_1 = c_2 = \frac{1}{3}a$)[a]

h/a	0.01		0.1		0.2	
solution	present	FEM[b]	present	FEM[b]	present	FEM[b]
W_c	2.13333	2.10513	2.55008	2.51538	3.42764	3.38374
W_m	0.15055	0.15300	0.40066	0.39056	0.99227	0.97492
$\overline{M}_{xc}$	2.77060	2.77666	2.93697	2.92900	3.03741	3.03547
$\overline{M}_{yc}$	3.30007	3.28833	3.45242	3.42967	3.57844	3.54900
$\overline{M}_{xyc}$	0.37852	0.38755	0.35755	0.35505	0.22406	0.22264

[a] $W_c = w_c D/(10^{-3}\times qa^4)$; $W_m = w_m D/(10^{-3}\times qa^4)$; $\overline{M}_{xc} = M_{xc}/(10^{-2}\times qa^2)$; $\overline{M}_{yc} = M_{yc}/(10^{-2}\times qa^2)$; $\overline{M}_{xyc} = M_{xyc}/(10^{-2}\times qa^2)$. where w_m is the deflection at the mid-side of $x = 0$.

[b] The finite element results were generated using ANSYS 5.3, shell 93 element was selected and 2821 grid points (actual number of active DOF is 15994) were used.

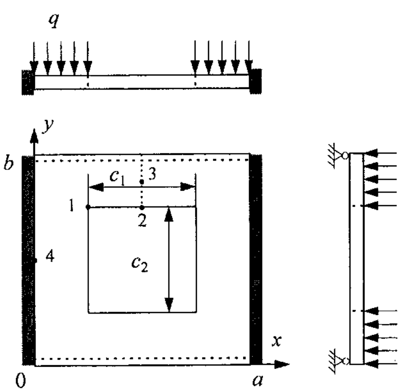

Fig. 6 Uniformly loaded square plate with CSCS outer boundaries and a free central square cutout

all the deflections and moments. This has verified the applicability of the differential quadrature element method in solution of this kind of problems.

4.3 Example 3: A Uniformly Loaded Rectangular Plate with a Rectangular Cutout. The last example given here is to analyze the rectangular plate with the discontinuous geometrical domain such as the cutout by the differential quadrature element method. A uniformly loaded square plate with the CSCS outer boundaries and a free central square cutout as shown in Fig. 6 is considered. The numerical results for the deflections at the three points, 1, 2, and 3, as shown in Fig. 6, the moment, $\bar{M}_x$, and the shear force, $\bar{Q}_x$ at the midpoint of side $x = 0$ (point 4), are tabulated in Table 8. The present differential quadrature element method results are compared with those obtained using finite element method, and again the agreement has been found to be very good.

Table 8 Numerical results for a uniformly loaded square plate with CSCS outer boundaries and a free central square cutout ($c_1 = c_2 = 0.5a$)[a]

h/a	W_1	W_2	W_3	$\overline{M}_{x4}$	$\overline{Q}_{x4}$
0.01	0.62224	1.15595	0.60430	-4.10040	0.30396
FEM[b]	0.63372	1.15888	—	-4.04230	—
0.1	0.76822	1.44426	0.75273	-4.09502	0.31157
FEM[b]	0.77234	1.42645	—	-4.04067	—
0.2	1.13237	2.06526	1.09995	-3.88612	0.30930
FEM[b]	1.13852	2.20142	—	-3.88267	—

[a] $W_1 = w_1 D/(10^{-3}\times qa^4)$; $W_2 = w_2 D/(10^{-3}\times qa^4)$; $W_3 = w_3 D/(10^{-3}\times qa^4)$; $\overline{M}_{x4} = M_{x4}/(10^{-2}\times qa^2)$; $\overline{Q}_{x4} = Q_{x4}/(qa)$. where 1, 2, 3 and 4 stand for the four points on the plate as shown in Fig. 6.

[b] The finite element results were generated using ANSYS 5.3, shell 93 element was selected and 2230 grid points (actual number of active DOF is 12474) were used.

5 Conclusion

In this paper, the two-dimensional differential quadrature element method has been developed for the bending analysis of Reissner-Mindlin plates by combining the domain decomposition method with the two-dimensional differential quadrature method. The reliability of the bending solutions computed in this study using the differential quadrature element method has been established through convergence studies for different boundary conditions in light of the element refinement and the grid point refinement in each element. In addition, the reliability of the differential quadrature element method solutions has been further established by comparing with analytical solutions.

The differential quadrature element method has been successfully applied to analyze several bending problems of Reissner-Mindlin plates with different discontinuities including the discontinuous loading, mixed boundaries, and cutouts. The accuracy and applicability of this method have been examined by comparing with the existing solutions obtained using analytical or other numerical methods. It is found that the differential quadrature element method possesses both the advantages of differential quadrature method and the flexibility of the finite element method.

References

Bert, C. W., and Malik, M., 1996, "Differential quadrature method in computational mechanics: A review," ASME *Applied Mechanics Reviews*, Vol. 49, pp. 1–28.

Bert, C. W., and Malik, M., 1995, "Differential quadrature analysis of free vibration of symmetric cross-ply laminates with shear deformation and rotatory inertia," *Shock and Vibration*, Vol. 2, pp. 321–338.

Bert, C. W., Jang, S. K., and Striz A. G., 1988, "Two new approximate methods for analyzing free vibration of structural components," *AIAA J.*, Vol. 26, pp. 612–618.

Bert, C. W., Jang, S. K., and Striz, A. G., 1989, "Nonlinear bending analysis of orthotropic rectangular plates by the method of differential quadrature," *Computa. Mechanics*, Vol. 5, pp. 217–226.

Civan, F., and Sliepcevich, C. M., 1985, "Application of differential quadrature to solution of pool boiling in cavities," *Proc. of Oklahoma Academy of Science*, Vol. 65, pp. 73–78.

Chen, W., Striz, A. G., and Bert, C. W., 1997, "Free Vibration of High-Accuracy Plate Elements by the Quadrature Element Method," *J. of Sound and Vibration*, Vol. 202, pp. 689–702.

Liew, K. M., Han, J.-B., Xiao, Z. M., and Du, H., 1996, "Differential quadrature method for Mindlin plates on Winkler foundations," *Int. J. Mech. Sci.*, Vol. 38, pp. 405–421.

Mindlin, R. D., 1951, "Influence of Rotatory Inertia and Shear on Flexural Motion of Isotropic, Elastic Plates," Trans. ASME JOURNAL OF APPLIED MECHANICS, Vol. 18, pp. 31–38.

Pandya, M. D., and Sherbourne, A. N., 1991, "Buckling of anisotropic composite plates under stress gradient," *ASCE J. of Engrg. Mechanics*, Vol. 117, pp. 260–275.

Pilkey, W. D., 1994, *Formulas for Stress, Strain, and Structural Matrices*, John Wiley and Sons, New York.

Striz, A. G., Chen, W., and Bert, C. W., 1994, "Static analysis of structures by the quadrature element method (QEM)," *Int. J. Solids Struct.*, Vol. 31, pp. 2807–2818.

Shu, C., and Richards, B. E., 1992, "Parallel simulation of incompressible viscous flows by generalized differential quadrature," *Computing Systems in Engrg.*, Vol. 3, pp. 271–281.

Timoshenko, S. P., and Woinowsky-Krieger, S., 1959, *Theory of Plates and Shells*, 2nd Ed., McGraw-Hill, New York.

Zhen-qiang Cheng[1]
Associate Professor,
Department of Modern Mechanics,
University of Science and
Technology of China
Hefei, Anhui 230026, P. R. China

S. Kitipornchai
Professor,
Department of Civil Engineering,
The University of Queensland,
Brisbane, QLD 4072, Australia

Nonlinear Theory for Composite Laminated Shells With Interfacial Damage

Interfacial damage is incorporated in the proposed nonlinear theory for composite laminated shells. A spring-layer model is employed to characterize damaged interfaces spanning from perfect bonding to different degrees of imperfect bonding in shear. By enforcing compatibility conditions for transverse shear stresses both at interfaces and on two bounding surfaces of a laminated shell, only five unknowns are needed for modeling its behavior. The principle of virtual work is used to derive the governing equations, which are of 14th order in lines of curvature coordinates, variationally self-consistent with seven prescribed boundary conditions. This theory includes the conventional higher-order zigzag model for a perfectly bonded shell as a special case. Numerical results provide a physical understanding of the effect of interfacial damage on bending and buckling responses of composite laminated shells.

1 Introduction

Damage in composite laminates may take many forms at different geometric scales. At the reinforcements-matrix level, damage can include fiber fracture, matrix cracks, and degradation of fiber/matrix interfaces. At the ply level, it can include bond deterioration and nucleation of microcracks pertinent to layer interfaces. In the former case, much micromechanics-based research has been completed. By contrast, research on the effects of damaged composite laminates at the ply level, despite its importance, appears to be in the early stages.

Composite materials are used in all kinds of engineering structures, medical prosthetic devices, electronic circuit boards, and sports equipment. A comprehensive review can be found in the detailed coverage presented by Reddy (1997) for the first time of traditional theories and refined theories of laminated composite materials. Recently, Cheng et al. (1996a, b, 1997) proposed linear and geometrically nonlinear theories for composite laminated plates incorporating interfacial imperfections. Numerical examples revealed the important influence of damaged interfaces on linear bending, buckling, and vibration behavior of laminated plates, as well as on their static large-deflection characteristics of von Karman's type. The well-developed higher-order zigzag theory, or termed as the equivalent single-layer theory (Reddy and Robbins, Jr., 1994), for composite laminated plates with perfect interfaces (Di Sciuva, 1992; Gaudenzi, 1992; Cho and Parmerter, 1992, 1993; He, 1993) can be recovered as a special case of those presented by Cheng et al. (1996a, b, 1997). In a separate development, Schmidt and Librescu (1996) presented a similar theory which was based on a piecewise linear variation of inplane displacements. As an alternative way to assessing the proposed theoretical model using numerical results, the paper made some remarks on several counterparts of general theorems in three-dimensional elasticity.

This paper is an extension of the previous work on plates (Cheng et al., 1996a, b, 1997) to composite laminated shells in general configurations, where the reference surface of the shells has an arbitrary geometry and each lamina is anisotropic and reflectional symmetry of materials is only assumed in surfaces parallel to the shell reference surface. Exact representation of displacement variation through the thickness of a laminated shell renders the incorporation of the interfacial damage, which is then modeled linearly by the use of a spring layer. The requirement for transverse shear stresses being zero on the two bounding surfaces and continuous across each interface is accommodated so that there is no need for the use of shear correction factors.

Although the term "damaged interface" is emphasized in this paper, the proposed theory could also be widely applied with significant ramifications for practical laminated structures, including those in the presence of *interphase*, i.e., a very thin adhesive layer between adjacent laminae. One purpose of the interphase material is to increase the interfacial bonding strength, while another purpose is to reduce the residual stresses generated from curing process so as to prevent premature delamination. Where this theory is applied for such materials, interfacial parameters would be micromechanically estimated and expressed in terms of properties and microstructures of the interphase material.

2 General Expression of Displacements

Consider an undeformed laminated shell, as shown in Fig. 1, consisting of k homogeneous anisotropic layers of uniform thickness in a curvilinear coordinate system $\{\theta^i\}$ $(i = 1, 2, 3)$, where θ^3-axis is normal to the shell surface. For convenience, the undeformed bottom surface of the shell is chosen as the reference surface defined by $\theta^3 = 0$. The bottom surface $(m = 0)$, the $k-1$ interfaces $(m = 1, \ldots, k-1)$ and the top surface $(m = k)$ are denoted by ${}^{(m)}\Omega (m = 0, \ldots, k)$ in the sequence. Thus, the range of the mth layer in the θ^3-direction is $[{}^{(m-1)}h, {}^{(m)}h]$, where ${}^{(m)}h (m = 0, \ldots, k)$ is the distance between ${}^{(m)}\Omega$ and ${}^{(0)}\Omega$. Obviously, ${}^{(0)}h = 0$, ${}^{(k)}h = h$, where h is the total thickness of the shell.

In what follows, a comma followed by a subscript denotes a partial derivative with respect to the corresponding spatial coordinate. The Einsteinian summation convention applies to repeated indices of tensor components, with Latin indices ranging from 1 to 3 while Greek indices over 1 and 2.

The displacement vector $\mathbf{V}(\boldsymbol{\theta})$ of any point of the shell can be expressed as (He, 1994, 1995)

[1] Visiting Fellow, Department of Civil Engineering, The University of Queensland, Brisbane, QLD 4072, Australia.

Contributed by the Applied Mechanics Division of THE AMERICAN SOCIETY OF MECHANICAL ENGINEERS for publication in the ASME JOURNAL OF APPLIED MECHANICS.

Discussion on the paper should be addressed to the Technical Editor, Professor Lewis T. Wheeler, Department of Mechanical Engineering, University of Houston, Houston, TX 77204-4792, and will be accepted until four months after final publication of the paper itself in the ASME JOURNAL OF APPLIED MECHANICS.

Manuscript received by the ASME Applied Mechanics Division, July 30, 1997; final revision, Nov. 3, 1997. Associate Technical Editor: J. N. Reddy.

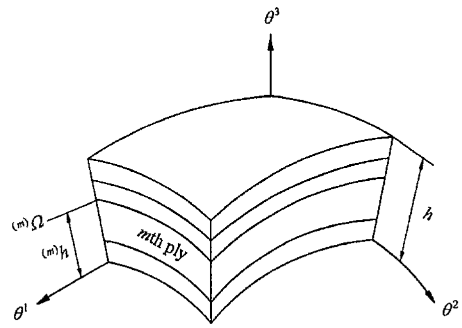

Fig. 1 Geometry of a laminated shell

$$\mathbf{V}(\boldsymbol{\theta}) = \sum_{m=0}^{k-1} [{}^{(m+1)}\mathbf{V}(\boldsymbol{\theta}) - {}^{(m)}\mathbf{V}(\boldsymbol{\theta})]H(\theta^3 - {}^{(m)}h), \quad (1)$$

where ${}^{(m)}\mathbf{V}(\boldsymbol{\theta})$ is the displacement vector of the mth layer with ${}^{(0)}\mathbf{V}(\boldsymbol{\theta}) \equiv \mathbf{0}$, and $H(\theta^3 - {}^{(m)}h)$ is the Heaviside step function. Taylor expansion of ${}^{(m)}\mathbf{V}(\boldsymbol{\theta})$ $(m = 0, \ldots, k)$ with respect to θ^3 gives an alternative form of Eq. (1) as

$$\mathbf{V}(\boldsymbol{\theta}) = \sum_{m=1}^{k-1} \sum_{n=0}^{\infty} {}^{(m)}\mathbf{U}^{(n)}(\theta^1, \theta^2)(\theta^3 - {}^{(m)}h)^n H(\theta^3 - {}^{(m)}h), \quad (2)$$

$${}^{(m)}\mathbf{U}^{(n)}(\theta^1, \theta^2) = \frac{1}{n!} {}^{(m+1)}\mathbf{V}^{(n)}(\theta^1, \theta^2, {}^{(m)}h) - \frac{1}{n!} {}^{(m)}\mathbf{V}^{(n)}(\theta^1, \theta^2, {}^{(m)}h), \quad (3)$$

where the following term has been retained, but excluded for perfect interfaces as by He (1994, 1995),

$${}^{(m)}\Delta\mathbf{V}(\theta^1, \theta^2) \equiv {}^{(m)}\mathbf{U}^{(0)}(\theta^1, \theta^2) = {}^{(m+1)}\mathbf{V}(\theta^1, \theta^2, {}^{(m)}h) - {}^{(m)}\mathbf{V}(\theta^1, \theta^2, {}^{(m)}h). \quad (4)$$

This term implies that the displacements are allowed to be discontinuous across each interface, so as to provide a possible incorporation of damaged interfaces of laminated shells, such as bond deterioration or even delamination. The case of perfect bonding corresponds to this term being a null vector.

Let the covariant base vectors $\mathbf{a}_i$ and contravariant base vectors $\mathbf{a}^i$ of the reference surface and the space covariant base vectors $\mathbf{g}_i$ and contravariant base vectors $\mathbf{g}^i$ be introduced in the undeformed state of the shell, with

$$\mathbf{a}^3 = \mathbf{a}_3 = \frac{\mathbf{a}_1 \times \mathbf{a}_2}{|\mathbf{a}_1 \times \mathbf{a}_2|}, \quad \mathbf{g}_\alpha = \mu_\alpha^\beta \mathbf{a}_\beta, \quad \mathbf{g}_3 = \mathbf{a}_3,$$
$$\mathbf{g}^\beta = (\mu^{-1})_\alpha^\beta \mathbf{a}^\alpha, \quad \mathbf{g}^3 = \mathbf{a}^3, \quad (5)$$

where μ_α^β denotes the shifter tensor generalized for composite laminated shells which, as shown by Naghdi (1963), is nonsingular. μ_α^β and its inverse, denoted by $(\mu^{-1})_\alpha^\beta$, are expressed as

$$\mu_\alpha^\beta = \delta_\alpha^\beta - \theta^3 b_\alpha^\beta, \quad (\mu^{-1})_\alpha^\beta = \frac{1}{\mu} \epsilon^{\beta\lambda}\epsilon_{\alpha\nu}\mu_\lambda^\nu, \quad (6)$$

where δ_α^β is the mixed Kronecker delta function, $\epsilon^{\beta\lambda}$ and $\epsilon_{\alpha\nu}$ are the two-dimensional permutation tensors, and

$$\mu = \det(\mu_\alpha^\beta), \quad b_\alpha^\beta = b_{\alpha\gamma}a^{\beta\gamma},$$
$$b_{\alpha\beta} = -\mathbf{a}_\alpha \cdot \mathbf{a}_{3,\beta} = \mathbf{a}_3 \cdot \mathbf{a}_{\alpha,\beta}, \quad (7)$$

in which b_α^β is the mixed curvature tensor and $b_{\alpha\beta}$ is the coefficient of second fundamental form of the reference surface ${}^{(0)}\Omega$, according to differential geometry. The components of the metric tensor for the undeformed reference surface are

$$a_{\alpha\beta} = \mathbf{a}_\alpha \cdot \mathbf{a}_\beta, \quad a_{\alpha 3} = \mathbf{a}_\alpha \cdot \mathbf{a}_3 = 0, \quad a_{33} = \mathbf{a}_3 \cdot \mathbf{a}_3 = 1,$$
$$a^{\alpha\beta} = \mathbf{a}^\alpha \cdot \mathbf{a}^\beta, \quad a^{\alpha 3} = \mathbf{a}^\alpha \cdot \mathbf{a}^3 = 0, \quad a^{33} = \mathbf{a}^3 \cdot \mathbf{a}^3 = 1, \quad (8)$$

where $a_{\alpha\beta}$ is also called the coefficient of the first fundamental form of the reference surface in the theory of the differential geometry. The components of the spatial metric tensor for the shell space are connected with their counterparts of the reference surface by

$$g_{\alpha\beta} = \mu_\alpha^\omega \mu_\beta^\rho a_{\omega\rho}, \quad g_{\alpha 3} = g^{\alpha 3} = 0, \quad g_{33} = g^{33} = 1. \quad (9)$$

The displacement vector $\mathbf{V}(\boldsymbol{\theta})$ of the shell can be expressed in terms of the spatial and their shifted components as

$$\mathbf{V} = V_\alpha \mathbf{g}^\alpha + V_3 \mathbf{g}^3 = v_\alpha \mathbf{a}^\alpha + v_3 \mathbf{a}^3, \quad (10)$$

$$V_\alpha = \mu_\alpha^\beta v_\beta, \quad V_3 = v_3. \quad (11)$$

The relationships between covariant differentiation of the space components of the displacement tensor and their surface counterparts referred to ${}^{(0)}\Omega$ are expressed as (Naghdi, 1963; Librescu, 1975)

$$V_{\alpha\|\beta} = \mu_\alpha^\nu (v_{\nu|\beta} - b_{\nu\beta}v_3), \quad V_{\alpha\|3} = \mu_\alpha^\nu v_{\nu,3},$$
$$V_{3\|\alpha} = v_{3,\alpha} + b_\alpha^\nu v_\nu, \quad V_{3\|3} = v_{3,3}, \quad (12)$$

where the double and single vertical lines designate covariant differentiation with respect to the space and surface metrics, respectively.

In view of Eq. (10), Eq. (2) can be rewritten in the following surface component form:

$$v_j(\theta^i) = \sum_{m=0}^{k-1} \sum_{n=0}^{\infty} {}^{(m)}u_j^{(n)}(\theta^\alpha)(\theta^3 - {}^{(m)}h)^n H(\theta^3 - {}^{(m)}h). \quad (13)$$

3 Formulation of Boundary Value Problem

Interfacial damage between adjacent laminae can be modeled by a mathematical surface across which material properties change discontinuously, with the interfacial tractions being continuous while the displacements are discontinuous (see, e.g., Aboudi, 1987; Achenbach and Zhu, 1989; Benveniste and Dvorak, 1990; Dvorak and Benveniste, 1992; Hashin, 1990; Qu, 1993a, b; Zhong and Meguid, 1996). To characterize the damaged interfaces in the evaluation of composite behavior, one simple approach is to use a linear spring-layer model as follows:

$$\sigma^{\beta 3}(\theta^\rho, {}^{(m)}h^+) = \sigma^{\beta 3}(\theta^\rho, {}^{(m)}h^-),$$
$$\sigma^{33}(\theta^\rho, {}^{(m)}h^+) = \sigma^{33}(\theta^\rho, {}^{(m)}h^-),$$
$$(m = 1, \ldots, k-1), \quad (14)$$
$${}^{(m)}\Delta V_\alpha = {}^{(m)}R_{\alpha\beta}(\theta^\rho)\sigma^{\beta 3}(\theta^\rho, {}^{(m)}h),$$
$${}^{(m)}\Delta V_3 = {}^{(m)}R_{33}(\theta^\rho)\sigma^{33}(\theta^\rho, {}^{(m)}h),$$
$$(m = 1, \ldots, k-1), \quad (15)$$

where σ^{ij} is the component of the second Piola-Kirchhoff stress tensor, ${}^{(m)}R_{\alpha\beta}$ and ${}^{(m)}R_{33}$ in Eq. (15) represent the spatial compliance coefficients of the mth spring-layer interface ${}^{(m)}\Omega$. It is clear from Eq. (15) that a perfect interface corresponds to ${}^{(m)}R_{\alpha\beta} = 0$ and ${}^{(m)}R_{33} = 0$, while ${}^{(m)}R_{\alpha\beta} \to \infty$ and ${}^{(m)}R_{33} \to \infty$ represent complete debonding, i.e., $\sigma^{i3} = 0$ on ${}^{(m)}\Omega$. From this point of view, a damaged interface may be modeled by finite values of ${}^{(m)}R_{\alpha\beta}$ and ${}^{(m)}R_{33}$. The fact that the interface parameters ${}^{(m)}R_{\alpha\beta}$ and ${}^{(m)}R_{33}$ depend upon θ^ρ implies that the degree of the interfacial damage over ${}^{(m)}\Omega(m = 1, \ldots, k-1)$ may be nonuniform.

When ${}^{(m)}R_{33} = 0$ in conjunction with finite values of ${}^{(m)}R_{\alpha\beta}$, this constitutive relation of the interface ${}^{(m)}\Omega$ means relative sliding between the two adjacent surfaces, but no separation.

Table 1 Central deflection and stresses of an infinitely long three-ply (90 deg/0 deg/90 deg) laminated circular cylindrical panel under sinusoidal loading ($\Phi = \pi/3$)

S		Ren (1987)	Xavier *et al.*(1993)	$\bar{R}=0$	$\bar{R}=0.2$	$\bar{R}=0.4$	$\bar{R}=0.6$
2	$\bar{V}_{(3)}(\frac{\pi}{6},0)$	1.436	1.0878	1.10533	1.20259	1.25766	1.28591
4		0.457	0.4410	0.44452	0.54059	0.63062	0.71158
10		0.144	0.1426	0.14291	0.16496	0.18957	0.21633
50		0.0808	0.0810	0.08078	0.08170	0.08276	0.08397
100		0.0787	0.0788	0.07856	0.07879	0.07906	0.07936
500		0.0773	0.0779	0.07767	0.07768	0.07769	0.07770
2	$-\bar{\sigma}_{(11)}(\frac{\pi}{6},0)$	0.0347	0.04901	0.04922	0.05430	0.05758	0.05962
4		0.0177	0.01978	0.01977	0.02294	0.02599	0.02879
10		0.0100	0.01005	0.01003	0.01064	0.01133	0.01208
50		0.0080	0.00801	0.00799	0.00801	0.00804	0.00807
100		0.0079	0.00789	0.00787	0.00787	0.00788	0.00789
500		0.0078	0.00782	0.00779	0.00779	0.00779	0.00779
2	$\bar{\sigma}_{(11)}(\frac{\pi}{6},h)$	0.0871	0.01974	0.02006	0.02207	0.02341	0.02429
4		0.0293	0.01352	0.01357	0.01553	0.01741	0.01915
10		0.0115	0.00896	0.00895	0.00944	0.01001	0.01064
50		0.0079	0.00785	0.00783	0.00785	0.00788	0.00791
100		0.0078	0.00781	0.00779	0.00779	0.00780	0.00781
500		0.0077	0.00779	0.00778	0.00778	0.00778	0.00778
2	$-\bar{\sigma}_{(22)}(\frac{\pi}{6},0)$	3.467	4.886	4.92227	5.43001	5.75782	5.96208
4		1.772	1.972	1.97720	2.29398	2.59858	2.87875
10		0.995	1.003	1.00324	1.06380	1.13256	1.20831
50		0.798	0.799	0.79859	0.80091	0.80365	0.80680
100		0.786	0.787	0.78675	0.78733	0.78800	0.78878
500		0.780	0.779	0.77925	0.77927	0.77930	0.77933
2	$\bar{\sigma}_{(22)}(\frac{\pi}{6},h)$	2.463	1.968	2.00591	2.20682	2.34146	2.42922
4		1.367	1.350	1.35745	1.55258	1.74105	1.91505
10		0.897	0.894	0.89452	0.94436	1.00102	1.06350
50		0.782	0.783	0.78267	0.78490	0.78753	0.79056
100		0.781	0.779	0.77891	0.77947	0.78014	0.78090
500		0.768	0.778	0.77769	0.77771	0.77774	0.77777
2	$\bar{\sigma}_{(23)}(0,\frac{h}{2})$	0.394	0.200	0.19779	0.12417	0.07401	0.04069
4		0.476	0.447	0.44602	0.39784	0.35088	0.30719
10		0.525	0.524	0.52388	0.51370	0.50204	0.48912
50		0.526	0.525	0.52533	0.52491	0.52441	0.52384
100		0.523	0.524	0.52340	0.52330	0.52318	0.52303
500		0.525	0.522	0.52153	0.52153	0.52152	0.52152

Furthermore, the free-sliding case can be achieved by setting ${}^{(m)}R_{\alpha\beta} \to \infty$ with ${}^{(m)}R_{33} = 0$. When ${}^{(m)}\Delta V_3 < 0$, this mathematical model results in a physically impossible phenomenon because one constituent would have to penetrate another, as noticed by Achenbach and Zhu (1989) and Qu (1993b). This violates the compatibility requirements and therefore the model is apparently unreasonable for such a case. However, the normal stress σ^{33} for the shell problem under consideration is assumed to be negligibly small compared with other stress components, so that it is ignored in this paper as in most other theories for plates and shells. This automatically leads to an identity Eq. $(14)_2$ and a vanishing displacement jump ${}^{(m)}\Delta V_3$ from Eq. $(15)_2$, regardless of the value of the interface parameter ${}^{(m)}R_{33}$. Therefore it seems reasonable to characterize interfacial damage in shear by use of this spring layer model.

For most shell problems transverse normals do not experience significant extensions and therefore it is assumed, without significant loss of accuracy, that v_3 is independent of the thickness coordinate. Although theories higher than third order for laminated shells may be proposed on the basis of the general representation of the displacement variation (13), they are not used in the absence of debonding because the extra accuracy achieved is so little that the effort required to solve the equations is not justified. Therefore, in view of ${}^{(m)}\Delta v_3 = {}^{(m)}\Delta V_3 = 0$, $(m = 1, \ldots, k-1)$ from Eqs. $(11)_2$ and $(15)_2$, the displacement model of the shell can be approximately expressed by truncating Eq. (13) as

$$v_\alpha(\theta^i) = u_\alpha + \psi_\alpha\theta^3 + \varphi_\alpha(\theta^3)^2 + \eta_\alpha(\theta^3)^3 + \sum_{m=1}^{k-1} [{}^{(m)}\Delta v_\alpha + {}^{(m)}u_\alpha(\theta^3 - {}^{(m)}h)]H(\theta^3 - {}^{(m)}h),$$

$$v_3(\theta^i) = u_3, \qquad (16)$$

where ${}^{(0)}u_i^{(0)}$, ${}^{(0)}u_\alpha^{(1)}$, ${}^{(0)}u_\alpha^{(2)}$, ${}^{(0)}u_\alpha^{(3)}$, ${}^{(m)}u_\alpha^{(0)}$, and ${}^{(m)}u_\alpha^{(1)}$ in Eq. (13) have been replaced by the quantities u_i, ψ_α, φ_α, η_α, ${}^{(m)}\Delta v_\alpha$, and ${}^{(m)}u_\alpha$, respectively. Of course, theories developed for calculating an extreme case of damage, i.e., general delamination, need more terms than are retained by Eqs. (16) (see Gu and Chattopadhyay, 1996).

Since small initial deviations from perfect geometry may have a significant influence on responses of structures, the existence of an initial stress-free geometric imperfection, which refers to the transverse displacement V_3^0, is assumed. By convention, the transverse deflection V_3 is then measured from the imperfect surface. The Lagrangian strain components e_{ij}, in the sense of von Karman partial nonlinearity, and the second Piola-Kirchhoff stress components of the shell can be obtained from (see Librescu, 1975)

$$e_{\alpha\beta} = \tfrac{1}{2}(V_{\alpha\|\beta} + V_{\beta\|\alpha} + V_{3\|\alpha}V_{3\|\beta} + V_{3\|\alpha}V^0_{3\|\beta} + V^0_{3\|\alpha}V_{3\|\beta}),$$

$$e_{\alpha3} = \tfrac{1}{2}(V_{\alpha\|3} + V_{3\|\alpha}), \quad e_{33} = V_{3\|3}, \qquad (17)$$

$$\sigma^{\alpha\beta} = H^{\alpha\beta\omega\rho}e_{\omega\rho}, \quad \sigma^{\alpha3} = 2E^{\alpha3\omega3}e_{\omega3}, \qquad (18)$$

where E^{ijkl} is the spatial component of the elasticity tensor associated with an elastic anisotropic body, and $H^{\alpha\beta\omega\rho} = E^{\alpha\beta\omega\rho} - E^{\alpha\beta33}E^{33\omega\rho}/E^{3333}$. Equations (18) hold valid only under the assumptions that each layer possesses elastic symmetry with respect to surfaces parallel to the reference surface and that σ^{33} is vanishingly small.

The compatibility conditions of transverse shear stresses on the two bounding surfaces of the shell, as well as the relationships characterizing the damaged interfaces, are now used to reduce the number of unknowns in Eq. $(16)_1$. The absence of tangential tractions on ${}^{(0)}\Omega$ and ${}^{(k)}\Omega$ yields, through Eqs. (16), $(12)_{2,3}$, $(17)_2$, and $(18)_2$,

Table 2 Central deflection and stresses of an infinitely long two-ply (0 deg/90 deg) laminated circular cylindrical panel under sinusoidal loading ($\Phi = \pi/3$)

S		Ren (1987)	Xavier *et al.* (1993)	$\bar{R} = 0$	$\bar{R} = 0.2$	$\bar{R} = 0.4$	$\bar{R} = 0.6$
2	$\bar{V}_{(3)}(\frac{\pi}{6},0)$	2.079	1.534	1.74234	1.79954	1.83270	1.84517
4		0.854	0.7196	0.75743	0.78164	0.80454	0.82582
10		0.493	0.4730	0.47754	0.48173	0.48608	0.49057
50		0.409	0.4090	0.40836	0.40852	0.40869	0.40887
100		0.403	0.4039	0.40312	0.40316	0.40321	0.40325
500		0.399	0.4002	0.39943	0.39943	0.39943	0.39944
2	$-\bar{\sigma}_{(11)}(\frac{\pi}{6},0)$	0.1610	0.07760	0.09546	0.08874	0.08266	0.07740
4		0.0960	0.07026	0.07376	0.07146	0.06911	0.06675
10		0.0693	0.06490	0.06528	0.06487	0.06443	0.06395
50		0.0601	0.06000	0.05991	0.05989	0.05987	0.05985
100		0.0592	0.05930	0.05916	0.05916	0.05915	0.05915
500		0.0587	0.05867	0.05855	0.05855	0.05855	0.05855
2	$\bar{\sigma}_{(11)}(\frac{\pi}{6},h)$	0.0960	0.03814	0.03831	0.04018	0.04168	0.04282
4		0.0407	0.02694	0.02692	0.02759	0.02826	0.02891
10		0.0250	0.02285	0.02281	0.02293	0.02306	0.02320
50		0.0218	0.02181	0.02168	0.02168	0.02169	0.02169
100		0.0216	0.02164	0.02159	0.02159	0.02159	0.02160
500		0.0215	0.02158	0.02153	0.02153	0.02153	0.02153
2	$-\bar{\sigma}_{(22)}(\frac{\pi}{6},0)$	0.644	0.310	0.38184	0.35498	0.33065	0.30961
4		0.384	0.281	0.29504	0.28584	0.27643	0.26701
10		0.277	0.260	0.26114	0.25949	0.25771	0.25582
50		0.240	0.240	0.23963	0.23956	0.23949	0.23941
100		0.237	0.237	0.23665	0.23664	0.23662	0.23660
500		0.234	0.234	0.23421	0.23421	0.23421	0.23421
2	$\bar{\sigma}_{(22)}(\frac{\pi}{6},h)$	3.348	3.803	3.83110	4.01756	4.16790	4.28171
4		2.511	2.687	2.69225	2.75929	2.82594	2.89095
10		2.245	2.279	2.28135	2.29339	2.30617	2.31965
50		2.165	2.166	2.16784	2.16833	2.16885	2.16942
100		2.158	2.158	2.15913	2.15925	2.15938	2.15952
500		2.153	2.151	2.15297	2.15298	2.15298	2.15299
2	$\bar{\sigma}_{(23)}(0,\frac{3h}{4})$	0.851	1.133	1.14997	1.20927	1.26200	1.30673
4		0.871	0.987	0.97451	0.99246	1.01086	1.02933
10		0.879	0.899	0.89870	0.90172	0.90497	0.90846
50		0.869	0.870	0.87028	0.87040	0.87053	0.87067
100		0.867	0.867	0.86732	0.86735	0.86739	0.86742
500		0.865	0.865	0.86503	0.86503	0.86503	0.86503

$$\psi_\alpha = -u_{3,\alpha} - b_\alpha^\beta u_\beta,$$

$$-\frac{3}{2h}\hat{\mu}_\omega^\beta \eta_\beta = \frac{1}{h^2}\left(\delta_\omega^\beta - \frac{h}{2} b_\omega^\beta\right)\varphi_\beta + \frac{1}{2h^3}\sum_{m=1}^{k-1}[b_\omega^{\beta(m)}\Delta v_\beta + (\delta_\omega^\beta - {}^{(m)}hb_\omega^\beta)^{(m)}u_\beta], \quad (19)$$

where $\hat{\mu}_\omega^\beta = \mu_\omega^\beta|_{\theta^3=2h/3}$ with its determinant $\hat{\mu} \neq 0$ as proved by Naghdi (1963). Therefore, Eq. $(19)_2$ gives

$$\eta_\alpha = d_\alpha^\beta \varphi_\beta + \sum_{m=1}^{k-1}(e_\alpha^{\beta(m)}\Delta v_\beta + {}^{(m)}f_\alpha^{\beta(m)}u_\beta), \quad (20)$$

in which

$$d_\alpha^\beta = \epsilon_{\alpha\lambda}\epsilon^{\omega\nu}(2hb_\nu^\lambda - 3\delta_\nu^\lambda)(2\delta_\omega^\beta - hb_\omega^\beta)/(9h\hat{\mu}),$$
$$e_\alpha^\beta = \epsilon_{\alpha\lambda}\epsilon^{\omega\nu}(2hb_\nu^\lambda - 3\delta_\nu^\lambda)b_\omega^\beta/(9h^2\hat{\mu}),$$
$${}^{(m)}f_\alpha^\beta = \epsilon_{\alpha\lambda}\epsilon^{\omega\nu}(2hb_\nu^\lambda - 3\delta_\nu^\lambda)(\delta_\omega^\beta - {}^{(m)}hb_\omega^\beta)/(9h^2\hat{\mu}). \quad (21)$$

The conditions $(14)_1$ and $(15)_1$ for damaged interfaces lead to the following $4(k-1)$ linearly algebraic equations involving the $4(k-1)$ unknowns ${}^{(i)}u_\alpha$ and ${}^{(i)}\Delta v_\alpha$, $(i = 1, \ldots, k-1)$, through Eqs. (16), $(19)_1$, (20), (11), $(12)_{2,3}$, $(17)_2$, $(18)_2$, $(14)_1$, and $(15)_1$:

$$({}^{(i+1)}E^{\alpha3\omega3} - {}^{(i)}E^{\alpha3\omega3})\{[2\delta_\omega^{\beta(i)}h - b_\omega^{\beta(i)}h^2 + d_\lambda^\beta(3\delta_\omega^{\lambda(i)}h^2 - 2b_\omega^{\lambda(i)}h^3)]\varphi_\beta + \sum_{m=1}^{i}[b_\omega^{\beta(m)}\Delta v_\beta + (\delta_\omega^\beta - {}^{(m)}hb_\omega^\beta)^{(m)}u_\beta] + (3\delta_\omega^{\lambda(i)}h^2 - 2b_\omega^{\lambda(i)}h^3)\sum_{m=1}^{k-1}(e_\lambda^{\beta(m)}\Delta v_\beta + {}^{(m)}f_\lambda^{\beta(m)}u_\beta)\} + {}^{(i)}E^{\alpha3\omega3}[b_\omega^{\beta(i)}\Delta v_\beta + (\delta_\omega^\beta - {}^{(i)}hb_\omega^\beta)^{(i)}u_\beta] = 0,$$

$${}^{(i)}\mu_\rho^{\alpha(i)}\Delta v_\alpha = {}^{(i)}R_{\rho\nu}(\theta^\rho)^{(\mathrm{bi}+1)}E^{\nu3\omega3}\{[2\delta_\omega^{\beta(i)}h - b_\omega^{\beta(i)}h^2 + d_\lambda^\beta(3\delta_\omega^{\lambda(i)}h^2 - 2b_\omega^{\lambda(i)}h^3)]\varphi_\beta + \sum_{m=1}^{i}[b_\omega^{\beta(m)}\Delta v_\beta + (\delta_\omega^\beta - {}^{(m)}hb_\omega^\beta)^{(m)}u_\beta] + (3\delta_\omega^{\lambda(i)}h^2 - 2b_\omega^{\lambda(i)}h^3)\sum_{m=1}^{k-1}(e_\lambda^{\beta(m)}\Delta v_\beta + {}^{(m)}f_\lambda^{\beta(m)}u_\beta)\}, \quad (i = 1, \ldots, k-1), \quad (22)$$

where ${}^{(i)}\mu_\rho^\alpha = \mu_\rho^\alpha|_{\theta^3={}^{(i)}h}$. These equations determine the relationship between ${}^{(i)}u_\alpha$, ${}^{(i)}\Delta v_\alpha$ and φ_λ as

$${}^{(i)}u_\alpha = {}^{(i)}a_\alpha^\lambda \varphi_\lambda, \quad {}^{(i)}\Delta v_\alpha = {}^{(i)}c_\alpha^\lambda \varphi_\lambda, \quad (i = 1, \ldots, k-1), \quad (23)$$

in which the coefficients ${}^{(i)}a_\alpha^\lambda$ and ${}^{(i)}c_\alpha^\lambda$ depend only on the material elasticity properties and geometry of each lamina and the characteristics of the interfacial damage.

Table 3 Critical buckling load $\bar{M}$ for a three-ply (90 deg/0 deg/90 deg) laminated circular cylindrical panel ($S = 4$, $L/h = 20$, $\Phi = \pi/3$)

λ	Xavier *et al.* (1995)	$\bar{R} = 0$	$\bar{R} = 0.2$	$\bar{R} = 0.4$	$\bar{R} = 0.6$
0.1	5.3829	5.42679	4.10149	3.61733	3.45825
0.5	4.6339	4.63564	3.74557	3.24852	2.95808
1.0	4.0960	4.06401	3.34937	2.87716	2.55433
5.0	3.1263	3.02073	2.67520	2.38744	2.14638

Table 4 Critical buckling load $\bar{M}$ for a two-ply (90 deg/0 deg) laminated circular cylindrical panel ($S = 4$, $L/h = 20$, $\Phi = \pi/3$)

λ	Xavier *et al.* (1995)	$\bar{R} = 0$	$\bar{R} = 0.2$	$\bar{R} = 0.4$	$\bar{R} = 0.6$
0.1	5.2566	5.17588	5.17055	5.16553	5.16082
0.5	4.5219	4.03686	3.98506	3.94384	3.91279
1.0	3.3517	3.16232	3.07356	2.99694	2.93187
5.0	1.7319	1.66979	1.57971	1.49615	1.41912

Substitution of Eqs. $(19)_1$, (20), and (23) into Eq. $(16)_1$ yields the following displacement expression:

$$v_\alpha = \mu_\alpha^\beta u_\beta - \theta^3 u_{3,\alpha} + h_\alpha^\beta \varphi_\beta, \tag{24}$$

in which

$$h_\alpha^\beta \equiv h_\alpha^\beta(\theta^i) = \delta_\alpha^\beta(\theta^3)^2 + g_\alpha^\beta(\theta^3)^3 + \sum_{m=1}^{k-1} [{}^{(m)}c_\alpha^\beta + {}^{(m)}a_\alpha^\beta(\theta^3 - {}^{(m)}h)]H(\theta^3 - {}^{(m)}h), \tag{25}$$

$$g_\alpha^\beta = d_\alpha^\beta + \sum_{m=1}^{k-1} (e_\alpha^{\lambda(m)} c_\lambda^\beta + {}^{(m)}f_\alpha^{\lambda(m)} a_\lambda^\beta). \tag{26}$$

By using the displacement expressions (24) and $(16)_2$, the associated strain and stress components can be obtained from Eqs. (17) and (18) but are not explicitly given here.

From the principle of virtual work, the nonlinear static fundamental equations are obtained as

$$\begin{aligned} &M^{(1)\alpha\beta}{}_{|\beta} - N^{(1)\alpha} - R^{(1)\alpha} = 0, \\ &M^{(2)\alpha\beta}{}_{|\alpha\beta} + N^{(1)3} + R^{(2)\alpha}{}_{|\alpha} + P^3 = 0, \\ &M^{(3)\alpha\beta}{}_{|\beta} - N^{(2)\alpha} - N^{(3)\alpha} - R^{(3)\alpha} = 0, \end{aligned} \tag{27}$$

and the associated boundary conditions are specified as

$$\begin{aligned} &n_\beta M^{(1)\alpha\beta}, \quad \text{or} \quad u_\alpha, \\ &n_\beta(M^{(2)\beta\alpha}{}_{|\alpha} + R^{(2)\beta}), \quad \text{or} \quad u_3, \\ &n_\beta M^{(3)\alpha\beta}, \quad \text{or} \quad \varphi_\alpha, \\ &n_\beta M^{(2)\alpha\beta}, \quad \text{or} \quad u_{3,\alpha}, \end{aligned} \tag{28}$$

where

$$[N^{(1)\alpha}, N^{(2)\alpha}, N^{(1)3}] = \int_0^h \sigma^{\lambda\beta}\mu_\lambda^\nu [\mu_{\nu|\beta}^\alpha, h_{\nu|\beta}^\alpha, b_{\nu\beta}]\mu d\theta^3,$$

$$N^{(3)\alpha} = \int_0^h \sigma^{\lambda 3}(\mu_\lambda^\nu h_{\nu,3}^\alpha + b_\lambda^\nu h_\nu^\alpha)\mu d\theta^3,$$

$$[M^{(1)\alpha\beta}, M^{(2)\alpha\beta}, M^{(3)\alpha\beta}] = \int_0^h \sigma^{\lambda\beta}\mu_\lambda^\nu [\mu_\nu^\alpha, \theta^3\delta_\nu^\alpha, h_\nu^\alpha]\mu d\theta^3,$$

$$[R^{(1)\alpha}, R^{(2)\alpha}, R^{(3)\alpha}] = \int_0^h \sigma^{\lambda\beta}(V_{3\|\lambda} + V_{3\|\lambda}^0)[b_\beta^\nu \mu_\nu^\alpha, \mu_\beta^\alpha, b_\beta^\nu h_\nu^\alpha]\mu d\theta^3, \tag{29}$$

$$P^3 = {}^{(k)}\mu^{(k)}p^3 + {}^{(0)}p^3, \tag{30}$$

with ${}^{(0)}p^3$ and ${}^{(k)}p^3$ denoting normal loads exerted on the bottom surface ${}^{(0)}\Omega$ and top surface ${}^{(k)}\Omega$, respectively.

The set of governing Eqs. (27), if expressed in terms of five generalized displacement functions u_i and φ_α in lines of curvature coordinates (ensuring $a_{12} = b_{12} = 0$), can be shown to have 14th order, which is variationally self-consistent with the seven prescribed boundary conditions (28). For brevity, however, the displacement-based governing equations are not explicitly given herein.

An appropriate simplification $\mu_\alpha^\beta \to \delta_\alpha^\beta$ can be taken for shallow shells. As a result,

$$g_{\alpha\beta} \to a_{\alpha\beta}, \quad g^{\alpha\beta} \to a^{\alpha\beta},$$

$$\mu = \sqrt{\frac{g}{a}} = 1 - 2H\theta^3 + K(\theta^3)^2 \to 1, \tag{31}$$

where $g = \det(g_{ij})$ and $a = \det(a_{ij})$, while $H = \frac{1}{2}b_\alpha^\alpha$ and $K = \det(b_\alpha^\beta)$ denote the mean curvature and the Gaussian curvature of the reference surface ${}^{(0)}\Omega$, respectively.

By collapsing the general shell theory presented here to the flat-plate limit, the theory given by Cheng et al. (1996b) is recovered. As another limit case where the interfacial parameters and the initial imperfection vanish, this theory exactly reduces to the one given by He (1995) for perfectly bonded shells, which is also similar to those given by Di Sciuva and Icardi (1993) and Xavier et al. (1993).

4 Illustrative Examples and Discussion

In the case of flat laminated plates, the influence of interfacial damage on the global and local behavior of composite laminates has been reported by Cheng et al. (1996a, b, 1997). This work is an extension to examine the behavior of composite laminated shells featuring interfacial damage. Because of the complexity of the governing equations, a simple example, a circular cylindrical laminated panel with inner radius r_0, length L, and central angle Φ, is used to verify the primary contribution of this theory. The panel is simply supported at edges $\theta^1 = 0, L$ and $\theta^2 = 0, \Phi$. Uniform interfacial damage is assumed. Each lamina has the following stiffness properties:

$$\begin{aligned} &E_L/E_T = 25, \quad G_{LT}/E_T = 0.5, \\ &G_{TT}/E_T = 0.2, \quad \nu_{LT} = \nu_{TT} = 0.25, \end{aligned} \tag{32}$$

where E is the tensile modulus, G is the shear modulus, ν is Poisson's ratio, and the subscripts L and T refer to the directions parallel and normal to the fibers, respectively. Unless specified otherwise, each lamina has same thickness.

Under the action of normal pressure ${}^{(k)}p^3 = p_0 \sin(\pi\theta^1/L) \sin(\pi\theta^2/\Phi)$ on the outer surface of the panel, a closed-form solution of the linear bending problem has the following form:

$$\begin{aligned} &[u_1, \varphi_1] = [U_1, \Phi_1] \cos\frac{\pi\theta^1}{L} \sin\frac{\pi\theta^2}{\Phi}, \\ &[u_2, \varphi_2] = [U_2, \Phi_2] \sin\frac{\pi\theta^1}{L} \cos\frac{\pi\theta^2}{\Phi}, \\ &u_3 = U_3 \sin\frac{\pi\theta^1}{L} \sin\frac{\pi\theta^2}{\Phi}. \end{aligned} \tag{33}$$

The solution for linear buckling of such a panel subjected to constant uniaxial edge compression $\hat{M}^{(1)11}$ in the θ^1-direction can be expressed in the same form as (33), such a buckling mode being assumed to enable the present results to be compared with those given by Xavier et al. (1995) for perfect interfaces. From these expressions, exact solutions can easily be given for linear bending and for linear buckling (taking $p_0 \to 0$). For brevity, an overview of the procedure for obtaining closed-form solutions is not given. Of course, the physical components of tensors in the orthogonal bases should be finally transformed by

$$\begin{aligned} &{}^{(m)}R_{\langle\alpha\beta\rangle} = \frac{1}{\sqrt{g_{AA}g_{BB}}}{}^{(m)}R_{\alpha\beta}, \quad V_{\langle i\rangle} = v_{\langle i\rangle} = \frac{1}{\sqrt{a_{II}}}v_i, \\ &e_{\langle ij\rangle} = \frac{1}{\sqrt{g_{II}g_{JJ}}}e_{ij}, \quad \sigma_{\langle ij\rangle} = \sqrt{g_{II}g_{JJ}}\sigma^{ij}, \end{aligned} \tag{34}$$

where an upper case subscript takes the same value as the corresponding lower case index, but no implicit summation applies between them.

Based on a three-phase model and generalized self-consistent scheme for random composites, a theoretical evaluation of interfacial damage parameters was made by Hashin (1991) in terms of interphase characteristics for isotropic deformation. However, such an efficient scheme only applies to random composites. Further theoretical work is needed on the estimation of the interfacial parameters, which requires a knowledge of interfacial microstructures and is beyond the scope of this paper. In an alternative way they can be determined experimentally either by direct shear test or through statistically equivalent macroscopic moduli for imperfectly bonded layered media (Lai

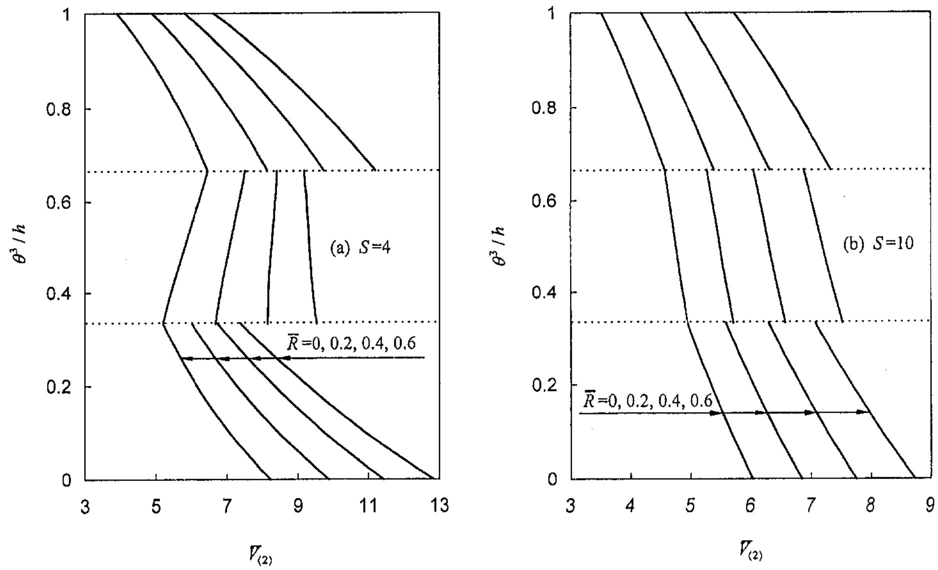

Fig. 2 Through-the-thickness variation of in-surface displacement at $\theta^2 = 0$, for an infinitely long three-ply (90 deg/0 deg/90 deg) laminated circular cylindrical panel ($\Phi = \pi/3$)

et al. 1997), in turn to determine the interfacial damage parameters.

Numerical results are tabulated in Tables 1–4 and plotted in Figs. 2–4 by taking, for each interface, ${}^{(m)}R_{\langle\alpha\beta\rangle} = \delta_{\alpha\beta}\bar{R}h/E_T$, where $\bar{R}$ is a dimensionless quantity. The following dimensionless quantities are used:

$$S = \frac{r_0}{h} + 0.5, \quad \lambda = \frac{{}^{(2)}h}{{}^{(1)}h} - 1,$$

$$\bar{V}_{\langle 2\rangle} = \frac{100E_T}{p_0hS^3} V_{\langle 2\rangle}, \quad \bar{V}_{\langle 3\rangle} = \frac{10E_T}{p_0hS^4} V_{\langle 3\rangle},$$

$$\bar{\sigma}_{\langle 11\rangle} = \frac{1}{p_0S^2}\sigma_{\langle 11\rangle}, \quad \bar{\sigma}_{\langle 22\rangle} = \frac{1}{p_0S^2}\sigma_{\langle 22\rangle},$$

$$\bar{\sigma}_{\langle 23\rangle} = \frac{1}{p_0S}\sigma_{\langle 23\rangle}, \quad \bar{M} = \left(1 - \frac{1}{2S}\right)\frac{\hat{M}^{(1)11}}{E_Th}. \quad (35)$$

The exact three-dimensional elasticity solution for bending of an infinitely long circular cylindrical panel excluding interfacial damage (Ren, 1987) is also used for comparison. As usual, the transverse shear stresses have been obtained through an a posteriori calculation, i.e., $\sigma^{\alpha k}{}_{\|k} = 0$. Some comments on the use of the a posteriori calculation of such components by means of three-dimensional equilibrium and constitutive relations were given by Noor and Peters (1989), Noor and Burton (1990), and Lee and Cao (1996).

The present predictions of deflection and stresses for perfect interfaces ($\bar{R} = 0$), as shown in Tables 1 and 2, are generally close to the exact solution (Ren, 1987) for $S \geq 4$. These bending results and buckling load shown in Tables 3 and 4 are also very close to the results from a slightly different theory for perfect shells (Xavier et al., 1993, 1995) for all values of S, where they have confirmed the high accuracy in comparison with Reddy and Liu's (1985) higher-order theory and some other

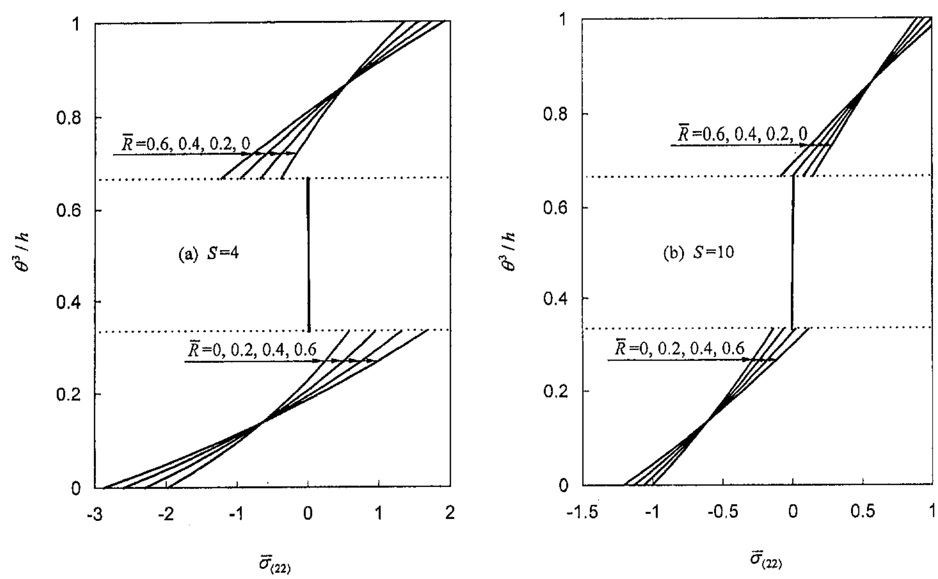

Fig. 3 Through-the-thickness variation of bending stress at $\theta^2 = \Phi/2$, for an infinitely long three-ply (90 deg/0 deg/90 deg) laminated circular cylindrical panel ($\Phi = \pi/3$)

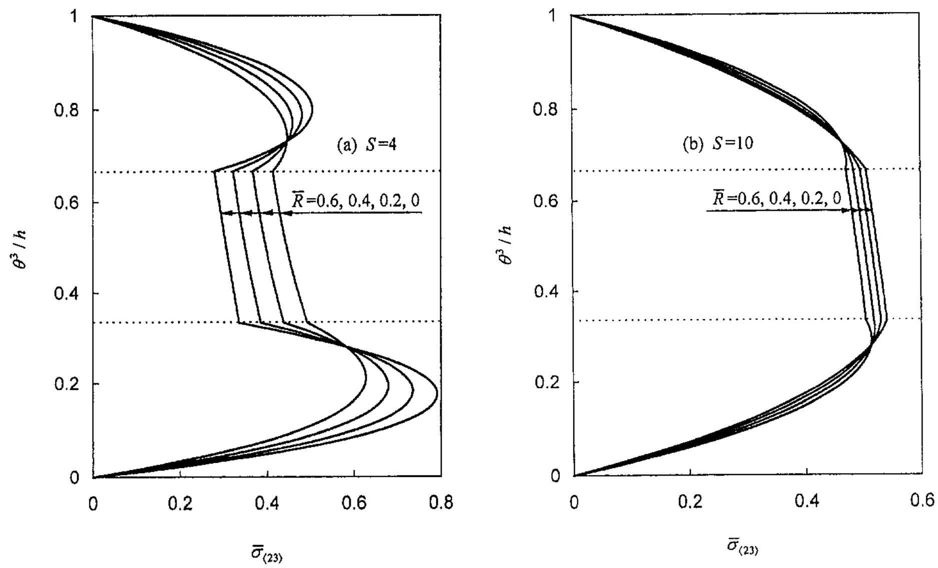

Fig. 4 Through-the-thickness variation of transverse shear stress at $\theta^2 = 0$, for an infinitely long three-ply (90 deg/0 deg/90 deg) laminated circular cylindrical panel ($\Phi = \pi/3$)

theories in this case. The dimensionless central deflection and buckling load in Tables 1–4 show the overall elastic response of laminated panels. As expected, interfacial damage reduces the rigidity of panels, and hence leads to an increasing bending deflection and a decreasing buckling load. The variation of stresses in Tables 1 and 2 and Figs. 3 and 4 for bending problems gives a better understanding of the way in which local elastic response is affected by the progressive interfacial damage. As in the case of flat plates, Fig. 4 confirms that the interfacial stress decreases with increasing interfacial parameter. This is significant for small values of S.

As an extreme case of damaged interfaces, delamination may allow laminates failure initiated by delamination buckling and thus greatly reduce the load capacity. Indeed, transverse normal stress often precipitates failure of laminates, which implies that transverse normal stress is an important cause of delamination. Therefore an appropriate kinematic description which allows for separation and slipping is required to model the delamination in laminated composite shells, as proposed by Gu and Chattopadhyay (1996) where more terms are retained than those truncated as Eq. (16) in this paper. Because of neglect of transverse normal stress in the present theory, perfect bonding in the thickness direction is assumed and hence it is impossible to study the case of separation delamination by this theory. However, it could possibly be improved for analyzing the case of shearing delamination.

5 Conclusions

Interfacial damage at the ply level of composite laminates is modeled by a spring layer. By invoking the principle of virtual work and an approximate displacement model, a geometrically nonlinear theory is presented for composite laminated shells featuring damaged interfaces. The proposed theory has the same advantages as conventional higher-order theories. Moreover, the third-order zigzag theory for a perfectly bonded shell can be recovered from this theory in the special case of vanishing interfacial parameters. An an extension of composite laminated plates, numerical results provide further confirmation of how the interfacial damage affects the overall and local responses of composite laminated shells.

Acknowledgment

This work was partly supported by the National Natural Science Foundation of China.

References

Aboudi, J., 1987, "Damage in composites—Modelling of imperfect bonding," *Composites Science and Technology,* Vol. 28, pp. 103–128.

Achenbach, J. D., and Zhu, H., 1989, "Effect of interfacial zone on mechanical behaviour and failure of fibre-reinforced composites," *Journal of the Mechanics and Physics of Solids,* Vol. 37, pp. 381–393.

Benveniste, Y., and Dvorak, G. J., 1990, "On a correspondence between mechanical and thermal fields with slipping interfaces," *Inelastic Deformation of Composite Materials* (IUTAM Symposium), G. J. Dvorak ed., Springer-Verlag, New York, pp. 77–98.

Cheng, Z. Q., Howson, W. P., and Williams, F. W., 1997, "Modelling of weakly bonded laminated composite plates at large deflections," *International Journal of Solids and Structures,* Vol. 34, pp. 3583–3599.

Cheng, Z. Q., Jemah, A. K., and Williams, F. W., 1996a, "Theory for multilayered anisotropic plates with weakened interfaces," ASME Journal of Applied Mechanics, Vol. 63, pp. 1019–1026.

Cheng, Z. Q., Kennedy, D., and Williams, F. W., 1996b, "Effect of interfacial imperfection on buckling and bending behavior of composite laminates," *AIAA Journal,* Vol. 34, pp. 2590–2595.

Cho, M., and Parmerter, R. R., 1992, "An efficient higher-order plate theory for laminated composites," *Composite Structures,* Vol. 20, pp. 113–123.

Cho, M., and Parmerter, R. R., 1993, "Efficient higher order composite plate theory for general lamination configurations," *AIAA Journal,* Vol. 31, pp. 1299–1306.

Di Sciuva, M., 1992, "Multilayered anisotropic plate models with continuous interlaminar stresses," *Composite Structures,* Vol. 22, pp. 149–167.

Di Sciuva, M., and Icardi, U., 1993, "Discrete-layer models for multilayered shells accounting for interlayer continuity," *Meccanica,* Vol. 28, pp. 281–291.

Dvorak, G. J., and Benveniste, Y., 1992, "On the thermomechanics of composites with imperfectly bonded interfaces and damage," *International Journal of Solids and Structures,* Vol. 29, pp. 2907–2919.

Gaudenzi, P., 1992, "A general formulation of higher-order theories for the analysis of laminated plates," *Composite Structures,* Vol. 20, pp. 103–112.

Gu, H. Z., and Chattopadhyay, A., 1996, "Delamination buckling and postbuckling of composite cylindrical shells," *AIAA Journal,* Vol. 34, pp. 1279–1286.

Hashin, Z., 1990, "Thermoelastic properties of fibre composites with imperfect interface," *Mechanics of Materials,* Vol. 8, pp. 333–348.

Hashin, Z., 1991, "Thermoelastic properties of particulate composites with imperfect interface," *Journal of the Mechanics and Physics of Solids,* Vol. 39, pp. 745–762.

He, L. H., 1993, "A novel Karman-type nonlinear theory of anisotropic laminated plates," *Proceedings of the 2nd International Conference on Nonlinear Mechanics,* W. Z. Chien, ed., Beijing University Press, Beijing, pp. 237–240.

He, L. H., 1994, "A linear theory of laminated shells accounting for continuity of displacements and transverse shear stresses at layer interfaces," *International Journal of Solids and Structures,* Vol. 31, pp. 613–627.

He, L. H., 1995, "Non-linear theory of laminated shells accounting for continuity conditions of displacements and tractions at layer interfaces," *International Journal of Mechanical Sciences,* Vol. 37, pp. 161–173.

Lai, Y. S., Wang, C. Y., and Tien, Y. M., 1997, "Micromechanical analysis of imperfectly bonded layered madia," *Journal of Engineering Mechanics,* Vol. 123, pp. 986–995.

Lee, K. H., and Cao, L., 1996, ''A predictor-corrector zigzag model for the bending of laminated composite plates,'' *International Journal of Solids and Structures,* Vol. 33, pp. 879–897.

Librescu, L., 1975, *Elastostatics and Kinetics of Anisotropic and Heterogeneous Shell-type Structures,* Noordhoff, Leyden, Netherlands.

Naghdi, P. M., 1963, ''Foundation of elastic shell theory,'' *Progress of Solid Mechanics,* Vol. 4, I. N. Sneddon and R. Hill, eds., North-Holland, Amsterdam.

Noor, A. K., and Burton, W. S., 1990, ''Assessment of computational models for multilayered composite shells,'' ASME *Applied Mechanics Reviews,* Vol. 43, pp. 67–97.

Noor, A. K., and Peters, J. M., 1989, ''*A posteriori* estimates for shear correction factors in multilayered composite cylinders,'' *Journal of Engineering Mechanics,* Vol. 115, pp. 1225–1244.

Qu, J., 1993a, ''Eshelby Tensor for an Elastic Inclusion With Slightly Weakened Interfaces,'' ASME JOURNAL OF APPLIED MECHANICS, Vol. 60, pp. 1048–1050.

Qu, J., 1993b, ''The effect of slightly weakened interfaces on the overall elastic properties of composite materials,'' *Mechanics of Materials,* Vol. 14, pp. 269–281.

Reddy, J. N., 1997, *Mechanics of Laminated Composite Plates: Theory and Analysis,* CRC Press, Boca Raton, FL.

Reddy, J. N., and Liu, C. F., 1985, ''A higher-order shear deformation theory of laminated elastic shells,'' *International Journal of Engineering Science,* Vol. 23, pp. 319–330.

Reddy, J. N., and Robbins, Jr., D. H., 1994, ''Theories and computational models for composite laminates,'' ASME *Applied Mechanics Reviews,* Vol. 47, pp. 147–169.

Ren, J. G., 1987, ''Exact solutions for laminated cylindrical shells in cylindrical bending,'' *Composites Science Technology,* Vol. 29, pp. 169–187.

Schmidt, R., and Librescu, L., 1996, ''Geometrically nonlinear theory of laminated anisotropic composite plates featuring interlayer slips,'' *Nova Journal of Mathematics, Game Theory, and Algebra,* Vol. 5, pp. 131–147.

Xavier, P. B., Chew, C. H., and Lee, K. H., 1995, ''Buckling and vibration of multilayer orthotropic composite shells using a simple higher-order layerwise theory,'' *International Journal of Solids and Structures,* Vol. 32, pp. 3479–3497.

Xavier, P. B., Lee, K. H., and Chew, C. H., 1993, ''An improved zigzag model for the bending of laminated composite shells,'' *Composite Structures,* Vol. 26, pp. 123–138.

Zhong, Z., and Meguid, S. A., 1996, ''On the Eigenstrain Problem of a Spherical Inclusion With an Imperfectly Bonded Interface,'' ASME JOURNAL OF APPLIED MECHANICS, Vol. 63, pp. 877–883.

Conservation Principles for Systems With a Varying Number of Degrees-of-Freedom

S. Djerassi
RAFAEL,
P.O. Box 2250
Haifa, Israel

This paper is the third in a trilogy dealing with simple, nonholonomic systems which, while in motion, change their number of degrees-of-freedom (defined as the number of independent generalized speeds required to describe the motion in question). The first of the trilogy introduced the theory underlying the dynamical equations of motion of such systems. The second dealt with the evaluation of noncontributing forces and of noncontributing impulses during such motion. This paper deals with the linear momentum, angular momentum, and mechanical energy of these systems. Specifically, expressions for changes in these quantities during imposition and removal of constraints are formulated in terms of the associated changes in the generalized speeds.

1 Introduction

A new approach to the analysis of systems with a varying number of degrees-of-freedom has been introduced by Djerassi (1994, 1997). Such systems undergo, *while in motion*, imposition or removal of constraints. A spacecraft docking at a space station, and a robot endeffector coming into contact with a work surface, provide examples of systems undergoing imposition of constraints; whereas an aircraft ejecting a pilot seat, and an athlete throwing a ball, provide examples of systems undergoing removal of constraints. With reference to such systems, three phases of motion can be identified: a phase where the motion is defined as unconstrained, a phase where the motion is defined as constrained, and a transition phase, where constraints are imposed or removed. It is the imposition and/or removal of these constraints which causes a change in the number of degrees-of-freedom.

Three-phase motions are governed by the following sets of equations: (a) Equations governing the motion in the unconstrained phase; (b) Constraint equations; (c) Certain relative velocities of particles and/or relative angular velocities of rigid bodies, if the ejection of these objects is under consideration; (d) Conditions, the satisfaction of which initiates the transition; (e) Equations governing the motion of the constrained system; and (f) Equations enabling the evaluation of the changes in the generalized speeds associated with the transition. Traditionally, the latter are generated by the integration of both sides of the motion equations of the system in its *unconstrained* phase, the integration time limits indicating the duration of the transition (which is assumed to be infinitely small). However, the integration is preceded by the introduction of contributions to the equations of motion of certain forces, namely forces associated with imposition or removal of constraints. These forces are assumed to be of unbounded magnitudes and of infinitely small duration. Thus, the integration gives rise to algebraic equations with two sets of unknowns. One set comprises changes in the generalized speeds, and another comprises impulses associated with the indicated forces; and the latter must be eliminated before the former can be evaluated (Levinson and Kane, 1983; Fitz-Coy and Cochran, 1986; Rhody et al., 1993). In accordance with the new approach introduced by Djerassi (1994), algebraic equations are generated, that contain changes in the generalized speeds as the only unknowns. This end is achieved if the equations being integrated during the transition phase are those governing the *constrained* motion (rather than those governing the unconstrained motion). Thus, the indicated impulses do not appear in the algebraic equations, and hence are referred to as ''noncontributing'' impulses. With the changes in the generalized speeds in hand, one can simulate the entire three-phase motion (Djerassi, 1994), and, in addition, evaluate quantities of interest in the transition phase, such as ''noncontributing'' impulses (Djerassi, 1997).

Here, expressions for changes in the linear momentum, angular momentum, and mechanical energy during the transition phase are obtained in terms of changes in the generalized speeds. Two kinds of systems, called noncontact force system (denoted here as NCF system) and contact force system (denoted here as CF system), are discussed. Particles of an NCF system exert no contact forces on particles not belonging to the system throughout the three-phase motion. A CF system is defined as one with particles exerting such contact forces during at least two of the phases.

The paper is organized as follows. The theory of imposition and removal of constrained is reviewed in Section 2. Expression for the changes in the linear momentum, angular momentum and mechanical energy during the transition phase are developed in Section 3 for NCF and for CF systems. An example is used throughout the paper, illustrating the use of the theoretical results.

2 Theory of Imposition-Removal of Constraints: Main Results

Let S be a simple nonholonomic system of υ particles P_i ($i = 1, \ldots, \upsilon$) of mass m_i possessing $\bar{n}$ generalized coordinates $q_1, \ldots, q_n$ and n (where $n < \bar{n}$) generalized speeds $u_1, \ldots, u_n$ in N, a Newtonian reference frame. Let S undergo three phases of motion as follows. Phase a occurs in the time interval of $0 \leq t \leq t_1$. The motion of S in N is *defined* as unconstrained, and is governed by n dynamical equations, namely,

$$F_r + F_r^* = 0 \quad (r = 1, \ldots, n) \tag{1}$$

where F_r and F_r^* are the rth generalized active force and the rth generalized inertia force for S, respectively. Phase b occurs in the time interval $t_1 \leq t \leq t_2$, where $t_2 - t_1$ is ''infinitely

Contributed by the Applied Mechanics Division of THE AMERICAN SOCIETY OF MECHANICAL ENGINEERS for publication in the ASME JOURNAL OF APPLIED MECHANICS.

Discussion on the paper should be addressed to the Technical Editor, Professor Lewis T. Wheeler, Department of Mechanical Engineering, University of Houston, Houston, TX 77204-4792, and will be accepted until four months after final publication of the paper itself in the ASME JOURNAL OF APPLIED MECHANICS.

Manuscript received by the ASME Applied Mechanics Division, Sept. 16, 1997; final revision, Dec. 20, 1997. Associate Technical Editor: N. C. Perkins.

small,'' e.g., as compared with time constants associated with the motion of S. Then m constraints of the form

$$u_k = \sum_{r=1}^{p} C_{kr}u_r + D_k \quad (k = p + 1, \ldots, n) \tag{2}$$

are imposed on S, where

$$p \triangleq n - m, \tag{3}$$

and C_{kr} and D_k are functions of $q_1, \ldots, q_n$ and time t. The configuration of S in N remains unaltered, that is,

$$q_r(t_2) = q_r(t_1) \quad (r = 1, \ldots, \bar{n}), \tag{4}$$

and the number of independent generalized speeds is reduced from n to p. The relations between $u_k(t_2)$ $(k = p + 1, \ldots, n)$, the values of the dependent generalized speeds at t_2, and $u_k(t_2)$ $(r = 1, \ldots, p)$, the values of the independent generalized speeds at t_2, is given by

$$u_k(t_2) = \sum_{r=1}^{p} C_{kr}u_r(t_2) + D_k \quad (k = p + 1, \ldots, n). \tag{5}$$

Additionally, if the magnitudes of the active forces contributing to Eqs. (1) are all bounded during Phase b, and if points of S exert contact forces on one another, and possibly on R_B, a set of particles with motions unaffected by contact forces exerted on them by particles of S, then p relations between $u_s(t_2)$ $(s = 1, \ldots, n)$ and $u_s(t_1)$ $(s = 1, \ldots, n)$ are given by

$$\sum_{s=1}^{n} (m_{rs} + \sum_{k=p+1}^{n} C_{kr}m_{ks})\Delta u_s = 0 \quad (r = 1, \ldots, p), \tag{6}$$

where

$$\Delta u_s \triangleq u_s(t_2) - u_s(t_1) \quad (s = 1, \ldots, n). \tag{7}$$

Here, m_{rs}, the element in row r, column s of the mass matrix associated with Eqs. (1), is defined

$$m_{rs} \triangleq -\sum_{i=1}^{\nu} m_i \mathbf{v}_r^{P_i} \cdot \mathbf{v}_s^{P_i} \quad (r, s = 1, \ldots, n), \tag{8}$$

where $\mathbf{v}_r^{P_i} \triangleq \partial \mathbf{v}^{P_i}/\partial u_r$, $\mathbf{v}_s^{P_i} \triangleq \partial \mathbf{v}^{P_i}/\partial u_s$, $\mathbf{v}^{P_i}$ being the velocity of P_i in N. Equations (5), (6), and (7) furnish $m + p$ relations between $u_s(t_2)$ and $u_s(t_1)$ $(s = 1, \ldots, n)$ that enable evaluation of the former, given the latter, with C_{kr}, D_k $(k = p + 1, \ldots, n;\ r = 1, \ldots, p)$ and m_{rs} $(r, s = 1, \ldots, n)$ calculated at t_1. Phase c occurs when $t \geq t_2$. Then the motion of S in N is *defined* as constrained, and is governed by p dynamical equations, namely,

$$F_r + F_r^* + \sum_{k=p+1}^{n} C_{kr}(F_k + F_k^*) = 0 \quad (r = 1, \ldots, p). \tag{9}$$

It is then said that the constraints in Eqs. (2) are *imposed* on the motion of S, and the process is called *imposition of constraints.*

Now, it may occur that Eqs. (2) are satisfied at $t = t_1$, that is,

$$u_k(t_1) = \sum_{r=1}^{p} C_{kr}u_r(t_1) + D_k \quad (k = p + 1, \ldots, n), \tag{10}$$

equations which, combined with Eqs. (5) and (7), lead to

$$\Delta u_k = \sum_{r=1}^{p} C_{kr}\Delta u_r \quad (k = p + 1, \ldots, n). \tag{11}$$

Equations (11) and (6) constitute a set of n homogeneous equations in n unknowns Δu_s $(s = 1, \ldots, n)$, having the unique, null solution, which, by virtue of Eqs. (7), yields

$$u_s(t_2) = u_s(t_1) \quad (s = 1, \ldots, n). \tag{12}$$

Equations (12) imply that no impulsive forces arise; therefore, the process is called *soft* imposition of constraints. If, on the other hand, Eqs. (2) are not satisfied at $t = t_1$, then Eqs. (5), (6), and (7), when solved for $u_s(t_2)$ $(s = 1, \ldots, n)$, given $u_s(t_1)$ $(s = 1, \ldots, n)$, decree changes in the values of the generalized speeds. These changes are associated with impulsive forces; therefore the process is called *hard* imposition of constraints.

When the chain of events described above occurs in reverse order, then Eqs. (9) govern Phase a. Phase b is governed by Eqs. (4), (6), and (10), and Phase c is governed by Eqs. (1). It is then said that the constraints in Eqs. (2) are *removed* from S, and the process is called *removal of constraints.*

Now, it may occur that $u_k(t_2)$ $(k = 1, \ldots, n)$ are interrelated as follows:

$$u_k(t_2) = \sum_{r=1}^{p} C_{kr}u_r(t_2) + D_k + E_k \quad (k = p + 1, \ldots, n), \tag{13}$$

where E_k $(k = p + 1, \ldots, n)$ is a function of $q_1, \ldots, q_n$ and t. If

$$E_k = 0 \quad (k = p + 1, \ldots, n), \tag{14}$$

then Eqs. (13) reduce to Eq. (5) which, with Eqs. (10), (7), and (6) yield Eqs. (11) and (12). As before, Eqs. (12) imply that no impulsive forces arise; therefore, the process is called *soft* removal of constraints. If, on the other hand, Eqs. (14) are not satisfied, then Eqs. (6), (13), and (7), when solved for $u_s(t_2)$ $(s = 1, \ldots, n)$, given $u_s(t_1)$ $(s = 1, \ldots, n)$, decree changes in the values of the generalized speeds. These changes are associated with impulsive forces; therefore the process is called *hard* removal of constraints.

Example I. Consider the system S described in Fig. 1, consisting of an axisymmetric, spinning top A, and of a rigid body E, initially undergoing an unconstrained motion in N. To discuss motions of S in N proceed as follows. Let $\mathbf{a}_i$, $\mathbf{e}_i$ and $\mathbf{n}_i$ $(i = 1, 2, 3)$ be three sets of three dextral, mutually perpendicular unit vectors fixed in A, E, and N, respectively, and let

$$A_{ij} \triangleq \mathbf{e}_i \cdot \mathbf{a}_j \quad (i, j = 1, 2, 3), \quad E_{ij} \triangleq \mathbf{n}_i \cdot \mathbf{e}_j \quad (i, j = 1, 2, 3).$$

Moreover, let A^* and E^* be the mass centers of A and E, respectively; and let q_4, q_5, and q_6 be the $\mathbf{e}_1$, $\mathbf{e}_2$, and $\mathbf{e}_3$ components of $\mathbf{p}^{\bar{E}/A^*}$, the position vector of A^* relative to $\bar{E}$, the

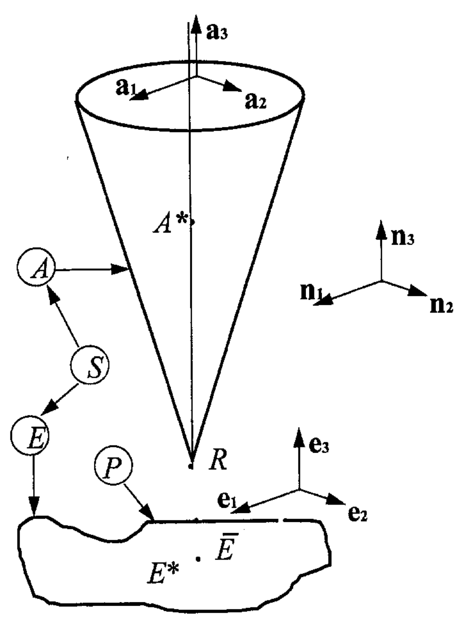

Fig. 1 A system undergoing three-phase motion: An example

projection of E^* on plane P of E. Similarly, let q_{10}, q_{11}, and q_{12} be the $\mathbf{n}_1$, $\mathbf{n}_2$, and $\mathbf{n}_3$ components of the position vector of E^* relative to a point fixed in N. Define $u_1, \ldots, u_{12}$, 12 generalized speeds for S, as follows:

$$u_r \triangleq {}^E\omega^A \cdot \mathbf{a}_r \quad (r = 1, 2, 3), \quad u_r \triangleq {}^E\mathbf{v}^{A^*} \cdot \mathbf{e}_{r-3} \quad (r = 4, 5, 6) \quad (a)^1$$

$$u_r \triangleq {}^N\omega^E \cdot \mathbf{e}_{r-6} \quad (r = 7, 8, 9), \quad u_r \triangleq {}^N\mathbf{v}^{E^*} \cdot \mathbf{n}_{r-9} \quad (r = 10, 11, 12) \quad (b)$$

where ${}^E\omega^A$ and ${}^N\omega^E$ are the angular velocities of A and E in N, and ${}^E\mathbf{v}^{A^*}$ and ${}^N\mathbf{v}^{E^*}$ are the velocities of A^* in E and of E^* in N, respectively. Hence,

$${}^E\omega^A = u_1\mathbf{a}_1 + u_2\mathbf{a}_2 + u_3\mathbf{a}_3, \quad {}^E\mathbf{v}^{A^*} = u_4\mathbf{e}_1 + u_5\mathbf{e}_2 + u_6\mathbf{e}_3 \quad (c)$$

$${}^N\omega^E = u_7\mathbf{e}_1 + u_8\mathbf{e}_2 + u_9\mathbf{e}_3, \quad {}^N\mathbf{v}^{E^*} = u_{10}\mathbf{n}_1 + u_{11}\mathbf{n}_2 + u_{12}\mathbf{n}_3. \quad (d)$$

The kinematical equations for S are $\dot{q}_r = u_r$ ($r = 4, 5, 6; 10, 11, 12$) and $\dot{A}_{13} = A_{12}u_3 - A_{13}u_2, \ldots, \dot{E}_{33} = E_{31}u_8 - E_{32}u_7$, relationships based on Poisson's kinematical equations. The dynamical equations are obtained by substitution in Eqs. (1) for $n = 12$. If the moments of inertia for A and E are chosen to be central principal, and if A_i ($i = 1, 2, 3$) are defined $A_i \triangleq A_{1i}u_7 + A_{2i}u_8 + A_{3i}u_9$ ($i = 1, 2, 3$), one obtains, for $r = 1, 4, 7$, and 12, the following respective equations:

$$-I_{A1}(\dot{u}_1 + \dot{A}_1) - (I_{A3} - I_{A2})(u_2 + A_2)(u_3 + A_3) = 0$$

$$-m_A(\dot{u}_4 + E_{11}\dot{u}_{10} + E_{21}\dot{u}_{11} + E_{31}\dot{u}_{12}) + m_A(u_5u_9 - u_6u_8 - gq_4/|\mathbf{p}^{E^*/A^*}|) = 0$$

$$-I_{A1}(\dot{u}_1 + \dot{A}_1)A_{11} - I_{A2}(\dot{u}_2 + \dot{A}_2)A_{12} - \mathrm{I}_{A3}(\dot{u}_3 + \dot{A}_3)A_{13} - I_{E3}\dot{u}_7$$
$$-(I_{A3} - I_{A2})(u_3 + A_3)(u_2 + A_2)A_{11} - (I_{A1} - I_{A3})(u_1 + A_1)(u_3 + A_3)A_{12}$$
$$-(I_{A2} - I_{A1})(u_2 + A_2)(u_1 + A_1)A_{13} - (I_{E3} - I_{E2})u_8u_9 = 0$$

$$-m_A(E_{31}\dot{u}_4 + E_{32}\dot{u}_5 + E_{33}\dot{u}_6) - (m_A + m_E)\dot{u}_{12}$$
$$-m_A[E_{32}(u_4u_9 - u_6u_7) - E_{31}(u_5u_9 - u_6u_8) - E_{33}(u_4u_8 - u_5u_7)] = 0 \quad (e)$$

where self-explanatory notations are used to denote inertial properties. Also, it is assumed that E^* exerts on A^* a force $\mathbf{F}^{E^*/A^*} = -m_A g\mathbf{p}^{E^*/A^*}/|\mathbf{p}^{E^*/A^*}|$, where $\mathbf{p}^{E^*/A^*}$ is the position vector from E^* to A^*, and g is the gravitational constant.

Next, let $\mathbf{p}^{A^*/R}$ and $\mathbf{p}^{\bar{E}/R}$ be the position vectors from A^* and from $\bar{E}$ to R, the vertex of A, respectively. Then

$$\mathbf{p}^{A^*/R} = r\mathbf{a}_3, \quad \mathbf{p}^{\bar{E}/R} = q_4\mathbf{e}_1 + q_5\mathbf{e}_2 + q_6\mathbf{e}_3 + r\mathbf{a}_3 \quad (f)$$

where r is the distance from A^* to R. If h denotes the distance from R to P, then

$$h \triangleq \mathbf{p}^{\bar{E}/R} \cdot \mathbf{e}_3 = q_6 + rE_{33}. \quad (g)$$

Now, suppose the motion of S in N is simulated, starting with the following initial conditions: $A_{ij} = E_{ij} = \delta_{ij}$ ($i, j = 1, 2, 3$), $q_4(0) = q_5(0) = 0$, $q_6(0) = 0.2$ m, $q_{10}(0) = q_{11}(0) = q_{12}(0) = 0$ m, $u_1(0) = u_2(0) = 0.2$ rad/sec, $u_3(0) = 104.72$ rad/sec, $u_6(0) = -0.1$ m/sec, $u_r(0) = 0$ ($r = 4, 5, 7, \ldots, 12$) (so that with $r = 0.04$ m, $h(0) = 0.16$ m). Then A approaches P, and h becomes smaller with time. Denote by t_1 the time h becomes zero; and suppose that at t_1 point R hits P, establishes contact with P between t_1 and t_2, and remains in contact with P throughout the remainder of the motion. This means that ${}^E\mathbf{v}^R \cdot \mathbf{e}_3$, the $\mathbf{e}_3$ component of ${}^E\mathbf{v}^R$, the velocity of R in E, vanishes from t_2 onwards; and, since ${}^E\mathbf{v}^R$ is given by

$${}^E\mathbf{v}^R = u_4\mathbf{e}_1 + u_5\mathbf{e}_2 + u_6\mathbf{e}_3 + u_2r\mathbf{a}_1 - u_1r\mathbf{a}_2, \quad (h)$$

the constraint equation ${}^E\mathbf{v}^R \cdot \mathbf{e}_3 = 0$ becomes, in view of Eq. (h),

$$u_6 = rA_{32}u_1 - rA_{31}u_2. \quad (i)$$

Hence, Eq. (i) plays the role of Eqs. (2) with $m = 1$ (note that the dependent variable is u_6, not u_{12} as implied by Eqs. (2) when $n = 12$ and $m = 1$; and that Eqs. (6) and (9) have to be rearranged accordingly). C_{6r} ($r = 1, \ldots, 5, 7, \ldots, 12$) can be determined by inspection of Eq. (i), and read

$$C_{61} = rA_{32}, \quad C_{62} = -rA_{31}, \quad C_{6s} = 0 \quad (s = 3, 4, 5, 7, \ldots, 12). \quad (j)$$

Substitutions from Eqs. (e) and (j) into Eqs. (9) (rearranged) give rise to equations governing the constrained motion of S, i.e., when R is constrained to remain in contact with P. These are

$$F_1 + F_1^* + rA_{32}(F_6 + F_6^*) = 0,$$
$$F_2 + F_2^* - rA_{31}(F_6 + F_6^*) = 0$$
$$F_r + F_r^* = 0 \quad (r = 3, 4, 5, 7, \ldots, 12). \quad (k)$$

The changes in the generalized speeds associated with the transition can be evaluated when equations obtained by substitutions from Eqs. (e) and (j) in Eqs. (5) and (6) (rearranged) are solved, in conjunction with Eqs. (7), for Δu_r ($r = 1, \ldots, 12$). If $m_A = 0.1$ kg, $I_{A1} = I_{A2} = 0.00003$, $I_{A3} = 0.00002$ kg $-$ m^2, $m_E = 100{,}000$ kg, $I_{E1} = I_{E2} = 30$, and $I_{E3} = 20$ kg $-$ m^2, the following changes in the generalized speeds result in

$$\Delta u_1 = -0.05801, \quad \Delta u_2 = -0.6624,$$
$$\Delta u_3 = \Delta u_4 = \Delta u_5 = 0, \quad \Delta u_6 = 1800 \quad (l)$$

$$\Delta u_7 = 6.0267\ 10^{-7}, \quad \Delta u_8 = 2.811\ 10^{-7},$$
$$\Delta u_r = 0\ (r = 9, 10, 11), \quad \Delta u_{12} = -0.0018. \quad (m)$$

Figure 2 shows u_1, u_2, and u_3, and Fig. 3 shows u_4, u_5, and u_6 as functions of time resulting from a one-second simulation, the transition occurring at $t = 0.16$ sec.

Similarly, suppose S initially undergoes a constrained motion with R in contact with P, starting with the following initial conditions: $A_{ij} = E_{ij} = \delta_{ij}$ ($i, j = 1, 2, 3$), $q_4(0) = q_5(0) = 0$ m, $q_6(0) = 0.04$ m, $q_{10}(0) = q_{11}(0) = q_{12}(0) = 0$ m, $u_1(0) = u_2(0) = 0.2$ rad/sec, $u_3(0) = 104.72$ rad/sec, $u_r(0) = 0$ ($r = 4, \ldots, 12$). Furthermore, suppose that after 0.5 sec, A is ejected from E so that ${}^E\mathbf{v}^R(t_2) = v\mathbf{e}_3$. Equation ($h$) is valid from t_2 on, hence at $t = t_2$

$$v\mathbf{e}_3 = u_4(t_2)\mathbf{e}_1 + u_5(t_2)\mathbf{e}_2 + u_6(t_2)\mathbf{e}_3 + \mathrm{u}_2(t_2)r\mathbf{a}_1 - u_1(t_2)r\mathbf{a}_2 \quad (n)$$

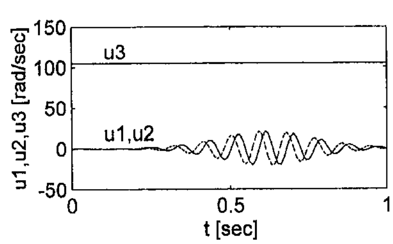

Fig. 2 u_1, u_2, and u_3 in hard imposition of constraints

[1] Equations associated with the examples are denoted with letters.

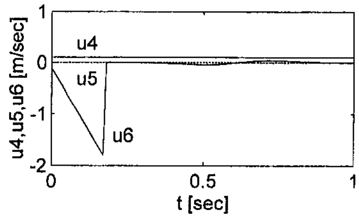

Fig. 3 u_4, u_5, and u_6 in hard imposition of constraints

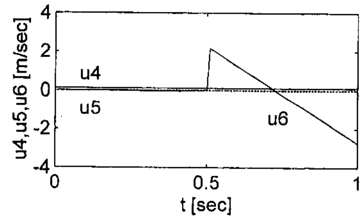

Fig. 5 u_4, u_5, and u_6 in hard removal of constraints

where v is a constant. If both sides of Eq. (n) are dot multiplied by $\mathbf{e}_3$, one has

$$u_6(t_2) = rA_{31}u_1(t_2) - rA_{31}u_2(t_2) + v, \qquad (o)$$

an equation playing the role of Eqs. (13) with $E_6 = v$ and $D_6 = 0$ (note that, if ${}^E\mathbf{v}^R = v\mathbf{e}_3$ not only at t_2, but throughout the remainder of the motion, then $E_6 = 0$ and $D_6 = v$. Such a state of affairs involves an instantaneous change in the constraint equation, i.e., form Eq. (i) to $u_6 = rA_{32}u_1 - rA_{31}u_2 + v$; and, since no change in the number of degrees of freedom is involved, the problem is beyond the scope of this paper). Thus Eqs. (k) govern the constrained motion of S, Eqs. (e) govern the unconstrained motion, i.e., the motion following the ejection; and Eq. (i) is the constraint being removed. The changes in the generalized speeds associated with the removal of this constraint are obtained by substitution from Eqs. (e) in Eq. (6) (rearranged) in conjunction with Eqs. (o) and (7). The following changes in the generalized speeds, associated with the transition, are obtained if $v = 6$ m/sec:

$$\Delta u_1 = -167.5, \quad \Delta u_2 = 7.995,$$

$$\Delta u_3 = \Delta u_4 = \Delta u_5 = 0, \quad \Delta u_6 = 2250 \qquad (p)$$

$$\Delta u_7 = -1.664\ 10^{-4}, \quad \Delta u_8 = 2.123\ 10^{-5},$$

$$\Delta u_r = 0\ (r = 9, 10, 11), \quad \Delta u_{12} = -0.00225. \qquad (q)$$

Figure 4 shows u_1, u_2, and u_3, and Fig. 5 shows u_4, u_5, and u_6 as functions of time resulting form a one-second simulation, the transition occurring at $t = 0.5$ sec.

In what follows, expressions for changes in the linear momentum, angular momentum, and mechanical energy of S *during* imposition and removal of constraints are formulated in terms of the associated changes in the generalized speeds.

3 Linear Momentum, Angular Momentum, and Mechanical Energy

3.1 NCF Systems.

3.1.1 Preliminaries. Let P_1 and P_2 be two particles of S, chosen so that S^*, the mass center of S, does not lie on the line passing through P_1 and P_2; and let B be a reference frame, and $\mathbf{b}_1$, $\mathbf{b}_2$, and $\mathbf{b}_3$ be three dextral, mutually perpendicular unit vectors fixed in B and oriented such that the plane defined by S^*, P_1, and P_2 is perpendicular to $\mathbf{b}_3$, with $\mathbf{b}_1$ parallel to the line passing through S^* and P_1. Define the six first generalized speeds for S as

$$u_s \triangleq {}^N\mathbf{v}^{S^*} \cdot \mathbf{n}_s\ (s = 1, 2, 3) \qquad (15)$$

$$u_{3+s} \triangleq {}^N\omega^B \cdot \mathbf{n}_s\ (s = 1, 2, 3), \qquad (16)$$

where ${}^N\mathbf{v}^{S^*}$ is the velocity of S^* in N, ${}^N\omega^B$ is the angular velocity of B in N, and $\mathbf{n}_s$ ($s = 1, 2, 3$) are three dextral, mutually perpendicular unit vectors fixed in N. Hence[2],

$${}^N\mathbf{v}^{S^*} \underset{(15)}{=} u_1\mathbf{n}_1 + u_2\mathbf{n}_2 + u_3\mathbf{n}_3 \qquad (17)$$

$${}^N\omega^B \underset{(16)}{=} u_4\mathbf{n}_1 + u_5\mathbf{n}_2 + u_6\mathbf{n}_3. \qquad (18)$$

Next, regard S as undergoing an unconstrained motion, and introduce $u_7, \ldots, u_{3v+3}$ as

$$u_7 \triangleq {}^B\mathbf{v}^{P_1} \cdot \mathbf{b}_1, \quad u_{7+i} \triangleq {}^B\mathbf{v}^{P_2} \cdot \mathbf{b}_i \quad (i = 1, 2)$$

$$u_{3i+k} \triangleq {}^B\mathbf{v}^{P_i} \cdot \mathbf{b}_k \quad (k = 1, 2, 3;\ i = 3, \ldots, v), \qquad (19)$$

where ${}^B\mathbf{v}^{P_i}$ is the velocity of P_i in B. Note that, since $\sum_{i=1}^{v} m_i{}^B\mathbf{v}^{P_i} = 0$, only $3v - 6$ of $u_7, \ldots, u_{3v+3}$, say $u_7, \ldots, u_{3v}$ are independent (hence u_{3v+1}, u_{3v+2} and u_{3v+3} are dependent); and that when S is a simple nonholonomic system possessing n independent generalized speeds, then only $n - 6$ of $u_7, \ldots, u_{3v}$ are independent. Now ${}^N\mathbf{v}^{P_i}$, the velocity of P_i in N, can be expressed as

$${}^N\mathbf{v}^{P_i} = {}^N\mathbf{v}^{S^*} + {}^B\mathbf{v}^{P_i} + {}^N\omega^B \times \mathbf{r}^{S^*P_i} \qquad (20)$$

where $\mathbf{r}^{S^*P_i}$ is the position vector of P_i relative to S^*; or, in view of Eqs. (17) and (18),

$${}^N\mathbf{v}^{P_i} = u_1\mathbf{n}_1 + u_2\mathbf{n}_2 + u_3\mathbf{n}_3 + (u_4\mathbf{n}_1 + u_5\mathbf{n}_2 + u_6\mathbf{n}_3) \times \mathbf{r}^{S^*P_i} + {}^B\mathbf{v}^{P_i} \quad (i = 1, \ldots, v). \qquad (21)$$

Moreover, ${}^N\mathbf{v}^{P_i}$ can be expressed as (Kane, 1985, Section 2.14)

$${}^N\mathbf{v}^{P_i} = \sum_{r=1}^{n} {}^N\mathbf{v}_r^{P_i} \cdot u_r + {}^N\mathbf{v}_t^{P_i} \qquad (22)$$

where ${}^N\mathbf{v}_r^{P_i}$ is called the rth partial velocity of P_i, and ${}^N\mathbf{v}_r^{P_i}$ ($r = 1, \ldots, n$) and ${}^N\mathbf{v}_t^{P_i}$ are functions of $q_1, \ldots, q_n$ and t. Thus, ${}^N\mathbf{v}_r^{P_i}$ ($r = 1, \ldots, n$) can be identified by comparison of the coefficients of $u_1, \ldots, u_n$ in Eqs. (21) and (22). For $r = 1, \ldots, 6$ one has

$${}^N\mathbf{v}_r^{P_i} = \mathbf{n}_r \quad (r = 1, 2, 3;\ i = 1, \ldots, v) \qquad (23)$$

$${}^N\mathbf{v}_{3+r}^{P_i} = \mathbf{n}_r \times \mathbf{r}^{S^*P_i} \quad (r = 1, 2, 3;\ i = 1, \ldots, v), \qquad (24)$$

equations which are not affected by the fact that only $n - 6$ of $u_7, \ldots, u_{3v}$ are independent. Now, it is implied by Eqs. (19) that ${}^B\mathbf{v}^{P_i}(i = 1, \ldots, v)$ in Eq. (21) are not functions of $u_1, \ldots, u_6$. If, in connection with three-phase motions, m constraints having the form of Eqs. (2) are imposed on S so that

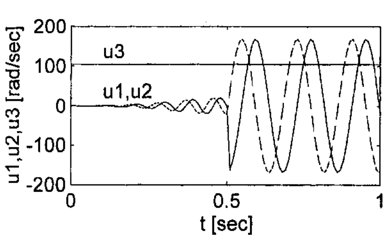

Fig. 4 u_1, u_2, and u_3 in hard removal of constraints

[2] Numbers appearing beneath expressions or equal signs refer to equations numbered correspondingly.

particles of S remain without contact with particles not belonging to S throughout the motion, then, $u_1, \ldots, u_6$ play no part in Eqs. (2); that is,

$$C_{kr} = 0 \quad (r = 1, \ldots, 6) \tag{25}$$

$$u_k = \sum_{r=7}^{p} C_{kr} u_r + D_k \quad (k = p + 1, \ldots, n). \tag{26}$$

Consequently, Eqs. (6), shown by Djerassi (1994) to be valid in this case, can be replaced with

$$\sum_{s=1}^{n} m_{rs} \Delta u_s \underset{(25)}{=} 0 \quad (r = 1, \ldots, 6) \tag{27}$$

and

$$\sum_{s=1}^{n} (m_{rs} + \sum_{k=p+1}^{n} C_{kr} m_{ks}) \Delta u_s = 0 \quad (r = 7, \ldots, p). \tag{28}$$

Similarly, Eqs. (27) and (28) apply if in Phase (a) S is subject to m constraints given by Eqs. (26), and if these constraints are removed from S during Phase b.

3.1.2 Linear Momentum and Angular Momentum. Let $\mathbf{L}$ be the linear momentum of S in N, defined as

$$\mathbf{L} \triangleq \sum_{i=1}^{\upsilon} m_i {}^N\mathbf{v}^{P_i}, \tag{29}$$

and let $\mathbf{H}^{S^*}$ be the central angular momentum of S in N, defined as

$$\mathbf{H}^{S^*} \triangleq \sum_{i=1}^{\upsilon} m_i \mathbf{r}^{S^* P_i} \times {}^N\mathbf{v}^{P_i}. \tag{30}$$

Then imposition and removal of constraints are events occurring such that

$$\mathbf{L}(t_2) - \mathbf{L}(t_1) = 0 \tag{31}$$

$$\mathbf{H}^{S^*}(t_2) - \mathbf{H}^{S^*}(t_1) = 0. \tag{32}$$

Proof. $\mathbf{L}$ can be written

$$\begin{aligned}
\mathbf{L} &= \sum_{s=1}^{3} \mathbf{L} \cdot \mathbf{n}_s \mathbf{n}_s \underset{(29)}{=} \sum_{s=1}^{3} \sum_{i=1}^{\upsilon} m_i {}^N\mathbf{v}^{P_i} \cdot \underset{(23)}{{}^N\mathbf{v}_s^{P_i}} \mathbf{n}_s \\
&\underset{(22)}{=} \sum_{s=1}^{3} \sum_{i=1}^{\upsilon} m_i (\sum_{r=1}^{n} {}^N\mathbf{v}_r^{P_i} u_r + {}^N\mathbf{v}_t^{P_i}) \cdot {}^N\mathbf{v}_s^{P_i} \mathbf{n}_s \\
&\underset{(8)}{=} \sum_{s=1}^{3} (-\sum_{r=1}^{n} m_{rs} u_r + \sum_{i=1}^{\upsilon} m_i {}^N\mathbf{v}_t^{P_i} \cdot {}^N\mathbf{v}_s^{P_i}) \mathbf{n}_s .
\end{aligned}$$

${}^N\mathbf{v}_t^{P_i}$ and ${}^N\mathbf{v}_s^{P_i}$ $(s = 1, 2, 3;\ i = 1, \ldots, \upsilon)$ are functions of $q_1, \ldots, q_n$ and t, so that in view of Eqs. (4)

$$\mathbf{L}(t_2) - \mathbf{L}(t_1) \underset{(7)}{=} -\sum_{s=1}^{3} (\sum_{r=1}^{n} m_{rs} \Delta u_r) \mathbf{n}_s. \tag{33}$$

The right-hand side of Eq. (33) vanishes by virtue of the first three of Eqs. (27); hence Eq. (33) reduces to Eq. (31) in connection with both imposition and removal of constraints. Similarly, $\mathbf{H}^{S^*} = \sum_{s=1}^{3} \mathbf{H}^{S^*} \cdot \mathbf{n}_s \mathbf{n}_s$ so that, in view of Eqs. (30), (24), (22), (8), and (4) one can show that

$$\mathbf{H}^{S^*}(t_2) - \mathbf{H}^{S^*}(t_1) = -\sum_{s=1}^{3} (\sum_{r=1}^{n} m_{r,3+s} \Delta u_r) \mathbf{n}_s. \tag{34}$$

The right-hand side of Eq. (34) vanishes by virtue of the last three of Eqs. (27); hence Eq. (32) is established in connection with both imposition and removal of constraints.

S in Example I is an NCF system. Substitutions from Eqs. $(l)-(m)$ and $(p)-(q)$ in the left-hand sides of Eqs. (27), with m_{rs} $(r, s = 1, \ldots, 12)$ obtained from Eqs. (e), reveal that Eqs. (27) are satisfied. Consequently, Eqs. (31) and (32) are satisfied both in connection with impositions of constraints and in connection with removal of constraints.

3.1.3 Mechanical Energy. Let K be the kinetic energy of S in N, defined

$$K \triangleq \frac{1}{2} \sum_{i=1}^{\upsilon} m_i {}^N\mathbf{v}^{P_i} \cdot {}^N\mathbf{v}^{P_i}; \tag{35}$$

let V, a function of $q_1, \ldots, q_n$ and t, be a potential energy of S in N, and let E be the mechanical energy of S in N, defined

$$E \triangleq K + V. \tag{36}$$

If

$$\sum_{i=1}^{\upsilon} m_i {}^N\mathbf{v}_t^{P_i} \cdot [{}^N\mathbf{v}^{P_i}(t_2) - {}^N\mathbf{v}^{P_i}(t_1)] = 0 \tag{37}$$

and

$$\sum_{s=1}^{n} \sum_{k=p+1}^{n} D_k m_{ks} \Delta u_s = 0 \tag{38}$$

then imposition of constraints is an event occurring such that

$$E(t_2) - E(t_1) = \frac{1}{2} \sum_{r=1}^{n} \sum_{s=1}^{n} m_{rs} \Delta u_r \Delta u_s, \tag{39}$$

whereas removal of constraints is an event occurring such that

$$E(t_2) - E(t_1) = -\frac{1}{2} \sum_{r=1}^{n} \sum_{s=1}^{n} m_{rs} \Delta u_r \Delta u_s. \tag{40}$$

The right-hand sides of Eqs. (39) and (40) comprise negative definite and positive definite quantities, respectively. Note that, if no prescribed motion is involved, then $\mathbf{v}_t^{P_i} = 0$ $(i = 1, \ldots, \upsilon)$ and $D_k = 0$ $(k = p + 1, \ldots, n)$; hence Eqs. (37) and (38) are satisfied indentically.

Proof. Consider imposition of constraints first, and note that substitutions from Eq. (22) in Eq. (35) for $t = t_1$ leads to

$$K(t_1) = \frac{1}{2} \sum_{i=1}^{\upsilon} m_i [\sum_{r=1}^{n} {}^N\mathbf{v}_r^{P_i} u_r(t_1) + {}^N\mathbf{v}_t^{P_i}] \cdot [\sum_{s=1}^{n} {}^N\mathbf{v}_s^{P_i} u_s(t_1) + {}^N\mathbf{v}_t^{P_i}]$$

or, when use is made of Eqs. (8),

$$K(t_1) = -\frac{1}{2} \sum_{r=1}^{n} \sum_{s=1}^{n} m_{rs} u_r(t_1) u_s(t_1) + \sum_{i=1}^{\upsilon} m_i {}^N\mathbf{v}_t^{P_i} \cdot {}^N\mathbf{v}^{P_i}(t_1) - E_t \tag{41}$$

where $E_t \triangleq \frac{1}{2} \sum_{i=1}^{\upsilon} m_i {}^N\mathbf{v}_t^{P_i} \cdot {}^N\mathbf{v}_t^{P_i}$. Similarly, for $t = t_2$

$$K(t_2) = \frac{1}{2} \sum_{i=1}^{\upsilon} m_i [\sum_{r=1}^{p} ({}^N\mathbf{v}_r^{P_i} + \sum_{k=p+1}^{n} C_{kr} {}^N\mathbf{v}_k^{P_i}) u_r(t_2) + \sum_{k=p+1}^{n} D_k {}^N\mathbf{v}_k^{P_i} + {}^N\mathbf{v}_t^{P_i}] \cdot [\sum_{s=1}^{n} {}^N\mathbf{v}_s^{P_i} u_s(t_2) + {}^N\mathbf{v}_t^{P_i}] \tag{42}$$

an expression obtained with substitutions from Eq. (2) in Eq. (22), and then in Eq. (35). In view of Eqs. (8), Eqs. (42) becomes

$$K(t_2) = -\frac{1}{2} \sum_{r=1}^{p} \sum_{s=1}^{n} (m_{rs} + \sum_{k=p+1}^{n} C_{kr} m_{ks}) u_s(t_2) u_r(t_2) - \frac{1}{2} \sum_{s=1}^{n} \sum_{k=p+1}^{n} D_k m_{ks} u_s(t_2) + \sum_{i=1}^{\upsilon} m_i {}^N\mathbf{v}_t^{P_i} \cdot {}^N\mathbf{v}^{P_i}(t_2) - E_t. \tag{43}$$

Next, the following relationship is formed by the addition of all p of Eqs. (6) after the rth equation is multiplied with $u_r(t_2)$ $(r = 1, \ldots, p)$:

$$\sum_{r=1}^{p}\sum_{s=1}^{n}\left(m_{rs} + \sum_{k=p+1}^{n} C_{kr}m_{ks}\right)u_s(t_2)u_r(t_2) = \sum_{r=1}^{p}\sum_{s=1}^{n}\left(m_{rs} + \sum_{k=p+1}^{n} C_{kr}m_{ks}\right)u_s(t_1)u_r(t_2). \quad (44)$$

When $\sum_{s=1}^{n}\sum_{k=p+1}^{n} D_k m_{ks}u_s(t_1)$ is added to and subtracted from the right-hand side of Eq. (44), one obtains, after a rearrangement involving Eqs. (5),

$$\sum_{r=1}^{p}\sum_{s=1}^{n}\left(m_{rs} + \sum_{k=p+1}^{n} C_{kr}m_{ks}\right)u_s(t_2)u_r(t_2) = \sum_{r=1}^{n}\sum_{s=1}^{n} m_{rs}u_r(t_2)u_s(t_1) - \sum_{s=1}^{n}\sum_{k=p+1}^{n} D_k m_{ks}u_s(t_1). \quad (45)$$

This relation leads, when used in Eq. (43) in conjunction with Eq. (38), to

$$K(t_2) = -\tfrac{1}{2}\sum_{r=1}^{n}\sum_{s=1}^{n} m_{rs}u_r(t_2)u_s(t_1) + \sum_{i=1}^{\upsilon} m_i\,{}^N\mathbf{v}_t^{P_i}\cdot{}^N\mathbf{v}^{P_i}(t_2) - E_t. \quad (46)$$

Two alternative forms of $K(t_2)$, denoted $\bar{K}(t_2)$ and $\bar{\bar{K}}(t_2)$, can be introduced as follows:

$$\bar{K}(t_2) = -\tfrac{1}{2}\sum_{r=1}^{n}\sum_{s=1}^{n} m_{rs}u_r(t_1)u_s(t_2) + \sum_{i=1}^{\upsilon} m_i\,{}^N\mathbf{v}_t^{P_i}\cdot{}^N\mathbf{v}^{P_i}(t_2) - E_t \quad (47)$$

$$\bar{\bar{K}}(t_2) = -\tfrac{1}{2}\sum_{r=1}^{n}\sum_{s=1}^{n} m_{rs}u_r(t_2)u_s(t_2) + \sum_{i=1}^{\upsilon} m_i\,{}^N\mathbf{v}_t^{P_i}\cdot{}^N\mathbf{v}^{P_i}(t_2) - E_t. \quad (48)$$

Equation (47) is identical with Eq. (46) in view of the fact that the mass matrix is symmetric (see Eqs. (8)); and Eq. (48) is the counterpart of Eq. (41) for $t = t_2$. The motivation for writing $\bar{K}(t_2)$ and $\bar{\bar{K}}(t_2)$ becomes apparent when $K(t_2) - K(t_1)$ is formed in the following manner:

$$K(t_2) - K(t_1) = -\bar{\bar{K}}(t_2) + K(t_2) + \bar{K}(t_2) - K(t_1). \quad (49)$$

Then the right-hand side of Eq. (49) reduces, in view of Eq. (37) and (7), to the right-hand side of Eq. (39); and, because V is a function solely of $q_1, \ldots, q_n$ and t, then $V(t_2) = V(t_1)$, and the validity of Eq. (39) is established. The right-hand side of Eq. (39) is negative definite because, by definition (Eqs. (8)), $m_{rs} < 0$ $(r = s = 1, \ldots, n)$ (Strang, 1980).

The validity of Eq. (40) can be established similarly. Equations (41)–(49) can all be rewritten with t_1 and t_2 replacing one another. Thus, one can rewrite Eq. (41) for $t = t_2$, Eq. (42) and (43) for $t = t_1$; form Eq. (44) by multiplication with $u_r(t_1)$ $(r = 1, \ldots, p)$; rewrite Eq. (45) using Eq. (10) instead of Eq. (5), etc.

It is finally worth noting that when soft imposition or soft removal of constraints is under consideration, then Eqs. (12) are valid, which means that $\mathbf{v}^{P_i}(t_2) = \mathbf{v}^{P_i}(t_1)$ $(i = 1, \ldots, \upsilon)$, so that Eqs. (37) and (38) are satisfied identically, and the right-hand sides of Eqs. (39) and (40) vanish.

Substitutions from Eqs. (l)–(m) in Eqs. (39) yield $E(t_2) - E(t_1) = -0.162$ N–m; and substitutions from Eqs. (p)–(q) in Eq. (40) yield $E(t_2) - E(t_1) = 0.675$ N–m. Identical results are obtained if the mechanical energy of S is formulated in the usual manner, and evaluated at t_1 and t_2.

3.2 CF Systems.

3.2.1 Preliminaries. Here, the following assumption is made, namely, that throughout at least two of the phases, particles of S exert contact forces on one another and on points of E, a rigid body moving in N. As before, S is assumed to be a simple, nonholonomic system of υ particles, possessing n generalized speeds. Now, before linear momentum, angular momentum and mechanical energy of S can be discussed in connection with imposition and removal of constraints, one has to define conditions, satisfaction of which ensure that Eqs. (6) can be applied to S. To this end, let S_E be a simple, nonholonomic system of υ_E particles and $n + 6$ generalized speeds $\bar{u}_1, \ldots, \bar{u}_{n+6}$, consisting of a rigid body E of $\upsilon_E - \upsilon$ particles, and of a system $\bar{S}$ of υ particles, which is identical to, and undergoes a motion identical with that of S when E is fixed in N. Accordingly, define $\bar{u}_{n+1}, \ldots, \bar{u}_{n+6}$ so as to describe the motion of E in N, and define $\bar{u}_1, \ldots, \bar{u}_n$ so that, when E is fixed in N

$$\bar{u}_r = u_r \quad (r = 1, \ldots, n), \quad \bar{u}_{n+k} = 0 \quad (k = 1, \ldots, 6). \quad (50)$$

Suppose that between $t = t_1$ and $t = t_2$ m constraints of the form

$$\bar{u}_k = \sum_{r=1}^{p} C_{kr}\bar{u}_r + D_k \quad (k = p + 1, \ldots, n) \quad (51)$$

are imposed on S_E, and that m constraints of the form of Eqs. (2) are imposed on S; and make analogous suppositions in connection with removal of constraints if S_E and S undergo initially constrained motions. Now, particles of S exert contact forces on particles not belonging to S (i.e., of N), and are acted upon by the associated reaction forces (themselves contact forces). The latter, like other active forces, contribute to Eqs. (1); and, like other contact forces, are not bounded during Phase b. Hence, the requirement preceding Eqs. (6) is not satisfied, and the use of Eqs. (6) for the evaluation of $u_1(t_2), \ldots, u_n(t_2)$ leads to erroneous results. Similarly, particles of $\bar{S}$ exert contact forces on particles of E. Here, however, all the particles in question belong to S_E, and contributions from contact forces do not appear in equations corresponding to Eqs. (1) when written for S_E. Hence, equations corresponding to Eqs. (6) can be used to evaluate $\bar{u}_1(t_2), \ldots, \bar{u}_{n+6}(t_2)$. These are

$$\sum_{s=1}^{n+6}\left[(m_{rs} + M_{rs}) + \sum_{k=p+1}^{n} C_{kr}(m_{ks} + M_{ks})\right]\Delta\bar{u}_s = 0 \quad (r = 1, \ldots, p, n + 1, \ldots, n + 6), \quad (52)$$

where $\Delta\bar{u}_s$ is defined similarly to Δu_s in Eqs. (7), and where m_{rs} and M_{rs} $(r, s = 1, \ldots, n + 6)$ are contributions of $\bar{S}$ and of E to the mass matrix. Noting that $M_{rs} = 0$ for $r, s \neq n + 1, \ldots, n + 6$, and that $\bar{u}_{n+1}, \ldots, \bar{u}_{n+6}$ play no part in Eqs. (51) (hence $C_{kr} = 0$ for $k = p + 1, \ldots, n$, $r = n + 1, \ldots, n + 6$), one can replace Eqs. (52) with

$$\sum_{s=1}^{n+6}\left(m_{rs} + \sum_{k=p+1}^{n} C_{kr}m_{ks}\right)\Delta\bar{u}_s = 0 \quad (r = 1, \ldots, p) \quad (53)$$

and

$$\sum_{s=1}^{n+6} m_{rs}\Delta\bar{u}_s + \sum_{s=n+1}^{n+6} M_{rs}\Delta\bar{u}_s = 0 \quad (r = n + 1, \ldots, n + 6). \quad (54)$$

Now suppose that Eqs. (53)–(54) are used to evaluate $\Delta\bar{u}_1, \ldots, \Delta\bar{u}_{n+6}$ for S_E, and Eqs. (6) are used to evaluate $\Delta u_1, \ldots, \Delta u_n$ for S. Furthermore, suppose that

$$M_{ij} \gg m_{rs} \; (i = j = n + 1, \ldots, n + 6; \; r, s = 1, \ldots, n + 6), \quad (55)$$

which mean that the inertial properties of E exceed those of $\bar{S}$ "significantly." Then

$$\Delta u_r = \Delta \bar{u}_r \quad (r = 1, \ldots, n) \tag{56}$$

$$\Delta \bar{u}_{n+k} = 0 \quad (k = 1, \ldots, 6). \tag{57}$$

Equations (57) indicate that neither imposition of constraints nor removal of constraints affect the motion of E; and Eqs. (56) indicate that, under these circumstances, Eqs. (6) can be applied to S.

Proof. Without a loss of generality, $\bar{u}_{n+1}, \ldots, \bar{u}_{n+6}$ can be chosen in such a way that they all have the dimension of m/sec, and

$$M_{rs} = 0 \quad r \neq s \quad (r, s = n + 1, \ldots, n + 6) \tag{58}$$

(such is the case if $\bar{u}_{n+1}, \ldots, \bar{u}_{n+6}$ are defined as follows: $\bar{u}_{n+r+3} \triangleq {}^N\mathbf{v}^{E^*} \cdot \mathbf{e}_r$ $(r = 1, 2, 3)$, $\bar{u}_{n+1} \triangleq \mathbf{v}^{P_2} \cdot \mathbf{e}_3 - \bar{u}_{n+6}$, $\bar{u}_{n+2} \triangleq \mathbf{v}^{P_3} \cdot \mathbf{e}_1 - \bar{u}_{n+4}$ and $\bar{u}_{n+3} \triangleq \mathbf{v}^{P_1} \cdot \mathbf{e}_2 - \bar{u}_{n+5}$, where $\mathbf{e}_r$ $(r = 1, 2, 3)$, E^* and ${}^N\mathbf{v}^{E^*}$ are defined as in Example I, and P_r $(r = 1, 2, 3)$ are three points of E located with respect to E^* at $d\mathbf{e}_r$ $(r = 1, 2, 3)$, where d is a constant. Then ${}^N\omega^E = (\bar{u}_{n+1}\mathbf{e}_1 + \bar{u}_{n+2}\mathbf{e}_2 + \bar{u}_{n+3}\mathbf{e}_3)/d$, ${}^N\mathbf{v}^{E^*} = \bar{u}_{n+4}\mathbf{n}_1 + \bar{u}_{n+5}\mathbf{n}_2 + \bar{u}_{n+6}\mathbf{n}_3$. The motion equations follow straightforwardly, and satisfy Eqs. (58)). Defining $\bar{M}$ as the 6×6 coefficient matrix of $\Delta\bar{u}_{n+1}, \ldots, \Delta\bar{u}_{n+6}$ in Eqs. (54), one may conclude that $m_{rs} + M_{rs}\delta_{rs}$ is the element in row r, column s of $\bar{M}$ $(r, s = n + 1, \ldots, n + 6)$; and that, in view of Eqs. (55), the diagonal elements of $\bar{M}$ are significantly larger than the nondiagonal elements. Consequently, the elements of $\bar{M}^{-1}$, the inverse of $\bar{M}$, designated $M_{rs}^{(-1)}$ $(r, s = n + 1, \ldots, n + 6)$ are related to those of $\bar{M}$ as follows:

$$O(M_{rs}^{(-1)}) = O(M_{ij}^{-1}) \quad (r = s; i = j = n + 1, \ldots, n + 6) \tag{59}$$

$$O(M_{rs}^{(-1)}) = O(m_{rs}M_{ij}^{-2}) \quad (r \neq s, i = j = n + 1, \ldots, n + 6), \tag{60}$$

where $O(\cdot)$ denotes order of magnitude. Solving Eqs. (54) for $\Delta\bar{u}_{n+1}, \ldots, \Delta\bar{u}_{n+6}$ one reveals that

$$O(\Delta\bar{u}_{n+k}/\Delta\bar{u}_s) = O(m_{rs}M_{ij}^{-1}) \quad (k = 1, \ldots, 6; r, s = 1, \ldots, n; i = j = 1, \ldots, 6), \tag{61}$$

so that in view of Eqs. (55), Eqs. (57) are nearly satisfied. Moreover, using Eqs. (61) one finds that terms associated with $s = n + 1, \ldots, n + 6$ in each of Eqs. (53) nearly vanish. Hence Eqs. (53), when applied to S_E, become identical to Eqs. (6) when applied to S, a result validating Eqs. (56) in connection with both imposition and removal of constraints. Moreover, suppose that R_B comprises a number of rigid bodies $E_1, \ldots, E_N$, each having inertial properties significantly exceeding those of S. If the steps leading to Eqs. (56) and (57) are carried out in connection with $E_1, \ldots, E_N$, one at a time, then Eq. (56) remains valid, and equations analogous to Eq. (57) are valid in connection with each of $E_1, \ldots, E_N$. Finally, if E is fixed in N, then Eqs. (57) are satisfied identically. Consequently, Eqs. (53) yield the same results for $\Delta\bar{u}_r$ as do Eqs. (6) for Δu_r $(r = 1, \ldots, n)$, as indicated by Eqs. (56). Thus, the requirement preceding Eqs. (6) concerning particles of R_B—here comprising E—is justified; and a significant simplification is obtained, namely, the replacement of an $n + 6$ degrees-of-freedom system with one of n degrees-of-freedom.

Example II. Suppose E in Fig. 1 is fixed in N (i.e., $u_7 \equiv 0, \ldots, u_{12} \equiv 0$), so that S, consisting now of A alone, undergoes three-phase motions similar to those in Example I. Note that here, a particle of S is in contact with a particle of N during two of the three phases. Accordingly, Eqs. (a) and (c) are valid if E is replaced with N (and $\mathbf{e}_i$ with $\mathbf{n}_i$ $(i = 1, 2, 3)$) in these equations; and, assuming that A is subject to a gravitational force given by $\mathbf{F} = -m_A g \mathbf{n}_3$, one can show that the following equations govern the unconstrained motion of A in N:

$$-I_{A1}\dot{u}_1 - (I_{A3} - I_{A2})u_2u_3 = 0, \ldots, -m_A\dot{u}_6 - m_A g = 0. \quad (r)$$

With reference to the constrained motion of A, Eqs. $(f)-(j)$ are valid if E is replaced with N (and $\mathbf{e}_i$ with $\mathbf{n}_i$ $(i = 1, 2, 3)$) in these equations, if $\bar{N}$, a point fixed in N, replaces $\bar{E}$, and if A_{ij} are redefined as $\mathbf{n}_i \cdot \mathbf{a}_j$ $(i, j = 1, 2, 3)$. Moreover, the first five of Eqs. (k) are valid if $F_r + F_r^*$ $(r = 1, \ldots, 6)$ are taken to be the respective left-hand sides of Eqs. (r). Now, consider an unconstrained motion of S starting with the same initial conditions for A_{ij} $(i, j = 1, 2, 3)$, q_r $(r = 4, 5, 6)$ and u_r $(r = 1, \ldots, 6)$ as in Example I. Then R comes into contact with P after 0.16 sec, and u_r $(r = 1, \ldots, 6)$ behave in a manner indistinguishable from that in Figs. 2 and 3. For, E in Example I is initially at rest, and relations (55) are satisfied by the entries of the mass matrix associated with Eqs. (e) in Example I. Hence, the system described in Example I can be regarded as playing the role of S_E, and the changes in the generalized speeds resulting from the solution of Eqs. (5)–(7) in conjunction with Eqs. (r) and (i) are identical with those in Eqs. (l) (obtained for S_E), in agreement with Eqs. (56).

Similarly, suppose A undergoes initially a constrained motion with R in contact with P; and that after 0.5 sec A is ejected in a manner characterized by Eqs. (o) with A_{31} and A_{32} redefined as $\mathbf{n}_3 \cdot \mathbf{a}_i$ $(i = 1, 2)$. Then, with the same initial conditions for A_{ij} $(i, j = 1, 2, 3)$, q_r $(r = 4, 5, 6)$ and u_r $(r = 1, \ldots, 6)$ as in Example I, the changes in the generalized speeds, evaluated by substitutions form Eqs. (r) and (o) into Eqs. (5), (6), and (13), are as in Eqs. (p), in agreement with Eqs. (56); and u_r $(r = 1, \ldots, 6)$ behave in a manner indistinguishable from that in Figs. 4 and 5.

Note that if the inertial properties of E and A are of the same order of magnitude, and if S is defined as A alone, then the theory of imposition and removal of constraints does not apply. However, one can always associate with S, here a CF system, an NCF system—for which the theory applies—redefining S so as to include E, as in Example I.

3.2.2 Linear Momentum and Angular Momentum. Imposition and removal of constraints are events occurring such that

$$\mathbf{L}(t_2) - \mathbf{L}(t_1) = I_1\mathbf{n}_1 + I_2\mathbf{n}_2 + I_3\mathbf{n}_3 \tag{62}$$

$$\mathbf{H}^{S^*}(t_2) - \mathbf{H}^{S^*}(t_1) = I_4\mathbf{n}_1 + I_5\mathbf{n}_2 + I_6\mathbf{n}_3 \tag{63}$$

where I_r is the rth generalized impulse, defined as (Kane, 1985, Section 7.8)

$$I_r \triangleq \int_{t_1}^{t_2} F_r dt. \tag{64}$$

Equations (31) and (32) can be regarded as special cases of Eqs. (62) and (63), as NCF systems are special cases of CF systems.

Proof. ${}^N\mathbf{a}^{P_i}$, the acceleration of P_i in N can be written

$${}^N\mathbf{a}^{P_i} \underset{(22)}{=} \sum_{s=1}^{n} {}^N\mathbf{v}_s^{P_i} \cdot \dot{u}_s + \sum_{s=1}^{n} {}^N\dot{\mathbf{v}}_s^{P_i} \cdot u_s + {}^N\dot{\mathbf{v}}_t^{P_i}. \tag{65}$$

By definition, the rth generalized inertia force F_r^* is given by (Kane, 1985, Section 4.11)

$$F_r^* \triangleq \sum_{i=1}^{\nu} {}^N\mathbf{v}_r^{P_i} \cdot (-m_i {}^N\mathbf{a}^{P_i}) = -\sum_{i=1}^{\nu} m_i {}^N\mathbf{v}_r^{P_i} \cdot \sum_{s=1}^{n} {}^N\mathbf{v}_s^{P_i}\dot{u}_s + R_r^* \underset{(8)}{=} \sum_{s=1}^{n} m_{rs}\dot{u}_s + R_r^* \tag{66}$$

where

$$R_r^* = -\sum_{i=1}^{v} m_i {}^N\mathbf{v}_r^{P_i} \cdot (\sum_{s=1}^{n} {}^N\mathbf{v}_s^{P_i} u_s + {}^N\mathbf{v}_t^{P_i}).$$

Because $R_1^*, \ldots, R_n^*$ are bounded functions of time, then $\int_{t_1}^{t_2} R_r^* dt = 0$ $(r = 1, \ldots, n)$, hence,

$$\int_{t_1}^{t_2} F_r^* dt \underset{(66),(7)}{=} \sum_{s=1}^{n} m_{rs} \Delta u_s. \quad (67)$$

When both sides of Eqs. (1) are integrated from t_1 to t_2 one has, in view of Eqs. (64) and (67),

$$I_r + \sum_{s=1}^{n} m_{rs} \Delta u_s = 0 \quad (r = 1, \ldots, n). \quad (68)$$

Equations (68) indicate that the left-hand sides of Eqs. (27) are the generalized impulses for $r = 1, \ldots, 6$. These differ from zero when S is a CF system since F_r $(r = 1, \ldots, 6)$ include contributions from contact forces exerted on particles of S by particles not belonging to S. Thus, Eqs. (62) and (63) are obtained by substitutions from Eqs. (68) in Eqs. (33) and (34), respectively. Note that applying Eqs. (27) to S_E (see Section 3.2.1)—then n is replaced with $n + 6$ and Δu_s with $\Delta \bar{u}_s$—one obtains Eqs. (54). These reduce to $I_r = \sum_{s=n+1}^{n+6} M_{rs} \Delta \bar{u}_s$ $(r = n + 1, \ldots, n + 6)$ in view of Eqs. (61) and (68).

Substitutions from Eqs. (l) and (p), in conjunction with Eqs. (r), in the left-hand side of Eqs. (27), reveal that Eqs. (27) are not satisfied. Consequently, changes occur in both the linear momentum and in the angular momentum as in Eqs. (62) and (63), in connection with both impositions removal of constraints.

3.2.3 Mechanical Energy. Equations (39) and (40) are applicable to CF systems if Eqs. (37) and (38) are satisfied, and if particles of S exert contact forces on one another and on particles of R_B.

Proof. If Eqs. (37) and (38) are satisfied in connection with S_E, then Eqs. (39) can be applied (see Section 3.2.1), yielding

$$E(t_2) - E(t_1) = \frac{1}{2} \sum_{r=1}^{n} \sum_{s=1}^{n} m_{rs} \Delta \bar{u}_r \Delta \bar{u}_s + \frac{1}{2} \sum_{r=1}^{n} \sum_{s=n+1}^{n+6} m_{rs} \Delta \bar{u}_r \Delta \bar{u}_s$$
$$+ \frac{1}{2} \sum_{r=n+1}^{n+6} \sum_{s=1}^{n} m_{rs} \Delta \bar{u}_r \Delta \bar{u}_s + \frac{1}{2} \sum_{r=n+1}^{n+6} \sum_{s=n+1}^{n+6} m_{rs} \Delta \bar{u}_r \Delta \bar{u}_s \quad (69)$$

Suppose, in addition, that particles of S exert contact forces on one another and on particles of R_B. Then Eqs. (61) can be used to show that the last three terms on the right-hand side of Eq. (69) are negligible as compared with the first; and the first term is identical with the right-hand side Eq. (39) by virtue of Eq. (56). Equation (39) can thus be applied to S. An analogous proof applies to Eq. (40). In summary, Eqs. (39) and (40) are applicable if the theory of imposition and removal of constraints is.

Substitutions from Eqs. (l) and (r) in Eqs. (39) yield $E(t_2) - E(t_1) = -0.162$ N–m; and substitutions from Eqs. (p) and (r) in Eq. (40) yield $E(t_2) - E(t_1) = 0.675$ N–m. These results are identical with those obtained in Example I, as implied by Eqs. (69).

Suppose the mechanical energy, the linear momentum and the angular momentum of a system undergoing a three phase motion are evaluated throughout Phases a and c. Then the changes in these quantities during the transition can be evaluated. Suppose that, in addition, these changes are evaluated with the aid of Eqs. (39), (or (40)), (62), and (64), and compared with the changes evaluated earlier. Identical results support the following conclusion, namely, that the theory of imposition and removal of constraints has been properly used. These tests are reminiscent of energy and momentum associated integrals, used to test numerical integration of equations of motion. Finally, note that the change in the mechanical energy is meaningful in its own right, for it comprises the energy which must be dissipated by, or supplied to the system in question during transition, if the total energy of the system (of which the mechanical energy forms a part) is to be conserved.

4 Conclusions

Simple, nonholonomic systems undergoing imposition or removal of constraints are the subject of the present work. Expressions for changes in the mechanical energy, the linear momentum and the angular momentum of such systems during the transition phases are formulated in terms of the associated changes in the generalized speeds. These expressions not only play a role in the understanding of the process of imposition and removal of constraints, but also enable to test the implementation of the theory. However, they apply only to NCF systems and to CF systems interacting with particles which belong to R_B, as does the theory of imposition and removal of constraints. This observation simplifies the analytical treatment of such systems considerably, and imply that a good analitical practice would be to define the system accordingly.

References

Djerassi, S., 1994, "Imposition of Constraints," ASME Journal of Applied Mechanics, Vol. 61, pp. 434–439.

Djerassi, S., 1997, "Determination of Noncontributing Forces and Noncontributing Impulses in Three-Phase Motions," ASME Journal of Applied Mechanics, Vol. 64, pp. 000–000.

Fitz-Coy, N. G., and Cochran, J. E., 1986, "Space Station/Shuttle Orbiter Dynamics During Docking," *Structural Dynamics and Control Interaction of Flexible Structure Conference,* Huntsville, AL, NASA Conference Publication 2467, Part 1, pp. 133–174.

Levinson, D. A., and Kane, T. R., 1983, "Docking of a Spacecraft with an Unrestrained Orbiting Structure," *The Journal of the Astronautical Sciences,* Vol. 31, No. 1, pp. 23–48.

Rhody, B. J., Heppler, G. R., and Golnaraghi, M. F., 1993, "Modeling the Dynamics of Mass Captured by a Single Flexible Link," *Proceedings of the 2nd International Conference on Dynamics and Control of Structure in Space,* Cranfield, England.

Strang, G., 1980, *Linear Algebra and Application,* Academic Press, New York.

R. P. S. Han[1]
Professor,
Department of Mechanical Engineering,
University of Iowa,
2136 Seamans Center,
Iowa City, IA 52242-1527
Mem. ASME

A. C. J. Luo
Assistant Professor,
Department of Mechanical Engineering,
University of Southern Illinois
at Edwardsville,
Edwardsville, IL 62026
Mem. ASME

Resonant Layers in Nonlinear Dynamics

A new method based on an incremental energy approach and the standard mapping technique is proposed for the study of resonant layers in nonlinear dynamics. To demonstrate the procedure, the method is applied to four types of Duffing oscillators. The appearance, disappearance and accumulated disappearance strengths of the resonant layers for each type of oscillator are derived. A quantitative check of the appearance strength is performed by computing its value using three independent methods: Chirikov overlap criterion, renormalization group technique, and numerical simulations. It is also observed that for the case of the twin-well Duffing oscillator, its perturbed left and right wells are asymmetric.

Introduction

In Luo and Han (1998), the stochastic layers near the homoclinic and the heteroclinic orbits were discussed. In this paper, we look at another type of stochastic layer, one that is located in the vicinity of the resonant orbit. To avoid confusion with the stochastic layer located in the vicinity of the separatrix, the region of stochasticity near the resonant orbit is usually termed the *resonant* layer. The condition of resonance with the unperturbed oscillation at frequency ω (Abraham and Marsden, 1978) is

$$m\omega = n\Omega \tag{1}$$

in which Ω denotes the excitation frequency, and m, n are positive integers. Thus, the resonant orbit leads to a separation between the actions of neighboring resonances. In the case of two-dimensional Poincare maps, resonant layers are isolated from each other by means of invariant curves or periodic orbits, and motion from one layer to another is generally forbidden except when the external excitation is very strong. When this happens, the last invariant curve separating the layers surrounding the adjacent elliptic orbits is destroyed and the layers merge together. We can now talk of *global* resonant layers, in analogy to *global* stochastic layers as described in Luo and Han (1998) and Luo (1995).

Using the Melnikov method (Melnikov 1963), Holmes (1980) developed an analytical technique to determine the occurrence of the transverse intersections of the stable and unstable eigencurves. Holmes and Marsden (1981, 1982a, b, 1983) applied the method to multi-degrees-of-freedom autonomous Hamiltonian systems to determine chaotic motion and Arnold diffusion. Other notable applications of the Melnikov method in this area of research include Greenspan and Holmes (1982, 1983) and Wiggins (1988, 1990). The Melnikov method is able to predict the existence of transverse intersections in the stochastic and resonant layers (Guckenheimer and Holmes, 1983) but it is unable to determine their strengths (or widths and chaotic conditions). Reichl and Zheng (1984a, b) and Reichl (1992) derived the strength of a stochastic layer for the twin-well Duffing oscillator using the Chirikov overlap criterion (Chirikov, 1979). In a subsequent publication, Lin and Reichl (1986) computed the strength of the stochastic layer for a particle in an infinite square well potential using the renormalization group technique (Escande and Doveil, 1981; Escande, 1985). Adopting an incremental energy approach, Luo and Han (1998) presented the strength of the stochastic layer for the twin-well Duffing oscillator. In a similar fashion, one can also talk of the strength of *resonant* layers. The strength of the resonant layer for four types of the Duffing oscillator is determined in Han and Luo (1997) by applying the Chirikov overlap criterion, and in Luo, Han, and Xiang (1995) using the renormalization group method. In this paper, a better understanding of resonant layers via the development of an analytical model is presented. The underlying theory is based on an incremental energy approach first developed for our previous work on stochastic layers as presented in Luo and Han (1998) and the standard mapping methods in Greene (1968, 1979). For completeness, four types of the Duffing oscillator are investigated in this work. Strength computations with respect to the appearance, disappearance, and accumulated disappearance of the resonance layer are presented. To verify our results, comparisons with those obtained using the Chirikov overlap criterion, the renormalization group technique, and through numerical experimentations are made.

Stochasticity Near a Resonant Orbit

We consider a time-periodic system defined by

$$\dot{x} = f(x) + g(x, t); \quad x = \begin{pmatrix} x \\ y \end{pmatrix} \in R^2, \tag{2}$$

where $f(x)$ is a Hamiltonian vector field defined on R^2, $g(x, t)$ is a $T = 2\pi/\Omega$-periodic (fixed period) Hamiltonian in time t, and Ω denotes the excitation frequency. Specifically, they are of the form

$$f(x) = \begin{pmatrix} f_1(x) \\ f_2(x) \end{pmatrix}, \quad \text{and} \quad g(x, t) = \begin{pmatrix} g_1(x, t) \\ g_2(x, t) \end{pmatrix}, \tag{3}$$

and are assumed to be sufficiently smooth (C^r, $r \geq 2$) and bounded on bounded sets $D \subset R^2$ in the phase space. The total energy of the system is

$$H(x, y, t) = H_0(x, y) + H_1(x, y, t), \tag{4}$$

where $H_0(x, y)$ and $H_1(x, y, t)$ are the energy functions of the conservative system and external excitation (unperturbed and perturbed Hamiltonians), respectively. For a given energy level, i.e., $H_0 = E_0$ = constant, the nonlinear natural frequency and the unperturbed solution can be obtained as described in Han

[1] To whom correspondence should be addressed. e-mail: ray_han@uiowa.edu.

Contributed by the Applied Mechanics Division of THE AMERICAN SOCIETY OF MECHANICAL ENGINEERS for publication in the ASME JOURNAL OF APPLIED MECHANICS.

Discussion on the paper should be addressed to the Technical Editor, Professor Lewis T. Wheeler, Department of Mechanical Engineering, University of Houston, Houston, TX 77204-4792, and will be accepted until four months after final publication of the paper itself in the ASME JOURNAL OF APPLIED MECHANICS.

Manuscript received by the ASME Applied Mechanics Division, Jan. 23, 1997; final revision, Dec. 10, 1997. Associate Technical Editor: S. W. Shaw.

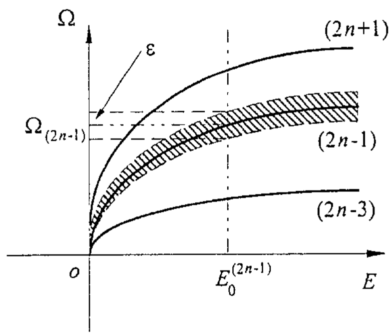

Fig. 1 Neighborhood of the (2n − 1)th resonant frequency

and Luo (1997). Applying Fourier series expansion to the perturbed Hamiltonian H_1, the resonant condition of Eq. (1) is given by

$$\Omega_{(m/n)} = \frac{m}{n}\Omega, \tag{5}$$

in which $\Omega_{(m/n)}$ denotes the $(m:n)$ resonant frequency. A neighborhood of a natural frequency ω close to $\Omega_{(m/n)}$ can be defined as

$$|\omega - \Omega_{(m/n)}| \le \varepsilon \quad \text{and} \quad T(E_0) = \frac{2\pi}{\Omega_{(m/n)}},$$

$$T(E_1) = \frac{2\pi}{\omega}, \tag{6}$$

where $\varepsilon \ll 1$ and $T(E)$ is the nonlinear period. Choosing the odd-order subharmonic resonance as an example, Eq. (6) is illustrated as shown in Fig. 1. To estimate the energy increment of the perturbed orbit, we consider the sketch in Fig. 2. All thin line curves (including the dash line curve) pertain to the unperturbed orbits of Eq. (2). The dash line curve denotes an unperturbed resonant orbit which is an unperturbed orbit that satisfy the resonant condition $\omega = (m/n)\Omega$. To compute the energy increment of the perturbed orbit shown by the bold line curve, it is assumed that the perturbed orbit lies in the neighborhood of the unperturbed resonant orbit with its frequency and period governed by Eq. (6). Thus, the energies of the two orbits are related by $|E - E_0| \le \varepsilon_1$ where $\varepsilon_1 > 0$ is a small parameter. Under this situation, the energy increment of the perturbed orbit can be approximated by the energy increment of the unperturbed resonant orbit. That is, over one period, we have

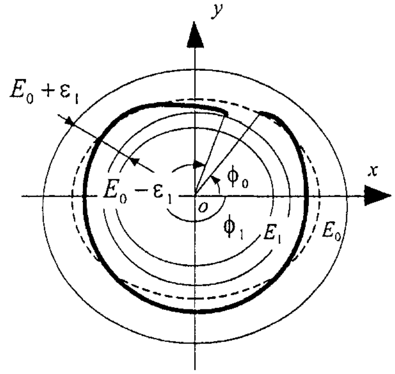

Fig. 2 A perturbed orbit in the neighborhood of the unperturbed resonant orbit

$$\Delta H_0 = E_1 - E_0 = \int_{t_0}^{T(E_1)+t_0} \frac{dH(x, y, t)}{dt}\, dt$$

$$\approx \int_{t_0}^{T(E_0)+t_0} \frac{dH(x, y, t)}{dt}\, dt = \int_{t_0}^{T(E_0)+t_0} \{H_0, H_1\}_{\text{Poisson}} dt$$

$$= \int_{t_0}^{T(E_0)+t_0} (f_1 g_2 - f_2 g_1) dt, \tag{7}$$

where t_0 is the initial time. If f_1, f_2, g_1, g_2 are given, Eq. (7) can be integrated into the following form:

$$\Delta H_0 \approx F(U_0, \phi_0), \tag{8}$$

in which U_0 is a system parameter function excluding the initial phase angle $\phi_0 = \Omega t_0$ and $F(U_0, \phi_0)$ is a bounded and periodic function. For the perturbed orbit in the neighborhood of a given unperturbed resonant orbit, its phase angle change over one period of the unperturbed orbit is

$$\Delta\phi = \phi_{i+1} - \phi_i \approx \Omega T(E_1) = \frac{2\pi\Omega}{\omega} \equiv V_0(E_1), \tag{9}$$

where V_0 is a function associated with the energy E_1. Introducing the following notation, $E_1 = w_{i+1}$ at the $(i+1)$th period and the corresponding phase angle is ϕ_{i+1}, Eqs. (8)–(9) can now be rewritten as

$$\left.\begin{aligned} w_{i+1} &= w_i + F(U_0, \phi_i) \\ \phi_{i+1} &= \phi_i + V_0(w_{i+1}) \end{aligned}\right\}. \tag{10}$$

Observe that Eq. (10) is now expressed in a form that permits the resonant layer to be investigated iteratively. It is a map of the energy change and phase angle change of a trajectory for each period of its motion. It resembles a perturbed twist map and when applied to the Duffing oscillator, it becomes the whisker map. In the neighborhood of the resonant layer, V_0 in Eq. (10) can be linearized about a fixed point and we obtain a map similar to the standard map. Considering the period-1 motion, its fixed point can be easily determined: $w_{i+1} = w_i = w_0$ and $\phi_{i+1} = \phi_i + 2m\pi/n = \phi_0 + 2m\pi/n$. This implies

$$\left.\begin{aligned} F(U_0, \phi_0) &= 0 \\ V_0(w_0) &= 2\pi\frac{m}{n} \end{aligned}\right\}. \tag{11}$$

Defining a new dimensionless energy

$$\hat{E}_i = \left.\frac{\partial V_0(w_j)}{\partial w_j}\right|_{w_j=w_0} (w_i - w_0), \tag{12}$$

and linearizing V_0 in Eq. (10) about the fixed point yields

$$\left.\begin{aligned} \hat{E}_{i+1} &= \hat{E}_i + F_1(K, \phi_i) \\ \phi_{i+1} &= \phi_i + \hat{E}_{i+1} \end{aligned}\right\}, \tag{13}$$

where $K = U_0 \partial V_0/\partial w_0$ and $F_1(K, \phi_0)$ is a bounded and periodic function. Observe that Eq. (13) resembles the standard map and as shown in the next section, when applied to the Duffing oscillator, becomes the standard map. From Eq. (13) the mechanism involved in the transition to global stochasticity (see Lichtenberg and Lieberman, 1992) in a conservative system is very clear. The coefficient K is the only control parameter for the characterization of the KAM tori. For instance, for the standard map, a critical value of K is attained when $K = K^* = 0.9716354$ . . . , since at this value, the last remaining KAM torus is broken. When this happens we have

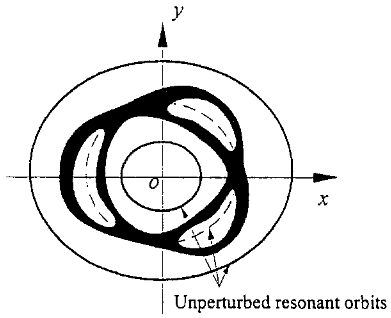

(a)

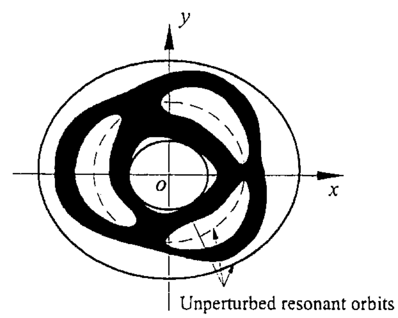

(b)

Fig. 3 Resonant layer: (*a*) appearance and (*b*) disappearance

$$U_0 \frac{\partial V_0}{\partial w_0} = K^*. \tag{14}$$

Increasing the excitation results in the merging of the primary resonant layers until they come into contact the closest unperturbed resonant orbit. When this happens, the resonant layers will be destroyed, and a new stochastic motion near that orbit will appear. This is qualitatively sketched in Fig. 3 where Figs. 3(a) and 3(b) show, respectively, appearance and disappearance of the resonant layer near the closest inner unperturbed resonant orbit. Depending on the physical system modeled, it is also possible for the resonant layer to come into contact with the closest outer unperturbed resonant orbit as depicted.

We postulate that when the resonant layer is destroyed, the energy increment in Eq. (7) is given by the energy difference between the two closest unperturbed resonant orbits, one of which is associated with the destroyed resonant layer. That is

$$\min\left(|E_0^{2n-3} - E_0^{2n-1}|,\ |E_0^{2n+1} - E_0^{2n-1}|\right) = |\Delta H_0^{(2n-1)}| \approx |F(U_0, \phi_0)|. \tag{15}$$

Equation (15) constitutes the critical condition for the disappearance of the resonant layer. From this equation, the *disappearance* strength of the resonant layer can be computed. To compute the *appearance* strength, we have to resort back to Eq. (12). For greater accuracy, we should consider the effects of the secondary resonances in the neighborhood of the intermediate resonant layer.

Resonant Layers for the Undamped Duffing Oscillator

The resonant layers for the four undamped Duffing oscillators are discussed in this section. By suitably varying α_1 and α_2, four types of the Duffing oscillator as listed in Table 1 can be simulated where parameters α_1 and α_2 are the linear stiffness and nonlinear stiffness coefficients respectively; and Q_0 and Ω are the external excitation amplitude and frequency.

Table 1 Four types of Duffing oscillators

Type I	$\alpha_1 > 0$ and $\alpha_2 > 0$	$\ddot{x} + \alpha_1 x + \alpha_2 x^3 = Q_o \cos\Omega t$
Type II	$\alpha_1 > 0$ and $\alpha_2 < 0$	$\ddot{x} + \alpha_1 x - \lvert\alpha_2\rvert x^3 = Q_o \cos\Omega t$
Type III	$\alpha_1 = 0$ and $\alpha_2 > 0$	$\ddot{x} + \alpha_2 x^3 = Q_o \cos\Omega t$
Type IV	$\alpha_1 < 0$ and $\alpha_2 > 0$ (a) $E_0 > 0$ (b) $E_0 < 0$	$\ddot{x} - \lvert\alpha_1\rvert x + \alpha_2 x^3 = Q_o \cos\Omega t$

Type I Duffing Oscillator. Resonant layers for the Type I Duffing oscillator are qualitatively sketched in Fig. 4. The *outer* dark patch associated with the first resonant orbit and the *inner* dark patch associated with the third resonant orbit are termed respectively the resonant layers of the first and third orders. Note there exist other resonant layers in the neighborhood of the origin O, but these are not shown.

From Table 1, the Hamiltonian for Type I is given by

$$H = \tfrac{1}{2} y^2 + \tfrac{1}{2} \alpha_1 x^2 + \tfrac{1}{4} \alpha_2 x^4 - x Q_0 \cos \Omega t. \tag{16}$$

where $y = \dot{x}$. This Hamiltonian can be separated into the non-time-dependent part H_0 and the time-dependent part H_1. That is

$$H = H_0 + H_1, \tag{17}$$

where

$$H_0 = \tfrac{1}{2} y^2 + \tfrac{1}{2} \alpha_1 x^2 + \tfrac{1}{4} \alpha_2 x^4, \tag{18}$$

and

$$H_1 = -x Q_0 \cos \Omega t. \tag{19}$$

Solving Eq. (18) for $H_0 = E_0$, the results are (Han and Luo 1997)

$$x = e \operatorname{cn}\left[\frac{2K(k)\,\theta}{\pi}, k\right], \tag{20}$$

$$y = \pm\sqrt{\frac{\alpha_2}{2}}\frac{e^2}{k} \operatorname{sn}\left[\frac{2K(k)\theta}{\pi}, k\right] \operatorname{dn}\left[\frac{2K(\theta)}{\pi}, k\right], \tag{21}$$

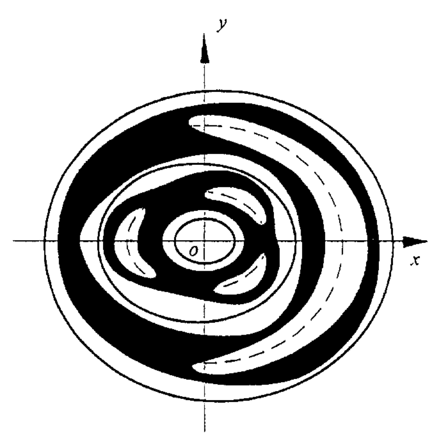

Fig. 4 Resonant layers near the first and third resonant orbits for Type I Duffing oscillator

in which cn, sn and dn are the Jacobi-elliptic functions, $K(k)$ the complete elliptic integral of the first kind, and k the modulus of the Jacobi-elliptic function. The other parameters e and θ in these expressions are defined by

$$e^2 = \frac{2k^2\alpha_1}{(1 - 2k^2)\alpha_2}, \quad \theta = \omega t, \tag{22}$$

where ω is the nonlinear natural frequency of the undamped Type I Duffing oscillator. It can be computed from

$$\omega = \frac{1}{2}\sqrt{\frac{\alpha_2}{2}}\,\frac{e\pi}{kK(k)}. \tag{23}$$

The particular energy level E_0 can then be calculated using

$$E_0 = \frac{k^2(1 - k^2)\alpha_1^2}{(1 - 2k^2)^2\alpha_2}, \tag{24}$$

and the action variable J for an orbit is given by

$$J = \frac{\sqrt{2\alpha_2}e^3}{3\pi k^3}[(1 - k^2)K(k) + (2k^2 - 1)E(k)], \tag{25}$$

where $E(k)$ denotes the complete elliptic integral of the second kind. Substituting Eqs. (20)–(21) into Eq. (16) and expanding the time-dependent term, the complete Hamiltonian now becomes

$$H = H_0(J) - Q_0 \sum_{n=1}^{\infty} Q_{2n-1}\{\cos[(2n - 1)\omega - \Omega]t + \cos[(2n - 1)\omega + \Omega]t\} \tag{26}$$

in which

$$Q_{2n-1} = \frac{\pi e}{2kK \cosh\left[\pi\left(n - \frac{1}{2}\right)\frac{K'(k)}{K(k)}\right]}, \tag{27}$$

where $K'(k) = K(k')$ and $k' = 1 - k^2$. Except for the term of the $(2n - 1)$th primary resonance, all other terms in H will average to zero over the period $2\pi/\Omega$. The resonant condition is

$$\omega = \Omega_{2n-1} = \frac{\Omega}{2n - 1}. \tag{28}$$

The period of the resonant orbit is computed using Ω_{2n-1}. However, for all other orbits in the resonant layer, the period at energy E_1 is calculated based on ω, that is

$$T(E_1) = \frac{2\pi}{\omega}. \tag{29}$$

The change of phase angle over one period $T(E_1)$ is

$$\Delta\phi = \Omega T(E_1) = V_0 \tag{30}$$

in which

$$V_0 = 4\Omega K(k)\sqrt{\frac{2}{\alpha_2}}\,\frac{k}{e}. \tag{31}$$

Thus, from Eq. (7), the energy increment over one period $T(E_1)$ can be approximated by

$$\Delta H_0 \approx \int_{t_0}^{T(E_0)+t_0} yQ_0 \cos(\Omega t)dt = U_0 \sin(\Omega t_0), \tag{32}$$

where

$$U_0 = \frac{2\sqrt{2}\pi\Omega Q_0}{\sqrt{\alpha_2}} \operatorname{sech}\left[\left(n - \frac{1}{2}\right)\pi\frac{K'(k_{2n-1})}{K(k_{2n-1})}\right]. \tag{33}$$

Note that $K'(k) = K(k')$. Observe that Eq. (33) describes the function U_0 identified in the previous section and as shown, comprises only of system parameters. Following the procedure outlined in previous section, Eqs. (30) and (32) are written as

$$\left.\begin{aligned} w_{i+1} &= w_i + U_0 \sin(\phi_i) \\ \phi_{i+1} &= \phi_i + V_0(w_{i+1}) \end{aligned}\right\}. \tag{34}$$

Observe that Eq. (34) is the whisker map. To obtain the standard map, we linearize V_0 in Eq. (34) in the neighborhood of the unperturbed resonant orbit about the period-1 fixed point $w_{i+1} = w_i = w_0$ and $\phi_{i+1} - \phi_i = 2(2n - 1)\pi$. The resonant energy is given by

$$2(2n - 1)\pi = V_0(w_0). \tag{35}$$

From Eq. (12) a new dimensionless energy $\hat{E}_i = G_1\Delta w_i$ can be defined, where the function $G_1 = \partial V_0/\partial w_{i+1}$ at $w_{i+1} = w_i = w_0$, is given by

$$G_1 = -\frac{2\Omega\alpha_2}{(k_{2n-1})^2}\left(\frac{1 - 2(k_{2n-1})^2}{\alpha_1}\right)^{5/2} \times \left[K(k_{2n-1}) - \frac{1 - 2(k_{2n-1})^2}{1 - (k_{2n-1})^2}E(k_{2n-1})\right]. \tag{36}$$

Linearizing Eq. (34) about the fixed point we get

$$\left.\begin{aligned} \hat{E}_{i+1} &= \hat{E}_i \pm K \sin\phi_i \\ \phi_{i+1} &= \phi_i + \hat{E}_{i+1} \end{aligned}\right\}, \tag{37}$$

where $K = U_0|G_1|$. Note that Eq. (37) is now the standard map. Employing the universal constant of the standard map, i.e., $K = K^* = 0.9716354\ldots$, we can compute the *appearance* strength of the resonant layer and the result is

$$Q_0 \approx \frac{0.9716354\sqrt{\alpha_2}}{2\sqrt{2}\pi\Omega|G_1|}\cosh\left[\left(n - \frac{1}{2}\right)\pi\frac{K'(k_{2n-1})}{K(k_{2n-1})}\right]. \tag{38}$$

As a check of Eq. (38), any one of the three methods can be used: Chirikov overlap criterion, renormalization group technique and numerical simulation; to independently compute the appearance strength. The results based on the Chirikov overlap criterion and the renormalization group technique are available, respectively, in Han and Luo (1997) and Luo, Han, and Xiang (1995). We will simply quote them here. Based on Chirikov overlap criterion, the appearance strength is

$$Q_0 = \frac{\Omega^2}{4(2n - 1)^2(2n + 1)^2G_0}\left(\frac{1}{\sqrt{Q_{2n-1}} + \sqrt{Q_{2n+1}}}\right)^2. \tag{39}$$

Using the renormalization group technique, the appearance strength is

$$Q_0 = \frac{0.49\Omega^2}{4(2n - 1)^2(2n + 1)^2G_0}\left(\frac{1}{\sqrt{Q_{2n-1}} + \sqrt{Q_{2n+1}}}\right)^2 \tag{40}$$

where

$$Q_{2n-1} = \frac{\sqrt{2}\Omega}{\sqrt{\alpha_2}(2n - 1)\cosh\left[\pi\left(n - \frac{1}{2}\right)\frac{K'(k_{2n-1})}{K(k_{2n-1})}\right]}, \tag{41}$$

$$Q_{2n+1} = \frac{\sqrt{2}\Omega}{\sqrt{\alpha_2}(2n + 1)\cosh\left[\pi\left(n + \frac{1}{2}\right)\frac{K'(k_{2n+1})}{K(k_{2n+1})}\right]}. \tag{42}$$

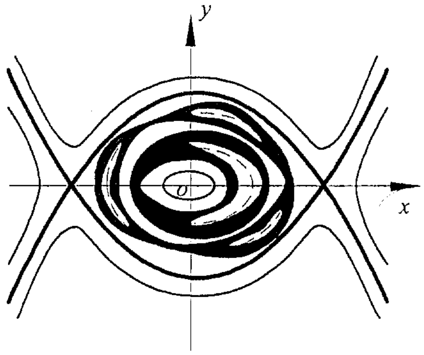

Fig. 5 Resonant layers near the first and third resonant orbits for Type II Duffing oscillator

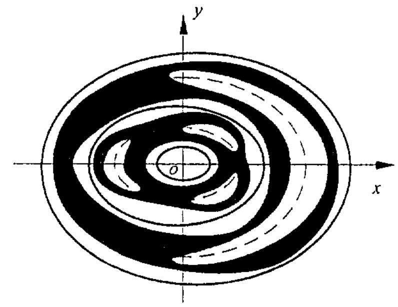

Fig. 6 Resonant layers near the first and third resonant orbits for Type III Duffing oscillator

Observe that Eqs. (39) and (40) differ only by a factor of 0.49. A comparison of our results based on the incremental energy approach with the predictions of the Chirikov overlap criterion, renormalization group technique, and numerical simulations is listed in the next section.

To compute the *disappearance* strength we assume that our energy postulate which is described mathematically by Eq. (15) still holds. This yields the critical condition for the disappearance of the resonant layer from which the disappearance strength of the resonant layer can be estimated. The result is

$$2Q_0\pi\Omega\sqrt{\frac{2}{\alpha_2}}\,\mathrm{sech}\left[\left(n-\frac{1}{2}\right)\pi\,\frac{K'(k_{2n-1})}{K(k_{2n-1})}\right]$$

$$= \min\{|E_0^{2n+1}-E_0^{2n-1}| \quad \text{and} \quad |E_0^{2n-1}-E_0^{2n-3}|\}. \quad (43)$$

If the incremental energy along a resonant obit is set equal to $|E_0^{2n-1}-E_0^c|$, where $E_0^c=0$ is the energy at the origin, Eq. (43) describes the *accumulated* disappearance strength of all the possible resonances higher than order $(2n-1)$ of the system. Therefore, we get the *maximum* critical condition for the accumulated disappearance strength:

$$2Q_0\pi\Omega\sqrt{\frac{2}{\alpha_2}}\,\mathrm{sech}\left[\left(n-\frac{1}{2}\right)\pi\,\frac{K'(k_{2n-1})}{K(k_{2n-1})}\right] = E_0^{2n-1}. \quad (44)$$

A more accurate model is to sum the effects of each individual resonant layer instead of simply setting the incremental energy to $|E_0^{2n-1}-E_0^c|$.

Type II Duffing Oscillator. Resonant layers for the Type II Duffing oscillator are qualitatively sketched in Fig. 5. The structure of the resonant layer differs from that of the Type I oscillator because as shown in Fig. 5, we now have a heteroclinic orbit. For this situation, the resonant layer exist only inside the heteroclinic orbit, otherwise, this layer will lose its stability when it comes into contact with the heteroclinic orbit. The maximum critical condition for instability of the resonant layer is

$$2Q_0\pi\Omega\sqrt{\frac{2}{|\alpha_2|}}\,\mathrm{csch}\left[\left(n-\frac{1}{2}\right)\pi\,\frac{K'(k_{2n-1})}{K(k_{2n-1})}\right]$$

$$= |E_0^{sx}-E_0^{2n-1}|, \quad (45)$$

in which E_0^{sx} is the energy of the separatrix, i.e., $E_0^{sx}=\alpha_1^2/(4|\alpha_2|)$. For brevity, all the results pertaining to the appearance and disappearance strengths are listed in the Appendix.

Type III Duffing Oscillator. Resonant layers for the Type III Duffing oscillator are qualitatively sketched in Fig. 6. This oscillator is a special situation of Type I and therefore, all its results, with the exception of the maximum critical condition for the accumulated disappearance strength, are summarized in the Appendix. The maximum critical condition is

$$2Q_0\pi\Omega\sqrt{\frac{2}{\alpha_2}}\,\mathrm{sech}\left[\left(n-\frac{1}{2}\right)\pi\right] = E_0^{2n-1}. \quad (46)$$

Type IV Duffing Oscillator. For the Type IV Duffing oscillator, there are two kinds of resonant layers as qualitatively sketched in Fig. 7, representing $E_0<0$ and $E_0>0$. Note that Type IV(c) which is described by $E_0=0$ possesses only stochastic layers as discussed in Luo and Han (1998). Once again, for these two situations, all their results listed in the Appendix, with exception of the maximum critical condition for the accumulated disappearance strength. The result for Type IV(a) is obtained by noting that $E_0^c=0$. That is

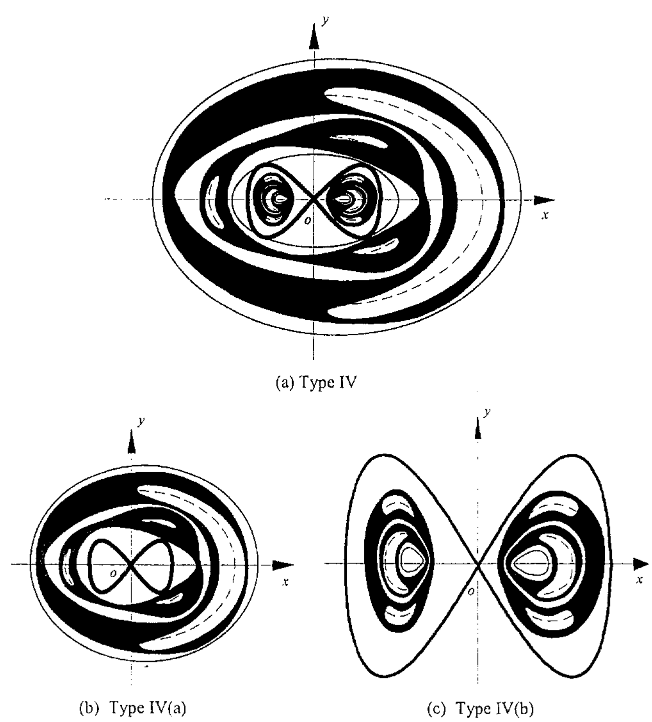

Fig. 7 Resonant layers for Type IV, Type IV(*a*) and Type IV(*b*) Duffing oscillators

Table 2 Comparison of the appearance strength computations

Oscillator Type	Order of Resonance	Input Energy	Computed Excitation Frequency	Appearance Strength Q_0			
		E_0	Ω	IE	CC[a]	RG[b]	NS
Type I	1st	52.75000	3.28244	3.04401	3.22748	1.58146	3.04995
	3rd	18.25000	7.64562	4.25025	13.09158	6.41488	3.60555
	5th	15.95000	12.34715	33.14722	142.48083	69.21561	33.20000
Type II	1st	0.10013	0.91064	0.08633	---	---	0.02873
	3rd	0.15638	2.51709	0.28158	0.25983	0.12732	0.25875
	5th	0.19800	3.80845	1.02497	1.32309	0.64831	1.02500
Type IV(a)	1st	48.75000	3.11743	2.53486	1.99073	0.97513	2.54550
	3rd	5.17500	5.19563	0.77066	1.66639	0.81653	0.75750
	5th	6.02500	9.01816	5.60285	17.47684	8.56365	5.90000
Type IV(b)	1st	-0.18413	1.33650	0.04687	0.06420	0.03145	0.03547
	2nd	-0.15038	2.57721	0.08425	0.16379	0.08026	0.10500
	3rd	-0.12413	3.73699	0.21239	0.49209	0.24109	0.19985

[a]Han and Luo (1997); [b]Luo, Han and Xiang (1995).

$$2Q_0\pi\Omega\sqrt{\frac{2}{\alpha_2}}\,\mathrm{sech}\left[\left(n-\frac{1}{2}\right)\pi\,\frac{K'(k_{2n-1})}{K(k_{2n-1})}\right]=E_0^{2n-1}, \quad (47)$$

and for the Type IV(b) we have

$$Q_0\pi\Omega\sqrt{\frac{2}{\alpha_2}}\,\mathrm{sech}\left[n\pi\,\frac{K'(k_n)}{K(k_n)}\right]=|E_0^n|. \quad (48)$$

Comparison of Appearance Strength of Resonant Layers

Having obtained the appearance strength of resonant layers based on our proposed incremental energy approach (**IE**), we will now present verification of our results by comparing with three independent methods: Chirikov overlap criterion (**CC**), renormalization group technique (**RG**), and numerical simulations (**NS**). For simplicity, we set $|\alpha_1| = |\alpha_2| = 1.0$ for all the four types of Duffing oscillator. The appearance strength is computed as follows. From the specified initial energy E_0, and choosing say, the Type I Duffing oscillator, we can compute k and e via Eqs. (24) and (22), respectively. Then, we can determine the natural frequency ω and the initial condition (x, y) using Eqs. (23) and (20)–(21), respectively. The excitation frequency Ω can then be evaluated from the resonant condition in Eq. (28) corresponding to a selected order of resonance n. The various strength computations are carried out using Eqs. (38), (43), and (44). We can also perform the same process but in a different order of execution if either the Ω or (x, y) is given. In our example, we assumed that E_0 is known, and the excitation frequency Ω (and the initial condition (x, y)) are to be computed. The results are tabulated in Table 2. The appearance strengths of the Type I Duffing oscillator are calculated using Eq. (38) for **IE**, Eq. (39) for **CC**, and Eq. (40) for **RG**. To compute the appearance strength of Type II-IV Duffing oscillators, their corresponding equations listed in the Appendix can be used.

Two integration techniques are used for the numerical experimentations: a second-order symplectic scheme (Feng and Qin 1991, and McLachlan and Atela 1992) with time-step $\Delta t = 10^{-5} \sim 10^{-7}T$ (where T is the excitation period) and precision 10^{-6}; and an adaptive fourth-order Runge-Kutta method with tolerance set between $10^{-8} \sim 10^{-9}$. The numerical simulations are performed over 10^5T and we find that both methods yield almost identical solutions, thereby confirming the reliability of the two schemes. To determine the appearance strength during **NS**, we check for the appearance of the resonance. For example, if input parameters pertaining to the third-order resonance are employed for the numerical runs, the appearance strength corresponding to the visually observed third-order resonance is computed. However, this is easier said than done because the precise determination of the appearance of a resonance layer during **NS** is based wholly on visual observations and thus, a highly subjective process. The **NS** results tabulated in Table 2 for all the four types of Duffing oscillator correspond to the most *visually distinctive* appearance of the resonance layers and are generated via the Runge-Kutta integrator. Observe that the agreement among **IE**, **CC**, and **RG** are generally better at lower-order resonances and this is attributed to the fact **CC** and **RG** are based on a two-term approximation which becomes increasingly less accurate as the order of resonance increases. On the other hand, the agreement between **IE** and **NS** is quite good.

We should also point out that since there are no currently known procedures for independently computing the disappearance strength and the accumulated disappearance strength, other than our proposed incremental energy method, no comparisons of these results are given.

Numerical Simulations of Resonant Layers

In this section, we present the results of numerical simulation of the resonant layers via their Poincare mapping sections. Only results for Type I, II, and IV(b) Duffing oscillators are given. The results for Type III and IV(a) oscillators are very similar to that of Type I oscillator and hence, not shown here. The computed input parameters for the numerical experimentations are summarized in Table 3. The use of these computed parameters ensures that resonant layers are obtained during the numerical runs. Once again, $|\alpha_1| = |\alpha_2| = 1.0$ is employed.

Figure 8 depicts the resonance layers produced by Type I, II, and IV(b) Duffing oscillators. Figure 8(a) shows the third

Table 3 Computed input data for numerical simulations of resonant layers

Figure No.	Oscillator Type	Order of Resonance	Analytically Computed Parameters (x,y)	Ω	Numerically Simulated Q_0
Figure 8(a)	Type I	3rd	(-2.75723145, 0.00000000)	7.64562	10.415
		5th	(0.71630084, 5.59064277)	12.34715	105.000
Figure 8(b)	Type II	1st	(0.47510649, 0.00000000)	0.91064	0.027
		5th	(0.32752924, 0.45959614)	2.51709	0.310
Figure 8(c)	Type IV(b)	2nd (R)	(1.27721125, 0.00000000)	2.57721	0.110
		2nd (L)	(-0.60723259, 0.00000000)	2.57721	0.110
		3rd (R)	(1.30750807, 0.00000000)	3.73699	0.376
		3rd (L)	(-0.53890877, 0.00000000)	3.73699	0.376

and fifth-order resonant layers for the Type I oscillator, Fig. 8(b) depicts the first and third-order resonant layers for the Type II oscillator, and Fig. 8(c) displays the second and third-order resonant layers for the Type IV(b) oscillator. Observe the presence of higher order islands in Type II and IV(b) oscillators. Another interesting observation is the nonsymmetry of the perturbed left and right potential wells in the Type IV(b) oscillator.

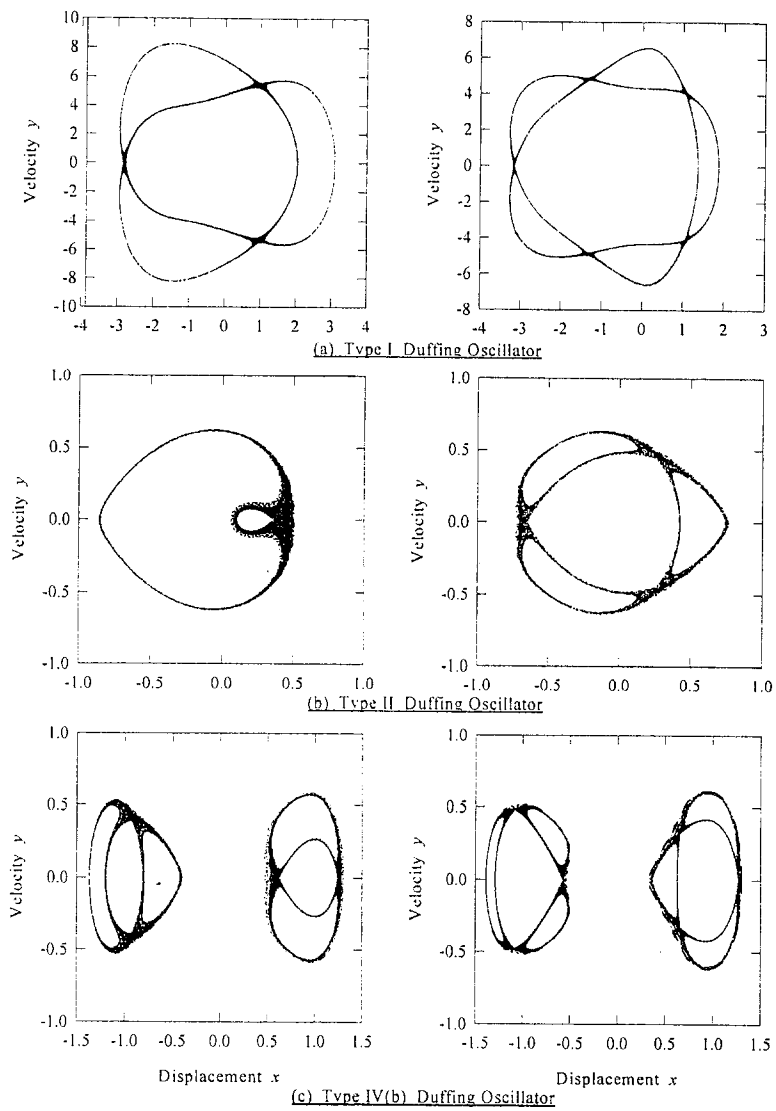

Fig. 8 Resonant layers for undamped Type I, II, and IV(b) Duffing oscillators via NS

Conclusions

A study of the resonant layers for all four types of Duffing oscillators is presented here. The approach is based on an incremental energy technique implemented into the standard mapping approach and can be quite easily extended to other nonlinear dynamical systems. Using this approach, the appearance, disappearance, and accumulated disappearance strengths of the resonant layers are derived. For the case of the appearance strength computations, they are quantitatively checked against the values obtained via three independent methods: Chirikov overlap criterion, renormalization group theory, and numerical simulations. The agreement between **IE** and **NS** is quite good. It is also found that the perturbed left and right potential wells are asymmetric for the case of the Type IV(b) twin-well Duffing oscillator.

Acknowledgment

This work was supported by an operating grant from the Natural Sciences and Engineering Research Council of Canada and a University of Manitoba doctoral fellowship for the second author during his study. We would also like to acknowledge the contributions of the reviewers for this paper.

References

Abraham, R., and Marsden, J. E., 1978, *Foundations of Mechanics*, Benjamin/Cummings, London.

Chirikov, B. V., 1979, "A Universal Instability of Many-Dimensional Oscillator System," *Phys. Rep.*, Vol. 52, pp. 263–379.

Escande, D. F., 1985, "Stochasticity in Classical Hamiltonian Systems: Universal Aspects," *Phys. Rep.*, Vol. 121, pp. 165–261.

Escande, D. F., and Doveil, F., 1981, "Renormalization Method for the Onset of Stochasticity in a Hamiltonian System," *Phys. Lett.*, Vol. 83A, pp. 307–310.

Feng, K., and Qin, M. Z., 1991, "Hamiltonian Algorithms for Hamiltonian Systems and a Comparative Numerical Study," *Comput. Phys. Commun.*, Vol. 65, pp. 173–187.

Greene, J. M., 1968, "Two-Dimensional Measure-Preserving Mappings," *J. of Math. Phys.*, Vol. 9, pp. 760–768.

Greene, J. M., 1979, "A Method for Computing the Stochastic Transition," *J. of Math. Phys.*, Vol. 20, pp. 1183–1201.

Greenspan, B. D., and Holmes, P. J., 1982, "Homoclinic Orbits, Subharmonics and Global Bifurcations in Forced Oscillations," *Nonlinear Dynamics and Turbulence*, G. Barenblatt, G. Iooss, and D. D. Joseph, eds., Pitman, London, pp. 172–214.

Greenspan, B. D., and Holmes, P. J., 1983, "Repeated Resonance and Homoclinic Bifurcations in a Periodically Forced Family of Oscillators," *SIAM J. Math. Anal.*, Vol. 15, pp. 69–97.

Guckenheimer, J., and Holmes P., 1983, *Nonlinear Oscillations, Dynamical Systems, and Bifurcations of Vector Fields*, Springer-Verlag, New York.

Han, Ray P. S., and Luo, Albert C. J., 1997, "Analytical Predictions of Chaos in a Nonlinear Rod," *Chaos, Solitons and Fractals*, submitted for publication.

Holmes, P. J., 1980, "Averaging and Chaotic Motion in Forced Oscillations," *SIAM J. Appl. Math.*, Vol. 38, pp. 65–80.

Holmes, P. J., and Marsden, J. E., 1981, "A Partial Differential Equation with Infinitely Many Periodic Orbits: Chaotic Oscillations of a Forced Beam," *Arch. Ration. Mech. Anal.*, Vol. 76, pp. 135–166.

Holmes, P. J., and Marsden, J. E., 1982a, "Horseshoes in Perturbations of Hamiltonians with Two Degrees of Freedom," *Comm. Math. Phys.*, Vol. 82, pp. 523–544.

Holmes, P. J., and Marsden, J. E., 1982b, "Perturbations of *n* Degree of Freedom Hamiltonian Systems with Symmetry," *J. Math. Phys.*, Vol. 23, No. 4, pp. 669–675.

Holmes, P. J., and Marsden, J. E., 1983, "Horseshoes and Arnold Diffusion for Hamiltonian Systems on Lie Groups," *Indiana University Math. J.*, Vol. 32, pp. 237–310.

Lichtenberg, A. J., and Lieberman, M. A., 1992, *Regular and Chaotic Dynamics*, 2nd ed., Springer-Verlag, New York.

Lin, W. A., and Reichl, L. E., 1986, "External Field Induced Chaos in an Infinite Square Well Potential," *Physica*, Vol. 19D, pp. 145–152.

Luo, Albert C. J., 1995, "Analytical Modeling of Bifurcations, Chaos, and Multifractals in Nonlinear Dynamics," Ph. D. dissertation, University of Manitoba.

Luo, Albert C. J., and Han, Ray P. S., 1998, "The Mechanism of Stochastic Layers Characterized by Inherent Resonance in the Vicinity of a Separatrix," *Proc. Royal Society, London*, submitted for publication.

Luo, A. C. J., Han, R. P. S., and Xiang, Y. M., 1995, "Chaotic Analysis of Subharmonic Resonant Waves in Undamped and Damped Srings," *J. Hydrodynamics*, Vol. 7B, pp. 92–104.

McLachlan, R., and Atela, P., 1992, "The Accuracy of Symplectic Integrators," *Nonlinearity*, Vol. 5, pp. 541–562.

Reichl, L. E., 1992, *The Transition to Chaos in Conservative Classic System: Quantum Manifestations*, Spring-Verlag, New York.

Reichl, L. E., and Zheng, W. M., 1984a, "Field-Induced Barrier Penetration in the Quadratic Potential," *Phys. Rev.*, Vol. 29A, pp. 2186–2193.

Reichl, L. E., and Zheng, W. M., 1984b, "Perturbed Double-Well System: The Pendulum Approximation and Low-Frequency Effect," *Phys. Rev.*, Vol. 30A, pp. 1068–1077.

Wiggins, S., 1988, *Global Bifurcations and Chaos: Analytical Methods*, Spring-Verlag, New York.

Wiggins, S., 1990, *Introduction to Applied Nonlinear Dynamical Systems and Chaos*, Spring-Verlag, New York.

APPENDIX

Computation of the Strength of Resonant Layers for the Undamped Type II-IV Duffing Oscillators

The equations governing the undamped Type II-IV(b) Duffing oscillators are summarized here. Their derivations are similar to that for the Type I oscillator.

Type II Oscillator. The results are

$$E_0 = \frac{k^2\alpha_1^2}{(1+k^2)^2|\alpha_2|}, \quad e^2 = \frac{2k^2\alpha_1}{(1+k^2)|\alpha_2|},$$

$$\omega = \frac{\sqrt{|\alpha_2|}e\pi}{2\sqrt{2}kK(k)}. \tag{A1}$$

The resonant condition is

$$\Omega = (2n-1)\omega. \tag{A2}$$

The appearance strength of the resonant layer based on Chirikov overlap criterion (**CC**) is

$$Q_0 = \frac{\Omega^2}{4(2n-1)^2(2n+1)^2G_0}\left(\frac{1}{\sqrt{Q_{2n-1}}+\sqrt{Q_{2n+1}}}\right)^2; \tag{A3}$$

the appearance strength of the resonant layer based on the renormalization group method (**RG**) is

$$Q_0 = \frac{0.49\Omega^2}{4(2n-1)^2(2n+1)^2G_0}\left(\frac{1}{\sqrt{Q_{2n-1}}+\sqrt{Q_{2n+1}}}\right)^2; \tag{A4}$$

and, the appearance strength of the resonant layer based on the incremental energy (**IE**) is

$$Q_0 \approx \frac{0.9716354\sqrt{|\alpha_2|}}{2\sqrt{2}\pi\Omega|G_1|}\sinh\left[\left(n-\frac{1}{2}\right)\pi\frac{K'(k_{2n-1})}{K(k_{2n-1})}\right]. \tag{A5}$$

The disappearance strength of the resonant layer based on the incremental energy is

$$Q_0 = \frac{|E_0^{2n+1}-E_0^{2n-1}|\sqrt{|\alpha_2|}}{2\sqrt{2}\pi\Omega}\sinh\left[\left(n-\frac{1}{2}\right)\pi\frac{K'(k_{2n-1})}{K(k_{2n-1})}\right]; \tag{A6}$$

in which

$$Q_{2n-1} = \frac{\sqrt{2}\Omega}{\sqrt{|\alpha_2|}(2n-1)}\operatorname{sech}\left[\pi\left(n-\frac{1}{2}\right)\frac{K'(k_{2n-1})}{K(k_{2n-1})}\right], \tag{A7}$$

$$Q_{2n+1} = \frac{\sqrt{2}\Omega}{\sqrt{|\alpha_2|}(2n+1)}\operatorname{sech}\left[\pi\left(n+\frac{1}{2}\right)\frac{K'(k_{2n+1})}{K(k_{2n+1})}\right], \tag{A8}$$

$$G_0 = \frac{\pi^2}{4e^2(k'_{2n-1})^2K(k_{2n-1})^3}\left[K(k_{2n-1}) - \frac{1+(k_{2n-1})^2}{1-(k_{2n-1})^2}E(k_{2n-1})\right], \tag{A9}$$

$$G_1 = -\frac{2\Omega|\alpha_2|}{k_{2n-1}(k'_{n-1})^2}\left(\frac{1+(k_{2n-1})^2}{\alpha_1}\right)^{5/2}\left[K(k_{2n-1}) - \frac{1+(k_{2n-1})^2}{1-(k_{2n-1})^2}E(k_{2n-1})\right]. \quad (A10)$$

Type III Oscillator. The results are

$$k = \frac{1}{\sqrt{2}},\ e = \left(\frac{4E_0}{\alpha_2}\right)^{1/4},\ K(k) \approx 1.8541,\ \omega = \frac{(4\alpha_2 E_0)^{1/4}\pi}{3.7082}. \quad (A11)$$

The resonant condition is

$$\Omega = (2n-1)\omega. \quad (A12)$$

The appearance strength of the resonant layer based on Chirikov overlap criterion (**CC**) is

$$Q_0 = \frac{6.3738151\Omega^3\{\sqrt{(2n-1)\ \text{sech}\,[\pi(n-1/2)]} + \sqrt{(2n+1)\ \text{sech}\,[\pi(n+1/2)]}\}^{-2}}{(2n-1)^3(2n+1)\pi^3\sqrt{\alpha_2}}; \quad (A13)$$

the appearance strength of the resonant layer based on the renormalization group method (**RG**) is

$$Q_0 = \frac{3.1231694\Omega^3\{\sqrt{(2n-1)\ \text{sech}\,[\pi(n-1/2)]} + \sqrt{(2n+1)\ \text{sech}\,[\pi(n+1/2)]}\}^{-2}}{(2n-1)^3(2n+1)\pi^3\sqrt{\alpha_2}}; \quad (A14)$$

and, the appearance strength of the resonant layer based on the incremental energy (**IE**) is

$$Q_0 \approx \frac{0.524046923\alpha_2^2 e^5}{16\sqrt{2}\Omega^2\pi}\cosh\left[\left(n-\frac{1}{2}\right)\pi\right]. \quad (A15)$$

The disappearance strength of the resonant layer based on the incremental energy is

$$Q_0 = \frac{|E_0^{2n+1} - E_0^{2n-1}|\sqrt{\alpha_2}}{2\sqrt{2}\Omega\pi}\cosh\left[\left(n-\frac{1}{2}\right)\pi\right]. \quad (A16)$$

Type IV(a) Oscillator. The results are

$$E_0 = \frac{(1-k^2)k^2\alpha_1^2}{(2k^2-1)^2\alpha_2},\quad e^2 = \frac{2k^2|\alpha_1|}{(2k^2-1)\alpha_2},\quad \omega = \frac{\sqrt{\alpha_2}e\pi}{2\sqrt{2}kK(k)}. \quad (A17)$$

The resonant condition is

$$\Omega = (2n-1)\omega. \quad (A18)$$

The appearance strength of the resonant layer based on Chirikov overlap criterion (**CC**) is

$$Q_0 = \frac{\Omega^2}{4(2n-1)^2(2n+1)^2G_0}\left(\frac{1}{\sqrt{Q_{2n-1}}+\sqrt{Q_{2n+1}}}\right)^2; \quad (A19)$$

the appearance strength of the resonant layer based on the renormalization group method (**RG**) is

$$Q_0 = \frac{0.49\Omega^2}{4(2n-1)^2(2n+1)^2G_0}\left(\frac{1}{\sqrt{Q_{2n-1}}+\sqrt{Q_{2n+1}}}\right)^2; \quad (A20)$$

and, the appearance strength of the resonant layer based on the incremental energy (**IE**) is

$$Q_0 \approx \frac{0.9716354\sqrt{\alpha_2}}{2\sqrt{2}\Omega\pi|G_1|}\cosh\left[\left(n-\frac{1}{2}\right)\pi\frac{K'(k_{2n-1})}{K(k_{2n-1})}\right]. \quad (A21)$$

The disappearance strength of the resonant layer based on the incremental energy is

$$Q_0 = \frac{|E_0^{2n+1} - E_0^{2n-1}|\sqrt{\alpha_2}}{2\sqrt{2}\Omega\pi}\cosh\left[\left(n-\frac{1}{2}\right)\pi\frac{K'(k_{2n-1})}{K(k_{2n-1})}\right]; \quad (A22)$$

in which

$$G_0 = \frac{\pi^2}{4e^2K(k_{2n-1})^3}\left[K(k_{2n-1}) - \frac{1-2(k_{2n-1})^2}{1-(k_{2n-1})^2}E(k_{2n-1})\right], \quad (A23)$$

$$G_1 = -\frac{2\Omega\alpha_2}{(k_{2n-1})^2}\left(\frac{2(k_{2n-1})^2-1}{\alpha_1}\right)^{5/2}\left[K(k_{2n-1}) - \frac{1-2(k_{2n-1})^2}{1-(k_{2n-1})^2}E(k_{2n-1})\right], \quad (A24)$$

$$Q_{2n-1} = \frac{\sqrt{2}\Omega}{\sqrt{\alpha_2}(2n-1)}\,\text{sech}\left[\pi\left(n-\frac{1}{2}\right)\frac{K'(k_{2n-1})}{K(k_{2n-1})}\right], \quad (A25)$$

$$Q_{2n+1} = \frac{\sqrt{2}\Omega}{\sqrt{\alpha_2}(2n+1)}\,\text{sech}\left[\pi\left(n+\frac{1}{2}\right)\frac{K'(k_{2n+1})}{K(k_{2n+1})}\right]. \quad (A26)$$

Type IV(b) Oscillator. The results are

$$E_0 = \frac{(k^2-1)\alpha_1^2}{(2-k^2)^2\alpha_2},\quad e^2 = \frac{2|\alpha_1|}{(2-k^2)\alpha_2},\quad \omega = \frac{\sqrt{\alpha_2}e\pi}{\sqrt{2}K(k)}. \quad (A27)$$

The resonant condition is

$$\Omega = n\omega. \tag{A28}$$

The appearance strength of the resonant layer based on Chirikov overlap criterion (**CC**) is

$$Q_0 = \frac{\Omega^2}{4n^2(n+1)^2 G_0}\left(\frac{1}{\sqrt{Q_n}+\sqrt{Q_{n+1}}}\right)^2; \tag{A29}$$

the appearance strength of the resonant layer based on the renormalization group method (**RG**) is

$$Q_0 = \frac{0.49\Omega^2}{4n^2(n+1)^2 G_0}\left(\frac{1}{\sqrt{Q_n}+\sqrt{Q_{n+1}}}\right)^2; \tag{A30}$$

and, the appearance strength of the resonant layer based on the incremental energy (**IE**) is

$$Q_0 \approx \frac{0.9716354\sqrt{\alpha_2}}{\sqrt{2}\pi\Omega|G_1|}\cosh\left[n\pi\frac{K'(k_n)}{K(k_n)}\right]. \tag{A31}$$

The disappearance strength of the resonant layer based on the incremental energy is

$$Q_0 = \frac{|E_0^{n+1}-E_0^n|\sqrt{\alpha_2}}{\sqrt{2}\pi\Omega|G_1|}\cosh\left[n\pi\frac{K'(k_n)}{K(k_n)}\right]; \tag{A32}$$

in which

$$Q_n = \frac{\sqrt{2}\Omega}{\sqrt{\alpha_2 n}}\operatorname{sech}\left[\pi n\frac{K'(k_n)}{K(k_n)}\right], \tag{A33}$$

$$Q_{n+1} = \frac{\sqrt{2}\Omega}{\sqrt{\alpha_2(n+1)}}\operatorname{sech}\left[\pi(n+1)\frac{K'(k_{n+1})}{K(k_{n+1})}\right], \tag{A34}$$

$$G_0 = \frac{\pi^2}{e^2 k_n^4 K(k_n)^3}\left[2K(k_n) - \frac{2-(k_n)^2}{1-(k_n)^2}E(k_n)\right], \tag{A35}$$

$$G_1 = -\frac{\Omega\alpha_2}{(k_n)^4}\left(\frac{2-(k_n)^2}{\alpha_1}\right)^{5/2}\left[2K(k_n) - \frac{2-(k_n)^2}{1-(k_n)^2}E(k_n)\right]. \tag{A36}$$

Discrete Modeling of a String and Analysis of a Loop Soliton

K. Nishinari
Department of Mechanical Engineering,
School of Engineering,
Yamagata University,
Yonezawa, yamagata 992, Japan
e-mail: knishi@dips.dgw.yz.yamagata-u.ac.jp

A discrete model for an extensible string is proposed and analyzed by a discrete soliton theory and computer simulations. The relation between tension of the string and the size of a loop propagating on the string is obtained analytically by using the soliton theory. We use this relation to investigate dynamics and stability of loops, and it is found that one loop is stable against various kinds of perturbation. It is confirmed numerically that the loop can be formed by moving a boundary along a semicircle. If the moment of the string is introduced, behaviors of the formation are drastically changed and there is a critical value of stiffness of the string beyond which the loop cannot be formed. As for collision of two loops, we found that two loops do not break after collision if the two are similar. This result of collision can be well explained by our former analysis of a continuous string theory (Nishinari, 1997).

1 Introduction

Research on the dynamics of large deformation of one-dimensional elastic media, such as rods, strings, and polymers are important both for engineering and physics. In analyzing the behavior of these media, it is one way to treat such a continuous string as a discrete system, such as a combination of beads and springs. The merit of using discrete models is obvious: We can treat various one-dimensional objects generally, and it is suitable for computer simulations including various boundary conditions.

In this paper, we propose a discrete model of an extensible string, which coincides with a usual continuous string in the continuous limit. By using the model we analyze the nonlinear dynamics of the string, including the effect of boundary conditions.

Recently Goldstein and Petrich (1991) have discovered the connection between dynamics of curves and soliton theory. They have shown that the dynamics of a curve in a plane is governed geometrically by the modified KdV (mKdV) equation in a particular case. We use the discrete version of their theory (Doliwa and Santini, 1994) and apply it to the dynamics of the discrete string by the way we have proposed in our previous paper (Nishinari, 1997).

This paper is organized as follows. Basic equations and constitutive equations for a discrete string are given in Section 2. We summarize the analysis of discrete curves by the soliton approach in Section 3. Comparison of the discrete soliton theory with the discrete string theory is given in Section 4. Results of numerical simulations are given in Section 5 and concluding discussions are given in Section 6.

2 Basic Equations for a Discrete String

Let us consider a motion of an extensible discrete string in a plane. The basic equation for a balance of forces is given by

$$\rho \frac{d^2\mathbf{r}_n}{dt^2} = (N_n - N_{n-1}\cos\Delta_{n-1} + Q_{n-1}\sin\Delta_{n-1})\frac{\mathbf{t}_n}{l} + (N_{n-1}\sin\Delta_{n-1} - (Q_n - Q_{n-1}\cos\Delta_{n-1}))\frac{\mathbf{n}_n}{l}. \quad (1)$$

Here ρ is mass density along the string defined by $\rho = m/l$, where m is mass of a bead, l is an unstretched length of a spring. $\mathbf{r}_n$ is a position vector in a plane, and Δ_{n-1} is defined as $\Delta_{n-1} \equiv \theta_n - \theta_{n-1}$, where θ_n is an angle between the x-axis and $\mathbf{t}_n$. The unit vectors $\mathbf{t}_n$ and $\mathbf{n}_n$ are related by the Serret-Frenet formula of a discrete version

$$\begin{pmatrix} \mathbf{t}_{n+1} \\ \mathbf{n}_{n+1} \end{pmatrix} = \begin{pmatrix} \cos\Delta_n & \sin\Delta_n \\ -\sin\Delta_n & \cos\Delta_n \end{pmatrix}\begin{pmatrix} \mathbf{t}_n \\ \mathbf{n}_n \end{pmatrix}. \quad (2)$$

N_n and Q_n are the axial force and the shear force of a spring, respectively (Fig. 1a)). Assuming that springs are linear, the constitutive equation for N_n is given by

$$N_n = k\frac{(|\mathbf{r}_{n+1} - \mathbf{r}_n| - l)}{l} \equiv k\frac{(G_n - l)}{l}, \quad (3)$$

where k is a spring constant.

Let us consider effects of the bending moment of the string. We assume that there occurs a moment at each segments due to a kind of torsional spring (Fig. 1(a)). The moment is considered to be proportional to the difference of the angle Δ_n. Then we set

$$M_n = K\frac{\Delta_{n-1}}{l}, \quad (4)$$

where K is a stiffness constant. Then we can determine Q_n by considering the balance of moment as

$$Q_n = \frac{M_{n+1} - M_n}{G_n}, \quad (5)$$

where G_n is defined in (3).

The position of the string is given by

$$\mathbf{r}_n = \mathbf{r}_0 + \sum_{k=0}^{n-1} G_k\mathbf{t}_k, \quad (6)$$

where $\mathbf{r}_0$ represents the position of the left boundary of the string. The proposed Eq. (1) and the constitutive Eq. (3) and (4) are simple discrete models for an extensible string with the bending moment. This model is the same as the Gaussian chain (see Doi and Edwards, 1986), which is a model of polymers, except for the bending moment and the shear force.

Let us consider the correspondence of the proposed model and the continuous string. We take $l \to 0$, and using the formula $G_n/l \to \sqrt{g}$ we obtain, from (3) and (4),

Contributed by the Applied Mechanics Division of THE AMERICAN SOCIETY OF MECHANICAL ENGINEERS for publication in the ASME JOURNAL OF APPLIED MECHANICS.

Discussion on the paper should be addressed to the Technical Editor, Professor Lewis T. Wheeler, Department of Mechanical Engineering, University of Houston, Houston, TX 77204-4792, and will be accepted until four months after final publication of the paper itself in the ASME JOURNAL OF APPLIED MECHANICS.

Manuscript received by the ASME Applied Mechanics Division, Feb. 12, 1997; final revision, March 2, 1998. Associate Technical Editor: T. R. Akylas.

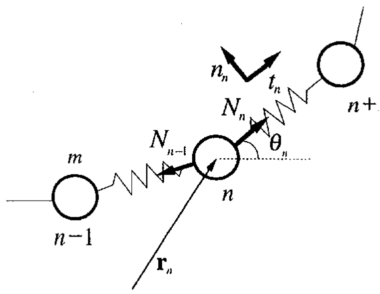

Fig. 1(a)

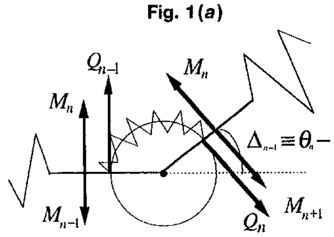

Fig. 1(b)

Fig. 1 (a) Configuration of the segment of a discrete string and (b) a mechanism for the moment generation between segments

$$N = k(\sqrt{g} - 1), \tag{7}$$

$$M = K\kappa\sqrt{g}, \tag{8}$$

where $\kappa = \partial\theta/\partial s$ and s is the arclength of the string defined by (Nishinari, 1997)

$$s = \int_0^\sigma \sqrt{g(\sigma', t)}\, d\sigma'. \tag{9}$$

In (9), σ represents the unstretched length of a string and g is a metric given by

$$g = \frac{\partial \mathbf{r}}{\partial\sigma}\cdot\frac{\partial \mathbf{r}}{\partial\sigma}. \tag{10}$$

Taking $l \to 0$, we obtain from (1) the continuous limit of the equation of motion

$$\rho\frac{d^2\mathbf{r}}{dt^2} = \left(\frac{\partial N}{\partial\sigma} + \sqrt{g}\kappa Q\right)\mathbf{t} + \left(-\frac{\partial Q}{\partial\sigma} + \sqrt{g}\kappa N\right)\mathbf{n}. \tag{11}$$

Here ρ represents a line density of the string. We divide (2) by G_n and also taking $l \to 0$, we obtain the Serret-Frenet formula

$$\frac{\partial}{\partial s}\begin{pmatrix}\mathbf{t}\\ \mathbf{n}\end{pmatrix} = \begin{pmatrix}0 & \kappa\\ -\kappa & 0\end{pmatrix}\begin{pmatrix}\mathbf{t}\\ \mathbf{n}\end{pmatrix}. \tag{12}$$

Equation (5) becomes, in the continuous limit,

$$Q = \frac{\partial M}{\partial s}. \tag{13}$$

Equations (11) and (13) and constitutive Eqs. (7) and (8) are been shown in our previous paper (Nishinari, 1997). The usual equation for the balance of moments is (Nishinari, 1997)

$$\frac{\rho I}{\sqrt{g}}\frac{d^2\theta}{dt^2} = \frac{\partial M}{\partial s} - Q, \tag{14}$$

where I the geometrical moment of inertia of the string. Thus our model corresponds to the case $I = 0$, i.e., we neglect an effect of inertia. This assumption is usually used to treat a narrow rod or a string (Ichikawa, Konno, and Wadati, 1981).

3 Analysis of a Discrete String by the Soliton Theory

In this section, we show a way of the analyzing of a discrete curve by the soliton theory (Doliwa and Santini, 1994). Let the curve dynamics in the plane be of the form

$$\frac{d\mathbf{r}_n}{dt} = U_n\mathbf{t}_n + W_n\mathbf{n}_n. \tag{15}$$

We summarize (15) and (2) into the matrix form as

$$\frac{d}{dt}\begin{pmatrix}\mathbf{r}_n\\ \mathbf{t}_n\\ \mathbf{n}_n\end{pmatrix} = \begin{pmatrix}0 & U_n & W_n\\ 0 & 0 & A_n\\ 0 & -A_n & 0\end{pmatrix}\begin{pmatrix}\mathbf{r}_n\\ \mathbf{t}_n\\ \mathbf{n}_n\end{pmatrix} \tag{16}$$

$$E_n\begin{pmatrix}\mathbf{r}_n\\ \mathbf{t}_n\\ \mathbf{n}_n\end{pmatrix} = \begin{pmatrix}1 & G_n & 0\\ 0 & \cos\Delta_n & \sin\Delta_n\\ 0 & -\sin\Delta_n & \cos\Delta_n\end{pmatrix}\begin{pmatrix}\mathbf{r}_n\\ \mathbf{t}_n\\ \mathbf{n}_n\end{pmatrix}, \tag{17}$$

where E_n is a shift operator defined by $E_n f(n) = f(n+1)$. From

$$[E_n, \partial_t] = 0, \tag{18}$$

we obtain

$$A_nG_n = -W_n + \cos\Delta_n W_{n+1} + \sin\Delta_n U_{n+1}, \tag{19}$$

$$\frac{d}{dt}G_n = -U_n + \cos\Delta_n U_{n+1} - \sin\Delta_n W_{n+1}, \tag{20}$$

$$\frac{d}{dt}\Delta_n = A_{n+1} - A_n. \tag{21}$$

The crucial point in using the discrete soliton theory is that if we put

$$U_n = 2q_nq_{n-1} \tag{22}$$

$$W_n = \frac{q_n - q_{n-2}}{G_{n-1}} - G_{n-1}q_{n-1}^2(q_n + q_{n-2}), \tag{23}$$

where

$$\frac{1}{G_n}\tan\frac{\Delta_n}{2} \equiv q_n. \tag{24}$$

Then we obtain from (20)

$$\frac{d}{dt}G_n = 0. \tag{25}$$

We can put

$$G_n = l(1+\epsilon) \equiv G, \tag{26}$$

where ϵ is a constant, which represents an initial tension of the string. Then using (26) we obtain from (21)

$$\frac{2G\dot{q}_n}{1 + G^2q_n^2} = A_{n+1} - A_n, \tag{27}$$

where

$$A_n = \frac{1}{G^2}((1 + G^2q_n^2)q_{n+1} - (1 - G^2q_n^2)q_{n-1}$$
$$- (1 - G^2q_{n-1}^2)q_n + (1 + G^2q_{n-1}^2)q_{n-2}), \tag{28}$$

or substituting (28) into (27) we obtain

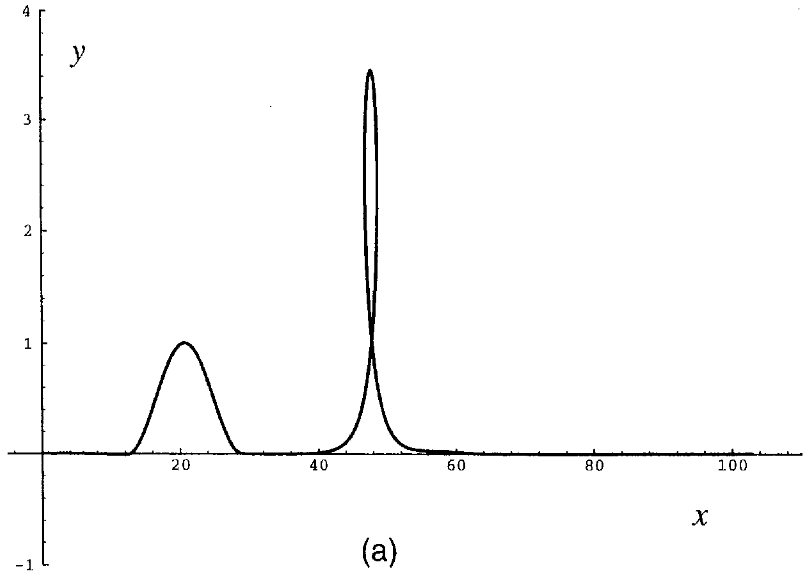

Fig. 2(*a*)

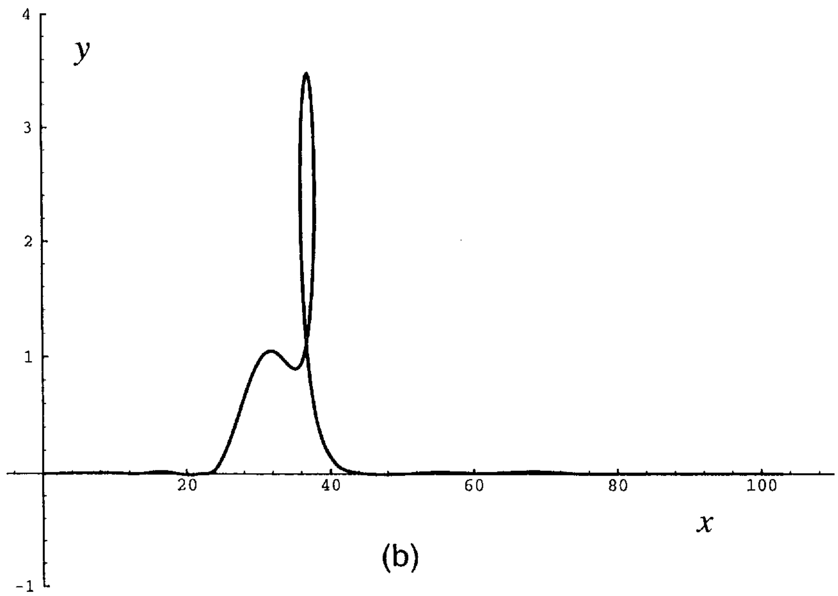

Fig. 2(*b*)

$$2G^3 \frac{dq_n}{dt} = (1 + G^2q_n^2)((1 + G^2q_{n+1}^2)q_{n+2} - (1 + G^2q_{n-1}^2)q_{n-2} + G^2(q_{n+1}^2 - q_{n-1}^2)q_n - 2(q_{n+1} - q_{n-1})). \quad (29)$$

This is called the second-order dmKdV equation, which is completely integrable by the soliton theory. One soliton solution, which correspond to a discrete loop of the dmKdV equation, is given by

$$Gq_n = \frac{p^n \exp(\omega t)}{1 + Ap^{2n}\exp(2\omega t)}, \quad A = \frac{p^2}{(p^2-1)^2}, \quad \omega = \frac{(p^2-1)(p-1)^2}{2G^3p^2}, \quad (30)$$

or

$$q_n = \frac{p^2-1}{2Gp}\,\mathrm{sech}\,(\log pn + wt). \quad (31)$$

Now let us consider the continuous limit $l \to 0$ of the above equations. Since we can see from (24) that q_n becomes $\kappa/2$ in the limit, we obtain $U_n \to \kappa^2/2$ and $W_n \to \kappa_s$, which coincide with the continuous case (Goldstein and Petrich, 1991; Nishinari, 1997). Moreover, (29) becomes

$$\frac{\partial \kappa}{\partial t} = \frac{\partial^3 \kappa}{\partial s^3} + \frac{3}{2}\kappa^2 \frac{\partial \kappa}{\partial s} \quad (32)$$

and the solution (31) becomes

$$\kappa = 2a\,\mathrm{sech}\,(a(s + a^2)t), \quad (33)$$

where a is a constant. Thus the equation and the solution also coincide with the continuous case in the previous papers. In deriving (33) we use $Gn \to s$ when $l \to 0$ and

$$p = \exp(aG). \quad (34)$$

It should be noted that there are other possibilities of choosing U_n and W_n in order to satisfy (25). The simplest one is

$$U_n = 1, \quad (35)$$

$$W_n = -G_{n-1}q_{n-1}. \quad (36)$$

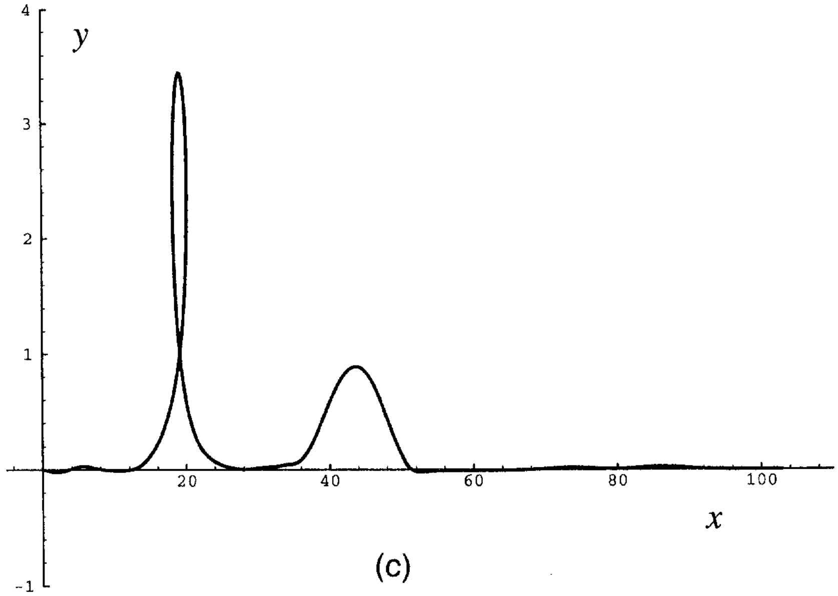

Fig. 2(c)

Fig. 2 A loop with transverse perturbation at (a) t = 86.9, (b) t = 119.5, and (c) t = 173.7

In this case, we obtain from (21) the lowest-order dmKdV equation

$$2G \frac{dq_n}{dt} = (1 + G^2 q_n^2)(q_{n+1} - q_{n-1}), \tag{37}$$

which is also completely integrable, and will be used in the following.

4 Comparison and a Discrete Loop

In order to utilize the soliton approach discussed in the previous section to analyze the nonlinear deformation of the discrete string, we must compare the dynamics of (15) with that of (1) (Nishinari, 1997). Differentiating (15) with respect to time gives

$$\frac{d^2\mathbf{r}_n}{dt^2} = \left(\frac{dU_n}{dt} - W_n A_n\right)\mathbf{t}_n + \left(\frac{dW_n}{dt} + U_n A_n\right)\mathbf{n}_n. \tag{38}$$

The compatibility conditions for (38) and (1) are

$$\frac{dU_n}{dt} - W_n A_n = \frac{1}{\rho l}(N_n - N_{n-1}\cos\Delta_{n-1} + Q_{n-1}\sin\Delta_{n-1}), \tag{39}$$

$$\frac{dW_n}{dt} + U_n A_n = \frac{1}{\rho l}(N_{n-1}\sin\Delta_{n-1} - (Q_n - Q_{n-1}\cos\Delta_{n-1})). \tag{40}$$

Therefore, Eqs. (20), (21), (39), and (40) for G_n, θ_n, W_n, and U_n are considered as the basic equations which connect the dynamics of the string and the discrete soliton theory. It should be noted here that these basic equations are general and we can apply them to any one-dimensional media like string.

In the following analyses, we will use the assumptions (22) and (23), and focus on a loop soliton (31). It is easily checked that (31) does not satisfy (39) and (40) exactly. In the continuous case, however, there is a famous solution which represents a loop (Ichikawa et al., 1981; Cohen and Epstein, 1994). Therefore we expect that (31) would satisfy (39) and (40) in the the continuous limit under some conditions.

First, we consider a loop soliton in the continuous case. If we neglect the bending moment and assuming G_n is a constant and we take the continuous limit $l \to 0$, the compatibility conditions (39) and (40) give

$$\frac{dU}{dt} - W\left(\frac{\partial W}{\partial s} + \kappa U\right) = \frac{k}{\rho}\sqrt{g}\,\frac{\partial\sqrt{g}}{\partial s}, \tag{41}$$

$$\frac{dW}{dt} + U\left(\frac{\partial W}{\partial s} + \kappa U\right) = \frac{k}{\rho}\kappa\sqrt{g}(\sqrt{g} - 1), \tag{42}$$

and (20) and (21) give

$$U_s = \kappa W, \tag{43}$$

$$\kappa_t = \frac{\partial}{\partial s}\left(\kappa U + \frac{\partial W}{\partial s}\right). \tag{44}$$

These coincide with the continuous case obtained in our previous paper (Nishinari, 1997).

Exact solution of these continuous equations is given as

$$\sqrt{g} = 1 + \epsilon, \tag{45}$$

$$W = \kappa_s, \tag{46}$$

$$U = \frac{\kappa^2}{2}, \tag{47}$$

$$\kappa_{ss} + \frac{\kappa^3}{2} = v\kappa, \tag{48}$$

$$v^2 = \frac{k}{\rho}(1 + \epsilon)\epsilon, \tag{49}$$

where κ is the one soliton solution of the mKdV equation with the velocity v, which solves (48). The velocity v is related by the initial tension ϵ through (49). This relation is the most important relation for realizing the continuous loop on the string.

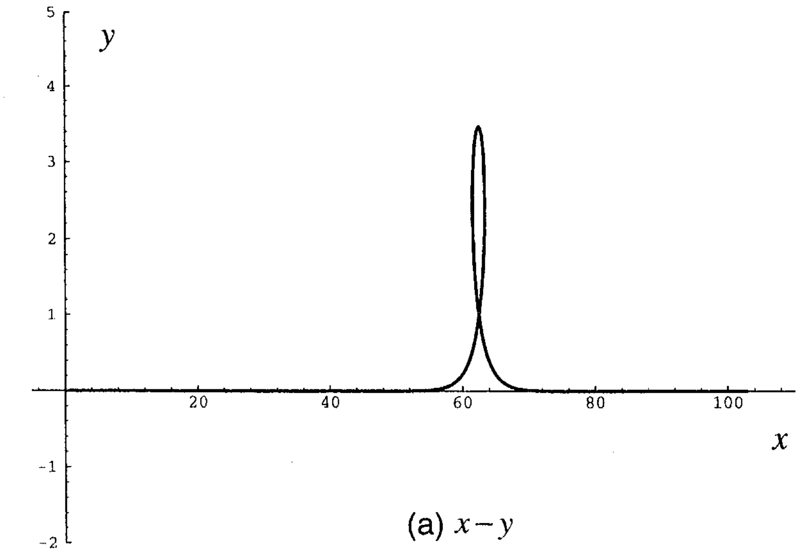

Fig. 3(a.1)

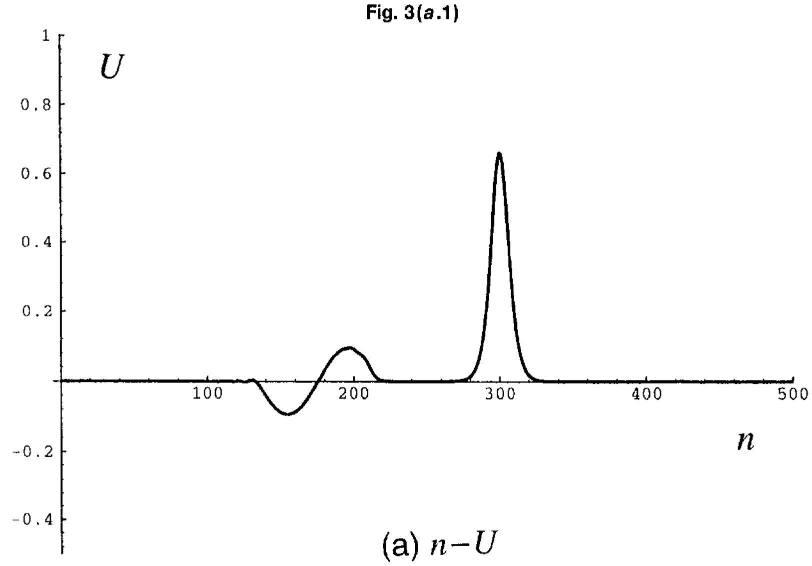

Fig. 3(a.2)

In order to coincide the discrete loop solution (31) in our model with the above continuous solution in the limit $l \to 0$, we must calculate the relation between parameters p and G which correspond to (49). From the symmetry analysis (Nishinari, 1997) and using (37), we obtain the following identity valid for one soliton solution (31):

$$\frac{dq_n}{dt} = \frac{(p-1)^2}{2G^3 p}(1 + G^2 q_n^2)(q_{n+1} - q_{n-1}). \qquad (50)$$

For A_n, the equation

$$A_n = \frac{d\theta_n}{dt} = \sum_{k=-\infty}^{n-1} \dot{\Delta}_n \qquad (51)$$

holds, then using (50) we obtain

$$A_n = \frac{(p-1)^2}{G^2 p}(q_n + q_{n-1}), \qquad (52)$$

which is valid for one soliton solution (31). By using these equations, we can calculate the left-hand side of (39) and (40) as

$$\frac{dU_n}{dt} - W_n A_n = \frac{(p-1)^4}{G^3 p^2} q_{n-1}(q_n + q_{n-1}), \qquad (53)$$

$$\frac{dW_n}{dt} + U_n A_n = \frac{(p-1)^4}{2G^4 p^2}(2(q_{n-1} + q_n) - (1 + G^2 q_{n-1}^2)(q_n - q_{n-2})). \qquad (54)$$

Neglecting the bending moment on the string, we obtain from (39) and (40)

$$\frac{(p-1)^4}{G^3 p^2} q_{n-1}(q_n + q_{n-1}) = \frac{k\epsilon}{\rho l} \frac{2G^2 q_{n-1}}{1 + G^2 q_{n-1}^2} \qquad (55)$$

$$\frac{(p-1)^4}{2G^4 p^2}(2(q_{n-1} + q_n) - (1 + G^2 q_{n-1}^2)(q_n - q_{n-2})) = \frac{k\epsilon}{\rho l} \frac{2G q_{n-1}^2}{1 + G^2 q_{n-1}^2} \qquad (56)$$

In order to satisfy both (55) and (56) simultaneously in the continuous limit $l \to 0$, we must put

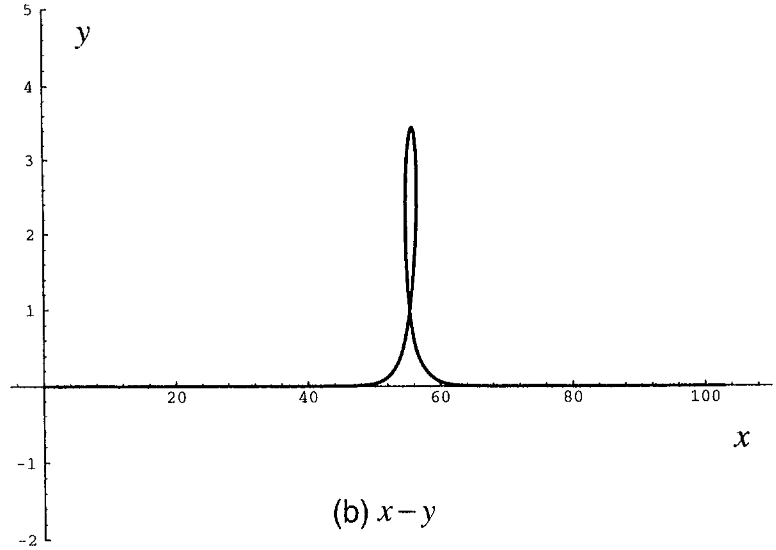

Fig. 3(b.1)

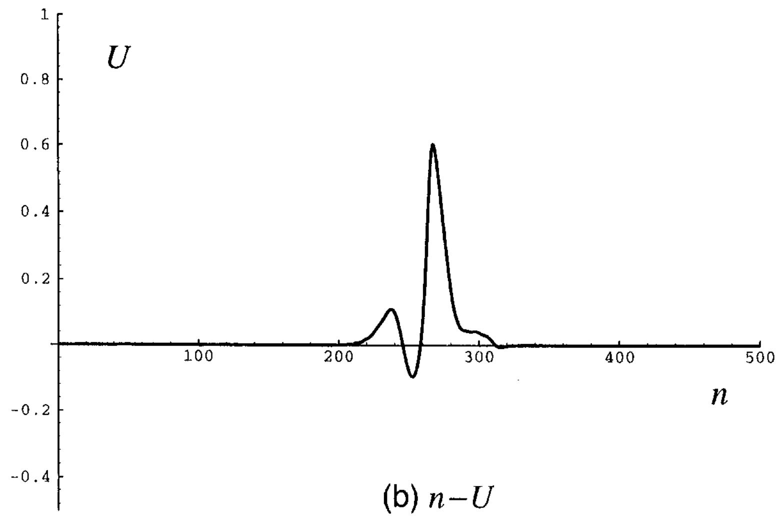

Fig. 3(b.2)

$$\frac{(p-1)^4}{p^2G^4} = \frac{k}{\rho}\,\epsilon(1+\epsilon). \tag{57}$$

Since p and a are related by (34), the left-hand side of (57) become a^4 in the continuous limit. Since from (33), a^2 is the velocity of the loop, we see that (57) coincides with (49) in this limit. This is a crucial relation of the parameters which connects the discrete and the continuous theories. As we can see from the above procedure, we usually neglect the bending moment when we consider loops. The effect of the bending moment will be investigated numerically in the next section.

5 Numerical Simulations

In this section, we will simulate the dynamics of the string by using the discrete model proposed in Section 2. The dynamics and stability of loops is investigated in the following three ways. As we mentioned before, (31) is not an exact solution of (39) and (40), but if we take l to be small enough and keep the relation (57), then we can simulate the loop soliton by using the general basic Eqs. (20), (21), (39), and (40) in a desired order of accuracy.

In the simulations, the fifth-order Runge-Kutta method with adaptive step-size control is used in order to integrate the time derivative. We set $l = 0.2$, and the number of beads is 500 in all the simulations.

5.1 Stability of a Loop. First, we check the stability of a single loop against some kinds of perturbations. In these simulations, we add two kind of perturbation to the loop: one is the transverse perturbation, and the other is longitudinal. When we add transverse perturbation, it is observed that the perturbated wave will go through the loop after a collision (Fig. 2), and we can observe that the loop keeps its shape and velocity. In the case of adding longitudinal perturbation, it is interesting to mention that the perturbated wave is reflected after the collision instead of going through the loop (Fig. 3). In both cases, we can show by simulations that the loop is stable due to the small amplitude perturbation. These results may be shown by the stability of the one soliton solution of the mKdV equation (Kuznetsov, Rubenchik, and Zakharov, 1986). We can rewrite the mKdV equation

$$\kappa_t = \kappa_{sss} + \frac{3}{2}\kappa^2\kappa_s \tag{58}$$

as a canonical form

$$\kappa_t = -\frac{\partial}{\partial s}\frac{\delta H}{\delta \kappa}, \tag{59}$$

where H is the third conserved quantity of the mKdV equation

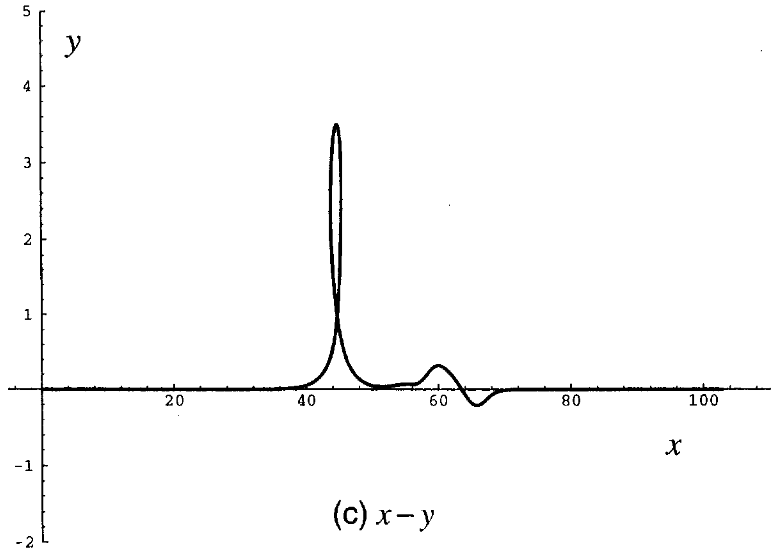

Fig. 3(c.1)

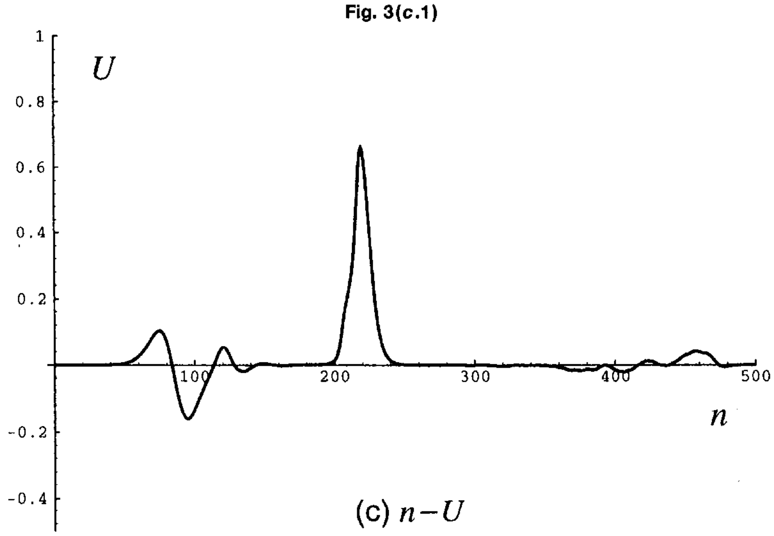

Fig. 3(c.2)

Fig. 3 A loop with longitudinal perturbation and the longitudinal velocity *U* versus the number of bead at (*a*) *t* = 43.3, (*b*) *t* = 64.9, and (*c*) *t* = 97.4

$$H = \int_{-\infty}^{\infty} \left(\frac{\kappa_s^2}{2} - \frac{\kappa^4}{8} \right) ds. \tag{60}$$

There are other conserved quantities

$$I_1 = \int_{-\infty}^{\infty} \kappa ds, \tag{61}$$

$$I_2 = \int_{-\infty}^{\infty} \frac{\kappa^2}{2} ds. \tag{62}$$

Here we assume traveling wave type solution $\kappa = \kappa(s - Vt)$, then substituting this into the mKdV equation and integrating it once with respect to s gives

$$\kappa_{ss} + \frac{\kappa^3}{2} + V\kappa = 0. \tag{63}$$

The crucial step is that we can rewrite this into the variation problem

$$\frac{\delta}{\delta \kappa}(H - VI_2) = 0, \tag{64}$$

where V plays the role of a Lagrangian multiplier. Though we would not discuss in detail in this paper, we can show that the bounded solution of the mKdV equation is obtained only in the case $V < 0$ and also we can prove the boundedness of the Hamiltonian (Kuznetsov et al., 1986). Considering these facts and (64), the stability of the one soliton solution is shown in the Lyapunov sense.

5.2 Making of a Loop. Let us consider the way of making of the loop soliton by moving a boundary. When we focus on one point on the string during the loop propagation, we can show that the point moves as

$$x_0 = h + h \tanh\left(\left(\frac{2}{h} \right)^3 (t + C) \right) \tag{65}$$

$$y_0 = h \operatorname{sech}\left(\left(\frac{2}{h} \right)^3 (t + C) \right) \tag{66}$$

in the continuous case. In deriving (65) and (66), we use the relation

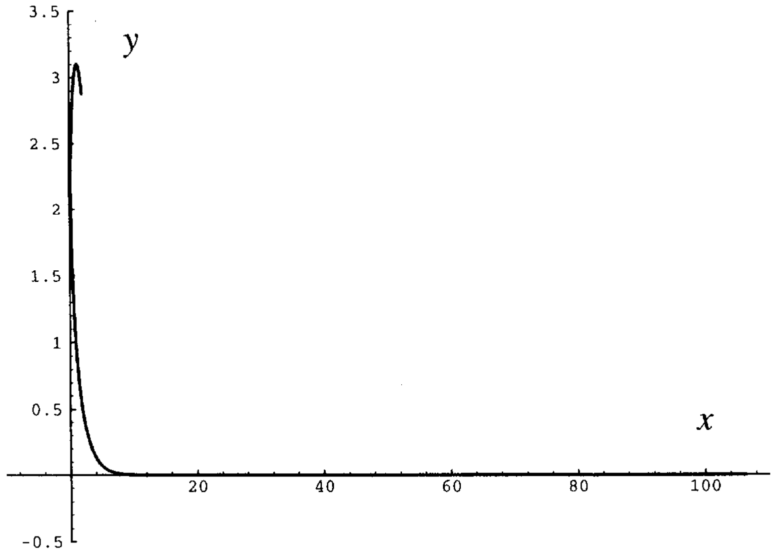

Fig. 4(*a*)

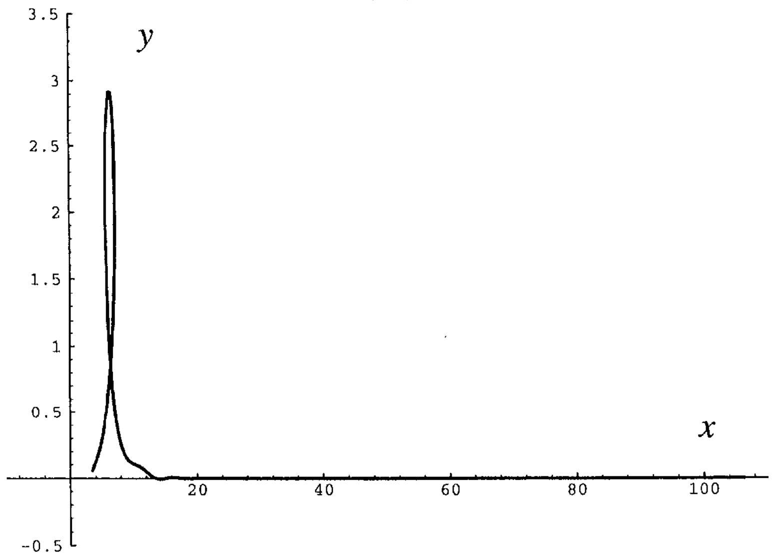

Fig. 4(*b*)

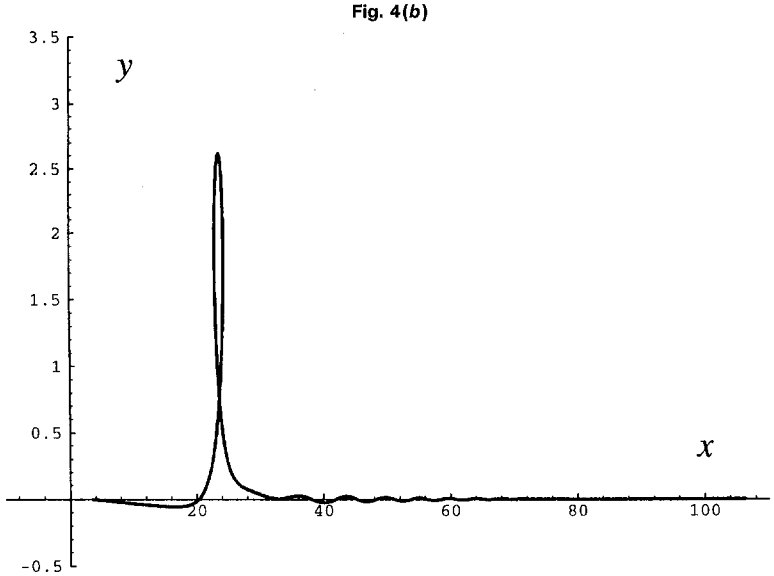

Fig. 4(*c*)

Fig. 4 Making a loop before critical value of K (K = 0.10) at (a) t = 203.3, (b) t = 225.0, and (c) t = 290.0. We start moving a boundary at t = −200.0.

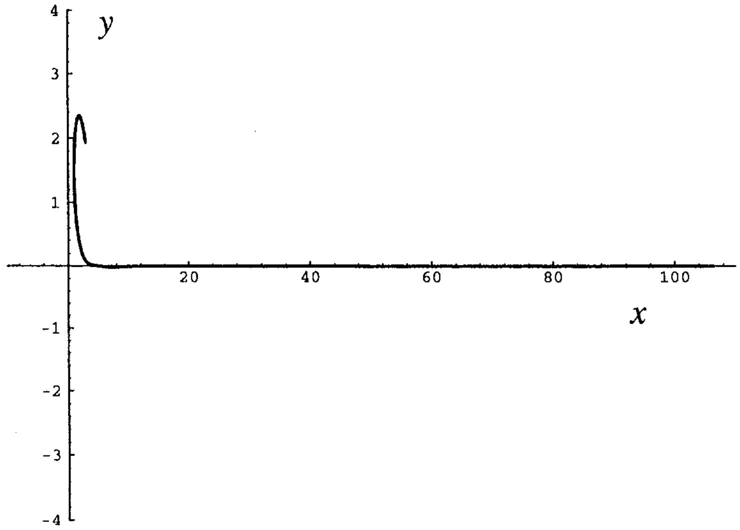

Fig. 5(*a*)

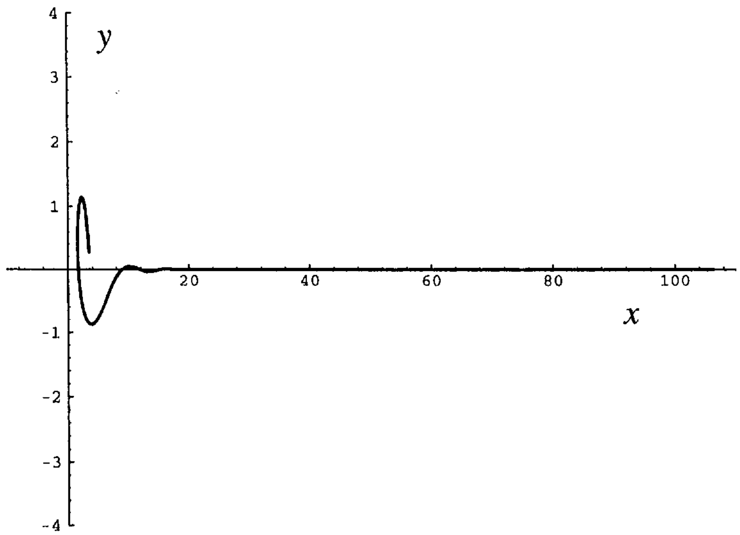

Fig. 5(*b*)

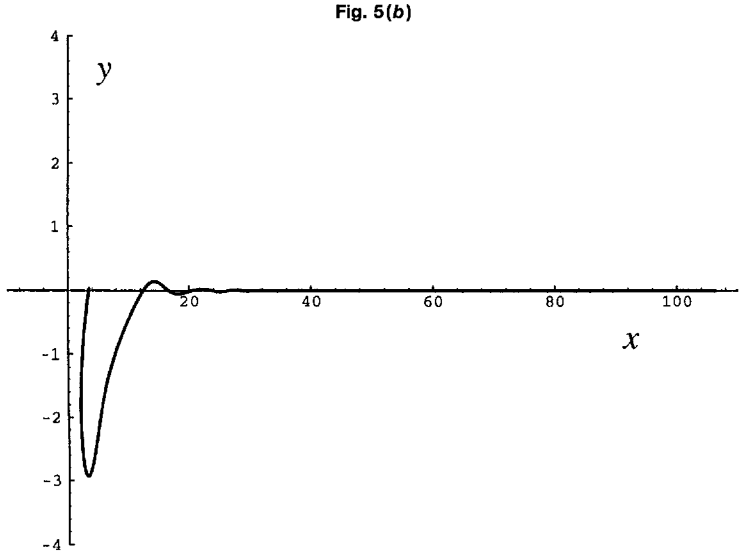

Fig. 5(*c*)

Fig. 5 Making a loop after critical value of K (K = 0.15) at (*a*) t = 206.2, (*b*) t = 217.1, and (*c*) t = 228.0. We start moving a boundary at t = −200.0.

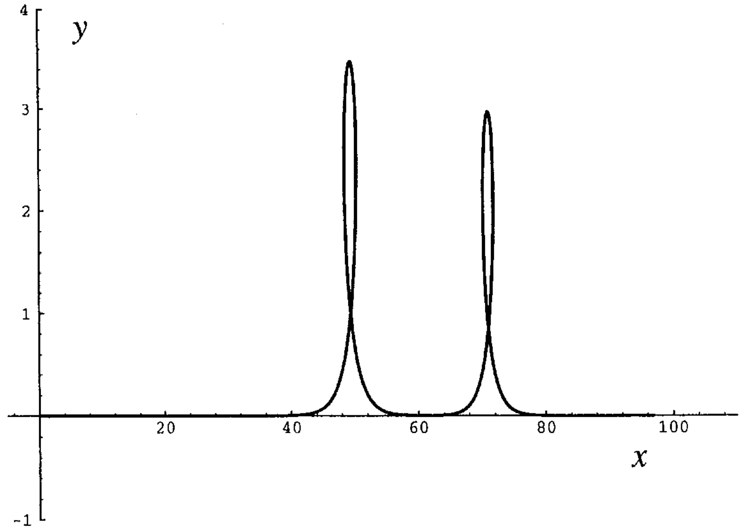

Fig. 6(*a*)

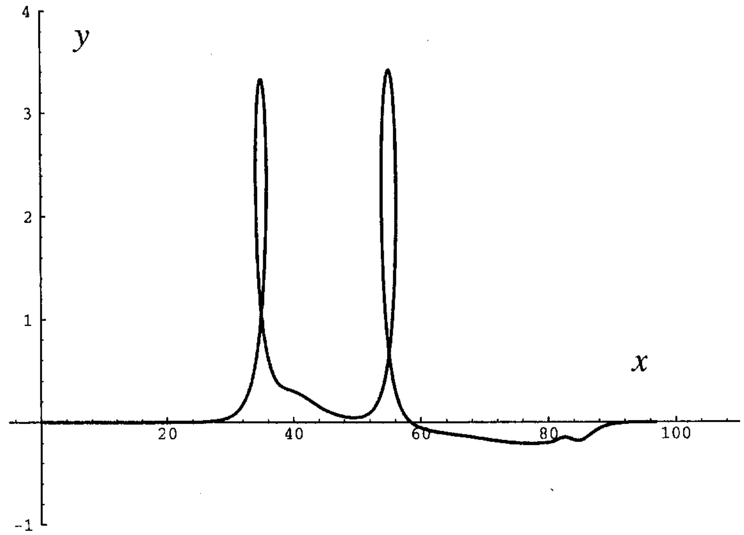

Fig. 6(*b*)

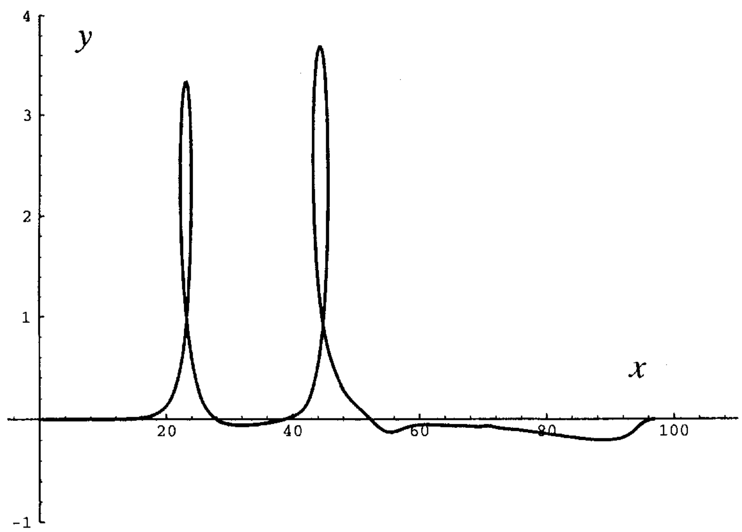

Fig. 6(*c*)

Fig. 6 Collision of similar loops at (*a*) $t = 0.0$, (*b*) $t = 43.4$, and (*c*) $t = 76.0$

$$\frac{dx}{ds} = \cos\left(\int \kappa ds\right), \quad \frac{dy}{ds} = \sin\left(\int \kappa ds\right). \qquad (67)$$

Subtracting t from (65) and (66) we obtain

$$(x_0 - h)^2 + y_0^2 = h^2. \qquad (68)$$

Therefore if we move left boundary along a semicircle, then we can make a loop on the string. First, we move the boundary by the exact functions (65) and (66), then it is observed numerically that a loop is formed without any radiation and it propagates stably.

As discussed in the previous section, we neglected the effect of bending moment up to now. Let us consider the effect when we make a loop by the above means. Numerical results show that there occurs an interesting phenomena when we change the bending stiffness K. When the stiffness is small, the loop is made with a little radiation, and propagates stably (Fig. 4). When the stiffness becomes large, then the velocity of the loop becomes slower. At the critical value of $K \sim 0.11$, the loop ceases to move forward and stands still at the boundary. Beyond the critical value $K \sim 0.11$, as soon as we move the boundary, the loop is reflected and goes around to the opposite side (Fig. 5). Then the loop disappears and only flexuous wave propagates on the string. Therefore, we have found that there is a maximum value of K beyond which the loop cannot be formed.

5.3 Collision of Two Loops. Finally let us consider a collision of loops. We initially set two different loops going in the same direction. Since the smaller one is faster than the larger one, the former will overtake and interact with the latter. If the difference of the two loops is small, we can see that the collision is not destructive to each loop (Fig. 6) and maintains its shape after the collision. This situation can be considered as the special case of two soliton solutions. In our previous paper (Nishinari, 1997), we have shown that only the soliton solution of traveling wave type can satisfy the elastic theory by using the reductive perturbation method. One soliton solution can, of course, satisfy this condition, and the special cases of two soliton solutions can also satisfy the condition up to some perturbated order, i.e., breather soliton and two similar loops' solution (Nishinari, 1997). Since we can see that the collision of two similar loops seems to keep the nature of the traveling wave type in the course of time, the result of the stable collision in Fig. 6 coincides with the fact that we have shown in this paper. On the other hand, in the case where the difference of the two loops are not small, we can see that the loops are largely disturbed by the collision. This result makes us sure of the fact that only the soliton solution of the traveling wave type can satisfy the elastic theory and general soliton solutions, and that more than two soliton solutions do not exist in the real elastic string.

6 Concluding Discussions

In this paper we have proposed a discrete model for an extensible string which coincides with the continuous theory in the limit. We have also obtained the general equations which connect the discrete string theory and the discrete soliton theory, i.e., (20), (21), (39), and (40). By using these basic equations, we investigate numerically the dynamics and stability of the loop soliton from various points of view.

First, we have obtained the analytical relation between the width of the loop and the initial tension of the string, which is the most important relation for analyzing loops by those basic equations. Next, it is found numerically that a one-loop soliton is stable against large perturbation and the direction of the reflected wave changes due to a kind of perturbation. When we move a boundary along a semicircle including the effect of the bending moment, there is a critical value of stiffness which can form a loop. We think that at the critical value, the stress in the string balances the initial accelerating force at the boundary. It is a future problem to calculate this critical value analytically. As for the collision of loops, if the two are similar, then it is observed that the two loops do not break after collision. Comparing a continuous string and a discrete string, this result coincides with our former analysis by the soliton theory (Nishinari, 1997). This stability is also explained clearly as follows: From (57), we see that there is a one-to-one correspondence between the initial tension and the size of the loop. Thus, it is impossible for there to exist more than two loops, which have different sizes, on one string.

Since there has been much research on strings, such as cables, polymers, vortex filaments and magnetic fields, we expect that our formulation can apply to the analysis of these fields.

Acknowledgment

The author is grateful to Prof. Kazumi Watanabe for fruitful discussions and helpful comments. He also would like to express his sincere gratitude to Prof. Junkichi Satsuma, Dr. Yasuhiro Ohta, and Dr. Shigeki Matsutani for stimulating discussions and valuable comments. This work is partially supported by Grant-in-Aid from the Ministry of Education, Science and Culture (No. 08750080).

References

Cohen, H., and Epstein, M., 1994, "On a Class of Planer Motions of Flexible Rods," ASME JOURNAL OF APPLIED MECHANICS, Vol. 61, pp. 206–208.

Doi, M., and Edwards, S. F., 1986, *The Theory of Polymer Dynamics*, Clarendon Press, Oxford, UK.

Doliwa, A., and Santini, P. M., 1994, "Integrable dynamics of a discrete curve and the Ablowitz-Ladik hierarchy," preprint IFT UW/6/94.

Goldstein, R. E., and Petrich, D. M., 1991, "The Korteweg-de Vries Hierarchy as Dynamics of Closed Curves in the Plane," *Physical Review Letters*, Vol. 67, pp. 3203–3206.

Ichikawa, Y. H., Konno, K., and Wadati, M., 1981, "Nonlinear Transverse Oscillation of Elastic Beams under Tension," *Journal of the Physical Society of Japan*, Vol. 50, pp. 1799–1802.

Kuznetsov, E. A., Rubenchik, A. M. and Zakharov, V. E., 1986, "Soliton Stability in Plasmas and Hydrodynamics," *Physics Reports*, Vol. 142, pp. 103–165.

Nishinari, K., 1997, "Nonlinear Dynamics of Solitary Waves in an Extensible Rod," *Proceedings of the Royal Society of London*, Vol. A453, pp. 817–833.

Elastoplastic Micromechanical Modeling of Two-Dimensional Irregular Convex and Nonconvex (Re-entrant) Hexagonal Foams

D. W. Overaker
Mem. ASME

A. M. Cuitiño
Mem. ASME

N. A. Langrana
Fellow ASME

Department of Mechanical and Aerospace Engineering, Rutgers, The State University of New Jersey, Piscataway, NJ 08854

A nonlinear micromechanical model for two-dimensional irregular hexagonal foams has been developed that allows for anisotropy in morphology and/or material. Based upon the orientation, cross section, length, and material properties of each strut, the resulting microlevel beam behavior within the unit cell determines its structural properties. Nonlinearity is introduced as coupled elastoplastic beam behavior, where the elastoplastic behavior of each beam is considered. The analytical formulation for the stiffness matrix of the general elastoplastic unit cell is found by considering compatibility and equilibrium of the unit cell. The structural properties of the elastoplastic unit cell are embedded in a continuum finite element model as material properties, thus capturing the microstructure of the foam in an accurate and efficient model. Structural nonlinearity is therefore directly linked to localized plasticity and its evolution at the microlevel. Elastic analyses investigated the degree of anisotropy in structural properties that was induced by various morphological changes. The differences in stress and deformation behavior between a regular hexagonal foam and a re-entrant foam were also demonstrated. Plastic analyses showed how structural nonlinearity could be explained by localized microstructural behavior. The advantage of this micromechanical model is that it allows a study of the effects of morphology and/or material anisotropies on the overall foam behavior.

1 Introduction

Many familiar materials have a cellular, or foam, structure in order to provide a certain amount of stiffness and strength with minimal weight. Biological materials tend to arrange into an architecture that satisfies the mechanical requirements of the environment with the least amount of material. Trabecular bone, for example, is a porous material with architectural symmetry that depends on the loading situation. Cork is a common cellular material having a closed-celled hexagonal (honeycomb) architecture that, conveniently, has a Poisson's ratio of zero for loading in the out-of-plane direction. Man-made honeycomb structures are used in aerospace structures, skis, and other applications where a stiff structure with minimal weight is required. Cellular materials occurring in nature as well as most of those manufactured by man have a cell structure with interior angles that are convex, resulting in a structure with a positive value of Poisson's ratio. Foams in which some of the interior angles of the cell structure are concave are commonly called "re-entrant" foams, and have the special characteristic of negative Poisson's ratio. Closed and open-celled polymer foams are used in a wide range of applications in the aerospace and automotive industries.

Early work in elastic foam mechanics was conducted by Gent and Thomas (1959, 1963), in which the foam was modeled as thin threads connecting rigid joints. The effective Young's modulus of an open-celled foam was related to the relative density of material by assuming that the threads only transmit axial loads. A number of later analytical studies have incorporated bending deformations of struts (Choi and Lakes, 1995; Gibson and Ashby, 1982; Ko, 1965; Menges and Knipschild, 1975; Patel and Finnie, 1970; Warren and Kraynik, 1987, 1988, 1991), which is understood to be the dominant deformation mechanism for small deformations of an open-celled foam. The negative Poisson's ratio behavior of re-entrant honeycomb has been investigated in several studies (Lee et al., 1996; Gibson and Ashby, 1988; T. L. Warren, 1990). Lakes (1987) was the first to report successful fabrication of three-dimensional re-entrant foam materials. Friis, Lakes, and Park (1988) gave transformation and mechanical test results for both polymer and metallic (copper) re-entrant foams. This inspired further experimental (Choi and Lakes, 1992) and analytical (Choi and Lakes, 1995) studies of re-entrant foam mechanics. Comprehensive reviews of experimental and theoretical work on foams has been provided by Gibson and Ashby (1988) and Hilyard (1982).

Gibson et al. (1982) considered the mechanics of a two-dimensional regular hexagonal foam. The four independent elastic constants were found using standard beam analysis to describe bending of the cell walls, and the elastic and plastic collapse stresses were calculated (axial beam deformations not considered). The work was then extended to the study of three-dimensional foams (Gibson and Ashby, 1982), where a simple dimensional analysis provided expressions for the dependence of foam properties on density. Extensive comparison with experiments proved that the mechanics of foams could be understood in terms of the mechanisms of bending, elastic buckling, and plastic collapse of the cell walls. Huber and Gibson treated anisotropic foams by considering a cell shape-anisotropy ratio, R, relating the mean intercept lengths in the out-of-plane and in-plane directions (Huber and Gibson, 1988). The in-plane architecture was regular in their analysis. Ratios of the moduli, the elastic, plastic, and brittle collapse stresses and of the fracture toughnesses in the out-of-plane direction to those in-plane

Contributed by the Applied Mechanics Division of THE AMERICAN SOCIETY OF MECHANICAL ENGINEERS for publication in the ASME JOURNAL OF APPLIED MECHANICS.

Discussion on the paper should be addressed to the Technical Editor, Professor Lewis T. Wheeler, Department of Mechanical Engineering, University of Houston, Houston, TX 77204-4792, and will be accepted until four months after final publication of the paper itself in the ASME JOURNAL OF APPLIED MECHANICS.

Manuscript received by the ASME Applied Mechanics Division, Apr. 22, 1997; final revision, July 24, 1997. Associate Technical Editor: R. Abeyaratne.

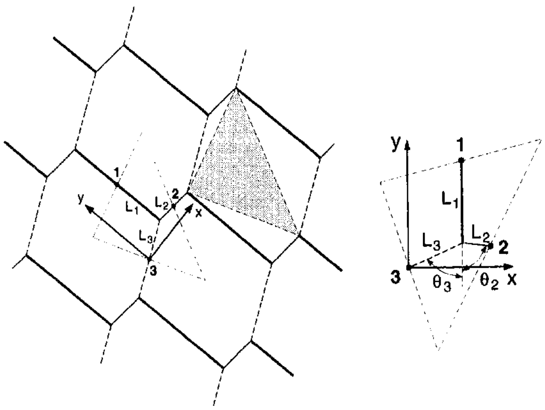

Fig. 1(*a*) The hexagonal array and (*b*) the periodically repeating unit cell for the array

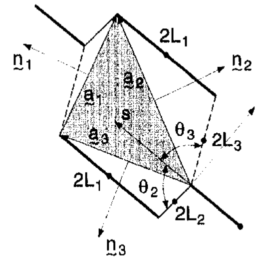

Fig. 2 The element face areas and outward unit normals

were given, and it was found that the elastic modulus and plastic collapse ratio, the two properties most sensitive to cell shape, fit well with experiments.

Warren and Kraynik provided a more rigorous formulation of the properties of cellular materials by fully exploiting the symmetries associated with a spatially periodic structure. They modeled a two-dimensional regular hexagonal foam by analyzing the structural properties of the smallest repeating element defining the spatially periodic array (Warren and Kraynik, 1987). Considering both axial and bending deformations of the cell walls, they showed that such a foam is elastically isotropic in the plane, and therefore transversely isotropic. The in-plane elastic constants were defined completely in terms of the axial and bending compliances of the unit cell beams and of the cell material. The ability to treat different strut morphologies (other than uniform) is an attractive advantage of the method. The same formulation methodology was extended to the case of the three-dimensional open-cell foam comprised of regular tetrahedral unit cells (Warren and Kraynik, 1988), and the elastic properties were determined exactly. Warren, Kraynik, and Stone formulated a constitutive model for the nonlinear elastic behavior of a two-dimensional regular hexagonal foam, where the large deformation effects were modeled by a foam with a pin-jointed structure (Warren et al., 1989). The same formulation was extended to the finite deformations of the regular tetrahedron by Warren and Kraynik (1991).

This work extends upon the two-dimensional hexagonal foam work presented by Warren and Kraynik (1987) to the more general two-dimensional anisotropic hexagonal foam. The model is more general in the sense that this formulation will treat the unit cell having struts of different lengths, orientations, and material properties. Nonlinearity is introduced as coupled elastoplastic beam behavior. An analytical expression for the stiffness of the elastoplastic unit cell will be derived by considering compatibility and equilibrium requirements of the unit cell in an incremental formulation. Based upon the available literature, this is the first presentation of the full linear elastic and nonlinear plastic behavior of the hexagonal foam with general structural and material anisotropy.

2 Analytical Formulation

2.1 Unit Cell Equilibrium and Constitutive Relations.

2.1.1 The Unit Cell. The two-dimensional formulation of the mechanics of the general anisotropic hexagonal foam begins by identifying the unit cell of the spatially periodic array. Figure 1 shows an array of hexagonal cells, where the dashed triangle between points 1, 2, and 3 identifies the area within the symmetry planes surrounding the unit cell. This is the smallest cell which, when mirrored and inverted about the faces of the element in all directions, will produce the hexagonal array shown. Notice that this model accommodates the most general degree of anisotropy in the foam, as described by different line styles for each of the three legs of the unit cell. Each leg can have its own length, cross section (regular or tapered), material properties, and orientation. By specifying L_1, L_2, L_3, θ_2, and θ_3 along with the cross section and material properties of each beam of the unit cell, the mechanical behavior of the whole structure is defined. The $x-y$ coordinate frame to be used in developing the structural model is as shown. The frame is attached to node number 3 such that the relative displacements of nodes 1 and 2 with respect to node 3 can be described, thus reducing the number of unknowns in the system. Deformations of this whole structure are therefore completely defined by the displacement of the two beam midpoints of the unit cell, where the beams are modeled as having unit depth in the out-of-plane direction.

Before proceeding to the structural formulation, the expressions for the element facial areas and unit normals must first be derived. Notice first from Fig. 1 that the volume element delineated by the dashed triangle can be shifted such that it fits exactly within one of the hexagons of the array, as shown by the shaded triangle in Fig. 1. Figure 2 shows that element, with all of the known geometric parameters indicated. The vectors $\mathbf{a}_1$, $\mathbf{a}_2$, $\mathbf{a}_3$ are expressed in terms of the unit cell geometry by attaching a new $r-s$ coordinate frame as shown in the Fig. 2. The s-direction is always aligned with leg 1 of the unit cell. The vectors are then found to be

$$\mathbf{a}_2 = 2L_3 \sin(\theta_3)\mathbf{i} + 2(L_1 + L_3 \cos(\theta_3))\mathbf{j}$$

$$\mathbf{a}_3 = -2L_2 \sin(\theta_2)\mathbf{i} + 2(L_1 + L_2 \cos(\theta_2))\mathbf{j}$$

$$\mathbf{a}_1 = \mathbf{a}_2 - \mathbf{a}_3.$$

The length of each face of the unit element is found by calculating the magnitude of the corresponding vector, which yields

$$A_1 = 2\sqrt{L_2^2 + L_3^2 - 2L_2L_3(\cos(\theta_2)\cos(\theta_3) - \sin(\theta_2)\sin(\theta_3))} \quad (1)$$

$$A_2 = 2\sqrt{L_1^2 + L_3^2 + 2L_1L_3\cos(\theta_3)} \quad (2)$$

$$A_3 = 2\sqrt{L_1^2 + L_2^2 + 2L_1L_2\cos(\theta_2)}. \quad (3)$$

The outward normals to each face are easily found from the vectors $\mathbf{a}_1$, $\mathbf{a}_2$, $\mathbf{a}_3$. Realizing that the y-component of $\mathbf{n}_1$ will always be positive and that of $\mathbf{n}_2$ and $\mathbf{n}_3$ will always be negative, the outward normals must satisfy

$$\mathbf{n}_1 \cdot \mathbf{a}_1 = 0, \quad \mathbf{n}_2 \cdot \mathbf{a}_2 = 0, \quad \mathbf{n}_3 \cdot \mathbf{a}_3 = 0, \quad (4)$$

which yields

$$\mathbf{n}_1 = n_{x1}\mathbf{i} + n_{y1}\mathbf{j}, \quad (5)$$

$$\mathbf{n}_2 = n_{x2}\mathbf{i} + n_{y2}\mathbf{j}, \quad (6)$$

$$\mathbf{n}_3 = n_{x3}\mathbf{i} + n_{y3}\mathbf{j}, \quad (7)$$

where

$$n_{x1} = \frac{L_2 \cos(\theta_2) - L_3 \cos(\theta_3)}{(L_3 \sin(\theta_3) + L_2 \sin(\theta_2)) \sqrt{\frac{(L_3 \cos(\theta_3) - L_2 \cos(\theta_2))^2}{(L_3 \sin(\theta_3) + L_2 \sin(\theta_2))^2} + 1}}, \tag{8}$$

$$n_{y1} = \frac{1}{\sqrt{\frac{(L_3 \cos(\theta_3) - L_2 \cos(\theta_2))^2}{(L_3 \sin(\theta_3) + L_2 \sin(\theta_2))^2} + 1}}, \tag{9}$$

$$n_{x2} = \frac{L_1 + L_3 \cos(\theta_3)}{L_3 \sin(\theta_3) \sqrt{\frac{(L_1 + L_3 \cos(\theta_3))^2}{L_3^2(\sin(\theta_3))^2} + 1}}, \tag{10}$$

$$n_{y2} = -\frac{1}{\sqrt{\frac{(L_1 + L_3 \cos(\theta_3))^2}{L_3^2(\sin(\theta_3))^2} + 1}}, \tag{11}$$

$$n_{x3} = \frac{-(L_1 + L_2 \cos(\theta_2))}{L_2 \sin(\theta_2) \sqrt{\frac{(L_1 + L_2 \cos(\theta_2))^2}{L_2^2(\sin(\theta_2))^2} + 1}}, \tag{12}$$

$$n_{y3} = -\frac{1}{\sqrt{\frac{(L_1 + L_2 \cos(\theta_2))^2}{L_2^2(\sin(\theta_2))^2} + 1}}. \tag{13}$$

2.1.2 Kinematics of the unit cell. The kinematics of the unit cell is completely defined by the relative displacements of the beam midpoints and the relative displacement and rotation of the junction point. Notice that the rotations of the beam midpoints are not independent variables since the moments there are zero due to symmetry conditions. We consider that the deformation field describes the relative motion of the beam midpoints while the location and rotation of the junction point is determined by enforcing local equilibrium.

Consider now a homogeneous strain increment $\mathbf{d}\epsilon$. The relative incremental displacements $\mathbf{d}\delta_1$, $\mathbf{d}\delta_2$ are given by

$$\begin{pmatrix} d\delta_{xi} \\ d\delta_{yi} \end{pmatrix} = \begin{bmatrix} d\epsilon_{xx} & d\epsilon_{xy} \\ d\epsilon_{xy} & d\epsilon_{yy} \end{bmatrix} \begin{pmatrix} r_{xi} \\ r_{yi} \end{pmatrix}, \tag{14}$$

for $i = 1, 2$, where $\mathbf{r_1}$, $\mathbf{r_2}$ are the position vectors of nodes 1 and 2, respectively, from node 3. Looking at Fig. 1, the position vectors are

$$\mathbf{r_1} = (L_3 \sin(\theta_3))\mathbf{i} + (L_1 + L_3 \cos(\theta_3))\mathbf{j}, \tag{15}$$

$$\mathbf{r_2} = (L_3 \sin(\theta_3) + L_2 \sin(\theta_2))\mathbf{i} + (L_3 \cos(\theta_3) - L_2 \cos(\theta_2))\mathbf{j}. \tag{16}$$

The incremental displacements in Eq. (14) are relative displacements of nodes 1 and 2 with respect to node 3. If the incremental displacements of the three nodes are $\mathbf{d\Delta_1}$, $\mathbf{d\Delta_2}$, and $\mathbf{d\Delta_3}$, then the relative displacements are

$$\mathbf{d}\delta_1 = \mathbf{d\Delta_1} - \mathbf{d\Delta_3} = d\delta_{x1}\mathbf{i} + d\delta_{y1}\mathbf{j}, \tag{17}$$

$$\mathbf{d}\delta_2 = \mathbf{d\Delta_2} - \mathbf{d\Delta_3} = d\delta_{x2}\mathbf{i} + d\delta_{y2}\mathbf{j}. \tag{18}$$

Expanding the system in (14) with Eqs. (15)–(16), the components of the incremental displacements in terms of the strain increment are

$$d\delta_{x1} = d\epsilon_{xx}L_3 \sin(\theta_3) + d\epsilon_{xy}(L_1 + L_3 \cos(\theta_3)), \tag{19}$$

$$d\delta_{y1} = d\epsilon_{xy}L_3 \sin(\theta_3) + d\epsilon_{yy}(L_1 + L_3 \cos(\theta_3)), \tag{20}$$

$$d\delta_{x2} = d\epsilon_{xx}(L_2 \sin(\theta_2) + L_3 \sin(\theta_3)) + d\epsilon_{xy}(L_3 \cos(\theta_3) - L_2 \cos(\theta_2)), \tag{21}$$

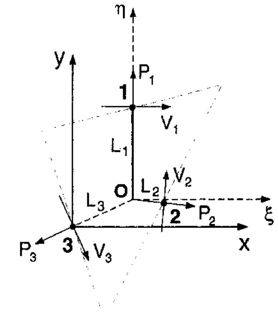

Fig. 3 Free-body diagram of the unit cell

$$d\delta_{y2} = d\epsilon_{xy}(L_2 \sin(\theta_2) + L_3 \sin(\theta_3)) + d\epsilon_{yy}(L_3 \cos(\theta_3) - L_2 \cos(\theta_2)). \tag{22}$$

2.1.3 Displacement-Force Relations for the Unit Cell. To establish the displacement-force relations for the structure, another coordinate system (ξ, η) is placed with its origin at the junction point O as shown in Fig. 3. Notice that the (ξ, η) frame is parallel to the (x, y) frame, but shifted from point 3 to point O. Isolating the unit cell in Fig. 3 as a free body in equilibrium, we denote the force at the three beam midpoints in terms of components P_i parallel to the beam axis and V_i normal to the beam axis, where the index i refers to the node number. Only axial and bending deformations of each beam are considered, where the P_i are axial forces and the V_i are transverse forces. Since shear deflections of beams are neglected and conventional beam theory is used to model the unit cell strut deformations, the current model is only valid for *porous* foams consisting of long, slender struts. The spatially periodic nature of the cell array requires that the individual beams deform symmetrically about their midpoints, so there is no resultant moment across the section at the beam midpoints.

Now consider some increment in the forces P_i and V_i as a result of an incremental deformation. In the general coupled beam, the axial and transverse tip displacements are affected by *both* forces. The incremental axial and transverse tip displacements for the ith beam in terms of the incremental forces are therefore

$$d\Delta_{ai} = M_{Pi}dP_i + M_{Vi}dV_i, \tag{23}$$

$$d\Delta_{ti} = N_{Pi}dP_i + N_{Vi}dV_i, \tag{24}$$

respectively, where M_{Pi}, M_{Vi} are the axial compliances due to the incremental forces dP_i, dV_i and N_{Pi}, N_{Vi} are the bending compliances due to dP_i, dV_i. Consider further an incremental rotation $\mathbf{dR} = d\psi\mathbf{k}$ of the junction point O, where $d\psi$ is the relative rotation of the junction point with respect to the rigid rotation of the cell. The resulting incremental displacements of nodes 1–3 are found from $du_i = \mathbf{R} \times \rho_i$, where ρ_i is the position vector from O to node i as follows:

$$\rho_1 = L_1\mathbf{j}$$

$$\rho_2 = L_2 \sin(\theta_2)\mathbf{i} - L_2 \cos(\theta_2)\mathbf{j}$$

$$\rho_3 = -L_3 \sin(\theta_3)\mathbf{i} - L_3 \cos(\theta_3)\mathbf{j}.$$

Combining tip deflections due to incremental axial and transverse forces and a junction point rotation, the total incremental tip deflections of each node are

$$d\Delta_1 = (d\Delta_{t1} - d\psi L_1)\mathbf{i} + (d\Delta_{a1})\mathbf{j}, \tag{25}$$

$$d\Delta_2 = (d\Delta_{a2} \sin(\theta_2) + d\Delta_{t2} \cos(\theta_2) + d\psi L_2 \cos(\theta_2))\mathbf{i} + (-d\Delta_{a2} \cos(\theta_2) + d\Delta_{t2} \sin(\theta_2) + d\psi L_2 \sin(\theta_2))\mathbf{j} \tag{26}$$

$$d\Delta_3 = (-d\Delta_{a3}\sin(\theta_3) + \Delta_{t3}\cos(\theta_3) + d\psi L_3\cos(\theta_3))\mathbf{i} + (-\Delta_{a3}\cos(\theta_3) - \Delta_{t3}\sin(\theta_3) - d\psi L_3\sin(\theta_3))\mathbf{j}, \quad (27)$$

where the $d\Delta_{ai}$, $d\Delta_{ti}$ are as defined in Eqs. (23)–(24). To reduce the number of unknowns in the problem, the displacements of nodes 1 and 2 will be expressed relative to node 3 as described by Eqs. (17) and (18).

Substituting Eqs. (23)–(24) into Eqs. (25)–(27), the components of Eqs. (17)–(18) in terms of the incremental forces are

$$d\delta_{x1} = N_{V1}dV_1 + N_{P1}dP_1 + (M_{P3}dP_3 + M_{V3}dV_3)\sin(\theta_3) - (N_{P3}dP_3 + N_{V3}dV_3)\cos(\theta_3) - d\psi(L_1 + L_3\cos(\theta_3)), \quad (28)$$

$$d\delta_{y1} = M_{V1}dV_1 + M_{P1}dP_1 + (M_{P3}dP_3 + M_{V3}dV_3)\cos(\theta_3) + (N_{P3}dP_3 + N_{V3}dV_3)\sin(\theta_3) + d\psi L_3\sin(\theta_3), \quad (29)$$

$$d\delta_{x2} = (M_{P2}dP_2 + M_{V2}dV_2)\sin(\theta_2) + (N_{P2}dP_2 + N_{V2}dV_2)\cos(\theta_2) + (M_{P3}dP_3 + M_{V3}dV_3)\sin(\theta_3) - (N_{P3}dP_3 + N_{V3}dV_3)\cos(\theta_3) + d\psi(L_2\cos(\theta_2) - L_3\cos(\theta_3)), \quad (30)$$

$$d\delta_{y2} = -(M_{P2}dP_2 + M_{V2}dV_2)\cos(\theta_2) + (N_{P2}dP_2 + N_{V2}dV_2)\sin(\theta_2) + (M_{P3}dP_3 + M_{V3}dV_3)\cos(\theta_3) + (N_{P3}dP_3 + N_{v3}dV_3)\sin(\theta_3) + d\psi(L_2\sin(\theta_2) + L_3\sin(\theta_3)). \quad (31)$$

Equations (28)–(31) expresses the two components of the relative incremental displacements of nodes 1 and 2 with respect to node 3 in terms of seven unknowns: $dP_1 - dP_3$, $dV_1 - dV_3$, and $d\psi$. The equations of equilibrium will provide the three additional equations needed to solve the system.

2.1.4 Cell Equilibrium. Equilibrium is governed by two force balances and one moment balance, as follows:

$$\sum dF_x = dP_2\sin(\theta_2) - dP_3\sin(\theta_3) + dV_1 + dV_2\cos(\theta_2) + dV_3\cos(\theta_3) = 0, \quad (32)$$

$$\sum dF_y = dP_1 - dP_2\cos(\theta_2) - dP_3\cos(\theta_3) + dV_2\sin(\theta_2) - dV_3\sin(\theta_3) = 0, \quad (33)$$

$$\sum dM_z = -dV_1L_1 + dV_2L_2 + dV_3L_3 = 0. \quad (34)$$

This brings the total system to seven equations with seven unknowns. The solution to the system is a set of incremental reaction forces $dP_1 - dP_3$, $dV_1 - dV_3$, and junction point rotation $d\psi$ that equilibrate the structure under the given relative incremental displacements $d\delta_1$, $d\delta_2$. Once the incremental reactions are known by simultaneously solving Eqs. (28)–(31) and (32)–(34), the incremental stresses acting on the area element enclosing the unit cell can be calculated.

2.1.5 Stress-Strain Relations. The incremental tractions on faces 1 and 2 are defined as

$$\mathbf{dt_1} = dt_{x1}\mathbf{i} + dt_{y1}\mathbf{j} = \mathbf{n_1}\cdot d\sigma = (d\sigma_{xx}n_{x1})\mathbf{i} + (d\sigma_{xy}n_{y1})\mathbf{j} \quad (35)$$

$$\mathbf{dt_2} = dt_{x2}\mathbf{i} + dt_{y2}\mathbf{j} = \mathbf{n_2}\cdot d\sigma = (d\sigma_{xx}n_{x2})\mathbf{i} + (d\sigma_{xy}n_{y2})\mathbf{j} \quad (36)$$

where n_{x1}, n_{y1}, n_{x2}, n_{y2} are the unit normals given in Eqs. (9)–(13). The incremental surface tractions can be calculated directly from the incremental forces as

$$\mathbf{dt_1} = \frac{dV_1}{A_1}\mathbf{i} + \frac{dP_1}{A_1}\mathbf{j} \quad (37)$$

$$\mathbf{dt_2} = \frac{dP_2\sin(\theta_2) + dV_2\cos(\theta_2)}{A_2}\mathbf{i} + \frac{-dP_2\cos(\theta_2) + dV_2\sin(\theta_2)}{A_2}\mathbf{j}. \quad (38)$$

Substituting Eqs. (37)–(38) into (35)–(36), the stresses in terms of the unit normals and the incremental forces are

$$d\sigma_{xx} = \frac{-dV_1A_2n_{y2} + dP_2\sin(\theta_2)A_1n_{y1} + dV_2\cos(\theta_2)A_1n_{y1}}{A_1A_2(n_{x2}n_{y1} - n_{x1}n_{y2})} \quad (39)$$

$$d\sigma_{yy} = \frac{dP_1A_2(n_{x2}n_{y1} - n_{x1}n_{y2}) - dV_1A_2n_{x1}n_{x2} + (dP_2\sin(\theta_2) + dV_2\cos(\theta_2))A_1n_{x1}^2}{A_1A_2n_{y1}(n_{x2}n_{y1} - n_{x1}n_{y2})} \quad (40)$$

$$d\sigma_{xy} = \frac{dV_1A_2n_{x2} - dP_2\sin(\theta_2)A_1n_{x1} - dV_2\cos(\theta_2)A_1n_{x1}}{A_1A_2(n_{x2}n_{y1} - n_{x1}n_{y2})}. \quad (41)$$

Given some increment in the strain field on the unit cell, the incremental displacements can be found from Eqs. (19)–(22). Equilibrium and compatibility conditions then yield the corresponding increment in the stress field, given by Eqs. (39)–(41). The incremental stiffness matrix is then computed by

$$C_{ijkl} = \frac{\partial\sigma_{ij}}{\partial\epsilon_{kl}} = \frac{\partial\sigma_{ij}}{\partial t_m}\frac{\partial t_m}{\partial F_n}\frac{\partial F_n}{\partial\delta_p}\frac{\partial\delta_p}{\partial\epsilon_{kl}}. \quad (42)$$

The analytical expressions for the terms in (42) are extremely large for the general model with the seventeen variables $M_{P1} - M_{P3}$, $M_{V1} - M_{V3}$, $N_{P1} - N_{P3}$, $N_{V1} - N_{V3}$, $L_1 - L_3$, θ_2, θ_3. It is left to the reader to use a symbolic math software package to solve the given system of equations and generate the stiffness expressions.

For the special case of the elastic (decoupled) regular hexagonal cell, where $L_1 = L_2 = L_3 = L$, $M_{P1} = M_{P2} = M_{P3} = M$, $M_{V1} = M_{V2} = M_{V3} = N_{P1} = N_{P2} = N_{P3} = 0$, $N_{V1} = N_{V2} = N_{V3} = N$, $\theta_2 = \theta_3 = 60$ deg, the analytical expression for C reduces to

$$\mathbf{C} = \begin{pmatrix} \frac{\sqrt{3}(N+3M)}{12M(N+M)} & \frac{\sqrt{3}(N-M)}{12M(N+M)} & 0 \\ \frac{\sqrt{3}(N-M)}{12M(N+M)} & \frac{\sqrt{3}(N+3M)}{12M(N+M)} & 0 \\ 0 & 0 & \frac{\sqrt{3}}{6(N+M)} \end{pmatrix}, \quad (43)$$

which is the same result given by Warren and Kraynik (1987).

Given the stiffness matrix, the effective Poisson's ratio ν_{12}^e relates the lateral deformation in the 2-direction to the deformation in the 1-direction under uniaxial load in the 1-direction. This is computed by

$$\nu_{12}^e = -\frac{\epsilon_{22}^1}{\epsilon_{11}^1} = \frac{C_{12}C_{33} - C_{13}C_{23}}{C_{22}C_{33} - C_{23}^2}, \tag{44}$$

where the 1 superscript indicates that the load is in the 1-direction. Similarly, the effective Poisson's ratio ν_{21}^e relating the lateral deformation in the 1-direction to the 2-direction deformation under uniaxial load in the 2-direction is

$$\nu_{21}^e = -\frac{\epsilon_{11}^2}{\epsilon_{22}^2} = \frac{C_{12}C_{33} - C_{13}C_{23}}{C_{11}C_{33} - C_{13}^2}, \tag{45}$$

where the 2 superscript indicates that the load is in the 2-direction.

The effective moduli in the 1 and 2-directions under uniaxial stresses σ_1 and σ_2, respectively, are

$$E_1^e = \frac{\sigma_1}{\epsilon_1} = \frac{-C_{11}C_{22}C_{33} + C_{11}C_{23}^2 + C_{12}^2C_{33} - 2C_{12}C_{13}C_{23} + C_{13}^2C_{22}}{-C_{22}C_{33} + C_{23}^2} \tag{46}$$

$$E_2^e = \frac{\sigma_2}{\epsilon_2} = \frac{-C_{11}C_{22}C_{33} + C_{11}C_{23}^2 + C_{12}^2C_{33} - 2C_{12}C_{13}C_{23} + C_{13}^2C_{22}}{-C_{11}C_{33} + C_{13}^2}. \tag{47}$$

It is useful to introduce a parameter that may be used to measure the degree of anisotropy in material behavior of a general hexagonal foam. For an elastically isotropic material the constitutive matrix must have the following form:

$$\mathbf{C} = \begin{pmatrix} \lambda + 2\mu & \lambda & 0 \\ \lambda & \lambda + 2\mu & 0 \\ 0 & 0 & \mu \end{pmatrix}.$$

A measure of the degree of anisotropy is therefore indicated by the values of the following anisotropy parameters:

$$J_1 = \frac{C_{11}}{C_{22}}, \tag{48}$$

$$J_2 = \frac{C_{12} + 2C_{33}}{C_{11}}. \tag{49}$$

An elastically isotropic foam will have $J_1 = J_2 = 1$, while any anisotropy will result in values other than 1.

2.2 Square Beam Compliances. For the analysis, the beams of the unit cell will be modeled as a regular square beams having side dimensions of $2b_1$, $2b_2$, and $2b_3$ for beams 1, 2, and 3, respectively. Nonlinearity will be introduced by considering that the beams are composed of elastic-perfectly plastic material. The elastoplastic behavior of a square beam with axial and transverse tip loads P and F is well known from classical solutions. The beam can exist in one of three deformation modes:

1 Elastic: $F \le F_{\rm el}$
2 Mode 1 Plastic: $F_{\rm el} < F \le F_{\rm 1crit}$,
3 Mode 2 Plastic: $F > F_{\rm 1crit}$,

where

$$F_{\rm el} = \frac{I}{Lb}\left(\sigma_y - \frac{P}{A}\right) = \frac{4b^3}{3L}\left(\sigma_y - \frac{P}{4b^2}\right), \tag{50}$$

$$F_{\rm 1crit} = \frac{1}{6bL\sigma_y}(8b^4\sigma_y^2 - P^2 + 2Pb^2\sigma_y), \tag{51}$$

where I is the area moment of inertia of the beam cross section. Mode 1 plastic corresponds to the case when yield is only occurring on one surface of the beam, while mode 2 plastic corresponds to that when both surfaces are at yield.

The elastic compliances of a square beam are

$$M_P = \frac{L}{AE} = \frac{L}{4b^2E}, \tag{52}$$

$$M_V = 0, \tag{53}$$

$$N_P = 0, \tag{54}$$

$$N_V = \frac{L^3}{3EI} = \frac{L^3}{4b^4E}. \tag{55}$$

The analytical solutions for mode 1 tip deflections in the axial and transverse directions are, respectively,

$$\Delta_a^1 = \frac{1}{12FEb}(-P^2 + c_1P + c_2), \tag{56}$$

$$\Delta_t^1 = \frac{1}{108F^2Eb}(-P^3 + c_3P^2 + c_4P + c_5), \tag{57}$$

and for mode 2 deflections are

$$\Delta_a^2 = \frac{1}{12FEb}((4b - 1)P^2 + d_1P + d_2), \tag{58}$$

$$\Delta_t^2 = \frac{1}{108F^2Eb}(-13P^3 + d_3P^2 + d_4P + d_5), \tag{59}$$

where the coefficients in each set of equations may be found in the Appendix.

The mode 1 and mode 2 compliances then arise from taking derivatives of (56)–(59) with respect to the forces

$$M_P^i = \frac{\partial \Delta_a^i}{\partial P}, \quad M_V^i = \frac{\partial \Delta_a^i}{\partial F}, \tag{60}$$

$$N_P^i = \frac{\partial \Delta_t^i}{\partial P}, \quad N_V^i = \frac{\partial \Delta_t^i}{\partial F}. \tag{61}$$

Depending on the mode of the beam, the appropriate compliances are used in the formulation of the incremental constitutive relations described in the previous section. The analytical expressions for (60)–(61) are fairly lengthy for modes 1 and 2, and are not given here for brevity.

3 Finite Element Procedure

The power of the structural formulation developed in Section 2 is its ability to model the evolution of plasticity at the beam level within the unit cell. Finite element analysis of the mechanics of a plastic foam requires an incremental procedure, since the stiffness of each cell will change as the plasticity evolves. By embedding the unit cell incremental constitutive model into a continuum finite element model, localized plastic regions within the structure can be followed. An important requirement is that the foam specimen be large compared to the scale of the unit cell. In such a case, the assumption that the unit cell approaches a continuum element is reasonable.

An explicit integration of the constitutive relations is used in this article. The corresponding strain-controlled finite element algorithm proceeds as follows:

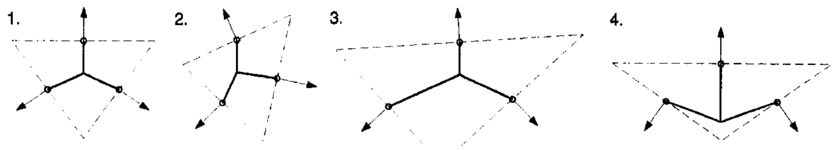

Fig. 4 The unit cells for groups 1–4

1 Given a strain increment $(d\epsilon_{xx}, d\epsilon_{yy}, d\epsilon_{xy})$, obtain the unit cell incremental displacements using Eqs. (19)–(22).

2 Determine the compliance of each beam based upon the cell reaction forces from the previous step.

- If the beam is elastic, use Eqs. (52)–(55).
- If the beam is plastic, use Eqs. (60)–(61) for the appropriate mode.

3 With the known geometry and compliance parameters and the incremental displacements, solve Eqs. (28)–(31) and (32)–(34) for the incremental reaction forces $dP_1 - dP_3$, $dV_1 - dV_3$, and $d\psi$.

4 Compute the total reaction forces (previous plus current increment) and find the stresses using Eqs. (39)–(41).

Global equilibrium is enforced at each step by means of a Newton iterative procedure. Our numerical experimentation shows that convergence is achieved in two iterations with an imposed tolerance of 10^{-9} of the initial unbalanced quantity.

4 Results

4.1 Linear Elastic Behavior. The mechanical behavior is strongly dependent on the morphology of the foam, even for samples having equivalent relative densities. This knowledge can be exploited in designing special purpose or ad-hoc foams with desired directional properties. As an example of the strong influence that foam morphology has on the mechanical behavior, we present the following four unit cell cases:

1 Regular: $L_1 = L_2 = L_3 = 1$ mm, $b_1 = b_2 = b_3 = 0.1$ mm, $\theta_2 = \theta_3 = 60$ deg, $E_1 = E_2 = E_3 = 10$ GPa,
2 Orientation anisotropy: $L_1 = L_2 = L_3 = 1.1239$ mm, same b's, $\theta_2 = 80$ deg, $\theta_3 = 20$ deg, $E_1 = E_2 = E_3 = 10$ GPa,
3 Length anisotropy: $L_1 = 1$ mm, $L_2 = 1.5$ mm, $L_3 = 2$ mm, $b_1 = b_2 = b_3 = 0.1444$ mm, $\theta_2 = \theta_3 = 60$ deg, $E_1 = E_2 = E_3 = 10$ G Pa,
4 Re-entrant: $L_1 = L_2 = L_3 = 1.576$ mm, $b_1 = b_2 = b_3 = 0.075$ mm, $\theta_2 = \theta_3 = 110$ deg, $E_1 = E_2 = E_3 = 10$ GPa.

The morphologic parameters have been chosen such that the relative density of the unit cell in each group is identical, having a value of 0.1155. The relative density is calculated from $\Sigma\, t_i L_i / A$, where A is the area of the triangular element surrounding the unit cell and $t_i = 2b_i$ are the beam thicknesses. The purpose of enforcing that the cells have the same density is to isolate the effects of various architectural anisotropies.

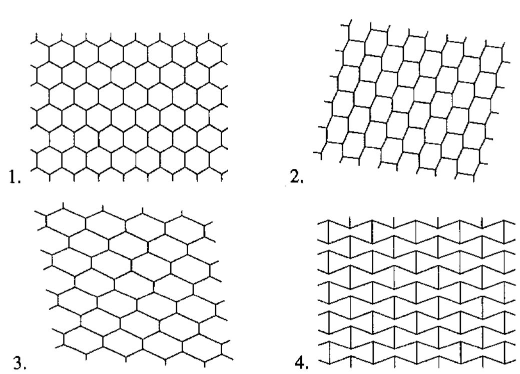

Fig. 5 Foam specimens of groups 1–4, (thicknesses not to scale)

Figure 4 shows the unit cells for each group, with the element areas and outward normals indicated. Figure 5 shows a foam specimen of each group. The constitutive matrices for each group, obtained through the procedure described in the first section, are

$$\mathbf{C}^1 = \begin{pmatrix} 5.8878 & 5.6592 & 0 \\ 5.6592 & 5.8878 & 0 \\ 0 & 0 & 0.1143 \end{pmatrix} \times 10^4,$$

$$\mathbf{C}^2 = \begin{pmatrix} 0.8847 & 3.0580 & 0.4158 \\ 3.0580 & 13.0444 & 1.7971 \\ 0.4158 & 1.7971 & 0.3071 \end{pmatrix} \times 10^4,$$

$$\mathbf{C}^3 = \begin{pmatrix} 11.4480 & 8.0107 & 0.9753 \\ 8.0107 & 5.8884 & 0.6296 \\ 0.9753 & 0.6296 & 0.3640 \end{pmatrix} \times 10^4,$$

$$\mathbf{C}^4 = \begin{pmatrix} 7.3112 & -1.8490 & 0 \\ -1.8490 & 0.4804 & 0 \\ 0 & 0 & 0.0038 \end{pmatrix} \times 10^4. \quad (62)$$

The anisotropy parameters for each foam are shown in Table 1. Notice again that the regular hexagonal cell (group 1) is transversely isotropic and normal stresses are unaffected by shear deformations (independent of coordinate frame). As soon as geometric or material anisotropy is introduced, as in groups 2 and 3, the stiffness matrix is no longer isotropic and shear coupling is introduced. The constitutive matrix for group 2 is more strongly anisotropic than that for group 3, indicated by larger deviations of J_1 and J_2 from 1 for group 2. The stiffness properties of the re-entrant foam cell (group 4) are interesting in that the cell is not isotropic and the normal stresses are unaffected by shear for the particular reference frame chosen (a coordinate rotation would change this). In any elastic foam the stiffness matrix will always be symmetric. This is a consequence of the fact that the system of incremental displacement Eqs. (23)–(24) describing the elastic beam behavior is symmetric (recall that M_V and N_P are zero for the elastic beam). Symmetry of the elasticity tensor is associated with the existance of a potential function or strain energy function, in this case with quadratic terms on the strain components.

It is instructive at this juncture to discuss the differences between the present model and that of Gibson and Ashby (1982), in which axial strut deformations are neglected. Table 2 shows the moduli (multiplied by t to account for depth) and

Table 1 Anisotropy parameters and Poisson's ratios for foam groups 1–4

	Group 1	Group 2	Group 3	Group 4
J_1	1.0000	0.0678	1.9442	15.2196
J_2	1.0000	4.1509	0.7633	-0.2519
ν_{12}^e	0.9612	0.7281	1.4933	-3.8491
ν_{21}^e	0.9612	2.4753	0.6640	-0.2529

Table 2 Moduli and Poisson's ratios for a re-entrant foam with decreasing beam thicknesses from Gibson and Ashby (1982) and current model ($L_1 = L_2 = L_3 = l = 1$ mm, $2b_1 = 2b_2 = 2b_3 = t$, $\theta_2 = \theta_3 = 110$ deg, $E_1 = E_2 = E_3 = 10$ GPa)

	Gibson & Ashby				Overaker, Cuitiño, Langrana			
t/l	E_1^* (Pa)	E_2^* (Pa)	ν_{12}^*	ν_{21}^*	E_1^c (Pa)	E_2^c (Pa)	ν_{12}^c	ν_{21}^c
0.2	2.442×10^4	1.586×10^3	-3.924	-0.255	2.270×10^4	1.549×10^3	-3.612	-0.246
0.02	2.442	1.586×10^{-1}	-3.924	-0.255	2.440	1.586×10^{-1}	-3.920	-0.255
0.002	2.442×10^{-4}	1.586×10^{-5}	-3.924	-0.255	2.442×10^{-4}	1.586×10^{-5}	-3.924	-0.255

Poisson's ratios for a re-entrant foam from both Gibson and Ashby and the current model for varying beam thicknesses. Notice that as the beam thickness decreases, the values predicted by the two models approach each other. As the cross section becomes very small, the bending deformations dominate and the current model approaches the model of Gibson and Ashby.

Finite element simulations of compression of 5×5 cm foam specimens of groups 1–4 were performed. The boundary conditions on the lower surface were fixed displacements in the x-direction and y-direction. The upper surface had an imposed y-displacement of 0.1 mm and fixed x-displacement. All simulations were performed in one step since the slope is constant.

Figure 6 shows the resulting distributions for specimens 1–3 (left to right), respectively, for σ_{xx}, σ_{xy}, and σ_{yy} (top to bottom). Different plot ranges were used for each of the σ_{yy} plots since the values were quite different between specimens. For the other stress plots, the same range was used for all specimens for ease of comparison. The stress results for the re-entrant foam, specimen 4, are given in Fig. 7. All stresses are normalized by $E \times 10^{-6}$, where E is 10 GPa for each of the specimens.

The stronger anisotropy of the group 2 versus group 3 foams is clearly indicated in the stress plots. Comparing the results of the re-entrant foam (group 4) with the regular foam (group 1), notice that σ_{xx} has opposite signs between the groups. Compression of the re-entrant foam in the y-direction produces tensile stresses in the x-direction at upper and lower surfaces (to maintain the rigid boundary condition), a result of the negative Poisson's ratio behavior of the structure. Magnification of the small deformation of the foams in Fig. 8 shows the regular foam expanding laterally while the re-entrant foam contracts laterally under compression. The plots clearly demonstrate the significant influence that structural morphology has on the mechanical properties of the foams.

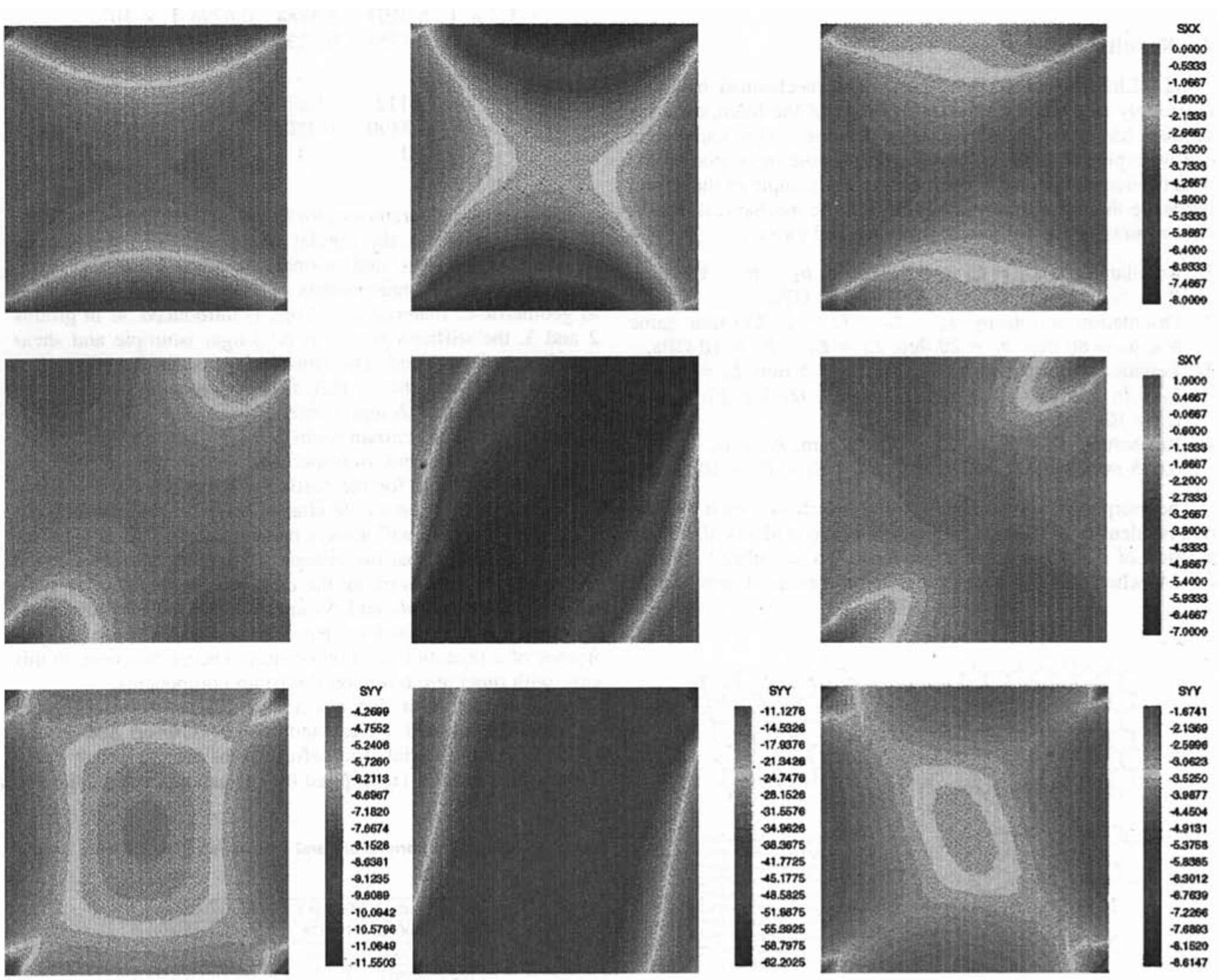

Fig. 6 Stresses obtained for specimens 1–3, respectively, normalized by $E \times 10^{-6}$ (left to right)

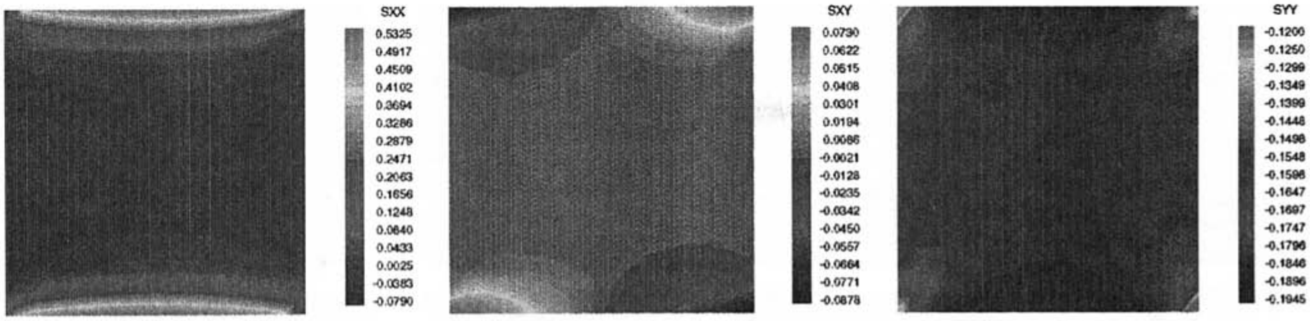

Fig. 7 Stresses obtained for the specimen 4, normalized by $E \times 10^{-6}$

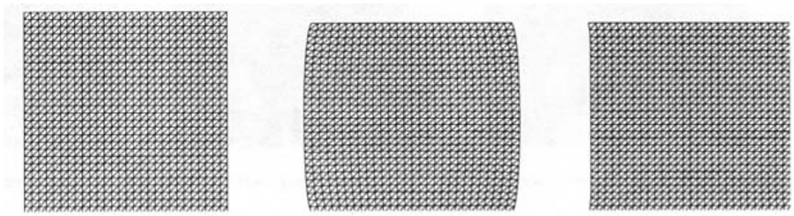

Fig. 8 Original configuration and 30× magnification of the deformation of the finite element mesh for elastic compression of group 1 and group 4 foams (left to right, respectively)

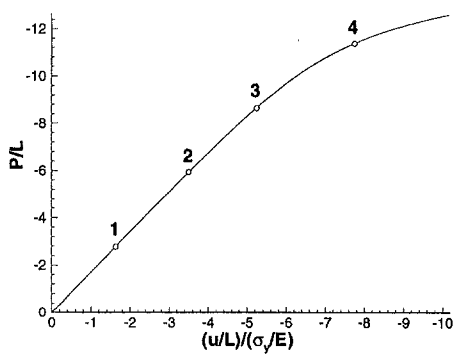

Fig. 9 Resultant load versus displacement from a simulation of compression of an elastoplastic foam (L_1 = 1 mm, L_2 = 1.5 mm, L_3 = 2 mm, $b_1 = b_2 = b_3$ = 0.0625 mm, $\theta_2 = \theta_3$ = 60 deg, $E_1 = E_2 = E_3$ = 10 GPa)

4.2 Nonlinear Elastoplastic Behavior. An interesting effect of the onset of beam plasticity is that the stiffness matrix for the unit cell can become nonsymmetric. This nonsymmetry arises directly from the introduction of the plastic beam behavior (coupling of axial and transverse forces) with nonsymmetry in the system of incremental displacement Eqs. (23)–(24).

A finite element simulation of compression of a foam specimen was performed with the same boundary conditions used in the elastic analysis. The specimen had the same geometric parameters as specimen 3 from the elastic analysis, except that the beam cross sections were reduced to $b_1 = b_2 = b_3 = 0.0625$ mm. This was done to ensure that the smallest beam length-to-diameter ratio was larger than 5. The elastic part of the simulation was performed in one step, while much smaller steps were taken beyond the yield limit in order to follow the changing stiffness of the structure.

Figure 9 shows the resultant load versus displacement from the compression simulation, where the load has been nondimensionalized by the width of the specimen (0.05 m) and the strain (u/L) has been nondimensionalized by σ_y/E of the beam material. The four points marked 1–4 denote points at which the yield and stress contours will be observed. Point 1 corresponds to initial yield within the structure. Notice that the structure does not begin to yield significantly until the displacement has proceeded considerably beyond the yield point. This can be explained by observing the contours of yielding material. Figure 10 shows the yield and σ_{yy} contours at the four points along the load-displacement curve. Notice that the yield is very localized at point 1, and still is not widely spread at point 2. At the third point a larger percentage of the structure is yielding and the rate of growth of the plastic region increases as the load is transferred to the ever shrinking elastic regions. At point 4 a considerable amount of the structure is yielding, indicated by the greatly diminished slope of the load-displacement curve.

Delving deeper to look at the deformation modes of individual beams, Fig. 11 shows contours of deformation modes for beams 1–3 corresponding to point 3 on the load-displacement curve. The results show how the plasticity of each beam contributes to the overall plastic behavior of the unit cell that is given in Fig. 10. Notice that at point 3, the 1-beams are almost entirely elastic. Both the 2-beams and 3-beams are predominantly elastic or mode 2 plastic, with the 2-beams having further developed plasticity than the 3-beams. This directly explains why the yield contours in Fig. 10 are skewed in the direction of the 2-beams.

5 Conclusions

A general formulation for the two-dimensional anisotropic hexagonal foam with coupled deformation behavior has been developed in an incremental form that accommodates elastoplastic analysis. The system of governing equations has been given so that the constitutive relations may be generated using any symbolic math software package.

Elastic analyses demonstrated the effects of strut orientations and lengths on the elastic properties of the structure. The stiffness matrix of the elastic foam is always symmetric and the degree of anisotropy is dictated by the degree of material and/or morphological anisotropy introduced in the unit cell. The re-entrant foam shows the same behavior, except that the re-entrant morphology introduces a negative Poisson's ratio effect to the deformation behavior. Sensitivity studies can be performed to more closely study the effects of any morphological or material parameter. The elastic foam has a symmetric stiffness matrix because axial and transverse beam deflections are decoupled.

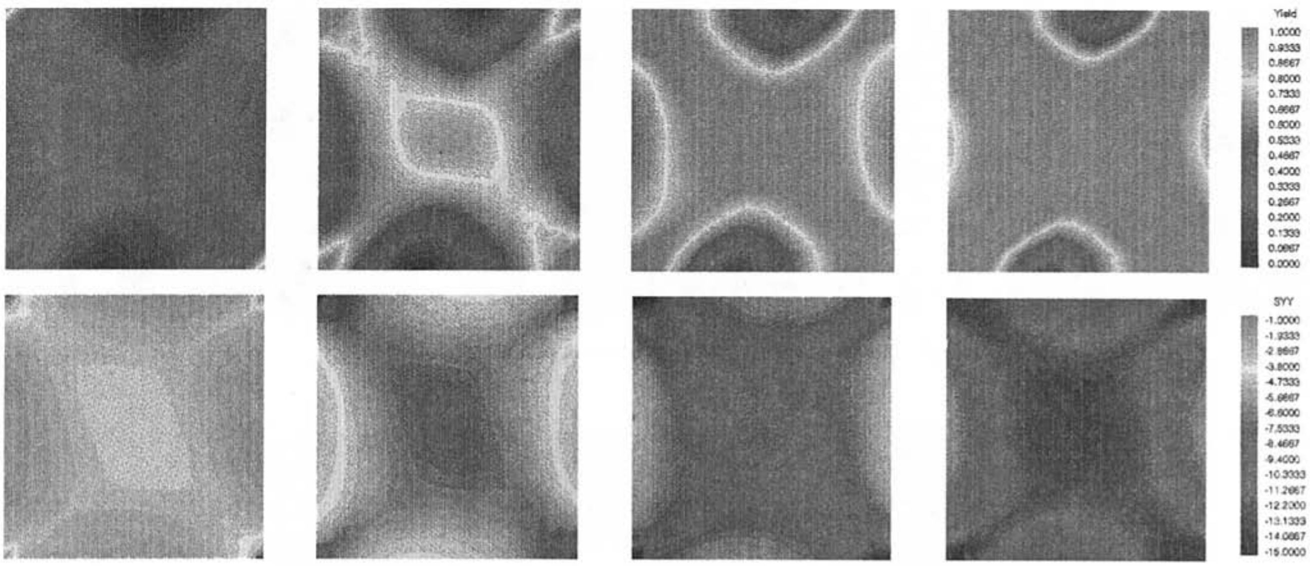

Fig. 10 Yield and σ_{yy} (normalized by $E \times 10^{-6}$) contours at points 1–4, respectively (left to right), on the load-displacement curve in Fig. 9

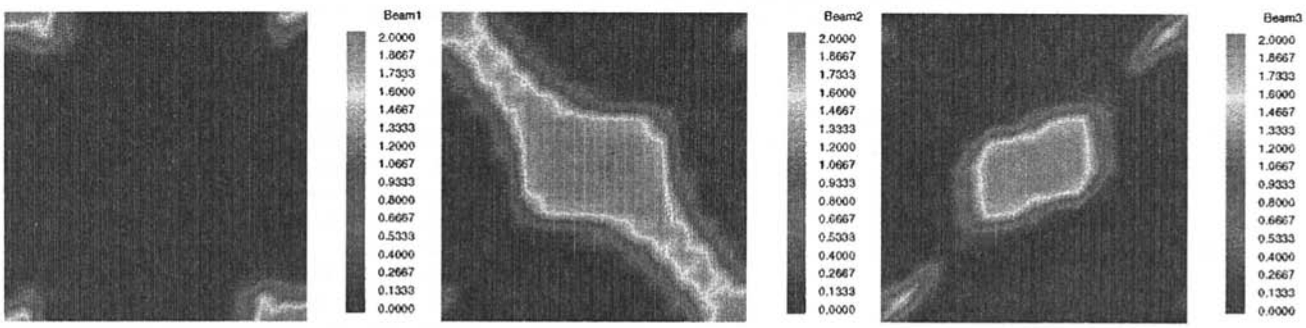

Fig. 11 Mode contours for beams 1–3, respectively, corresponding to point 3 on the load-displacement curve in Fig. 9 (elastic: mode = 0; mode 1 plastic: mode = 1; mode 2 plastic: mode = 2)

Plastic analyses showed how localized regions of plasticity develop and grow within the foam structure with continued loading. The changes in the load-displacement behavior of the foam were explained in terms of the stage of development of localized plasticity. As the plastic region expands its rate of expansion increases, which is indicated in a strain-controlled test by a decrease in the slope of the load-displacement curve. The coupled elastoplastic beam model yields a nonsymmetric stiffness matrix for the unit cell as soon as nonsymmetry in beam behavior of any of the cell beams is introduced.

The potential of this formulation for use in design of foams is particularly attractive. The simplicity and flexibility of the formulation allows comparison of many different structural and material arrangements, which could prove useful in determining a design that has a particular required mechanical behavior for a given application.

Acknowledgments

This work has been performed in partial fulfillment of the requirements for the doctoral dissertation of the first author. Support of this work was provided by the Rutgers Department of Mechanical and Aerospace Engineering.

References

Ashby, M. F., 1983, "The mechanical properties of cellular solids," *Metallurgical Transactions*, Vol. 14A, p. 1755.

Christensen, R. M., 1986, "Mechanics of low density materials," *Journal Mech. Phys. Solids*, Vol. 34, pp. 563–578.

Choi, J. B., and Lakes, R. S., 1992, "Nonlinear properties of metallic cellular materials with a negative Poisson's ratio foams," *Journal of Materials Science*, Vol. 27, pp. 5375–5381.

Choi, J. B., and Lakes, R. S., 1995, "Nonlinear analysis of the Poisson's ratio of negative Poisson's ratio foams," *Journal of Composite Materials*, Vol. 29, No. 1, pp. 113–128.

Friis, E. A., Lakes, R. S., and Park, J. B., 1988, "Negative Poisson's ratio of polymeric and metallic foams," *Journal of Materials Science*, Vol. 23, pp. 4406–4414.

Gent, A. N., and Thomas, A. G., 1959, "The deformation of foamed elastic materials," *Journal of Applied Polymer Science*, Vol. 1, No. 1, pp. 107–113.

Gent, A. N., and Thomas, A. G., 1963, "Mechanics of foamed elastic materials," *Rubber Chemistry and Technology*, Vol. 63, pp. 597–610.

Gibson, L. J., et al., 1982, "The mechanics of two-dimensional cellular materials," *Proceedings of the Royal Society of London*, Vol. A382, pp. 25–42.

Gibson, L. J., and Ashby, M. F., 1982, "The mechanics of three-dimensional cellular materials," *Proceedings of the Royal Society of London*, Vol. A382, pp. 43–59.

Gibson, L. J., and Ashby, M. F., 1988, *Cellular Solids*, Pergamon, Oxford, U.K.

Hilyard, N. C., ed., 1982, *Mechanics of Cellular Plastics*, Macmillan, New York.

Huber, A. T., and Gibson, L. J., 1988, "Anisotropy of foams," *Journal of Materials Science*, Vol. 23, pp. 3031–3040.

Ko, W. L., 1965, "Deformations of foamed elastomers," *Journal of Cellular Plastics*, Vol. 1, pp. 45–50.

Lakes, R. S., 1987, "Foam structures with a negative Poisson's ratio," *Science*, Vol. 235, pp. 1038–1040.

Lee, J., Choi, J. B., and Choi, K., 1996, "Application of homogenization FEM analysis to regular and re-entrant honeycomb structures," *Journal of Materials Science*, Vol. 31, pp. 4105–4110.

Menges, G., and Knipschild, F., 1975, "Estimation of mechanical properties for rigid polyurethane foams," *Polymer Engineering Science*, Vol. 15, pp. 623–627.

Patel, M. R., and Finnie, I., 1970, "Structural features and mechanical properties of rigid cellular plastics," *Journal of Materials*, Vol. 5, pp. 909–932.

Warren, T. L., 1990, "Negative Poisson's ratio in a transversely isotropic foam structure," *Journal of Applied Physics*, Vol. 67, No. 12, pp. 7591–7594.

Warren, W. E., and Kraynik, A. M., 1987, "Foam mechanics: The linear elastic response of two-dimensional spatially periodic cellular materials," *Mechanics of Materials*, Vol. 6, pp. 27–37.

Warren, W. E., and Kraynik, A. M., 1988, "The Linear Elastic Properties of Open-Cell Foams," ASME JOURNAL OF APPLIED MECHANICS, Vol. 55, pp. 341–346.

Warren, W. E., Kraynik, A. M., and Stone, C. M., 1989, "A constitutive model for two-dimensional nonlinear elastic foams," *Journal Mech. Phys. Solids*, Vol. 37, No. 6, pp. 717–733.

Warren, W. E., and Kraynik, A. M., 1991, "The Nonlinear Elastic Behavior of Open-Cell Foams," ASME JOURNAL OF APPLIED MECHANICS, Vol. 58, pp. 376–381.

APPENDIX

Coefficients in Eqs. (56)–(57):

$$c_1 = -4b^2\sigma_y(2b + 4bA - 4bB - 1),$$

$$c_2 = -8b^2\sigma_y(-4b^3\sigma_y - 8b^3\sigma_y A + 8b^3\sigma_y B + 3FL),$$

$$c_3 = 36b^2\sigma_y(1 + 2A - 2B),$$

$$c_4 = 24\sigma_y b(-24b^3\sigma_y A - 10b^3\sigma_y + 24b^3\sigma_y B + 3FL),$$

$$c_5 = -32b^3\sigma_y^2(-36b^3\sigma_y A - 14b^3\sigma_y + 36b^3\sigma_y B + 9FL),$$

$$A = \ln\left(-\frac{2b}{3}(-P + 4b^2\sigma_y)\right),$$

$$B = \ln(Pb - 4b^3\sigma_y + FL).$$

Coefficients in Eqs. (58)–(59):

$$d_1 = -2b(8b^2\sigma_y - 8b^2\sigma_y B + 8b^2\sigma_y C - 2b\sigma_y + D - A),$$

$$d_2 = 64b^5\sigma_y^2(C - B),$$

$$d_3 = -5A + 3\sqrt{D} - 72b^2\sigma_y B + 72b^2\sigma_y C + 108b^2\sigma_y,$$

$$d_4 = -4\sigma_y b^2(-144b^2\sigma_y B + 60b^2\sigma_y + 144b^2\sigma_y C - A),$$

$$d_5 = 4\sigma_y b(16b^5\sigma_y^2 + 288b^5\sigma_y^2 C - 288b^5\sigma_y^2 B + 16b^3A\sigma_y - 12b^3\sigma_y\sqrt{D} - 3\sqrt{D}FL),$$

$$A = \sqrt{(-P + 4b^2)^2},$$

$$B = \ln\left(\frac{1}{6b\sigma_y}(-P + 4b^2)^2\right),$$

$$C = \ln\left(\frac{2b}{3}(-P + 4b^2)\right),$$

$$D = -24FbL\sigma_y + 48b^4\sigma_y^2 - 3P^2.$$

Bernoulli Numbers and Rotational Kinematics

F. Pfister
IPG Automotive Engineering Software
+ Consulting GmbH
Postfach 210522,
D-76155 Karlsruhe, Germany

The representation of rotation operators in the form of infinite tensor power series, $\mathbf{R} = exp(\hat{\mathbf{\Psi}})$, has been found to be a valuable tool in multibody dynamics and nonlinear finite element analysis. This paper presents analogous formulations for the kinematic differential equations of the Euler-vector $\mathbf{\Psi}$ and elucidates their connection to Bernoulli-numbers. New power series such as the Bernoulli- and the Gibbs series are shown to provide compact expressions and a simple means for understanding and computing some of the fundamental formulae of rotational kinematics. The paper includes an extensive literature review, discussions of isogonal rotations, and a kinematic singularity measure.

1 Introduction and Overview

Through some two centuries the problem of describing the orientation of bodies in our three-dimensional world has facinated men. The names of some of the most distinguished savants, such as Euler, Monge, Gauss, Rodrigues, Hamilton, Jacobi, Klein, and Darboux appear in a historical development of the theory. Perhaps all of them were, as (Pars, 1965), "influenced as much by the intrinsic elegance of the theory [of finite rotations] as by its immediate relevance." A couple of decades ago the subject still seemed of interest to only a small group of mathematicians and mechanicians and Pars claimed that it "has been inadequately represented in some expositions."

There is certainly no reason to repeat Pars' words today. During the last decades wide areas of applications and an enormous number of papers applying rotational kinematics to the field of computational geometry, multibody dynamics, and finite element analysis appeared. Wertz (1980), Argyris (1982), Hiller (1985), Spring (1986), Shuster (1993), Schaub (1996), Géradin (1995), and others review the subject as it now stands.

Since Gibbs' time it is known that the *rotation tensor* $\mathbf{R}$ is expressible in form of an infinite tensor power series (ITPSs), $\mathbf{R} = \exp(\hat{\mathbf{\Psi}})$, the *exponential* of a skew-symmetric tensor $\hat{\mathbf{\Psi}}$; (Gibbs, 1884). It is rewarding and enlightening to extend the idea of ITPSs to the kinematic differential equations (KDEs) of the finite rotation vector $\mathbf{\Psi}$. Peres (1979), using Lie-algebra, obtained

$$\mathbf{\Omega} = \mathrm{coe}(\hat{\mathbf{\Psi}}) \cdot \dot{\mathbf{\Psi}}. \tag{1}$$

($\mathbf{\Omega}$: Angular velocity; $\dot{\mathbf{\Psi}}$: time derivative of $\mathbf{\Psi}$; $\mathrm{coe}(\hat{\mathbf{\Psi}})$ the *coexponential,* (Langner, 1997), of $\hat{\mathbf{\Psi}}$, see below.) Except, perhaps, for use in quantum mechanics, this result remained virtually unknown in kinematics. In most elementary and advanced texts on the subject, even the "scalar forms" of Eq. (1) remain unmentioned. One possible reason for this gap might be the often-cited paper of Stuelpnagel (1964), in which he applied involved arguments that eventually led him to rather complex expressions. Asserting that the derivation of his final result ". . . requires some lengthy computations, which are omitted," his exposé is not easy to follow and leaves the reader with the unjustified perception of the KDEs of $\mathbf{\Psi}$ as being clumsy and unattractive.

Sections 2 and 3 derive the fundamental formulae (rotation operator, KDEs) in terms of tensor and scalar power series, respectively. In an attempt to unify various results and to obtain computationally efficient formulations, new power series such as the Bernoulli and Gibbs series are defined, in which the rotation angle Ψ appears always quadratically. The results are derived using only elementary tensor algebra, not Lie algebra. By this, we hope to make them accessible to a broader class of readers. Section 4 discusses isogonal rotations and introduces a new singularity measure for parametrizations of $SO(3)$. Section 5 gives additional material such as composition formulae, historical remarks, and a literature review.

2 Tensor Power Series

2.1 Rotation Tensor. The theorem of Euler is without much question the most important single theorem in rotational kinematics. It states that a general displacement of a rigid body $\mathcal{B}$ for which a point O is fixed may be regarded as a rotation about an axis through O. Hence the displacement of $\mathcal{B}$ that relates the reference configuration $\mathcal{B}_0$ to a subsequent configuration $\mathcal{B}_1$ is determined by the finite rotation (or Euler) vector

$$\mathbf{\Psi} = \Psi \mathbf{n}, \tag{2}$$

where Ψ is the angle of rotation and the unit vector $\mathbf{n}$ points along the axis of rotation. The correspondence between rotations $\mathcal{R}$ and their representation $\mathbf{\Psi}$ is multivalued. Symbolically,

$$\mathcal{R} = \{\mathbf{\Psi} + n\mathbf{\Psi}_{id}\}, \tag{3}$$

with $\mathbf{\Psi}_{id}$ being $2\pi\mathbf{n}$ (the identity rotation) and n being any integer. We reduce the multiplicity of this correspondence by imposing upon $\mathbf{\Psi}$ the condition

$$\Psi \equiv \|\mathbf{\Psi}\| \equiv \sqrt{\mathbf{\Psi} \cdot \mathbf{\Psi}} \leq \pi. \tag{4}$$

Equation (4) shows that for any rotation, except for rotations on the sphere $\|\mathbf{\Psi}\| = \pi$, the map is one to one. For $\|\mathbf{\Psi}\| = \pi$ the vectors $\mathbf{\Psi}$ and $-\mathbf{\Psi}$ denote the same orientation. Treating, (pretty much as in elliptic geometry) every pair of diametrically opposite points on the sphere as one single point, we eliminate this multiplicity. In group theory this fact is expressed by saying that the rotation group $SO(3)$ is topologically equivalent to a ball of radius π with diametrically opposite points on the surface of the ball identified (Srinivasa, 1996, p. 290).

$\mathbf{\Psi}$ is a tensor of first order. It can be replaced by a skew-symmetric tensor of second-order $\hat{\mathbf{\Psi}}$ such that $\forall \mathbf{a}$:

Contributed by the Applied Mechanics Division of THE AMERICAN SOCIETY OF MECHANICAL ENGINEERS for publication in the ASME JOURNAL OF APPLIED MECHANICS.

Discussion on the paper should be addressed to the Technical Editor, Professor Lewis T. Wheeler, Department of Mechanical Engineering, University of Houston, Houston, TX 77204-4792, and will be accepted until four months after final publication of the paper itself in the ASME JOURNAL OF APPLIED MECHANICS.

Manuscript received by the ASME Applied Mechanics Division, June 6, 1997; final revision, Mar. 10, 1998. Associate Technical Editor: N. C. Perkins.

$$\hat{\mathbf{\Psi}}\cdot\mathbf{a} = \mathbf{\Psi}\times\mathbf{a}. \quad (5)$$

$((\times)$: cross product) $\hat{\mathbf{\Psi}}$ as we shall see, forms the backbone of the theory of finite rotations.

Now, let M_0 and M_1 be the initial and a subsequent position of some point $M\cdot \in \mathcal{B}$ which experiences the rotation (2). The mapping $M_0 \to M_1$ can be represented by a unimodular, proper orthogonal tensor $\mathbf{R}$, called the rotation tensor or rotation operator:

$$\overline{OM}_1 = \mathbf{R}\cdot\overline{OM}_0. \quad (6)$$

Since both $\mathbf{R}$ and $\mathbf{\Psi}$ describe rotations, $\mathbf{R}$ must be expressible in terms of $\mathbf{\Psi}$ and vice versa. This relationship consists of carrying the rotation operator in its exponential form (Gibbs, 1884):

$$\mathbf{R} = \exp(\hat{\mathbf{\Psi}}). \quad (7)$$

The exponential has an inverse, the logarithm. Consequently, the inverse mapping of (7), if it exists (see below), is (Gibbs, 1884)

$$\hat{\mathbf{\Psi}} = \ln(\mathbf{R}). \quad (8)$$

The above tensor power series are

$$\exp(\hat{\mathbf{\Psi}}) \equiv \mathbf{1} + \frac{(\hat{\mathbf{\Psi}})^1}{1!} + \frac{(\hat{\mathbf{\Psi}})^2}{2!} + \ldots \equiv \sum_{\nu=0}^{\infty}\frac{(\hat{\mathbf{\Psi}})^\nu}{\nu!}, \quad (9)$$

$$\ln(\mathbf{R}) \equiv -\frac{(\mathbf{1}-(\mathbf{R}))^1}{1} - \frac{(\mathbf{1}-(\mathbf{R}))^2}{2} - \ldots$$
$$\equiv -\sum_{\nu=1}^{\infty}\frac{(\mathbf{1}-(\mathbf{R}))^\nu}{\nu}, \quad (10)$$

where $\mathbf{1}$ is the unit operator. Additionally, one has

$$\exp(\mathbf{T}\hat{\mathbf{\Psi}}\mathbf{T}^{-1}) = \mathbf{T}\exp(\hat{\mathbf{\Psi}})\mathbf{T}^{-1} \quad \text{and} \quad (11)$$

$$\ln(\mathbf{T}\mathbf{R}\mathbf{T}^{-1}) = \mathbf{T}\ln(\mathbf{R})\mathbf{T}^{-1}, \quad (12)$$

where $\mathbf{T}$ is an arbitrary nonsingular tensor and $\mathbf{T}^{-1}$ is its inverse.

Hensel (1926) first showed, and it is now well known that a power series of some tensor $\mathbf{T}$ converges if and only if every proper number of $\mathbf{T}$ lies inside or on the circle of convergence of the corresponding scalar series. The proper numbers of $\mathbf{R}$ are $\{1, \exp(i\Psi), \exp(-i\Psi)\}$ and the radius convergence of ln x in the scalar x is $-1 < x \le 1$. As a consequence, (8) becomes singular for $\|\mathbf{\Psi}\| = \pi$, thereby nicely reflecting the abovementioned fact that oppositely directed rotations with $\|\mathbf{\Psi}\| = \pi$ are indistinguishable. Hence, in this case, $\mathbf{R}$ does not determine $\mathbf{\Psi}$ uniquely. Equation (7), however, is convergent for all finite $\mathbf{\Psi}$.

An alternative formulation of (7) is (Argyris, 1982)

$$\exp(\hat{\mathbf{\Psi}}) = \mathbf{1} + \frac{\sin\Psi}{\Psi}\hat{\mathbf{\Psi}} + \frac{1}{2}\frac{\sin^2(\Psi/2)}{(\Psi/2)^2}\hat{\mathbf{\Psi}}^2. \quad (13)$$

Such kinds of scalar power series are the subject of Section 3.

The review of familiar ideas and equations given in this subsection should provide sufficient background and motivation for obtaining similar results for kinematic differential equations (KDEs).

2.2 Kinematic Differential Equations. We denote by $(\bullet)$ a scalar, a second-order tensor, or an element of any other algebra which is representable by square matrices of finite order.

The following power series are sufficiently important to warrant a special and easily recognizable name.

- Coexponential Series:

$$\text{coe}(\bullet) := 1 + \frac{(\bullet)^1}{2!} + \frac{(\bullet)^2}{3!} + \frac{(\bullet)^3}{4!} + \ldots$$
$$\equiv \sum_{\nu=0}^{\infty}\frac{(\bullet)^\nu}{(\nu+1)!}. \quad (14)$$

$\text{coe}(x)$, $x \in \mathbb{R}$, converges for all finite x.

- Bernoulli Series:

$$\text{Ber}(\bullet) := \frac{B_1}{2!}(\bullet) + \frac{B_2}{4!}(\bullet)^2 + \frac{B_3}{6!}(\bullet)^3 + \ldots$$
$$\equiv \sum_{\nu=1}^{\infty}\frac{B_\nu}{(2\nu)!}(\bullet)^\nu. \quad (15)$$

The scalar constants $\{B_\nu\}$, $\nu = 1, 2, 3 \ldots$ are the Bernoulli numbers. They have been introduced by J. Bernoulli, (Bernoulli, 1713), and have a long and interesting bibliography in and of itself (Dilcher, 1991). In our notation, which follows (Saalschütz, 1893) and (Whittaker, 1958), the B_i's are generated by the expansion of

$$\text{Ber}(x^2) \equiv 1 - \frac{x}{2}\cot\left(\frac{x}{2}\right), \quad x \in \mathbb{R}. \quad (16)$$

From (16) it is easily verified that Ber (x) converges if and only if $\|x\| < 4\pi^2$. From Hensel's theorem a generalization to tensor series follows easily. The reader should note that we write Ber (x), not ber (x), because it is customary to use ber (x) for $\Sigma_{\nu=0}^{\infty}(-1)^\nu(\frac{1}{2}x)^{4\nu})/((2n)!)^2$; see, e.g., Watson (1958).

The following relationships can be verified by consulting Bromwich (1955), Abramowitz (1964), or any other handbook of mathematical functions:

$$\exp(\bullet) - \mathbf{1} = (\bullet)\cdot\text{coe}(\bullet), \quad (17)$$

$$\text{Ber}(-(\bullet)^2) = 1 - \frac{(\bullet)}{2}\coth\left(\frac{(\bullet)}{2}\right) \quad (18)$$

$$\text{coe}(\bullet)\cdot(\mathbf{1} - \tfrac{1}{2}(\bullet) - \text{Ber}(-(\bullet)^2)) = \mathbf{1}. \quad (19)$$

Equation (19) shows that $(\mathbf{1} - \frac{1}{2}(\bullet) - \text{Ber}(-(\bullet)^2)$ is the inverse of coe $(\bullet)$.

If $\mathcal{B}$ is in smooth motion, it is, with respect to $\mathcal{B}_0$, endowed with a unique angular velocity $\mathbf{\Omega}$. $\dot{\mathbf{\Psi}}$, being the time rate of change of $\mathbf{\Psi}$ as observed from $\mathcal{B}_0$, we have the following.

Lemma 1: $\sigma := \mathbf{\Omega} - \dot{\mathbf{\Psi}}$, the so-called noncommutativity rate vector (Bortz, 1971), is perpendicular to $\mathbf{\Psi}$:

$$\mathbf{\Psi}\cdot\mathbf{\Omega} = \mathbf{\Psi}\cdot\dot{\mathbf{\Psi}}. \quad (20)$$

Proof: Our plan is (we modify slightly the demonstration first given by Nazaroff (1979)) to equalize $A := (d/dt)(\text{tr}\,\mathbf{R})$ and $B := \text{tr}\,(d\mathbf{R}/dt)$; tr $(\cdot)$ is the trace of the tensor argument $(\cdot)$.

First, because the sum of the proper values of $\mathbf{R}$ being $1 + 2\cos\Psi$ (or from the canonical form of $\mathbf{R}$), we have $\text{tr}(\mathbf{R}) = 1 + 2\cos\Psi$ and hence $A = -2\dot{\Psi}\sin\Psi$.

Next, on applying Poisson's differential equation $(d/dt)\mathbf{R} = \hat{\mathbf{\Omega}}\cdot\mathbf{R}$ and the trace operation to (13) we find $B = (\sin\Psi/\Psi)\,\text{tr}\,(\hat{\mathbf{\Omega}}\cdot\hat{\mathbf{\Psi}})$. This is clear from the fact that for any symmetric tensor $\mathbf{S}$ (such as $\mathbf{1}$ and $\hat{\mathbf{\Psi}}^2$ in (13)) $\text{tr}\,(\hat{\mathbf{\Omega}}\cdot\mathbf{S}) = 0$ because $\hat{\mathbf{\Omega}}$ is skew-symmetric. Then, using the fact that the tensors $\hat{\mathbf{\Psi}}$ and $\mathbf{\Omega}$ are both skew-symmetric, we get $\text{tr}\,(\hat{\mathbf{\Omega}}\cdot\hat{\mathbf{\Psi}}) = -2\mathbf{\Omega}\cdot\mathbf{\Psi}$ and therefore $B = -2\sin\Psi/\Psi\mathbf{\Omega}\cdot\mathbf{\Psi}$.

Finally $A = B$ gives $\Psi\dot{\Psi} = \mathbf{\Omega}\cdot\mathbf{\Psi}$. Now $\Psi\dot{\Psi} = \mathbf{\Psi}\cdot\dot{\mathbf{\Psi}}$, from which follows Lemma 1. □

Theorem 1: The kinematic differential equations of $\dot{\boldsymbol{\Psi}}$ are the equations which relate $\dot{\boldsymbol{\Psi}}$ to $\boldsymbol{\Omega}$. We have

$$\boldsymbol{\Omega} = \mathrm{coe}\,(\hat{\boldsymbol{\Psi}})\cdot\dot{\boldsymbol{\Psi}}, \tag{21}$$

$$\dot{\boldsymbol{\Psi}} = (\mathbf{1} - \tfrac{1}{2}\hat{\boldsymbol{\Psi}} - \mathrm{Ber}\,(-\hat{\boldsymbol{\Psi}}^2)\cdot\boldsymbol{\Omega}. \tag{22}$$

$\mathrm{coe}\,(\hat{\boldsymbol{\Psi}})$ *is convergent for every finite* $\boldsymbol{\Psi}$. $\mathrm{Ber}\,(-\hat{\boldsymbol{\Psi}}^2)$ *converges for all* Ψ *with* $\|\boldsymbol{\Psi}\| < 2\pi$.

Proof. $\boldsymbol{\Psi}$ is an eigenvector of $\mathbf{R}$. Therefore, observers fixed in $\mathcal{B}_0$ and $\mathcal{B}_1$ measure the same time rate of change of $\boldsymbol{\Psi}$:

$$\mathring{\boldsymbol{\Psi}} = \mathbf{R}\cdot\dot{\boldsymbol{\Psi}}. \tag{23}$$

The circle ($\circ$) stands for time derivatives as observed from $\mathcal{B}_1$. Equation (23) holds for any vector $\mathbf{a}(t)$, which $\forall t$ is an eigenvector of $\mathbf{R}(t)$. If one gets confused about (23), the best plan is to resolve $\mathring{\boldsymbol{\Psi}}$ in $\mathcal{B}_1$ and $\dot{\boldsymbol{\Psi}}$ in $\mathcal{B}_0$ and then to interpret $\mathbf{R}$ as a coordinate transformation rather than a rotation operator.

Substituting (23) into the formula of the moving base, $\dot{\boldsymbol{\Psi}} = \boldsymbol{\Omega}\times\boldsymbol{\Psi} + \mathring{\boldsymbol{\Psi}}$, allows us to eliminate $\mathring{\boldsymbol{\Psi}}$ and to obtain a linear relationship between $\boldsymbol{\Omega}$ and $\dot{\boldsymbol{\Psi}}$:

$$\hat{\boldsymbol{\Psi}}\cdot\boldsymbol{\Omega} = \mathbf{R}\cdot\dot{\boldsymbol{\Psi}} - \mathbf{1}\cdot\dot{\boldsymbol{\Psi}}. \tag{24}$$

Thus we read from (17) the equivalence

$$\hat{\boldsymbol{\Psi}}\cdot\boldsymbol{\Omega} = \hat{\boldsymbol{\Psi}}\cdot\mathrm{coe}\,(\hat{\boldsymbol{\Psi}})\cdot\dot{\boldsymbol{\Psi}}. \tag{25}$$

As easily verified,

$$\boldsymbol{\Omega} = \mathrm{coe}\,(\hat{\boldsymbol{\Psi}})\cdot\dot{\boldsymbol{\Psi}} + \dot{\alpha}\boldsymbol{\Psi} \tag{26}$$

satisfies (25) for arbitrary values of the scalar variable $\dot{\alpha}$. Since $\boldsymbol{\Psi}$ spans the nullspace of $\hat{\boldsymbol{\Psi}}$, (26) is the general solution of (25).

Note that $\boldsymbol{\Psi}$ is an eigenvector of $\mathrm{coe}\,(\hat{\boldsymbol{\Psi}})$. Scalar multiplication of (26) with $\boldsymbol{\Psi}$ leads to $\boldsymbol{\Psi}\cdot\boldsymbol{\Omega} = \boldsymbol{\Psi}\cdot\dot{\boldsymbol{\Psi}} + \dot{\alpha}\Psi^2$. Applying Lemma 1 we find that

$$\dot{\alpha} = 0. \tag{27}$$

This completes the proof of (21).

Thanks to (19) and Hensel's theorem, (22) should come as no surprise. The proper values of $\hat{\boldsymbol{\Psi}}$ are $\{0, \exp(i\Psi), \exp(-i\Psi)\}$. Equation (22) therefore converges for all $\|\boldsymbol{\Psi}\| < 2\pi$. $\square$

Equations (7), (21), and (22) uniquely determine three of the fundamental tensors involved in rotational kinematics in terms of their vector invariant $\boldsymbol{\Psi}$. The formal anology between $\exp(\hat{\boldsymbol{\Psi}})$ and $\mathrm{coe}\,(\hat{\boldsymbol{\Psi}})$ contains a certain elegance. A development of higher-order time derivatives (angular acceleration, jerk, . . .) in terms of ITPSs would perhaps show that it results from some as yet undiscovered even more general rule.

3 Scalar Power Series

This section presents formulations for $\mathbf{R}$ and the KDEs (21), (22) in terms of scalar power series. Scalar series are less elegant and lengthen and complicate the formulae in which they appear, but they give additional insight and eventually simplify computational problems.

The reader is presumed familiar (see, e.g., Argyris (1982)) with the following crucial identities that transform tensor power series into scalar power series:

$$\hat{\boldsymbol{\Psi}}^{2\nu-1} \equiv (-1)^{\nu-1}\Psi^{2(\nu-1)}\hat{\boldsymbol{\Psi}} \quad \text{and}$$
$$\hat{\boldsymbol{\Psi}}^{2\nu} \equiv (-1)^{\nu-1}\Psi^{2(\nu-1)}\hat{\boldsymbol{\Psi}}^2. \tag{28}$$

Rotation Tensor. By the aid of (28), we may express Gibbs' formulation (6) in the form

$$\begin{aligned}\overline{OM}_1 &= (\mathbf{1} + \mathrm{gib}_1(\Psi^2)\hat{\boldsymbol{\Psi}} + \mathrm{gib}_2(\Psi^2)\hat{\boldsymbol{\Psi}}^2)\cdot\overline{OM}_0,\\ &= \mathrm{gib}_0(\Psi^2)\overline{OM}_0 + \mathrm{gib}_1(\Psi^2)\boldsymbol{\Psi}\\ &\qquad\times\overline{OM}_0 + \mathrm{gib}_2(\Psi^2)(\boldsymbol{\Psi}\cdot\overline{OM}_0)\boldsymbol{\Psi}\end{aligned} \tag{29}$$

or

$$\mathbf{R} \equiv \mathbf{1} + \underline{\mathrm{gib}_1}(\underline{\Psi}^2)\hat{\boldsymbol{\Psi}} + \underline{\mathrm{gib}_2}(\underline{\Psi}^2)\hat{\boldsymbol{\Psi}}^2, \tag{30}$$

where

$$\mathrm{gib}_i(\bullet) := \sum_{\nu=0}^{\infty}\frac{(-1)^\nu(\bullet)^\nu}{(2\nu+i)!}, \quad i = 1, 2, 3\ldots. \tag{31}$$

We call these functions Gibbs' series of type i, without any certainty that we have settled on this name permanently.

One could have written, as it is usually (see, e.g., (13)) done, $\mathrm{gib}_0(\Psi^2) = \cos(\Psi)$, $\mathrm{gib}_1(\Psi^2) = \sin\Psi/\Psi$ and $\mathrm{gib}_2(\Psi^2) = [\sin^2(\Psi/2)]/[(\Psi/2)^2] = (1 - \cos(\Psi))/\Psi^2$. Our reasons for preferring the present course are two: (i) it is formally much simpler, and (ii)—and this is important—it shows that (29) depends on $\Psi^2 = \boldsymbol{\Psi}\cdot\boldsymbol{\Psi}$ only, and not on Ψ as such. Evaluation of $\mathrm{gib}_i(\Psi^2)$ allows to overcome the drawback of superflous and computationally expensive root calculations like $\Psi = +\sqrt{\boldsymbol{\Psi}\cdot\boldsymbol{\Psi}}$. This fact, it seems, has not previously been realized.

Kinematic Differential Equation. By (28) and (14), (21):

$$\boldsymbol{\Omega} = (\mathbf{1} + \mathrm{gib}_2(\Psi^2)\hat{\boldsymbol{\Psi}} + \mathrm{gib}_3(\Psi^2)\hat{\boldsymbol{\Psi}}^2)\cdot\dot{\boldsymbol{\Psi}} \tag{32}$$

$$= \mathrm{gib}_1(\Psi^2)\dot{\boldsymbol{\Psi}} + \mathrm{gib}_2(\Psi^2)\boldsymbol{\Psi}\times\dot{\boldsymbol{\Psi}} + \mathrm{gib}_3(\Psi^2)(\boldsymbol{\Psi}\cdot\dot{\boldsymbol{\Psi}})\boldsymbol{\Psi}, \tag{33}$$

or

$$\mathrm{coe}\,(\hat{\boldsymbol{\Psi}}) \equiv \mathbf{1} + \mathrm{gib}_2(\Psi^2)\hat{\boldsymbol{\Psi}} + \mathrm{gib}_3(\Psi^2)\hat{\boldsymbol{\Psi}}^2. \tag{34}$$

Equations (32)–(34) show—and here again comes the punchline—the dependence of the scalar KDEs on Ψ^2 only and not on Ψ itself.

Inverse Kinematic Differential Equation. From (28), (31), and (22) we get

$$\dot{\boldsymbol{\Psi}} = \left(\mathbf{1} - \frac{1}{2}\hat{\boldsymbol{\Psi}} - \frac{\mathrm{Ber}\,(\Psi^2)}{\Psi^2}\hat{\boldsymbol{\Psi}}^2\right)\cdot\boldsymbol{\Omega}, \tag{35}$$

$$= (1 - \mathrm{Ber}\,(\Psi^2))\boldsymbol{\Omega} - \tfrac{1}{2}\boldsymbol{\Psi}\times\boldsymbol{\Omega} - \frac{\mathrm{Ber}\,(\Psi^2)}{\Psi^2}(\boldsymbol{\Psi}\cdot\boldsymbol{\Omega})\boldsymbol{\Psi}, \tag{36}$$

or

$$\mathrm{Ber}\,(-\hat{\boldsymbol{\Psi}}^2) \equiv \frac{\mathrm{Ber}\,(\Psi^2)}{\Psi^2}\hat{\boldsymbol{\Psi}}^2. \tag{37}$$

4 Further Considerations

4.1 Isogonal Rotations. There are two major families of rotations, isoaxial rotations and isogonal rotations, defined by special conditions we place on $\boldsymbol{\Psi}$:

Isoaxial rotations are the family of rotations where only the amount of rotation, but not the direction changes; $\{\boldsymbol{\Psi} = \Psi\mathbf{n}\,|\,\mathbf{n} = \text{const}\}$. They form a one parameter subgroup of $SO(3)$ which is elementary, but nevertheless of fundamental importance.

Conversely we shall say that isogonal rotations are the family of rotations where only the direction changes but not the amount: $\{\boldsymbol{\Psi} = \Psi\mathbf{n} \mid \Psi = \text{const}\}$. Isogonal rotations do *not* form a subgroup of $SO(3)$.

An interesting aspect of isogonal motions follows from Lemma 1. For these motions $\boldsymbol{\Psi}\cdot\boldsymbol{\Omega} = 0$, since (by definition) $\boldsymbol{\Psi}\cdot\dot{\boldsymbol{\Psi}} = 0$. That is: *whatever the isogonal motion, $\boldsymbol{\Psi}$ is perpendicular to a plane Π whose spanning vectors are $\dot{\boldsymbol{\Psi}}$ and $\boldsymbol{\Omega}$.*

Now, let us define three vectors $\mathbf{n}_1 = \boldsymbol{\Psi}/\|\boldsymbol{\Psi}\|$, $\mathbf{n}_2 = \dot{\boldsymbol{\Psi}}/\|\dot{\boldsymbol{\Psi}}\|$, $\mathbf{n}_3 = \boldsymbol{\Omega}/\|\boldsymbol{\Omega}\|$, and two scalars $\dot{\Psi} = \|\dot{\boldsymbol{\Psi}}\|$ and $\Omega = \|\boldsymbol{\Omega}\|$. Clearly, the quadratic form

$$N(\Psi) \equiv \left(\frac{\boldsymbol{\Omega}\cdot\dot{\boldsymbol{\Psi}}}{\dot{\Psi}^2}\right) = \mathbf{n}_2\cdot\operatorname{coe}(\hat{\boldsymbol{\Psi}})\cdot\mathbf{n}_2 = \frac{\sin\Psi}{\Psi} \tag{38}$$

as well as

$$D(\Psi) \equiv \frac{\|\dot{\boldsymbol{\Psi}}\|\|\boldsymbol{\Omega}\|}{\dot{\Psi}^2} = \frac{\Omega\dot{\Psi}}{\dot{\Psi}^2} = \|\operatorname{coe}(\hat{\boldsymbol{\Psi}})\cdot\mathbf{n}_2\| = \frac{\sqrt{2(1-\cos\Psi)}}{\Psi} \tag{39}$$

are functions of Ψ only and therefore constant if the motion is isogonal. When α represents the angle between $\dot{\boldsymbol{\Psi}}$ and $\boldsymbol{\Omega}$:

$$\cos\alpha = \frac{\boldsymbol{\Omega}\cdot\dot{\boldsymbol{\Psi}}}{\|\dot{\boldsymbol{\Psi}}\|\|\boldsymbol{\Omega}\|} = \frac{N(\Psi)}{D(\Psi)} = \frac{\sin\Psi}{\sqrt{2(1-\cos\Psi)}} = \cos\left(\frac{\Psi}{2}\right) \text{ or} \tag{40}$$

$$\alpha = \frac{\Psi}{2}. \tag{41}$$

Collecting the above into words we may conclude with the following.

Theorem 2. If the motion is isogonal, the trihedral $F := \{O, \mathbf{n}_1, \mathbf{n}_2, \mathbf{n}_3\}$ *is rigid. It is* $\mathbf{n}_1 \perp \mathbf{n}_2$, $\mathbf{n}_1 \perp \mathbf{n}_3$ *and* $\alpha \equiv \angle(\mathbf{n}_2, \mathbf{n}_3) = \Psi/2$.

4.2 Singularities. Writers on finite rotations sometimes find it interesting to state that "no 3-dimensional parametrization can be both global and nonsingular." Apart from the fact of its being true we are unable to find reasons for ascribing much practical relevance to this statement. These singularities are situated at $\Psi = 2\pi$ and therefore (far) outside configuration space!

In order to make this point a little clearer, let us define a new dimensionless quantity:

$$\beta(P_i) = \frac{V_{cs}(P_i)}{V_{ns}(P_i)}. \tag{42}$$

$\beta(P_i)$ is called kinematic singularity measure for the parameterization P_i of $SO(3)$. Equation (42) applies to parameterizations of $SO(3)$, which are expressible as $f_i(\Psi)\mathbf{n}$, where $f_i(\Psi)$ is some scalar function in Ψ and $\mathbf{n}$ is, as previously, the unit vector of the rotation axis. (Generalizations to other three-dimensional parameterizations (Euler angles, etc.) are obvious. They are not discussed here.)

$V_{cs}(P_i)$ and $V_{ns}(P_i)$ is explained and the use of $\beta(P_i)$ is illustrated by considering three examples:

1 P_1: the Euler vector: $\Psi\mathbf{n}$,
2 P_2: the Rodrigues vector (Gibbs vector): $\tan(\Psi/2)\mathbf{n}$, and
3 P_3: the (not so well-known) Wiener vector: $\tan(\Psi/4)\mathbf{n}$; Wiener (1962), Milenkovic (1982), McPhee (1991), Schaub (1996), and the literature cited there.

$V_{cs}(P_i)$ is the volume of the configuration space of P_i. For the rotation group, as discussed in Section 2.1, $V_{cs}(P_i)$ is equivalent to the volume of a ball of radius π: $V_{cs}(P_i) = \frac{4}{3}\pi\pi^3\ \forall i \in \{1, 2, 3\}$.

$V_{ns}(P_i)$ is the volume of the ball in which the KDEs are nonsingular. To be more precise, the radius of this ball is $\Psi_{\text{sing}}(P_i)$, this being the smallest positive value of Ψ where singularities of the (inverse) KDEs occur:

1 $V_{cs}(P_1) = \frac{4}{3}\pi(2\pi)^3$, see above,
2 $V_{cs}(P_2) = \frac{4}{3}\pi\pi^3$, see any textbook on this subject, and
3 $V_{cs}(P_3) = \frac{4}{3}\pi(2\pi)^3$ see, e.g., Schaub (1996).

It is now seen that

$$1 = \beta(P_2) > \beta(P_3) = \beta(P_1) = 0.125 > 0. \tag{43}$$

Conclusion:

- P_1 as well as P_3 are examples of globally defined nonsingular parameterizations of $SO(3)$.
- No other well-known set of parameters P_x possess a smaller $\beta(P_x)$ than the Euler vector or the Wiener vector.

Remark: The problem of "globally nonsingular" attitude description (and related additional results) has been recently addressed in Pfister (1995), Schaub (1995), and Tsiotras (1997). Reference may also be made to Schaub (1996) who constructed an interpretation of the Rodrigues and Wiener vector as special cases of a whole family of stereographic parameters derived from Euler parameters (unit quaternions) by stereographic projection and derived related additional results. These parameters have a singularity measure anywhere between 1 and 0.125.

5 Remarks in Passing

This paper does not attempt to discuss the relative advantages of the various ways to represent finite rotations. A large literature on this subject exists; references have been given in the Introduction. As a rule, those most desirous of generality are least successful in grasping the pecularities afforded by a special case. Contentions that claim that some set of parameters is better than all others are futile. In view of the fundamental importance of the exponential form in great many applications, with $\hat{\boldsymbol{\Psi}}$ as the natural variable and because of $\hat{\boldsymbol{\Psi}}$'s geometrically vivid and physically meaningfull sense, we regard these parameters as fundamental.

Composition Formula. For some problems it is of interest to determine the Euler vector $\boldsymbol{\Psi}_3$ of a combined rotation in terms of two individual rotations $\boldsymbol{\Psi}_1$ and $\boldsymbol{\Psi}_2$.

In exponential form

$$\exp(\hat{\boldsymbol{\Psi}}_3(\hat{\boldsymbol{\Psi}}_1, \hat{\boldsymbol{\Psi}}_2)) = \exp(\hat{\boldsymbol{\Psi}}_2)\cdot\exp(\hat{\boldsymbol{\Psi}}_1). \tag{44}$$

From the composite rotation formula of Rodrigues (see, e.g., Gibbs (1884)) or from the Baker-Campbell-Hausdorff (BHC) formula for the rotation group we obtain in an abridged notation in which $c_i = \cos(\Psi_i/2)$ and $s_i = \sin(\Psi_i/2)/\Psi_i$:

$$\Psi_3 = 2\arcsin(c_1c_2 - s_1s_2\boldsymbol{\Psi}_1\cdot\boldsymbol{\Psi}_2) \tag{45}$$

and

$$\boldsymbol{\Psi}_3 = \frac{\Psi^3}{c_3}(s_1c_2\boldsymbol{\Psi}_1 + s_2c_1\boldsymbol{\Psi}_2 + s_1s_2\boldsymbol{\Psi}_2\times\boldsymbol{\Psi}_1). \tag{46}$$

Baker-Campbell-Hausdorff (BHC) formulas give the product of exponentials in terms of one single exponential: $\exp(C(A, B)) = \exp(A)\exp(B)$, where A and B are generators of the Lie-group in question. This, as well as the derivation of $\boldsymbol{\Psi}_3 = \boldsymbol{\Psi}_3(\boldsymbol{\Psi}_1, \boldsymbol{\Psi}_2)$ from Pauli matrices, are quite standard in quantum mechanics (Santiago, 1976; Harter, 1978), in engineering mechanics, however, these ideas only received little attention until now, an exception is Tsiotras (1993).

Readers interested in noncommutative solutions of $\exp(X)\exp(Y) = \exp(X + Y)$, where X and Y are matrices, may consult Rinehart (1959) and the literature cited there.

Historical Perspective, Literature Review.

Rotation Tensor: Gibbs, as it seems, first realized the importance of the tensor formulae (7) and (8). In the pioneer work (Gibbs, 1884) he created what is essentially our modern symbolism of vector algebra and analysis (Crowe, 1994). So, interesting enough, (7) and (8) (see Gibbs' Chapter V) are as old as the vector calculus itself. Among other (early) authors who followed Gibbs we cite Spielrein (1926) and Hamel, who found important enough to mention it in his *Foundations of Mechanics;* (Hamel, 1909). It has to be noted that (Wilson's, (1901)) influential book (subtitled *Founded upon the Lectures of J. Willard Gibbs*) does *not* mention (7), (8) or other transcendental functions of tensors. This remark is relevant because it was Wilson who first popularized Gibbs' ideas on vector algebra and analysis. Gibbs' connection with the exponential form of **R** disappeared from mechanicians' collective conciousness, otherwise one would certainly find it mentioned in the comprehensive surveys compiled in the last two decades. For much detailed information on the relationships between Cayley transforms, proper orthogonal matrices, and matrix exponentials the reader is referred to (Tsiotras, 1997).

Kinematic Differential Equations: There is no classical treatise on rational kinematics, dynamics or differential geometry which presents the kinematic differential equation of the Euler vector. As a consequence they have never been taught and remained unknown to most kinematicians working in this field. This gap is serious, reasons to explain it are difficult to find; one possible reason has been mentioned in the Introduction.

In aerospace dynamics the Euler vector became somewhat popular with the work of Bortz (1971). He derived, if rather obscurely, an equation equivalent to (32). Nazaroff (1979) replaced Bortz' analysis by a short and elegant demonstration. An alternative approach is due to Pfister (1996). Perhaps the earliest recorded statement of an equation equivalent to (32) is (Laning, 1949). We have been unable to see this work, it is included in Bortz' bibliography. Apparently Laning did not think of his development as a contribution original enough to warrant publication; his notes were circulated among only a limited number of people.

An excellent review that contains Eq. (32) has recently been published by Shuster (1993). In this study (and in most others) the focus is on scalar power series. What remains largely undiscussed in the realm of rational kinematics are tensor power series formulations like (21) and (22).

Peres (1979), working in the field of quantum mechanics, first derived a formula which is essentially our (21) and which therefore may well be named the Peres formula. Never, to the best of our knowledge, has an engineer referred to Peres work. A more elaborate but equivalent derivation of (21) is to be found in Sudarshan (1974), who does not mention previous work. This reference seems to be the only book containing (21). Both Peres and Sudarshan use mathematical concepts that are involved and somewhat sophisticated, namely Lie algebra. In this article it was shown how ordinary tensor algebra can be used to obtain the same results.

Neither Peres nor Sudarshan derived the inverse KDEs. Also, they did not introduce coexponential, Gibbs or Bernoulli series. These series provide compact expressions and an efficient means for computing some of the fundamental relationships of the rotation vector. The resulting formulae are easy to memorize. These series are certainly useful in their own right.

Langner (1997) originated the term coexponential series. The term Bernoulli series goes back to Hill (1857) or earlier. A somewhat different definition to ours was given by Langner (1997).

6 Conclusion

In modern mechanics, as in any other scientific research today, we find two tendencies present: on the one hand, the tendency which seeks to crystallize the structure inherent in the material that is studied and on the other hand, the tendency toward computational efficient algorithms. These two tendencies are, of course, interrelated closely and quite often unexpectedly.

This paper tries to contribute to the first rather than to the second. We aimed at understanding the mathematical structure of the kinematic differential equations of the Euler vector $\mathbf{\Psi}$. This vector definitively is "the stuff" of which rotational kinematics is made. As a conclusion of the literature review at the end of the preceding section one may say: Our approach is not completely new, but it is new in the way equations are derived and results are presented. Most of the more or less known results have been scattered in areas as diverse as quantum, space, and continuum mechanics and have been collected here for the first time, together with a multitude of detailed citations.

One further point concerning computational efficiency is worth noting in conclusion: Transcendental functions such as sin (x) or cos (x) are so ingrained in our daily repetition that we are easily led to regard them as a "primitive," more "beautiful," or more natural concept and then to look at other, "unorthodox," transcendental functions like $\text{gib}_i(x)$ in (29) or Ber (x) in (35) as a "defined" and, by consequence, "extravagant," inattractive and/or computational expensive one. None of these functions, however, is anything more than a power series. Indeed, for some formulations in kinematics it is artificial and unnecessary to introduce sin (x) or cos (x), because Ber (x) and coe (x), etc., are sufficient. The development of computational efficient algorithms in kinematics therefore calls for the development of compilers (or, even better, hardware implementations) that without "detour" evaluate these series.

Our last remark is a couple of questions that seem to be nontrivial and unanswered. They arise from the definition of $\beta(P_i)$, the kinematic singularity measure. Is there a "natural" lower bound $\beta_{\min} > 0$ for this measure? If yes, What is the three-system of parameters that corresponds to this bound? If no, What is (are) the limit process(es) that allow one to obtain $\beta_{\min} \to 0$? As we feel it (without being able to prove it), $\beta = \frac{1}{8}$ might be the lower bound.

Acknowledgments

The author is indebted to Drs. K. Wohlhart (University of Graz, Austria) and J. G. Papastavridis (Georgia Institute of Technology, U.S.A.) for bringing his attention to the works of Peres and Sudarshan and Mukunda. He is extremely grateful for comments received from Dr. R. Langner (University of Karlsruhe, Germany) without which this paper would have been substantially poorer. He also acknowledges with appreciation discussions with Drs. M. Fayet (INSA de Lyon, France) and S. K. Agrawal (University of Delaware, U.S.A.). He owes thanks for the financial support of the Alexander von Humboldt Foundation, who made it possible for him to work in Delaware. The author will be grateful to readers who make him aware of other work, especially other parametrization of $SO(3)$ (not contained in the cited literature) and early literature containing $\exp(\hat{\mathbf{\Psi}})$ or $\text{coe}(\hat{\mathbf{\Psi}})$.

References

Abramowitz, M., and Stegun, I. A., eds., 1964, *Handbook of Mathematical Functions*, Applied Mathematics Series, Vol. 55, U.S. Department of Commerce, National Bureau of Standards, Washington, DC.

Argyris, J., 1982, "An excursion into large rotations," *Computer Methods in Applied Mechanics and Engineering,* Vol. 32, pp. 85–155.

Bernoulli, J., 1713, *Ars conjectandi, opus posthum. Accedit Tractatus de seriebus Infinitis, et epistola Gallicè scripta de Ludo Pilae recticularis,* Basel (Reprint: *Culture et Civilisation* 1968, Bruxelles).

Bortz, J. E., 1971, "A new Mathematical Formulation for Strapdown Inertial Navigation," *IEEE Trans. Aerospace Electronic Systems,* Vol. AES-7, No. 1, pp. 61–66.

Bromwich, T. J. I'a, 1955, *An Introduction to the Theory of Infinite Series,* 2nd ed., Macmillan London.

Crowe, M. J., 1994, *A History of Vector Calculus,* Dover, New York (unabriged and corrected republication of a work originally published in 1967 by Notre Dame Press).

Dilcher, K., et al., 1991, *Bernoulli Numbers Bibliography (1713–1990),* Queen's University, Kingston, Ontario, Queen's Papers in Pure and Applied Mathematics, Vol. 87.

Gibbs, J. W., 1984, *Elements of Vector Analysis,* New Haven, CT, privately printed. pp. 1–36, 1881; pp. 37–83, 1884 (reprint in *The collected Works of J. Willard Gibbs,* Vol. 2, Part 2, Longmans, Green and Co., New York, 1928).

Harter, W. G., and Dos Santos, N., 1978, "Double-group theory on the half-shell and the two-level system. I. Rotation and half-integral spin states," *American Journal of Physics,* Vol. 46, No. 3, pp. 251–263.

Géradin, M., and Rixen, D., 1995, "Parametrization of Finite Rotations in Computational Dynamics, A Review," *Revue Europénne des Eléments Finis (Numéro spécial: Rotations Finies en Mécanique des Solides et des Structures),* Vol. 4, No. 5–6, pp. 497–553.

Hamel, G., 1909, "Über die Grundlagen der Mechanik," *Mathematische Annalen,* Vol. 66, pp. 350–397.

Hensel, K., 1926, "Über Potenzreihen von Matrizen," *Journal für die Reine und Angewandte Mathematik,* Vol. 155, p. 107–110.

Hill, C. J. D., 1857, "När äro de n första termene af Bernoullis serie gifven funktion af den i den sista ingående derivatan?" *Öfersigt af Kongl. Vetenskaps-akademiens forhandlingar,* Vol. 14, pp. 259–261.

Hiller, M., and Woernle, C., 1985, "A unified representation of spatial displacements," *Mechanism and Machine Theory,* Vol. 19, No. 6, pp. 477–486.

Langner, R., 1997–1998, "Arbeitsumdrucke zur Mechanik der Punkt- und Starrkörper," Karlsruhe, Germany: Institut für Theoretische Mechanik, Universität Karlsruhe (TH), Karlsruhe, Germany, internal publication.

Laning, J. H., Jr., 1949, "The Vector Analysis of Finite Rotations and Angles," Massachusetts Institute of Technology, Cambridge, MA, MIT/IL Special Rept. 6398-S-3.

McPhee, J. J., and Dubey, R. N., 1991, "Dynamics of Multibody Systems with Known Configuration Changes," ASME JOURNAL OF APPLIED MECHANICS, Vol. 58, 1991, pp. 215–220.

Milenkovic, V., 1982, "Coordinates Suitable for Angular Motion Synthesis in Robots," *Robotics International of the Society of Manufacturing Engineers (SME): Proceedings of Robots VI Conference,* Detroit, MI, Mar 2–4. pp. 407–420.

Nazaroff, G. J., 1979, "The Orientation Vector Differential Equation," *Journal of Guidance and Control,* Vol. 2, No. 4, pp. 351–352.

Pars, L. A., 1965, *A Treatise on Analytical Dynamics,* John Wiley and Sons, New York.

Peres, A., 1979, "Finite Rotations and Angular Velocity," *American Journal of Physics,* Vol. 48, No. 1, pp. 70–71.

Pfister, F., 1995, "Contributions à la Mécanique Analytique des Systèmes Multicorps," Ph.D. thesis, Lyon, France: Institut National des Sciences Appliquées (INSA) de Lyon, Lyon, France.

Pfister, F., 1996, "A three parametric "singularity free" representation of finite spatial rotations," *Zeitschrift für angewandte Mathematik und Mechanik (ZAMM),* Vol. 76, No. S5, pp. 383–384.

Rinehart, R. F., 1959, "The Equation $e^x e^y = e^{x+y}$ in quaternions," *Rendiconti del Circolo Matematico di Palermo, Serie II,* Vol. 8, pp. 160–162.

Saalschütz, L., 1893, *Vorlesungen über Bernoullische Zahlen,* Springer, Berlin.

Santiago, M. A. M., and Vaidya, A. N., 1976, "Baker-Campbell-Hausdorff formulae and spherical and hyperbolic rotations," *The Journal of Astronomical Sciences,* Vol. 44, No. 1, pp. 1–19.

Schaub, H., et al., 1995, "Principal Rotation Representation of Proper $N \times N$ Orthotogonal Matrices," *International Journal of Engineering Science,* Vol. 33, No. 15, pp. 2277–2295.

Schaub, H., and Junkins, J. L., 1976, "Stereographic Orientation Parameters for Attitude Dynamics: A Generalization of the Rodrigues Parameters," *J. Phys. A: Math. Gen.* Vol. 9, No. 6, pp. 897–904.

Shuster, M. D., 1993, "A Survey of Attitude Representations," *Journal of the Astronautical Sciences,* Vol. 41, No. 4, pp. 439–517.

Spielrein, J., 1926, *Lehrbuch der Vektorrechnung nach den Bedürfnissen in der technischen Mechanik und Elektrizitätslehre,* 2nd Ed., Verlag von Konrad Wittwer, Stuttgart.

Spring, K. W., 1986, "Euler Parameters and the use of quaternion algebra in the manipulation of finite rotations: A review," *Mechanism and Machine Theory,* Vol. 21, No. 5, pp. 365–373.

Srinivasa, K. N. R., 1996, *Linear Algebra and Group Theory for Physicists,* John Wiley and Sons, New York.

Stuelpnagel, J., 1964, "On the parametrization of the three-dimensional rotation-group," *SIAM Review,* Vol. 6, No. 4, pp. 422–430.

Sudarshan, E. C. G., and Mukunda, N., *Classical Dynamics: A Modern Perspective,* John Wiley and Sons, New York.

Tsiotras, P., and Longuski, J. M., 1994, "New Kinematic Relations for the large angle problem in rigid body attitude dynamics," *Acta Astronautica,* Vol. 32, No. 3, pp. 181–190.

Tsiotras, P., 1996, "Stabilization and Optimality Results for the Attitude Control Problem," *AIAA Journal of Guidance, Control, and Dynamics,* Vol. 19, No. 4, pp. 772–779.

Tsiotras, P., et al., 1997, "Higher Order Cayley Transforms with Applications to Attitude Representations," *AIAA Journal of Guidance, Control, and Dynamics,* Vol. 20, No. 3, pp. 528–534.

Watson, G. N., 1958, *A Treatise on the Theory of Bessel Functions,* 2nd Ed., Cambridge University Press, London.

Wertz, J. R., ed., 1980, *Spacecraft Attitude Determination and Control,* D. Reidel, Dordrecht, The Netherlands.

Wiener, T. F., 1962, "Theoretical Analysis of Gimballess Inertial Reference Equipment Using Delta-Modulated Instruments," dissertation, Department of Aeronautical and Astronautical Engineering, Massachusetts Institute of Technology, Cambridge, MA.

Wilson, E. B., 1901, *Vector Analysis,* New Haven: Yale University Press, New Haven, CT (reprint: Dover, New York, 1960).

Whittaker, E. T., and Watson, G. N., 1958, *A Course of Modern Analysis* 4th Ed., Cambridge University Press, Cambridge, UK.

Thermodynamical Modeling of Boundary Layer Flow With Suction and Injection

M. Chandrasekar
Lecturer,
Department of Mathematics,
Vellore Engineering College,
Vellore—632014, Tamilnadu,
India

The variational principle developed by Gyarmati embodying the principles of non-equilibrium thermodynamics is employed to investigate the laminar boundary layer effect on wedge flows with suction and injection. The velocity function is assumed as a simple third-degree polynomial and the variational principle is formulated. The hydrodynamical boundary layer thickness is derived as the Euler-Lagrange equation of the variational principle. The velocity profiles and skin friction values were computed for various values of suction and injection parameter and wedge angle parameter. The comparison of the present solution with an available exact solution establishes the fact that the accuracy is remarkable.

1 Introduction

The present study deals with the application of the Governing Principle of Dissipative Processes to boundary layer flows with suction and injection over a wedge whose apex angle is $\pi\beta$. The interest in the boundary layer flow with suction and injection is due to numerous engineering problems that occur. There are several methods which have been developed for the purpose of artificially controlling the behavior of the boundary layer. The purpose of these methods is to affect the whole flow in a desired direction by influencing the structure of the boundary layer. Prandtl (1904) described several experiments in which the boundary layer was controlled. The problem of boundary layer control has become very important in recent times, particularly in the field of aerospace engineering. In actual applications it is often necessary to prevent separation in order to reduce the drag and to attain lift. The boundary layer can be effectively controlled by the methods of suction and injection inside the boundary layer.

The effect of suction consists in the removal of decelerated fluid particles from the boundary layer before they are given a chance to cause separation. The application of suction, first tried by Prandtl, was later widely used in the design of aircraft wings. By applying suction, considerably greater pressure increases on the upper side of the aerofoil are obtained at large angles of incidence, and consequently, much larger maximum lift values. Recently suction was also applied to reduce the drag. The method of boundary layer control by suction, together with the prevention of transition on laminar aerofoils, have the greatest practical importance. Another method of preventing separation is by supplying additional energy to particles of the fluid which are being retarded in the boundary layer by injecting fluid from the interior of the body with the help of a special blower. A new boundary layer, which is again capable of overcoming a certain adverse pressure gradient, is allowed to form in the region behind the slit. With a suitable arrangement of the slits and under favorable conditions separation can be prevented completely. Simultaneously, the amount of pressure drag is greatly reduced owing to the absence of separation.

Contributed by the Applied Mechanics Division of THE AMERICAN SOCIETY OF MECHANICAL ENGINEERS for publication in the ASME JOURNAL OF APPLIED MECHANICS.

Discussion on the paper should be addressed to the Technical Editor, Professor Lewis T. Wheeler, Department of Mechanical Engineering, University of Houston, Houston, TX 77204-4792, and will be accepted until four months after final publication of the paper itself in the ASME JOURNAL OF APPLIED MECHANICS.

Manuscript received by the ASME Applied Mechanics Division, May 7, 1997; final revision, Nov. 1, 1997. Associate Technical Editor: S. Lichter.

Schrenk (1941) investigated a large number of different arrangements of suction slits and their effect on maximum lift. Poisson-Quiton (1956) performed experiments to apply blowing at the trailing edge of an aerofoil in order to increase its maximum lift. A detailed investigation into the flow before the asymptotic state has been reached was carried out by Iglisch (1949). A solution for the flat plate with uniform suction in a compressible stream was found by Lew (1955); the same problem for cylindrical bodies of arbitrary cross section was solved by Wuest (1955). Kay (1948) undertook to verify these theoretical results for the flat plate at zero incidence with the aid of experiments. The assumption that uniform suction begins at the leading edge, which formed the basis of Iglisch's theoretical calculations, was not satisfied in the test plate. Extensive tables for boundary layers on a plate with suction ($m = 0$) covering a wide range of values of the parameter H were calculated by Emmons and Leigh (1954). For cases when $m \neq 0$ there exist additional numerical solutions extending over a wide range of values of the parameters were investigated by Nickel (1962).

The classical problem of boundary layer flow with suction and injection over a flat plate was investigated by many researchers both theoretically and experimentally and the above-mentioned works are with respect to a flat plate. Relatively speaking, considerably less study has been made of the problem when the boundary layer flow with suction and injection over a wedge. Therefore, the main aim of the present investigation is to study the boundary layer effect on wedge flows with suction and injection.

2 Gyarmati's Variational Principle

Gyarmati (1969, 1970) proposed a variational principle by means of which evolution of dissipative transport processes can be described in space and time. This principle, based on Onsager's linear theory and reciprocal relations (Onsager, 1931), is called the "Governing Principle of Dissipative Processes." The most general form of the principle is given by (Gyarmati, 1969)

$$\delta \int_V [\sigma - \psi - \Phi] dV = 0 \tag{1}$$

for any instant of time under the constraints that the balance equations

$$\dot{\rho}_i + \nabla \cdot \mathbf{J}_i = \sigma_i \quad (i = 1, 2, 3 \ldots, f) \tag{2}$$

are satisfied. Here V denotes the volume of the thermodynamic system, and σ the entropy production per unit time and unit volume, which is expressed as a bilinear function of thermodynamic forces and fluxes,

$$\sigma = \sum_{i=1}^{f} \mathbf{J}_i \cdot \mathbf{X}_i \geq 0. \tag{3}$$

This is a definite positive quantity according to the second law of thermodynamics. f is the number of independent fluxes $\mathbf{J}_i$, and thermodynamic forces $\mathbf{X}_i$. In the linear Onsager theory, the fluxes $\mathbf{J}_i$ and the forces $\mathbf{X}_i$ are related by the linear constitutive equations

$$\mathbf{J}_i = \sum_{i=1}^{f} L_{ik}\mathbf{X}_k \tag{4}$$

$$\mathbf{X}_i = \sum_{i=1}^{f} R_{ik}\mathbf{J}_k \tag{5}$$

where L_{ik} and R_{ik} satisfy the relations

$$\sum_{m=1}^{f} L_{im}R_{mk} = \sum_{m=1}^{f} R_{im}L_{mk} \quad (i, k = 1, 2, 3 \ldots, f) \tag{6}$$

and

$$L_{ik} = L_{ki}; \quad R_{ik} = R_{ki}. \tag{7}$$

Using Eqs. (4) and (5), σ can be expressed as

$$\sigma \equiv \sum_{i,k=1}^{f} L_{ik}\mathbf{X}_i\mathbf{X}_k \equiv \sum_{i,k=1}^{f} R_{ik}\mathbf{J}_i\mathbf{J}_k \geq 0. \tag{8}$$

These two forms of σ are called force and flux representation of the entropy production. The nonequilibrium local potentials (Gyarmati, 1969) ψ and Φ, which are equal to half of the entropy production, are given by

$$\Psi(\mathbf{X}, \mathbf{X}) \equiv (1/2) \sum_{i,k=1}^{f} L_{ik}\mathbf{X}_i \cdot \mathbf{X}_k \geq 0, \tag{9}$$

$$\Phi(\mathbf{J}, \mathbf{J}) \equiv (1/2) \sum_{i,k=1}^{f} R_{ik}\mathbf{J}_i \cdot \mathbf{J}_k \geq 0. \tag{10}$$

Ψ and Φ are also the local measures of irreversibility. The potential character of ψ and Φ can be obtained from the relations

$$\mathbf{J}_i = (\partial\Psi/\partial\mathbf{X}_i) = \sum_{k=1}^{f} L_{ik}\mathbf{X}_k \quad (i = 1, 2, 3 \ldots, f) \tag{11}$$

$$\mathbf{X}_i = (\partial\Phi/\partial\mathbf{J}_i) = \sum_{k=1}^{f} R_{ik}\mathbf{J}_k \quad (i = 1, 2, 3 \ldots, f) \tag{12}$$

which are the linear Eqs. (4) and (5). Using the expressions of σ, ψ, and Φ in principle (1), we get

$$\delta \int_v [\sum_{i=1}^{f} \mathbf{J}_i \cdot \nabla\Gamma_i - (1/2) \sum_{i,k=1}^{f} L_{ik}\nabla\Gamma_i \cdot \nabla\Gamma_k - (1/2) \sum_{i,k=1}^{f} R_{ik}\mathbf{J}_j \cdot \mathbf{J}_k]dV = 0, \tag{13}$$

where the dissipative forces X_i can be generated as the gradients of certain Γ variables which are state parameters and simultaneously internal parameters with respect to forces (Gyarmati, 1969)

$$\mathbf{X}_i = \nabla\Gamma_i. \tag{14}$$

The principle (13) is operative if and only if the balance equations are treated as auxiliary conditions for whose variations the restrictions

$$\delta(\dot{\rho}_i - \sigma_i) = -\delta(\nabla \cdot \mathbf{J}_i) = -\nabla \cdot (\delta\mathbf{J}_i) \quad (i = 1, 2, 3 \ldots, f) \tag{15}$$

are valid.

3 Formulation of Governing Principle of Dissipative Processes

Prandtl's boundary layer equations for two-dimensional incompressible steady fluid flow are

$$(\partial u/\partial x) + (\partial v/\partial y) = 0 \tag{16}$$

$$u(\partial u/\partial x) + v(\partial u/\partial y) = U(dU/dx) + \gamma(\partial^2 u/\partial y^2) \tag{17}$$

where u, v are the velocity components along x and y-directions, respectively, and γ is the kinematic viscosity. The boundary conditions of the system are

$$y = 0; \quad u = 0, v = v_0(x)$$

$$y \to \infty; \quad u \to U(x) \tag{18}$$

where $v_0(x)$ is the suction/injection velocity. It is well known that in the formulation of Gyarmati's principle the transport Eqs. (16) and (17) play the basic role which in this case are

$$\nabla \cdot \mathbf{V} = 0 \; (\mathbf{V} = iu + jv) \tag{19}$$

$$\rho(\mathbf{V} \cdot \nabla)\mathbf{V} + \nabla \cdot \bar{\bar{P}} = 0. \tag{20}$$

These equations represent the mass and the momentum balance, respectively. Here $\bar{\bar{P}}$ denotes the pressure tensor and it takes the form for the present problem (Gyarmati, 1969)

$$\bar{\bar{P}} = p\bar{\bar{\delta}} + \overset{0}{\bar{\bar{P}}}{}^{vs}, \tag{21}$$

where p is the hydrostatic pressure and $\overset{0}{\bar{\bar{P}}}{}^{vs}$ is the symmetrical part of the viscous pressure tensor, whose trace is zero. In the study of fluid flow problems, the energy picture of Gyarmati's principle is preferable over entropy picture. Therefore, we use the energy dissipation $T\sigma$ instead of entropy production σ. The energy dissipation for the problem is (Gyarmati, 1969)

$$T\sigma = -\overset{0}{\bar{\bar{P}}}{}^{vs}: (\nabla^0 V)^s = -P_{12}(\partial u/\partial y) \geq 0, \tag{22}$$

where $(\nabla^0 V)^s$ is the symmetrical part of the velocity gradient tensor and its trace is zero. In this case it has only one component $(\nabla^0 V)^s = (\partial u/\partial y)$. The viscous pressure tensor $\overset{0}{\bar{\bar{P}}}{}^{vs}$ also has only one component P_{12}. The double dots denote the scalar product of two tensors. The linear constitutive relation for the present case is

$$P_{12} = -\mu(\partial u/\partial y). \tag{23}$$

The dissipation potentials ψ and Φ in the energy picture are

$$T\psi \equiv (\mu/2)(\partial u/\partial y)^2 \geq 0 \tag{24}$$

$$T\Phi \equiv (1/2\mu)P_{12}^2 \geq 0. \tag{25}$$

Using the Eqs. (23), (24), and (25) the energy picture of principle (1) assumes the form

$$\delta \int_0^L \int_0^\infty [-P_{12}(\partial u/\partial y) - (\mu/2)(\partial u/\partial y)^2 - (1/2\mu)P_{12}^2]dydx = 0, \tag{26}$$

where L is the characteristic length of the body. Following the dual field method (Stark, 1974) we introduce a new velocity field u^* through the approximate constitutive equation

$$P_{12} = -\mu(\partial u^*/\partial y). \tag{27}$$

It is assumed that u^* satisfies the same boundary conditions as u. The momentum balance Eq. (17) and the principle (26) become

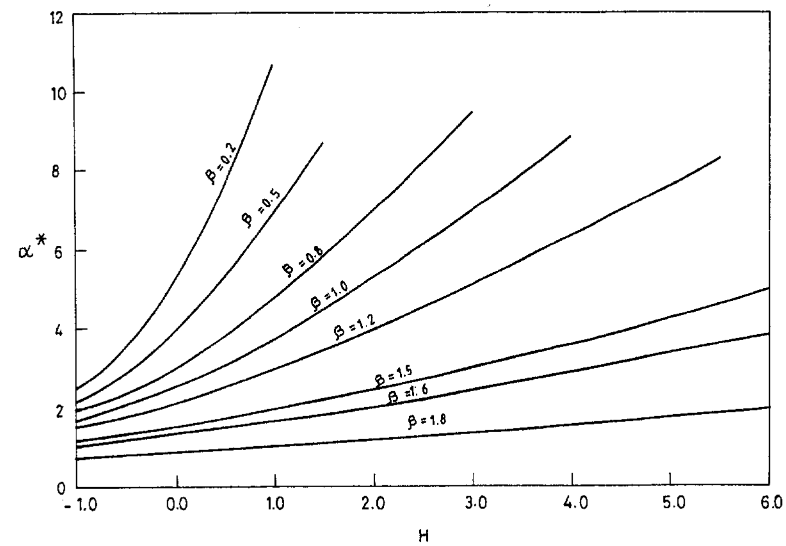

Fig. 1 Hydrodynamical boundary layer thickness as a function of H

$$u(\partial u/\partial x) + v(\partial u/\partial y) = U(dU/dx) + \gamma(\partial^2 u^*/\partial y^2) \quad (28)$$

$$\delta \int_0^L \int_0^\infty [(\partial u/\partial y)(\partial u^*/\partial y) - (1/2)(\partial u/\partial y)^2 - (1/2)(\partial u^*/\partial y)^2]dydx = 0. \quad (29)$$

4 Method of Solution

We consider the system of two-dimensional, laminar inviscid potential flow past an unlimited wedge placed symmetrically in a stream with apex at the origin and the center line on the positive x-axis. The flow creates along the surface a velocity variation like

$$U(x) = ax^m, \quad (30)$$

where a is a constant and the exponent m is connected with the apex-angle $\pi\beta$ by the relation

$$m = \beta/(2 - \beta). \quad (31)$$

Here we confine our analysis to realistic flows only, that is, when $0 \le m < \infty$ or $0 \le \beta < 2$.

Let us assume that the velocity distribution in the boundary layer is as follows:

$$u/U(x) = 3y/\alpha - 3y^2/\alpha^2 + y^3/\alpha^3 \quad (0 \le y \le \alpha)$$
$$u = U(x) \quad (y \ge \alpha) \quad (32)$$

which satisfies the compatibility conditions

$$y = 0;\ u = 0$$
$$y = \alpha;\ u = U(x), \quad (\partial u/\partial y) = 0, \quad (\partial^2 u/\partial y^2) = 0. \quad (33)$$

Here $\alpha = \alpha(x)$ is the extent of the hypothetical hydrodynamical boundary layer thickness which is to be determined from the present thermodynamic analysis.

The transverse velocity component v is obtained from the mass balance Eq. (16) as

$$v/U(x) = \alpha'[3y^2/2\alpha^2 - 2y^3/\alpha^3 + 3y^4/4\alpha^4] - m[3y^2/2\alpha - y^3/\alpha^2 + y^4/4\alpha^3]/x + v_0 \quad (34)$$

where a prime indicates differentiation with respect to x. The

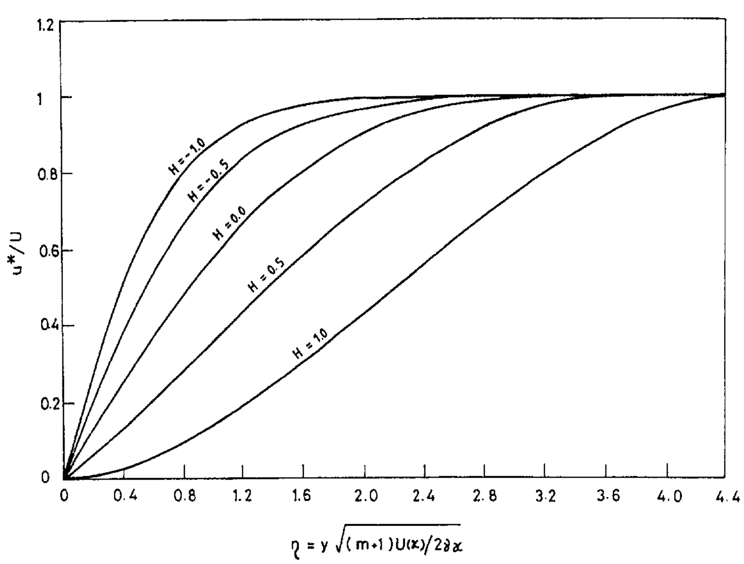

Fig. 2 Velocity distribution for $\beta = 0.2$

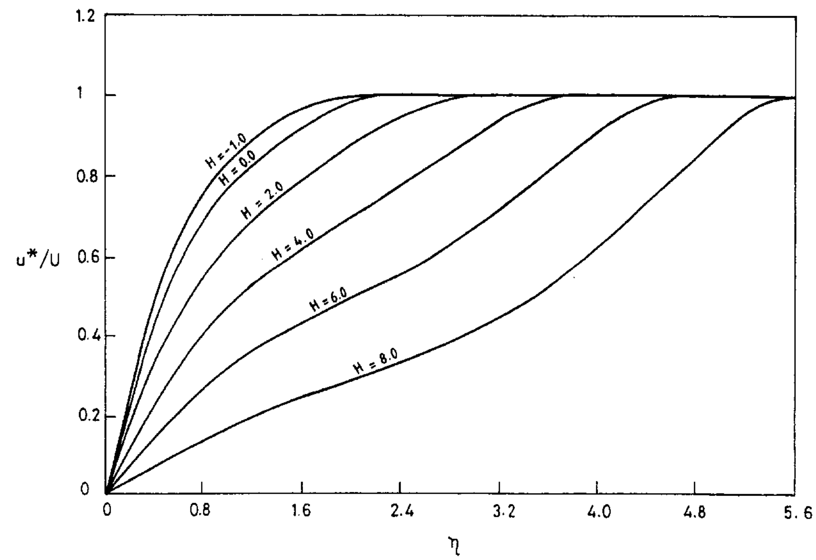

Fig. 3 Velocity distribution for $\beta = 1.8$

velocity distribution (32) and (34) and the boundary conditions (33) are used in the balance Eq. (20) to determine the following expression for momentum flux:

$$-P_{12}/\mu = (\partial u^*/\partial y) = [U/\alpha] + U^2\alpha'[9/160 - 3y^3/2\alpha^3 + 3y^4/\alpha^4 - 9y^5/4\alpha^5 + 3y^6/4\alpha^6 - 3y^7/28\alpha^7]/\gamma + mU^2[53\alpha/160 - y + 3y^3/2\alpha^2 - 3y^4/2\alpha^3 + 3y^5/4\alpha^4 - y^6/4\alpha^5 + y^7/28\alpha^6]/\gamma x + Uv_0[-3/4 + 3y/\alpha - 3y^2/\alpha^2 + y^3/\alpha^3]/\gamma \quad (35)$$

where u^* is the dual field velocity. Using the Eqs. (32) and (35) in the principle (29) and integrating with respect to y, we get

$$\delta \int_0^L [U^3\alpha\alpha'(0.034821428)\gamma x^2 - U^2(0.4)\gamma^2 x^2 + mU^3\alpha^2(0.124107142)\gamma x - U^4\alpha^2\alpha'^2(0.000812449)x^2 - m^2U^4\alpha^4(0.009715542) - mU^4\alpha^3\alpha'(0.005284936)x - U^2\alpha v_0(0.25)\gamma x^2 - U^2\alpha^2 v_0^2(0.0401785)x^2 + mU^3\alpha^3 v_0(0.0393877)x + U^3\alpha^2\alpha' v_0(0.0104095)x^2]dx = 0. \quad (36)$$

Let us introduce the dimensionless boundary layer thickness α^* by the relation

$$\alpha = \alpha^*\sqrt{\gamma x/U} \quad (37)$$

in the variational principle (36). If the concise formulation of the variational principle (36) is given with the help of Lagrangian density L as

$$\delta \int_0^L L dx = 0, \quad (38)$$

the Euler-Lagrange equation of the principle (38) turns out to be

$$\partial L/\partial \alpha^* = 0 \quad (\text{or}) \quad (39)$$

$$\alpha^{*4}[m^2(0.021828558) + m(0.006708731) + 0.000609336] - \alpha^{*3}H[m(0.0683659) + 0.0104095] + \alpha^{*2}[H^2(0.0401785) - m(0.106696428) - 0.017410714] - 0.4 = 0, \quad (40)$$

where H the dimensionless injection speed is given by

$$H = v_0\sqrt{R_x}/U. \quad (41)$$

Here R_x denotes the Reynolds number $(Ux)/\gamma$. Suction and injection are represented by $H < 0$ and $H > 0$, respectively.

Equation (40) is a simple algebraic equation in terms of the boundary layer thickness whose coefficients depend on the injection speed H and the wedge parameter m. The algebraic Eq. (40) is solved easily for the given values of m and H, and the corresponding hydrodynamical boundary layer thickness α^* is obtained as the only positive root. In order to study the effects of suction and injection on local shear stress, we calculate its dimensionless value

$$\tau_w^* = (\partial u^*/\partial y)_{y=0}. \quad (42)$$

It is noteworthy that the nonlinear partial differential Eqs. (16) and (17) are reduced to simple algebraic Eq. (40), which is of much practical use to any practicing engineer.

5 Discussion of Results

The dimensionless boundary layer thickness α^* which is the solution of (40) is graphically presented in Fig. 1. The boundary layer thickness α^* is shown as a function of injection parameter H for the values of wedge parameter $\beta = 0.2$, 0.5, 0.8, 1.0, 1.2, 1.5, 1.6, and 1.8. From this figure, we observe that the boundary layer thickness increases with H and the increase is very rapid when β is small.

Figures 2 and 3 represent velocity distribution inside the boundary layer for various values of H. The figures correspond to the values of the wedge parameter $\beta = 0.2$, and 1.8. Since we confined our analysis to realistic flows only, we can determine the velocity distributions inside the boundary layer for various values of H ranging from the wedge parameter $\beta \geq 0$ and $\beta < 2$. It can be easily observed from each figure that the dimensionless velocity increases from 0 to 1, more rapidly in the case of suction ($H < 0$).

It is customary that when a new mathematical method is applied to a problem, the obtained results are compared with the available exact solution in order to determine the error in-

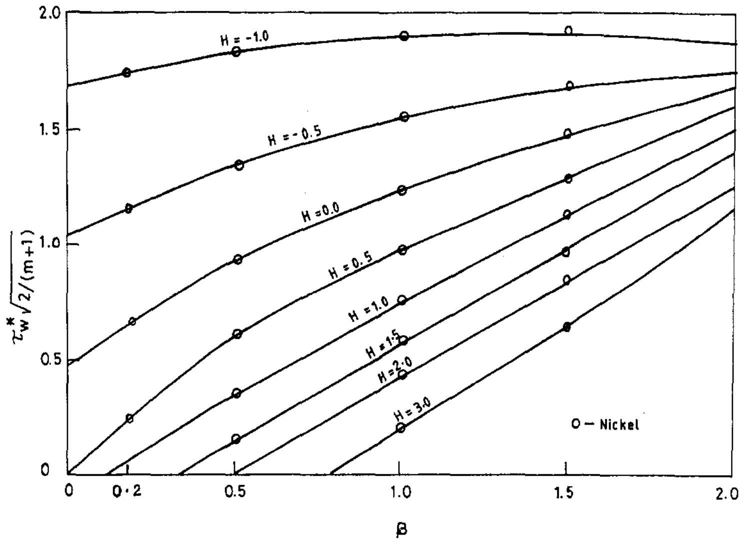

Fig. 4 Skin friction as a function of the wedge parameter β

volved in the results. The main result of engineering interest is the local values of shear stress. Accordingly, we compute the skin friction values and Fig. 4 displays skin friction values as a function of the wedge parameter β. It is demonstrated that the skin friction values are decreasing function of H. The intention of this figure is to compare the present solution with the exact solution of Nickel (1962). The agreement of the results is excellent and thus we find our present variational method produces results with a very high order of accuracy.

The boundary layer separation by plotting the separation values of H against β is exhibited in Fig. 5. By a separation value of H we mean the H value which causes separation. We observe from the figure that the increase in the value of the wedge parameter β delays the separation.

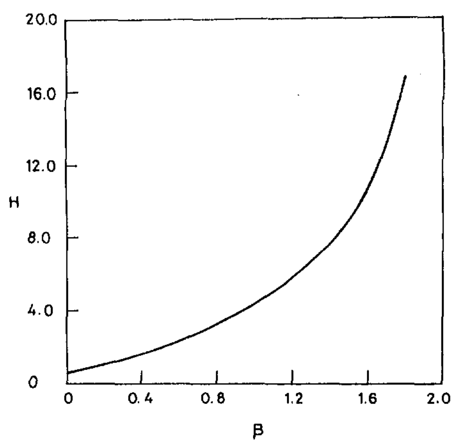

Fig. 5 Separation values of H versus β

One can note that this variational procedure yields results which are analytical and almost exact. The great advantage of this analysis is that the amount of calculation is considerably less. Thus we observe from the present investigation that the comparably easier variational procedure for solving the partial differential equations governing the present system yields results with remarkable accuracy.

Acknowledgment

The author gratefully acknowledges the encouragements and suggestions of Prof. S. Antony Raj, Department of Mathematics, Presidency College, Madras-5, India.

References

Emmons, H. W., and Leigh, D. C., 1954, ARC Report and Memo No. 157.

Gyarmati, I., 1969, *Ann. Phys.*, Vol. 23, pp. 353–378.

Gyarmati, I., 1970, *Non-equilibrium Thermodynamics, Field Theory and Variational Principles*, Springer-Verlag, Berlin, p. 95.

Iglisch, R., 1949, NACA Tech. Memo No. 1205.

Kay, J. M., 1948, ARC Report and Memo No. 2628.

Lew, H. G., 1955, *Jour. Aero. Sci.*, Vol. 22, pp. 589–597.

Nickel, K., 1962, *Ing. Arch.*, Vol. 31, pp. 85–100.

Onsager, L., 1931, *Phys. Rev.*, Vol. 37, p. 405.

Onsager, L., 1931, *Phys. Rev.*, Vol. 38, p. 2265.

Poisson-Quiton, P., 1956, ONERA Publication, Note Technique Vol. 37.

Prandtl, L., 1904, *Proc. III. Intern. Maths Congr.*, Heidelberg, pp. 484–491.

Schrenk, O., 1941, NACA Tech. Mem. No. 974.

Stark, A., 1974, *Ann. Physik., Leipzig*, Vol. 31, pp. 53–75.

Wuest, W., 1955, *Ing. Arch.*, Vol. 23, pp. 198–208.

Journal of Applied Mechanics

Brief Notes

A Brief Note is a short paper that presents a specific solution of technical interest in mechanics but which does not necessarily contain new general methods or results. A Brief Note should not exceed 1500 words *or equivalent* (a typical one-column figure or table is equivalent to 250 words; a one line equation to 30 words). Brief Notes will be subject to the usual review procedures prior to publication. After approval such Notes will be published as soon as possible. The Notes should be submitted to the Technical Editor of the JOURNAL OF APPLIED MECHANICS. Discussions on the Brief Notes should be addressed to the Editorial Department, ASME, United Engineering Center, 345 East 47th Street, New York, N. Y. 10017, or to the Technical Editor of the JOURNAL OF APPLIED MECHANICS. Discussions on Brief Notes appearing in this issue will be accepted until two months after publication. Readers who need more time to prepare a Discussion should request an extension of the deadline from the Editorial Department.

A Note on the Effective Lamé Constants of Polycrystalline Aggregates of Cubic Crystals

V. A. Lubarda[1]

It is well known that the Voigt and Reuss estimates of the effective shear modulus of a polycrystalline aggregate of cubic crystals are, respectively, the upper and lower bounds for this constant ($\mu^R \leq \mu \leq \mu^V$). It is pointed out in this note that the opposite is true for the Lamé constant λ ($\lambda^V \leq \lambda \leq \lambda^R$).

1 Introduction

According to the Voigt (1889) assumption, when a polycrystalline aggregate is subjected to the overall uniform strain, the individual crystals are all in the same state of applied strain. From this assumption it follows that the effective elastic moduli of an isotropic aggregate are directional averages of the corresponding moduli of individual crystals. Thus, the effective Lamé and bulk moduli of a polycrystalline aggregate of cubic crystals are

$$\lambda^V = \frac{1}{5}(c_{11} + 4c_{12} - 2c_{44}), \quad \mu^V = \frac{1}{5}(c_{11} - c_{12} + 3c_{44}),$$

$$\kappa^V = \frac{1}{3}(c_{11} + 2c_{12}), \tag{1}$$

where superscript V designates the Voigt assumption. The constants c_{11}, c_{12}, and c_{44} are the elastic moduli of individual crystals.

According to the Reuss (1929) assumption, when a polycrystalline aggregate is subjected to overall uniform stress, the individual crystals are all in the same state of applied stress. From this assumption it follows that the effective elastic compliances of an isotropic aggregate are directional averages of the corresponding compliances of individual crystals. Expressing the result in terms of elastic moduli, this gives

$$\lambda^R = \frac{(c_{11} - c_{12})(c_{11} + 2c_{12}) - 2c_{44}(c_{11} - 3c_{12})}{3(c_{11} - c_{12}) + 4c_{44}},$$

$$\mu^R = \frac{5c_{44}(c_{11} - c_{12})}{3(c_{11} - c_{12}) + 4c_{44}}, \tag{2}$$

and $\kappa^R = (c_{11} + 2c_{12})/3$. Evidently, $\kappa^V = \kappa^R$, since cubic crystals under hydrostatic state of stress behave as isotropic materials. Comparing Eqs. (1) and (2), we further have

$$\lambda^V = \lambda^R - \frac{2}{5}\frac{(c_{11} - c_{12} - 2c_{44})^2}{3(c_{11} - c_{12}) + 4c_{44}},$$

$$\mu^V = \mu^R + \frac{3}{5}\frac{(c_{11} - c_{12} - 2c_{44})^2}{3(c_{11} - c_{12}) + 4c_{44}}. \tag{3}$$

Since from the stability conditions for a single crystal $c_{11} - c_{12} > 0$ and $c_{44} > 0$, from Eq. (3) it follows that

$$\lambda^V \leq \lambda^R, \quad \mu^V \geq \mu^R. \tag{4}$$

2 Bounds

Hill (1952) has shown that the strain energy density in a polycrystalline aggregate with the true effective moduli is not greater than the corresponding energy in the aggregate with the Voigt estimates of the elastic moduli. Likewise, the complementary energy in a polycrystalline aggregate with the true effective compliances is not greater than the corresponding energy in the aggregate with the Reuss estimates of the elastic compliances. From this it follows that the true shear and bulk moduli are related to their Voigt and Reuss estimates by

$$\mu^R \leq \mu \leq \mu^V, \quad \kappa^R = \kappa = \kappa^V. \tag{5}$$

The other well-known consequences are that the effective Young's modulus and Poisson's ratio are bounded by

$$E^R \leq E \leq E^V, \quad \nu^V \leq \nu \leq \nu^R. \tag{6}$$

The bounds on the Lamé constant λ are easily identified. Indeed,

$$\kappa - \frac{2}{3}\mu^V \leq \lambda = \kappa - \frac{2}{3}\mu \leq \kappa - \frac{2}{3}\mu^R, \tag{7}$$

and since $\kappa = \kappa^V = \kappa^R$, we obtain

[1] Department of Applied Mechanics and Engineering Sciences, University of California, San Diego, La Jolla, CA 92093-0411.

Contributed by the Applied Mechanics Division of THE AMERICAN SOCIETY OF MECHANICAL ENGINEERS for publication in the ASME JOURNAL OF APPLIED MECHANICS. Manuscript received by the ASME Applied Mechanics Division, May 13, 1996; final revision, Oct. 21, 1997. Associate Technical Editor: J. L. Bassani.

$$\lambda^V \le \lambda \le \lambda^R. \quad (8)$$

Thus, the upper bound for the Lamé constant λ is the Reuss estimate of this constant, while the lower bound for this constant is given by its Voigt estimate.

This is the message of this brief note. It is brought to the attention of the reader, because a statement appears in the literature that all effective elastic moduli are bounded from above by their Voigt estimates and from below by their Reuss estimates (e.g., Barsch, 1968, p. 3782; Mura, 1987, Eq. (45.19.13) on p. 428).

References

Barsch, G. R., 1968, "Relation between third-order elastic constants of single crystals and polycrystals," *J. Appl. Phys.*, Vol. 39, pp. 3780–3793.

Hill, R., 1952, "The elastic behavior of a crystalline aggregate," *Proc. Phys. Soc. London*, Vol. A65, pp. 349–354.

Mura, T., 1987, *Micromechanics of Defects in Solids*, 2nd ed., Martinus Nijhoff Publishers, Dordrecht, The Netherlands.

Reuss, A., 1929, "Berechnung der Fliessgrenze von Mischkristallen auf Grund der Plastizitätsbedingung für Einkristalle," *Z. angew. Math. Mech.*, Vol. 9, pp. 49–58.

Voigt, W., 1889, "Über die Beziehung zwischen den beiden Elastizitätskonstanten isotroper Körper," *Wied. Ann.*, Vol. 38, pp. 573–587.

Natural Frequencies and Normal Modes for Externally Damped Spinning Timoshenko Beams With General Boundary Conditions

J. W. Zu[1,3] and J. Melanson[2,3]

Vibration analysis of externally damped spinning Timoshenko beams with general boundary conditions is performed analytically. Exact solutions for natural frequencies and normal modes for the six classical boundary conditions are derived for the first time. In the numerical simulations, the trend between the complex frequencies and the damping coefficient is investigated, and complex mode shapes are presented in three-dimensional space.

1 Introduction

Most research in analytical modeling of Timoshenko beams spinning along the longitudinal axis that has been conducted is limited to undamped vibrations. Zu and Han (1992) developed analytical solutions for the natural frequencies and normal modes for a spinning Timoshenko beam with six different boundary conditions. Lee (1995) formulated the equations of motion for a simply supported beam subjected to axial forces and moving loads by Hamilton's principle. Argento (1995) investigated the response and resonance of simply supported and clamped-clamped spinning beams subjected to moving loads using Galerkin's method. Tan and Kuang (1995) obtain closed-form solutions for both Rayleigh and Timoshenko beams by means of a distributed transfer function and a generalized displacement formulation for stepped beams.

For damped vibration of Timoshenko beams, Singh and Abdelnaser (1993) presented a general modal solution to a stationary Timoshenko beam with external damping. They include both external transverse and rotary viscous damping as well as viscoelastic damping. Extensive research on externally damped spinning Timoshenko beams is lacking at the present time. One of the very few papers on external damping is by Medgyesi (1991), in which the external damping was studied in the case of a Jeffcott rotor.

The objective of this paper is to develop analytical solutions for the complex eigenvalues and complex normal modes of an externally damped Timoshenko beam with general boundary conditions. This is a continuation of the work done by Zu and Han (1992) in which undamped natural frequencies and normal modes were solved analytically.

2 Equations of Motion

The equations of motion based on an inertial frame $oxyz$ for a spinning uniform Timoshenko beam are based on the equations presented by Han and Zu (1992) with the inclusion of the external viscous damping. The equations of motion are

$$\frac{\partial^2 u}{\partial t^2} + \frac{c}{\rho A}\frac{\partial u}{\partial t} + \frac{\kappa G}{\rho l^2}\left[l\frac{\partial \psi}{\partial \zeta} - \frac{\partial^2 u}{\partial \zeta^2}\right] = 0 \quad (1)$$

$$\frac{\partial^2 \psi}{\partial t^2} - i\frac{\Omega J_z}{\rho I}\frac{\partial \psi}{\partial t} - \frac{E}{\rho l^2}\frac{\partial^2 \psi}{\partial \zeta^2} + \frac{\kappa A G}{\rho I l}\left[l\psi - \frac{\partial u}{\partial \zeta}\right] = 0 \quad (2)$$

where ρ is the mass density; A is the cross-sectional area; I is the transverse moment of inertia of an axisymmetric cross section; J_z is the polar moment of inertia; c is the viscous damping coefficient; and E, G, and κ are Young's modulus, shear modulus, and shear coefficient, respectively. $\zeta = z/l$ is the nondimensional variable, and $u = u_x + iu_y$, $\psi = \psi_x + i\psi_y$ are the complex transverse deflections the corresponding bending angles. Note that only transverse damping is included while rotary damping is ignored since the effect of rotary damping is much smaller than the transverse damping.

Assume that the solutions to Eqs. (1) and (2) are

$$u = W_u(\zeta)e^{\lambda t}$$
$$\psi = W_\psi(\zeta)e^{\lambda t}. \quad (3)$$

Here $W_u(\zeta)$ and $W_\psi(\zeta)$ are complex normal modes and λ is the complex eigenvalue and they are expressed by

$$W_u(\zeta) = W_{uR}(\zeta) + iW_{uI}(\zeta)$$
$$W_\psi(\zeta) = W_{\psi R}(\zeta) + iW_{\psi I}(\zeta) \quad (4)$$

$$\lambda = \lambda_R + i\lambda_I. \quad (5)$$

Thus the substitution of Eq. (3) into Eqs. (1) and (2) becomes

$$-\lambda\left(\lambda + \frac{c}{\rho A}\right)W_u(\zeta) = \frac{\kappa G}{\rho l}W'_\psi(\zeta) - \frac{\kappa G}{\rho l^2}W''_u(\zeta) \quad (6)$$

$$\left[\lambda^2 - i\frac{\Omega J_z \lambda}{\rho I} + \frac{\kappa A G}{\rho I}\right]W_\psi(\zeta) - \frac{E}{\rho l^2}W''_\psi(\zeta) = \frac{\kappa A G}{\rho I l}W'_u(\zeta). \quad (7)$$

The solutions to Eqs. (6) and (7) can be derived as follows:

[1] Assistant Professor.

[2] Graduate Student.

[3] Department of Mechanical and Industrial Engineering, University of Toronto, Toronto, Ontario M5S 3G8, Canada.

Contributed by the Applied Mechanics Division of THE AMERICAN SOCIETY OF MECHANICAL ENGINEERS for publication in the ASME JOURNAL OF APPLIED MECHANICS. Manuscript received by the ASME Applied Mechanics Division, Mar. 4, 1997; final revision, Nov. 25, 1997. Associate Technical Editor: N. C. Perkins.

$$\lambda^V \le \lambda \le \lambda^R. \tag{8}$$

Thus, the upper bound for the Lamé constant λ is the Reuss estimate of this constant, while the lower bound for this constant is given by its Voigt estimate.

This is the message of this brief note. It is brought to the attention of the reader, because a statement appears in the literature that all effective elastic moduli are bounded from above by their Voigt estimates and from below by their Reuss estimates (e.g., Barsch, 1968, p. 3782; Mura, 1987, Eq. (45.19.13) on p. 428).

References

Barsch, G. R., 1968, "Relation between third-order elastic constants of single crystals and polycrystals," *J. Appl. Phys.*, Vol. 39, pp. 3780–3793.

Hill, R., 1952, "The elastic behavior of a crystalline aggregate," *Proc. Phys. Soc. London*, Vol. A65, pp. 349–354.

Mura, T., 1987, *Micromechanics of Defects in Solids*, 2nd ed., Martinus Nijhoff Publishers, Dordrecht, The Netherlands.

Reuss, A., 1929, "Berechnung der Fliessgrenze von Mischkristallen auf Grund der Plastizitätsbedingung für Einkristalle," *Z. angew. Math. Mech.*, Vol. 9, pp. 49–58.

Voigt, W., 1889, "Über die Beziehung zwischen den beiden Elastizitätskonstanten isotroper Körper," *Wied. Ann.*, Vol. 38, pp. 573–587.

Natural Frequencies and Normal Modes for Externally Damped Spinning Timoshenko Beams With General Boundary Conditions

J. W. Zu[1,3] and J. Melanson[2,3]

Vibration analysis of externally damped spinning Timoshenko beams with general boundary conditions is performed analytically. Exact solutions for natural frequencies and normal modes for the six classical boundary conditions are derived for the first time. In the numerical simulations, the trend between the complex frequencies and the damping coefficient is investigated, and complex mode shapes are presented in three-dimensional space.

1 Introduction

Most research in analytical modeling of Timoshenko beams spinning along the longitudinal axis that has been conducted is limited to undamped vibrations. Zu and Han (1992) developed analytical solutions for the natural frequencies and normal modes for a spinning Timoshenko beam with six different boundary conditions. Lee (1995) formulated the equations of motion for a simply supported beam subjected to axial forces and moving loads by Hamilton's principle. Argento (1995) investigated the response and resonance of simply supported and clamped-clamped spinning beams subjected to moving loads using Galerkin's method. Tan and Kuang (1995) obtain closed-form solutions for both Rayleigh and Timoshenko beams by means of a distributed transfer function and a generalized displacement formulation for stepped beams.

For damped vibration of Timoshenko beams, Singh and Abdelnaser (1993) presented a general modal solution to a stationary Timoshenko beam with external damping. They include both external transverse and rotary viscous damping as well as viscoelastic damping. Extensive research on externally damped spinning Timoshenko beams is lacking at the present time. One of the very few papers on external damping is by Medgyesi (1991), in which the external damping was studied in the case of a Jeffcott rotor.

The objective of this paper is to develop analytical solutions for the complex eigenvalues and complex normal modes of an externally damped Timoshenko beam with general boundary conditions. This is a continuation of the work done by Zu and Han (1992) in which undamped natural frequencies and normal modes were solved analytically.

2 Equations of Motion

The equations of motion based on an inertial frame $oxyz$ for a spinning uniform Timoshenko beam are based on the equations presented by Han and Zu (1992) with the inclusion of the external viscous damping. The equations of motion are

$$\frac{\partial^2 u}{\partial t^2} + \frac{c}{\rho A}\frac{\partial u}{\partial t} + \frac{\kappa G}{\rho l^2}\left[l\frac{\partial \psi}{\partial \zeta} - \frac{\partial^2 u}{\partial \zeta^2}\right] = 0 \tag{1}$$

$$\frac{\partial^2 \psi}{\partial t^2} - i\frac{\Omega J_z}{\rho I}\frac{\partial \psi}{\partial t} - \frac{E}{\rho l^2}\frac{\partial^2 \psi}{\partial \zeta^2} + \frac{\kappa A G}{\rho I l}\left[l\psi - \frac{\partial u}{\partial \zeta}\right] = 0 \tag{2}$$

where ρ is the mass density; A is the cross-sectional area; I is the transverse moment of inertia of an axisymmetric cross section; J_z is the polar moment of inertia; c is the viscous damping coefficient; and E, G, and κ are Young's modulus, shear modulus, and shear coefficient, respectively. $\zeta = z/l$ is the nondimensional variable, and $u = u_x + iu_y$, $\psi = \psi_x + i\psi_y$ are the complex transverse deflections the corresponding bending angles. Note that only transverse damping is included while rotary damping is ignored since the effect of rotary damping is much smaller than the transverse damping.

Assume that the solutions to Eqs. (1) and (2) are

$$u = W_u(\zeta)e^{\lambda t}$$
$$\psi = W_\psi(\zeta)e^{\lambda t}. \tag{3}$$

Here $W_u(\zeta)$ and $W_\psi(\zeta)$ are complex normal modes and λ is the complex eigenvalue and they are expressed by

$$W_u(\zeta) = W_{uR}(\zeta) + iW_{uI}(\zeta)$$
$$W_\psi(\zeta) = W_{\psi R}(\zeta) + iW_{\psi I}(\zeta) \tag{4}$$

$$\lambda = \lambda_R + i\lambda_I. \tag{5}$$

Thus the substitution of Eq. (3) into Eqs. (1) and (2) becomes

$$-\lambda\left(\lambda + \frac{c}{\rho A}\right)W_u(\zeta) = \frac{\kappa G}{\rho l}W'_\psi(\zeta) - \frac{\kappa G}{\rho l^2}W''_u(\zeta) \tag{6}$$

$$\left[\lambda^2 - i\frac{\Omega J_z \lambda}{\rho I} + \frac{\kappa A G}{\rho I}\right]W_\psi(\zeta) - \frac{E}{\rho l^2}W''_\psi(\zeta) = \frac{\kappa A G}{\rho I l}W'_u(\zeta). \tag{7}$$

The solutions to Eqs. (6) and (7) can be derived as follows:

---

[1] Assistant Professor.

[2] Graduate Student.

[3] Department of Mechanical and Industrial Engineering, University of Toronto, Toronto, Ontario M5S 3G8, Canada.

Contributed by the Applied Mechanics Division of THE AMERICAN SOCIETY OF MECHANICAL ENGINEERS for publication in the ASME JOURNAL OF APPLIED MECHANICS. Manuscript received by the ASME Applied Mechanics Division, Mar. 4, 1997; final revision, Nov. 25, 1997. Associate Technical Editor: N. C. Perkins.

Table 1 Comparison of complex eigenvalues varying with viscous damping

Damping (Ns/m) C	Hinged-Hinged Real	Hinged-Hinged Imaginary	Clamped-Clamped Real	Clamped-Clamped Imaginary	Hinged-Free Real	Hinged-Free Imaginary
0	0	2445	0	4827	0	3874
100000	-233	2435	-227	4822	-233	3868
200000	-467	2402	-430	4806	-430	3849
300000	-701	2348	-683	4780	-701	3816
400000	-936	2269	-910	4743	-935	3770
500000	-1173	2164	-1138	4694	-1171	3710
600000	-1413	2028	-1366	4634	-1407	3635
700000	-1658	1853	-1594	4562	-1646	3545
800000	-1913	1627	-1823	4478	-1886	3437
900000	-2190	1326	-2051	4381	-2129	3311
1000000	-2551	890	-2280	4269	-2377	3163

Damping (Ns/m) C	Clamped-Free Real	Clamped-Free Imaginary	Free-Free Real	Free-Free Imaginary	Clamped-Hinged Real	Clamped-Hinged Imaginary
0	0	907	0	5595	0	3570
100000	-240	877	-228	5590	-230	3563
200000	-485	779	-456	5578	-430	3541
300000	-747	581	-684	5557	-689	3505
400000	-1226	216	-913	5527	-919	3454
500000	-1857	146	-1142	5489	-1150	3386
600000	-2390	131	-1372	5442	-1381	3302
700000	-2889	124	-1602	5386	-1613	3200
800000	-3373	120	-1833	5320	-1846	3078
900000	-3848	117	-2065	5245	-2081	2933
1000000	-4316	115	-2299	5159	-2318	2762

$$W_u(\zeta) = A_1e^{s_1\zeta} + A_2e^{s_2\zeta} + A_3e^{s_3\zeta} + A_4e^{s_4\zeta} \tag{8}$$

$$W_\psi(\zeta) = B_1e^{s_1\zeta} + B_2e^{s_2\zeta} + B_3e^{s_3\zeta} + B_4e^{s_4\zeta} \tag{9}$$

where

$$s_{1,2,3,4} = \pm\sqrt{\frac{-k_2 \pm \sqrt{k_2^2 - 4k_1k_3}}{2k_1}} \tag{10}$$

$$k_1 = -\frac{\kappa GE}{\rho^2 l^4}$$

$$k_2 = \frac{1}{\rho l^2}\left[(\kappa G + E)\lambda^2 + \left(E\frac{c}{\rho A} - i\frac{\kappa G\Omega J_z}{\rho I}\right)\lambda\right]$$

$$k_3 = -\lambda^4 + \left(-\frac{c}{\rho A} + i\frac{\Omega J_z}{\rho I}\right)\lambda^3 + \left(-\frac{\kappa AG}{\rho I} + i\frac{\Omega J_z c}{\rho^2 AI}\right)\lambda^2 - \frac{\kappa Gc}{\rho^2 I}\lambda. \tag{11}$$

$A_1 - A_4$ and $B_1 - B_4$ in Eqs. (8) and (9) are complex integration constants. Since only half of the integration constants, $A_1 - A_4$ or $B_1 - B_4$, are independent, a relationship between A_i and B_i can be found by substituting Eqs. (8) and (9) into Eq. (6) or Eq. (7).

3 Determination of Complex Eigenvalues and Complex Normal Modes

By applying boundary conditions (Zu and Han, 1992) to Eqs. (8) and (9), a set of four simultaneous, homogeneous equations in terms of A_1, A_2, A_3, and A_4 will be generated. For a nontrivial solution, the determinant of the A_i coefficient matrix is set to equal zero. The resulting characteristic equation can be split into real and imaginary components. Consequently, two real nonlinear equations in terms of two real unknowns, λ_R and λ_I, are obtained:

$$\Delta_R = f_1(\lambda_R, \lambda_I) \tag{12}$$

$$\Delta_I = f_2(\lambda_R, \lambda_I). \tag{13}$$

Due to the high nonlinearity and the complexity of Eqs. (12) and (13), obtaining explicit expressions for f_1 and f_2 is too cumbersome and virtually impossible, even with the aid of mathematical symbolic packages. Therefore, a numerical scheme based on a standard root solver is adopted to solve the eigenvalues without explicit expressions for f_1 and f_2. Initial guesses for λ_R and λ_I are given and the values for Δ_R and Δ_I are calculated to check whether they are equal to zero. This step is repeated until both values of Δ_R and Δ_I converge to within a tolerance value.

4 Numerical Simulations

Numerical simulations of an externally damped, spinning Timoshenko beam for each of the six different boundary conditions (Zu and Han, 1992) are presented here. The same data and the same parameters $\bar{\Omega} = 2.5$ and $\beta = 0.15$ are used.

Table 1 shows the variation of the first complex frequency with damping coefficient c in each boundary condition. Only forward precession frequencies are presented. For $c = 0$, the results agree completely with the undamped natural frequencies obtained in Zu and Han (1992). It is shown that with the increase of damping, the natural frequency, which is the imaginary component of the complex frequency, is decreasing. As well, the real component, which reflects the rate of decay of the vibration, increases in value. Note in every case, except for clamped-free, the real component decrease linearly. This is consistent with single-degree-of-freedom systems with damping.

5 Conclusions

A free-vibration analysis of an externally damped spinning Timoshenko beam with general boundary conditions is performed analytically for the first time. It is found from numerical simulations that the real component of the complex natural frequency increases in value linearly with damping, where the imaginary component decrease nonlinearly.

References

Argento, A., 1995, "A Spinning Beam Subjected to a Moving Deflection Dependent Load, Part I: Response and Resonance," *Journal of Sound and Vibration,* Vol. 182, pp. 595–615.

Lee, H. P., 1995, "Dynamic Response of a Rotating Timoshenko Shaft Subjected to Axial Forces and Moving Loads," *Journal of Sound and Vibration,* Vol. 181, pp. 169–177.

Medgyesi, E., 1991, "Stability of a Simple Rotor with Nonlinear Internal Damping," *ASME Vibration Analysis—Analytical and Computational,* DE-Vol. 37, pp. 233–237.

Singh, M. P., and Abdelnaser, A. S., 1993, "Random Vibrations of Externally Damped Viscoelastic Timoshenko Beams With General Boundary Conditions," ASME JOURNAL OF APPLIED MECHANICS, Vol. 60, pp. 149–156.

Tan, C. A., and Kuang, W., 1995, "Vibration of a Rotating Discontinuous Shaft by the Distributed Transfer Function Method," *Journal of Sound and Vibration,* Vol. 183, pp. 451–474.

Zu, J. W., and Han, R. P. S., 1992, "Natural Frequencies and Normal Modes of a Spinning Timoshenko Beam With General Boundary Conditions," ASME JOURNAL OF APPLIED MECHANICS, Vol. 59, pp. 197–204.

Pseudo-Linear Vibro-Impact System With a Secondary Structure: Response to a White-Noise Excitation

M. F. Dimentberg[1] and H. G. Haenisch[1,2]

Introduction

Many structural systems can be modeled for a dynamic analysis by a primary mass, suspended on nonlinear spring(s), with a linear secondary structure attached to this mass. A two-step procedure for response prediction of such a structure to an excitation, applied to the primary mass, may be based on a so-called "cascade" approximation, which actually implies decomposition of the original nonlinear multi-degree-of-freedom system into a nonlinear single-degree-of-freedom one and a linear multi-degree-of-freedom one. The advantage of the procedure is that it does not need to rely on any assumption(s) of small nonlinearity.

Step 1. Response prediction for a single-degree-of-freedom nonlinear system, as obtained from the original one by assuming a *rigid* attachment of the secondary structure to the primary one.

Step 2. Response of the primary mass, as predicted at the Step 1, is considered as a base excitation for the (linear) secondary structure, with subsequent predictions being straightforward, provided that all necessary information of the base excitation is available.

The approximation should certainly be adequate for the cases, where secondary mass is small compared with the primary one. This sufficient condition may be relaxed sometimes, particularly if suspension springs of the secondary structure are much stiffer than those of the primary one—such as in case of a moored body with (small) primary suspension stiffness being solely due to buoyancy. This topic, however, will not be considered here.

The above procedure seems to be straightforward for the case of a sinusoidal excitation of the primary mass. However, in case of a random excitation it faces an intrinsic difficulty due to necessity for predicting the power spectral density of the primary mass response at the Step 1. The latter problem is very difficult, even for a single-degree-of-freedom system under a white-noise excitation. Thus, any approximate analytical method (e.g., based on moment closure), as well as a direct numerical (Monte-Carlo) simulation study, may benefit from some benchmark exact solution that can be used to check accuracy of the analytical or numerical results.

Such a solution is actually available for the case, where nonlinearity in the suspension is due to a rigid barrier at the system's static equilibrium position, with perfectly elastic rebound of the mass after impact. For the case of a white-noise excitation of such a "pseudo-linear" system a closed-form exact solution for the autocorrelation function of the response has been obtained by Dimentberg et al. (1995). The corresponding power spectral density of the response acceleration is studied in this brief note, both analytically and numerically. It is shown that this power spectral density has peaks at even integer multiples (harmonics) of the natural frequency of the system without barrier, the heights of the peaks decreasing with the number of the harmonic. Furthermore, asymptotic evaluation of the integral expression for the power spectral density at high frequencies indicates that the power spectral density of the response acceleration approaches a constant value and provides an explicit formula for this limiting level within the "inertia-dominated range." This formula illustrates strong influence of the impacts for lightly damped systems. The results are used for predicting mean-square response of the secondary mass to a base excitation from the primary one. While these results seem to be of importance mostly as benchmark ones, for developing and/or testing various procedures for approximate analysis and/or numerical simulation, they also may be of a direct use for a moored body with a weightless inextensible mooring line, which doesn't have any slack or preload at its static equilibrium position.

Autocorrelation Function and Power Spectral Density of the Primary Mass Response

A single-degree-of-freedom system is considered, which has a rigid barrier at its static equilibrium position $y = 0$. The system's motion between impacts is governed by equation

$$\ddot{y} + 2\alpha\dot{y} + \Omega^2 y = \zeta(t),\ y > 0 \tag{1}$$

where $\zeta(t)$ is a stationary zero-mean Gaussian white-noise with intensity D. The condition for perfectly elastic impact at $y = 0$ can be written as

$$\dot{y}_+ = -\dot{y}_-,\ \dot{y}_\pm = \dot{y}(t_* \pm 0),\ y(t_*) = 0 \tag{2}$$

where subscripts minus and plus are used for values of the velocity immediately before and after the impact instant t_*. Dimentberg et al. (1995) obtained for this system the following exact solution for the autocorrelation function $K_{yy}(\tau)$ of the stationary response $y(t)$ (the solution is based on a certain piecewise-linear transformation of state variables, as proposed originally by Zhuravlev (1976), which makes the new state variables continuous at the impact instants, thereby transferring all nonlinearity to the transformation and reducing the nonlinear system (1), (2) to a linear one)

$$K_{yy}(\tau) = (2\sigma^2/\pi)[R(\tau)\sin^{-1}R(\tau) + \sqrt{1 - R^2(\tau)}]$$
$$R(\tau) = \exp(-\alpha|\tau|)\cdot[\cos\omega_d\tau + (\alpha/\omega_d)\sin\omega_d|\tau|],$$
$$\omega_d = \sqrt{\Omega^2 - \alpha^2},\ \sigma^2 = D/4\alpha\Omega^2. \tag{3}$$

[1] Mechanical Engineering Department, Worcester Polytechnic Institute, 100 Institute Road, Worcester, MA 01609.

[2] Presently with Raytheon Co., 1001 Boston Post Road, Marlborough, MA 01752.

Contributed by the Applied Mechanics Division of THE AMERICAN SOCIETY OF MECHANICAL ENGINEERS for publication in the ASME JOURNAL OF APPLIED MECHANICS. Manuscript received by the ASME Applied Mechanics Division, July 8, 1997; final revision, Jan. 10, 1998. Associate Technical Editor: M. Shinozuka.

simulations that the real component of the complex natural frequency increases in value linearly with damping, where the imaginary component decrease nonlinearly.

References

Argento, A., 1995, "A Spinning Beam Subjected to a Moving Deflection Dependent Load, Part I: Response and Resonance," *Journal of Sound and Vibration,* Vol. 182, pp. 595–615.

Lee, H. P., 1995, "Dynamic Response of a Rotating Timoshenko Shaft Subjected to Axial Forces and Moving Loads," *Journal of Sound and Vibration,* Vol. 181, pp. 169–177.

Medgyesi, E., 1991, "Stability of a Simple Rotor with Nonlinear Internal Damping," *ASME Vibration Analysis—Analytical and Computational,* DE-Vol. 37, pp. 233–237.

Singh, M. P., and Abdelnaser, A. S., 1993, "Random Vibrations of Externally Damped Viscoelastic Timoshenko Beams With General Boundary Conditions," ASME JOURNAL OF APPLIED MECHANICS, Vol. 60, pp. 149–156.

Tan, C. A., and Kuang, W., 1995, "Vibration of a Rotating Discontinuous Shaft by the Distributed Transfer Function Method," *Journal of Sound and Vibration,* Vol. 183, pp. 451–474.

Zu, J. W., and Han, R. P. S., 1992, "Natural Frequencies and Normal Modes of a Spinning Timoshenko Beam With General Boundary Conditions," ASME JOURNAL OF APPLIED MECHANICS, Vol. 59, pp. 197–204.

Pseudo-Linear Vibro-Impact System With a Secondary Structure: Response to a White-Noise Excitation

M. F. Dimentberg[1] and H. G. Haenisch[1,2]

Introduction

Many structural systems can be modeled for a dynamic analysis by a primary mass, suspended on nonlinear spring(s), with a linear secondary structure attached to this mass. A two-step procedure for response prediction of such a structure to an excitation, applied to the primary mass, may be based on a so-called "cascade" approximation, which actually implies decomposition of the original nonlinear multi-degree-of-freedom system into a nonlinear single-degree-of-freedom one and a linear multi-degree-of-freedom one. The advantage of the procedure is that it does not need to rely on any assumption(s) of small nonlinearity.

Step 1. Response prediction for a single-degree-of-freedom nonlinear system, as obtained from the original one by assuming a *rigid* attachment of the secondary structure to the primary one.

Step 2. Response of the primary mass, as predicted at the Step 1, is considered as a base excitation for the (linear) secondary structure, with subsequent predictions being straightforward, provided that all necessary information of the base excitation is available.

The approximation should certainly be adequate for the cases, where secondary mass is small compared with the primary one. This sufficient condition may be relaxed sometimes, particularly if suspension springs of the secondary structure are much stiffer than those of the primary one—such as in case of a moored body with (small) primary suspension stiffness being solely due to buoyancy. This topic, however, will not be considered here.

The above procedure seems to be straightforward for the case of a sinusoidal excitation of the primary mass. However, in case of a random excitation it faces an intrinsic difficulty due to necessity for predicting the power spectral density of the primary mass response at the Step 1. The latter problem is very difficult, even for a single-degree-of-freedom system under a white-noise excitation. Thus, any approximate analytical method (e.g., based on moment closure), as well as a direct numerical (Monte-Carlo) simulation study, may benefit from some benchmark exact solution that can be used to check accuracy of the analytical or numerical results.

Such a solution is actually available for the case, where nonlinearity in the suspension is due to a rigid barrier at the system's static equilibrium position, with perfectly elastic rebound of the mass after impact. For the case of a white-noise excitation of such a "pseudo-linear" system a closed-form exact solution for the autocorrelation function of the response has been obtained by Dimentberg et al. (1995). The corresponding power spectral density of the response acceleration is studied in this brief note, both analytically and numerically. It is shown that this power spectral density has peaks at even integer multiples (harmonics) of the natural frequency of the system without barrier, the heights of the peaks decreasing with the number of the harmonic. Furthermore, asymptotic evaluation of the integral expression for the power spectral density at high frequencies indicates that the power spectral density of the response acceleration approaches a constant value and provides an explicit formula for this limiting level within the "inertia-dominated range." This formula illustrates strong influence of the impacts for lightly damped systems. The results are used for predicting mean-square response of the secondary mass to a base excitation from the primary one. While these results seem to be of importance mostly as benchmark ones, for developing and/or testing various procedures for approximate analysis and/or numerical simulation, they also may be of a direct use for a moored body with a weightless inextensible mooring line, which doesn't have any slack or preload at its static equilibrium position.

Autocorrelation Function and Power Spectral Density of the Primary Mass Response

A single-degree-of-freedom system is considered, which has a rigid barrier at its static equilibrium position $y = 0$. The system's motion between impacts is governed by equation

$$\ddot{y} + 2\alpha\dot{y} + \Omega^2 y = \zeta(t),\ y > 0 \tag{1}$$

where $\zeta(t)$ is a stationary zero-mean Gaussian white-noise with intensity D. The condition for perfectly elastic impact at $y = 0$ can be written as

$$\dot{y}_+ = -\dot{y}_-,\ \dot{y}_\pm = \dot{y}(t_* \pm 0),\ y(t_*) = 0 \tag{2}$$

where subscripts minus and plus are used for values of the velocity immediately before and after the impact instant t_*. Dimentberg et al. (1995) obtained for this system the following exact solution for the autocorrelation function $K_{yy}(\tau)$ of the stationary response $y(t)$ (the solution is based on a certain piecewise-linear transformation of state variables, as proposed originally by Zhuravlev (1976), which makes the new state variables continuous at the impact instants, thereby transferring all nonlinearity to the transformation and reducing the nonlinear system (1), (2) to a linear one)

$$K_{yy}(\tau) = (2\sigma^2/\pi)[R(\tau)\sin^{-1}R(\tau) + \sqrt{1 - R^2(\tau)}]$$
$$R(\tau) = \exp(-\alpha|\tau|)\cdot[\cos\omega_d\tau + (\alpha/\omega_d)\sin\omega_d|\tau|],$$
$$\omega_d = \sqrt{\Omega^2 - \alpha^2},\ \sigma^2 = D/4\alpha\Omega^2. \tag{3}$$

[1] Mechanical Engineering Department, Worcester Polytechnic Institute, 100 Institute Road, Worcester, MA 01609.

[2] Presently with Raytheon Co., 1001 Boston Post Road, Marlborough, MA 01752.

Contributed by the Applied Mechanics Division of THE AMERICAN SOCIETY OF MECHANICAL ENGINEERS for publication in the ASME JOURNAL OF APPLIED MECHANICS. Manuscript received by the ASME Applied Mechanics Division, July 8, 1997; final revision, Jan. 10, 1998. Associate Technical Editor: M. Shinozuka.

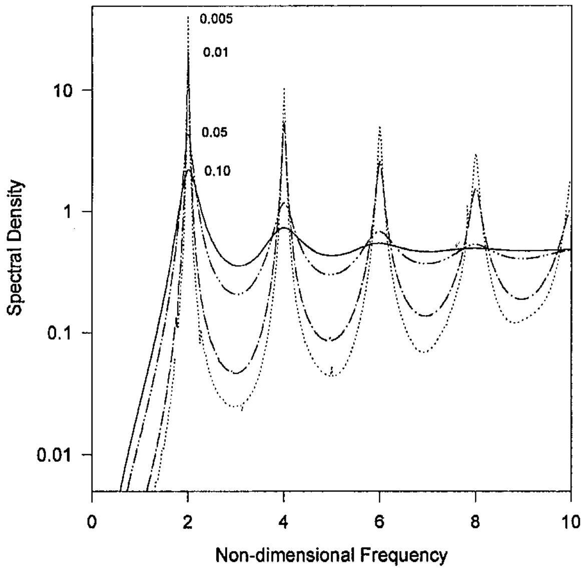

Fig. 1 Response acceleration power spectral densities for various damping ratios of the primary mass α/Ω. The nondimensional frequency is ω/Ω.

The power spectral density of the zero-mean part of the response $y(t)$ can be obtained now as a Fourier transform

$$\Phi_{yy}(\omega) = \frac{1}{2\pi}\int_{-\infty}^{\infty}[K_{yy}(\tau) - K_{yy}(\infty)]e^{-i\omega\tau}d\tau$$
$$= \frac{1}{\pi}\int_{0}^{\infty}[K_{yy}(\tau) - K_{yy}(\infty)]\cos\omega\tau d\tau. \quad (4)$$

Expansion of expression (3) for $K_{yy}(\tau)$ in a power series in $R^2(\tau)$, which converges for nonzero time shifts (where $R < 1$), and thus for finite frequencies for power spectral density shows that the response power spectral density has peaks at

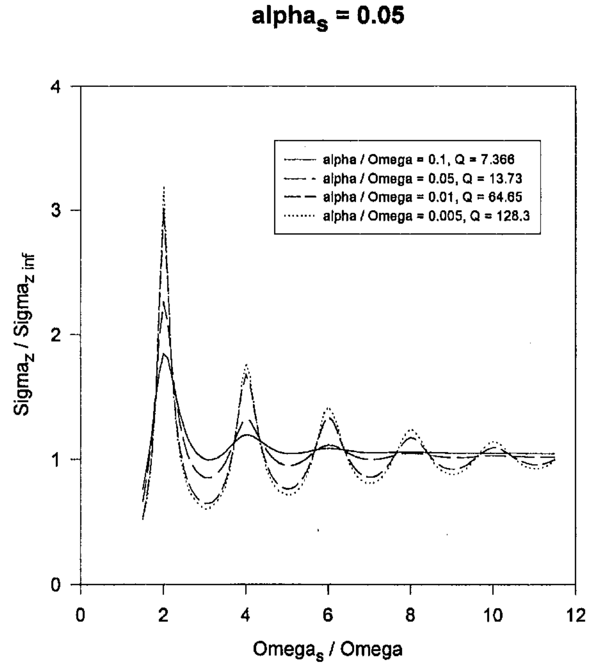

Fig. 3 Normalized rms displacement of the secondary mass $\sigma_z/\sigma_{z\infty}$ versus natural frequency ratio Ω_s/Ω for several values of the primary damping ratio α/Ω and secondary damping ratio $\alpha_s/\Omega_s = 0.05$.

even harmonics of the system's natural frequency without barrier. The peaks are attenuated with increasing harmonic number, the attenuation rate increasing with damping ratio α/Ω. These conclusions are clearly supported by the numerical integration results as presented in Fig. 1 for several values of the damping ratio.

On the other hand, it is worthwhile to study asymptotic behavior of the response power spectral density at high frequencies, by using successive integration by parts (Bender and Ors-

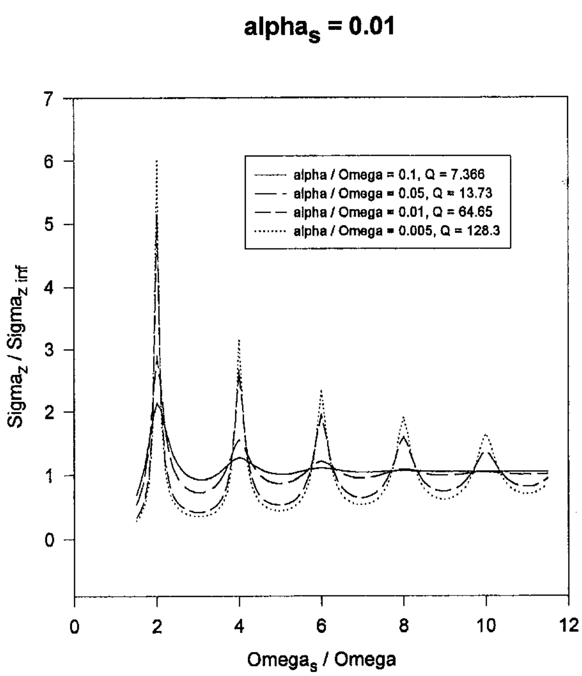

Fig. 2 Normalized rms displacement of the secondary mass $\sigma_z^2/\sigma_{z\infty}^2$ versus natural frequency ratio Ω_s/Ω for several values of the primary damping ratio α/Ω and secondary damping ratio $\alpha_s/\Omega_s = 0.01$

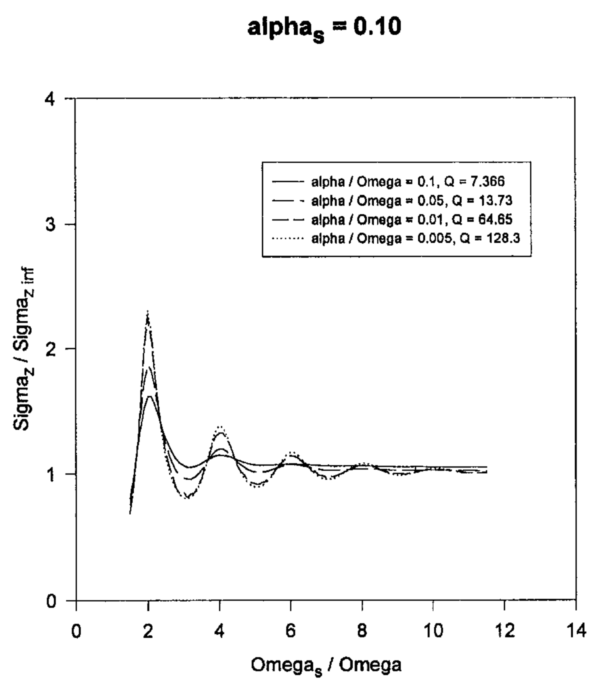

Fig. 4 Normalized rms displacement of the secondary mass $\sigma_z/\sigma_{z\infty}$ versus natural frequency ratio Ω_s/Ω for several values of the primary damping ratio α/Ω and secondary damping ratio $\alpha_s/\Omega_s = 0.1$.

zag, 1978). As long as each integration brings an additional factor ω into denominator, the first nonzero term in the sequence will be a leading one in the expansion in the inverse powers of frequency. This leading term is found to be

$$\Phi_{yy}(\omega) = (\Omega^3/\pi\omega^4)K'''_{yy}(0) + o(\omega^{-4}) \quad (5)$$

so that using formula (3) yields

$$\lim_{\omega\to\infty}\Phi_{\ddot{y}\ddot{y}}(\omega) = \lim_{\omega\to\infty}\omega^4\Phi_{yy}(\omega) = (D/2\pi)Q,$$
$$Q = 1 + 2\Omega/\pi\alpha. \quad (6)$$

The first co-factor in formula (4) for the limiting value of the response acceleration power spectral density is seen to be just a power spectral density of the original white-noise excitation in the Eq. (1). Therefore, it corresponds to the response acceleration power spectral density *of the (linear) system without a barrier* in the ''inertia-dominated'' high-frequency range. The factor Q may be called an ''impact magnification factor,'' as long as it appears solely due to impacts. The expression (6) shows that the influence of the impacts persists to indefinitely high frequencies, and relative contribution of the impacts, as governed by the second term in the expression for Q, may be quite large, particularly for lightly damped systems. This dominating contribution of the impacts may form a basis for developing a procedure for approximate analysis for the cases, which are not amenable to exact solution.

Mean-Square Response of a Secondary Structure

Consider now the response $y(t)$ as a base excitation for the (linear) secondary structure according to the ''cascade'' approximation. For simplicity, the case of a single secondary response variable $z(t)$ will be considered, with the corresponding transfer function from base acceleration to this variable being denoted as $H_s(i\omega)$. Then the mean-square response of the secondary structure can be represented as

$$\langle z^2 \rangle = \sigma_z^2 = \int_{-\infty}^{\infty} |H_s^2(\omega)|\omega^4\Phi_{yy}(\omega)d\omega. \quad (7)$$

Specific results of numerical integration are presented below for the case, where $z(t)$ is a relative displacement of a secondary mass-spring-dashpot system with natural frequency and damping ratio Ω_s, α_s/Ω_s, respectively, so that

$$H_s(i\omega) = (-\omega^2 + 2i\omega\alpha_s + \Omega_s^2)^{-1}. \quad (8)$$

It can be seen from the Eqs. (7) and (8), that if Ω_s is very large compared with Ω and lies far enough within the inertia-dominated frequency range—one with a constant power spectral density of the base acceleration—then the rms relative displacement of the secondary mass should approach the limiting value $\sigma_{z\infty}^2 = (D/4\alpha_s\Omega_s^2)Q = \sigma^2(\alpha/\alpha_s)(\Omega/\Omega_s)^2Q$. The convergence to this limit is illustrated by the results of numerical integration according to Eqs. (4), (7), and (8), as presented in Figs. 2, 3 and 4, for values of the secondary system's damping ratio $\alpha_s/\Omega_s = 0.01$; 0.05 and 0.1, respectively. Each figure contain a set of curves of $\sigma_z/\sigma_{z\infty}$ versus secondary/primary natural frequency ratio Ω_s/Ω for several selected values of the primary system's damping ratio α/Ω. Each curve approaches, as expected, the unit level, which corresponds to the predicted inertia-dominated limit, *accounting for the impacts via factor Q according to the formula (6).* All curves exhibit resonant peaks at even integer values of the natural frequency ratio. Decreasing primary and/or secondary system's damping ratio is seen to make the peaks more sharp and less rapidly attenuated with increasing natural frequency ratio.

Finally, a comment can be made on accounting for possible impact losses, as described by a restitution factor $r < 1$, introduced into an RHS of the impact condition (2). Asymptotic analysis by stochastic averaging shows (Dimentberg, 1988) that it can be done for small values of $1 - r$ by using an equivalent apparent viscous damping ratio $\alpha/\Omega + (1 - r)/\pi$ (this can be also shown easily by considering free decaying vibrations with impacts and enforcing the condition of same rebound velocities at each two consecutive cycles as one for equivalence between systems with impact damping and with viscous one). Of course the results should be regarded then as approximate ones, their accuracy increasing with decreasing $1 - r$ (decreasing impact losses).

Acknowledgment

This work was sponsored by ONR-URI Grant No. N00014-93-1-0917. This support is greatfully acknowledged.

References

Bender, C. M., and Orszag, S. A., 1976, *Advanced Mathematical Methods for Scientists and Engineers*, McGraw-Hill, New York.

Dimentberg, M. F., 1988, *Statistical Dynamics of Nonlinear and Time-Varying Systems*, Research Studies Press, Taunton, UK.

Dimentberg, M. F., Hou, Z., and Noori, M., 1995, ''Spectral Density of a Non-Linear Single-Degree-of-Freedom System's Response to a White-Noise Random Excitation: A Unique Case of an Exact Solution,'' *International Journal of Non-Linear Mechanics*, Vol. 30, No 5, pp. 673–676.

Zhuravlev, V. F., 1976, ''A Method for Analyzing Vibration-Impact Systems by means of Special Functions,'' *Mech. Solids*, Vol. 11, pp. 23–27.

Lateral Vibration Instability Mechanisms in a Constrained Rotating String

Jifang Tian[1,3] and S. G. Hutton[2,3]

1 Introduction

The development of instabilities due to lateral vibration is of concern in many industries with applications as diverse as floppy disk drives and guided saw blades. In such systems, energy provided to drive the system in rotation may be diverted, by virtue of interaction between the rotating and the nonrotating components, into unwanted vibration of the system.

Iwan and Moeller (1976), Hutton et al. (1987), Ono, Chen, and Bogy (1991), and other researchers have analyzed mathematically the vibration characteristics of a constrained rotating disk. However, these investigations have not concentrated on defining the physical mechanisms that are responsible for the development of the instabilities that occur in such systems. Shen and Mote (1991) presented an explanation of the instability mechanisms of a stationary circular plate subjected to a rotating spring-dashpot-mass system. However, in general, the physical mechanisms involved in the instabilities that occur in constrained rotating disks have not been adequately explained in previous papers, especially for instability mechanisms caused by an arbitrary interactive conservative or nonconservative force. In the present note the string model considered by Yang and Hutton (1995), which contains the essential elements of

[1] Graduate Student.

[2] Professor. Mem. ASME.

[3] Department of Mechanical Engineering, University of British Columbia, Vancouver, BC V6T 1Z4, Canada.

Contributed by the Applied Mechanics Division of THE AMERICAN SOCIETY OF MECHANICAL ENGINEERS for publication in the ASME JOURNAL OF APPLIED MECHANICS. Manuscript received by the ASME Applied Mechanics Division, May 1, 1997; final revision, Dec. 18, 1997. Associate Technical Editor: M. Ortiz.

zag, 1978). As long as each integration brings an additional factor ω into denominator, the first nonzero term in the sequence will be a leading one in the expansion in the inverse powers of frequency. This leading term is found to be

$$\Phi_{yy}(\omega) = (\Omega^3/\pi\omega^4)K'''_{yy}(0) + o(\omega^{-4}) \quad (5)$$

so that using formula (3) yields

$$\lim_{\omega\to\infty}\Phi_{\ddot{y}\ddot{y}}(\omega) = \lim_{\omega\to\infty}\omega^4\Phi_{yy}(\omega) = (D/2\pi)Q,$$
$$Q = 1 + 2\Omega/\pi\alpha. \quad (6)$$

The first co-factor in formula (4) for the limiting value of the response acceleration power spectral density is seen to be just a power spectral density of the original white-noise excitation in the Eq. (1). Therefore, it corresponds to the response acceleration power spectral density *of the (linear) system without a barrier* in the "inertia-dominated" high-frequency range. The factor Q may be called an "impact magnification factor," as long as it appears solely due to impacts. The expression (6) shows that the influence of the impacts persists to indefinitely high frequencies, and relative contribution of the impacts, as governed by the second term in the expression for Q, may be quite large, particularly for lightly damped systems. This dominating contribution of the impacts may form a basis for developing a procedure for approximate analysis for the cases, which are not amenable to exact solution.

Mean-Square Response of a Secondary Structure

Consider now the response $y(t)$ as a base excitation for the (linear) secondary structure according to the "cascade" approximation. For simplicity, the case of a single secondary response variable $z(t)$ will be considered, with the corresponding transfer function from base acceleration to this variable being denoted as $H_s(i\omega)$. Then the mean-square response of the secondary structure can be represented as

$$\langle z^2 \rangle = \sigma_z^2 = \int_{-\infty}^{\infty} |H_s^2(\omega)|\omega^4\Phi_{yy}(\omega)d\omega. \quad (7)$$

Specific results of numerical integration are presented below for the case, where $z(t)$ is a relative displacement of a secondary mass-spring-dashpot system with natural frequency and damping ratio Ω_s, α_s/Ω_s, respectively, so that

$$H_s(i\omega) = (-\omega^2 + 2i\omega\alpha_s + \Omega_s^2)^{-1}. \quad (8)$$

It can be seen from the Eqs. (7) and (8), that if Ω_s is very large compared with Ω and lies far enough within the inertia-dominated frequency range—one with a constant power spectral density of the base acceleration—then the rms relative displacement of the secondary mass should approach the limiting value $\sigma_{z\infty}^2 = (D/4\alpha_s\Omega_s^2)Q = \sigma^2(\alpha/\alpha_s)(\Omega/\Omega_s)^2Q$. The convergence to this limit is illustrated by the results of numerical integration according to Eqs. (4), (7), and (8), as presented in Figs. 2, 3 and 4, for values of the secondary system's damping ratio $\alpha_s/\Omega_s = 0.01$; 0.05 and 0.1, respectively. Each figure contain a set of curves of $\sigma_z/\sigma_{z\infty}$ versus secondary/primary natural frequency ratio Ω_s/Ω for several selected values of the primary system's damping ratio α/Ω. Each curve approaches, as expected, the unit level, which corresponds to the predicted inertia-dominated limit, *accounting for the impacts via factor Q according to the formula (6)*. All curves exhibit resonant peaks at even integer values of the natural frequency ratio. Decreasing primary and/or secondary system's damping ratio is seen to make the peaks more sharp and less rapidly attenuated with increasing natural frequency ratio.

Finally, a comment can be made on accounting for possible impact losses, as described by a restitution factor $r < 1$, introduced into an RHS of the impact condition (2). Asymptotic analysis by stochastic averaging shows (Dimentberg, 1988) that it can be done for small values of $1 - r$ by using an equivalent apparent viscous damping ratio $\alpha/\Omega + (1 - r)/\pi$ (this can be also shown easily by considering free decaying vibrations with impacts and enforcing the condition of same rebound velocities at each two consecutive cycles as one for equivalence between systems with impact damping and with viscous one). Of course the results should be regarded then as approximate ones, their accuracy increasing with decreasing $1 - r$ (decreasing impact losses).

Acknowledgment

This work was sponsored by ONR-URI Grant No. N00014-93-1-0917. This support is greatfully acknowledged.

References

Bender, C. M., and Orszag, S. A., 1976, *Advanced Mathematical Methods for Scientists and Engineers*, McGraw-Hill, New York.

Dimentberg, M. F., 1988, *Statistical Dynamics of Nonlinear and Time-Varying Systems*, Research Studies Press, Taunton, UK.

Dimentberg, M. F., Hou, Z., and Noori, M., 1995, "Spectral Density of a Non-Linear Single-Degree-of-Freedom System's Response to a White-Noise Random Excitation: A Unique Case of an Exact Solution," *International Journal of Non-Linear Mechanics*, Vol. 30, No 5, pp. 673–676.

Zhuravlev, V. F., 1976, "A Method for Analyzing Vibration-Impact Systems by means of Special Functions," *Mech. Solids*, Vol. 11, pp. 23–27.

Lateral Vibration Instability Mechanisms in a Constrained Rotating String

Jifang Tian[1,3] and S. G. Hutton[2,3]

1 Introduction

The development of instabilities due to lateral vibration is of concern in many industries with applications as diverse as floppy disk drives and guided saw blades. In such systems, energy provided to drive the system in rotation may be diverted, by virtue of interaction between the rotating and the nonrotating components, into unwanted vibration of the system.

Iwan and Moeller (1976), Hutton et al. (1987), Ono, Chen, and Bogy (1991), and other researchers have analyzed mathematically the vibration characteristics of a constrained rotating disk. However, these investigations have not concentrated on defining the physical mechanisms that are responsible for the development of the instabilities that occur in such systems. Shen and Mote (1991) presented an explanation of the instability mechanisms of a stationary circular plate subjected to a rotating spring-dashpot-mass system. However, in general, the physical mechanisms involved in the instabilities that occur in constrained rotating disks have not been adequately explained in previous papers, especially for instability mechanisms caused by an arbitrary interactive conservative or nonconservative force. In the present note the string model considered by Yang and Hutton (1995), which contains the essential elements of

[1] Graduate Student.

[2] Professor. Mem. ASME.

[3] Department of Mechanical Engineering, University of British Columbia, Vancouver, BC V6T 1Z4, Canada.

Contributed by the Applied Mechanics Division of THE AMERICAN SOCIETY OF MECHANICAL ENGINEERS for publication in the ASME JOURNAL OF APPLIED MECHANICS. Manuscript received by the ASME Applied Mechanics Division, May 1, 1997; final revision, Dec. 18, 1997. Associate Technical Editor: M. Ortiz.

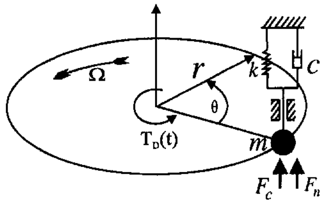

Fig. 1 A rotating string subjected to stationary interactive forces

more general problems, is further analyzed with a view to providing an analysis that illustrates, on a simple a model as possible, the physical mechanisms that are responsible for the development of vibrational instabilities.

New developments in this note involve an identification of the energy flux into the rotating system that is responsible for the instabilities and a definition of the relationship between the interactive forces involved and this energy flux.

2 Energy Flux Considerations

The idealized system under consideration is shown in Fig. 1. The equation governing the lateral vibration $u(\theta, t)$ of the circular string of radius r, rotating at a constant angular velocity Ω, and constrained by an arbitrary constraint at $(r, \theta = 0)$; together with the force boundary condition, can be expressed with respect to stationary coordinates as (Yang and Hutton, 1995):

$$u_{,tt} + 2\Omega u_{,\theta t} - [P/(\rho r^2) - \Omega^2]u_{,\theta\theta} = 0 \quad (1)$$

$$u(0, t) - u(2\pi, t) = 0,$$

$$\rho r(S^2 - \Omega^2)[u_{,\theta}(2\pi, t) - u_{,\theta}(0, t)] + F_I(0, t) = 0 \quad (2)$$

where $F_I(0, t) = F_c(0, t) + F_n(0, t)$, represents an arbitrary constraint force consisting of a conservative component $F_c(0, t)$ and a nonconservative component $F_n(0, t)$. $S^2 = P/(\rho r^2)$, P and ρ are the flexural wave speed, string tension (assumed constant), and density per unit length, respectively.

The rate of change of total vibration energy $E_{,t}$ in the system can be shown to be

$$E_{,t} = -r\Omega F_c(0, t)\bar{u}_{,s}(0, t) - F_n(0, t)[u_{,t}(0, t) + r\Omega\bar{u}_{,s}(0, t)] \quad (3)$$

where $\bar{u}_{,s}(0, t) = [u_{,\theta}(2\pi, t) + u_{,\theta}(0, t)]/(2r)$ is the average slope of the string at the constraint location. Equation (3) can also be rewritten in the following forms:

$$E_{,t} = -r\Omega[F_{\theta c}(t) + F_{\theta n}(t)] - F_n(0, t)u_{,t}(0, t)$$
$$= -\Omega T_c(t) + [-\Omega T_n(t) - F_n u_{,t}(0, t)] \quad (4)$$

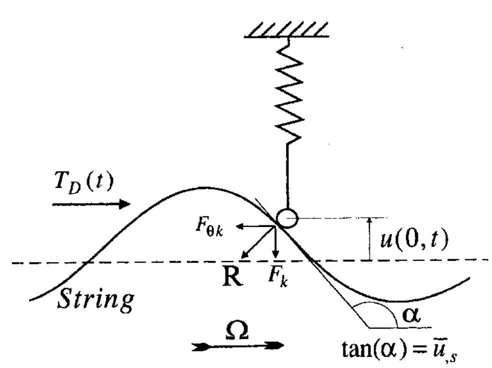

Fig. 2 Interactive forces applied to the rotating string due to a spring constraint

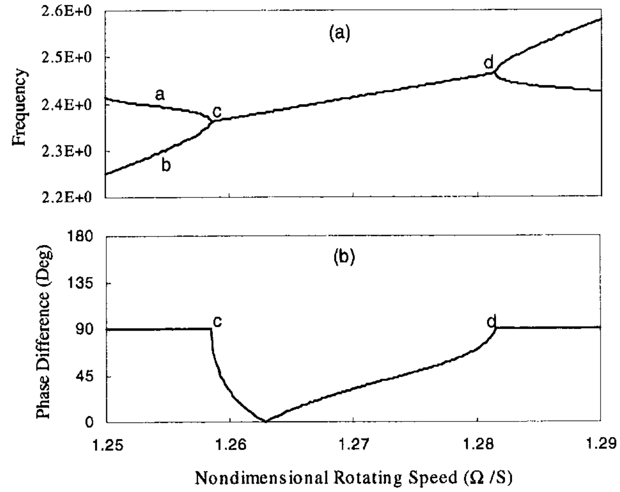

Fig. 3 Response characteristics due to stiffness constraint ($k' = kr/P = 2.0$); (*a*) modal frequencies, (*b*) the phase differences

where, $F_{\theta c}(t) = F_c(t)\bar{u}_{,s}(0, t)$ and $F_{\theta n}(t) = F_n(t)\bar{u}_{,s}(0, t)$ are the circumferential components of the interactive conservative and nonconservative forces, respectively. The torques produced by these circumferential components can be expressed as $T_c(t) = F_{\theta c}(t)r$ and $T_n(t) = F_{\theta n}(t)r$.

3 Instability Mechanisms for Some Particular Cases

Figure 2 illustrates the forces involved for the case where the constraint consists only of a linear stiffness component. The lateral component F_k of the interactive elastic force must balance the spring force $ku(0, t)$ whereas the horizontal component $F_{\theta k}(t)$ of this force will result in a torque $F_{\theta k}r$ applied to the string. This torque must be balanced by the driving torque T_D in order for the system to rotate at constant speed. If $\int(-F_{\theta k})r\Omega dt = \int(-ku(0, t))r\Omega dt > 0$, i.e., the work done by T_D is greater than zero over a complete cycle of motion, instability will result.

For the case of nonconservative forces it can be seen from Eq. (3) that the driving energy required for steady rotation will be transferred into lateral vibration if the lateral interactive force $(-F_n(t))$ is in phase with the absolute lateral velocity $\dot{u}_r(0, t) = u_{,t}(0, t) + r\Omega\bar{u}_{,s}(0, t)$, which is also the velocity measured in the coordinates rotating with the string. However, in the case of conservative forces, the system becomes unstable when the lateral force $F_c(t)$ is in phase with the slope $\bar{u}_{,s}(0, t)$, because

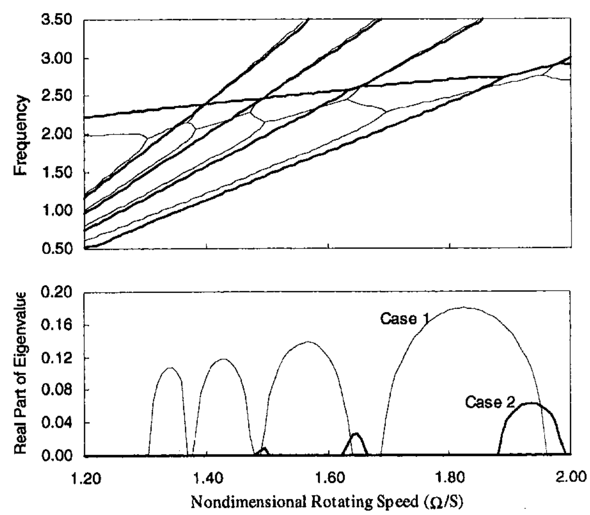

Fig. 4 Effect of system parameters on stability characteristics. Case 1: $m' = m/(\rho r) = 0.6$ and $k' = 0.0$; Case 2: $m' = 0.6$ and $k'3.31$ ($\bar{\omega}_i = 2.35$).

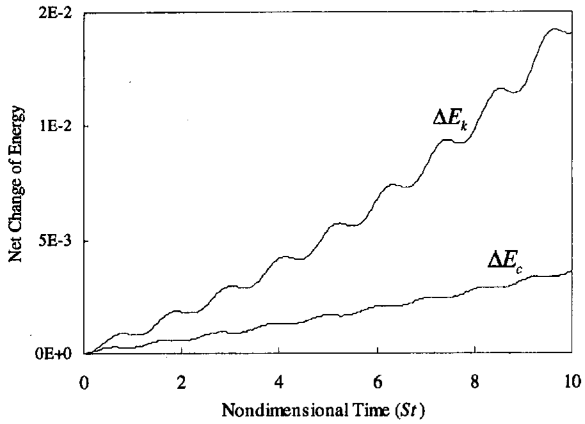

Fig. 5 Net energy changes of the fourth backward mode due to a stationary spring ($k' = 1.8$) and a viscous damper ($c' = c/\sqrt{\rho P} = 0.75$) at $\Omega' = 1.72$

the conservative forces, such as the inertial and elastic forces, are always 90 degrees out of phase with the velocity $u_{,t}(0, t)$.

When the rotating speed Ω equals the wave speed S, the backward-wave mode shape appears as a stationary wave (i.e., $u_{,tt}(0, t) = u_{,t}(0, t) = 0$) when observed from stationary coordinates. It can then be noted from Eq. (2) that divergence instability cannot occur because the interactive force $F_l(0, t)$ becomes zero when $\Omega = S$, so that $E_{,t}(t) = 0$, i.e., there is zero energy input into the system. The instabilities that occur in the present problem are either flutter or terminal instabilities.

4 Flutter and Terminal Instabilities

Flutter instability is a type of dynamic instability characterized by oscillations with increasing amplitude. The flutter instability due to a stationary stiffness (or mass) always occurs in conjunction with the coupling of two modes in a given speed region, as shown in Fig. 3(a). It can be easily proven that the phase difference between the lateral interactive force ($-ku(0, t)$) and the average slope $\bar{u}_{,si}(0, t)$ for a single mode is always 90 deg in an uncoupled region. In the flutter region, the coupled modes have identical frequencies and mode shapes. In this case the phase difference between F_{ki} and $\bar{u}_{,si}(0, t)$ varies from 90 deg to 0 deg, as shown in Fig. 3(b).

Within the flutter region, the total circumferential force generated by a constraint having both mass and stiffness characteristics is given by

$$F_c = F_{\theta k} + F_{\theta m} = m(\omega_0^2 - \omega_i^2)u(0, t)\bar{u}_{,s}(0, t) \quad (5)$$

where $\omega_0^2 = k/m$. ω_i is a frequency in the flutter region. The flutter instability can therefore be minimized by setting $\omega_0^2 = \bar{\omega}_i^2$, where $\bar{\omega}_i$ is an average frequency over the flutter region. Figure 4 illustrates four flutter instability regions before and after such a modification is made. The flutter regions reduce or even disappear due to a significant reduction of the resultant circumferential force.

Terminal instability refers to a special flutter instability which occurs at all speeds above a particular rotating speed. A typical example of terminal instability is that caused by a stationary viscous damper. For a constraint consisting only of a stationary damper, the resultant energy change in the system can be expressed from Eq. (3) as

$$\Delta E = \int_0^T F_d[u_{,t}(0, t) + r\Omega\bar{u}_{,s}(0, t)]dt$$
$$= \int_0^T [r\Omega F_d\bar{u}_{,s}(0, t) - cu_{,t}^2(0, t)]dt \quad (6)$$

where $F_d = -cu_{,t}(0, t)$. It is noted from Eq. (6) that the energy into the system equals the difference between the input energy required to overcome the resistant torque induced by the damper and the energy dissipated by the same damper. It can be shown that instability occurs only when the backward-wave mode is excited by the stationary damping force at supercritical speeds. In this case the lateral damping force is always in phase with its velocity, measured in the string-fixed coordinates, which is independent of the rotating speed.

Figure 5 shows the net energy changes for the fourth backward-wave mode caused individually by a spring and by a viscous damper that provide approximately equal transverse forces to the string. It can been seen from this figure that the net energy into the system through the damper is relatively small compared to that of the spring because the damper dissipates a portion of the input energy.

5 Conclusions

The stability characteristics of a constrained rotating string are determined by the ability of the system to divert driving energy into vibrational energy. When the interactive force between a stationary constraint and a rotating string is in phase with the absolute velocity for nonconservative forces, or in phase with the average slope $\bar{u}_{,s}(0, t)$ for conservative forces, driving energy will be switched into vibration energy which leads to unstable behavior. This behavior has been mathematically characterized in this note. The strength of the instability in a given flutter region can be minimized by choosing the natural frequency of the constraint to coincide with a frequency in the instability region.

References

Hutton, S. G., Chonan, S., and Lehmann, B. F., 1987, "Dynamics Response of a Guided Circular Saw," *Journal of Sound and Vibration*, Vol. 112, No. 3, pp. 527–539.

Iwan, W. D., and Moeller, T. L., 1976, "The Stability of a Spinning Elastic Disk With a Transverse Load System," ASME JOURNAL OF APPLIED MECHANICS, Vol. 43, pp. 485–490.

Ono, K., Chen, J. S., and Bogy, D. B., 1991, "Stability Analysis for the Head-Disk Interface in a Flexible Disk Drive," ASME JOURNAL OF APPLIED MECHANICS, Vol. 58, pp. 1005–1014.

Shen, I. Y., and Mote Jr., C. D., 1991, "On the Mechanism of Instability of a Circular Plate under a Rotating Spring-Mass-Dashpot," *Journal of Sound and Vibration*, Vol. 148, No. 2, pp. 307–318.

Yang, L., and Hutton, S. G., 1995, "Interactions between an Idealized Rotating String and Stationary Constraints," *Journal of Sound and Vibration*, Vol. 185, pp. 139–154.

Circular Arc Rigid Line Problem With Loading On-Line

Y. Z. Chen[1]

1 Introduction

The significance of the rigid line problem was pointed by Dundurs and Markenscoff (1989). The singular integral equation approach was suggested to solve the curve rigid line prob-

[1] Guest researcher at the Laboratory for Nonlinear Mechanics of Continuous Media, Institute of Mechanics, Chinese Academy of Sciences, Beijing 100080, P. R. China. Permanent address: Division of Engineering Mechanics, Jiangsu University of Science and Technology, Zhenjiang, Jiangsu 212013, P. R. China.

Contributed by the Applied Mechanics Division of THE AMERICAN SOCIETY OF MECHANICAL ENGINEERS for publication in the ASME JOURNAL OF APPLIED MECHANICS. Manuscript received by the ASME Applied Mechanics Division, Aug. 26, 1997; final revision, Jan. 23, 1998. Associate Technical Editor: J. R. Barber.

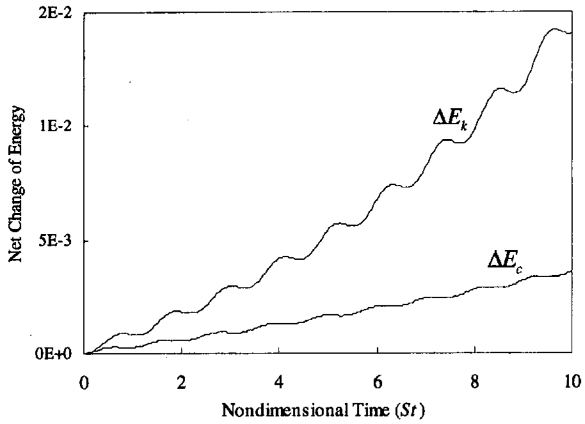

Fig. 5 Net energy changes of the fourth backward mode due to a stationary spring ($k' = 1.8$) and a viscous damper ($c' = c/\sqrt{\rho P} = 0.75$) at $\Omega' = 1.72$

the conservative forces, such as the inertial and elastic forces, are always 90 degrees out of phase with the velocity $u_{,t}(0, t)$.

When the rotating speed Ω equals the wave speed S, the backward-wave mode shape appears as a stationary wave (i.e., $u_{,tt}(0, t) = u_{,t}(0, t) = 0$) when observed from stationary coordinates. It can then be noted from Eq. (2) that divergence instability cannot occur because the interactive force $F_l(0, t)$ becomes zero when $\Omega = S$, so that $E_{,t}(t) = 0$, i.e., there is zero energy input into the system. The instabilities that occur in the present problem are either flutter or terminal instabilities.

4 Flutter and Terminal Instabilities

Flutter instability is a type of dynamic instability characterized by oscillations with increasing amplitude. The flutter instability due to a stationary stiffness (or mass) always occurs in conjunction with the coupling of two modes in a given speed region, as shown in Fig. 3(*a*). It can be easily proven that the phase difference between the lateral interactive force ($-ku(0, t)$) and the average slope $\bar{u}_{,si}(0, t)$ for a single mode is always 90 deg in an uncoupled region. In the flutter region, the coupled modes have identical frequencies and mode shapes. In this case the phase difference between F_{ki} and $\bar{u}_{,si}(0, t)$ varies from 90 deg to 0 deg, as shown in Fig. 3(*b*).

Within the flutter region, the total circumferential force generated by a constraint having both mass and stiffness characteristics is given by

$$F_c = F_{\theta k} + F_{\theta m} = m(\omega_0^2 - \omega_i^2)u(0, t)\bar{u}_{,s}(0, t) \qquad (5)$$

where $\omega_0^2 = k/m$. ω_i is a frequency in the flutter region. The flutter instability can therefore be minimized by setting $\omega_0^2 = \bar{\omega}_i^2$, where $\bar{\omega}_i$ is an average frequency over the flutter region. Figure 4 illustrates four flutter instability regions before and after such a modification is made. The flutter regions reduce or even disappear due to a significant reduction of the resultant circumferential force.

Terminal instability refers to a special flutter instability which occurs at all speeds above a particular rotating speed. A typical example of terminal instability is that caused by a stationary viscous damper. For a constraint consisting only of a stationary damper, the resultant energy change in the system can be expressed from Eq. (3) as

$$\Delta E = \int_0^T F_d[u_{,t}(0, t) + r\Omega\bar{u}_{,s}(0, t)]dt$$
$$= \int_0^T [r\Omega F_d\bar{u}_{,s}(0, t) - cu_{,t}^2(0, t)]dt \qquad (6)$$

where $F_d = -cu_{,t}(0, t)$. It is noted from Eq. (6) that the energy into the system equals the difference between the input energy required to overcome the resistant torque induced by the damper and the energy dissipated by the same damper. It can be shown that instability occurs only when the backward-wave mode is excited by the stationary damping force at supercritical speeds. In this case the lateral damping force is always in phase with its velocity, measured in the string-fixed coordinates, which is independent of the rotating speed.

Figure 5 shows the net energy changes for the fourth backward-wave mode caused individually by a spring and by a viscous damper that provide approximately equal transverse forces to the string. It can been seen from this figure that the net energy into the system through the damper is relatively small compared to that of the spring because the damper dissipates a portion of the input energy.

5 Conclusions

The stability characteristics of a constrained rotating string are determined by the ability of the system to divert driving energy into vibrational energy. When the interactive force between a stationary constraint and a rotating string is in phase with the absolute velocity for nonconservative forces, or in phase with the average slope $\bar{u}_{,s}(0, t)$ for conservative forces, driving energy will be switched into vibration energy which leads to unstable behavior. This behavior has been mathematically characterized in this note. The strength of the instability in a given flutter region can be minimized by choosing the natural frequency of the constraint to coincide with a frequency in the instability region.

References

Hutton, S. G., Chonan, S., and Lehmann, B. F., 1987, "Dynamics Response of a Guided Circular Saw," *Journal of Sound and Vibration,* Vol. 112, No. 3, pp. 527–539.
Iwan, W. D., and Moeller, T. L., 1976, "The Stability of a Spinning Elastic Disk With a Transverse Load System," ASME JOURNAL OF APPLIED MECHANICS, Vol. 43, pp. 485–490.
Ono, K., Chen, J. S., and Bogy, D. B., 1991, "Stability Analysis for the Head-Disk Interface in a Flexible Disk Drive," ASME JOURNAL OF APPLIED MECHANICS, Vol. 58, pp. 1005–1014.
Shen, I. Y., and Mote Jr., C. D., 1991, "On the Mechanism of Instability of a Circular Plate under a Rotating Spring-Mass-Dashpot," *Journal of Sound and Vibration,* Vol. 148, No. 2, pp. 307–318.
Yang, L., and Hutton, S. G., 1995, "Interactions between an Idealized Rotating String and Stationary Constraints," *Journal of Sound and Vibration,* Vol. 185, pp. 139–154.

Circular Arc Rigid Line Problem With Loading On-Line

Y. Z. Chen[1]

1 Introduction

The significance of the rigid line problem was pointed by Dundurs and Markenscoff (1989). The singular integral equation approach was suggested to solve the curve rigid line prob-

[1] Guest researcher at the Laboratory for Nonlinear Mechanics of Continuous Media, Institute of Mechanics, Chinese Academy of Sciences, Beijing 100080, P. R. China. Permanent address: Division of Engineering Mechanics, Jiangsu University of Science and Technology, Zhenjiang, Jiangsu 212013, P. R. China.
Contributed by the Applied Mechanics Division of THE AMERICAN SOCIETY OF MECHANICAL ENGINEERS for publication in the ASME JOURNAL OF APPLIED MECHANICS. Manuscript received by the ASME Applied Mechanics Division, Aug. 26, 1997; final revision, Jan. 23, 1998. Associate Technical Editor: J. R. Barber.

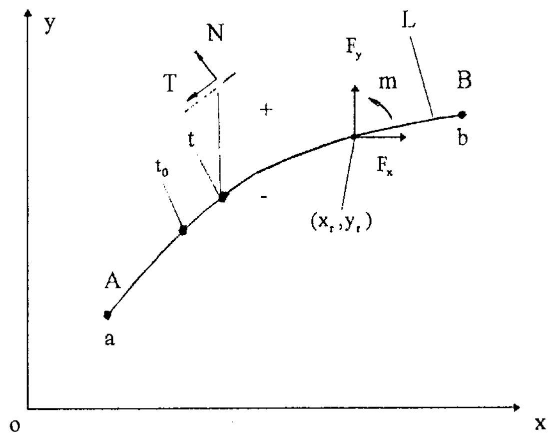

Fig. 1 A curve rigid line problem in an infinite plate

lem (Chen and Hasebe, 1992). However, the formulation was only used to the case that the rigid line was in a floating state. This means no forces are applied on the rigid line. In the meantime, for the rigid straight line with loading on-line, the problem was proposed and solved by Dundurs and Markenscoff (1989).

In this note, the circular rigid line problem with loading online is studied and solved. It was found that, for the aforementioned particular case, an explicit form for the kernels in the singular integral equation can be obtained. The form of the investigated function in the equation ($h(t)$ in the following analysis) can be assumed from a direct inspection. Finally, the solution in a closed form is obtainable.

2 Formulation of the Problem in a General Case

The following analysis depends on the complex variable function method in plane elasticity (Muskelishvili, 1953). In this method the stresses $(\sigma_x, \sigma_y, \sigma_{xy})$, the displacements (u, v), and the resultant force function (X, Y) are expressed in terms of two complex potentials $\phi(z)$, $\psi(z)$ such that

$$\sigma_x + \sigma_y = 4 \operatorname{Re} \phi'(z)$$

$$\sigma_y - \sigma_x + 2i\sigma_{xy} = 2[\bar{z}\phi''(z) + \psi'(z)] \quad (1)$$

$$f = -Y + iX = \phi(z) + z\overline{\phi'(z)} + \overline{\psi(z)} \quad (2)$$

$$2G(u + iv) = \kappa\phi(z) - z\overline{\phi'(z)} - \overline{\psi(z)} \quad (3)$$

where G is the shear modulus of elasticity, $\kappa = (3 - \nu)/(1 + \nu)$ is the plane stress problem, and ν is the Poisson's ratio.

In the problem we assume that (1) the stresses and the rotation $(\partial v/\partial x - \partial u/\partial y)$ vanish at infinity and (2) the forces F_x, F_y and the moment m are applied at the point (x_r, y_r) (Fig. 1). In the actual analysis, the second condition is satisfied in the sense that the distributing forces applied on the rigid line are statically equivalent to the aforementioned forces F_x, F_y and the moment m in Fig. 1.

The appropriate complex potential for the curve rigid line problem has been obtained previously by Chen and Hasebe (1992), which is as follows:

$$\phi(z) = -\frac{1}{2\pi}\int_L \operatorname{Log}(z - t)h(t)dt$$

$$\psi(z) = \frac{\kappa}{2\pi}\int_L \operatorname{Log}\overline{(z - t)}\,\overline{h(t)}\,d\bar{t} - \frac{1}{2\pi}\int_L \frac{\bar{t}h(t)dt}{t - z} \quad (4)$$

where $h(t)$, $t \in L$ takes the complex value in general. Physically, the function $h(t)$ represents the body force density. Previously, we obtain the following relation (Chen and Hasebe, 1992):

$$[N(t) + iT(t)]^+ - [N(t) + iT(t)]^-$$
$$= [N_b(t) + iT_b(t)] = i(\kappa + 1)h(t), \quad t \in L \quad (5)$$

where $[N_b(t) + iT_b(t)](t \in L)$ denotes the distributing forces applied along the curve rigid line.

The relevant singular integral equation takes the form (Chen and Hasebe, 1992)

$$\frac{\kappa}{\pi}\int_L \frac{h(t)dt}{t - t_0} + \frac{\kappa}{2\pi}\int_L K_1(t, t_0)h(t)dt$$
$$- \frac{1}{2\pi}\int_L K_2(t, t_0)\overline{h(t)}\,d\bar{t} = 2G\gamma i \quad (t_0 \in L) \quad (6)$$

where γ denotes the rotation of the rigid line and

$$K_1(t, t_0) = \frac{d}{dt_0}\left(\operatorname{Log}\frac{t_0 - t}{\bar{t}_0 - \bar{t}}\right),$$

$$K_2(t, t_0) = -\frac{d}{dt_0}\left(\frac{t_0 - t}{\bar{t}_0 - \bar{t}}\right). \quad (7)$$

Since the distributing forces $[N_b(t) + iT_b(t)]$ are statically equivalent to the forces F_x, F_y and the moment m, thus we have

$$(\kappa + 1)\int_L h(t)dt = F_x + iF_y \quad (8)$$

$$(\kappa + 1)\operatorname{Im}\int_L \bar{t}h(t)dt = m + x_rF_y - y_rF_x. \quad (9)$$

The stress singularity coefficient at the tips A and B in Fig. 1 can be evaluated by (Chen and Hasebe, 1992)

$$(K_{1R} - iK_{2R})_A = (2\pi)^{1/2}\lim_{t\to a}\sqrt{|t - a|}\,h(t)$$

$$(K_{1R} - iK_{2R})_B = -(2\pi)^{1/2}\lim_{t\to b}\sqrt{|t - b|}\,h(t). \quad (10)$$

3 Solution for the Circular Rigid Line Case

In the circular arc rigid line case (Fig. 2), a solution in closed form is obtainable. In this case, we have

$$t\bar{t} = t_0\bar{t}_0 = R^2, \quad d\bar{t} = -R^2dt/t^2 \quad (t, t_0 \in L). \quad (11)$$

Here, L denotes the circular arc configuration (Fig. 2). Substituting (11) into (7), Eq. (6) becomes

$$\frac{\kappa}{\pi}\int_L \frac{h(t)dt}{t - t_0} + \frac{\kappa}{2\pi}\int_L \frac{1}{t_0}h(t)dt$$
$$+ \frac{1}{2\pi}\int_L \frac{1}{t}\overline{h(t)}\,dt = 2G\gamma i \quad (t_0 \in L). \quad (12)$$

To solve the equation, we introduce the following function:

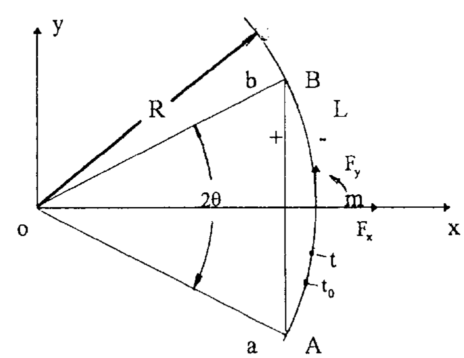

Fig. 2 A circular arc rigid line problem in an infinite plate

$$X(z) = \sqrt{(z-a)(z-b)},$$

$$\text{(taking the branch } \lim_{z\to\infty} X(z)/z = 1) \quad (13)$$

where $a = R\exp(-i\theta)$, $b = R\exp(i\theta)$. In addition, we define

$$X(t) = X^+(t) \quad (t \in L). \quad (14)$$

From the assumed definition, it follows that

$$X(t) = X^+(t) = -X^-(t),\ \overline{X(t)} = RX(t)/t\ (t \in L). \quad (15)$$

In the meantime, it is easy to quadrature the following integrals (Chen, 1994):

$$\int_L \frac{1}{X(t)} \frac{dt}{t-t_0} = 0,\quad \int_L \frac{t}{RX(t)} \frac{dt}{t-t_0} = -\frac{\pi i}{R},$$

$$\int_L \frac{R}{tX(t)} \frac{dt}{t-t_0} = \frac{\pi i}{t_0} \quad (t_0 \in L) \quad (16)$$

$$\int_L \frac{dt}{X(t)} = -\pi i,\quad \int_L \frac{tdt}{RX(t)} = -\pi i(\cos\theta),$$

$$\int_L \frac{Rdt}{tX(t)} = -\pi i,\quad \int_L \frac{R^2}{t^2} \frac{dt}{X(t)} = -\pi i(\cos\theta). \quad (17)$$

The solution will be investigated in two groups.

(1) In the first group we let $F_x \neq 0$, $F_y = 0$, $m = 0$. In this case, it is suitable to assume

$$h(t) = i\left(c_1 + c_2\frac{t}{R} + c_3\frac{R}{t}\right)\frac{1}{X(t)}. \quad (18)$$

Substituting (18) into (12), (8), (9), and using (16), (17), we obtain the following solution:

$$c_1 = \frac{2\kappa - 1 - \cos^2\theta}{2\kappa - 1 + \cos\theta}\frac{F_x}{2\pi(\kappa+1)},$$

$$c_2 = \frac{1+\cos\theta}{2\kappa - 1 + \cos\theta}\frac{F_x}{2\pi(\kappa+1)},$$

$$c_3 = \frac{F_x}{2\pi(\kappa+1)},\quad \gamma = 0. \quad (19)$$

In addition, substituting (18) into (10), the stress singularity coefficients at the tips A and B are obtainable

$$(K_{1R} - iK_{2R})_A = i\sqrt{\frac{\pi}{R\sin\theta}}\,[c_1 + c_2\exp(-i\theta)$$

$$+ c_3\exp(i\theta)]\exp(i\theta/2) \quad (20)$$

$$(K_{1R})_B = (K_{1R})_A,\quad (K_{2R})_B = -(K_{2R})_A \quad (21)$$

(2) In the second group, we assume $F_y \neq 0$, $m \neq 0$, $F_x = 0$,. In this case, it is suitable to assume

$$h(t) = \left(d_1 + d_2\frac{t}{R} + d_3\frac{R}{t}\right)\frac{1}{X(t)}. \quad (22)$$

Substituting (22) into (12), (8), (9), and using (16), (17), we obtain the following solution:

$$d_1 = \frac{1}{2\pi(\kappa+1)}\left(\frac{2\cos\theta}{1-\cos\theta}\frac{m}{R} - (1-\cos\theta)F_y\right),$$

$$d_2 = \frac{1}{2\pi(\kappa+1)}\left(-\frac{2}{1-\cos\theta}\frac{m}{R} - F_y\right),$$

$$d_3 = -\frac{F_y}{2\pi(\kappa+1)},$$

$$\gamma = -\frac{1}{4GR}(d_1 + (2\kappa+1)d_2 + d_3\cos\theta). \quad (23)$$

In addition, substituting (22) into (10), the stress singularity coefficients at the tips A and B are obtainable:

$$(K_{1R} - iK_{2R})_A = \sqrt{\frac{\pi}{R\sin\theta}}\,[d_1 + d_2\exp(-i\theta)$$

$$+ d_3\exp(i\theta)]\exp(i\theta/2) \quad (24)$$

$$(K_{1R})_B = -(K_{1R})_A,\quad (K_{2R})_B = (K_{2R})_A. \quad (25)$$

Acknowledgment

The research project is support by National Natural Science Fund of China.

References

Chen, Y. Z., and Hasebe, N., 1992, "Integral Equation Approaches for Curved Rigid Line Problem in an Infinite Plate," *International Journal of Fracture*, Vol. 58, pp. 1–20.

Chen, Y. Z., 1994, "New Singular Integral Equations for Circular Arc Crack and Rigid Line Problem," *Engineering Fracture Mechanics*, Vol. 47, pp. 139–145.

Dundurs, J., and Markenscoff, X., 1989, "A Green's Function Formulation of Anticracks and Their Interaction with Load-Induced Singularities," ASME JOURNAL OF APPLIED MECHANICS, Vol. 56, pp. 550–555.

Muskhelishvili, N. I., 1953, *Some Basic Problems in the Theory of Elasticity*, Noordhoff, Leyden, The Netherlands.

Analysis of a Rotating Pendulum With a Mass Free to Move Radially

B. A. Schmidt[1] and D. G. McDowell[1]

Analysis of a pendulum pivoted on a rotating shaft. The mass of the pendulum is free to move radially. The shaft is nearly horizontal.

Introduction

Pendulums with imposed oscillations have been studied by many researchers. Stephenson (1908) presented the inverted pendulum. Lowenstern (1932) analyzed the inverted spherical pendulum and compound pendulums with excitation. Miles (1962) investigated stability of the downward vertical position of a spherical pendulum with horizontal excitation. Sethna and Hemp (1964) analyzed a gyroscopic spherical pendulum with an imposed vertical oscillation. Phelps and Hunter (1965) presented an analytical solution for the linearized inverted pendulum with harmonic excitation at an unrestricted frequency. Mitchell (1972) investigated the inverted pendulum with almost periodic excitation and with stochastic excitation. Howe (1974) described a theory of stabilization of the inverted position by

[1] Mathematics Department, Central Michigan University, Mt. Pleasant, MI 48859.

Contributed by the Applied Mechanics Division of THE AMERICAN SOCIETY OF MECHANICAL ENGINEERS for publication in the ASME JOURNAL OF APPLIED MECHANICS. Manuscript received by the ASME Applied Mechanics Division, Feb. 15, 1996; final revision, Dec. 10, 1997. Associate Technical Editor: S. W. Shaw.

$$X(z) = \sqrt{(z-a)(z-b)},$$

$$\text{(taking the branch } \lim_{z\to\infty} X(z)/z = 1) \quad (13)$$

where $a = R\exp(-i\theta)$, $b = R\exp(i\theta)$. In addition, we define

$$X(t) = X^+(t) \quad (t \in L). \quad (14)$$

From the assumed definition, it follows that

$$X(t) = X^+(t) = -X^-(t),\ \overline{X(t)} = RX(t)/t\ (t \in L). \quad (15)$$

In the meantime, it is easy to quadrature the following integrals (Chen, 1994):

$$\int_L \frac{1}{X(t)}\frac{dt}{t-t_0} = 0,\quad \int_L \frac{t}{RX(t)}\frac{dt}{t-t_0} = -\frac{\pi i}{R},$$

$$\int_L \frac{R}{tX(t)}\frac{dt}{t-t_0} = \frac{\pi i}{t_0} \quad (t_0 \in L) \quad (16)$$

$$\int_L \frac{dt}{X(t)} = -\pi i,\quad \int_L \frac{tdt}{RX(t)} = -\pi i(\cos\theta),$$

$$\int_L \frac{Rdt}{tX(t)} = -\pi i,\quad \int_L \frac{R^2}{t^2}\frac{dt}{X(t)} = -\pi i(\cos\theta). \quad (17)$$

The solution will be investigated in two groups.

(1) In the first group we let $F_x \neq 0$, $F_y = 0$, $m = 0$. In this case, it is suitable to assume

$$h(t) = i\left(c_1 + c_2\frac{t}{R} + c_3\frac{R}{t}\right)\frac{1}{X(t)}. \quad (18)$$

Substituting (18) into (12), (8), (9), and using (16), (17), we obtain the following solution:

$$c_1 = \frac{2\kappa - 1 - \cos^2\theta}{2\kappa - 1 + \cos\theta}\frac{F_x}{2\pi(\kappa+1)},$$

$$c_2 = \frac{1+\cos\theta}{2\kappa - 1 + \cos\theta}\frac{F_x}{2\pi(\kappa+1)},$$

$$c_3 = \frac{F_x}{2\pi(\kappa+1)},\quad \gamma = 0. \quad (19)$$

In addition, substituting (18) into (10), the stress singularity coefficients at the tips A and B are obtainable

$$(K_{1R} - iK_{2R})_A = i\sqrt{\frac{\pi}{R\sin\theta}}[c_1 + c_2\exp(-i\theta)$$

$$+ c_3\exp(i\theta)]\exp(i\theta/2) \quad (20)$$

$$(K_{1R})_B = (K_{1R})_A,\quad (K_{2R})_B = -(K_{2R})_A \quad (21)$$

(2) In the second group, we assume $F_y \neq 0$, $m \neq 0$, $F_x = 0$,. In this case, it is suitable to assume

$$h(t) = \left(d_1 + d_2\frac{t}{R} + d_3\frac{R}{t}\right)\frac{1}{X(t)}. \quad (22)$$

Substituting (22) into (12), (8), (9), and using (16), (17), we obtain the following solution:

$$d_1 = \frac{1}{2\pi(\kappa+1)}\left(\frac{2\cos\theta}{1-\cos\theta}\frac{m}{R} - (1-\cos\theta)F_y\right),$$

$$d_2 = \frac{1}{2\pi(\kappa+1)}\left(-\frac{2}{1-\cos\theta}\frac{m}{R} - F_y\right),$$

$$d_3 = -\frac{F_y}{2\pi(\kappa+1)},$$

$$\gamma = -\frac{1}{4GR}(d_1 + (2\kappa+1)d_2 + d_3\cos\theta). \quad (23)$$

In addition, substituting (22) into (10), the stress singularity coefficients at the tips A and B are obtainable:

$$(K_{1R} - iK_{2R})_A = \sqrt{\frac{\pi}{R\sin\theta}}[d_1 + d_2\exp(-i\theta)$$

$$+ d_3\exp(i\theta)]\exp(i\theta/2) \quad (24)$$

$$(K_{1R})_B = -(K_{1R})_A,\quad (K_{2R})_B = (K_{2R})_A. \quad (25)$$

Acknowledgment

The research project is support by National Natural Science Fund of China.

References

Chen, Y. Z., and Hasebe, N., 1992, "Integral Equation Approaches for Curved Rigid Line Problem in an Infinite Plate," *International Journal of Fracture*, Vol. 58, pp. 1–20.

Chen, Y. Z., 1994, "New Singular Integral Equations for Circular Arc Crack and Rigid Line Problem," *Engineering Fracture Mechanics*, Vol. 47, pp. 139–145.

Dundurs, J., and Markenscoff, X., 1989, "A Green's Function Formulation of Anticracks and Their Interaction with Load-Induced Singularities," ASME JOURNAL OF APPLIED MECHANICS, Vol. 56, pp. 550–555.

Muskhelishvili, N. I., 1953, *Some Basic Problems in the Theory of Elasticity*, Noordhoff, Leyden, The Netherlands.

Analysis of a Rotating Pendulum With a Mass Free to Move Radially

B. A. Schmidt[1] and D. G. McDowell[1]

Analysis of a pendulum pivoted on a rotating shaft. The mass of the pendulum is free to move radially. The shaft is nearly horizontal.

Introduction

Pendulums with imposed oscillations have been studied by many researchers. Stephenson (1908) presented the inverted pendulum. Lowenstern (1932) analyzed the inverted spherical pendulum and compound pendulums with excitation. Miles (1962) investigated stability of the downward vertical position of a spherical pendulum with horizontal excitation. Sethna and Hemp (1964) analyzed a gyroscopic spherical pendulum with an imposed vertical oscillation. Phelps and Hunter (1965) presented an analytical solution for the linearized inverted pendulum with harmonic excitation at an unrestricted frequency. Mitchell (1972) investigated the inverted pendulum with almost periodic excitation and with stochastic excitation. Howe (1974) described a theory of stabilization of the inverted position by

[1] Mathematics Department, Central Michigan University, Mt. Pleasant, MI 48859.

Contributed by the Applied Mechanics Division of THE AMERICAN SOCIETY OF MECHANICAL ENGINEERS for publication in the ASME JOURNAL OF APPLIED MECHANICS. Manuscript received by the ASME Applied Mechanics Division, Feb. 15, 1996; final revision, Dec. 10, 1997. Associate Technical Editor: S. W. Shaw.

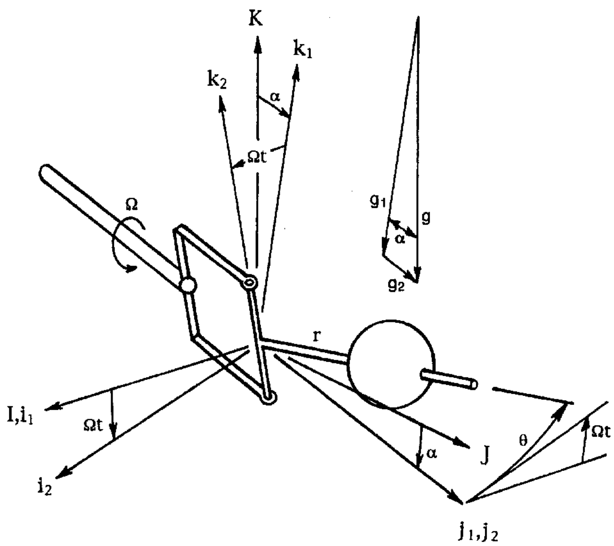

Fig. 1 The pendulum

imposed random oscillations. Ryland and Meirovitch (1977) investigated the radially flexible pendulum with vertical excitation. Stability boundaries for the upward and downward vertical positions were established. Levi (1988) presented a topological proof of stability of the inverted pendulum. Schmidt (1980, 1981, 1983, 1990) investigated several parametrically excited pendulums with various characteristics such as radial flexibility, rotational flexibility, and imposed rotational oscillations. Interesting equilibrium positions were found. Schmidt and McDowell (1992) analyzed a pendulum pivoted on a rotating arm. A surprising stable equilibrium position was found. Acheson (1993) established a stability theorem for compound inverted pendulums. Acheson and Mullin (1993) presented experimental results for compound inverted pendulums. Levi and Weckesser (1995) presented a geometrical explanation of the inverted pendulum.

In this work we consider a pendulum pivoted on a rotating rigid shaft. (See Fig. 1.) The shaft is horizontal or nearly horizontal and is rotating at a constant speed. The angle between the shaft and the horizontal plane is denoted by α. The pendulum is made up of a rigid weightless rod and a spherical mass. The mass is allowed to slide freely on the rod and, by some unspecified design, the radius of the mass is allowed to be positive, negative, or zero. The expectation is that the pendulum would swing outward and the mass would slide off the rod. While this motion can occur, we find that there can be a steady-state motion with the pendulum remaining near the axis of the shaft and with the mass remaining near the pivot. We employ the method of averaging to describe this steady-state motion.

The motion is described by two second-order differential equations. We use a transformation which gives four first-order differential equations in the standard form for the method of averaging (See Bogoliuboff and Mitropolskiy 1962). We use the improved first approximation of the method of averaging to find the steady-state motion of the pendulum along with the transcient motion near the steady-state motion. Since we must approximate the differential equations in order to make our analysis, we verify our result with a modest numerical investigation.

The Analysis

The equations of motion are

$$m\frac{d^2r}{dt^2} - mr\Omega^2\sin^2\theta - mr\left(\frac{d\theta}{dt}\right)^2 + c_1\frac{dr}{dt} - mg_2\cos\theta + mg_1\sin\theta\sin\Omega t = 0$$

and

$$(I + mr^2)\frac{d^2\theta}{dt^2} + 2mr\frac{dr}{dt}\frac{d\theta}{dt} - mr^2\Omega^2\sin\theta\cos\theta + c_2\frac{d\theta}{dt} + mg_2r\sin\theta + mg_1r\cos\theta\sin\Omega t = 0, \quad (1a,b)$$

where m is the mass, r is the radius, θ is the angle of the pendulum measured from the axis of the shaft, I is the moment of inertia of the mass, g is gravity, g_1 is the component of gravity perpendicular to the shaft, g_2 is the component of gravity in the direction of the shaft, Ω is the angular rate of the shaft, c_1 and c_2 are damping coefficients, and t is time. We establish dimensionless parameters and variables.

Let

$$x = \frac{r}{r_e}, \quad \tau = \Omega t, \quad \epsilon = \frac{g}{r_e\Omega^2}, \quad \epsilon\gamma_1 = \frac{g_1}{r_e\Omega^2},$$

$$\epsilon^3\gamma_2 = \frac{g_2}{r_e\Omega^2}, \quad \epsilon a_1 = \frac{c_1}{m\Omega}, \quad \text{and} \quad \epsilon a_2 = \frac{c_2}{mr_e^2\Omega}$$

where r_e is the radius of gyration of the mass. This yields

$$\frac{d^2x}{d\tau^2} - x\sin^2\theta - x\left(\frac{d\theta}{d\tau}\right)^2 + \epsilon a_1\frac{dx}{d\tau} - \epsilon^3\gamma_2\cos\theta + \epsilon\gamma_1\sin\theta\sin\tau = 0$$

and

$$(1 + x^2)\frac{d^2\theta}{d\tau^2} + 2x\frac{dx}{d\tau}\frac{d\theta}{d\tau} - x^2\sin\theta\cos\theta + \epsilon a_2\frac{d\theta}{d\tau} + \epsilon^3\gamma_2 x\sin\theta + \epsilon\gamma_1 x\cos\theta\sin\tau = 0. \quad (2a,b)$$

Up to this point, no approximations have been made. We now restrict the problem so that x and θ are near zero.

Let

$$\epsilon y = x,$$

and

$$\epsilon\phi = \theta. \quad (3a,b)$$

We approximate Eq. (2) by substituting Eq. (3) in Eq. (2) and discarding third-order terms. This gives

$$\frac{d^2y}{d\tau^2} - \epsilon^2y\phi^2 - \epsilon^2y\left(\frac{d\phi}{d\tau}\right)^2 + \epsilon a_1\frac{dy}{d\tau} - \epsilon^2\gamma_2 + \epsilon\gamma_1\phi\sin\tau = 0$$

and

$$\frac{d^2\phi}{d\tau^2} + 2\epsilon^2y\frac{dy}{d\tau}\frac{d\phi}{d\tau} - \epsilon^2y^2\phi + \epsilon a_2\frac{d\phi}{d\tau} + \epsilon\gamma_1 y\sin\tau = 0. \quad (4a,b)$$

To express Eqs. (4) in the standard form for the method of averaging, we introduce the transformation

$$\frac{dy}{d\tau} = \epsilon z + \epsilon\gamma_1\phi\cos\tau$$

and

$$\frac{d\phi}{d\tau} = \epsilon\psi + \epsilon\gamma_1 y\cos\tau. \quad (5a,b)$$

Substituting Eq. (5) in Eq. (4) gives two first-order differential equations involving $(dz/d\tau)$ and $(d\Psi/d\tau)$. These along with Eqs. (5) give four first-order differential equations in the variables y, z, ϕ, and ψ. They are

$$\frac{dy}{d\tau} = \epsilon(z + \gamma_1\phi \cos \tau),$$

$$\frac{dz}{d\tau} = \epsilon(-\gamma_1(\psi + \gamma_1 y \cos \tau) \cos \tau - a_1(z + \gamma_1\phi \cos \tau) + y\phi^2 + \gamma_2),$$

$$\frac{d\phi}{d\tau} = \epsilon(\psi + \gamma_1 y \cos \tau),$$

and

$$\frac{d\psi}{d\tau} = \epsilon(-\gamma_1(z + \gamma_1\phi \cos \tau) \cos \tau + y^2\phi - a_2(\psi + \gamma_1 y \cos \tau)). \quad (6a,b,c,d)$$

We have discarded second-order terms in Eq. (6). We apply the averaging process to Eqs. (6). This yields

$$\frac{dY}{d\tau} = \epsilon Z,$$

$$\frac{dZ}{d\tau} = \epsilon\left(-\frac{1}{2}\gamma_1^2 Y - a_1 Z + Y\Phi^2 + \gamma_2\right),$$

$$\frac{d\Phi}{d\tau} = \epsilon\Psi,$$

and

$$\frac{d\Psi}{d\tau} = \epsilon\left(-\frac{1}{2}\gamma_1^2\Phi + Y^2\Phi - a_2\Psi\right), \quad (7a,b,c,d)$$

where Y, Z, Φ, Ψ are the slow parts of y, z, ϕ, and ψ. If we could solve Eqs. (7), we could use the improved first approximation of the method of averaging to obtain approximate solutions for y and ϕ. This would give

$$y = Y + \epsilon\gamma_1\Phi \sin \tau$$

and

$$\phi = \Phi + \epsilon\gamma_1 Y \sin \tau, \quad (8a,b)$$

where Y and Φ are solutions of Eqs. (7). We cannot solve Eqs. (7). We approximately find a solution by linearizing near the equilibrium solution $Y_E = (2\gamma_2/\gamma_1^2)$ and $\Phi_E = 0$. We do not consider other equilibrium positions. We substitute

$$Y = \frac{2\gamma_2}{\gamma_1^2} + \Delta Y$$

and

$$\Phi = \Delta\Phi \quad (9a,b)$$

in Eq. (7) and discard products of ΔY and $\Delta\Phi$. This gives a linear system in ΔY and $\Delta\Phi$ which is easy to solve. Then the approximate solution to Eq. (7) is given by Eqs. (9) in which

$$\Delta Y = \begin{cases} C_1 e^{-m_1\epsilon\tau} + C_2 e^{-m_2\epsilon\tau}, \text{ if } m_1 \neq m_2 \\ \text{or } C_1 e^{-m_1\epsilon\tau} + C_2\epsilon\tau e^{-m_1\epsilon\tau}, \text{ if } m_1 = m_2, \end{cases}$$

and

$$\Delta\Phi = \begin{cases} E_1 e^{-n_1\epsilon\tau} + E_2 e^{-n_2\epsilon\tau}, \text{ if } n_1 \neq n_2 \\ \text{or } E_1 e^{-n_1\epsilon\tau} + E_2\epsilon\tau e^{-n_1\epsilon\tau}, \text{ if } n_1 = n_2, \end{cases} \quad (10a,b)$$

and

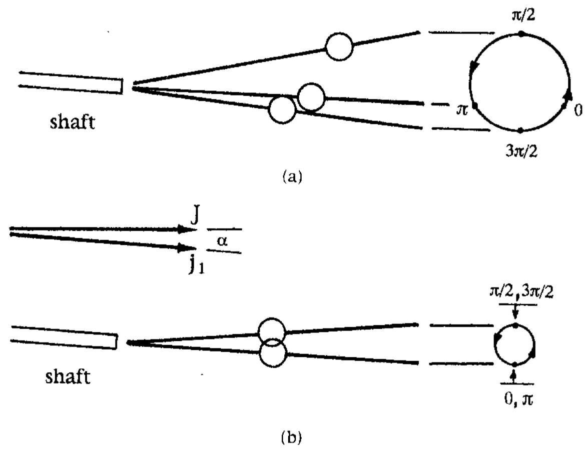

Fig. 2 **(a) The motion when $\Delta Y > 0$ and $\Delta\Phi > 0$ (b) the steady-state motion**

$$m_1 = \tfrac{1}{2}(a_1 - \sqrt{a_1^2 - 2\gamma_1^2}),$$

$$m_2 = \tfrac{1}{2}(a_1 + \sqrt{a_1^2 - 2\gamma_1^2}),$$

$$n_1 = \frac{1}{2}\left(a_2 - \sqrt{a_2^2 - 2\left(\gamma_1^2 - \frac{8\gamma_2^2}{\gamma_1^4}\right)}\right),$$

$$n_2 = \frac{1}{2}\left(a_2 + \sqrt{a_2^2 - 2\left(\gamma_1^2 - \frac{8\gamma_2^2}{\gamma_1^4}\right)}\right). \quad (11a,b,c,d)$$

In order that the real part of n_1 in Eq. (11c) be positive, we impose the condition

$$\gamma_1^2 - \frac{8\gamma_2^2}{\gamma_1^4} > 0. \quad (12)$$

Condition (12) causes the equilibrium positions of Eqs. (7) ($Y_E = (2\gamma_2/\gamma_1^2)$ and $\Phi_E = 0$) to be stable and with condition (12), ΔY and $\Delta\Phi$ are diminishing exponentials or damped oscillations. Combining Eqs. (3), (8), and (9), we obtain our approximate solution for x and θ. It is

$$x = \epsilon\left(\frac{2\gamma_2}{\gamma_1^2} + \Delta Y\right) + \epsilon^2\gamma_1\Delta\Phi \sin \tau$$

and

$$\theta = \epsilon\Delta\Phi + \epsilon^2\gamma_1\left(\frac{2\gamma_2}{\gamma_1^2} + \Delta Y\right) \sin \tau, \quad (13a,b)$$

where $\Delta\Phi$ and ΔY are given by Eqs. (10) along with Eqs. (11).

Equation (13) is an approximate solution of Eq. (2) when ΔY and $\Delta\Phi$ are small. As ΔY and $\Delta\Phi$ approach zero, the approximate solution Eqs. (13) approach the approximate steady-state solution

$$x = \epsilon\frac{2\gamma_2}{\gamma_1^2}$$

and

$$\theta = \epsilon^2\frac{2\gamma_2}{\gamma_1} \sin \tau. \quad (14a,b)$$

We present Eqs. (14) along with Eqs. (13) as our result. Equation (14a) indicates the radius of the pendulum is approximated by the positive constant $\epsilon(2\gamma_2/\gamma_1^2)$. Equation (14b) indicates θ makes a small conical motion near the axis of the shaft. The cone angle is $\epsilon^2(2\gamma_2/\gamma_1) \approx 2\alpha$. Figure 2(a) shows the

Table 1 The numerical solution and the method of averaging solution

τ	k	Numerical Solution $x\times10^2$	$\theta\times10^3$	Method of Av. Sol. $x\times10^2$	$\theta\times10^3$
0		1.40000	6.00000	1.40000	6.00000
.5π	0	1.40819	6.24335	1.40863	6.25714
2.5π	1	1.39652	6.17842	1.39532	6.16654
6.5π	3	1.37709	6.09775	1.36956	5.98939
10.5π	5	1.36068	6.05001	1.34493	5.81749
14.5π	7	1.34591	6.01504	1.32136	5.65068
20.5π	10	1.32545	5.96792	1.28791	5.40968
40.5π	20	1.26496	5.77349	1.19119	4.68046
80.5π	40	1.16423	5.18463	1.05155	3.51274
140.5π	70	1.04538	4.07371	0.92986	2.30279
200.5π	100	0.95729	2.99659	0.86714	1.53028
400.5π	200	0.82848	0.90953	0.80757	0.46962
600.5π	300	0.80649	0.33547	0.80089	0.23014
800.5π	400	0.80354	0.20043	0.80011	0.17591
1000.5π	500	0.80317	0.16931	0.80002	0.16361
1200.5π	600	0.80312	0.16216	0.80000	0.16082

pendulum with $\Delta Y > 0$ and $\Delta\Phi > 0$. Figure 2(b) shows the pendulum in steady-state motion. The pendulum is shown for shaft rotation angles 0, $(1/2)\pi$, π, $(3/2)\pi$. In order to depict the motion clearly, we have distorted the scale in Fig. 2. The angles are exaggerated and the mass is diminished.

Some thought about Fig. 2 can provide some understanding of the phenomenon. To gain a better understanding of the phenomenon, we consider some terms in Eqs. (2). The term $-\epsilon^3\gamma_2\cos\theta$ in Eq. (2a) represents the component of the gravitational force in the positive radial direction. It would be expected that this force would destroy the steady-state motion by causing the radius to increase. The term $\epsilon\gamma_1\sin\theta\sin\tau$ seems to be an oscillating term, but it has a slow part which mostly cancels $-\epsilon^3\gamma_2\cos\theta$. To see this, we consider the slow parts of these terms with x and θ replaced by Eqs. (13). We use the overbar to denote the slow part. This gives

$$\overline{-\epsilon^3\gamma_2\cos\theta} + \overline{\epsilon\gamma_1\sin\theta\sin\tau} \approx \epsilon^3\tfrac{1}{2}\gamma_1^2\Delta Y.$$

In this approximation small angle formulas were used. The positive radial force is cancelled. The slow parts of these terms combine to give a term which represents a negative radial force when ΔY is positive.

We consider the moment caused by the centrifugal force. The third term in Eq. (2b), $-x^2\sin\theta\cos\theta$, represents the moment (about $\mathbf{k}_2$) caused by the centrifugal force. This moment acts to enlarge θ and degrade steady-state motion. The sixth term counteracts this. To see this, we substitute our approximate solution, Eq. (13), into the third and sixth terms of Eq. (2b) and consider the slow parts. This gives the approximation

$$\overline{-x^2\sin\theta\cos\theta} + \overline{\epsilon\gamma_1 x\cos\theta\sin\tau} \approx \epsilon^3\left(\frac{1}{2}\gamma_1^2 - \frac{4\gamma_2^2}{\gamma_1^4}\right)\Delta\Phi.$$

In this approximation, small angle formulas were used and products of ΔY and $\Delta\Phi$ were discarded. This indicates that the moment caused by the centrifugal force has been cancelled and these two terms approximately cause a restoring moment if $(\frac{1}{2})\gamma_1^2 - 4(\gamma_2^2/\gamma_1^4) > 0$, i.e., if condition (12) holds.

Considering these terms in Eqs. (2) with x and θ approximated by Eq. (13) strongly suggest that forces and moments acting to destroy steady-state motion are cancelled by the parametric excitation in Eqs. (2).

Numerical Analysis

In our analysis, Eqs. (2) were approximated by Eqs. (4). Because of this, a brief numerical analysis seemed appropriate. We applied the Runge-Kutta method of order four to Eqs. (2). The step size is $(\pi/200) \approx .016$.

In Table 1 we present some numerical results with printout at $\tau = (\pi/2) + 2k\pi$ for some different integer values of k for this example: $\epsilon = .02$, $\gamma_1 = 1$, $\gamma_2 = .2$, $a_1 = 3$, $a_2 = 3$, $x(0) = .014$, $x'(0) = 9.8745 \times 10^{-5}$, $\theta(0) = .006$, $\theta'(0) = 2.658433 \times 10^{-4}$. The corresponding points obtained from Eqs. (13) are also shown. The values of the constants C_1, C_2, E_1, and E_2 in Eqs. (10), for the above example, are $C_1 = .3$, $C_2 = 0$, $E_1 = .3$, $E_2 = 0$.

There is close agreement between the numerical results and the analytical approximation given by Eq. (13). Numerical results (not shown in Table 1) were obtained, for the above example, for $\tau = 2k\pi$, $\tau = \pi + 2k\pi$ and $\tau = (\frac{3}{2})\pi + 2k\pi$. These results agree well with Eq. (13). However, for large τ the numerical approximation of x shows a small oscillation which does not appear in Eq. (14a). For $\tau = (\frac{1}{2})\pi + 2k\pi$ and $\tau = (\frac{3}{2})\pi + 2k\pi$ (k large), the numerical x stabilizes at .0080106. For $\tau = 2k\pi$ and $\tau = \pi + 2k\pi$, x stabilizes at .0080027. Apparently there is a small oscillation in x even when τ is large. Figure 2(b) suggests an oscillation in x should occur. Equation (14a) indicates that x approaches .0080000.

Conclusion

Our analysis shows that gravity combined with the rotation of the shaft causes a parametric excitation which can create a surprising steady-state motion.

Conventional intuition would suggest that the pendulum would swing briskly away from the axis of the shaft and the mass would slide off the rod. While this motion can happen and is likely, our analysis shows that the pendulum can take on this motion: The pendulum oscillates near the axis of the shaft and the mass approximately maintains a constant radius. The motion is described by Eqs. (14). In terms of the original variables and parameters, the motion is described by

$$r = \frac{2g_2 I\Omega^2}{g_1^2 m}$$

and

$$\theta = \frac{2g_2}{g_1}\sin\Omega t. \qquad (15a,b)$$

Equations (15) approximately satisfy Eqs. (1) for the restrictions we impose.

References

Acheson, D. J., 1993, "A Pendulum Theorem," *Proc. R. Soc. Lond.*, Vol. A443, pp. 239–245.

Acheson, D. J., and Mullin, T., 1993, "Upside-Down Pendulums," *Nature*, Vol. 366, pp. 215–216.

Bogoliuboff, N. M., and Mitropolskiy, Yu. A., 1962, *Asymptotic Methods in the Theory of Nonlinear Oscillations*, Gordon and Breach, New York.

Howe, M. S., 1974, "The mean Square Stability of an Inverted Pendulum Subject to Random Parametric Excitation," *Journal of Sound and Vibration*, Vol. 32, No. 3, pp. 407–421.

Levi, M., 1988. "Stability of the Inverted Pendulum-A Topological Explanation," *SIAM Review*, Vol 30, pp 639–644.

Levi, M., and Weckesser, W., 1995, "Stabilization of the Inverted Linearized Pendulum by High Frequency Vibrations," *SIAM Review*, Vol. 37, pp. 219–223.

Lowenstern, E. R., 1932, "The Stabilizing Effect of Imposed Oscillations of High Frequency on a Dynamical System," *Philosophical Magazine*, Vol. 13, pp. 458–486.

Miles, J. W., 1962, "Stability of Forced Oscillations of a Spherical Pendulum," *Quarterly of Applied Mathematics*, Vol. 20, No. 1, pp. 21–32.

Mitchell, R., 1972, "Stability of the Inverted Pendulum Subjected to Almost Periodic and Stochastic Base Motion—An Application of the Method of Averaging," *International Journal of Non-Linear Mechanics*, Vol. 7, pp. 101–123.

Phelps, F. M., III, and Hunter, J. H., Jr., 1965, "An Analytical Solution of The Inverted Pendulum," *American Journal of Physics*, Vol. 33, pp. 285–295.

Ryland, G., II, and Meirovitch, L., 1977, "Stability Boundaries of a Swinging Spring with Oscillatory Support," *Journal of Sound and Vibration*, Vol. 51, pp. 547–560.

Schmidt, B. A., 1980, "Vibrated Pendulum with a Mass Free to Move Radially," ASME Journal of Applied Mechanics, Vol. 47, pp. 428–430.

Schmidt, B. A., 1981, "Pendulum with a Rotational Vibration," ASME Journal of Applied Mechanics, Vol. 48, pp. 200–203.

Schmidt, B. A., 1983, "The Radially Flexible Pendulum Subjected to a High Frequency Excitation," ASME Journal of Applied Mechanics, Vol. 50, pp. 443–448.

Schmidt, B. A., 1990, "The Rotationally Flexible Pendulum Subjected to a High Frequency Excitation," ASME JOURNAL OF APPLIED MECHANICS, Vol. 57, pp. 725–730.

Schmidt, B. A., and McDowell, D. G., 1992, "Analysis of a Pendulum on a Rotating Arm," ASME JOURNAL OF APPLIED MECHANICS, Vol 59, pp. 233–234.

Sethna, P. R., and Hemp, G. W., 1964, "Nonlinear Oscillation of a Gyroscopic Pendulum with an Oscillatory Point of Suspension," *Proc. Colloq. International du Centre National de la Reserche Scientifique, N-148, Les vibration forcées dans les systemes non-lineaires,* pp. 375–392.

Stephenson, A., 1908, "On a New Type of Dynamical Stability," *Manchester Memoirs,* Vol. 52, pp. 1–10.

Measurement of Tensile Properties of Metallic Foils

V. Sharma[1], J. B. Isaacs[2], and S. Nemat-Nasser[2]

A fixture has been developed for testing thin specimens under uniaxial tension. The fixture consists of two cantilever beams with strain gauges attached to them close to their fixed ends. The displacement of one beam is used to measure the force and the difference in the displacements of the beams is used to measure the sample displacement. The tensile properties of 0.025 mm by 1.25 mm by 5 mm iron-nickel specimens were measured. The tensile plastic yield point of the specimens was observed to be 1.4 GPa and the total elongation to failure turned out to be five percent and eight percent, for the two tested specimens.

Introduction

Tension tests are widely used to measure the strength and ductility of different materials under uniaxial tensile stresses. A variety of tension testing machines are available commercially with a wide range of loading rate and load capacity, with interchangeable grips to hold various test specimens. A majority of commercially available tension testing machines are not capable of testing tensile properties of very thin and small specimens due to the small loads required for failure and inability to mount the specimens in the grips.

The tensile properties of thin films has been studied by using mini tensile testers (Rudd et al., 1993; Griffin et al., 1992; Noyan and Sheikh, 1993). Rudd et al. (1993) measured the strains in thin films by monitoring the position of laser spots diffracted from a grating created on the surface of the specimen. Griffin et al. (1992) measured stress from the load cell and strain from the rotational speed of their screw driven tensile tester. Noyan and Sheikh (1993) used a standard uniaxial tensile test with X-ray diffraction techniques to measure mechanical stress-strain relations and X-ray stress and strain in the diffracting regions of the specimen. In this study, the tensile properties of thin metallic foils are studied on a new test fixture, which allows the measurement of the tensile properties of very small metallic foils, in conjunction with any standard testing machine.

[1] Samsung Information Systems America, 75 West Plumeria Drive, San Jose, CA 95134.

[2] Center for Excellence for Advanced Materials, University of California, San Diego, La Jolla, CA 92093-0416.

Contributed by the Applied Mechanics Division of THE AMERICAN SOCIETY OF MECHANICAL ENGINEERS for publication in the ASME JOURNAL OF APPLIED MECHANICS. Manuscript received by the ASME Applied Mechanics Division, Nov. 19, 1996; final revision, Feb. 17, 1998. Associate Technical Editor: V. K. Kinra.

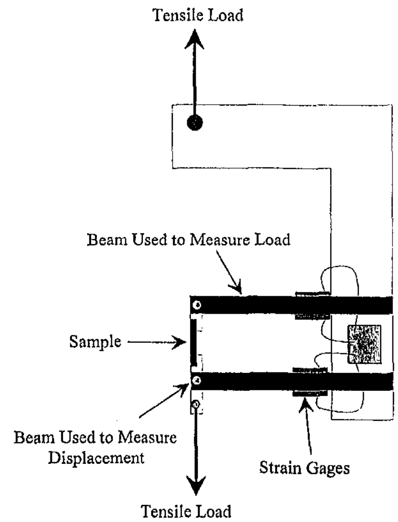

Fig. 1 Schematic diagram of the load fixture used to measure the tensile properties of metallic foils

Experimental Procedure

Iron-nickel foils were used in these experiments. The dimensions of the foils were 0.025 mm by 1.25 mm by 5 mm. Figure 1 is the schematic diagram of the load fixture. It consists of two cantilever beams with strain gauges mounted on them close to their fixed ends. The calibrated displacement of one beam gives the force applied to the sample, whereas the difference in the displacement between the two beams gives the displacement of the sample.

A system of alignment pins and hinges were used to eliminate bending loads on the foils and to facilitate sample installation. The sample is glued and clamped in place between the two cantilevers. The lower beam is loaded through a spring, the other end of which is connected to the lower ram of a servohydraulic machine. The strain gauge outputs were digitized and the force-displacement curves were computed, from which stress-strain curves were obtained.

Results and Discussions

Two iron-nickel samples were tested to failure under tension. Figure 2 shows the stress-strain curve for both samples. The tensile yield point for both samples was measured to be about 1.4 GPa, while the total elongation varied between five percent and eight percent. Both samples failed near the interface with the grip, indicating a possible stress concentration problem due to sample geometry.

The total elastic displacement of the sample was of the order of 12 microns. Because of the small elastic displacement and the limits set by the precision of the pins and hinges, it was not possible to measure the Young modulus with this load frame which was designed to measure the initial yield and ultimate strength of the material.

The cross section of the samples tested in this study was uniform. Hence, the grips apply shear stress in the region where the compressive load is maximum. Consequently, the samples were observed to fail near the interface with the grip. By using a "dogbone" shaped geometry for the samples, the failure can be expected to occur at the center of the gage section, rather than near the gage ends.

Conclusions

The extremely small size of the samples introduced a number of difficulties, such as sample handling and attaching the sample to the grips. In spite of these, a good measurement of the yield point and the ultimate strength was made. By changing the geometry of

Schmidt, B. A., 1990, "The Rotationally Flexible Pendulum Subjected to a High Frequency Excitation," ASME JOURNAL OF APPLIED MECHANICS, Vol. 57, pp. 725–730.

Schmidt, B. A., and McDowell, D. G., 1992, "Analysis of a Pendulum on a Rotating Arm," ASME JOURNAL OF APPLIED MECHANICS, Vol 59, pp. 233–234.

Sethna, P. R., and Hemp, G. W., 1964, "Nonlinear Oscillation of a Gyroscopic Pendulum with an Oscillatory Point of Suspension," *Proc. Colloq. International du Centre National de la Reserche Scientifique, N-148, Les vibration forcées dans les systemes non-lineaires,* pp. 375–392.

Stephenson, A., 1908, "On a New Type of Dynamical Stability," *Manchester Memoirs,* Vol. 52, pp. 1–10.

Measurement of Tensile Properties of Metallic Foils

V. Sharma[1], J. B. Isaacs[2], and S. Nemat-Nasser[2]

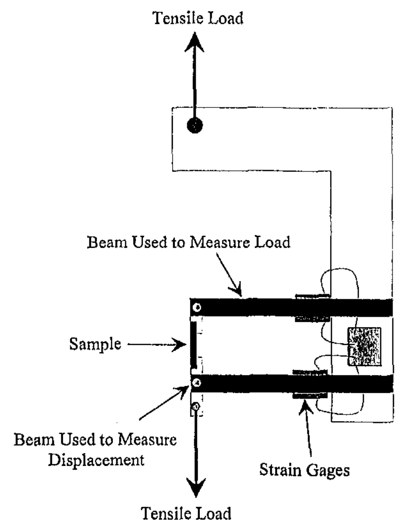

Fig. 1 Schematic diagram of the load fixture used to measure the tensile properties of metallic foils

A fixture has been developed for testing thin specimens under uniaxial tension. The fixture consists of two cantilever beams with strain gauges attached to them close to their fixed ends. The displacement of one beam is used to measure the force and the difference in the displacements of the beams is used to measure the sample displacement. The tensile properties of 0.025 mm by 1.25 mm by 5 mm iron-nickel specimens were measured. The tensile plastic yield point of the specimens was observed to be 1.4 GPa and the total elongation to failure turned out to be five percent and eight percent, for the two tested specimens.

Introduction

Tension tests are widely used to measure the strength and ductility of different materials under uniaxial tensile stresses. A variety of tension testing machines are available commercially with a wide range of loading rate and load capacity, with interchangeable grips to hold various test specimens. A majority of commercially available tension testing machines are not capable of testing tensile properties of very thin and small specimens due to the small loads required for failure and inability to mount the specimens in the grips.

The tensile properties of thin films has been studied by using mini tensile testers (Rudd et al., 1993; Griffin et al., 1992; Noyan and Sheikh, 1993). Rudd et al. (1993) measured the strains in thin films by monitoring the position of laser spots diffracted from a grating created on the surface of the specimen. Griffin et al. (1992) measured stress from the load cell and strain from the rotational speed of their screw driven tensile tester. Noyan and Sheikh (1993) used a standard uniaxial tensile test with X-ray diffraction techniques to measure mechanical stress-strain relations and X-ray stress and strain in the diffracting regions of the specimen. In this study, the tensile properties of thin metallic foils are studied on a new test fixture, which allows the measurement of the tensile properties of very small metallic foils, in conjunction with any standard testing machine.

Experimental Procedure

Iron-nickel foils were used in these experiments. The dimensions of the foils were 0.025 mm by 1.25 mm by 5 mm. Figure 1 is the schematic diagram of the load fixture. It consists of two cantilever beams with strain gauges mounted on them close to their fixed ends. The calibrated displacement of one beam gives the force applied to the sample, whereas the difference in the displacement between the two beams gives the displacement of the sample.

A system of alignment pins and hinges were used to eliminate bending loads on the foils and to facilitate sample installation. The sample is glued and clamped in place between the two cantilevers. The lower beam is loaded through a spring, the other end of which is connected to the lower ram of a servohydraulic machine. The strain gauge outputs were digitized and the force-displacement curves were computed, from which stress-strain curves were obtained.

Results and Discussions

Two iron-nickel samples were tested to failure under tension. Figure 2 shows the stress-strain curve for both samples. The tensile yield point for both samples was measured to be about 1.4 GPa, while the total elongation varied between five percent and eight percent. Both samples failed near the interface with the grip, indicating a possible stress concentration problem due to sample geometry.

The total elastic displacement of the sample was of the order of 12 microns. Because of the small elastic displacement and the limits set by the precision of the pins and hinges, it was not possible to measure the Young modulus with this load frame which was designed to measure the initial yield and ultimate strength of the material.

The cross section of the samples tested in this study was uniform. Hence, the grips apply shear stress in the region where the compressive load is maximum. Consequently, the samples were observed to fail near the interface with the grip. By using a "dogbone" shaped geometry for the samples, the failure can be expected to occur at the center of the gage section, rather than near the gage ends.

Conclusions

The extremely small size of the samples introduced a number of difficulties, such as sample handling and attaching the sample to the grips. In spite of these, a good measurement of the yield point and the ultimate strength was made. By changing the geometry of

[1] Samsung Information Systems America, 75 West Plumeria Drive, San Jose, CA 95134.

[2] Center for Excellence for Advanced Materials, University of California, San Diego, La Jolla, CA 92093-0416.

Contributed by the Applied Mechanics Division of THE AMERICAN SOCIETY OF MECHANICAL ENGINEERS for publication in the ASME JOURNAL OF APPLIED MECHANICS. Manuscript received by the ASME Applied Mechanics Division, Nov. 19, 1996; final revision, Feb. 17, 1998. Associate Technical Editor: V. K. Kinra.

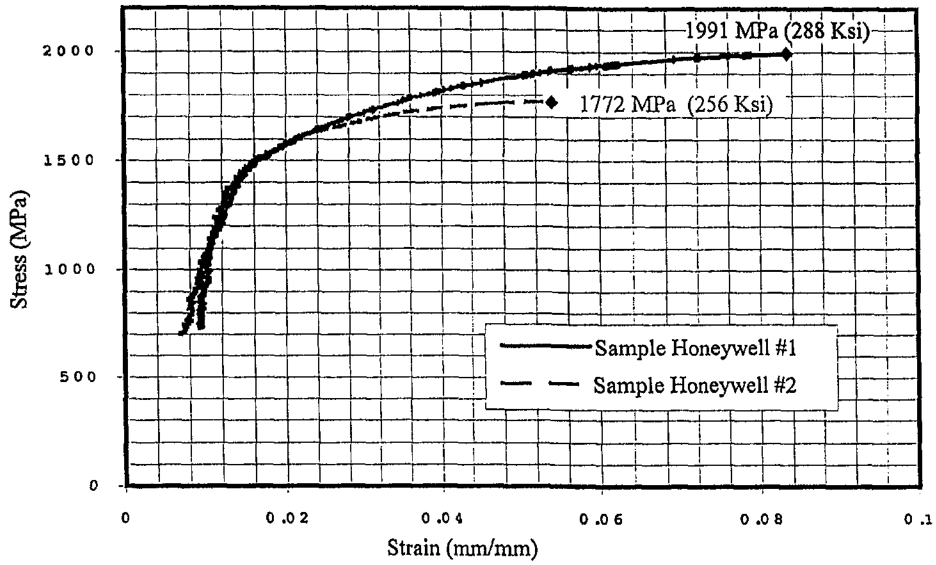

Fig. 2 Stress-strain curves for two iron-nickel foils under tension

the specimen, different metallic and nonmetallic foils with varying strengths can be tested with this kind of fixtures.

Acknowledgment

This research was supported by a grant from the Army Research Office under DAAL03-92-G-0108 to the University of California, San Diego.

References

Griffin, A. J., Brotzen, F. R., and Dunn, C. F., 1992, "Mechanical testing of thin metallic film," *Thin Solid Films*, Vol. 220, pp. 265–270.

Noyan, I. C., and Sheikh, G., 1993, "X-ray tensile testing of thin films," *J. Mater. Res.*, Vol. 8, No. 4, pp. 764–770.

Rudd, J. A., Josell, D., Spaepen, F., and Greer, A. L., 1993, "A new method for tensile testing of thin films," *J. Mater. Res.*, Vol. 8, No. 1, pp. 112–117.

A Comparison Between Direct and Indirect Friction Measurements in a Forced Oscillator

J.-W. Liang[1,3] and B. F. Feeny[2,3]

1 Introduction

Characterizing macroscopic friction behavior is important in many engineering tasks, such as those involving control, and squeak and squeal prediction. Two schools of thought for measuring macroscopic friction forces involve the employment of a load cell and the calculation of the friction force by measuring motion signals and applying them to the system's governing equation. Direct load-cell measurements are most often found in the literature. Examples can be found in recent books and reviews, such as Guran et al. (1996), Ibrahim (1994), Armstrong-Hélouvry et al. (1994), and Oden and Martins (1985), or in any journal on the topic.

Installing a load cell to frictional systems can be expensive, and is equivalent to adding a mass-spring subsystem and its dynamics to the main system (Streator and Bogy, 1994). Thus, the signal obtained from a load cell may not be able to completely depict actual friction forces. On the other hand, the "indirect" calculation of the friction force from the system's ordinary differential equation (ODE) requires more than one transducer. The indirect measurement is therefore liable to parasitic interference and calibration errors (Antoniou et al., 1965).

A brief comparison between friction signals from both direct and indirect friction measurements is presented in this note. The measurements displayed here are in a forced mass-spring system during macroscopic sliding and macroscopic stick-slip. More details on the classification and modeling of these motions for this system were given previously (Liang and Feeny, 1998).

2 Apparatus and Instrumentation

The apparatus (Fig. 1) consisted of a base-excited mass (m = 2.42 kg), helical springs with a total stiffness of k = 2310 N/m, and the friction-contact mechanism. The sliding mass moved in an air track. Motion in the air track was almost friction free, with a nondimensional viscous damping factor equal to 0.0008. This damping is subsequently neglected. The friction-contact mechanism consisted of a pinched-flange structure mounted through a roller bearing, which was designed for balancing the normal loads on both sliding surfaces, as depicted in the cross-section diagram.

The displacements of both the sliding mass and the base excitation were sensed by linear variable differential transformer (LVDT). The LVDT signal passed through a signal conditioner. This LVDT was made by Rabinson-Halpern Co. (Model 210A-0500) and had a resolution of 2.5 μm after quantization. A seismic accelerometer (PCB, Model 393C) was adopted to record the acceleration signal. This accelerometer had a frequency range of 0.025 Hz to 800 Hz with five percent transverse sensitivity and a resonant frequency of 3.5 kHz (125 Hz with its mounting). The friction force was measured by a

[1] Department of Mechanical Engineering, MingChi Institute of Technology, Taipei, Taiwan, R.O.C.

[2] Department of Mechanical Engineering, Michigan State University, East Lansing, MI 48824.

[3] Mem. ASME.

Contributed by the Applied Mechanics Division of The American Society of Mechanical Engineers for publication in the ASME Journal of Applied Mechanics. Manuscript received by the ASME Applied Mechanics Division, Mar. 18, 1997; final revision, Mar, 10, 1998. Associate Technical Editor: N. C. Perkins.

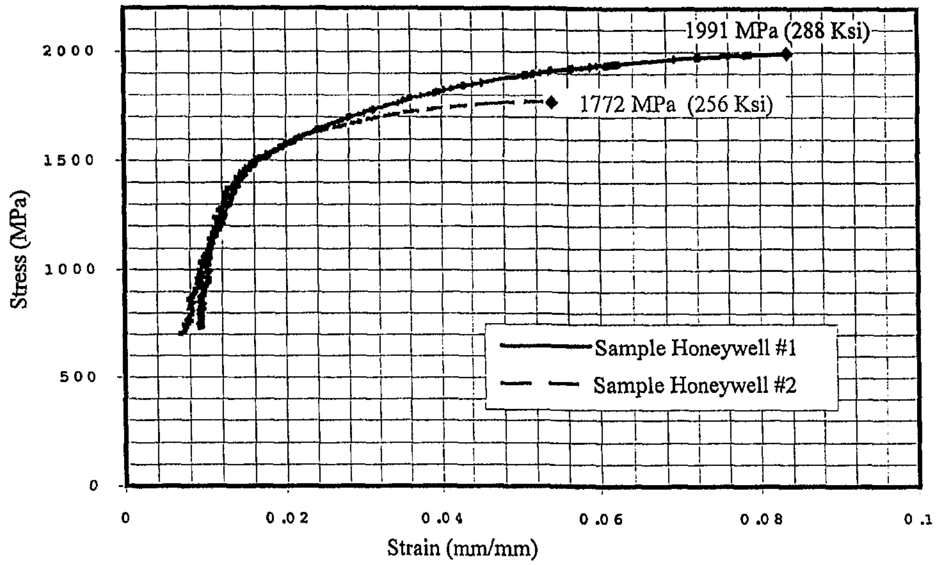

Fig. 2 Stress-strain curves for two iron-nickel foils under tension

the specimen, different metallic and nonmetallic foils with varying strengths can be tested with this kind of fixtures.

Acknowledgment

This research was supported by a grant from the Army Research Office under DAAL03-92-G-0108 to the University of California, San Diego.

References

Griffin, A. J., Brotzen, F. R., and Dunn, C. F., 1992, "Mechanical testing of thin metallic film," *Thin Solid Films*, Vol. 220, pp. 265–270.

Noyan, I. C., and Sheikh, G., 1993, "X-ray tensile testing of thin films," *J. Mater. Res.*, Vol. 8, No. 4, pp. 764–770.

Rudd, J. A., Josell, D., Spaepen, F., and Greer, A. L., 1993, "A new method for tensile testing of thin films," *J. Mater. Res.*, Vol. 8, No. 1, pp. 112–117.

A Comparison Between Direct and Indirect Friction Measurements in a Forced Oscillator

J.-W. Liang[1,3] and B. F. Feeny[2,3]

1 Introduction

Characterizing macroscopic friction behavior is important in many engineering tasks, such as those involving control, and squeak and squeal prediction. Two schools of thought for measuring macroscopic friction forces involve the employment of a load cell and the calculation of the friction force by measuring motion signals and applying them to the system's governing equation. Direct load-cell measurements are most often found in the literature. Examples can be found in recent books and reviews, such as Guran et al. (1996), Ibrahim (1994), Armstrong-Hélouvry et al. (1994), and Oden and Martins (1985), or in any journal on the topic.

Installing a load cell to frictional systems can be expensive, and is equivalent to adding a mass-spring subsystem and its dynamics to the main system (Streator and Bogy, 1994). Thus, the signal obtained from a load cell may not be able to completely depict actual friction forces. On the other hand, the "indirect" calculation of the friction force from the system's ordinary differential equation (ODE) requires more than one transducer. The indirect measurement is therefore liable to parasitic interference and calibration errors (Antoniou et al., 1965).

A brief comparison between friction signals from both direct and indirect friction measurements is presented in this note. The measurements displayed here are in a forced mass-spring system during macroscopic sliding and macroscopic stick-slip. More details on the classification and modeling of these motions for this system were given previously (Liang and Feeny, 1998).

2 Apparatus and Instrumentation

The apparatus (Fig. 1) consisted of a base-excited mass ($m = 2.42$ kg), helical springs with a total stiffness of $k = 2310$ N/m, and the friction-contact mechanism. The sliding mass moved in an air track. Motion in the air track was almost friction free, with a nondimensional viscous damping factor equal to 0.0008. This damping is subsequently neglected. The friction-contact mechanism consisted of a pinched-flange structure mounted through a roller bearing, which was designed for balancing the normal loads on both sliding surfaces, as depicted in the cross-section diagram.

The displacements of both the sliding mass and the base excitation were sensed by linear variable differential transformer (LVDT). The LVDT signal passed through a signal conditioner. This LVDT was made by Rabinson-Halpern Co. (Model 210A-0500) and had a resolution of 2.5 μm after quantization. A seismic accelerometer (PCB, Model 393C) was adopted to record the acceleration signal. This accelerometer had a frequency range of 0.025 Hz to 800 Hz with five percent transverse sensitivity and a resonant frequency of 3.5 kHz (125 Hz with its mounting). The friction force was measured by a

[1] Department of Mechanical Engineering, MingChi Institute of Technology, Taipei, Taiwan, R.O.C.

[2] Department of Mechanical Engineering, Michigan State University, East Lansing, MI 48824.

[3] Mem. ASME.

Contributed by the Applied Mechanics Division of The American Society of Mechanical Engineers for publication in the ASME Journal of Applied Mechanics. Manuscript received by the ASME Applied Mechanics Division, Mar. 18, 1997; final revision, Mar, 10, 1998. Associate Technical Editor: N. C. Perkins.

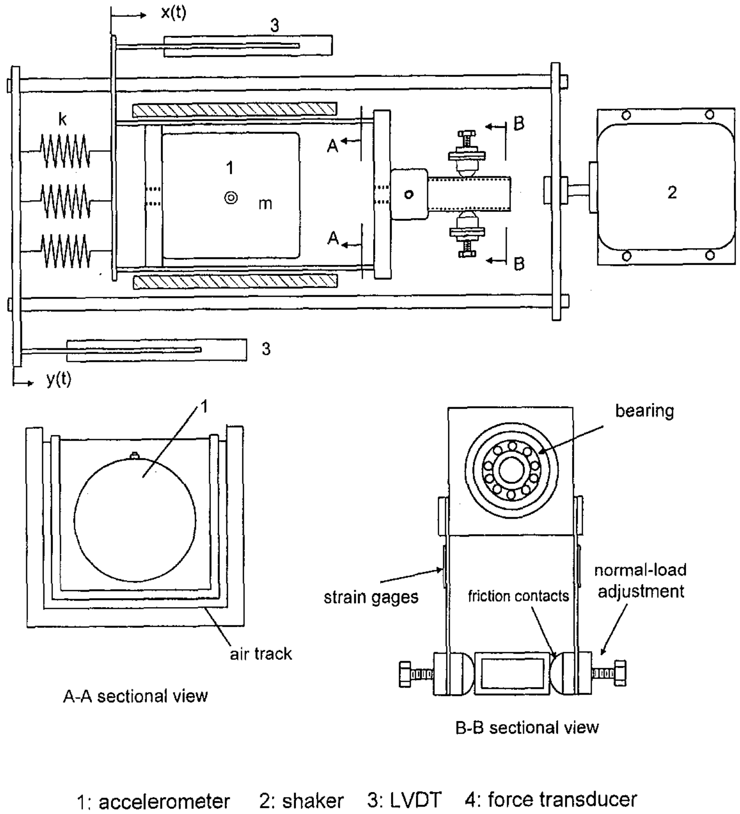

Fig. 1 Schematic diagram of the experimental apparatus

piezoelectric load cell (PCB, Model 208B) which had 0.00089 N resolution in a range of 44.8 N in both tension and compression. The nominal sensitivity was 110 mV/N with a stiffness of 1.75×10^9 N/m. The discharge time constant of this load cell was 50 sec and the resonant frequency was 70 kHz (250 Hz with its attachment). The sampling rate was 5 kHz.

The system was driven by an electromagnetic shaker (LDS, Model 400). The friction contact was steel-on-steel. The planar surfaces were ground and rubbed with 400-grit, silicon-carbide paper. The other contact surfaces had hemispherical geometry and were lathed with an engineering finish then rubbed by the same type of paper. Finally, the surfaces were cleaned by a degreaser (Measurement Group, Inc., Model CSM-1). The surfaces were then engaged in sliding motion for at least 30 minutes to attain a steady-state friction characteristic before the data were recorded.

A phase shift existed between the accelerometer and LVDT, probably caused by filtering in the LVDT signal conditioner. To determine this phase shift, a free-vibration test of the mass-spring system was conducted with the base constrained.

The measurements of displacement and acceleration are denoted as $x_m(t)$ and $\ddot{x}_m(t)$, respectively. There was a phase shift of $\phi = 0.0389$ radians by which the accelerometer signal leads the LVDT signal. This phase angle was converted to a time shift using $\tau = \phi/\omega_n$, and it was chosen such that the resultant force, namely $m\ddot{x}_m(t + \tau) + kx_m(t)$, was close to zero with some random noise. A strong source of random noise was induced by the sound pressure fluctuation of the air track.

Three sets of base-excited motion tests (Liang, 1996) indicated that the dependence of the phase shift on the excitation frequency was not significant over a reasonable range. The phase angles of accelerometer and the load cell were presumed to be approximately equal to zero based on their response characteristics and the low-frequency range of this study.

Here there was virtually no viscous friction. If viscous friction were significant, a velocity signal would be needed. Integrating the acceleration would involve an integration constant, which could be chosen to produce zero mean in the velocity. Differentiating the displacement would amplify noise, although in this case perhaps not to the level of noise that is present in $\ddot{x}_m$. If available, a velocity sensor such as a laser or LVT could be used, if care is taken in its calibration and phase determination.

3 The Comparison Between Friction Signals

To calculate the friction force from the system's equation of motion, namely $F(t) = ky_m(t) - kx_m(t) - m\ddot{x}_m(t + \tau)$, where $y_m(t)$ represents the measured motion of the base, motion signals $x_m(t)$, $\ddot{x}_m(t)$, and $y_m(t)$ are required.

Figure 2(a) illustrates the time-domain histories of the experimental inertial forces, $f_2 = m\ddot{x}(t + \tau)$, spring force, $f_1 = kx_m(t)$, and the base-excitation force, $f_3 = ky_m(t)$. The frequency of harmonic excitation is 5.5 Hz. The response of the slider is a stable pure-sliding motion. The calculated friction force is presented in Fig. 2(b) and denoted as $F(t)$. Random noise caused mostly by the air track on the accelerometer signal was superimposed on the calculated friction signal. To smoothen the signal, a five-point moving average (Liang, 1996) was applied to generate the data shown in Fig. 2(c) and labeled $F1(t)$. Next, the friction force obtained from the direct measurements of the load cell after the same smoothening process (for comparison) is illustrated in Fig. 2(d) as $F2(t)$. The signal $F2(t)$ is obtained by subtracting the inertial component on the load cell due to the mass of the flange from the readout of the load cell. The raw version of $F2(t)$ is very similar to the averaged version since it does not register much transient dynamics as in the computation case.

Three observations are made from these Figures. (1) During the whole test, the friction-force magnitudes are more or less constant. (2) Both methods are consistent regarding the macroscopic dynamics friction feature. (3) There are subtle differences between the two approaches at the change in sliding

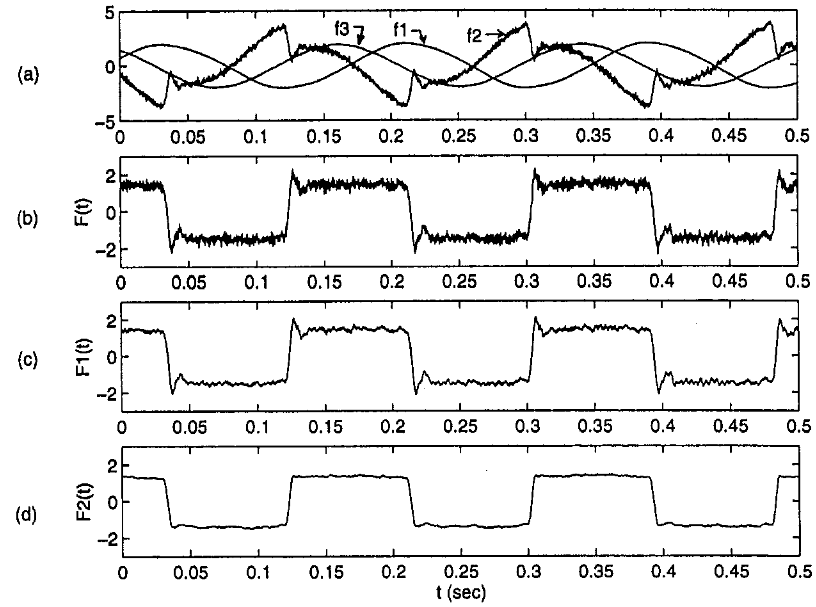

Fig. 2 Time-domain comparison of direct and indirect friction measurements, excitation frequency = 5.5 Hz, stable pure sliding case, in (*a*) f1 labels the experimental spring force $= kx_m(t)$; f2 labels the experimental inertial force $= m\ddot{x}_m(t+\tau)$; f3 labels the experimental excitation force $= ky_m(t)$; (*b*) $F(t)$ is the calculated friction force; (*c*) $F1(t)$ is the averaged version of $F(t)$; (*d*) $F2(t)$ represents the load cell measurement after averaging

direction. Regarding observation (3), a higher-frequency dynamical response is registered in the calculated friction force than in the directly measured friction force. This may be because the load cell, with its attached flange, acts as a low-pass filter, and attenuates high frequencies. (The stiffness and mass of the attachment has a natural frequency and a bandwidth.) Furthermore, some high-frequency oscillation is evident in the calculated friction signal immediately following a velocity reversal. We speculate that this may be due to the dynamics of the accelerometer mounting.

Two other stable pure-sliding cases were examined in which the excitation frequencies were 3.5 and 7.5 Hz (Liang, 1996). Consistencies and discrepancies between the two approaches are preserved in these tests, with the post-reversal oscillation slightly more prominent in the indirect signal of the latter case, and less evident in the former case. Since the same phase relationship was employed between the sensors at each excitation frequency, the consistent results indeed illustrate the reliability of the indirect approach over a reasonable frequency range.

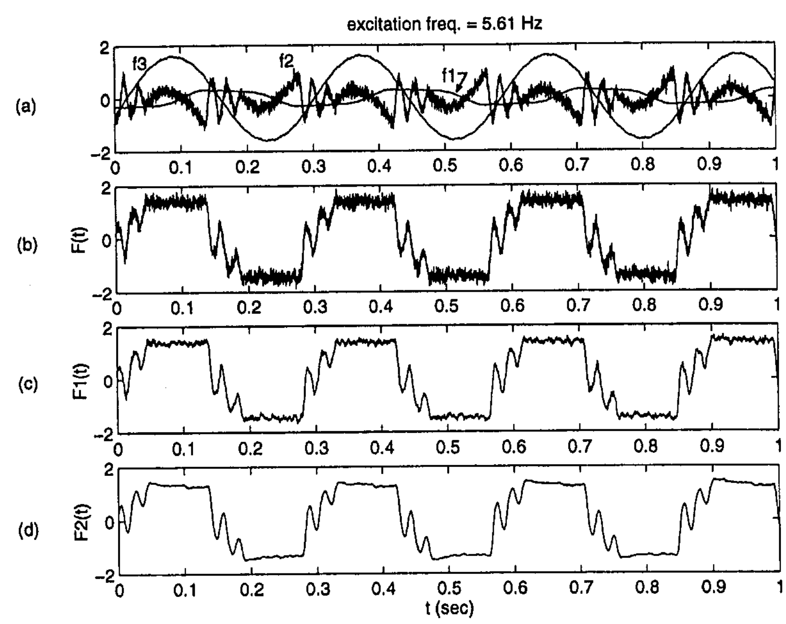

Fig. 3 Time-domain comparison of direct and indirect friction measurements, excitation frequency = 3.5 Hz, stick-slip motion case, in (*a*) f1: the experimental spring force $= kx_m(t)$; f2: the experimental inertial force $= m\ddot{x}_m(t+\tau)$; f3: the experimental excitation force $= ky_m(t)$; (*b*) $F(t)$ is the calculated friction force; (*c*) $F1(t)$ is the averaged version of $F(t)$; (*d*) $F2(t)$ represents the load cell measurement after averaging

Figure 3 illustrates a case that has stick-slip motion. The excitation frequency is 3.5 Hz. Due to the presence of stick-slip, features of the friction force are different, especially during the transition of sliding to sticking. A 47-Hz transition oscillation occurs during the sticking phase. This transition oscillation is likely to be caused by the compliance of the contact and its surrounding structure (Liang and Feeny, 1998). The averaged calculated force of Fig. 3(c) and the transducer force shown in (d) are consistent with the exception of a slight high-frequency noise in the calculated force.

4 Conclusion

In this study, we compared friction measurements computed from motion sensors with those obtained directly from a load cell. While there are high-frequency differences between the direct and indirect measurements, the the correlation in the results suggests that either method can be trusted for capturing the macroscopic friction behavior. This cross reference between two measurement techniques reinforces the applicability of the more commonly used load-cell technique. The indirect calculation measurement is only practical for simple oscillators, which may be useful in studying basic phenomena such as friction. In more general multi-degree-of-freedom systems, the indirect measurement based on measured states is impractical, as the number of measurements needed may be arbitrarily large, and knowledge of the system equations of motion may be limited.

Detailed comparisons of these measurement techniques showed that, although the load cell registered most of the friction dynamics in our system, its high-frequency contents were attenuated to some extent. Perhaps a better load-cell mounting strategy may have reduced this attenuation. Evidence elsewhere (e.g., Ibrahim, 1997) indicates that high-quality load cells effectively capture minute details such as the presence of a static friction peak (e.g., Ibrahim, 1996; Popp et al., 1996) or rate dependence (Polycarpou and Soom, 1996). In our system, the calculated friction may have caught more complete details over the low and high-frequency ranges and also captured the noise generated by the air track and possibly the dynamics of the mounting.

Acknowledgments

Years ago, Andy Ruina suggested estimating the friction force indirectly from the equations of motion. This work was supported by the National Science Foundation (CMS-9624347) and Ford Motor Company.

References

Antoniou, S. S., Cameron, A., and Gentle, C. R., 1976, "The friction-speed relationship from stick-slip data," *Wear*, Vol. 36, pp. 235–254.

Armstrong-Hélouvry, B., Dupont, P., and Canudas de Wit, C., 1994, "A survey of models, analysis tools and compensation methods for the control of machines with friction," *Automatica*, Vol. 30, No. 7, pp. 1083–1138.

Guran, A., Pfeiffer, F., and Popp, K., 1996, *Dynamics with Friction: Modeling, Analysis and Experiment. Part I*, World Scientific, River Edge, NJ.

Ibrahim, R. A., 1994, "Friction-induced vibration, chatter, squeal, and chaos: Part I—Mechanics of friction; Part II—Dynamics and modeling," ASME *Applied Mechanics Reviews*, Vol. 47, No. 7, pp. 209–253.

Ibrahim, R. A., 1996, *Proceedings of the symposium on Elasto-Impact and Friction in Dynamic Systems*, ASME International Congress and Exhibition, Atlanta, GA, Nov. 17–22.

Liang, J.-W., 1996, "Characterizing the Low-Order Friction Dynamics in a Forced Oscillator," Ph.D. thesis, Michigan State University, East Lansing, MI.

Liang, J.-W., and Feeny, B. F., 1998, "Dynamical Friction Behavior in a Forced Oscillator With a Compliant Contact," ASME JOURNAL OF APPLIED MECHANICS, Vol. 65, pp. 250–257.

Oden, J. T., and Martins, J. A. C., 1985, "Models and computational methods for dynamic friction phenomena," *Computer Methods in Applied Mechanics and Engineering*, Vol. 52, pp. 527–634.

Polycarpou, A., and Soom, A., 1996, "Modeling Unsteady Lubricated Friction," *Dynamics with Friction: Modeling, Analysis, and Experiments*, A. Guran, F. Pfeiffer, and K. Popp, eds., World Scientific, River Edge, NJ, 197–232.

Popp, K., Hinrichs, N., Oestreich, M., 1996, "Analysis of a Self-Excited Friction Oscillator with External Excitation," *Dynamics with Friction: Modeling, Analysis, and Experiments*, A. Guran, F. Pfeiffer, and K. Popp, eds., World Scientific, River Edge, NJ, pp. 1–35.

Streator, J. L., and Bogy, D. B., 1992, "Accounting for transducer dynamics in the measurement of friction," *Journal of Tribology*, Vol. 114, pp. 86–94.

On the Extreme Values of Young's Modulus, the Shear Modulus, and Poisson's Ratio for Cubic Materials

M. Hayes[1] and A. Shuvalov[1]

For homogeneous cubic elastic materials with positive definite stored energy it is shown that the maximum and minimum values of Young's modulus E are related to the maximum and minimum values of the shear modulus G through the simple connection

$$1/G_{\min} - 1/G_{\max} = 3(1/E_{\min} - 1/E_{\max}).$$

It is deduced that the ratio of compliances $-s_{12}/s_{44}$ *is the maximum value of Poisson's ratio* ν *in the cubic materials with a positive parameter* $\chi \equiv 2s_{11} - 2s_{12} - s_{44}$, *and the minimum value of* ν *in the cubic materials with negative* χ.

1 Introduction

Consider a homogeneous anisotropic elastic material with positive definite stored energy in the absence of body forces. The response of the material to uniaxial tension T in the direction $\mathbf{n}$: $t_{ij} = Tn_in_j$, (T constant, $\mathbf{n}\cdot\mathbf{n} = 1$), is characterized by Young's modulus $E(\mathbf{n})$. Indeed, $T = E(\mathbf{n})e_{ij}n_in_j$, where e_{ij} are the strain components. Similarly, the response to the shear stress $t_{ij} = S(n_im_j + n_jm_i)$, ($S$ constant, $\mathbf{n}\cdot\mathbf{n} = \mathbf{m}\cdot\mathbf{m} = 1$, $\mathbf{m}\cdot\mathbf{n} = 0$), is characterized by the shear modulus $G(\mathbf{m};\mathbf{n}) = G(\mathbf{n};\mathbf{m})$. In this case $S = 2G(\mathbf{m};\mathbf{n})e_{ij}m_in_j$. Poisson's ratio ν ($\mathbf{m}$; $\mathbf{n}$) is the ratio of the lateral contraction $-e_{ij}m_im_j$ along $\mathbf{m}$ to the longitudinal extension $e_{rs}n_rn_s$. If the elastic compliances are denoted by s_{ijkl}, which are assumed to possess the symmetries $s_{ijkl} = s_{jikl} = s_{klij} = s_{ijlk}$, then $1/E(\mathbf{n}) = s_{ijkl}n_in_jn_kn_l$, $1/G(\mathbf{m};\mathbf{n}) = 4s_{ijkl}n_im_jn_km_l$, $\nu(\mathbf{m};\mathbf{n}) = -s_{ijkl}m_im_jn_kn_l/s_{pqrs}n_pn_qn_rn_s$ (Sirotin and Shaskol'skaya, 1982). For anisotropic elastic materials Young's modulus E is a function of direction in the material, while the shear modulus G and Poisson's ratio ν are functions of a pair of orthogonal directions.

In the case of a cubic material there are only three independent compliances, usually denoted by s_{11}, s_{12}, s_{44}, where $s_{11} = s_{1111} = s_{2222} = s_{3333}$, $s_{12} = s_{1122} = s_{1133} = s_{2233}$, $s_{44} = 4s_{2323} = 4s_{1313} = 4s_{1212}$ (Sirotin and Shaskol'skaya, 1982). Then,

$$1/E(\mathbf{n}) = s_{12} + \tfrac{1}{2}s_{44} + \tfrac{1}{2}(2s_{11} - 2s_{12} - s_{44}) \times (n_1^4 + n_2^4 + n_3^4), \quad (1)$$

$$1/G(\mathbf{m};\mathbf{n}) = s_{44} + 2(2s_{11} - 2s_{12} - s_{44}) \times (m_1^2n_1^2 + m_2^2n_2^2 + m_3^2n_3^2), \quad (2)$$

[1] Department of Mathematical Physics, University College Dublin, Belfield, Dublin 4, Ireland.

Contributed by the Applied Mechanics Division of The American Society of Mechanical Engineers for publication in the ASME Journal of Applied Mechanics. Manuscript received by the ASME Applied Mechanics Division, July 30, 1997; final revision, May 4, 1998. Associate Technical Editor: M. M. Carroll.

Figure 3 illustrates a case that has stick-slip motion. The excitation frequency is 3.5 Hz. Due to the presence of stick-slip, features of the friction force are different, especially during the transition of sliding to sticking. A 47-Hz transition oscillation occurs during the sticking phase. This transition oscillation is likely to be caused by the compliance of the contact and its surrounding structure (Liang and Feeny, 1998). The averaged calculated force of Fig. 3(*c*) and the transducer force shown in (*d*) are consistent with the exception of a slight high-frequency noise in the calculated force.

4 Conclusion

In this study, we compared friction measurements computed from motion sensors with those obtained directly from a load cell. While there are high-frequency differences between the direct and indirect measurements, the the correlation in the results suggests that either method can be trusted for capturing the macroscopic friction behavior. This cross reference between two measurement techniques reinforces the applicability of the more commonly used load-cell technique. The indirect calculation measurement is only practical for simple oscillators, which may be useful in studying basic phenomena such as friction. In more general multi-degree-of-freedom systems, the indirect measurement based on measured states is impractical, as the number of measurements needed may be arbitrarily large, and knowledge of the system equations of motion may be limited.

Detailed comparisons of these measurement techniques showed that, although the load cell registered most of the friction dynamics in our system, its high-frequency contents were attenuated to some extent. Perhaps a better load-cell mounting strategy may have reduced this attenuation. Evidence elsewhere (e.g., Ibrahim, 1997) indicates that high-quality load cells effectively capture minute details such as the presence of a static friction peak (e.g., Ibrahim, 1996; Popp et al., 1996) or rate dependence (Polycarpou and Soom, 1996). In our system, the calculated friction may have caught more complete details over the low and high-frequency ranges and also captured the noise generated by the air track and possibly the dynamics of the mounting.

Acknowledgments

Years ago, Andy Ruina suggested estimating the friction force indirectly from the equations of motion. This work was supported by the National Science Foundation (CMS-9624347) and Ford Motor Company.

References

Antoniou, S. S., Cameron, A., and Gentle, C. R., 1976, "The friction-speed relationship from stick-slip data," *Wear*, Vol. 36, pp. 235–254.

Armstrong-Hélouvry, B., Dupont, P., and Canudas de Wit, C., 1994, "A survey of models, analysis tools and compensation methods for the control of machines with friction," *Automatica*, Vol. 30, No. 7, pp. 1083–1138.

Guran, A., Pfeiffer, F., and Popp, K., 1996, *Dynamics with Friction: Modeling, Analysis and Experiment. Part I*, World Scientific, River Edge, NJ.

Ibrahim, R. A., 1994, "Friction-induced vibration, chatter, squeal, and chaos: Part I—Mechanics of friction; Part II—Dynamics and modeling," ASME *Applied Mechanics Reviews*, Vol. 47, No. 7, pp. 209–253.

Ibrahim, R. A., 1996, *Proceedings of the symposium on Elasto-Impact and Friction in Dynamic Systems*, ASME International Congress and Exhibition, Atlanta, GA, Nov. 17–22.

Liang, J.-W., 1996, "Characterizing the Low-Order Friction Dynamics in a Forced Oscillator," Ph.D. thesis, Michigan State University, East Lansing, MI.

Liang, J.-W., and Feeny, B. F., 1998, "Dynamical Friction Behavior in a Forced Oscillator With a Compliant Contact," ASME JOURNAL OF APPLIED MECHANICS, Vol. 65, pp. 250–257.

Oden, J. T., and Martins, J. A. C., 1985, "Models and computational methods for dynamic friction phenomena," *Computer Methods in Applied Mechanics and Engineering*, Vol. 52, pp. 527–634.

Polycarpou, A., and Soom, A., 1996, "Modeling Unsteady Lubricated Friction," *Dynamics with Friction: Modeling, Analysis, and Experiments*, A. Guran, F. Pfeiffer, and K. Popp, eds., World Scientific, River Edge, NJ, 197–232.

Popp, K., Hinrichs, N., Oestreich, M., 1996, "Analysis of a Self-Excited Friction Oscillator with External Excitation," *Dynamics with Friction: Modeling, Analysis, and Experiments*, A. Guran, F. Pfeiffer, and K. Popp, eds., World Scientific, River Edge, NJ, pp. 1–35.

Streator, J. L., and Bogy, D. B., 1992, "Accounting for transducer dynamics in the measurement of friction," *Journal of Tribology*, Vol. 114, pp. 86–94.

On the Extreme Values of Young's Modulus, the Shear Modulus, and Poisson's Ratio for Cubic Materials

M. Hayes[1] and A. Shuvalov[1]

For homogeneous cubic elastic materials with positive definite stored energy it is shown that the maximum and minimum values of Young's modulus E are related to the maximum and minimum values of the shear modulus G through the simple connection

$$1/G_{\min} - 1/G_{\max} = 3(1/E_{\min} - 1/E_{\max}).$$

It is deduced that the ratio of compliances $-s_{12}/s_{44}$ *is the maximum value of Poisson's ratio* ν *in the cubic materials with a positive parameter* $\chi \equiv 2s_{11} - 2s_{12} - s_{44}$, *and the minimum value of* ν *in the cubic materials with negative* χ.

1 Introduction

Consider a homogeneous anisotropic elastic material with positive definite stored energy in the absence of body forces. The response of the material to uniaxial tension T in the direction $\mathbf{n}$: $t_{ij} = Tn_in_j$, (T constant, $\mathbf{n}\cdot\mathbf{n} = 1$), is characterized by Young's modulus $E(\mathbf{n})$. Indeed, $T = E(\mathbf{n})e_{ij}n_in_j$, where e_{ij} are the strain components. Similarly, the response to the shear stress $t_{ij} = S(n_im_j + n_jm_i)$, ($S$ constant, $\mathbf{n}\cdot\mathbf{n} = \mathbf{m}\cdot\mathbf{m} = 1$, $\mathbf{m}\cdot\mathbf{n} = 0$), is characterized by the shear modulus $G(\mathbf{m};\mathbf{n}) = G(\mathbf{n};\mathbf{m})$. In this case $S = 2G(\mathbf{m};\mathbf{n})e_{ij}m_in_j$. Poisson's ratio $\nu(\mathbf{m};\mathbf{n})$ is the ratio of the lateral contraction $-e_{ij}m_im_j$ along $\mathbf{m}$ to the longitudinal extension $e_{rs}n_rn_s$. If the elastic compliances are denoted by s_{ijkl}, which are assumed to possess the symmetries $s_{ijkl} = s_{jikl} = s_{klij} = s_{ijlk}$, then $1/E(\mathbf{n}) = s_{ijkl}n_in_jn_kn_l$, $1/G(\mathbf{m};\mathbf{n}) = 4s_{ijkl}n_im_jn_km_l$, $\nu(\mathbf{m};\mathbf{n}) = -s_{ijkl}m_im_jn_kn_l/s_{pqrs}n_pn_qn_rn_s$ (Sirotin and Shaskol'skaya, 1982). For anisotropic elastic materials Young's modulus E is a function of direction in the material, while the shear modulus G and Poisson's ratio ν are functions of a pair of orthogonal directions.

In the case of a cubic material there are only three independent compliances, usually denoted by s_{11}, s_{12}, s_{44}, where $s_{11} = s_{1111} = s_{2222} = s_{3333}$, $s_{12} = s_{1122} = s_{1133} = s_{2233}$, $s_{44} = 4s_{2323} = 4s_{1313} = 4s_{1212}$ (Sirotin and Shaskol'skaya, 1982). Then,

$$1/E(\mathbf{n}) = s_{12} + \tfrac{1}{2}s_{44} + \tfrac{1}{2}(2s_{11} - 2s_{12} - s_{44}) \times (n_1^4 + n_2^4 + n_3^4), \quad (1)$$

$$1/G(\mathbf{m};\mathbf{n}) = s_{44} + 2(2s_{11} - 2s_{12} - s_{44}) \times (m_1^2n_1^2 + m_2^2n_2^2 + m_3^2n_3^2), \quad (2)$$

[1] Department of Mathematical Physics, University College Dublin, Belfield, Dublin 4, Ireland.

Contributed by the Applied Mechanics Division of The American Society of Mechanical Engineers for publication in the ASME Journal of Applied Mechanics. Manuscript received by the ASME Applied Mechanics Division, July 30, 1997; final revision, May 4, 1998. Associate Technical Editor: M. M. Carroll.

$$\nu(\mathbf{m};\mathbf{n}) = -\frac{s_{12} + \frac{1}{2}(2s_{11} - 2s_{12} - s_{44})(m_1^2n_1^2 + m_2^2n_2^2 + m_3^2n_3^2)}{s_{12} + \frac{1}{2}s_{44} + \frac{1}{2}(2s_{11} - 2s_{12} - s_{44})(n_1^4 + n_2^4 + n_3^4)}. \tag{3}$$

By virtue of the assumption that the stored energy is positive definite it follows (Sirotin and Shaskol'skaya, 1982) that

$$s_{11} > |s_{12}|, \quad s_{11} + 2s_{12} > 0, \quad s_{44} > 0. \tag{4}$$

For an isotropic material, the combination χ, defined by

$$\chi = 2s_{11} - 2s_{12} - s_{44}, \tag{5}$$

is zero, and Young's modulus and the shear modulus are independent of direction(s) and then given by $1/E = s_{11}$, $1/G = s_{44}$, $\nu = -s_{12}/s_{11}$.

2 Extrema of Young's Modulus and the Shear Modulus

We proceed to determine the maximum and minimum values of $E(\mathbf{n})$ and $G(\mathbf{m};\mathbf{n})$ given by Eqs. (1) and (2).

Let us note the two identities for the unit orthogonal vectors $\mathbf{n}$ and $\mathbf{m}$:

$$n_1^4 + n_2^4 + n_3^4 = 1 - 2(n_1^2n_2^2 + n_1^2n_3^2 + n_2^2n_3^2)$$
$$= \frac{1}{3}[1 + (n_1^2 - n_2^2)^2 + (n_1^2 - n_3^2)^2 + (n_2^2 - n_3^2)^2], \tag{6}$$

$$m_1^2n_1^2 + m_2^2n_2^2 + m_3^2n_3^2 = \frac{1}{2}[1 - (m_1n_2 + m_2n_1)^2 - (m_1n_3 + m_3n_1)^2 - (m_2n_3 + m_3n_2)^2]. \tag{7}$$

Thus, by (6), the maximum value of $(n_1^4 + n_2^4 + n_3^4)$ is 1 and its minimum value is $(\frac{1}{3})$, taken at $\mathbf{n}$ parallel, respectively, to $\langle 001\rangle$ and to $\langle 111\rangle$, where $\langle\ldots\rangle$ is the conventional notation adopted in crystallography for a set of symmetrically equivalent directions defined by the enclosed coordinates of one of them. By (7), the maximum value of $(m_1^2n_1^2 + m_2^2n_2^2 + m_3^2n_3^2)$ is $(\frac{1}{2})$ attained when the mutually orthogonal vectors $\mathbf{m}$, $\mathbf{n}$ are parallel to $\langle 110\rangle$, $\langle -110\rangle$ (in arbitrary order), and its minimum value is zero, attained at $\mathbf{m}$, $\mathbf{n}$ parallel to $\langle 100\rangle$, $\langle 011\rangle$ (in arbitrary order).

We denote the maximum and minimum values of $E(\mathbf{n})$ by $E_{\max}$ and $E_{\min}$, respectively, and the maximum and minimum values of $G(\mathbf{m};\mathbf{n})$ by $G_{\max}$ and $G_{\min}$, respectively.

If $\chi > 0$, then

$$1/E_{\min} = s_{11}, \tag{8}$$

and

$$1/E_{\max} = \frac{1}{3}(s_{11} + 2s_{12} + s_{44}). \tag{9}$$

We note

$$3(1/E_{\min} - 1/E_{\max}) = \chi. \tag{10}$$

Also,

$$1/G_{\min} = 2(s_{11} - s_{12}), \tag{11}$$

and

$$1/G_{\max} = s_{44}. \tag{12}$$

Thus

$$1/G_{\min} - 1/G_{\max} = \chi. \tag{13}$$

Hence, using Eqs. (10) and (13),

$$1/G_{\min} - 1/G_{\max} = 3(1/E_{\min} - 1/E_{\max}). \tag{14}$$

Similar considerations apply if $\chi < 0$; the values of $E_{\min}$ and $E_{\max}$ given by Eqs. (8) and (9) are interchanged as are the values of $G_{\min}$ and $G_{\max}$ given by Eqs. (11) and (12). In any case the result (14) is valid.

3 Extrema of Poisson's Ratio

Similarly, it may be shown that Poisson's ratio $\nu(\mathbf{m};\mathbf{n})$ in a cubic body with compliances for which $\chi > 0$, attains its maximum value $\nu_{\max} = -s_{12}/s_{11}$ when $\mathbf{m}$, $\mathbf{n}$ are parallel to $\langle 100\rangle$, $\langle 011\rangle$, respectively, so that simultaneously the numerator in Eq. (3) taken with opposite sign attains its minimum value, and the positive denominator attains its maximum value. If $\chi < 0$, then the corresponding interchange of the maximum and minimum values of the numerator and denominator yields $\nu_{\min} = -s_{12}/s_{11}$ for the same directions interchanged. In both cases the extreme value $-s_{12}/s_{11}$, by virtue of (4), satisfies the inequalities: $-1 < -s_{12}/s_{11} < 0$ with $s_{12} > 0$; $0 < -s_{12}/s_{11} < \frac{1}{2}$ with $s_{12} < 0$. It is seen that these inequalities set bounds for possible values of the maximum Poisson's ratio in cubic materials with $\chi > 0$ and of minimum Poisson's ratio in cubic materials with $\chi < 0$.

Acknowledgment

One of us (A.S.) is grateful to Foirbairt for support under grant SC/96/736.

Reference

Sirotin, Yu. I., and Shaskol'skaya, M. P., 1982, *Fundamentals of crystal physics.* MIR Publishers, Moscow.

A Stress Analysis Method for Bi-axially Loaded Fastener Hole in Composite Laminate of Finite Geometry

Y. Xiong[1]

A stress analysis method has been developed for a bi-axially loaded fastener hole in a laminated plate of finite geometry. The method is based on a variational formulation involving complex variables. In this method, the equilibrium and compatibility equations are satisfied in the domain of the plate due to the employment of the complex stress potentials and all the boundary conditions are satisfied through a variational statement. Therefore, the requirement for finite width corrections in relatively large fastener hole cases is avoided. The method has been verified through comparison with finite element results.

Introduction

Stress analysis of fastener loaded holes is crucial in the design of mechanically fastened joints in composite structures. Extensive work has been devoted to mechanically fastened composite

[1] Structures, Materials and Propulsion Laboratory, Institute for Aerospace Research, National Research Council, Ottawa, Canada K1A 0R6.

Contributed by the Applied Mechanics Division of THE AMERICAN SOCIETY OF MECHANICAL ENGINEERS for publication in the ASME JOURNAL OF APPLIED MECHANICS. Manuscript received by the ASME Applied Mechanics Division, Aug. 2, 1997; final revision, Apr. 1, 1998. Associate Technical Editor: J. N. Reddy.

$$\nu(\mathbf{m};\mathbf{n}) = -\frac{s_{12}+\frac{1}{2}(2s_{11}-2s_{12}-s_{44})(m_1^2n_1^2+m_2^2n_2^2+m_3^2n_3^2)}{s_{12}+\frac{1}{2}s_{44}+\frac{1}{2}(2s_{11}-2s_{12}-s_{44})(n_1^4+n_2^4+n_3^4)}. \tag{3}$$

By virtue of the assumption that the stored energy is positive definite it follows (Sirotin and Shaskol'skaya, 1982) that

$$s_{11} > |s_{12}|, \quad s_{11}+2s_{12} > 0, \quad s_{44} > 0. \tag{4}$$

For an isotropic material, the combination χ, defined by

$$\chi = 2s_{11} - 2s_{12} - s_{44}, \tag{5}$$

is zero, and Young's modulus and the shear modulus are independent of direction(s) and then given by $1/E = s_{11}$, $1/G = s_{44}$, $\nu = -s_{12}/s_{11}$.

2 Extrema of Young's Modulus and the Shear Modulus

We proceed to determine the maximum and minimum values of $E(\mathbf{n})$ and $G(\mathbf{m};\mathbf{n})$ given by Eqs. (1) and (2).

Let us note the two identities for the unit orthogonal vectors $\mathbf{n}$ and $\mathbf{m}$:

$$n_1^4+n_2^4+n_3^4 = 1-2(n_1^2n_2^2+n_1^2n_3^2+n_2^2n_3^2)$$
$$= \tfrac{1}{3}[1+(n_1^2-n_2^2)^2+(n_1^2-n_3^2)^2+(n_2^2-n_3^2)^2], \tag{6}$$

$$m_1^2n_1^2+m_2^2n_2^2+m_3^2n_3^2 = \tfrac{1}{2}[1-(m_1n_2+m_2n_1)^2$$
$$-(m_1n_3+m_3n_1)^2-(m_2n_3+m_3n_2)^2]. \tag{7}$$

Thus, by (6), the maximum value of $(n_1^4+n_2^4+n_3^4)$ is 1 and its minimum value is $(\frac{1}{3})$, taken at $\mathbf{n}$ parallel, respectively, to $\langle 001\rangle$ and to $\langle 111\rangle$, where $\langle\ldots\rangle$ is the conventional notation adopted in crystallography for a set of symmetrically equivalent directions defined by the enclosed coordinates of one of them. By (7), the maximum value of $(m_1^2n_1^2+m_2^2n_2^2+m_3^2n_3^2)$ is $(\frac{1}{2})$ attained when the mutually orthogonal vectors $\mathbf{m}$, $\mathbf{n}$ are parallel to $\langle 110\rangle$, $\langle -110\rangle$ (in arbitrary order), and its minimum value is zero, attained at $\mathbf{m}$, $\mathbf{n}$ parallel to $\langle 100\rangle$, $\langle 011\rangle$ (in arbitrary order).

We denote the maximum and minimum values of $E(\mathbf{n})$ by $E_{\max}$ and $E_{\min}$, respectively, and the maximum and minimum values of $G(\mathbf{m};\mathbf{n})$ by $G_{\max}$ and $G_{\min}$, respectively.

If $\chi > 0$, then

$$1/E_{\min} = s_{11}, \tag{8}$$

and

$$1/E_{\max} = \tfrac{1}{3}(s_{11}+2s_{12}+s_{44}). \tag{9}$$

We note

$$3(1/E_{\min} - 1/E_{\max}) = \chi. \tag{10}$$

Also,

$$1/G_{\min} = 2(s_{11}-s_{12}), \tag{11}$$

and

$$1/G_{\max} = s_{44}. \tag{12}$$

Thus

$$1/G_{\min} - 1/G_{\max} = \chi. \tag{13}$$

Hence, using Eqs. (10) and (13),

$$1/G_{\min} - 1/G_{\max} = 3(1/E_{\min} - 1/E_{\max}). \tag{14}$$

Similar considerations apply if $\chi < 0$; the values of $E_{\min}$ and $E_{\max}$ given by Eqs. (8) and (9) are interchanged as are the values of $G_{\min}$ and $G_{\max}$ given by Eqs. (11) and (12). In any case the result (14) is valid.

3 Extrema of Poisson's Ratio

Similarly, it may be shown that Poisson's ratio $\nu(\mathbf{m};\mathbf{n})$ in a cubic body with compliances for which $\chi > 0$, attains its maximum value $\nu_{\max} = -s_{12}/s_{11}$ when $\mathbf{m}$, $\mathbf{n}$ are parallel to $\langle 100\rangle$, $\langle 011\rangle$, respectively, so that simultaneously the numerator in Eq. (3) taken with opposite sign attains its minimum value, and the positive denominator attains its maximum value. If $\chi < 0$, then the corresponding interchange of the maximum and minimum values of the numerator and denominator yields $\nu_{\min} = -s_{12}/s_{11}$ for the same directions interchanged. In both cases the extreme value $-s_{12}/s_{11}$, by virtue of (4), satisfies the inequalities: $-1 < -s_{12}/s_{11} < 0$ with $s_{12} > 0$; $0 < -s_{12}/s_{11} < \frac{1}{2}$ with $s_{12} < 0$. It is seen that these inequalities set bounds for possible values of the maximum Poisson's ratio in cubic materials with $\chi > 0$ and of minimum Poisson's ratio in cubic materials with $\chi < 0$.

Acknowledgment

One of us (A.S.) is grateful to Foirbairt for support under grant SC/96/736.

Reference

Sirotin, Yu. I., and Shaskol'skaya, M. P., 1982, *Fundamentals of crystal physics*. MIR Publishers, Moscow.

A Stress Analysis Method for Bi-axially Loaded Fastener Hole in Composite Laminate of Finite Geometry

Y. Xiong[1]

A stress analysis method has been developed for a bi-axially loaded fastener hole in a laminated plate of finite geometry. The method is based on a variational formulation involving complex variables. In this method, the equilibrium and compatibility equations are satisfied in the domain of the plate due to the employment of the complex stress potentials and all the boundary conditions are satisfied through a variational statement. Therefore, the requirement for finite width corrections in relatively large fastener hole cases is avoided. The method has been verified through comparison with finite element results.

Introduction

Stress analysis of fastener loaded holes is crucial in the design of mechanically fastened joints in composite structures. Extensive work has been devoted to mechanically fastened composite

[1] Structures, Materials and Propulsion Laboratory, Institute for Aerospace Research, National Research Council, Ottawa, Canada K1A 0R6.

Contributed by the Applied Mechanics Division of THE AMERICAN SOCIETY OF MECHANICAL ENGINEERS for publication in the ASME JOURNAL OF APPLIED MECHANICS. Manuscript received by the ASME Applied Mechanics Division, Aug. 2, 1997; final revision, Apr. 1, 1998. Associate Technical Editor: J. N. Reddy.

joints but the majority of the work has dealt with unidirectional loading conditions, as cited by Oplinger (1996). In most of the actual cases, the loading conditions around each fastener hole will not be unidirectional. The closed-form analytical approaches following Lekhnitskii (1968) have been used to deal with single fastener joints under uni-axial loading conditions, such as the work by de Jong (1977) and Zhang and Ueng (1985). Superposition procedures have to be employed if bi-axial loads are considered. In addition, in these analytical approaches, an infinite plate assumption is adopted. Another analytical work by Mangalgiri and Dattaguru (1986), involving complex stress potentials, dealt with the problem of misfit pin in an infinite plate under general biaxial loading in which a collocation technique was used to satisfy part of the boundary conditions.

The author has recently developed an analytical method to analyze multifastener composite joints under a unidirectional loading condition (Xiong, 1996). The method is based on complex variational formulations involving complex variables. The stress and displacement components in the joined members are represented using two complex stress potentials. The boundary effects are taken into account by the variational statement with the stress potentials being used as the trial functions. As a result, the approach can be used for composite joints with finite geometry without the requirement for a finite width correction.

In this paper, the complex variational approach is extended to calculate the stresses around a single fastener hole of finite geometry under bi-axial loading conditions. Results of stress analyses for a single fastener joint under bi-axial loads are presented along with a comparison to finite element data.

Statement of Problem

The problem under study is a rectangular laminated plate of length L and width W containing a centrally located hole with a radius of a, as shown in Fig. 1. This is a two-dimensional problem of an anisotropic plate under bi-axial loads, which are generally distributed along its four external edges. These given loads are shown in barred symbols in Fig. 1. The central hole is subjected to a bearing load by the fastener, which is in equilibrium with the external loads. In addition, the following assumptions are made in the analysis: (i) the pin is infinitely rigid and frictionless; (ii) the pin load is in a cosine distribution over one half of the hole edge; and (iii) the resultant of all the distributed normal loads is located at the mid-span of the respective edges. Assumption (i) has been used by numerous investigators and

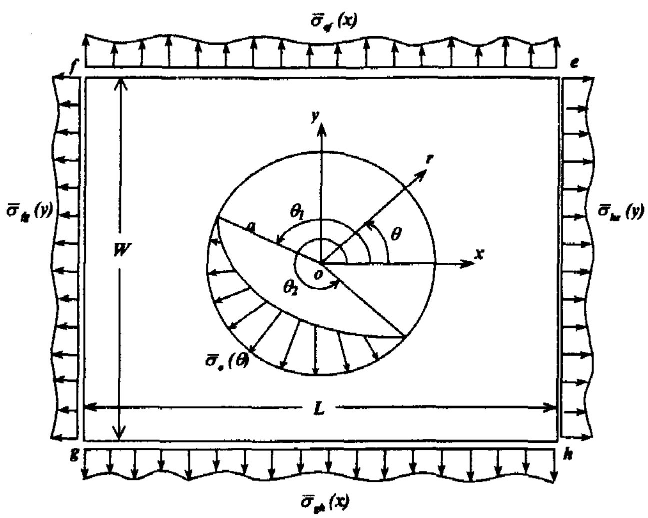

Fig. 1 Geometry configuration of a fastener hole

Table 1 Stress components around hold edge (Pa)

N	2	3	4	5	6
$(\sigma_\theta)_{max}$	7.78	7.83	7.82	7.96	7.97
$(\sigma_r)_{max}$	-5.03	-5.45	-5.46	-5.40	-5.38
$(\tau_{r\theta})_{max}$	-0.73	-0.21	-0.18	0.10	0.10
P_f (N)	0.217	0.217	0.217	0.217	0.216
ε	0.68%	0.67%	0.67%	0.65%	0.06%

its validity has been assessed by Hyer et al. (1987). Assumption (ii) is over simplified for a more orthotropic laminate, which is made here in order to ensure that only force boundary conditions are involved in the problem under consideration. It has been realized that the treatment of the pin-hole interaction by using displacement boundary conditions (Mangelgiri and Dattaquru, 1986) is more appropriate. The last assumption is made for simplicity of discussion in this paper. As a matter of fact, the edge normal loads can be arbitrarily distributed as long as they are in equilibrium with the fastener load.

A global coordinate system, x-y, is employed which is located at the center of the plate. The corresponding stress and displacement components in the plate are denoted as σ_x, σ_y, τ_{xy}, $\mathbf{u}$, and $\mathbf{v}$, respectively. For the purpose of convenience, a polar system, $\mathbf{r} - \theta$, is used on the periphery of the hole with the r-axis being the outer normal direction and $\theta = 0$ being the x-direction. Using the coordinate transformations, the stress and displacement components in the polar system can be derived, which are denoted as σ_r, σ_θ, $\tau_{r\theta}$, $\mathbf{u}_r$, and $\mathbf{u}_\theta$, respectively.

The problem is to find solutions for the stress and displacement components, which satisfy the equilibrium and compatibility equations in the plate. In addition, the solutions must satisfy the boundary conditions along all external and internal edges.

Complex Variational Formulation

In the theory of the two-dimensional anisotropic elasticity, two complex stress potentials, φ_1 and φ_2, are employed to derive the stress and displacement components. In doing so, the equilibrium and compatibility equations are automatically satisfied in the domain of the plate. The stress components take the following form:

$$\sigma_x = 2\,\mathrm{Re}[\mu_1^2\varphi_1'(\mathbf{z}_1) + \mu_2^2\varphi_2'(\mathbf{z}_2)]$$

$$\sigma_y = 2\,\mathrm{Re}[\varphi_1'(\mathbf{z}_1) + \varphi_2'(\mathbf{z}_2)]$$

$$\tau_{xy} = -2\,\mathrm{Re}[\mu_1\varphi_1'(\mathbf{z}_1) + \mu_2\varphi_2'(\mathbf{z}_2)] \qquad (1)$$

and the corresponding displacement components are

$$\mathbf{u} = 2\,\mathrm{Re}[\mathbf{p}_1\varphi_1(\mathbf{z}_1) + \mathbf{p}_2\varphi_2(\mathbf{z}_2)],$$

$$\mathbf{v} = 2\,\mathrm{Re}[\mathbf{q}_1\varphi_1(\mathbf{z}_1) + \mathbf{q}_2\varphi_2(\mathbf{z}_2)], \qquad (2)$$

where the conventional notation as used in Section 8, Chapter 2 of Lekhnitskii (1968) is employed in this paper.

Since the stress and displacement components expressed in terms of the two stress potentials as in Eqs. (1) and (2) satisfy the equilibrium and compatibility equations in the domain of the plate, the remaining task is to find appropriate stress potentials so that the respective boundary conditions can be satisfied. To this end, a variational formulation is established below with the energy functional written as

$$\Pi = \frac{1}{2}\int_\Omega \left\{ \mathbf{A}_{11}\left(\frac{\partial \mathbf{u}}{\partial \mathbf{x}}\right)^2 + 2\mathbf{A}_{12}\frac{\partial \mathbf{u}}{\partial \mathbf{x}}\frac{\partial \mathbf{v}}{\partial \mathbf{y}} + \mathbf{A}_{22}\left(\frac{\partial \mathbf{v}}{\partial \mathbf{y}}\right)^2 \right.$$

$$+ 2\left(\mathbf{A}_{16}\frac{\partial \mathbf{u}}{\partial \mathbf{x}} + \mathbf{A}_{26}\frac{\partial \mathbf{v}}{\partial \mathbf{y}}\right)\left(\frac{\partial \mathbf{u}}{\partial \mathbf{y}} + \frac{\partial \mathbf{y}}{\partial \mathbf{x}}\right)$$

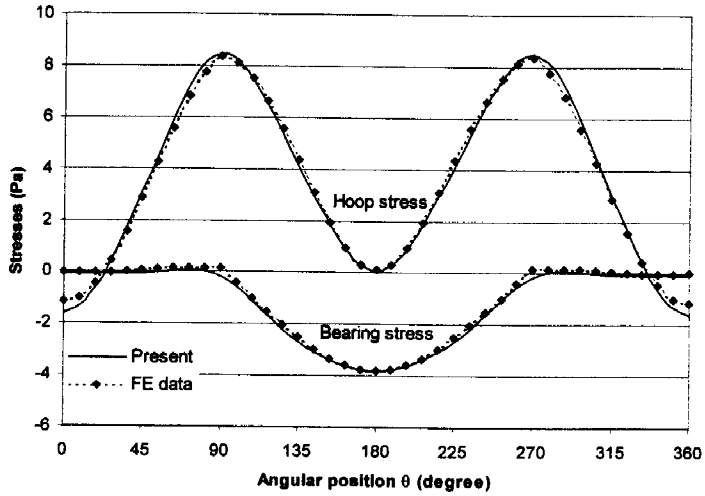

Fig. 2 Bearing and hoop stresses around fastener hole

$$+ \mathbf{A}_{66}\left(\frac{\partial \mathbf{u}}{\partial \mathbf{y}} + \frac{\partial \mathbf{v}}{\partial \mathbf{x}}\right)^2\Bigg\}\mathbf{dxdy} - \int_{x_e}^{x_f} \bar{\sigma}_{ef}(\mathbf{x})\mathbf{v}\left(\mathbf{x}, \frac{\mathbf{W}}{2}\right)\mathbf{dx}$$

$$- \int_{y_f}^{y_g} \bar{\sigma}_{fg}(\mathbf{y})\mathbf{u}\left(-\frac{\mathbf{L}}{2}, \mathbf{y}\right)\mathbf{dy} + \int_{x_g}^{x_h} \bar{\sigma}_{gh}(\mathbf{x})\mathbf{v}\left(\mathbf{x}, -\frac{\mathbf{W}}{2}\right)\mathbf{dx}$$

$$+ \int_{y_h}^{y_e} \bar{\sigma}_{he}(\mathbf{y})\mathbf{u}\left(\frac{\mathbf{L}}{2}, \mathbf{y}\right)\mathbf{dy} + \int_{\theta_1}^{\theta_2} \bar{\sigma}_0(\theta)\mathbf{u}_r(\mathbf{a}, \theta)\mathbf{a}\,\mathbf{d}\theta \quad (3)$$

where Ω denotes the domain of the plate. It can be shown, after cumbersome mathematical manipulations, that the vanishing condition of the energy functional in Eq. (3) is equivalent to the boundary conditions. That is, the minimization of the energy functional results in the correct solution of the problem under study. This condition can be written in a variational formulation, which involves boundary integrations only, as

$$\delta\Pi = \int_{x_e}^{x_f} \left[\sigma_y\left(\mathbf{x}, \frac{\mathbf{W}}{2}\right) - \bar{\sigma}_{ef}\right]\delta\mathbf{v}\mathbf{dx}$$

$$+ \int_{y_f}^{y_g} \left[\sigma_x\left(-\frac{\mathbf{L}}{2}, \mathbf{y}\right) - \bar{\sigma}_{fg}\right]\delta\mathbf{u}\mathbf{dy}$$

$$- \int_{x_g}^{x_h} \left[\sigma_y\left(\mathbf{x}, -\frac{\mathbf{W}}{2}\right) - \bar{\sigma}_{gh}\right]\delta\mathbf{v}\mathbf{dx}$$

$$- \int_{y_h}^{y_e} \left[\sigma_x\left(\frac{\mathbf{L}}{2}, \mathbf{y}\right) - \bar{\sigma}_{he}\right]\delta\mathbf{u}\mathbf{dy} + \int_{\theta_2 - 2\pi}^{\theta_1} \{\sigma_r(\mathbf{a}, \theta)\delta\mathbf{u}_r$$

$$+ \tau_{r\theta}(\mathbf{a}, \theta)\delta\mathbf{u}_\theta\}\mathbf{a}\,\mathbf{d}\theta + \int_{\theta_1}^{\theta_2} \{[\sigma_r(\mathbf{a}, \theta) + \bar{\sigma}_o(\theta)]\delta\mathbf{u}_r$$

$$+ \tau_{r\theta}(\mathbf{a}, \theta)\delta\mathbf{u}_\theta\}\mathbf{a}\,\mathbf{d}\theta = 0. \quad (4)$$

Now the problem is to select the appropriate stress potentials, φ_1 and φ_2, as the trial functions for the variational formulation derived. In this work, a truncated Laurent series with conformal mapping is used for the stress potentials, φ_1 and φ_2, as

$$\varphi_1 = \mathbf{C}_{10} \ln \zeta_1 + \sum_{n=1}^{N} (\mathbf{C}_{1n}\zeta_1^n + \mathbf{D}_{1n}\zeta_1^{-n})$$

$$\varphi_2 = \mathbf{C}_{20} \ln \zeta_2 + \sum_{n=1}^{N} (\mathbf{C}_{2n}\zeta_2^n + \mathbf{D}_{2n}\zeta_2^{-n}), \quad (5)$$

where the undetermined constants C_{1n}, D_{1n}, C_{2n}, and D_{2n} are, in general, complex and ζ_k are the mapping functions as used in Section 32, Chapter 6 of Lekhnitskii (1968). In addition, the following single-valued conditions are imposed for the logarithm terms in Eq. (5), as in Xiong (1996):

$$\mathrm{Im}(\mathbf{p}_1\mathbf{C}_{10} + \mathbf{p}_2\mathbf{C}_{20}) = 0, \quad \mathrm{Im}(\mathbf{q}_1\mathbf{C}_{10} + \mathbf{q}_2\mathbf{C}_{20}) = 0 \quad (6)$$

The complex constants in the trial functions are to be determined by the variational formulation derived and the number of constants in each of the stress potentials is $2N + 1$. Once these constants are computed, the stress and displacement components can be calculated using Eqs. (1) and (2).

Results and Discussion

To verify this analytical approach, a single fastener joint of finite geometry has been analyzed. The problem is a square AS4/3501-6 laminate with a centrally located hole. The plate edge length is $\mathbf{L} = \mathbf{W} = 152.4$ mm. The mechanical properties of each ply are: $\mathbf{E}_{11} = 140$ GPa, $\mathbf{E}_{22} = 8.2$ GPa, $\mathbf{G}_{12} = 6.2$ GPa, and $\nu_{12} = 0.3$. The layer thickness is 0.127 mm.

In the first case, an analysis is conducted to examine the convergence characteristics of the approach by changing the number of terms in the stress potentials. The lay-up of the laminate considered is quasi-isotropic $[45/0/-45/90]_{5s}$. The radius of the hole is $\mathbf{a} = 25.4$ mm and the four edge loads are $\bar{\sigma}_{ef} = 2$ Pa, $\bar{\sigma}_{fg} = 1$ Pa, $\bar{\sigma}_{gh} = 1$ Pa, and $\bar{\sigma}_{he} = 2$ Pa. The calculated peak stress components along the hole edge versus N, the number of terms in the series of the stress potentials, are presented in Table 1. It is shown that the calculations are stable and converged when the total number of terms in each of the stress potentials is 11 or more. It is also shown in Table 1 that the fastener load is relatively insensitive to the number of terms in the stress potentials as can be seen from the relative error, ϵ, between the calculated fastener load and the exact one which is in equilibrium with the external edge loads.

In the second case, the same joint under bi-axial and bypass loads is analyzed. The applied loads in this case are $\bar{\sigma}_{ef} = 0.5$ Pa, $\bar{\sigma}_{fg} = 1$ Pa, $\bar{\sigma}_{gh} = 0.5$ Pa, and $\bar{\sigma}_{he} = 2$ Pa. The hoop and bearing stress distributions along the fastener hole edge are shown in Fig. 2. Also shown in the figure are the results from a finite element analysis using MSC/NASTRAN with a very fine mesh. Good agreement between the analytical results using this method and the finite element data was obtained.

Conclusions

An analytical method based on a complex variational formulation has been developed for the stress analyses of composite laminates containing a single fastener hole. The variational formulation derived can deal with joints of finite geometry under bi-axial and bypass loading conditions without the requirement for finite width correction factors. The overall stress distribution in the joint as well as the fastener load can be determined. Results of example cases discussed have shown the effectiveness and accuracy of the complex variational approach developed.

References

de Jong, Th., 1977, "Stresses Around Pin-Loaded Holes in Elastically Orthotropic or Isotropic Plates," *Journal of Composite Materials*, Vol. 11, pp. 313–331.

Hyer, M. W., Klang, E. C., and Cooper, D. E., 1987, "The Effects of Pin Elasticity, Clearance, and Friction on the Stresses in a Pin-Loaded Orthotropic Plate," *Journal of Composite Materials*, Vol. 21, pp. 190–206.

Lekhnitskii, S. G., 1968, *Anisotropic Plates*, Gordon and Breach, New York.

Mangalgiri, P. D., and Dattaguru, B., 1986, "A Large Orthotropic Plate with Misfit Pin under Arbitrarily Oriented Biaxial Loading," *Composite Structures*, Vol. 6, pp. 271–281.

Oplinger, D. W., 1996, "Bolted Joints in Composite Structures: An Overview," *AGARD Conference Proceedings 590: Bolted/Bonded Joints in Polymeric Composites*, NATO, France.

Xiong, Y., 1996, "An Analytical Method for Failure Prediction of Multi-Fastener Composite Joints," *International Journal of Solids and Structures*, Vol. 33, pp. 4395–4409.

Zhang, K. D., and Veng, C. E. S., 1985, "Stresses Around a Pin-Loaded Hole in Orthotropic Plates with Arbitrary Loading Direction," *Composite Structures*, Vol. 3, pp. 119–142.

Journal of Applied Mechanics

Discussions

A Quasi-Decoupling Approach for Nonclassical Linear Systems in State Space[1]

S. M. Shahruz[2]. The authors consider the nonclassical linear system represented by

$$M\ddot{x}(t) + (G + C)\dot{x}(t) + (K + F)x(t) = f(t),$$
$$x(0) = x_0, \quad \dot{x}(0) = \dot{x}_0, \tag{1}$$

for all $t \geq 0$, where the real $n \times n$ matrices M, C, K, G, and F incorporate certain properties of the system. According to the authors (see [1, Section 7]) "The quasi-decoupling approach is attempted to provide a solution path for general nonclassical linear systems in state space." The proposed quasi-decoupling approach is as follows:

- Write the system (1) as

$$A\dot{y}(t) + By(t) = F(t), \quad y(0) = [x_0^T \quad \dot{x}_0^T]^T, \tag{2}$$

for all $t \geq 0$, where

$$A = \begin{bmatrix} G+C & M \\ -M & 0 \end{bmatrix}, \quad B = \begin{bmatrix} K+F & 0 \\ 0 & M \end{bmatrix}, \qquad (3a, b)$$

$$y(t) = \begin{bmatrix} x(t) \\ \dot{x}(t) \end{bmatrix}, \quad F(t) = \begin{bmatrix} f(t) \\ 0 \end{bmatrix}. \qquad (3c, d)$$

- By the QZ algorithm compute the matrices Q and Z such that

$$Q^T AZ = R, \quad Q^T BZ = S, \qquad (5),(6)$$

where R and S are block upper triangular and strict upper triangular matrices, or vice versa, with m blocks on their diagonals.

- Apply the linear transformation

$$y(t) = Zz(t), \tag{7}$$

to the system (2) and premultiply the resulting equation by Q^T to obtain

$$R\dot{z}(t) + Sz(t) = \bar{F}(t),$$
$$z(0) = [z_1^T(0) \quad z_2^T(0) \quad \dots \quad z_m^T(0)]^T = Z^{-1}y(0), \tag{8}$$

for all $t \geq 0$, where $\bar{F}(t) = Q^T F(t) = [\bar{f}_1^T(t) \ \bar{f}_2^T(t) \ \dots \ \bar{f}_m^T(t)]^T$. Finally, write the system (8) as

$$r_{ii}\dot{z}_i(t) + s_{ii}z_i(t) = \tilde{f}_i(t), \quad \text{initial conditions: } z_i(0), \tag{9}$$

for all $t \geq 0$, where $i = m, \dots, 1$ and $\tilde{f}_i(t) = \bar{f}_i(t) - \sum_{k=i+1}^{m} (r_{ik}\dot{z}_k(t) + s_{ik}z_k(t))$. Having the sets of equations in (9), the authors propose to solve them from the mth (last) set to the first set sequentially. Thus, by the proposed technique the vector $z(t) = [z_1^T(t) \quad z_2^T(t) \quad \dots \quad z_m^T(t)]^T$ can be obtained over a time interval $[0, T_f]$. It is certainly true that the proposed technique can provide a solution for the system (1). However, the efficacy of the technique is seriously questionable, because of the following:

(i) There is computational effort to obtain the matrices Q and Z that satisfy (5) and (6).

(ii) A set of equations in (9) is not decoupled because for an $i = 1, \dots, m$, either r_{ii} or s_{ii} can be a full matrix. Therefore, solving a set of equations in (9) is not as convenient as it seems. The authors never mention how a set of equations in (9) should be solved. It should be solved by direct numerical integration. Suppose that the jth set of equations, $1 \leq j \leq m$, is to be solved. On the right-hand side of this set, solutions of the $j+1$st, $j+2$nd, ..., mth sets of equations, which were obtained in pervious steps, as well as their time-derivatives, should be first substituted. This means that additional effort should be made to compute the time-derivatives of the previous solutions. Moreover, computing these derivatives can be quite inaccurate and noisy. Therefore, the computational error can propagate as the sets of equations are solved from the last set to the first.

The authors fail to show that their proposed technique to solve linear systems is superior over the existing techniques, such as direct numerical integration, in terms of computational effort (CPU time). Computational effort to compute the matrices Q and Z and to solve the sets of equations in (9) can be more than that of direct numerical integration of the system (1). With the advent of fast computers, the system (1) can be solved efficiently and accurately by direct numerical integration, and in particular by parallel integration algorithms when the system is large scale (see, e.g., Bennighof and Wu (1991), Harichandaran and Ye (1993), Shieh (1993), and the references therein).

References

Bennighof, J. K., and Wu, J.-Y., 1991, "An unconditionally stable parallel transient algorithm with multi-step independent subdomain computation," *Parallel Methods on Large-Scale Structural Analysis and Physics Applications*, O. O. Storaasli and E. A. Carmona, eds., Pergamon Press, Oxford, pp. 217–230.

Harichandaran, R. S., and Ye, B., 1993, "A method of deriving parallel algorithms for direct integration in structural dynamics," *Parallel Computational Methods for Large-Scale Structural Analysis and Design*, O. O. Storaasli, J. M. Housner, and D. T. Nguyen, eds., Elsevier, New York, pp. 415–420.

Shieh, R. C., 1993, "Massively parallel computational methods for finite element analysis of transient structural responses," *Parallel Computational Methods for Large-Scale Structural Analysis and Design*, O. O. Storaasli, J. M. Housner, and D. T. Nguyen, eds., Elsevier, New York, pp. 421–433.

[1] By G. Ren and Z. Zheng and published in the Dec. 1997 issue of the ASME JOURNAL OF APPLIED MECHANICS, Vol. 64, pp. 946–950.

[2] Research Scientist, Berkeley Engineering Research Institute, P.O. Box 9984, Berkeley, California 94709.

Nonlinear Waves in Strings: The Barrage Balloon Problem[1]

N. D. Cristescu[2]. One knows today much more about mechanics of extensible strings than mentioned by the author. Below I briefly present the early history of the problem. For further details see Cristescu, (1967, Chapter 4) and Cristescu (1960a), where some results, initially published in some other languages, are summarized in English.

The problem of plane motion of a string impacted obliquely with a punctual body, moving with constant velocity (i.e., due to its big mass the string is unable to reduce the speed of the impacting body) was studied by Rakhmatulin (1945). It is assumed that during impact the body is in contact with the same material point of the string, and that the tension-strain relationship is nonlinear. First propagate the longitudinal waves and afterwards the transverse shock waves (discontinuities of the tangent) (see Fig. 1 reproduced after Rakhmatulin's paper—see also Fig. V.1 from Cristescu (1960a)—which is self-explanatory). Several other cases have been considered: impact without friction when the body slides along the string, rectangular impact on the string, oblique impact, etc. Rakhmatulin writes also the general differential equations of plane motion of the string, and discovers the velocities of propagation (Rakhmatulin; 1947). Plane motion of elastic strings has been considered also by Cole et al. (1953), with the strong assumption that the displacements are linear functions on spatial and temporal coordinates. The oblique impact of elastic strings, assuming that the area of transverse cross sections remain constant, was considered by Ringleb (1957). A method to determine the constitutive relation $T = T(\epsilon)$ from orthogonal impact of a string was proposed by Rakhmatulin and Shapiro (1955). Impact of strings by bodies of finite mass was considered by Rakhmatulin (1951) and Ryabova (1953); thus the string may influence the motion of the impacted body. Both the elastic and plastic waves are considered. The dynamic unloading from a plastic state is also considered. The impact of a string with a wedge of arbitrary shape was studied by Rakhmatulin (1952). The motion of the string in contact with the surface of the wedge and in free motion is examined. The particular shape of the wedge is also considered, as well as impact with a circular cylinder. Experimental results of impact of rubber cables are also reported. Impact with a wedge of variable velocity (finite mass), leading to a variable impact velocity, was considered by Ryabova (1956). Transverse impact of a finite extensible string at midpoint was studied experimentally by Smith et al. (1956, 1958). Both longitudinal and transverse waves are considered, the transverse being a shock wave (traveling discontinuity of the tangent to the string). Figure 2 reproduced after Smith et al. (1956) is self-explanatory. A method was proposed to determine from tests the constitutive equation for the material (nylon, fortisan, etc.) (Smith et al., 1961). An experimental method to determine the velocity of propagation of longitudinal waves was developed by Smith et al. (1960). Specific breaking energies for various yarns and limiting breaking velocities are discussed by Smith et al. (1962b, c). An experimental technique of impacting yarns with a rifle bullet was developed by Smith et al. (1962a, 1963) and Fenstermaker and Smith (1965). The effect of the air drag on the motion of the yarn was analyzed by Smith et al. (1964).

Transverse impact of strings by bullets and a study of both longitudinal and transverse waves have been reported also by Petterson et al. (1960), Petterson and Stewart (1960), and

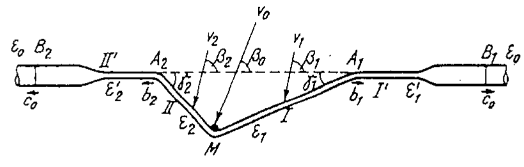

Fig. 1 Oblique impact on a string, according to Rakhmatulin (1945)

Jameson et al. (1962). Smith et al. (1965) arrived experimentally to the conclusion that during impact with rifle bullets creep and stress relaxation are significant.

The equation of motion in three-dimensions of an extensible string, for an arbitrary nonlinear stress-strain relation, finite strain, and arbitrary transverse motion are due to Cristescu (1954, 1960b). It is shown that the transverse and longitudinal waves propagate with the velocity

$$c_I^2 = \frac{1}{\varrho}\frac{T}{1+\epsilon} \quad \text{and} \quad c_{II}^2 = \frac{1}{\varrho}\frac{dT}{d\epsilon}, \tag{1}$$

respectively, where T is the "tension," ϵ the finite strain, ϱ the initial density, and $T = T(\epsilon)$ the nonlinear tension-strain relation. It is shown when one wave is propagating faster than the other, and when the two velocities are equal. The differential relation satisfied along characteristic lines show, in exact mathematical terms, how the two kinds of waves are influencing each other. Examples have been given by numerical integration on four characteristic lines: a semi-infinite string with a prescribed motion at the end (Cristescu, 1963); the finite string with one end fixed and the other end moving following a prescribed law (Cristescu, 1964); the problem of a finite extensible cable used to brake high-speed moving bodies (Cristescu, 1965a); and the motion of two bodies of distinct mass and moving initially with distinct velocities, connected by an extensible cable (Cristescu, 1965b).

The general three-dimensional equation of motion of extensible strings satisfying a constitutive equation of rate type of the form

$$\frac{\partial \epsilon}{\partial t} = g(T, \epsilon)\frac{\partial T}{\partial t} + f(T, \epsilon) \tag{2}$$

was also studied by Cristescu (1965c). This time there are five characteristic curves. The particular cases of (2) were considered. Manacorda (1958) has studied a certain rate influence and temperature changes on the motion of the string. Dinca (1967) has also considered the temperature influence on the dynamics of extensible strings which move in a resistive medium, for a tension-strain-temperature relationship written in finite form.

Transverse shock waves (traveling "kinks") have also been theoretically studied. For plane motion let us mention Rakhmatulin and Demianov (1961), Pérès (1953), Craggs (1954), and Pavlenko (1959). The three-dimensional motion was analyzed by Cristescu et al. (1966) where the general jump conditions have been given, (see also Cristescu (1967)). The velocities of propagation are now

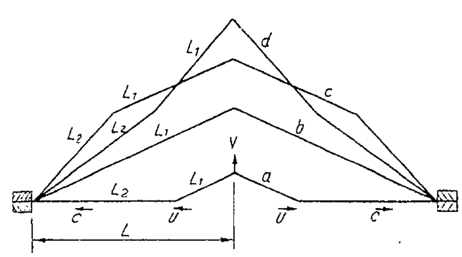

Fig. 2 Typical configuration of a yarn specimen after transverse impact, according to Smith et al. (1956)

[1] By J. F. Hall and published in the Mar. 1998 issue of the ASME Journal of Applied Mechanics, Vol. 65, pp. 141–149.

[2] Graduate Research Professor, Department of Aerospace Engineering, Mechanics, and Engineering Science, University of Florida, Gainesville, FL 32611-6250.

$$c_I^2 = \frac{T}{\varrho(1+\epsilon)} \quad \text{and} \quad c_{II}^2 = \frac{1}{\varrho}\frac{[T]}{[\epsilon]} \qquad (3)$$

where the brackets stand for "jump." Formula $(3)_1$ was obtained for elastic strings by Cristescu (1951; see also Cristescu, 1967) and by Pérès (1953) for general extensible strings. The cases when shock wave coincides or not with smooth waves was also discussed. The propagation of transverse shock waves in inextensible strings was studied using functional analysis by Moisil (1956).

All the above-mentioned results, as well as many other ones, are presented in Chapter 4 (pp. 181–291) of the book by Cristescu (1967). Thus, problems of the kind considered by the author, as well as much more general ones, concerning the mechanics of extensible strings (with nonlinear tension-strain relationship, finite strains, and arbitrary transverse motion), have been considered for a long time.

A "geographical" erratum: the Ploesti Oil Refinery mentioned by the author, is located in the town Ploesti which is not a town in Hungary, but in Romania.

References

Cole, J. D., Dougherty, C. B., and Huth, H. J., 1953, ASME JOURNAL OF APPLIED MECHANICS, Vol. 20, pp. 519–522.

Craggs, J. W., 1954, "Wave Motion in Plastic-Elastic Strings," *J. Mech. Phys. Solids,* Vol. 2, pp. 286–295.

Cristescu, N., 1951, "Discontinuities in the motion of perfectly flexible elastic strings," *Com. Acad. R.P.R.,* Vol. 1, pp. 439–445 (in Romanian).

Cristescu, N., 1954, "About the Loading and Unloading Waves which Can Appear in the Motion of elastic or plastic flexible strings," *Prikl. Mat. Mekh.,* Vol. 18, pp. 257–264 (in Russian).

Cristescu, N., 1960a, "European Contributions to Dynamic Loading and Plastic Waves," *Proc. Second Symp. On Naval Structural Mechanics—Plasticity,* Brown University, Pergamon Press, New York, pp. 385–442.

Cristescu, N., 1960b, "Elastic-Plastic Waves in Strings," *Arch. Mech. Stos.,* Vol. 12, pp. 597–615.

Cristescu, N., 1963, "Loading waves in transverse motion of extensible strings," *Arch. Mech. Stos.,* Vol. 15, pp. 47–61.

Cristescu, N., 1964, "Impact with variable velocity of a finite string," *Inj. Journal,* Vol. 4, pp. 140–147 (in Russian).

Cristescu, N., 1965a, "The braking of high speed moving bodies by extensible strings," *Proc. Of the Fourth Intern. Congr. On Rheology,* Part 3, Brown University 1963, John Wiley and Sons, New York, pp. 59–78.

Cristescu, N., 1965b, "Le mouvement de deux corps liés par un câble elastique," *Journal de Mécanique,* Vol. 4, pp. 151–160.

Cristescu, N., 1965c, "Loading/unloading criteria for rate sensitive materials," *Arch. Mech. Stos.,* Vol. 17, pp. 291–305.

Cristescu, N., Dinca, G., and Suliciu, I., 1966, "On the propagation of shock waves in extensible strings," *Analele Univ. Bucuresti, Seria Stiint. Naturii,* Vol. 15, pp. 65–73.

Cristescu, N., 1967, *Dynamic Plasticity,* John Wiley and Sons, New York.

Dinca, G., 1967, *Studii Cercetari Matematice,* Vol. 19, pp. 659–680.

Fenstermaker, C. A., and Smith, J. C., 1965, *Appl. Polymer Symposia,* Vol. 1, pp. 125–146.

Jameson, J. W., Stewart, G. M., Petterson, D. R., and Odell, F. A., 1962, *Textile Res. J.,* Vol. 32, pp. 858–860.

Manacorda, T., 1958, *Riv. Mat. Univ. Parma,* Vol. 9, pp. 13–19.

Moisil, Gr. C., 1956, "Shock waves in a cable," *The 9th Intern Congr. Appl. Mech.,* Bruxelles.

Pavlenko, A. L., 1959, "On the Propagation of Perturbations in a Flexible String," *Izv. Akad. Nauk, SSSR, Otd. Tekh. Nauk, Mekh. I Mash.,* No. 4, pp. 112–122 (in Russian).

Pérès, J., 1953, *Mécanique générale,* Masson, Paris.

Petterson, D. R., and Stewart, G. M., 1960, *Textile Res. J.,* Vol. 30, pp. 422–431.

Petterson, D. R., Stewart, G. M., Odell, F. A., and Maheux, R. C., 1960, *Textile Res. J.,* Vol. 30, pp. 411–421.

Rakhmatulin, H. A., 1945, "Oblique Shock with a Great Velocity on a Flexible String in Presence of Friction," *Prikl. Mat. Mekh.,* Vol. 9, pp. 449–462 (in Russian).

Rakhmatulin, H. A., 1947, "On the Shock of a Flexible String," *Prikl. Mat. Mekh,* Vol. 11, pp. 379–382 (in Russian).

Rakhmatulin, H. A., 1951, "Transverse Shock with Variable Velocity on a Flexible String," *Uch. Zap. Moskovsk gos. Univ.,* Vol. 4, p. 154 (in Russian).

Rakhmatulin, H. A., 1952, "Transverse Shock of a Flexible String by a Body of a Given Shape," *Prikl. Mat. Mekh.,* Vol. 16, pp. 23–34 (in Russian).

Rakhmatulin, H. A., and Shapiro, G. S. 1955, "The Propagation of Perturbations in Nonlinear Elastic and Non-elastic Media," *Izv. Akad. Nauk SSSR, Otd. Tekh. Nauk,* No. 2, pp. 68–89 (in Russian).

Rakhmatulin, H. A., and Demianov, Yu. A., 1961, *Strength under intensive momentary loads,* Moscow (in Russian).

Ringleb, F. O., 1957, ASME JOURNAL OF APPLIED MECHANICS, Vol. 24, pp. 417–425.

Ryabova, E. B., 1953, "Transverse Shock with Variable Velocity on a Flexible String," *Vestnik Moskovsk. Univ.,* No. 10, pp. 85–91 (in Russian).

Ryabova, E. B., 1956, "The Problems of the Shock of a Wedge by a String," *Vestnik Moskovsk. Univ.,* No. 1, pp. 57–62 (in Russian).

Smith, J. C., McCrackin, F. L., Schiefer, H. F., Stone, W. K., and Towne, K. M., 1956, *J. Res. Nat. Bur. Std,* Vol. 57, pp. 83–89.

Smith, J. C., McCrackin, F. L., and Schiefer, H. F., 1958, *J. Res. Nat. Bur. Std.,* Vol. 60, pp. 517–534.

Smith, J. C., Blandford, J. M., and Schiefer, H. F., 1960, *Textile Res. J.,* Vol. 30, pp. 752–760.

Smith, J. C., Shouse, P. J., Blandford, J. M., and Towne, K. M., 1961, *Textile Res. J.* Vol. 30, pp. 721–734.

Smith, J. C., Fenstermaker, C. A., and Shouse, P. J., 1962a, "Behaviour of filamentous materials subjected to high-speed tensile impact," *Proc. Symp. On Dynamic behaviour of materials* (Special Techn. Publ., No. 336), pp. 47–69.

Smith, J. C., Blandford, J. M., Shouse, P. J., and Towne, K. M., 1962b, *Textile Res. J.* Vol. 32, pp. 472–480.

Smith, J. C., Blandford, J. M., Shouse, P. J., and Towne, K. M., 1962c, *Textile Res. J.* Vol. 32, pp. 67–76.

Smith, J. C., Fenstermaker, C. A., and Shouse, P. J., 1963, *Textile Res. J.,* Vol. 33, pp. 919–934.

Smith, J. C., Fenstermaker, C. A., and Shouse, P. J., 1964, *J. Res. Nat. Bur. Std.,* Vol. 68, pp. 177–181.

Smith, J. C., Fenstermaker, C. A., and Shouse, P. J., 1965, *Textile Res. J.,* Vol. 35, p. 743.

Author's Closure[3]

In addition to thanking Professor Cristescu for his detailed early history of nonlinear string dynamics, the author would like to make a few comments regarding the role of the discussed paper. There were two purposes as stated in the Introduction. One was to describe an historically significant solution to the barrage balloon problem by George Housner, which may have been the first generalization of linear string theory to account for transverse waves of nonsmall slope. Housner's work in 1943 predates the references listed by Cristescu, including the one in 1945 by Rakhmatulin and the one from 1957 by Ringleb (which refers to and extends a 1948 then-classified Navy report by the same author) which dealt with the same mathematical problem. The application of Ringleb's work was to cables used as breaking devices for aircraft landing on ships.

The other purpose of the paper was to present some analytical solutions for the dynamics of strings of nonsmall slope which describe specific situations encountered in finite strings, such as reflections of transverse waves at a support and interaction between longitudinal and transverse waves. These solutions, which are limited to small strains, are used to investigate the limits of geometrically linear theory,[4] to gain insight into the wave mechanics,[5] and to extend Housner's analysis of the barrage balloon problem. In addition, the standard mass-spring model used in the paper to generate numerical solutions is a convenient alternative to the method of integrating along characteristic lines mentioned by Cristescu. The mass-spring technique can also easily accommodate the various generalizations described by Cristescu such as finite strains, plasticity, and interaction with bodies of finite mass.

[3] J. F. Hall, Professor, Department of Civil Engineering, Division of Engineering and Applied Science, California Institute of Science, Mail Code 104-44, Pasadena, CA 91125.

[4] An example result from the paper shows that a transverse wave with a slope angle of only six degrees which is travelling in a string with a longitudinal strain of 0.01 percent doubles this strain upon reflection at a fixed support. Linear theory predicts no change in the tension.

[5] For example, the paper shows how a longitudinal wave which meets a travelling kink (a wavefront for a transverse wave) undergoes partial reflection and transmission and also divides the kink into two kinks which then move apart.

$$c_I^2 = \frac{T}{\varrho(1+\epsilon)} \quad \text{and} \quad c_{II}^2 = \frac{1}{\varrho}\frac{[T]}{[\epsilon]} \qquad (3)$$

where the brackets stand for "jump." Formula $(3)_1$ was obtained for elastic strings by Cristescu (1951; see also Cristescu, 1967) and by Pérès (1953) for general extensible strings. The cases when shock wave coincides or not with smooth waves was also discussed. The propagation of transverse shock waves in inextensible strings was studied using functional analysis by Moisil (1956).

All the above-mentioned results, as well as many other ones, are presented in Chapter 4 (pp. 181–291) of the book by Cristescu (1967). Thus, problems of the kind considered by the author, as well as much more general ones, concerning the mechanics of extensible strings (with nonlinear tension-strain relationship, finite strains, and arbitrary transverse motion), have been considered for a long time.

A "geographical" erratum: the Ploesti Oil Refinery mentioned by the author, is located in the town Ploesti which is not a town in Hungary, but in Romania.

References

Cole, J. D., Dougherty, C. B., and Huth, H. J., 1953, ASME Journal of Applied Mechanics, Vol. 20, pp. 519–522.

Craggs, J. W., 1954, "Wave Motion in Plastic-Elastic Strings," *J. Mech. Phys. Solids,* Vol. 2, pp. 286–295.

Cristescu, N., 1951, "Discontinuities in the motion of perfectly flexible elastic strings," *Com. Acad. R.P.R.,* Vol. 1, pp. 439–445 (in Romanian).

Cristescu, N., 1954, "About the Loading and Unloading Waves which Can Appear in the Motion of elastic or plastic flexible strings," *Prikl. Mat. Mekh.,* Vol. 18, pp. 257–264 (in Russian).

Cristescu, N., 1960a, "European Contributions to Dynamic Loading and Plastic Waves," *Proc. Second Symp. On Naval Structural Mechanics—Plasticity,* Brown University, Pergamon Press, New York, pp. 385–442.

Cristescu, N., 1960b, "Elastic-Plastic Waves in Strings," *Arch. Mech. Stos.,* Vol. 12, pp. 597–615.

Cristescu, N., 1963, "Loading waves in transverse motion of extensible strings," *Arch. Mech. Stos.,* Vol. 15, pp. 47–61.

Cristescu, N., 1964, "Impact with variable velocity of a finite string," *Inj. Journal,* Vol. 4, pp. 140–147 (in Russian).

Cristescu, N., 1965a, "The braking of high speed moving bodies by extensible strings," *Proc. Of the Fourth Intern. Congr. On Rheology,* Part 3, Brown University 1963, John Wiley and Sons, New York, pp. 59–78.

Cristescu, N., 1965b, "Le mouvement de deux corps liés par un câble elastique," *Journal de Mécanique,* Vol. 4, pp. 151–160.

Cristescu, N., 1965c, "Loading/unloading criteria for rate sensitive materials," *Arch. Mech. Stos.,* Vol. 17, pp. 291–305.

Cristescu, N., Dinca, G., and Suliciu, I., 1966, "On the propagation of shock waves in extensible strings," *Analele Univ. Bucuresti, Seria Stiint. Naturii,* Vol. 15, pp. 65–73.

Cristescu, N., 1967, *Dynamic Plasticity,* John Wiley and Sons, New York.

Dinca, G., 1967, *Studii Cercetari Matematice,* Vol. 19, pp. 659–680.

Fenstermaker, C. A., and Smith, J. C., 1965, *Appl. Polymer Symposia,* Vol. 1, pp. 125–146.

Jameson, J. W., Stewart, G. M., Petterson, D. R., and Odell, F. A., 1962, *Textile Res. J.,* Vol. 32, pp. 858–860.

Manacorda, T., 1958, *Riv. Mat. Univ. Parma,* Vol. 9, pp. 13–19.

Moisil, Gr. C., 1956, "Shock waves in a cable," *The 9th Intern Congr. Appl. Mech.,* Bruxelles.

Pavlenko, A. L., 1959, "On the Propagation of Perturbations in a Flexible String," *Izv. Akad. Nauk, SSSR, Otd. Tekh. Nauk, Mekh. I Mash.,* No. 4, pp. 112–122 (in Russian).

Pérès, J., 1953, *Mécanique générale,* Masson, Paris.

Petterson, D. R., and Stewart, G. M., 1960, *Textile Res. J.,* Vol. 30, pp. 422–431.

Petterson, D. R., Stewart, G. M., Odell, F. A., and Maheux, R. C., 1960, *Textile Res. J.,* Vol. 30, pp. 411–421.

Rakhmatulin, H. A., 1945, "Oblique Shock with a Great Velocity on a Flexible String in Presence of Friction," *Prikl. Mat. Mekh.,* Vol. 9, pp. 449–462 (in Russian).

Rakhmatulin, H. A., 1947, "On the Shock of a Flexible String," *Prikl. Mat. Mekh,* Vol. 11, pp. 379–382 (in Russian).

Rakhmatulin, H. A., 1951, "Transverse Shock with Variable Velocity on a Flexible String," *Uch. Zap. Moskovsk gos. Univ.,* Vol. 4, p. 154 (in Russian).

Rakhmatulin, H. A., 1952, "Transverse Shock of a Flexible String by a Body of a Given Shape," *Prikl. Mat. Mekh.,* Vol. 16, pp. 23–34 (in Russian).

Rakhmatulin, H. A., and Shapiro, G. S. 1955, "The Propagation of Perturbations in Nonlinear Elastic and Non-elastic Media," *Izv. Akad. Nauk SSSR, Otd. Tekh. Nauk,* No. 2, pp. 68–89 (in Russian).

Rakhmatulin, H. A., and Demianov, Yu. A., 1961, *Strength under intensive momentary loads,* Moscow (in Russian).

Ringleb, F. O., 1957, ASME Journal of Applied Mechanics, Vol. 24, pp. 417–425.

Ryabova, E. B., 1953, "Transverse Shock with Variable Velocity on a Flexible String," *Vestnik Moskovsk. Univ.,* No. 10, pp. 85–91 (in Russian).

Ryabova, E. B., 1956, "The Problems of the Shock of a Wedge by a String," *Vestnik Moskovsk. Univ.,* No. 1, pp. 57–62 (in Russian).

Smith, J. C., McCrackin, F. L., Schiefer, H. F., Stone, W. K., and Towne, K. M., 1956, *J. Res. Nat. Bur. Std,* Vol. 57, pp. 83–89.

Smith, J. C., McCrackin, F. L., and Schiefer, H. F., 1958, *J. Res. Nat. Bur. Std.,* Vol. 60, pp. 517–534.

Smith, J. C., Blandford, J. M., and Schiefer, H. F., 1960, *Textile Res. J.,* Vol. 30, pp. 752–760.

Smith, J. C., Shouse, P. J., Blandford, J. M., and Towne, K. M., 1961, *Textile Res. J.* Vol. 30, pp. 721–734.

Smith, J. C., Fenstermaker, C. A., and Shouse, P. J., 1962a, "Behaviour of filamentous materials subjected to high-speed tensile impact," *Proc. Symp. On Dynamic behaviour of materials* (Special Techn. Publ., No. 336), pp. 47–69.

Smith, J. C., Blandford, J. M., Shouse, P. J., and Towne, K. M., 1962b, *Textile Res. J.* Vol. 32, pp. 472–480.

Smith, J. C., Blandford, J. M., Shouse, P. J., and Towne, K. M., 1962c, *Textile Res. J.* Vol. 32, pp. 67–76.

Smith, J. C., Fenstermaker, C. A., and Shouse, P. J., 1963, *Textile Res. J.,* Vol. 33, pp. 919–934.

Smith, J. C., Fenstermaker, C. A., and Shouse, P. J., 1964, *J. Res. Nat. Bur. Std.,* Vol. 68, pp. 177–181.

Smith, J. C., Fenstermaker, C. A., and Shouse, P. J., 1965, *Textile Res. J.,* Vol. 35, p. 743.

Author's Closure[3]

In addition to thanking Professor Cristescu for his detailed early history of nonlinear string dynamics, the author would like to make a few comments regarding the role of the discussed paper. There were two purposes as stated in the Introduction. One was to describe an historically significant solution to the barrage balloon problem by George Housner, which may have been the first generalization of linear string theory to account for transverse waves of nonsmall slope. Housner's work in 1943 predates the references listed by Cristescu, including the one in 1945 by Rakhmatulin and the one from 1957 by Ringleb (which refers to and extends a 1948 then-classified Navy report by the same author) which dealt with the same mathematical problem. The application of Ringleb's work was to cables used as breaking devices for aircraft landing on ships.

The other purpose of the paper was to present some analytical solutions for the dynamics of strings of nonsmall slope which describe specific situations encountered in finite strings, such as reflections of transverse waves at a support and interaction between longitudinal and transverse waves. These solutions, which are limited to small strains, are used to investigate the limits of geometrically linear theory,[4] to gain insight into the wave mechanics,[5] and to extend Housner's analysis of the barrage balloon problem. In addition, the standard mass-spring model used in the paper to generate numerical solutions is a convenient alternative to the method of integrating along characteristic lines mentioned by Cristescu. The mass-spring technique can also easily accommodate the various generalizations described by Cristescu such as finite strains, plasticity, and interaction with bodies of finite mass.

[3] J. F. Hall, Professor, Department of Civil Engineering, Division of Engineering and Applied Science, California Institute of Science, Mail Code 104-44, Pasadena, CA 91125.

[4] An example result from the paper shows that a transverse wave with a slope angle of only six degrees which is travelling in a string with a longitudinal strain of 0.01 percent doubles this strain upon reflection at a fixed support. Linear theory predicts no change in the tension.

[5] For example, the paper shows how a longitudinal wave which meets a travelling kink (a wavefront for a transverse wave) undergoes partial reflection and transmission and also divides the kink into two kinks which then move apart.